

UC Davis

UC Davis Electronic Theses and Dissertations

Title

Breakdown of Solid Foods During in Vitro Gastric Digestion

Permalink

<https://escholarship.org/uc/item/1gq6g218>

Author

Swackhamer, Clay

Publication Date

2022

Peer reviewed|Thesis/dissertation

Breakdown of Solid Foods During in Vitro Gastric Digestion

By

CLAY SWACKHAMER
DISSERTATION

Submitted in partial satisfaction of the requirements for the degree of

DOCTOR OF PHILOSOPHY

in

Biological Systems Engineering

in the

OFFICE OF GRADUATE STUDIES

of the

UNIVERSITY OF CALIFORNIA

DAVIS

Approved:

Gail M. Bornhorst, Chair

R. Paul Singh

Ameer Taha

Committee in Charge

2022

Abstract

Food breakdown during gastric digestion influences gastric emptying, satiety, and nutrient bioaccessibility. However, the engineering design of foods for targeted breakdown has remained a challenge. This is in part due to a lack of data on the breakdown of solid foods during gastric digestion, particularly regarding the influence of simulated peristalsis on the breakdown of solid food particles. In addition, there is a need for standardized model, solid foods for studying food breakdown which could be used to establish a more in-depth understanding of the physical property changes experienced by solid food matrices during in vitro gastric digestion. Such knowledge on the physical property changes of solid foods during in vitro gastric digestion could help to identify the influence of food properties on the mechanisms of particle breakdown during in vitro gastric digestion that includes simulated peristalsis. However, currently available systems for studying food breakdown in the presence of simulated peristalsis include the potential for interactions between food particles as well as for food breakdown due to the direct effect of the simulated peristaltic wave. Thus, there is a need for a new in vitro digestion system that can apply simulated peristaltic waves to single particles of solid food. In this study, progress toward addressing these gaps in the literature was made by assessing the breakdown of almond particles during in vitro digestion both in the presence and in the absence of simulated peristalsis, developing and characterizing standardized, model solid foods with varying breakdown rates during in vitro gastric digestion, and developing a new peristaltic simulator for digestion studies.

First, in vitro digestion of almond particles was conducted using a dynamic model (Human Gastric Simulator) and a static model (shaking water bath). This experiment was carried out to gather data on the breakdown of a solid food product during gastric digestion, and to determine whether the observed breakdown could be attributed to the peristaltic motion of the simulated stomach. Results showed that structural breakdown of particles occurred only in the Human Gastric Simulator, as evidenced by a reduction in particle size during the gastric phase of digestion ($15.89 \pm 0.68 \text{ mm}^2$ to $12.19 \pm 1.29 \text{ mm}^2$, $p < 0.05$). Fatty acid bioaccessibility at the end of the gastric phase was greater in the Human Gastric

Simulator than in the shaking water bath ($6.55 \pm 0.85\%$ vs. $4.54 \pm 0.36\%$, $p < 0.01$). Results indicated that the in vitro model of digestion incorporating simulated peristaltic contractions (Human Gastric Simulator) led to breakdown of almond particles during gastric digestion which increased fatty acid bioaccessibility. These results underscore the importance of simulated peristaltic contractions towards achieving realistic breakdown of solid food particles during in vitro digestion. However, due to the inhomogeneous microstructure and particle size distribution of almond particles, it was not possible to determine changes in mechanical properties of almond particles over time during digestion. This pointed to the need for standardized, model foods whose physical properties could be quantified over time during digestion and then related to particle breakdown during digestion experiments that include simulated peristalsis.

To meet this research need, standardized, model solid foods were developed based on the macronutrient composition of the Standard American Diet. The model foods were based on hydrogels, which allowed for controllable particle shapes and sizes to be prepared, allowing for assessment of their physical properties using texture analysis, rheology, and fracture property testing. A strong gel version and a weak gel version were created by modulating the pH at which the model foods were produced. Another class of model foods was developed using whey protein hydrogels to serve as a simpler model system. A strong gel and weak gel version of the whey protein model foods were produced by addition of pectin. The whey protein weak gel had the lowest initial hardness of the model foods (6.2 ± 1.0 N) which was significantly ($p < 0.05$) lower than that of the whey protein strong gel (56.2 ± 5.7 N), which had the highest hardness of the four model foods. The breakdown of model foods was assessed during in vitro gastric digestion using texture analysis, dry solids retention ratio analysis, and modeling of moisture diffusion into the model food matrix. The standard diet weak gel had the fastest softening half-time of the model foods (58 ± 5 min), which was significantly ($p < 0.05$) lower than that of the whey protein strong gel (775 ± 82 min) which had the longest softening half-time of the model foods.

Fracture properties of the model foods were assessed using wire cutting and knife cutting. Toughness, yield stress, and stiffness were significantly influenced by digestion time ($p < 0.01$). Rheological

properties of model foods were assessed using parallel plate oscillatory rheology, and it was found that the storage modulus (G'), loss modulus (G''), and $\tan \delta$ were significantly influenced by digestion time ($p < 0.01$).

One unexpected finding from the study of fracture properties was that the apparent toughness of the whey protein strong gel increased during the first three hours of in vitro gastric digestion but decreased after 24 hours of in vitro gastric digestion. The initial increase in toughness of this model food was attributed to a loss of brittleness due to moisture uptake, with the eventual decrease in apparent toughness due to the weakening of the food matrix by acid and enzymatic hydrolysis. This suggests that competing mechanisms operating on different time scales can lead to non-monotonic changes in food fracture properties during digestion, specifically, rapid moisture uptake can lead to increased toughness, whereas slower matrix hydrolysis eventually leads to decreased toughness. Taken together, these findings show that physical property changes in soft solid foods during in vitro gastric digestion are complex.

After characterizing the changes in textural, fracture, and rheological properties of the model foods over time during in vitro gastric digestion, it was desired to relate these properties to the breakdown mechanisms experienced by the model foods during in vitro gastric digestion that included simulated peristalsis. However, existing dynamic digestion systems apply simulated peristaltic contractions to numerous food particles simultaneously, meaning that particle/particle grinding could contribute to food breakdown in addition to the direct effect of the peristaltic wave. To address the need for a system that can apply simulated peristaltic contractions to food particles one at a time, a novel peristaltic simulator was designed and constructed. The new peristaltic simulator can apply simulated peristaltic contractions one at a time to a single food particle, and also allows for up to 12 digestion modules to be used simultaneously. This >10-fold improvement in throughput relative to previous state-of-the-art systems could allow for fast screening of food materials for health-promoting properties. The novel simulator was characterized using quantitative video analysis and computational fluid dynamics (CFD) simulations, the results of which were compared to physiological data on the motility of the human stomach and intestine.

This new digestion simulator could help future researchers identify the mechanisms leading to food breakdown by studying the effect of digesta rheology or peristaltic wave dynamics on food breakdown. One important characteristic of the novel peristaltic simulator is that it permits simulated peristaltic contractions of adjustable occlusion to be applied one at a time to individual food particles allowing their breakdown to be studied in more detail.

The model foods developed with varying breakdown rates during static in vitro digestion were then subjected to static in vitro digestion for varying lengths of time followed by digestion using either the Human Gastric Simulator (HGS) or the novel peristaltic simulator, systems which include simulated peristalsis. The HGS was used to study the breakdown of particles of model, solid foods under physiologically representative conditions which included the potential for breakdown due to the direct effect of the simulated peristaltic wave as well as due to particle/particle grinding. The novel peristaltic simulator was used to isolate the effect of the simulated peristaltic wave without the potential for breakdown due to particle/particle grinding. Results showed that the number and sizes of particles were significantly ($p < 0.05$) influenced by the type of model food and in vitro digestion time. Results from this study were used to establish the hypothesized breakdown mechanisms for the standardized, model, solid foods during in vitro digestion that includes simulated peristalsis. Specifically, the standard diet strong gel broke down by erosion as well as chipping, whereas the standard diet weak gel broke down by erosion, chipping, and fragmentation. The whey protein strong gel broke down by erosion with only minor breakdown overall, while the whey protein weak gel broke down by erosion, chipping, and fragmentation. Experiments using the peristaltic simulator suggested that the mechanisms of particle breakdown of the model, solid foods were influenced by the number of simulated peristaltic contractions that were applied to the particle. For example, the standard diet strong gel broke down by erosion and chipping until ca. 30 simulated peristaltic contractions had been applied, after which the breakdown could be ascribed to erosion, chipping, and fragmentation. These results demonstrated that the mechanisms which lead to particle breakdown during in vitro digestion that includes simulated peristalsis may be dynamic in time,

so that foods which initially break down only by erosion or erosion and chipping may be weakened by the progressive application of contractions, leading to breakdown at later times due to erosion, chipping, and fragmentation. Overall, the model foods, which were shown to fall into distinct classes in the Food Breakdown Classification System (FBCS), experienced differing hypothesized breakdown mechanisms which were related to their initial properties and kinetics of texture change. It was determined that that food particles with hardness < 6 N may break down by erosion, chipping, and fragmentation at the onset of simulated peristalsis but particles with hardness > 9 N may break down initially by erosion but transition to breakdown by erosion and chipping at later digestion times as the particle softens due to contact with simulated gastric fluid.

Collectively, the data gathered in these studies show that particle breakdown of solid foods during in vitro gastric digestion was driven by simulated peristaltic contractions, that the physical properties of solid foods influenced their breakdown rates during in vitro digestion, and that the progressive application of simulated peristaltic contractions can lead to transitions in the breakdown mechanisms of solid food particles. These findings could help future researchers develop foods with targeted rates of particle breakdown during gastric digestion, a potential means to modulate gastric emptying rates in vivo. The system of standardized model, solid foods and novel peristaltic simulator could serve as tools to help future researchers develop foods with targeted breakdown rates for controlled bioaccessibility or satiety, for example, by linking the initial values of food physical properties and their changes during in vitro gastric digestion to their expected mechanisms of breakdown during gastric digestion.

Acknowledgements

I would like to thank my major professor, Dr. Gail M. Bornhorst for her guidance, technical expertise, energy, mentorship, and support. In the spring of 2016, she called me on the phone when I was considering coming to Davis for graduate school and it was apparent that she was passionate about this research topic. I think back to this conversation sometimes. I picture myself asking questions which may have been ridiculous, and Dr. Bornhorst answering every one of them graciously and with enthusiasm.

I think the Food Breakdown Classification system will come to be widely used and may even revolutionize the field of Food Engineering. If so, it is due to Gail's research program. I thank her for letting me have the keys to this car for a few years, during which time I hope I have navigated to somewhere interesting and not scuffed up the paint too much.

Many thanks are owed to my committee members, Dr. R. Paul Singh, Dr. Ameer Taha, and Dr. Gail Bornhorst who have all guided me and shaped the way I think about this research project.

I am grateful for Dr. Jennifer Mullin who hired me as a teaching assistant nine separate times for the course Engineering 003: Engineering Design. I learned a lot of technical and professional skills through this experience, where Dr. Mullin teaches the teaching assistants and the undergraduates simultaneously, an impressive feat.

I am grateful for my lab mates: Dr. Yamile Mennah-Govela, Dr. Alex Olenskyj, Dr. Joanna Nadia, Dr. Silvia Keppler, Berta Lascuevas, Weiyi Sun, Karen Villa, and Ian Martin. I am also grateful for the undergraduates that have worked with me: Xiaohan Cao, Zhe Fu, and Raymond Doan. Each of you has helped me grow as an engineer and as a person. I am grateful for Dr. Zhichao Zhang, Dr. Ameer Taha, Dr. Bruce Hamaker, Dr. Mario Martinez, Yixing Lu, Adam Poltorak, Kyle Cheung, Nashea Awais, and all our lab's collaborators who have broadened my horizons. Thanks are owed to Dr. Ryan Kawakita, P.E. He was my roommate for three years. He coached me to masters in Teamfight Tactics and convinced me to take the professional engineering exam, two of my proudest accomplishments.

I would like to say thank you to everyone in the Biological and Agricultural Engineering Department at UC Davis. Thank you to Dr. Fadi Fathallah and Dr. Bryan Jenkins who led the department. Thanks to the graduate students in the department. I would like to thank all the professors who taught classes that were formative for me, especially Dr. Tina Jeoh, Dr. Shrinivasa Upadhyaya, Dr. David Slaughter, Dr. Ameer Taha, and Dr. Gail Bornhorst. I strive to emulate these people in the way I conduct myself as an engineer and carry out research tasks. Thank you.

I want to thank my parents Emelie and Scott Swackhamer. Thank you for making sacrifices so I could pursue research far away from home. Thank you for the patience to read me books when I was a kid. Thank you for always supporting me and being a great example. Thanks to my brother Cole for also being a great example and sharing my sense of humor. Thanks to my grandparents: Robert Seip, Cynthia Seip, Dr. Gene Swackhamer, and Sharon Swackhamer.

Thank you, Dr. Anna Hayes. I cannot express how much you have helped me and how fortunate I am to have your support and companionship. You make me excited for the future.

Table of Contents

Chapter 1	Introduction.....	1
1.1	Background.....	1
1.2	Research Objectives.....	4
Chapter 2	Review of Literature Part I: Food digestion and the importance of food properties on the breakdown of foods in the gastric environment.....	7
2.1	Food digestion.....	7
2.1.1	Food digestion in context of global challenges.....	7
2.1.2	Oral digestion.....	9
2.1.3	Esophageal transit.....	10
2.1.4	Gastric digestion.....	10
2.1.5	Small intestinal digestion.....	13
2.1.6	Large intestinal digestion.....	15
2.1.7	Engineering operations that parallel the food digestion process.....	16
2.2	Food breakdown during gastric digestion.....	18
2.2.1	Importance of food breakdown during gastric digestion.....	18
2.2.2	Gastric motility in relation to food breakdown during gastric digestion.....	19
2.2.3	Enzymes relevant to gastric digestion.....	21
2.3	In vitro gastric digestion: Experimental methods and applications.....	22
2.3.1	Models of gastric digestion.....	23
2.3.2	Conditions used in static and dynamic models of gastric digestion.....	24
2.3.3	Use of model foods for in vitro digestion.....	28
2.4	Food physical properties and their influence on food breakdown.....	29
2.4.1	Texture change of foods during gastric digestion.....	31
2.4.2	The Food Breakdown Classification System.....	31
2.5	Summary.....	32
Chapter 3	Review of Literature Part II: Fracture properties of foods: Experimental considerations and applications to mastication.....	34
3.1	Introduction.....	36
3.2	Fracture properties of foods.....	36

3.2.1	Steps in the fracture process.....	37
3.2.2	Energy approach to fracture.....	37
3.2.3	Criteria for fracture	39
3.2.4	Modes of fracture	41
3.3	Fracture indices for mastication.....	42
3.3.1	Displacement-limited index	43
3.3.2	Stress-limited index.....	45
3.3.3	Applications of displacement and stress-limited indices	46
3.4	Variables affecting food fracture during mastication.....	50
3.4.1	Variations in strain rates applied to foods by teeth	51
3.4.2	Multiple cycles of deformation	52
3.4.3	Saliva.....	52
3.4.4	Temperature	53
3.4.5	Fracture on multiple length scales.....	54
3.4.6	Fracture on multiple time scales	55
3.5	Experimental methods to measure fracture properties of foods relevant to mastication	56
3.5.1	Uniaxial compression test	56
3.5.2	Puncture test.....	58
3.5.3	Wedge test.....	59
3.5.4	Cutting test	61
3.5.5	Three-point bend test	62
3.5.6	Tensile test	64
3.5.7	Statistical approaches.....	64
3.6	Conclusion	70
Chapter 4 Fatty acid bioaccessibility and structural breakdown from in vitro digestion of almond particles 72		
4.1	Introduction.....	74
4.2	Materials and methods	76
4.2.1	Raw materials.....	76
4.2.2	Digestive juice formulation.....	76
4.2.3	Shaking water bath model.....	77
4.3	Human Gastric Simulator model using simulated digestive juices.....	78
4.4	Analysis of liquid phase.....	79
4.4.1	Fatty acid extraction and preparation.....	80
4.4.2	GC–FID analysis of fatty acids.....	81

4.5	Analysis of solid phase	82
4.5.1	Particle size analysis	82
4.5.2	Scanning electron microscopy	83
4.5.3	Almond composition.....	83
4.6	Statistical analysis.....	84
4.7	Results.....	84
4.7.1	Fatty acid bioaccessibility	84
4.7.2	Particle breakdown.....	87
4.7.3	°Brix of liquid phase and moisture content of solid phase.....	89
4.7.4	Scanning Electron Microscopy Images.....	90
4.8	Discussion	95
4.9	Limitations.....	101
4.10	Conclusions.....	102
Chapter 5 Development and characterization of standardized model, solid foods with varying		
breakdown rates during gastric digestion..... 103		
5.1	Introduction.....	105
5.2	Materials and Methods.....	107
5.2.1	Materials	107
5.2.2	Preparation of model foods	107
5.2.3	Simulated saliva and gastric juice formulation	111
5.2.4	In vitro digestion protocol.....	113
5.2.5	Moisture content analysis.....	114
5.2.6	Diffusion modeling	114
5.2.7	Texture analysis of model foods	115
5.2.8	Dry solids retention ratio analysis.....	116
5.2.9	Weibull analysis.....	116
5.2.10	Soluble solids analysis	117
5.2.11	Statistical analysis	117
5.3	Results.....	118
5.3.1	Texture and fracture properties of model foods.....	118
5.3.2	Dry solids retention ratio and soluble solids	132
5.3.3	Moisture uptake and diffusion modeling	133
5.3.4	Regression analysis.....	137
5.4	Discussion	139

5.4.1	Design of standard, model foods with varying breakdown properties.....	139
5.4.2	Physical property changes of model foods during in vitro digestion.....	143
5.4.3	Weibull analysis of softening using force at varying values of strain	147
5.4.4	Classification of the standardized, model solid foods using the FBCS	148
5.5	Limitations	151
5.6	Conclusions.....	152
Chapter 6	Video Analysis and Fluid Dynamic Modeling of a Novel Multi-Module Peristaltic Simulator for Gastrointestinal Research	153
6.1	Introduction.....	154
6.2	Materials and Methods.....	157
6.2.1	Design and construction of the peristaltic simulator.....	157
6.2.2	Characterization of the simulator	162
6.2.3	Statistical analysis	171
6.3	Results and discussion	171
6.3.1	Rheology of simulated digestion fluids.....	171
6.3.2	Characterization of the peristaltic simulator	172
6.4	Limitations	192
6.5	Conclusions.....	193
Chapter 7	Fracture and rheological properties of standardized, model solid foods influence their physical breakdown mechanisms during in vitro gastric digestion with simulated peristalsis	195
7.1	Introduction.....	197
7.2	Materials and Methods.....	201
7.2.1	Materials	201
7.2.2	Overall experimental design	202
7.2.3	Model food preparation.....	202
7.2.4	Rheological analysis of model food dispersions.....	203
7.2.5	Confocal laser scanning microscopy (CLSM)	204
7.2.6	Static in vitro gastric digestion.....	204
7.2.7	Fracture property analysis.....	207
7.2.8	Rheological property analysis.....	210
7.2.9	Assessment of mechanical breakdown in the Human Gastric Simulator (HGS).....	211
7.2.10	Assessment of free amino group concentration	214
7.2.11	Assessment of mechanical breakdown in the peristaltic simulator.....	215

7.2.12	Statistical analysis	218
7.3	Results	220
7.3.1	Microstructure of the model foods	220
7.3.2	Changes in fracture properties of model foods during static in vitro gastric digestion.....	223
7.3.3	Changes in rheological properties of model foods during in vitro digestion	229
7.3.4	Breakdown of model foods in the HGS	234
7.3.5	Free amino group concentration	245
7.3.6	Breakdown of model foods in the peristaltic simulator	247
7.4	Discussion	261
7.4.1	Fracture and rheological properties of model foods and relation to their microstructure.	261
7.4.2	Changes in fracture and rheological properties of model foods during in vitro digestion	265
7.4.3	Hypothesized mechanisms of breakdown of model foods in the HGS.....	270
7.4.4	Hypothesized mechanisms of breakdown of model foods in the peristaltic simulator	277
7.4.5	Implications for the FBCS	281
7.5	Limitations	283
	Conclusions	283
Chapter 8	Overall conclusions.....	286
Chapter 9	Recommendations for future work.....	292
Chapter 10	References.....	295

List of Figures

Figure 2.1. Illustration of the stomach showing selected anatomical features and approximate dimensions. 13

Figure 3.1: Examples of the three modes of fracture (A1, B1,C1), adapted from Berthaume, (2016). For each mode of fracture, examples of mechanical tests that lead to a fracture event in that mode are shown (A2, B2, C2) adapted from Berthaume, (2016). Similarly, loading geometries of teeth and a food particle are shown (A3, B3, C3) that may lead to each of the three modes of fracture. Red circles indicate contact points between teeth and the food particle. Mode I (A3) adapted from Agrawal et al., (1997) and Agrawal and Lucas (2003), mode II (B3) adapted from Xu (2016) and Zink et al., (2014), and mode III (C3) adapted from Wright and Vincent (1996). 42

Figure 3.2: Example loading geometry of a food sample (shown in blue) acting as a beam between cusps (A). Red circles indicate points of applied force, and arrows indicate the direction. The crack length is labeled “a.” For this loading geometry, an example correlation (B) is shown between the change in specific surface area (measured using image analysis) and the displacement limited index. Modified from Agrawal et al., (1997). 44

Figure 3.3: Loading geometry of an incisor driving a crack through a food particle, shown in blue (A). Red circles indicate points of applied force, and arrows indicate the direction. The crack length is labeled “a.” For this loading geometry, an example correlation (B) is shown between the product of fracture stress and crack length, measured during one chew, and the stress limited index $RE_{1/2}$, which was measured for the test foods using instrumental-mechanical methods. Modified from Agrawal and Lucas (2003). 46

Figure 3.4. Scanning electron microscopy images showing fractured microstructure of a cellular expanded rice snack. Fracture lines are visible between air cells (Roopa et al., 2009) (A). Environmental scanning electron microscopy images showing tensile fracture of a structural element (gluten strut) within bread crumb. Black arrows show the direction of applied force (Stokes and Donald, 2000) (B). Comparison of the two images shows that fracture occurs on multiple length scales. 55

Figure 3.5: The wedge test is used to measure toughness using a two-pass approach. The work of fracture is found by subtracting the work on the second pass from the first pass. Adapted from (Lucas et al., 2012) (A). The wire cutting test can be used to find the intrinsic toughness of a food material by repeating the test with wires of varying width, and then extrapolating to a theoretical wire width of zero. Adapted from Kamyab et al., (1998) (B). 62

Figure 3.6: Example Weibull survivability plot, showing how Weibull modulus, m , characterizes the consistency of the material. High values of m indicate that all samples fail within a narrow range of stress. By estimating the stress at which $Pf = 1 - 1/e = 0.63$, the characteristic stress, σ_0 , is determined. Adapted from Burrow et al., (2004). 65

Figure 3.7. Mechanical tests that can be used to measure the fracture properties of foods. Arrows indicate the direction of applied force. Food samples are colored in blue, and selected parts of the test apparatus used to conduct the test are colored grey. Dimensions of the food samples are labeled with lowercase letters and correspond to the variables in the relevant equation for each test (Equations 3.11 to 3.17). 66

Figure 4.1. The gastric phase of digestion was conducted in either the Human Gastric Simulator (HGS) or a shaking water bath. After the gastric phase, the intestinal digestion was always conducted in the shaking water bath. All digestions were conducted at 37 °C. 79

Figure 4.2. Total percent fatty acid bioaccessibility in the Human Gastric Simulator (●), shaking water bath (▲), and shaking water bath with only pH-adjusted water (■) models. All points represent the mean (n = 3) ± standard deviation. 86

Figure 4.3. Change in Rosin–Rammler x50 (Equation 4.1) at each timepoint from x50 of the initial almond particles subjected to in vitro digestion shown for Human Gastric Simulator (●), shaking water bath (▲), and shaking water bath with only pH-adjusted water (■) models. All points represent the mean (n = 3) ± standard deviation. 89

Figure 4.4. SEM images of an almond particle that was either (A) digested in the HGS for 180 min; (B) undigested. Scale bars represent 100 μm. 90

Figure 5.1. Process flow diagram showing steps in the preparation of model foods (A), and diagram showing the in vitro digestion protocol (B). All samples were subjected to in vitro oral digestion (2 min) followed by in vitro gastric digestion, for a maximum total time of 180 min. Samples were taken at 2, 15, 30, 60, 120, and 180 min. Each bottle containing cubes of model food was used for only one timepoint, i.e., no cubes were removed at 30 min from the bottle designated to be the 60 min timepoint. pH was adjusted to 2 ± 0.1 at 5, 30, 60, and 120 min. Note that bars in the diagram (B) are not to scale. 110

Figure 5.2. Images of undigested model foods cut into cubes of the size and shape that were used for in vitro digestion of the standard diet strong gel (A), standard diet weak gel (B), whey protein strong gel (C), and whey protein weak gel (D). 111

Figure 5.3. Example stress vs strain curves for cubes of the standard diet strong gel (A), standard diet weak gel (B), whey protein strong gel (C), whey protein weak gel (D) model foods before in vitro digestion (initial) and after in vitro digestion (180 min), showing the softening that occurred due to in vitro digestion. Note that the whey protein strong gel did not fracture during the compression and is shown with a different y axis range. The slope of the curve in the linear elastic region was used to define the elastic modulus. Photographs of the model foods before and after compression are shown in Figure 5.1 and Figure 5.9, respectively. 125

Figure 5.4. Normalized hardness of the standard diet strong gel (A), standard diet weak gel (B), whey protein strong gel (C), whey protein weak gel (D) model foods over time during in vitro digestion (0-180 min) with fit to the Weibull function (Equation 5.6). Markers represent averages with error bars as the standard deviation (n=3). Lines represent the Weibull model fit with average parameters (Table 2). 126

Figure 5.5. Normalized elastic modulus of the standard diet strong gel (A), standard diet weak gel (B), whey protein strong gel (C), whey protein weak gel (D) model foods over time during in vitro digestion (0-180 min) with fit to the Weibull function (Equation 6). Markers represent averages with error bars as the standard deviation (n=3). Lines represent the Weibull model fit with average parameters. 128

Figure 5.6. Parameters of the Weibull function (Equation 5.6) fit to the force at different values of strain during in vitro digestion. Weibull model parameter k (A) and β (B) are shown for the standard diet strong gel (●), standard diet weak gel (■), whey protein strong gel (★), and whey protein weak gel (▲). Markers

represent averages and error bars represent standard deviation (n=3). The region between 20% and 60% strain is shown between the vertical dashed lines as there were no statistically significant differences in the values of k or β between values of strain on this interval. 130

Figure 5.7. Normalized moisture content of standard diet strong gel (A), standard diet weak gel (B), whey protein strong gel (C), whey protein weak gel (D) model foods over time during in vitro digestion. Points represent the mean with error bars as \pm standard deviation, respectively. Error bars may be too small to see in some cases. Lines represent the diffusion model (Equation 5.1) fit with average parameters (Table 5.10). 135

Figure 5.8. Relationships between hardness, dry solids retention ratio, and normalized moisture content analyzed using linear regression, shown for standard diet strong gel (●), standard diet weak gel (■), whey protein strong gel (★), and whey protein weak gel (▲). There was a statistically significant, direct relationship between hardness and dry solids retention ratio for the standard diet model foods (A1) and for the whey protein model foods (A2). There was a statistically significant, inverse relationship between hardness and normalized moisture content for the standard diet model foods (B1) and for the whey protein model foods (B2). There was a statistically significant, inverse relationship between dry solids retention ratio and normalized moisture content for the standard diet model foods (C1) and for the whey protein model foods (C2). 137

Figure 5.9. Images of model foods after 180 minutes of digestion, as described in Section 2.6 of the standard diet strong gel (A), standard diet weak gel (B), whey protein strong gel (C), and whey protein weak gel (D). 142

Figure 5.10. Images of undigested model foods after compression to 75% strain, as described in Section 2.7 of the standard diet strong gel (A), standard diet weak gel (B), whey protein strong gel (C), and whey protein weak gel (D). The whey protein strong gel (C) did not fracture during the compression, and thus its fracture stress and fracture strain were not presented in Table 2. It should be noted that the whey protein strong gel (C) expressed water during the compression, resulting in the pool of liquid visible in panel C. 143

Figure 6.1. Three-dimensional CAD model of the peristaltic simulator showing a side view of the simulator and the Hoecken linkage (A); side view of the peristaltic simulator and the drive motor, digestion modules, base plate, and pulley/counterweight assembly (B); top view of the simulator (C); isometric view of the simulator with the endoscopic camera used for video analysis of the shape of the digestion modules shown in red (D); schematic view of the Hoecken linkage used to drive the motion of the rollers with individual parts shown in different colors for clarity (E); diagram of the control system (F). 160

Figure 6.2. Depiction of the simulated peristaltic wave applied to digestion modules by the simulator. Rollers approach the undeformed digestion modules (A1, B1), Rollers contact the digestion modules, initiating the simulated peristaltic wave (A2, B2), the simulated peristaltic wave progresses to the middle of the digestion modules (A3, B3), rollers reach the lowest point of the path (A4, B4), and rollers then separate and return to the top position, beginning the next cycle. Images in column A represent CAD views of the simulator, and images in column B represent a simplified view showing the interaction of a single digestion module with the rollers. 162

Figure 6.3. Video analysis of the peristaltic simulator. Original image acquired by the endoscopic video camera (A); Binary image showing the digestion module in white and the background in black (B); Points

defining the edges of the digestion module with the left edge marked by blue circles and the right edge by red circles (C); Edge points after smoothing, showing the direct fit of the three-parameter Gaussian distribution function (Equation 6.2) to points on the left side with the fit represented by a blue line and the fit to points on the right side of the digestion module represented by a red line (D); Gaussian function with averaged parameters used to model the deformation of both the left and right side of the digestion module (E); Curves generated by the process overlaying the original image (F). The distance axes (in mm) are valid in the plane of the digestion module, which was located approximately 20 cm from the aperture of the camera. 165

Figure 6.4. Pressure profiles in the digestion module were recorded using the thick rollers (◆) and thin rollers (●) over two simulated peristaltic waves (A). Calibration of the manometer was carried out to determine the estimated contraction force applied to the digestion module during the simulated peristaltic wave by applying force to the bulb using the texture analyzer and recording the resultant pressure recorded by the manometer (B). Force profiles in the digestion module are shown in panel C. The mean values ± standard deviation from three runs are shown. Error bars are shown on every third point for clarity. 173

Figure 6.5. Percent occlusion of the midpoint of the digestion module during two compression cycles as determined using video analysis for the thick rollers (◆) and thin rollers (●) over two simulated peristaltic waves, showing the mean values ± standard deviation from three runs. Every third point is shown for clarity. 177

Figure 6.6. Predicted velocity field inside of the peristaltic simulator module using either the thin rollers or thick rollers. The module is shown at three different elapsed times after the start of the simulation (2 s, 4 s, and 6 s) in both the xz and yz plane cutting through the center of the module. 180

Figure 6.7. Predicted shear field inside of the peristaltic simulator module using either the thin rollers or thick rollers. The module is shown at three different elapsed times after the start of the simulation (2 s, 4 s, and 6 s) in both the xz and yz plane cutting through the center of the module. 182

Figure 6.8. Predicted vorticity field inside of the peristaltic simulator module using either the thin rollers or thick rollers. The module is shown at three different elapsed times after the start of the simulation (2 s, 4 s, and 6 s) in both the xz and yz plane cutting through the center of the module. 183

Figure 6.9. Predicted pressure field inside of the peristaltic simulator module using either the thin rollers or thick rollers. The module is shown at three different elapsed times after the start of the simulation (2 s, 4 s, and 6 s) in both the xz and yz plane cutting through the center of the module. 185

Figure 6.10. Predicted CFD variables for the module in the peristaltic simulator undergoing deformation by either the thick rollers (◆) and thin rollers (●). Figures shown the volumetric average fluid velocity on the computational domain (A1), the average fluid velocity on the xy plane passing horizontally through the center of the module (A2), the volumetric maximum fluid velocity (global maximum on the computational domain, A3), the volumetric average shear rate (B1), the average shear rate on the xy plane passing horizontally through the center of the module (B2), the volumetric maximum shear rate (B3), the volumetric average vorticity magnitude rate (C1), the average vorticity magnitude on the xy plane passing horizontally through the center of the module (B2), the volumetric maximum vorticity magnitude (B3), the volumetric average fluid pressure (D1), the average fluid pressure on the xy plane passing horizontally through the center of the module (D2), the volumetric maximum fluid pressure (D3). 186

Figure 6.11. Correspondence between the shape of the peristaltic simulator module with either the thin or thick rollers as measured using video analysis with the predicted shape of the module based on the results of the CFD model (A) with a closer view of the occluded region (B)..... 187

Figure 6.12. Preliminary analysis of the shape of an *ex vivo* porcine intestine (A) and comparison to the peristaltic simulator using either thin or thick rollers (B). One individual image of the porcine intestinal tissue used for curve fitting, with points defining the edge of the intestine shown as red circles and the curve fit shown as green lines (A). The shape function of the digestion module in the peristaltic simulator was shown alongside the shape function from the porcine intestine on the entire region of the contraction (B). The red line represents the shape of the peristaltic simulator with thick rollers, the blue line represents the simulator with thin rollers, and the green line represents the average shape function from curve fitting four images of *ex vivo* intestinal tissue (Table 3). For the peristaltic simulator, error bars represent the standard deviation from three independent curve fits (Section 2.2.2), and for the intestinal tissue error bars represent the standard deviation from the curve fits generated using four images that were examined (Table 3). Error bars may be too small to be visible. 189

Figure 7.1. Sample geometries used for static *in vitro* digestion and flowchart showing how samples subjected to static *in vitro* digestion were then analyzed using fracture property testing (A), rheological property testing (B), or were processed and then subjected to subsequent dynamic *in vitro* digestion in the HGS (C), or peristaltic simulator (D). The asterisk (*) in row C, corresponding to experiments carried out in the HGS, indicates when a sample was taken for analysis of protein hydrolysis, as described in Section 7.2.10. 206

Figure 7.2. Texture analyzer attachment used to conduct wire cutting experiments (A). Wire cutting attachment in use with the texture analyzer (B). Typical curve of force versus distance obtained during wire cutting experiments, with labels showing the parameters of Equation 7.3 (C). Example plot showing regression and extrapolation to a theoretical wire width of zero as used to obtain the intrinsic toughness, R , and yield stress, σ_c (D). Parts C and D were adapted from Swackhamer et al (2019)..... 210

Figure 7.3. Overview of the mechanisms of simulated peristalsis applied to cubes of model food in the HGS (A) and peristaltic simulator (B). In the HGS, simulated peristaltic contractions were applied by external rollers that progressed along the side of the stomach liner from an initial contact point (A1) to the middle of the liner (A2) and ultimately releasing at the bottom of the liner (A3) after which they began to cycle back to the start position on a chain drive. Simulated peristaltic contractions in the HGS were applied to ca. 45 cubical particles of model food, leading to the possibility for particle breakdown due to particle-particle grinding as well as by direct contact with the liner as the simulated peristaltic wave advanced. The peristaltic simulator (B) consisted of vertical modules hanging from a top rack with the simulated peristaltic contraction applied by rollers that approached the module at a vertical height where the cube was located on the holding rig (B1) then made contact with the module and applied the simulated peristaltic contraction to the cube (B2) then eventually progressed downwards along the module (B3) returning to the top to apply the next simulated peristaltic wave (approximate path shown with dashed lines)..... 217

Figure 7.4. CLSM images of the model foods. Lower case letters indicate features in the images, with “a” indicating the protein network, “b” indicating the starch network, and “c” indicating the location of soybean oil droplets. showing the whey protein strong gel with the protein network shown in green (A), whey protein weak gel with the protein network shown in green (B), standard diet strong gel with the starch network shown in green (C), standard diet strong gel with the protein network shown in red (D), the composite (overlay) of the standard diet strong gel with the protein network shown in red and the

starch network shown in green (E), standard diet weak gel the starch network shown in green (F), standard diet weak gel with the protein network shown in red (G), the composite of the standard diet weak gel with the protein network shown in red and the starch network shown in green (H), standard diet strong gel with soybean oil droplets shown in blue (I), standard diet strong gel with the protein network shown in red (J), the composite of the standard diet strong gel with the protein network shown in red and soybean oil droplets shown in blue (K), standard diet weak gel with soybean oil droplets shown in blue (L), standard diet weak gel with the protein network shown in red (M), and the composite of the standard diet strong gel with the protein network shown in red and soybean oil droplets shown in blue (N). Scale bars represent 50 μm 222

Figure 7.5. Example force vs distance curves for wire cutting experiments on cubes of the standard diet strong gel (top row), standard diet weak gel (middle row), and whey protein weak gel (bottom row) after 30 or 180 min in vitro gastric digestion. 226

Figure 7.6. Example force vs distance curves for knife cutting experiments on cubes of the whey protein strong gel after 0, 30 or 180 min static in vitro gastric digestion, showing how the initial stiffness of the cubes tended to decrease with digestion time, but the maximum force achieved during the test increased. * indicates the initial fracture point, which occurred when the knife began to penetrate the surface of the model food cube..... 227

Figure 7.7. Results from wire cutting analysis for the standard diet strong gel (A), standard diet weak gel (B), and whey protein weak gel (C). Points represent the mean with error bars as the standard deviation ($n=3$). Lines represent the linear regression of F_{sce}/w onto wire diameter for each model food at each timepoint, with the R^2 values for the regression shown in the legend. The y-intercept represents the intrinsic toughness of the model food, R (N/m) and the slope represents the yield stress, (σ_y , Pa), which were quantified according to Equation 7.3. 227

Figure 7.8. Frequency sweeps for the standard diet strong gel (A), standard diet weak gel (B), whey protein strong gel (C), and whey protein weak gel (D). Filled symbols \bullet , \blacksquare , and \blacktriangle represent G' values at 0, 30, and 180 min digestion times, respectively. Open symbols \circ , \square , and \triangle represent G'' values at 0, 30, and 180 min digestion times, respectively. All points represent the mean with error bars as the standard deviation ($n=3$). Error bars may be too small to visualize. Lines represent the fit to Equation 7.5 for G' values and Equation 7.6 for G'' values..... 231

Figure 7.9. $\tan \delta$ values from frequency sweeps for the standard diet strong gel (A), standard diet weak gel (B), whey protein strong gel (C), and whey protein weak gel (D). Symbols \bullet , \blacksquare , and \blacktriangle represent $\tan \delta$ values at 0, 30, and 180 min digestion times, respectively. All points represent the mean with error bars as the standard deviation ($n=3$). Error bars may be too small to visualize. 231

Figure 7.10. Flow curves for the dispersion form of the standard diet model foods (A) as well as the whey protein model foods (B). All points represent the mean with error bars as the standard deviation ($n=3$). Error bars may be too small to visualize. Lines represent the fit to the power law model (Equation 7.1). Standard diet model food dispersions (A) were shown with a greater y-axis scale as they were more viscous than the whey protein model food dispersions (B). 233

Figure 7.11. Example photographs showing particles of the standard diet weak gel model food after being subjected to 0 min (A), 30 min (B), or 180 min (C) static in vitro digestion, followed by 90 contractions in the HGS..... 235

Figure 7.12. Cumulative particle area percentage after varying durations of static in vitro gastric digestion (0, 30, and 180 min), followed by application of 90 contractions in the HGS shown for the standard diet strong gel (A), standard diet weak gel (B), whey protein strong gel (C), and whey protein weak gel (D). All points represent the mean with error bars as the standard deviation (n=3). Lines represent the fit to the Mixed Weibull Model (Equation 7.7)..... 238

Figure 7.13. Representative binary images showing particles of model foods after static in vitro digestion followed by 90 contractions in the HGS, showing the standard diet strong gel with 0 min static in vitro digestion (A1), standard diet strong gel with 30 min static in vitro digestion (A2), standard diet strong gel with 180 min static in vitro digestion (A3), standard diet weak gel with 0 min static in vitro digestion (B1), standard diet weak gel with 30 min static in vitro digestion (B2), standard diet weak gel with 180 min static in vitro digestion (B3), whey protein strong gel with 0 min static in vitro digestion (C1), whey protein strong gel with 30 min static in vitro digestion (C2), whey protein strong gel with 180 min static in vitro digestion (C3), whey protein weak gel with 0 min static in vitro digestion (D1), whey protein weak gel with 30 min static in vitro digestion (D2), and the whey protein weak gel with 180 min static in vitro digestion (D3)..... 239

Figure 7.14. Particle size histograms used to classify the particles of model foods that arose from breakdown due to varying durations of static in vitro gastric digestion (0, 30, and 180 min), followed by application of 90 contractions in the HGS shown for the standard diet strong gel (A1-A3), standard diet weak gel (B1-B3), whey protein strong gel (C1-C3), and whey protein weak gel (D1-D3). 244

Figure 7.15. Total $[NH_2]$ as determined using OPA (Section 2.9). Bars within a given in vitro digestion time with different letters were significantly ($p<0.05$) different..... 246

Figure 7.16. Estimated percentage of total particle volume that remained on the holding rig after varying numbers of contractions in the peristaltic simulator (*PVc*) for the standard diet strong gel (A), standard diet weak gel (B), whey protein strong gel (C), and whey protein weak gel (D). All points represent the mean with error bars as the standard deviation (n=3)..... 249

Figure 7.17. Knife cutting was used to estimate the fracture properties of the whey protein strong gel, which was too strong to be cut with wires. Before digestion, the whey protein strong gel had higher stiffness but lower apparent toughness and fracture initiation energy than after 180 min static in vitro digestion (Table 7.1). It was observed that fracture was initiated by the knife blade after a small distance of indentation at the onset of fracture for the undigested samples (A) but after 180 min static in vitro digestion the cube deformed around the advancing knife blade resulting in a greater distance of indentation at the onset of fracture, greater force achieved at fracture, and greater apparent toughness (B). After 24 h digestion the distance of indentation at the onset of fracture was intermediate to the undigested and 180 min digested samples and the apparent toughness had decreased relative to its value at 180 min (C). These differences were shown using representative force vs distance profiles (D). It is hypothesized that these differences were due to changes in the microstructure of the whey protein strong gel that occurred during static in vitro digestion, namely that the microstructure was strong before digestion (E), after 180 min digestion was softened by moisture with a minor contribution of hydrolysis (F) causing the gel to become less stiff but able to dissipate energy by bending or flow of serum, resulting in the increased apparent toughness between 0 min and 180 min. After 24 h digestion it was hypothesized that the matrix was extensively weakened by hydrolysis (G), leading to the observed decrease in apparent toughness between 180 min and 24 h. Hypothesized microstructures of the whey protein model foods (E, F, and G) were adapted from Schmitt et. al., (2010)..... 269

Figure 7.18. Appearance of particles after application of 90 simulated peristaltic contractions in the HGS and hypothesized mechanisms of breakdown for the standard diet strong gel (A), standard diet weak gel (B), whey protein strong gel (C), and the whey protein weak gel (D). The hypothesized mechanisms of particle breakdown varied more between different model foods than between different static in vitro digestion times for a given model food. For instance, the hypothesized mechanism of breakdown for the whey protein strong gel was erosion regardless of static in vitro digestion time. The relation between changes in hardness and hypothesized mechanisms of breakdown are shown in panel E (modified from Chapter 5). 276

Figure 7.19. Appearance of particles during progressive application of contractions in the peristaltic simulator and hypothesized mechanism of breakdown. In general, variations in breakdown behavior were greater between different model foods than between different static in vitro digestion times for a given model food. 280

Figure 8.1. Overall conclusions from this project. Images of model foods cut into a cubical geometry are shown along with CLSM images from microstructural analysis. The initial hardness, softening half-time, and resulted FBCS classifications are provided, along with the hypothesized mechanisms of breakdown in the HGS. The number of contractions at which point particles began to break down by fragmentation in the peristaltic simulator are provided. 290

List of Tables

Table 2.1. Secretion rate of simulated gastric juice in the HGS based on the measured intragastric pH (Mennah-Govela et al., 2021), based on data from in vitro digestion in a growing pig model (Nadia et al., 2021b).	26
Table 3.1. Results from selected studies that explored relations between instrumentally measured properties of foods and mastication variables. The test food used in each study is indicated. The instrumentally measured property is shown, as well as the type of test used to obtain it where U: uniaxial compression test, P: puncture test, W: wedge test, C: cutting test, TPB: Three-point bending test, TEN: Tensile test. An upward pointing arrow indicates an increase in a certain instrumentally measured property, and its relationship with a specific mastication variable is indicated by the next arrow. For example, “↑ compression work: ↑ number of chews” indicates that a greater amount of work needed to compress the sample was associated with a higher number of chews before the food was swallowed.....	47
Table 3.2. Mechanical properties in three-point bending for two common food sample geometries. Δx_{frac} [m] is the displacement in the direction of the applied force when fracture occurs, F_{frac} [N] is the force when fracture occurs, dF/dx [N/m] is the slope of the linear-elastic region of the force-displacement curve, s [m] is the distance between the supports, D [m] is the diameter of a solid, cylindrical sample, h [m] is the height and w [m] the width of a rectangular prism-shaped sample (Figure 3.7 E).....	63
Table 3.3. Parameters of instrumental-mechanical tests used in selected studies to measure the fracture properties of foods. The test food used in each study is indicated. The sample geometry is shown, as well as the geometry of the test probe that was used, the speed at which it was used to deform the sample, and the condition for stopping the test.....	67
Table 4.1. Composition of simulated digestive juices (Bornhorst and Singh, 2013; Minekus et al., 2014; Roman et al., 2012).....	77
Table 4.2. Fatty acid composition of whole almonds used for in vitro digestion determined by direct acid extraction and Folch extraction (Section 4.4.1). Direct acid extraction was carried out on almond powder (10.08 ± 0.93 mg dry mass) and extractable fatty acid comprised $58.76 \pm 2.44\%$ of initial almond dry mass. Folch extraction was carried out on almond powder (10.42 ± 2.80 mg dry mass) and extractable fatty acid comprised $54.77 \pm 2.68\%$ of initial almond dry mass. All values are means \pm standard deviation ($n = 8$ for direct acid extraction and $n = 9$ for Folch extraction).....	87
Table 4.3. Bioaccessible fatty acid in liquid digesta as percentage of initial fatty acid content of almonds. All values are means ($n = 3$) \pm standard deviation. Values in each column with no letter in common (abc) represent significant differences ($p < 0.05$) within a certain model across different digestion times. Values in each row with no letter in common (xyz) represent significant differences ($p < 0.05$) at a certain digestion time across the gastric digestion models for each fatty acid. If no letter is listed, there were no significant differences.	91
Table 4.4. Parameters of the Rosin–Rammler model (Equation 4.1) and particles per gram dry solids. The coefficient of determination R^2 for the Rosin–Rammler distribution fit to the cumulative distribution of particle sizes was ≥ 0.99 in all cases. All values are means ($n = 3$) \pm standard deviation. Values in each column with no letter in common (abc) represent significant differences ($p < 0.05$) within a certain model	

across different digestion times. Values in each row with no letter in common (xyz) represent significant differences ($p < 0.05$) at a certain digestion time across the different models for each parameter. If no letter is listed, there were no significant differences..... 92

Table 4.5. Moisture content of solid particles (g moisture per g dry matter) and °Brix of liquid digesta. All values are means ($n = 3$) \pm standard deviation. Values in each column with no letter in common (abc) represent significant differences ($p < 0.05$) within a certain model across different digestion times. Values in each row with no letter in common (xyz) represent significant differences ($p < 0.05$) at a certain digestion time across the different models. If no letter is listed, there were no significant differences. 93

Table 4.6. pH of digesta. When a pH adjustment was called for by the digestion protocol (Section 4.2.3.1), the pH was recorded both before and after the adjustment was made. All values are means \pm standard deviation ($n = 3$). 94

Table 5.1. Chemicals and other ingredients used for preparation of model foods. All ingredients were dissolved in water so that the total mass of the dispersion was 100 g. 109

Table 5.2. Composition of simulated saliva and gastric juice..... 112

Table 5.3. Parameters of the Weibull function (Equation 5.6) fit to values of force measured at different levels of strain over time during in vitro digestion for the standard diet strong gel (standard diet model food prepared at pH 5.2). Values represent the mean ($n=3$) \pm standard deviation..... 121

Table 5.4. Parameters of the Weibull function (Equation 5.6) fit to values of force measured at different levels of strain over time during in vitro digestion for the standard diet weak gel (standard diet model food prepared at pH 2.5). Values represent the mean ($n=3$) \pm standard deviation. 122

Table 5.5. Parameters of the Weibull function (Equation 5.6) fit to values of force measured at different levels of strain over time during in vitro digestion for the whey protein strong gel (whey protein hydrogel model food with 0% pectin). Values represent the mean ($n=3$) \pm standard deviation. 123

Table 5.6. Parameters of the Weibull function (Equation 5.6) fit to values of force measured at different levels of strain over time during in vitro digestion for the whey protein weak gel (whey protein hydrogel model food with 0.6% pectin). Values represent the mean ($n=3$) \pm standard deviation. 124

Table 5.7. Hardness (N) of model foods over time during digestion. All values are mean ($n=3$) \pm standard deviation. Values in each column (abc) or each row (zyx) with different letters represent significant differences ($p < 0.05$) between means. If no letter is listed, there were no significant differences within that factor. 127

Table 5.8. Parameters of the Weibull function (Equation 5.6) used to fit normalized hardness, normalized elastic modulus, and dry solids retention ratio of model foods during in vitro digestion. Values in each row with no letter in common (zyx) represent significant differences ($p < 0.05$) across the different model foods. If no letter is listed, there were no significant differences. 129

Table 5.9. Elastic modulus (kPa), fracture stress (kPa), fracture strain (unitless), dry solids retention ratio (%), calculated using Equation 5), and soluble solids (°Brix) for model foods. The whey protein strong gel did not fracture during the compression test and thus its fracture stress and fracture strain are not

presented (NA). All values are means ($n=3$) \pm standard deviation. Values in each column (abc) or each row (zyx) with different letters represent significant differences ($p<0.05$) between means. If no letter is listed, there were no significant differences within that factor. Superscripts are not given for elastic modulus and fracture strain as the interaction effect of model food type and digestion time was not found to be significant for these variables..... 131

Table 5.10. Estimated effective diffusivity of moisture (D_{eff}) estimated equilibrium moisture content (C_e) and diffusion model metrics for model foods during in vitro digestion. The relative root mean square error (RRMSE) was calculated using Equation 5.2. Values represent the mean ($n=3$) \pm standard deviation. Values in each row with different letters (zyx) represent significant differences ($p<0.05$) between the model foods..... 135

Table 5.11. Dry basis moisture content (g moisture per g dry matter) of model foods over time during digestion. All values are mean ($n=3$) \pm standard deviation. Values in each column (abc) or each row (zyx) with different letters represent significant differences ($p<0.05$) between means. If no letter is listed, there were no significant differences within that factor..... 136

Table 5.12. Parameters from regression analysis used to determine the relationships between hardness, dry solids retention ratio, and normalized moisture content for model foods. RRMSE was calculated using Equation 5.2..... 138

Table 5.13. pH of digesta at each digestion time point. When the in vitro digestion protocol specified a pH adjustment (Section 2.4), the pH was recorded both before and after the adjustment was made. Values represent the mean ($n=3$) \pm standard deviation. NA indicates that a pH adjustment was not required at the given timepoint, because the pH was already within 2 ± 0.1 139

Table 5.14. FBCS classification criteria based on initial hardness (N) and softening half-time (min), modified from Bornhorst et al. (2015) and Drechsler and Bornhorst (2018). NA signifies that no food in the FBCS class was tested in the corresponding study. 151

Table 6.1. Parameters of the CFD model of fluid flow inside the peristaltic simulator..... 169

Table 6.2. Parameters of the shape function (Equation 6.1) obtained for the digestion module when either the thin rollers or the thick rollers were used..... 178

Table 6.3. Parameters from curve fitting the Gaussian (Equation 6.1) to images of ex vivo porcine intestinal tissue undergoing post mortem motility..... 190

Table 7.1. Fracture properties of model foods over time during in vitro digestion. All values are means ($n=3$) \pm standard deviation. Two-factor ANOVA was used to analyze results for the standard diet strong gel, standard diet weak gel, and whey protein weak gel. For these model foods, values in each column (abc) or each row (zyx) with different letters represent significant differences ($p < 0.05$) between means. If no letter is listed, there were no significant differences within that factor. For variables analyzed using two-factor ANOVA, if the interaction effect of type of model food and time point was not significant ($p > 0.05$), post-hoc tests were not conducted. One-factor ANOVA was used to analyze results for the whey protein strong gel, and values in each row (ijk) with different letters represent significant differences ($p < 0.05$) between means..... 228

Table 7.2. Rheological properties of model foods over time during in vitro digestion. All values are means ($n=3$) \pm standard deviation. Values in each column (abc) or each row (zyx) with different letters represent significant differences ($p < 0.05$) between means. If no letter is listed, there were no significant differences within that factor. 232

Table 7.3. Rheological properties of model foods in dispersion form with parameters from Equation 7.1. All values are means ($n=3$) \pm standard deviation. Values in each column (abc) with different letters represent significant differences ($p < 0.05$) between means. If no letter is listed, there were no significant differences within that factor. 234

Table 7.4. Parameters of the Mixed Weibull Model (Equation 7.7) and percentages of total particle area belonging to distinct size classes for model foods after being subjected to static in vitro digestion for varying time points (0, 30, or 180 min) followed by 90 contractions in the HGS. Values in each column (abc) or each row (zyx) with different letters represent significant differences ($p < 0.05$) between means. For variables where the interaction effect of type of model food and time point was not significant ($p > 0.05$), post-hoc tests were not conducted. 240

Table 7.5. Change in concentration of free amino groups in liquid digesta Δ [NH₂] (Mol/L) from the end of the static in vitro digestion in the shaking water bath to immediately after 90 simulated peristaltic contractions were applied in the HGS (approximately 30 min). Values in each column (abc) or each row (zyx) with different letters represent significant differences ($p < 0.05$) between means. 247

Table 7.6. Significance of factors used in three-factor ANOVA to analyze results from trials in the peristaltic simulator. Main effects consisted of the type of model food (F), static in vitro digestion time (T), and number of simulated peristaltic contractions (C). Interaction effects consisted of the interaction of the type of model food and the static in vitro digestion time (F*T), the type of model food and the number of simulated peristaltic contractions (F*C), the interaction of static in vitro digestion time and the number of simulated peristaltic contractions (T*C), and the three-way interaction of the type of model food, static in vitro digestion time, and the number of simulated peristaltic contractions (F*T*C). Significant factors were indicated as $p < 0.01$ or $p < 0.05$. NS indicated that the factor was not significant. Variables labeled as “Debris: N”, “Partially damaged: N”, and “Mostly undamaged: N” indicate the number of particles in each respective class. 251

Table 7.7. Characteristics of particles resulting from application of simulated peristaltic contractions to cubical particles of model food in the peristaltic simulator. For each treatment, consisting of a combination of type of model food (standard diet strong gel, standard diet weak gel, whey protein strong gel, whey protein weak gel), static in vitro digestion time (0, 30, or 180 min), and number of applied contractions (3, 10, 30, 90, or remainder), particles were classified as either debris, partially damaged, or mostly undamaged. The percentage of particles in each class (% total) were reported on an 2D area basis, as well as the number of particles in the respective class, N, and their average size, χ (mm²). For each treatment, values given are the average of three replicate experiments \pm the standard deviation of those three replicates. Each replicate consisted of results from 5 cubes of model food subjected to simulated peristalsis, each one attached to an individual holding rig. Thus, if in each column (abc) or each row (zyx) with different letters represent significant differences ($p < 0.05$) between means. For variables where the interaction effect of type of model food and number of applied contractions was not significant ($p > 0.05$), post-hoc tests were not conducted. If no particles in a given class were present for a given treatment (which consisted of a combination of type of model food, static in vitro digestion time, and number of contractions), the percent of the total area made up of particles in that class was 0% with $N = 0$, however, their average size was indicated by NA. For example, application of 3 simulated peristaltic contractions to

the standard diet strong gel did not result in any particles breaking away from the cube on the holding rig that were large enough to be classified as mostly intact, therefore their percent of total area was 0%, their number, N, was 0, and their average size was indicated by NA. 252

Table 7.8. Summary of FBCS classifications of the model foods used in the current study as described by Swackhamer et. al., (2022), along with summary of hypothesized mechanisms of breakdown in the HGS and peristaltic simulator. 282

Chapter 1 Introduction

1.1 Background

Digestion is the life-sustaining process by which food is broken down and nutrients are absorbed by the body. Gastric digestion refers to digestion in the stomach, which occurs after food has been processed in the mouth and swallowed, but before partially digested food in the form of chyme is discharged into the duodenum through a process called gastric emptying. Food breakdown during gastric digestion influences gastric emptying, satiety, and bioaccessibility of nutrients (Cisse et al., 2018; Gopirajah et al., 2016; L. Marciani et al., 2001a). Food breakdown during gastric digestion is influenced by the physical structure of food as well as the chemical environment achieved by the stomach, which in turn depends on food properties (Bornhorst et al., 2015; Mennah-Govela et al., 2021). However, the influence of food properties on the breakdown during gastric digestion is not fully understood.

The multitude of foods available for consumption throughout the world precludes characterization of the breakdown of every food through experimentation. One approach that has been used to study the breakdown of food during gastric digestion is the use of model foods, which are created for a specific research purpose but may lead to insights into the fundamental processes of digestion and additionally may display behavior that can be generalized to commercial food products with similar composition or structure (Campbell et al., 2016). Examples of model foods used to study the processes of gastric digestion include model carbohydrates to understand the effect of food structure on their breakdown during gastric digestion (Nadia et al., 2021b), model whey protein hydrogels to understand the effect of particle size on the buffering capacity of digesta (Mennah-Govela et al., 2019), model whey protein gels to quantify the diffusion of pepsin in a solid food matrix (Luo et al., 2017) and model plants that were used to study the enzymatic modification of antibiotics during gastric digestion (Keppler et al., 2021).

However, model foods that incorporate only one major macronutrient such as whey protein hydrogels may have limited applicability in studies on the release of nutrients from solid food matrices, as the human diet includes protein, lipid, and carbohydrate that are often consumed at the same time in the same

food product. To contend with this limitation, researchers have developed a model food to study the release of lycopene (Zhang et al., 2019a) and nanoparticles (Zhang et al., 2019b) during gastric digestion that was based on the Standard American Diet. This model food was proposed as a general-purpose food matrix in which compounds of interest could be incorporated, allowing for their release during gastric digestion to be studied in the presence of macronutrients in physiologically relevant proportion to one another. This model food was only developed in powder form, however, and thus there is a need for a version in the form of a solid matrix, as roughly 80% of calories in the Standard American Diet are consumed as part of solid foods (Mesirow and Welsh, 2015). Additionally, there is a need for foods with varying breakdown rates during gastric digestion, as it has been shown that foods with varying textural properties can differ greatly in their breakdown rates during digestion, and thus the availability of a fast-breakdown and a slow-breakdown version of any model food could extend its applicability to studying digestion.

Quantifying the breakdown rates of foods during digestion is complex. In general, previous approaches have involved texture analysis (Somaratne et al., 2020d) or particle size analysis (Nadia et al., 2021b) to determine changes to foods that occur due to the chemical and physical effects of the stomach. Relating the changes in texture or particle size to their associated mechanisms of breakdown has remained a challenge. Previous researchers have proposed that erosion and fragmentation represent the major mechanisms of breakdown of solid foods in the gastric environment, with erosion referring to the wearing away of the outer surface of food particles and fragmentation as the breakage of a food particle into multiple pieces (Guo et al., 2014a; Kong and Singh, 2009a). An additional mechanism has been proposed by Drechsler et al., (2016) who proposed that chipping, the breakage of small pieces away from a food particle, was a distinct mechanism from that of fragmentation, the breakage of the overall particle into pieces of comparable size to the original. Identifying the dominant mechanisms that are responsible for the breakdown of foods in the gastric environment is a goal of *in vitro* digestion research but more experimental data on the breakdown of foods is needed.

To study the breakdown of food during gastric digestion, previous researchers have used both in vivo (Bornhorst et al., 2013b, 2013d) and in vitro (Drechsler and Bornhorst, 2018; Olenskyj et al., 2020) models. In vitro models may have advantages in terms of reduced cost and lesser ethical considerations as compared to in vivo approaches (Somaratne et al., 2020a). However, the breakdown of food during gastric digestion depends on the motility of the stomach which is difficult to recreate using in vitro models. In recent years in vitro models have been developed that attempted to recreate simplified versions of the motility of the human stomach for the purpose of applying realistic conditions to food samples, usually achieved through simulated peristaltic contractions (Dupont et al., 2019). Despite these advancements, there is a need for in vitro models that permit simulated peristaltic contractions to be applied to a single food particle for the breakdown-inducing effect of simulated peristalsis to be isolated from additional possible mechanisms of food breakdown, such as particle-particle grinding. There is also a need for in vitro models including simulated peristalsis to have higher experimental throughput, as the currently available in vitro models are single chamber systems built at a 1:1 scale with the human stomach and require several hours for a single food product to be tested (Barros et al., 2016; Dang et al., 2020; Li et al., 2019; Liu et al., 2020).

To summarize the needs for research that were identified, the effect of simulated peristalsis on the breakdown of solid food particles during in vitro digestion has not been fully established, there is a need for model, solid foods based on the Standard American Diet but with varying softening rates, a need for a new in vitro digestion system that allows simulated peristaltic contractions to be applied to individual food particles, and a need for links to be established between the physical property changes in solid foods during digestion and the mechanisms of particle breakdown during in vitro digestion that includes simulated peristalsis. The overall hypothesis of this project was that in vitro gastric digestion with simulated peristalsis would lead to a greater rate of food particle breakdown than in vitro digestion without simulated peristalsis, and that food physical properties would influence the breakdown mechanisms of solid food particles during in vitro digestion that includes simulated peristalsis.

1.2 Research Objectives

The objectives of this project were as follows:

1. Quantify the breakdown of solid food particles during in vitro gastric digestion and determine whether the breakdown was affected by the presence or absence of simulated peristaltic contractions, and whether the degree of breakdown affected the bioaccessibility of nutrients. It was hypothesized that food particles would experience increased particle size reduction in the system that included simulated peristalsis, which would lead to increase bioaccessibility of nutrients relative to in vitro gastric digestion in a system that lacked simulated peristalsis.
2. Develop standardized, model solid foods with macronutrient composition matched to the Standard American Diet but with varying rates of softening during static in vitro gastric digestion. It was hypothesized that model solid foods could be developed with minimal differences in chemical formulation but with varying rates of softening, leading to placement in distinct classes under the FBCS, which would then experience differing rates of particle breakdown during in vitro gastric digestion that included simulated peristaltic contractions.
3. Develop a novel dynamic in vitro digestion system capable of applying adjustable simulated peristaltic contractions to individual food particles and with higher experimental throughput than currently available systems. It was hypothesized that the dynamics of the simulated peristaltic wave could be controlled by tuning the device so that variables such as percent occlusion of the peristaltic wave and force exerted on a simulated food particle would fall into a physiologically representative range.
4. Characterize changes in the texture, fracture, and rheological properties of the standardized, model solid foods during gastric digestion and determine their hypothesized mechanisms of breakdown during in vitro digestion that includes simulated peristaltic contractions. It was hypothesized that foods would experience decreases in empirical textural properties such as hardness, rheological properties such as G' and G'' , and fracture properties such as toughness,

but with differing rates depending on their class within the FBCS. Furthermore, it was hypothesized that model foods would experience mechanisms of particle breakdown dependent on their properties, for example, it was hypothesized that foods with high initial hardness and slow softening would experience particle breakdown only by erosion as compared to food particles with low initial hardness or rapid softening, which would experience particle breakdown due to erosion, chipping, and fragmentation.

These research objectives were approached through the research presented in Chapters 2 through 7. Chapter 2 presents an overview of the literature on the digestion process. Chapter 3 is a review of the literature on food fracture properties and their influence on food breakdown during mastication, which has parallels to food breakdown during gastric digestion. In Chapter 4, experiments using almonds to test the effect of simulated peristalsis on the breakdown of solid food particles were reported. In Chapter 5, model solid foods were developed to serve as a tool for linking food physical properties to particle breakdown. In Chapter 6, a novel device was developed to allow for simulated peristaltic contractions to be applied to model food particles, and in Chapter 7 the model foods developed in Chapter 5 were subjected to in vitro gastric digestion using the device developed in Chapter 6, with the goal of linking the properties of solid foods to their breakdown under simulated peristalsis.

Research objective 1 was addressed in Chapter 4, where almond particles were subjected to in vitro digestion that either included or lacked simulated peristaltic contractions in order to determine the influence of simulated peristalsis on the breakdown of solid food particles. In this study it was determined that almond particles experienced particle size reduction only in the in vitro system that included simulated peristaltic contractions. However, almonds are not preferable as a model food system as they have heterogeneous sizes and shapes, and do not contain the macronutrient ratios of the Standard American Diet.

Research objective 2 was the focus of Chapter 5, in which standardized, model solid foods with macronutrient composition based on the Standard American Diet were developed and their softening rates

during in vitro gastric digestion were determined. Two additional model foods were developed that also had varying breakdown rates during gastric digestion but with structure derived only from whey protein to serve as a simpler model system. The model foods were classified according to the Food Breakdown Classification System (FBCS) (Bornhorst et al., 2015) and it was confirmed that they were categorized into distinct classes.

Research objective 3 was the focus of Chapter 6, in which the design, construction, and characterization of a novel, multi-module peristaltic simulator for in vitro digestion studies was reported. This device was originally constructed as part of a senior design project at the University of California, Davis, by undergraduate students in the department of Biological and Agricultural Engineering and was further developed in the present work. This device can apply adjustable simulated peristaltic contractions to a single food particle at a time and as permits higher experimental throughput than previously available in vitro digestion systems that include simulated peristalsis.

Research question 4 was addressed in Chapter 7, in which the model foods developed in Chapter 5 were subjected to in vitro digestion and the changes in their rheological and fracture properties were quantified. In parallel experiments, the model foods were subjected to in vitro gastric digestion without simulated peristaltic contractions for varying lengths of time before then subjecting them to simulated in vitro digestion in either the Human Gastric Simulator (HGS) or the novel peristaltic simulator developed in Chapter 6, both of which included simulated peristaltic contractions. The hypothesized breakdown mechanisms of the model foods were determined and related to their texture, rheological, and fracture properties to shed light on the relationships between the physical properties of solid foods and their breakdown mechanisms under simulated peristalsis. These results could allow the model foods to serve in future studies as well-characterized food matrices for examining the effect of food properties on variables such as gastric emptying or satiety.

Chapter 2 Review of Literature Part I: Food digestion and the importance of food properties on the breakdown of foods in the gastric environment

Rationale

The rationale for this literature review was to introduce the process of digestion and the importance of studying food digestion. The physiology of the major steps in the digestion process were briefly reviewed to provide context for the in vitro models used in Chapters 4, 5, 6, and 7. Previous research on the breakdown of food during gastric digestion and the properties of foods that have been shown to influence breakdown were reviewed.

2.1 Food digestion

Food digestion is essential for human life. Digestion is the process by which foods are taken into the body's gastrointestinal tract and then broken down and processed by complex mechanical and chemical phenomena until nutrients can be absorbed. This occurs through a sequence of processes: ingestion, oral digestion, gastric digestion, small and large intestinal digestion, and excretion of waste. Although inter-individual variability affects the function of the digestion system, it has been analyzed as a sequence of processes comparable to a series of engineering unit operations (Bornhorst et al., 2016b). This perspective may enable the complex biological processes of digestion to be analyzed in terms of the underlying chemical and physical interactions between food and the body (Lamond et al., 2019). Furthering the understanding of digestion is essential for improving consumer health, which could come through health-promoting foods or through better therapies for individuals with medical conditions that affect their digestion process. There are significant opportunities in this area as it has been estimated that 60-90 % of all diseases that affect the human body are directly related to the digestive system (Welcome, 2018).

2.1.1 *Food digestion in context of global challenges*

The purpose of the global agriculture and food production system is to create products that enter and exit the digestion system and maximize human health while minimizing negative impacts on the environment. To this end, the global food system is the result of tremendous scientific and engineering

achievement. Nevertheless, this system emits more greenhouse gasses, causes more loss of biodiversity, degrades more ecosystems, consumes more fresh water, and produces more nitrogen and phosphorous pollutants than any other industry (Rockström et al., 2020). Furthermore, it has been estimated that between 2010 and 2050, changing global population and income levels will result in a 50-90% increase in the negative environmental impacts of the global food system in the absence of technological advancements (Springmann et al., 2018).

Despite the large resource investments into the food system, it is estimated that 711 million adults are obese (Afshin and Collaborators*, 2017), leading to \$2 trillion in annual costs in health care and lost productivity (Swinburn et al., 2019). At the same time, an estimated 462 million adults (Abarca-Gómez and Collaborators*, 2017) and 192 million children (Abarca-Gómez and Collaborators*, 2017) were moderately or severely underweight.

Food digestion is the crux of the food system, the critical process where valuable inputs of energy and resources from the environment are transformed into nutrients that sustain life. A more in-depth understanding of food digestion could help address these global challenges, whether through reducing obesity with highly-satiating functional foods (Norton et al., 2007), reducing the burden of undernutrition with nutrient-dense foods (Banerjee and Maitra, 2020), decreasing environmental impacts through innovations such as lab-grown or insect proteins (Herrero et al., 2020), or diversifying the human diet to include crops resilient to climate change (Meyer, 2020). From an engineering perspective, such improvements would be inherently scalable. There are 7.8 billion people on Earth (Klein and Anderegg, 2021). Almost all of them¹ must digest food.

¹ In cases where the digestive system cannot function individuals can be fed through an intravenous nutrient delivery system called total parenteral nutrition, used for ca. 40,000 individuals (ca. 0.01 % of the population) in the United States each year (John and Seifi, 2017).

2.1.2 Oral digestion

Food digestion begins with the oral phase which takes place in the mouth. During oral digestion, foods are physically broken down by teeth and the tongue through a process called mastication. It is during this phase of the digestion that sensory appreciation of food taste and texture greatly influence consumer acceptability of food products (Chen, 2009a). During the first bite, sensory information on the structure of the food is used to set the parameters for the remainder of oral processing, including the duration of chewing, how much force will be applied to teeth, and the frequency of chews, through a process called haptic exploration (Dan et al., 2007).

Oral digestion involves lubrication of the food with saliva (Sanahuja et al., 2017), which includes water, salts, and about 300 different proteins (Amado et al., 2005). Glycoproteins called salivary mucins contribute to lubrication of food particles (Gavião et al., 2004), assisting in the formation of food particles into a bolus that can be swallowed (Bornhorst and Singh, 2012a). The process of bolus formation depends on food properties as well as variables such as dentition status, gender, and age (Xu, 2016). During oral digestion, starch in the food can be hydrolyzed by salivary alpha-amylase (Joubert et al., 2017), which in turn affects the texture of the food bolus (Bornhorst et al., 2014a) and the rate of acid diffusion into the bolus that occurs in the stomach after swallowing (Mennah-Govela et al., 2015). Previous researchers have suggested that inter-individual differences in the degree of particle size reduction during mastication could be a potential cause of variability in the glycemic response to consumption of a given food between different consumers (Ranawana et al., 2010). Additionally, food physical properties such as hardness (Shiau et al., 1999), fracture stress (Kohyama et al., 2017), and moisture content (van der Bilt and Abbink, 2017) affect the number of chewing cycles needed to complete the mastication process. In total, oral digestion lasts for about 20 s – 30 s (Hutchings et al., 2011; Kohyama et al., 2015; Lin et al., 2021), with the duration dependent on the consumer and type of food. Previous researchers have developed mastication simulators which may help to shed light on the relationships between food properties and variables such as chewing effort (Peyron et al., 2019; Salles et al., 2007; Woda et al., 2010). This area of

investigation could help to promote health as difficulties in mastication have been linked to poor nutrition (Morais et al., 2003; N’Gom and Woda, 2002).

2.1.3 *Esophageal transit*

At the conclusion of oral digestion, food is swallowed through a process called deglutition and transported through the peristaltic motion of the esophagus from the upper esophageal sphincter to the lower esophageal sphincter where it enters the stomach (Bornhorst and Singh, 2012a). The total time for esophageal transit varies based on bolus characteristics, requiring only 15 s for a gelatin capsule but up to 120 s for a large cube of liver (Fisher et al., 1982). Additionally, oval shaped capsules may pass through the esophagus more quickly than round ones (Channer and Virjee, 1986). The muscles that trigger swallowing are coordinated by a central pattern generator, a type of neural circuit located in the medulla oblongata, a part of the brain stem (Jean, 2001).

An engineering approach to studying esophageal transit has been carried out by previous researchers who constructed a soft-bodied swallowing robot outfitted with sensors as well as an artificial central pattern generator with three neurons that allows for experiments to be conducted on the effect of bolus properties on the deformation of the soft, artificial esophagus (Dirven et al., 2017; Zhu et al., 2017). This could one day help to develop foods suitable for individuals with dysphagia (Witt and Stokes, 2015), a collection of swallowing disorders that affect about 8 % of the global population (Cichero et al., 2013) but are particularly common in elderly populations (Chen et al., 2013). Thickened liquids have been proposed as a solution to dysphagia as they may be more easily swallowed (Cichero et al., 2013), however, the risks of aspirating thickened liquids have not been fully studied and warrant further consideration (Nativ-Zeltzer et al., 2020).

2.1.4 *Gastric digestion*

After discharge from the lower esophageal sphincter, the bolus enters the upper region of the stomach, referred to as the proximal stomach (Figure 2.1). The proximal region of the stomach has been considered as the site of food storage. The stomach is roughly J-shaped (Ferrua and Singh, 2010), and

narrows in the distal region toward the pylorus, the valve which connects the stomach to the duodenum and has a diameter ca. 1 cm (Malik et al., 2015) (Figure 2.1). X-ray computed tomography has been used to quantify the approximate dimensions of the stomach, and it was found that the maximum width was 13 cm (range 9-16 cm), the maximum height was 10 cm (range 6-15 cm) and the volume ca. 372 cm³ for subjects having consumed 500-600 mL of liquid 30 min before the computed tomography scan and an additional 250-300 mL immediately before the scan (Lamart et al., 2013). The stomach on the inside is lined with folds of tissue lined with mucus called rugae (Schulze, 2006).

Cells in a region called the cardia, which exists near the top of the proximal stomach in close proximity to the lower esophageal sphincter, are responsible for secreting mucin (Landa et al., 2019). In addition to mucin, gastric secretions consist of hydrochloric acid, the proenzyme pepsinogen, bicarbonate, and a glycoprotein called intrinsic factor (Barrett, 2014). The secretions of the stomach are often referred to as gastric juice. The secretions of the stomach have acidity equivalent to 0.16 M HCl and their total volume consists of about 2-3 L per day (Schubert and Peura, 2008). Basal secretion rates (occurring between meals) have a flow rate of ca. 1 mL per minute, with rates after meal consumption up to ca. 6 mL per minute (Dressman et al., 1990; Malagelada et al., 1979).

The pH profile of stomach is dynamic both in time and location, with fasting pH values ca. 1.7 and increases following meal consumption to ca 7.0 (Dressman et al., 1990). The pH profile in the stomach following consumption of either brown or white rice has been studied using a growing pig model, where it was determined that pH was significantly affected by rice type ($p < 0.001$), postprandial time ($p < 0.001$) and stomach region ($p < 0.001$) with significant interaction effects of rice type \times stomach region ($p < 0.01$) in addition to stomach region \times postprandial time ($p < 0.001$) (Bornhorst et al., 2013a). It has been determined that pH is generally higher in the proximal region of the stomach than in the distal region during the postprandial period (Bornhorst et al., 2013a; Nadia et al., 2021b) despite the secretion of acid occurring in the proximal stomach. Previous researchers have hypothesized that this could be due to a “settling” effect of gastric acid in addition to a greater degree of mixing between gastric secretions and food particles in the distal region due to the presence of antral contraction waves in the distal stomach

(Bornhorst et al., 2013e). Motility of the stomach is discussed in Section 2.2.2. The pH of digesta may have important implications for protein digestion as the activity of pepsin is pH dependent, with optimal activity ca. pH 2.0 (Mennah-Govela and Bornhorst, 2021a, 2021b) and inactivation above ca. pH 7.0 (Gallier and Singh, 2012). Additional enzymes relevant to digestion such as salivary α -amylase and human gastric lipase have pH-dependent activity, as discussed in more detail in Section 2.2.3. Thus, use of appropriate pH values during in vitro gastric digestion studies is an important consideration. The presence of pH gradients in the stomach that vary spatially and temporally presents a challenge for development of physiologically relevant conditions in vitro. Previous researchers have implemented a pH control algorithm based on the available in vivo data using the Human Gastric Simulator (HGS), a dynamic in vitro model of human digestion (Mennah-Govela et al., 2021). The use of in vitro models to represent the gastric phase of digestion are discussed in Section 2.3.1. With regards to the pH of the stomach the buffering capacity of food may have an important effect, as foods with greater buffering capacity resist changes in pH due to secretion of gastric acids. Methods to quantify food buffering capacity in the context of gastric digestion have been reviewed by previous researchers (Mennah-Govela and Bornhorst, 2021b).

Food particles are not emptied from the stomach until they are approximately 1-2 mm in size (Bornhorst et al., 2013b; Guo et al., 2015) due to gastric sieving, the selective retention of large particles by the pyloric valve (Figure 2.1) (Bornhorst et al., 2013c; Marciani et al., 2012). When the stomach is full satiety is high, and thus it has been proposed that foods which resist breakdown in the stomach delay gastric emptying and prolong satiety (Luca Marciani et al., 2001; Santangelo et al., 1998). This suggests an opportunity to develop foods with targeted breakdown rates in gastric digestion for modulating satiety (Norton et al., 2007), and points to the need for an increased understanding of mechanical breakdown of solid foods during gastric digestion.

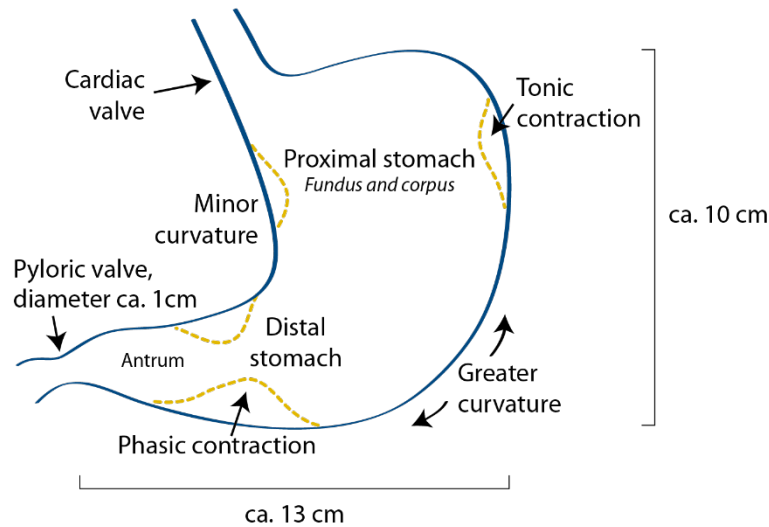


Figure 2.1. Illustration of the stomach showing selected anatomical features and approximate dimensions.

2.1.5 *Small intestinal digestion*

Partially digested food that is emptied from the stomach is referred to as chyme. Upon exit from the pyloric valve chyme enters the duodenum, which consists of the first 25 cm of the small intestine. The next portion of the small intestine is the jejunum which consists of about 40% of the total length of the small intestine, with the final 60% of the small intestine referred to as the ileum. The interior of the small intestine is referred to as the lumen and its surface is lined with finger-like structures ca. 500 μm in length called villi (Wang et al., 2010). Villi increase the surface area for nutrient absorption, and their motion may facilitate mixing by creating microscopic eddies in flowing fluid and increasing mass transfer of nutrients between the intestinal lumen and the intervillous space (Wang et al., 2010).

In the duodenum, the pH of chyme is raised by secretions of bicarbonate. Amphiphilic bile salts are secreted which emulsify lipids. Bile salts are produced in the liver and stored in the gallbladder, containing species such as taurocholic acid, taurodeoxycholic acid, and glycholic acid (Hofmann, 1999). Overall, approximately 10-30 % of lipid digestion occurs in the stomach due to gastric lipase with the remainder (70-90 %) occurring in the small intestine (Maldonado-Valderrama et al., 2011). Human pancreatic lipase, pancreatic triacylglycerol lipase, and carboxyl ester lipase are the enzymes responsible for hydrolysis of triacylglycerols, which occurs mostly in the upper region of the jejunum (Sun et al.,

2009). The activity of triacylglycerol lipase is regulated by colipase, a 10 kDa cofactor (non-enzymatic protein) which is secreted by the pancreas in the form of procolipase that must be cleaved by trypsin to reach a form in which it can interact with triacylglycerol lipase to hydrolyze lipids, a process that is also dependent on emulsification by bile salts (Erlanson-Albertsson et al., 1991). The secretion of hydrolytic enzymes in the form of proenzymes, also referred to as zymogens, is thought to prevent auto-hydrolysis of cellular components (Leach et al., 1991).

Trypsin and chymotrypsin are proteolytic enzymes secreted in the small intestine (Sandler and Lerch, 2020). In total, about 1.2-1.5 L of pancreatic juice is secreted daily (Shani-Levi et al., 2017). Starch digestion in the small intestine is carried out by pancreatic α -amylase, resulting in maltose, maltotriose, and α -limit dextrins. These oligosaccharides are hydrolyzed by brush border enzymes located on the villi to monosaccharides which can then be absorbed (Freitas et al., 2018). Starch digestion may impact intestinal motility through the ileal brake, a reduction in intestinal motility caused when incompletely digested carbohydrates reach the terminal ileum (Khalaf et al., 2018). This has been a hypothesized mechanism to explain the higher levels of satiety achieved after consumption of slowly digestible foods (Cisse et al., 2018; Poppitt et al., 2017). Starch digestion in relation to food structure, physiological outcomes such as glycemic response, and correlation between in vivo and in vitro models has been recently reviewed (Nadia et al., 2021a).

Intestinal motility consists of peristaltic contractions which propel chyme through the small intestine, as well as segmental contractions which introduce mixing in luminal contents (Schulze, 2015). Control of intestinal motility occurs through neural and hormonal control loops, and motility patterns vary between individuals (Lentle, 2018). The influence of intestinal motility on the fluid dynamics of the intestinal lumen are the subject of active research, where techniques such as smoothed particle hydrodynamics (Sinnott et al., 2017), the finite element method (Love et al., 2013), and the lattice-Boltzmann method (Loubens et al., 2013) have been applied. One finding from these computational studies is that intestinal contents are not homogeneous throughout the length of the intestine (Sinnott et al., 2017). Despite intestinal motility, luminal contents undergo laminar flow with Reynold's number less than 200, as

estimated by a computation study that considered luminal contents to be a Newtonian fluid with dynamic viscosity of 10^{-3} Pa-s (Love et al., 2013).

2.1.6 *Large intestinal digestion*

The large intestine is an anaerobic environment that serves as the site of microbial fermentation. In total, ca. 38 trillion microorganisms may be present, whose genomes collectively include 3 million genes (Sender et al., 2016; Valdes et al., 2018). The colon can contain one billion cells per mL (Sender et al., 2016). The impact of the colonic microbiome on human health goes beyond the presence or absence of pathogens. For example, short-chain fatty acid producing bacteria may confer benefits including improved postprandial glucose metabolism, production of vitamin B and antioxidants, and modulation of the immune system (Dewulf et al., 2013; Rivière et al., 2016). The colonic microbiome is shaped by the host's diet, especially the types and amounts of dietary fibers that are consumed. This is because fibers are not digested in the upper gastrointestinal tract and reach the colon where they can serve as substrates for microbial growth (Hamaker and Tuncil, 2014). In addition to short-chain fatty acids, water is absorbed during the large intestine phase of digestion.

Motility of the large intestine is complex, including patterns referred to as giant migrating contractions which are thought to compress digesta, extruding fluid from the material and preparing it for excretion (M. Costa et al., 2013; Lentle, 2018; Sakaguchi, 2003). In addition, low amplitude ripple contractions may promote mixing of the extruded fluid (Ehrlein et al., 1982). Colonic migrating motor complexes represent yet another motility pattern, which move digesta toward the anal canal (M. Costa et al., 2013). Similar to the small intestine, the surface of the large intestine is covered in a layer of mucus which protects intestinal surfaces from abrasion, particularly relevant in the large intestine as the progressive absorption of water throughout the digestive system results in the highest solids content in digesta in the colon (ca. 25 % w/w) (Lentle and Janssen, 2008). The digesta in the large intestine has been found to be viscoelastic (Lentle et al., 2006).

The last step in the digestion process is defecation. Anatomical factors, poor coordination of autonomic musculature, or unusual fecal rheology (de Loubens et al., 2020) can lead to difficult excretion of waste, with issues such as constipation or pain² arising in some individuals (Schwizer et al., 2006; Wang and Camilleri, 2019). Techniques such as magnetic resonance imaging, fluoroscopic defecography, and manometry have been applied to understand this final (but important) process of digestion (Samsom et al., 1998; Schwizer et al., 2006). Recently, a defecation simulator has been developed to help find solutions for individuals who experience problems with the defecation process (Tokoro et al., 2014), which includes workers on the international space station who have reported difficulty doing so in microgravity (Mullane, 2006).

2.1.7 Engineering operations that parallel the food digestion process

The digestive system, as outlined in the preceding sections, consists of different stages that have parallels with food and chemical process unit operations (Bornhorst et al., 2016b). For example, the function of the mouth is analogous to that of a mill through which food particle size is reduced. However, the mouth also involves mixing of food and saliva, an operation which parallels that of a mixing tank. Enzymatic hydrolysis of starch by alpha-amylase in saliva introduces the parallel of an enzymatic reactor. Finally, food particles and saliva are re-formed into a bolus which can be swallowed, a parallel with equipment that processes soft foods like dough into desired shapes. The breakdown of food particles and formation of the bolus is an example of what previous researchers have referred to as the de-structuring and re-structuring processes of digestion (Guo et al., 2020). In yet another parallel with engineering process operations, sensory feedback is incorporated to determine the force that will be applied to teeth and the duration of mastication (Morell et al., 2014). In summary, there is no unit operation that

² The wombat, an herbivorous, Australian marsupial, passes cubical feces with sharp corners without issue. Recently, a mathematical model has been developed to explain how fast transit through stiff regions of the intestine and slow transit through soft regions creates these structures (Yang et al., 2021).

completely overlaps with the human mouth, but parallels can be found in that of a mill, mixing tank, enzymatic bioreactor, and dough rounder.

Transport of the bolus through the esophagus can be considered analogous to the pumping of a viscoelastic fluid through a peristaltic pump (Lamond et al., 2019). The stomach functions as a mixing tank, mill, and bioreactor, as well as a sieve due to selective retention of large particles (Bornhorst et al., 2016b). The small and large intestines have functional parallels in those of a mixing tank, continuous flow reactor, enzymatic bioreactor, and membrane filter (Boland, 2016; Bornhorst et al., 2016b).

The engineering unit operations that are analogous to the different stages of digestion suggest the opportunity to apply physics-based models of mass transfer, reaction kinetics, and fluid flow to these systems, which could help to achieve greater understanding of the individual processes. Additionally, a better understanding of the body's control of the digestive process, mediated through modulating pH, enzyme levels, and motility patterns, could allow for engineering controls theory to be applied. This could allow for a new paradigm in the management of digestive disorders, specifically, by using the knowledge of a specific individual's digestive system and its associated controls to adjust process parameters with a forward engineering approach. This could have advantages beyond using only on population-level correlations and statistical risk factors. These opportunities have been noted by previous researchers who noted that specific human populations, such as infants and the elderly, could see improved quality of life from advancements in the understanding of the digestive system (Shani-Levi et al., 2017).

Elucidating the physical processes and controls of the digestion system could enable a digital twin to be developed for an individual, allowing treatments to be prototyped and tested in a digital environment (Corral-Acero et al., 2020). It has been previously suggested that digital twins of industrial food processing equipment could help reduce costs of troubleshooting (Verboven et al., 2020). Since the processes of digestion parallel those of industrial processing operations, there may be potential for interdisciplinary work in this area.

2.2 Food breakdown during gastric digestion

Previous experiments using *in vivo* (Bornhorst et al., 2013c) and *in vitro* (Guo et al., 2015; Kong and Singh, 2009b) models have shown that solid foods break down during gastric digestion. Factors that contribute to food breakdown include acid and enzymatic hydrolysis (Bornhorst and Singh, 2013; Luo et al., 2017; Mennah-Govela et al., 2015; Van Wey et al., 2014) as well as temperature and moisture-related softening (Kong and Singh, 2009a; Lewicki, 2004; McFeeters et al., 1995). Mechanical breakdown of food particles in gastric digestion could be caused by stresses exerted by contact with other particles, contact with stomach walls, and softening of the structure by components of gastric juice. The contact forces that act on food particles during gastric digestion are not well-understood due to the heterogeneous contents of the stomach (Kong and Singh, 2008a), mixing that rearranges loading geometries between particles and other contacting bodies (Bornhorst, 2017), and physiological variability between individuals.

2.2.1 Importance of food breakdown during gastric digestion

The breakdown of food during gastric digestion may affect the rate of gastric emptying due to gastric sieving, the selective retention of particles greater than ca. 2 mm in size (Bornhorst et al., 2013c). Gastric emptying represents an important control point in the overall digestion process (Boland, 2016), with longer gastric emptying rates associated with reduced postprandial glycemia (Gopirajah et al., 2016) and increased satiety (Cisse et al., 2018). Management of postprandial glycemia may be challenging for consumers with diabetes mellitus, and designing carbohydrate-based foods with targeted breakdown rates during gastric digestion could be beneficial (Drechsler and Bornhorst, 2018; Miao and Hamaker, 2021).

In vitro experiments using almond particles of initial size 2-4 mm showed that a significant ($p < 0.05$) reduction in particle size occurred in the HGS, an *in vitro* model that includes simulated peristaltic contractions, as described in Chapter 4. However, particle size reduction did not occur when particles were subjected to *in vitro* digestion in a shaking water bath, an *in vitro* model that lacks simulated peristalsis (Swackhamer et al., 2019). Although there is a lack of previous studies directly comparing particle breakdown from solid foods using an *in vitro* gastric digestion system that either include or lack simulated peristalsis, previous researchers have noted that particle size reduction of peanuts occurred in

an in vitro gastric digestion system that incorporated mechanical motion similar to that of the human stomach (Chen et al., 2011), whereas a study using in vitro gastric digestion of almond particles in the absence of simulated peristalsis found no significant change in particle size (Mandalari et al., 2014). Taken together, these results underscore the importance of simulated peristalsis on the particle breakdown of solid foods.

In addition, results showed that fatty acid bioaccessibility was significantly greater ($p < 0.05$) at the end of the gastric phase in the HGS as compared to the shaking water bath model. This demonstrates that particle breakdown during the gastric phase of digestion has implications for bioaccessibility of fatty acids, which suggests the opportunity to design functional foods with slow release of fatty acids for consumers with hyperlipidemia (Grundy et al., 2015a; Li et al., 2011; Nishinari and Fang, 2021).

2.2.2 Gastric motility in relation to food breakdown during gastric digestion

Contact between food particles and the stomach wall arises from the motility of the stomach. Gastric motility includes tonic contractions, waves of low amplitude and long duration (Lammers et al., 2009) (Figure 2.1). Motility also includes phasic contractions, which begin in the corpus and then travel through the antrum, with occlusion reaching approximately 70% near the pylorus (Ferrua and Singh, 2010; Kwiatek et al., 2006). The phasic contraction waves occur at a frequency of about 3 cycles/min (Gopirajah et al., 2016) and travels at 2.7 mm/s (Kwiatek et al., 2006). Gastric motility is regulated by electrical signals that propagate through the gastric wall, with electrophysiological motor regulatory patterns similar to those of the heart (Brandstaeter et al., 2019). At least two populations of cells are necessary to trigger gastric motility: smooth muscle cells that generate mechanical forces to cause contraction of the gastric wall, and interstitial cells of Cajal which stimulate smooth muscle cells via electrical signals (Sanders et al., 2016). The contractions of the stomach could have implications for food breakdown as they directly impinge on the digesta, particularly in the antral region located in the distal part of the stomach where the occlusion is greatest (L. Marciani et al., 2001a).

In addition to particle/stomach wall interactions, it has been proposed that particle/particle interactions contribute to mechanical breakdown (L. Marciani et al., 2001b). This hypothesis is supported by research that found the force on particles in the stomach was 1.5 N under fasted conditions and 1.9 N under fed conditions (Kamba et al., 2000). Due to the unknown loading geometry of particles in the stomach, it is not clear if particle/stomach wall or particle/particle contact leads to mechanical particle breakdown through static compression, through a sliding or grinding mechanism, or through the effects of both compression and grinding.

Additionally, mechanical breakdown of particles in the stomach could be caused by forces applied by fluids in the gastric system, including hydrostatic pressure and hydrodynamic shear. Hydrostatic pressure exerts an inward normal force at all points on the surface of a particle immersed in gastric juice, but the impact of this pressure on particle breakdown is not well-known. It is hypothesized that hydrostatic compression plays a negligible role in breakdown of poorly compressible foods such as hydrogels or water-saturated tissues, but that it may contribute to the breakdown of foods with closed air cells such as puffed rice (Jiamjariyatam et al., 2016; Roopa and Bhattacharya, 2009) or baked products (Castro-Prada et al., 2012).

Hydrodynamic shear on particles in the stomach arises from the flow field of gastric juice driven by peristaltic contractions. It has been proposed that the fluid flow in the stomach is laminar, with Reynold's numbers estimated between 0.2 and 125 (Ferrua and Singh, 2010; Kozu et al., 2014, 2010; Pal et al., 2007a, 2004). Previous researchers used computational fluid dynamics to estimate the average fluid velocity in the stomach (fluid viscosity 10^{-3} Pa-s) as 0.16 cm/s and the average shear rate as 0.45/s (Ferrua et al., 2014) during maximum antral contraction wave occlusion. An in vivo study using magnetic resonance imaging (MRI) found the maximum fluid velocity to be 5 cm/s (Boulby et al., 1999). The variability in these estimates may be due to inter individual differences, which have been noted to affect the digestion system (Dupont et al., 2019). It is hypothesized that hydrodynamic shear contributes to the breakdown of solid foods by wearing away the particle surface. Previous researchers observed such

breakdown using an in vitro digestion model that applied fluid shear to solid food particles (Kong and Singh, 2009a, 2008b).

2.2.3 *Enzymes relevant to gastric digestion*

The stomach is well-known as a site of proteolysis due to pepsin, which has its highest activity in the low pH of the gastric environment. Pepsinogen, an proenzyme form of pepsin, is secreted by chief cells and becomes active when the pH of the surrounding fluid is < 2.0 (Barrett, 2014). In addition to pepsin, human gastric lipase is secreted which may be responsible for 10-30% of total lipid digestion (Gargouri et al., 1986; Maldonado-Valderrama et al., 2011). Human gastric lipase is active at pH values between 2.0 and 7.0 (Ville et al., 2002). There is no carbohydrate hydrolyzing enzyme secreted by the stomach, however, salivary α -amylase may retain activity during gastric digestion and act on starch provided the pH is > 3 (Nadia et al., 2021b). These conditions may occur in the proximal stomach where pH is elevated due to food buffering capacity (Mennah-Govela and Bornhorst, 2021b; Reynaud et al., 2020).

Considering the enzymatic hydrolysis in the gastric phase of digestion could have implications for food safety. For example, previous researchers cultivated a model plant in antibiotic-rich media, causing the plant tissue to phytometabolize antibiotic molecules, however, these antibiotics were chemically modified by glycosylation leading to low abundance of the original (parent) antibiotic molecule in the raw plant tissues (Keppler et al., 2021). However, the parent antibiotic molecules were recovered in the liquid digesta after subjecting the plant material to in vitro digestion due to the glycosylated antibiotic conjugates being hydrolyzed and the parent antibiotic molecules released. Overall, the abundance of the parent antibiotic molecules was 4-5 times greater in digesta than in extracts from raw plant tissues, suggesting that food safety studies on potential contaminants such as antibiotics may consider using in vitro digestion to understand the chemical modifications to these chemicals that could occur in the human body.

2.3 In vitro gastric digestion: Experimental methods and applications

In vitro gastric digestion refers to experiments that seek to recreate the conditions of the stomach without the use of living organisms. In vitro experiments are generally more rapid, inexpensive, and involve fewer ethical considerations than in vivo methods (Colombo et al., 2021). In vitro experiments may also be more reproducible as they do not contend with the inter-individual variability in the digestive system of living organisms, and can test the effect of experimental variables that cannot be modified in vivo (Bornhorst et al., 2016b). For example, in vitro digestion systems can easily be carried out without a certain enzyme to test its effect on the digestion of a certain food, or can carry out digestion without simulated peristalsis to isolate the biochemical effects of food breakdown due to gastric juice.

Results from in vitro digestion experiments on different foods may be directly comparable between different laboratories if the same experimental protocols are followed. To this end, the INFOGEST research network has developed international consensus protocols for in vitro digestion that prescribe the composition of simulated digestive fluids as well as the ratios of food to digestive fluids (Brodkorb et al., 2019; Minekus et al., 2014). The international consensus protocol established by Minekus et. al., (2014) represents a significant development in the field of digestion research. Nevertheless, opportunities for future research to improve in vitro digestion protocols remain. For example, the current protocol recommends a constant pH of 3.0 be maintained throughout the gastric phase which does not reflect the dynamic pH changes that occur during gastric digestion, which are influenced by the buffering capacity of food (Mennah-Govela and Bornhorst, 2021b). Furthermore, simulated mastication remains a challenge with no currently available method to establish a realistic distribution of food particle sizes that would result from mastication in vivo, due to physiological feedback that adjusts mastication parameters based on food properties. Additionally, the consensus developed by Minekus et. al., (2014) does not recommend mucin in the simulated gastric juice in spite of the fact that mucins have been demonstrated to lead to emulsion destabilization in the gastric environment due to charge screening effects that dominate those of electrolytes (Scheuble et al., 2018). The lack of mucin in gastric juice could lead to emulsions that are more stable in vitro than in the physiological reality, which could have important consequences as

emulsion stability in the stomach is associated with decreased gastric emptying rates and prolonged satiety (Leal-Calderon and Cansell, 2012).

In general, a drawback of in vitro approaches is the lack of a perfectly physiologically accurate model. This does not mean that results from in vitro experiments cannot relate to the in vivo reality, however, as a correlation between in vitro and in vivo results may be sufficient to classify or compare foods based on in vitro data and then predict corresponding in vivo results (Bohn et al., 2018). This could be useful for screening food products before conducting more resource-intensive in vivo trials to confirm findings. This approach is used in the pharmaceutical industry to assist in the development of drug delivery systems and has led to a classification system for the disintegration profiles of drug delivery systems in the simulated gastric environment (Amidon et al., 1995). Previous researchers have discussed the different levels of in vitro in vivo correlations in the context of food digestion and identified the conditions under which in vitro in vivo correlations can be expected to occur (Bornhorst et al., 2015).

2.3.1 *Models of gastric digestion*

In vitro experiments have been carried out using both static and dynamic models of gastric digestion. Previous researchers have defined static models as those seeking to recreate the biochemical environment of the digestion system including appropriate enzymes, ratios of gastric fluids to food, and duration of time that is spent by food in the gastric environment, but without attempting to recreate the physical motion of the stomach (Colombo et al., 2021). Semi-dynamic models have been defined as those with accurate representation of biochemical conditions as well as some degree of physiological motility, emptying patterns, or changing levels of pH over time (Mulet-Cabero et al., 2020). Finally, dynamic models attempt to recreate the conditions of the stomach with as much resemblance to the physiological reality as possible (Dupont et al., 2019). These models may include simulated peristalsis (Keppler et al., 2020), control schemes for pH and temperature (Mennah-Govela et al., 2021), and intermittent emptying profiles to dispense digesta from the dynamic in vitro digestion system (Hayes et al., 2020).

The classification of in vitro digestion models as either “static” or “dynamic” is not sufficient to determine the nature of the system being used. For example, many static in vitro digestion models use either a shaking water bath (Mennah-Govela and Bornhorst, 2016a) or rotary shaker (Toro-Uribe et al., 2019) to mix the contents of the digestion, yet both could be referred to as static in vitro digestion systems according to the terminology in widespread use. Some static in vitro digestion systems simulate gastric emptying through progressive withdrawal of samples (Mulet-Cabero et al., 2019), or involve a simulated mastication step before the gastric phase so that the initial size of food particles is realistic (Floury et al., 2018). A more systematic classification system for in vitro digestion models is urgently needed and is suggested as an opportunity for future research. Such a classification system could develop a standardized reporting format for the conditions used in the in vitro digestion experiment including the composition of simulated digestive fluids and the timing of their addition, which could help to identify important differences between the methods used in different laboratories.

Finally, in silico approaches to studying digestion have been increasingly used. A recently developed multi-response model of lipid digestion has been found to closely correlate with in vivo data ($R^2_{\text{adj}} > 0.986$) (Verkempinck et al., 2019). The effect of pH and food composition on the transport of fluids into food matrices has been taken into consideration using numerical solutions to Darcy’s law for unsaturated porous media, and the model was shown to allow for prediction of the rate of soluble solids loss by cheese during gastric digestion (Van Wey et al., 2014). These approaches have been reviewed in detail by previous researchers (Le Feunteun et al., 2021, 2020).

2.3.2 Conditions used in static and dynamic models of gastric digestion

To simulate the conditions of the human stomach, previous researchers have developed static and dynamic models with varying designs. Static in vitro digestion models generally are conducted by placing food and simulated gastric juice in a glass flask or beaker in a shaking water bath (100 rpm, 37 °C). Simulated gastric juice incorporates sodium chloride, hydrochloric acid, mucin, and pepsin (Mennah-Govela and Bornhorst, 2016b) but may also include additional electrolytes (Minekus et al., 2014). The

ratio of simulated gastric juice to food used in previous experiments ranges from 1:1 (Egger et al., 2017) to 6:1 (Drechsler and Bornhorst, 2018; Swackhamer et al., 2022), however, the amount of saliva used for in vitro oral processing may also be included in this ratio. It has been recommended to use a ratio of simulated saliva to food of 1:1, followed by a 1:1 ratio of (simulated saliva + food):simulated gastric juice (Minekus et al., 2014). Some experiments have not involved the use of simulated saliva during simulated oral processing of food, which has been considered acceptable when the objective is to understand the breakdown of the food during gastric digestion, and the food contains little to no starch. This method, where food particles were generated in the absence of simulated saliva, has been used for in vitro digestion experiments involving almond particles (Grundy et al., 2015b; Mandalari et al., 2008; Swackhamer et al., 2019). Dynamic models of gastric digestion seek to recreate the motility of the stomach in addition to the biochemical environment. Unlike static models that generally combine food and simulated gastric juice at the beginning of the experiment, dynamic models may begin with a small volume of simulated gastric juice (ca. 75 mL) and then secrete additional simulated gastric juice at a rate of approximately 2.5 mL/min (Guo et al., 2015, 2014a; Hayes et al., 2020). Recently, the rate of secretion of simulated gastric juice has been carried out at varying rates according to intragastric pH (Table 2.1) which was based on in vivo data from a study using a growing pig model (Nadia et al., 2021b). Both of these approaches have been referred to as dynamic models of in vitro digestion even though they differ by using either constant secretion rates of simulated gastric juice or variable secretion rates based on intragastric pH, suggesting the need for a more systematic terminology to classify in vitro digestion systems.

Table 2.1. Secretion rate of simulated gastric juice in the HGS based on the measured intragastric pH (Mennah-Govela et al., 2021), based on data from in vitro digestion in a growing pig model (Nadia et al., 2021b).

Measured pH inside the HGS	Flow rate of simulated gastric juice (mL/min)
$5 \leq \text{pH}$	9.0
$4 \leq \text{pH} < 5$	6.0
$3 \leq \text{pH} < 4$	3.0
$2 \leq \text{pH} < 3$	2.5
$\text{pH} < 2$	1.5

Dynamic in vitro models of gastric digestion may apply simulated peristalsis using rollers driven by belts (Kong and Singh, 2008b), chains (Phinney, 2013), or ropes (Wang et al., 2019). Alternatively, contractions have been applied using pneumatically-actuated pistons (Li et al., 2019). Computer control systems with sophisticated human machine interfaces have been developed to allow for modification of experimental variables in the dynamic in vitro model (Barros et al., 2016). Dynamic gastric digestion models have been developed specifically to resemble the digestion system of infants (Bellmann et al., 2019; Oosterveld et al., 2016), the elderly (Denis et al., 2016) or animals such as rats (Wu et al., 2017), pigs (Avantaggiato et al., 2007; Martinez et al., 2013), or dogs (Smeets-Peeters et al., 1999). Models have developed 3D printed stomach chambers using molds based on cadaver tissues (Barros et al., 2016; Ranganathan et al., 2021). Dynamic in vitro digestion systems have been developed specifically to study gastric emptying (Wang et al., 2019), gastric mixing (Kozu et al., 2017), and particle breakdown (Wang et al., 2021). Dynamic in vitro digestion systems have been developed that can be studied using positron emission particle tracking to determine the paths made by food particles during digestion (Keppler et al., 2020), or that can be outfitted with particle imaging velocimetry devices (Kozu et al., 2014) or magnetic resonance imaging devices (Deng et al., 2022). An in vitro model developed by The Netherlands

organization for applied scientific research (TNO), referred to as the TNO (gastro)-Intestinal Model (TIM) system includes a dynamic gastric digestion model that connects directly to dynamic in vitro simulator of the intestines (Denis et al., 2016; Minekus et al., 1995). This paradigm of linking dynamic in vitro digestion systems in parallel could one day lead to simulation of the entire digestion system of the human body. Despite these advancements, one area of need is the development of multiplexed dynamic gastric models, as the use of single-chamber, 1:1 physiological-scale models presents drawbacks in terms of experimental throughput and cost. A more rapid method to screen food materials for health-promoting properties could result from the availability of a dynamic in vitro gastric digestion model with higher throughput. The advantages and limitations of currently available dynamic in vitro gastric digestion systems has been reviewed by previous researchers (Dupont et al., 2019; Liu et al., 2020).

Enzymes of porcine origin are commonly used during in vitro digestion studies (Minekus et al., 2014). Porcine pepsin is used in the formulation of simulated gastric juices. It has a high degree of structural homology with human pepsin (Fujinaga et al., 2008) as well as comparable hydrolysis kinetics (Tritsch and Sachatello, 1971). Porcine pancreatin contains enzymes necessary to prepare simulated intestinal juices. On the other hand, there is no commercially-available substitute for human gastric lipase, although previous researchers have reviewed the advantages and disadvantages of various potential substitutes (Sams et al., 2016). One drawback of commonly used substitutes for human gastric lipase is a lack of preference to hydrolyze triacylglycerol molecules at the sn-3 position, which is a characteristic of human gastric lipase (Rogalska et al., 1990). This may result in a reduced prevalence of 1,2-diacylglycerols as compared to the physiological reality (Guo et al., 2020). Additional considerations in the selection of an appropriate analogue for in vitro studies are that human gastric lipase is partially resistant to hydrolysis by pepsin and stable at low pH (Ville et al., 2002). Due to its partial resistance to pepsin and stability at low pH (Sams et al., 2016; Zentler-Munro et al., 1992), Lipase A derived from *Aspergillus niger* has been selected by previous researchers as appropriate analogue for human gastric lipase (Abrahamse et al., 2012b; Pinheiro et al., 2013).

2.3.3 Use of model foods for *in vitro* digestion

Model foods can be considered similar to model organisms. In the case of model organisms, the objective of studying *E. coli*, yeast, and *Arabidopsis* is not to develop a perfect understanding of only three organisms, but instead to obtain insights into the biology of bacterial cells, eukaryotic cells, and plants, respectively. By analogy, model foods are foods that can be used obtain insights that generalize to other foods with similar properties. There are too many foods to subject each one to *in vitro* digestion experiments, but by studying the breakdown of model dairy gels, for instance, insights into the digestion of cheese and other dairy products can be obtained (Fang et al., 2016). Model foods with the same protein content but varying texture have been developed in order to study the effect of texture on satiety (Campbell et al., 2016). Model foods with varying rheological properties have been developed to understand human sensory perception of food physical properties (Santagiuliana et al., 2018). By embedding peanuts in model food matrices with varying texture properties researchers were able to determine links between food texture and the sizes of particles in the bolus (Hutchings et al., 2012). Whey protein hydrogels were used as a model food to determine the factors such as protein content and particle size which affect buffering capacity of foods in the gastric environment (Mennah-Govela and Bornhorst, 2021b), and the factors that influenced buffering capacity of the model foods were found to relate to those that influenced buffering capacity of commercial food products (Yamile A Mennah-Govela et al., 2020), highlighting the usefulness of model foods to better understand gastric digestion.

Advantages of model foods can be an increased ability to control formulation, processing, and texture variables during laboratory experiments. Additionally, model foods with specific purposes have been designed, such as whey protein (Luo et al., 2017; Thévenot et al., 2017) or egg white gels (Somaratne et al., 2020b) to enable the diffusion of fluorescent labeled pepsin to be measured and related to the microstructure of the gel. A model food was developed to study how inclusion in a food matrix could modulate the bioaccessibility of ingested nanomaterials (Zhang et al., 2019b) or lycopene (Zhang et al., 2019a). In general, these studies have demonstrated that both the macronutrient composition of the food matrix as well as its structure can influence the bioaccessibility of nutrients during *in vitro* digestion.

Considering these previous studies, an important gap in the literature is that there is not currently a model solid food available which has macronutrient composition based on the average diet consumed by individuals in the United States. Recently, a model food based on the Standard American Diet was developed, but only in powder or liquid form (Zhang et al., 2019b). Using a model food based on the Standard American Diet could allow results from controlled release studies to be more generalizable to the broader population than studies conducted using model foods that incorporate only one macronutrient (such as whey protein gels or egg white gels), as consumers may intake multiple macronutrients in the same meal. Additionally, the availability of such a model food in solid form is important, as ca. 80 % of total calories consumed in the Standard American Diet are from solid foods (Mesirow and Welsh, 2015).

2.4 Food physical properties and their influence on food breakdown

Physical properties of foods may be categorized as extrinsic when the property is influenced by the size or shape of food particles, or intrinsic when the property is intensive to the food material itself (Campanella, 2011). Intrinsic properties have also been referred to as material properties by previous researchers (Harrison and Cleary, 2014). Material properties related to stress and strain relationships such as Young's modulus or shear modulus are considered intrinsic properties (Skamniotis and Charalambides, 2020) in addition to properties that relate to work or energy necessary to cause unit changes in surface area such as toughness or surface tension (Vincent et al., 1991). Food composition variables are considered intrinsic properties, including fat content, protein content, mineral content, and sugar content, as well as pH and water activity (Ranganathan et al., 2016). Sensory variables such as crispness have been considered intrinsic food properties (Chen et al., 2005), but such variables are defined only at the level of a particular consumer and not according to definitions from the field of materials science (Szczesniak, 2002). Additionally, sensory properties of foods are known to change rapidly over time even in ambient conditions (Rico et al., 2007). In summary, various properties can be defined for foods including intrinsic and extrinsic properties, compositional properties, and sensory properties. Determining the influence of food properties on the digestion process is an ongoing area of investigation.

Previous researchers reviewed the influence of food properties on mechanical breakdown during gastric digestion (Somaratne et al., 2020a) and proposed that soft foods such as baked goods tended to break down due to fragmentation whereas foods with a hard surface such as carrots broke down due to erosion (Ferrua et al., 2011). Previous in vivo research using MRI showed that agar gel beads with a hardness greater than 0.65 N were not broken down during gastric digestion, whereas those with lower hardness were susceptible to fragmentation (L. Marciani et al., 2001a). This study helped to estimate the relative magnitude of force applied to particles during digestion, but a limitation of the study was that the initial hardness of the particles may not have been the same as the hardness at the time fragmentation occurred, due to exposure to gastric juice. It has been stated that food particles fragment when the external destructive force due to contact with other bodies in the stomach exceeds the internal cohesive force of the particle (Ferrua et al., 2011; Kong and Singh, 2008a). However, it is not yet clear which properties influence the cohesive force of a food particle.

The breakdown of foods in gastric digestion has parallels to mastication, where food particles are contacted by saliva, teeth, and other particles until they are reduced to a small enough size to permit swallowing (Chen, 2009b; Harrison and Cleary, 2014). The fracture properties of foods are particularly influential during mastication (Koç et al., 2013). These properties include toughness and critical stress intensity factor, and their relation to mastication has been reviewed by previous researchers (Swackhamer and Bornhorst, 2019). During mastication and gastric digestion, loading geometries between food particles and contacting bodies are complex. This may include contact between food particles and other food particles, teeth, or stomach walls. Previous researchers have analyzed the contact between a food particle and tooth under simplified loading geometries in order to determine relationships between breakdown and mechanical properties of the food such as toughness and Young's modulus, resulting in the establishment of displacement-limited and stress-limited indices for food breakdown (Agrawal et al., 1998, 1997; Agrawal and Lucas, 2003). This demonstrates that the breakdown of the food particle had a different relationship with its mechanical properties depending on the loading geometry. Nevertheless, such work demonstrates that simplifying the loading geometries between food and contacting bodies in a

complex system can be used to obtain insights about the relationship between particle breakdown and the mechanical properties of the particle (Berthaume, 2016). Based on the results obtained for mastication, it is hypothesized that the mechanisms of breakdown that affect solid foods in gastric digestion will depend on the initial properties of the food as well as the changes in food properties that occur over time during gastric digestion. Previous researchers have recommended the measurement of food physical properties over time during digestion, although more data is needed (Bornhorst et al., 2015).

2.4.1 *Texture change of foods during gastric digestion*

Investigating the texture change of foods during gastric digestion is an active area of research. One texture property that has been established by previous researchers is hardness, defined as the maximum force exerted by a food particle on a flat plate during uniaxial compression to 50 % engineering strain (Bornhorst et al., 2015). The hardness of sweet potato (Mennah-Govela and Bornhorst, 2016b, 2016a), apple (Olenskyj et al., 2020), and egg white gels (Somaratne et al., 2020d) has been shown to decrease over time during *in vitro* gastric digestion.

The hardness of carbohydrate-based food particles was measured over time during digestion and it was found that certain food products such as pretzel experienced more rapid softening than foods such as pasta (Drechsler and Bornhorst, 2018). The use of simulated gastric juice led to a more rapid decrease in hardness in apple than when acidic water was used (Olenskyj et al., 2020). These results support the use of hardness to characterize the softening kinetics of foods during gastric digestion as it displays changes that are sensitive to the presence of simulated gastric juice and not merely related to moisture or temperature effects.

2.4.2 *The Food Breakdown Classification System*

To meet the need for an increased understanding of food breakdown during gastric digestion, previous researchers have developed a Food Breakdown Classification System (FBCS) (Bornhorst et al., 2015). The FBCS includes a protocol for testing food breakdown, in which 10 mm cubes of food are subjected to simulated gastric digestion in a shaking water bath. The breakdown behavior can be

classified into six categories based on the initial hardness of the cube and its softening half time. Hardness is defined as the maximum force that the cubical particle exerts on a probe during compression to 50% engineering strain. The softening half time is defined as the time during simulated gastric digestion when the cube's hardness is half of its initial value. The softening half time is appropriately determined by curve fitting the data consisting of normalized hardness (y variable) onto digestion time (x variable) using the Weibull function. This approach has been validated by previous studies, and it was shown that kinetic parameters from the Weibull function fit to hardness data are not strongly influenced by the duration of the experiment or by the level of strain used to define hardness. Specifically, it was shown that in vitro digestion experiments on carbohydrate-based foods could be carried out for 60-240 min, with the resulting kinetic parameters describing changes in hardness not strongly affected (Drechsler and Bornhorst, 2018). Additionally, experiments used model hydrogels showed that defining the dependent variable for Weibull analysis (hardness) at levels of strain between 20-60% did not affect the resulting kinetic parameters (Swackhamer et al., 2022). The classification of carbohydrate-based foods according to the FBCS (Drechsler and Bornhorst, 2018) were furthermore shown to align with trends in gastric emptying rates (Nadia et al., 2021b) and glycemic indices (Atkinson et al., 2008; Foster-Powell et al., 2002) for similar food products as reported by previous researchers. Taken together, these results show that the FBCS successfully classifies food according to breakdown rates during gastric digestion and may furthermore be predictive of physiological response to consumption of food products with varying rates of breakdown during gastric digestion. It is recommended that future researchers classify additional foods according to the FBCS. Future work could involve establishing correlations between hardness and particle size change during digestion.

2.5 Summary

Food digestion is essential for human life. Although much progress has been made in the scientific advancement of the food system, significant resources are expended in producing food which result in negative environmental consequences. Through design of functional food products it could be possible to

reduce environmental impacts, for example by using insect proteins or lab-grown proteins (Herrero et al., 2020), or alternatively to optimize human nutrition, such as by designing foods with rapid glucose hydrolysis for athletes or slow glucose hydrolysis for patients with diabetes (Bornhorst, 2012).

The overall process of food digestion consists of oral digestion, esophageal transit, gastric digestion, small intestinal digestion, large intestinal digestion, and excretion. Previous researchers have identified unit operations that parallel the different stages of food digestion (Bornhorst et al., 2016b). This approach could be used to help apply existing knowledge of industrial processing systems to better understand the body, and eventually even develop personalized medicine for consumers by understanding the intricacies of the digestive system that lead to inter-individual differences (Corral-Acero et al., 2020; Shani-Levi et al., 2017).

Food breakdown during gastric digestion is an important aspect of the overall digestion process with impacts on gastric emptying and satiety. To better understand food breakdown during gastric digestion, in vivo experiments have been carried out using a growing pig model to characterize the process-related changes that occur to food particles during the gastric phase (Bornhorst et al., 2013a, 2013e; Bornhorst and Singh, 2013). In vitro approaches have also been developed, which have the advantages of reduced cost and ethical considerations but suffer from the drawbacks associated with the lack of a perfectly physiologically-representative digestion model (Dupont et al., 2019; Somaratne et al., 2020a). In vitro models have been classified as either static or dynamic, although future researchers may consider establishing a more comprehensive terminology to better describe the differences between the available in vitro digestion systems.

Food physical properties have been shown to influence the breakdown of foods in the gastric environment, however, more data is needed to fully understand the relationships between food composition, structure, processing, and breakdown during gastric digestion and the associated impacts on the human body.

Chapter 3 Review of Literature Part II: Fracture properties of foods: Experimental considerations and applications to mastication

Originally published as:

Swackhamer, C., Bornhorst, G.M., 2019. Fracture properties of foods: experimental considerations and applications to mastication. *J. Food Eng.* 263, 213–226. <https://doi.org/10.1016/j.jfoodeng.2019.07.002>.

Rationale

In this chapter, research on the fracture properties of foods was reviewed. Food breakdown during oral processing has parallels to food breakdown during gastric digestion as both steps involve particle size reduction of foods. However, more research has been conducted on the breakdown of food particles in the mouth than during gastric digestion, and thus reviewing literature of the mastication process is important to the study of food breakdown during digestion. Additionally, the processing of foods in the mouth determines the initial condition of food particles entering the stomach, which suggests that food breakdown in the mouth is an important consideration for understanding food breakdown in the stomach. Selected fracture properties defined in this section were assessed for the model foods (initially developed in Chapter 4) in Chapter 7. Methods described in this section, such as uniaxial compression, wire cutting, and knife cutting, were used in Chapter 7 and thus reviewing the literature on these methods provided important context for the later chapters in this dissertation.

Abstract

Foods are broken down during oral processing, which for solid foods often involves fracture. The aim of this article is to review previous research applying fracture mechanics to mastication, the effect of selected physiological variables on the fracture of foods in the mouth, and certain experimental methods that can be used to quantify the fracture properties of foods relevant to mastication. Fracture mechanics defines food properties that influence mastication, such as fracture stress, fracture strain, and toughness. Additionally, fracture mechanics provides a quantitative way to interpret the effect of physiological variables that influence the fracture of foods in the mouth, for example saliva, temperature change, and variations in strain rates applied by the teeth for different types of food. Previous research has determined displacement and stress-limited indices to link fundamental fracture properties of foods to their behavior during mastication. There are several experimental methods to measure the fracture properties of foods, which include compression, wedge, puncture, and tensile tests. Finally, there are opportunities for future studies to establish structure—property—oral processing relationships, which could inform the design of novel processes and products.

3.1 Introduction

Oral processing is the first step in food digestion (Chen, 2009b). Oral processing refers to the combination of mastication (chewing), lubrication, and transport of food particles that results in bolus formation and swallowing. For solid foods, breakdown during mastication often involves fracture, the cleavage of food particles into smaller pieces (Koç et al., 2013). The relative ease or difficulty of fracturing food influences mastication variables such as the time before swallowing and the number of chews (Lucas et al., 2002). This in turn affects consumer preference (Szczesniak, 2002), satiety (Campbell et al., 2017), and nutrient absorption, by influencing the particle size distribution of fractured food particles that enter the digestive system (Gebauer et al., 2016). Increased knowledge about the mechanisms of food fracture could inform the design of products for targeted health outcomes or for consumption by individuals with challenges in mastication, for example the elderly (Xu, 2016). There is a need for additional studies that evaluate the properties of foods using a fracture mechanics approach, as well as a need for studies that quantify the relationships between food fracture properties and the physiological variables of mastication.

The aims of this review are to summarize the application of fracture mechanics to foods, discuss the influence of selected mastication variables (such as temperature and saliva) on the fracture process, and to present instrumental-mechanical methods to measure food fracture properties.

3.2 Fracture properties of foods

Fracture mechanics is a physical way of understanding the breakage of solids under large deformation (van Vliet, 2014). Previous studies have found that food properties measured under large deformation were more influential to human mastication than those measured under small deformation (Kohyama et al., 2008). This suggests the usefulness of studying food fracture to better understand food breakdown during mastication.

Fracture is a stochastic process, but the use of fracture mechanics allows the measurement of intrinsic food properties. Intrinsic properties depend on the material a food is comprised of, and do not depend on test parameters or sample geometries. Intrinsic properties relevant to fracture include Young's modulus,

fracture stress, fracture toughness, and the critical stress intensity factor (Atkins and Mai, 1985; Ross and Scanlon, 2004).

3.2.1 *Steps in the fracture process*

A fundamental concept in fracture mechanics is that all materials contain inhomogeneities, which are often called stress-concentrators because in their vicinity the local stress is higher than in the bulk of the material (Sala et al., 2009). When local stress reaches the fracture stress of the material an existing stress-concentrator may extend, forming a crack (Luyten et al., 1992). Fracture can be stopped when the crack becomes blunted, such as by intersecting a larger inhomogeneity in the food sample (Saeleaw and Schleining, 2011a). Therefore, the cracking mechanism has four steps:

1. Crack initiation
2. Crack extension or stoppage
3. Crack reaching boundary region
4. Failure

Thus, fracture requires the extension of a crack through a sample, which results in the following structural changes (Koç et al., 2013):

1. Breakage of bonds between structural elements in a macroscopic plane
2. Structural change on a length scale greater than the size of individual structural elements
3. Breakage of the test sample into multiple pieces

Fracture results in the creation of new surfaces and thus requires an input of energy (Courtney, 2005). Tougher materials require greater energy input to fracture. The relationship between energy input and surface creation enables the energy approach to fracture.

3.2.2 *Energy approach to fracture*

During deformation of a food sample, energy is imparted by the contacting object (ex. testing apparatus or teeth) and stored by the sample as elastic strain energy. When fracture occurs, energy is released as stress relaxes in the material surrounding an advancing crack and a new surface is created

(Luyten and Van Vliet, 2006). The following balance has been used to describe the energy of the fracture (Luyten et al., 2005):

$$U_s = U_f + U_p + U_d + U_e \quad 3.1$$

Where U_s is the total system energy, U_f is fracture energy, U_p is energy dissipated due to plastic deformation, U_d is the energy dissipated by other processes, and U_e is elastically stored energy (Luyten et al., 2005). All quantities have units [J]. Under linear elastic conditions, U_p and U_d are zero (Williams and Patel, 2016).

The total energy applied to the system can be expressed as $U_s = \int_0^h F(x)dx$, where F [N] is the force applied to the sample, x [m] is displacement, and h [m] is the net displacement achieved over the entire deformation (Luyten et al., 2005). This is a simplified approach, but useful because many experimental devices used to deform food samples contain a load cell which measures force.

The fracture energy, U_f , is the energy required to create new surfaces and is given by $U_f = RA_f$, where R [J/m²] is the toughness and A_f [m²] is the new surface area created during the fracture event (Luyten et al., 2005).

In food materials, which are not perfectly elastic, there is plastic deformation during fracture in the vicinity of the crack tip. Modeling the energy dissipated by plastic deformation, U_p , is a subject of current research, so there is no universal expression for this term (Boisly et al., 2016; Faber et al., 2017b). The plastic dissipation of energy is important because fracture energy can only come from the elastically stored strain energy of the sample (Atkins and Mai, 1985; Vincent, 2004). In other words, plastic deformation takes away energy that might otherwise be used to create new surfaces, contributing to the difficulty of fracturing foods like caramels during mastication, which dissipate significant energy by plastic deformation (Luyten et al., 2005).

There is no complete expression for the energy dissipated by other processes, U_d , but in fracture events involving foods it often includes sound wave production (Saeleaw and Schleinig, 2011b;

Taniwaki and Kohyama, 2012). Likewise, there is no universal expression for the elastically stored energy, U_e , as it depends on the geometry of the sample.

3.2.3 *Criteria for fracture*

For a crack to advance the system energy must go down (Courtney, 2005). Thus, whether a certain crack of length a [m] advances can be understood using:

$dU_s/da < 0$, crack extends

$dU_s/da = 0$, crack at unstable equilibrium

$dU_s/da > 0$, crack heals

For a crack to extend at constant rate the elastically stored strain energy, U_e , must be converted to fracture energy (consumed by surface creation) at the same rate that it is provided by the deformation of the sample (Sala et al., 2009). This can be described as:

$$\frac{dU_e}{da} = \frac{dU_f}{da} \quad 3.2$$

The elastically stored strain energy in a deformed sample depends on material properties and sample geometry, and thus the relationship between stored strain energy and stress can be complex. For more detail on such relationships the reader is referred to Atkins and Mai (Atkins and Mai, 1985) and Bower (2010). However, if the simple case of a large, thin sheet in plane stress is considered, the elastic energy can be expressed as $\pi\sigma^2 a^2/E$, where E [Pa] is Young's modulus (Courtney, 2005). Substituting into Equation 3.2 yields a statement that is true for steady crack extension in a thin sheet:

$$\frac{d}{da} \left(\frac{\pi\sigma^2 a^2}{E} \right) = \frac{d}{da} (2aR) \quad 3.3$$

Where R [J/m²] is the toughness and σ [N/m²] is the stress. By considering Equation 3.3 when the stress is equal to the fracture stress, σ_f , an expression for the fracture stress in terms of fundamental material properties and crack length is reached (Courtney, 2005):

$$\sigma_f = \left(\frac{RE}{\pi a} \right)^{1/2} \quad 3.4$$

For food samples with appreciable thickness, plane strain better describes the stress state (Berthoume, 2016), and the fracture stress is given as:

$$\sigma_f = \left(\frac{RE}{\pi a(1 - \nu^2)} \right)^{1/2} \quad 3.5$$

Where ν [m/m] is the Poisson ratio. During mastication, the fracture stress as given by Equations 4 and 5 is achieved at small inhomogeneities in the food (acting as stress-concentrators), which leads to crack extension (Luyten et al., 1992). The effect of this stress concentration is quantified by the stress intensity factor:

$$K = \sigma_o Y (\pi a)^{1/2} \quad 3.6$$

Where K is the stress intensity factor [$\text{Pa}\cdot\text{m}^{1/2}$], σ_o [Pa] is the magnitude of the nominal stress applied to the food sample, and Y [dimensionless] is a geometrical factor accounting for crack shape and sample geometry. Values of Y are given by Pilkey and Pilkey (2008).

Crack extension occurs when the stress intensity factor reaches a critical value, K_C . By taking Equation 3.6 at the point where conditions for fracture are met ($\sigma_o = \sigma_F, K = K_C$) and equating with the definitions of fracture stress in Equations 4 and 5, expressions are found for the critical stress intensity factor in terms of material properties (Rojo and Vincent, 2008; Vincent, 2004):

$$K_C = (RE)^{1/2} \quad 3.7$$

$$K_C = \left(\frac{RE}{1 - \nu^2} \right)^{1/2} \quad 3.8$$

Equation 3.7 holds in plane stress and Equation 3.8 in plane strain. The critical stress intensity factor characterizes the ability of the material to resist the extension of an existing crack. A lower critical stress intensity factor, K_C , means that for a given stress state the material can tolerate only a small crack before it extends. During mastication, the critical stress intensity factor has been found to correlate well with the sensory attribute crispness/crunchiness ($r = 0.97, P < 0.001$) (Kim et al., 2012), suggesting that these sensory terms relate to the perceived ease with which cracks can be extended through a food sample.

3.2.4 Modes of fracture

There are three fundamental ways that fracture can occur, which are referred to as modes of fracture (Figure 3.1 A1, B1, C1). The steps in fracture and the energy approach to fracture, (Section 3.2.1-3.2.3) apply to any mode, but during mechanical testing it is important to identify the mode of fracture that the food sample experiences. This is because food properties can depend on the mode of fracture. For example, the critical stress intensity factor in mode I fracture, K_{IC} , may be different from the critical stress intensity factor in mode II fracture, K_{IIC} .

All three modes of fracture are relevant during mastication (Sanson, 2016). Mode I fracture (Figure 3.1 A3) occurs by tension or crack opening and has been considered the most significant of the three modes overall for food breakdown (Alvarez et al., 2000). It can be investigated using wedge tests (Luyten et al., 1992). More information on tests for experimentally evaluating food fracture properties is provided in Section 5. Mode II fracture (Figure 3.1 B3) occurs by edge-sliding/in plane shear, which can result from contact with molar cusps (Wright and Vincent, 1996). The punch and die test has been used to evaluate foods under mode II fracture (Alfonso et al., 2002). Mode III fracture (Figure 3.1 C3) occurs by out of plane shear/tearing by teeth, and has been investigated using scissor tests and double blade cutting systems (Anderson and LaBarbera, 2008). Most of the research in mastication has focused on mode I fracture, and thus an opportunity for future work is to analyze loading geometries between food and teeth that could give rise to fracture under modes II or III.

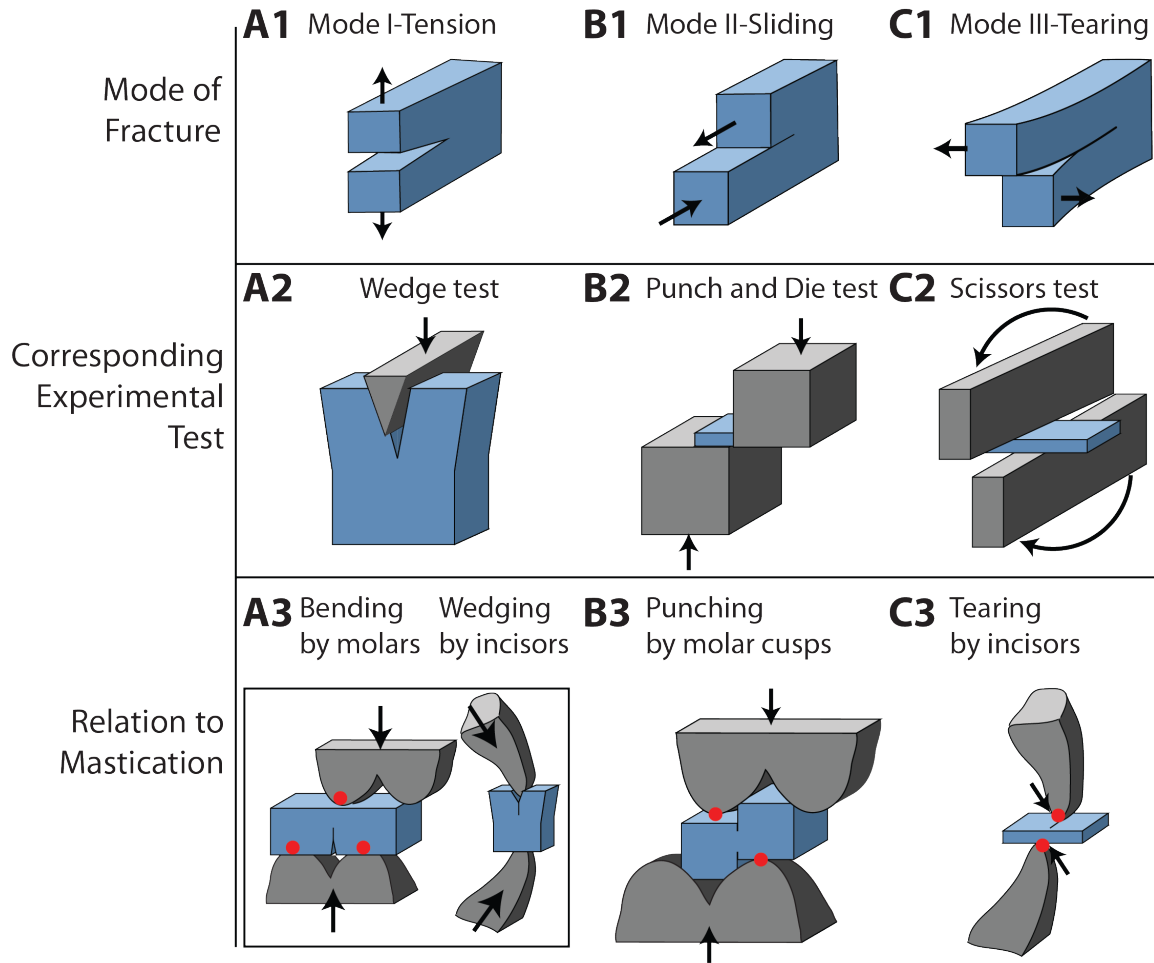


Figure 3.1: Examples of the three modes of fracture (A1, B1,C1), adapted from Berthaume, (2016). For each mode of fracture, examples of mechanical tests that lead to a fracture event in that mode are shown (A2, B2, C2) adapted from Berthaume, (2016). Similarly, loading geometries of teeth and a food particle are shown (A3, B3, C3) that may lead to each of the three modes of fracture. Red circles indicate contact points between teeth and the food particle. Mode I (A3) adapted from Agrawal et al., (1997) and Agrawal and Lucas (2003), mode II (B3) adapted from Xu (2016) and Zink et al., (2014), and mode III (C3) adapted from Wright and Vincent (1996).

3.3 Fracture indices for mastication

Engineering fracture mechanics can be used to define fracture properties of foods, including the toughness, R , fracture stress, σ_f , and the critical stress intensity factor, K_{IC} , but this approach does not

indicate how to best relate these properties to the breakdown of foods during mastication. Previous research has approached this by developing relationships between food breakdown and material properties for food particles subjected to certain loading situations that occur during mastication.

3.3.1 *Displacement-limited index*

Agrawal and Lucas (Agrawal et al., 1997) analyzed the loading of a food particle contacted at three points by molar cusps (Figure 3.2 A). Due to the shape of the tooth, the particle could not deflect more than a certain distance, and thus its ability to break was considered displacement-limited. Researchers proposed an index to relate the fracture properties of the food particle to its fragmentation under displacement-limited conditions. The fragmentation of the food particle was quantified by the amount of new surface area created during a single fracture event under displacement-limited conditions. The objective was to predict the fragmentation of different foods subjected to the same loading conditions based on their fracture properties. It was hypothesized that fragmentation would be related to fracture stress, σ_F , divided by the Young's modulus, E . Specifically, a food with a higher value of σ_F/E was hypothesized to experience a smaller increase in surface area than a food with a lower value of σ_F/E . To express σ_F/E in terms of food properties that could be experimentally measured, Equation 3.6 was taken at the critical case of mode I crack extension ($K = K_{IC}$ and $\sigma_o = \sigma_F$), combined with Equation 3.7 and divided by Young's modulus, giving:

$$\left(\frac{R}{E}\right)^{1/2} = \frac{\sigma_F(\pi a)^{1/2}}{E} \quad 3.9$$

Where R [J/m^2] is the toughness, E [Pa] is Young's modulus, σ_F [Pa] is the fracture stress, and a [m] is the crack length. Thus, $(R/E)^{1/2}$ was related to σ_F/E such that the quantity $(R/E)^{1/2}$ could be used as an index for the fragmentation of the food, under displacement-limited conditions. Stiff, brittle foods have a lower displacement-limited index than softer or tougher foods (Agrawal et al., 2000). It has been demonstrated (Figure 3.2 B) that foods with a lower displacement-limited index (ex. nuts, displacement-limited index ~ 3 [$\text{mm}^{1/2}$]) would generate a larger amount of new surface area when subjected to a single controlled compression under displacement-limited conditions than foods with a higher displacement-

limited index (ex. cheeses, displacement-limited index ~ 15 [$\text{mm}^{1/2}$]) (Agrawal et al., 1997). The influence of the displacement-limited index was further supported by a mastication study using standardized-volume portions of 15 different foods, in which displacement-limited index influenced total muscle activity during chewing, measured using electromyography (EMG) ($r = -0.86, P < 0.001$) (Agrawal et al., 1998). Another study found that the displacement-limited index influenced the closing angle of the jaw and the amplitude of jaw motion (Agrawal et al., 2000). Computational models using the finite element method have suggested that cracks can be initiated on the opposite side of a food particle from where it is contacted by molar cusps, lending further support to the idea that foods fracture under displacement-limited loading conditions (Berthaume et al., 2013).

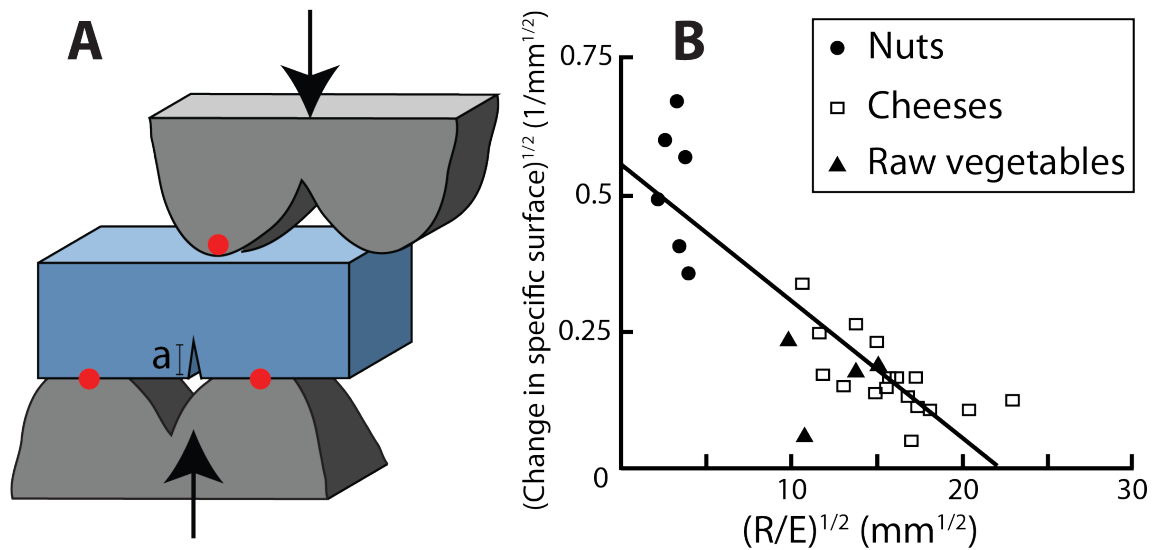


Figure 3.2: Example loading geometry of a food sample (shown in blue) acting as a beam between cusps (A). Red circles indicate points of applied force, and arrows indicate the direction. The crack length is labeled “a.” For this loading geometry, an example correlation (B) is shown between the change in specific surface area (measured using image analysis) and the displacement limited index. Modified from Agrawal et al., (1997).

3.3.2 Stress-limited index

In contrast to the loading geometry of the displacement-limited index, food can be contacted by an incisor tooth which initiates a crack directly at the contact point (Figure 3.3 A). It was found that under this loading geometry some foods fractured at small displacements relative to their thickness, since the fracture stress limited the fracture event prior to the fracture becoming displacement-limited (Agrawal et al., 1997). As a result, fracture of the food was considered stress-limited, and an alternative index for food breakdown was developed (Agrawal and Lucas, 2003). It was assumed that the material was in plane stress and fracture occurred at quasi-steady state, allowing Equation 3.6 to be equated with Equation 3.7 at the onset of fracture (Agrawal and Lucas, 2003), giving:

$$\sigma_F(\pi a)^{1/2} = (RE)^{1/2} \quad 3.10$$

Where σ_F [Pa] is the fracture stress, a [m] is the crack length, R [J/m^2] is the toughness, and E [Pa] the Young's modulus of the food. To experimentally test the validity of Equation 3.10, the Young's modulus, E , and the toughness, R , were measured for several test foods using instrumental methods, and the fracture stress, σ_F , and crack length, a , were measured after a controlled, single chew by a human subject (Agrawal and Lucas, 2003). A linear relationship was predicted between the quantity $(RE)^{1/2}$ and the quantity $\sigma_F a^{1/2}$ (Figure 3.3 B).

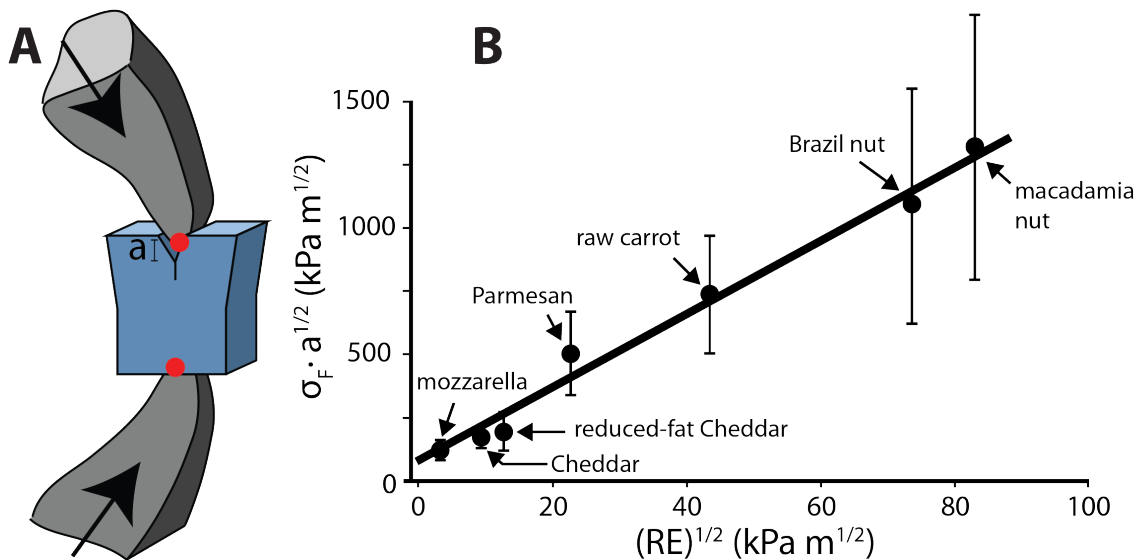


Figure 3.3: Loading geometry of an incisor driving a crack through a food particle, shown in blue (A). Red circles indicate points of applied force, and arrows indicate the direction. The crack length is labeled “a.” For this loading geometry, an example correlation (B) is shown between the product of fracture stress and crack length, measured during one chew, and the stress limited index $(RE)^{1/2}$, which was measured for the test foods using instrumental-mechanical methods. Modified from Agrawal and Lucas (2003).

3.3.3 Applications of displacement and stress-limited indices

The displacement and stress-limited indices have been used in many studies to describe the breakdown of foods during mastication (Laird et al., 2016; Vogel et al., 2014; Zink et al., 2014). The displacement-limited index allows for prediction of the relative increase in surface area for a food after loading in three-point bending between molar cusps, and the stress-limited index allows for prediction of the necessary combination of stress and crack length to cause fracture when a food is fractured directly at the point of contact with a tooth. Studies have qualitatively referred to foods as “displacement-limited” when they allow cracks to initiate easily but resist their propagation, which often includes meats (Vogel et al., 2014; Zink et al., 2014). Similarly, studies have referred to foods as “stress-limited” when they resist crack initiation but fail easily once a crack has been initiated, such as nuts (Vogel et al., 2014; Williams et al., 2005).

The predicted relationships between food behavior during mastication and stress and displacement-limited indices hold for a wide variety of foods, including vegetables, nuts, and cheeses (Agrawal and Lucas, 2003). One interesting finding has been that foods with a higher displacement-limited index (such as almonds) were chewed less efficiently than foods with a lower displacement-limited index (such as cooked chicken and sweet potato), when efficiency was defined as the change in the size of food particles divided by the work of chewing from EMG (Laird et al., 2016). Additional correlations between the stress and displacement-limited indices and mastication variables are summarized in Table 2.1.

A limitation of the stress and displacement-limited indices is that the classification of a food sample as “hard” or “tough” cannot be made by comparing the values of the two indices because such a comparison would only depend on the Young’s modulus of the food (Berthaume, 2016). In general, the stress and displacement-limited indices are useful but have limitations and should be considered a starting, rather than an end point for analyses relating food properties to food breakdown during mastication.

Table 3.1. Results from selected studies that explored relations between instrumentally measured properties of foods and mastication variables. The test food used in each study is indicated. The instrumentally measured property is shown, as well as the type of test used to obtain it where U: uniaxial compression test, P: puncture test, W: wedge test, C: cutting test, TPB: Three-point bending test, TEN: Tensile test. An upward pointing arrow indicates an increase in a certain instrumentally measured property, and its relationship with a specific mastication variable is indicated by the next arrow. For example, “↑ compression work: ↑ number of chews” indicates that a greater amount of work needed to compress the sample was associated with a higher number of chews before the food was swallowed.

Food sample	Instrumentally measured property	Test	Relation to mastication variables	Reference
Elastic (gelatin) and plastic (caramel) model foods	Hardness [N]	UC	↑ Hardness: ↑ time for oral processing, ↑ number of chews before swallowing, ↑ total impulse during mastication (from EMG), ↑ vertical amplitude of jaw during mastication	(Foster et al., 2006)

			(from electromagnetic induction motion tracking)	
Peanuts embedded in chocolate matrix	Chewiness, defined in terms of compression work [J]	UC	↑ Chewiness : ↑ number of chews before swallowing	(Hutchings et al., 2012)
Gels (gellan gum)	Fracture stress [Pa]	UC	↑ Fracture stress : ↑ time for oral processing, ↑ total impulse during mastication (from EMG)	(Kohyama et al., 2017)
Model brittle foods (tableted CaCO ₃ and cellulose)	Hardness [N]	P	↑ Hardness : ↑ total muscle activity on first three chews, ↑ muscle contractile duration (from EMG)	(Shiau et al., 1999)
Assorted Japanese foods	Maximum force [N]	P	↑ Maximum force : ↑ maximum bite force (from multiple point sheet sensor)	(Takahashi et al., 2009)
Bread (with crust)	Maximum force [N]	P	↑ Maximum force : ↑ total impulse during mastication (from EMG), ↓ mass fraction of large food particles at swallowing	(Gao et al., 2015)
Carrot, cheese, peanut, cake, gum, melba toast	Maximum force [N]	P	↑ Maximum force : ↑ chewing time, ↑ chewing work (from EMG)	(van der Bilt and Abbink, 2017)

Apple	Maximum force [N]	P	↑ Maximum force : ↑ hardness, ↑juiciness ↓ mealiness (from sensory analysis), ↑ total impulse during mastication (from EMG)	(Ioannides et al., 2009)
Cheese, nuts, raw carrot	Toughness, R [J/m ²], Young's modulus E [Pa], Stress-limited index $(RE)^{1/2}$ [Pa·m ^{1/2}], Displacement- limited index $(R/E)^{1/2}$ [m ^{1/2}]	W	↑ R, E, stress limited index : ↑ total impulse during mastication (from EMG) ↑ Displacement limited index : ↓ total impulse during mastication (from EMG)	(Agrawal et al., 1998)
Cooked chicken cooked sweet potato, raw sweet potato, celery	Toughness, R [J/m ²], Displacement- limited index, $(R/E)^{1/2}$ [m ^{1/2}]	W	↑ R, Displacement-limited index : ↓ chewing efficiency (change in particle size divided by chewing work, from EMG)	(Laird et al., 2016)
Beef muscle	Shear stress [N/m ²]	C	↑ Shear stress : ↑ mean impulse during mastication (from EMG)	(Mioche et al., 2003)
Various hydrocolloid gels	Cutting effort	C	↑ Cutting effort (from sensory analysis): ↑ chewing time, ↑ impulse during first stage of mastication (from EMG)	(Kohyama et al., 2015)

Processed cheeses	Maximum force [N]	TPB	↑ Maximum force : ↑ firmness, ↑ chewiness (from sensory analysis)	(Everard et al., 2007)
Cereals	Fracture force [N]	TPB	No significant correlation between fracture force and mastication variables chewing time, number of chews before swallowing (from EMG)	(Le Révérend et al., 2016)
Biscuits	Fracture stress [Pa], Critical stress intensity factor K_{IC} [Pa-m ^{1/2}]	TPB	↑ Fracture stress, K_{IC} : ↑ hardness, ↑ crispness, ↑ crunchiness (from sensory analysis on first bite)	(Kim et al., 2012)
Jelly and custard	Maximum tensile force [N], Impulse of tensile test [N-s]	TEN	↑ Maximum tensile force, impulse of tensile test : ↑ difficulty of swallowing (from sensory analysis)	(Chen and Lolivret, 2011)
Sticky semisolid foods	Maximum tensile force [N], Work of tensile test [J]	TEN	↑ Maximum tensile force, work of tensile test : ↑ stickiness (from sensory analysis)	(Chen et al., 2008)

3.4 Variables affecting food fracture during mastication

The application of fracture mechanics to food defines the fundamental fracture properties of food materials, including E , R , σ_f , and K_{IC} . However, there are additional variables during oral processing that influence the way foods fracture. Some of these variables have to do with the dynamic strain rates and multiple cycles of deformation that occur during mastication. Other variables have to do with the components of oral processing that do not directly involve contact of food by teeth, for example,

temperature and saliva. Lastly, foods are complex structures, and this can lead to fracture phenomena across multiple time and length scales.

3.4.1 *Variations in strain rates applied to foods by teeth*

Fracture mechanics have been reviewed (Section 3.2) for food materials under quasi-static loading conditions. However, loading conditions during mastication are dynamic. The rate that a food particle is deformed (strain rate) can vary within a single chew as well as between chews (Shimada et al., 2012; van der Bilt and Abbink, 2017).

Strain rates applied by the teeth during mastication may be influenced by food fracture properties (Mioche et al., 1999). The speed of teeth during the closing of the jaw (also called the occlusal phase of mastication) varies for different foods, with values between 34 mm/s (elastic model food) to 121 mm/s (soft gum) (Bhatka et al., 2004; Lassauzay et al., 2000). In general, tooth velocity is lower for foods with higher stiffness (Dan et al., 2007). This could be due to the fact that many materials cannot dissipate energy by plastic flow as rapidly as by fracture and thus contacting a food with high tooth velocity could lead to a stiffer response and too much force on the teeth, whereas a slower tooth speed allows the material to plastically deform and not lead to excessive force on the teeth (Lillford, 2011; van Vliet and Primo-Martin, 2011).

Although tooth speed varies for mastication of different foods, the speed of mechanical tests used to determine food properties is often chosen without regard for the speed that the food would be deformed by teeth in vivo. A future opportunity is to choose an appropriate test speed based on data from consumption of the same food by humans, which would require increased studies connecting food material properties to tooth speeds during mastication. This could be important as test speed has been shown to influence the results of mechanical tests involving food fracture. For example, a study found that uniaxial compression of almonds at 30 mm/s resulted in a particle size distribution of fractured particles that more closely reflected in vivo results than those from the same test conducted at 1 mm/s, likely because 30 mm/s was closer to the actual speed of teeth during mastication (Varela et al., 2008).

Modifying a test to account for variations in tooth speed during mastication could involve testing stiffer foods more slowly to better reflect their mastication in vivo.

3.4.2 *Multiple cycles of deformation*

In addition to tooth speed varying between foods, mastication of a food particle often requires more than one chew. This indicates the possibility for fatigue fracture, which occurs when multiple cycles of deformation cause a loss in mechanical toughness over time, ultimately leading to fracture (Courtney, 2005). Fatigue fracture still requires a concentration of stresses that extend a crack but differs from brittle fracture because it is preceded by multiple deformation cycles or a significant delay.

Due to the multiple cycles that typically occur during mastication, teeth periodically open and close. Food that remains stuck to teeth can experience fracture in tension as the jaw opens, which may involve ductile behavior of the food. Ductile fracture occurs due to tensile stresses. Previous research has suggested the importance of considering ductile fracture mechanisms in foods such as model gels and cooked apple (Dan et al., 2003; Harrison et al., 2014).

The multiple cycles of deformation that occur during mastication should be taken into consideration for selection of appropriate mechanical tests of food fracture properties. For example, tough or semisolid foods require many cycles of chewing, and thus instrumental-mechanical models used to study the behavior of these foods should consider applying multiple cycles of deformation to reflect their behavior in vivo.

3.4.3 *Saliva*

Oral processing was defined as the conversion of food into a swallowable bolus, and thus involves chewing, but also includes lubrication with saliva (Yven et al., 2010). The penetration of saliva into food changes its mechanical properties and helps prepare a swallowable bolus (Gao et al., 2015). Saliva acts as a plasticizer, which can affect the fracture properties of the food (Luyten et al., 2005). Water often acts as a plasticizer in foods, explaining why drying processes increase the tendency of a food to experience brittle fracture (Lewicki and Pawlak, 2003), whereas plasticizer addition (such as saliva) has the opposite

effect (Andreuccetti et al., 2012). Numerous studies have found a decline in brittle properties of foods with increasing moisture (Saeleaw et al., 2012).

In addition to moisture, saliva contains digestive enzymes, notably salivary alpha-amylase and lipase, which degrade the food and change its mechanical properties. Saliva also contains mucins, which give it a lubricating effect in the mouth (Carpenter et al., 2019). Overall, the effects of moisture, enzymes, and mucins in saliva can modify food properties and influence contact between teeth and food particles (Chen, 2009b). Nevertheless, instrumental testing of fracture properties often occurs in the absence of saliva. Thus, results from these tests are only descriptive of the food before it has absorbed saliva, which limits their utility for understanding fracture behavior of food after the first chew (Gao et al., 2015; Le Révérend et al., 2016). There is an opportunity to incorporate saliva (either real or simulated) into instrumental-mechanical tests of food fracture properties, especially if the objective is to understand the breakdown path of the food and not simply its properties on the first chew (van Vliet and Primo-Martin, 2011).

3.4.4 *Temperature*

During mastication, heat is transferred to food through contact with saliva and mouth surfaces. This may cause the food to transition from glassy and brittle to ductile (Van Der Bilt, 2011). Previous research has shown that higher temperature results in a loss of brittle behavior in foods (Schuldt et al., 2018). Since instrumental tests are often conducted at room temperature instead of physiological temperature, the results may not reflect the properties of the food after heating in the mouth (Harrison et al., 2014). Additionally, the interaction between temperature and plasticizer is important, because water decreases the glass transition temperature of many food materials (Lazou and Krokida, 2011). In other words, foods become more ductile/pliable with increasing temperature, but may experience this transition more rapidly under higher moisture conditions. A previous study found that less force was needed to chew a waxy model food after it had warmed up, indicating the importance of considering temperature effects on food properties that influence contact forces on teeth (Speksnijder et al., 2009). There is an opportunity to

develop novel instrumental-mechanical tests capable of controlling temperature to understand the fracture of food as it is heated during oral processing.

3.4.5 Fracture on multiple length scales

Foods can fracture on multiple length scales during mastication because the structural elements in foods exist at the nanoscale (nm), microscale (μm), as well as meso/macroscale ($mm - cm$) (Foegeding et al., 2017). Selection of an appropriate test for food fracture properties depends on identifying the length scales of interest. For example, indentation tests on tooth enamel have been conducted using micrometer-scale displacements to understand how teeth resist fracture during contact with hard foods (He and Swain, 2007). However, for the purpose of understanding how foods are fractured by teeth, testing occurs on $mm - cm$ length scales, because food particles must be reduced to roughly this size range before they can be assembled into a swallowable bolus (Bornhorst and Singh, 2012b).

The multiple length scales of fracture are especially relevant to foods with cellular structures, which refers to the food being comprised of a network of solid struts or plates surrounding cells, often filled with air (Ashby and Gibson, 1988; Butt et al., 2018). In these foods, fracture can occur on the length scale of a single cell (Mazumder et al., 2007) (Figure 3.4 A), but if the crack propagates, fracture can occur on the length scale of the entire food particle. Mechanical testing of cellular structures has been found to create jagged force vs displacement curves, with force rising as energy is stored elastically by the food and then periodically falling as energy is dissipated through fracture (Çarşamba et al., 2018). Previous research has found that brittle snack foods with larger air cells experienced a greater number of large force drops during uniaxial compression, and were perceived as more crispy during sensory evaluation (Rojo and Vincent, 2008; Vincent, 2004). Ensuring favorable sensory characteristics such as crispiness during mastication of a product is a goal in product and process engineering (Chen and Opara, 2013a).

Understanding the relevant length scales of fracture phenomena in food also has implications for mastication research. For instance, when a food sample is tested in compression, such as to mimic compression between molars, some of its structural elements may fracture due to tensile stresses as

observed by Stokes and Donald (Stokes and Donald, 2000) using bread (Figure 3.4 B). In this experiment, the food sample (length scale *cm*) fractured due to compressive forces, but some of its structural elements (length scale μm) fractured under tension. Understanding the multiscale fracture phenomena of food products is an opportunity in engineering functional foods, as small scale fractures may contribute to a large increase in surface area of fractured food particles entering the digestive system, influencing the kinetics of nutrient release from solid food matrices (Bornhorst et al., 2015).

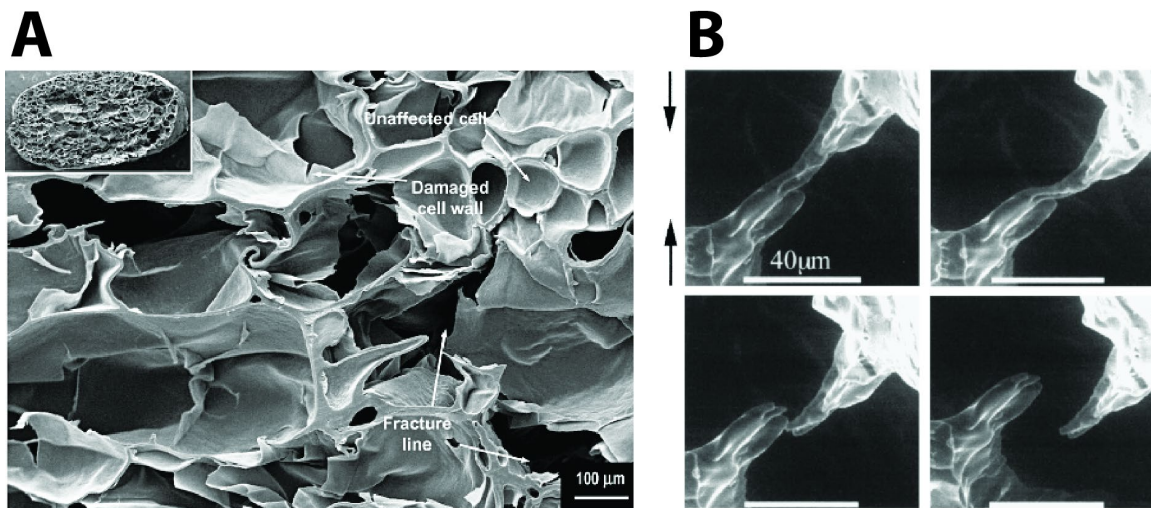


Figure 3.4. Scanning electron microscopy images showing fractured microstructure of a cellular expanded rice snack. Fracture lines are visible between air cells (Roopa et al., 2009) (A). Environmental scanning electron microscopy images showing tensile fracture of a structural element (gluten strut) within bread crumb. Black arrows show the direction of applied force (Stokes and Donald, 2000) (B). Comparison of the two images shows that fracture occurs on multiple length scales.

3.4.6 Fracture on multiple time scales

Another consideration for applying fracture mechanics to mastication is that fracture occurs on multiple time scales. For example, Castro-Prada et al., (Castro-Prada et al., 2012), Varela et al., (Varela et al., 2008), and Kong and Singh (Kong and Singh, 2009b) all used uniaxial compression to fracture brittle foods. However, the fracture phenomena investigated in these experiments differed in time scale. By recording the response of the food at 2^{16} Hz, Castro-Prada et al., (Castro-Prada et al., 2012) characterized

high frequency fractures that occurred from failure of individual air cells (more than 100 force peaks per test). These events were of interest for their influence on sensory characteristics during mastication (such as crispness). By recording at 500 Hz, Varela et al., (Varela et al., 2008) measured fracture properties on an intermediate time scale, finding roughly 10 peaks in the response curve from each test. These peaks represented larger fractures that resulted in fragmentation of the test sample into multiple pieces. Finally, Kong and Singh (Kong and Singh, 2009b) measured the endpoint value of force built up over the entire compression to calculate an overall stiffness value on the same time scale as the test itself. Endpoint measurements of compressive force may be useful for investigating features such as the maximum force during biting, but not for identifying high frequency events resulting from the fracture of individual structural elements. This is because decreasing the rate of data acquisition averages out high frequency (short time scale) features of the response curve.

The identification of the relevant time scales can be used to select appropriate tests for relation to mastication. For example, if the objective is to design foods that will not provide too much force for successful fracture in the mouth, then endpoint measurements may be of use. If the objective is instead to characterize fractures for relation to sensory descriptors such as crackly or crispy, recording data at high enough frequency (~50 kHz) to capture acoustic events may be necessary (Castro-Prada et al., 2007).

3.5 Experimental methods to measure fracture properties of foods relevant to mastication

Mastication is a complex process and cannot be exactly reproduced by any instrumental test. However, the fracture properties of foods can be related to food behavior during mastication, and instrumental-mechanical tests can be used to measure food fracture properties. Measured fracture properties are then either directly related to mastication variables or used to evaluate indices such as the stress and displacement-limited indices (Section 3.3) which can then be related to mastication variables.

3.5.1 *Uniaxial compression test*

In the uniaxial compression test, a food sample is placed on an unyielding platform and deformed by a probe (Figure 3.7 A). Test parameters include probe size and shape, probe speed, and the condition for

stopping the test (Chen and Opara, 2013b). Examples of experimental parameters used in previous uniaxial compression tests are provided in Table 3.3.

Advantages of the uniaxial compression test are that it does not require creating a specific sample shape or size and does not require attaching the sample to the test apparatus. Limitations are that the internal stress state causing fracture of the sample is complex, the path of the crack is generally not known, and the deformation of the sample is influenced by friction with the probe and platform (Canet et al., 2007). This prevents uniaxial compression from being used to determine toughness, R , or critical stress intensity factor, K_{IC} (Luyten et al., 1992). However, it can be used to determine Young's modulus, E [Pa]. For determination of Young's modulus using uniaxial compression, the force-time curve recorded by the texture analysis instrument must be represented as a stress-strain curve. This can be done using Equations 3.11 and 3.12 (Sharma and Bhattacharya, 2014):

$$\varepsilon_{true} = \ln\left(\frac{h}{h - \Delta h(t)}\right) \quad 3.11$$

$$\sigma_{true} = \frac{F(t)(h - \Delta h(t))}{A_o h} \quad 3.12$$

Where ε_{true} [m/m] is true strain, h [m] is initial sample height, $\Delta h(t)$ [m] is the change in height due to compression, σ_{true} [Pa] is true stress, $F(t)$ [N] is the force response of the sample, and A_o [m²] is the initial cross-sectional area of the sample. Typically, cylindrical samples are used so that $A_o = \pi r_o^2$, where r_o [m] is the initial sample radius. After transforming the curve of force vs time to σ_{true} vs ε_{true} , Young's modulus can be calculated as the slope of the initial linear region. Previous studies have used the region from 5% to 10% true strain (Vandenberghe et al., 2014). The region on which Young's modulus is calculated should not contain any significant fracture events. This value can then be used in the mastication indices defined in Section 3.3.

Several previous studies have related values from the uniaxial compression test to parameters measured during mastication (Table 3.1). For example, Hutchings et al., (Hutchings et al., 2012) used

two-cycle uniaxial compression to instrumentally measure the compression work needed to deform model foods (peanuts embedded in either chocolate or gelatin matrices). The same foods were then masticated, and it was found that the food which exhibited higher compression work during uniaxial compression required more chews before being swallowed. Takahashi et al., (Takahashi et al., 2009) measured the compression work needed to deform food samples (including cookie, radish, and tofu) in uniaxial compression, and then used a multiple point sheet sensor to record force vs time data during mastication of the same foods. It was found that the instrumental work of compression was correlated with the impulse (area under force-time curve) recorded during mastication. It was concluded that the compression test was useful for prediction of the ease of chewing a food sample. It has been proposed that uniaxial compression may better represent chewing by molars than tests such as the puncture or wedge test, which more closely resemble biting by incisors (Varela et al., 2009).

A future opportunity could be to estimate the fracture stress, σ_f , from a graph of σ_{true} vs ε_{true} , for instance by taking the value of σ_{true} at which the first major fracture event occurs, and then comparing it to the fracture stress from either Equations 3.4 or 3.5. Since the Young's modulus and toughness can be measured using other experimental tests (Sections 3.5.1 to 3.5.6), the equation could be solved for the critical crack length, a [m]. This approach could be used to obtain fundamental information about the sizes of inhomogeneities that function as stress-concentrators within the food sample.

3.5.2 Puncture test

In the puncture test, the loading geometry of the food sample is similar to the compression test (Figure 3.7 B) except in puncture testing the probe is smaller than the sample and is used to penetrate its interior. Puncture testing is commonly used to determine fracture properties of foods with crusts or shells (Jakubczyk et al., 2015). Selected test parameters used in previous puncture experiments are provided in Table 3.3.

In the context of mastication, puncture testing resembles the loading geometry of a food particle between incisors (Van Hecke et al., 1998). As with uniaxial compression testing, empirical indices of

food texture derived from puncture experiments have been successfully related to mastication (examples in Table 3.1). For example, foods with higher initial hardness as measured using a puncture test resulted in smaller particles in the masticated bolus (Chen et al., 2013). In another study, bread crust was punctured with a 2 mm diameter probe at 40 mm/s to simulate biting with the front teeth (Gao et al., 2015). The maximum force during the test was positively correlated with the total impulse from EMG during mastication. Takahashi et al., (Takahashi et al., 2009) found that maximum force during puncture was correlated with maximum bite force. These results showed that puncture testing can yield useful results to relate to mastication in foods such as abalone, cookie, tofu, radish, bread, chicken and pork meat (Takahashi et al., 2009).

An opportunity for puncture testing is the development of puncture probes with a tooth-like geometry. This could allow the direct relationship of empirical parameters from puncture testing (such as maximum force during the test) to results from mastication studies, such as the maximum force during biting.

3.5.3 *Wedge test*

In the wedge test a wedge-shaped probe is used to split the food sample (Figure 3.7 C). The goal of the test is to incrementally advance the wedge through the sample so that the test is conducted in the state of steady crack advance (Equation 3.2). The wedge splits the sample through internal tensile forces, thus testing the food's resistance to mode I fracture (Figure 3.1 A2). Experimental parameters include wedge speed, wedge angle, and radius of curvature of the wedge tip (examples of test setups provided in Table 3.3). It is important that the wedge is wider than the sample so that the sample completely splits, as this makes the area of fractured surface a known value (Lucas et al., 2012).

The wedge test can be used to measure the toughness of a food sample. This has been accomplished using a two-pass method (Lucas et al., 2012; Zink et al., 2014). First, the wedge is driven through the food sample, and the work of the test is determined in the region of steady crack propagation. Second, the wedge is withdrawn, the cleaved halves of the sample are gently pushed back together, and the test is run again. On the second pass, the force recorded is only due to friction between the wedge and the sample

($U_{f,pass\ 2} = 0$). In wedge testing, energy dissipated plastically or stored elastically in the sample offcuts is assumed to be negligible for both passes ($U_e = U_p = 0$). This allows the energy balance for each pass to be expressed as a simplified form of the general balance given in Equation 3.1.

$$U_{s,pass\ 1} = U_f + U_d \quad 3.13$$

$$U_{s,pass\ 2} = U_d \quad 3.14$$

Where $U_{s,pass\ 1}$ [J] is the energy imparted to the sample on the first test (causing fracture), and $U_{s,pass\ 2}$ [J] is the energy imparted to the sample on the second test (empty pass). The fracture energy, U_f [J], can be found by subtraction (Figure 3.5 A). The fracture energy is also given by Equation 3.15, provided the wedge is wider than the sample and completely splits it.

$$U_f = Rwh \quad 3.15$$

Where R [J/m²] is the toughness, w [m] is the width, and h [m] the height of the sample. The energy imparted to the sample can be expressed as the integral of the force vs displacement curve in the region of steady crack propagation (McCarthy et al., 2007). Thus, the toughness can be calculated as:

$$R = \frac{1}{wh} \left[\left(\int_0^h F(x) dx \right)_{pass\ 1} - \left(\int_0^h F(x) dx \right)_{pass\ 2} \right] \quad 3.16$$

In the context of mastication, the wedge test could be useful to determine food fracture properties for loading geometries such as splitting by incisors or bending by contact with molar cusps (Primo-Martín et al., 2009; Sui et al., 2006). Jiang, et al., (Jiang et al., 2008) created a model incisor tooth (length 34.0 mm, width 9.9 mm, and thickness 1.5 mm), attached it to a texture analyzer, and used it as a wedge to test texture of fish fillets. The maximum force during the compression at 2 mm/s was taken as an index for difficulty of penetration by an incisor into the fillet during mastication. Examples of previous experiments in which wedge tests were used to measure food properties that were then related to mastication variables are given in Table 3.1. However, there is opportunity for more studies to relate fracture properties of foods measured using the wedge test to those from controlled bite experiments using only the incisors, as

this is the loading geometry under which the results of the wedge test are predicted to most directly relate to mastication variables.

3.5.4 Cutting test

Cutting is a common method for determining fracture properties of foods such as toughness. A few specific test setups used by previous researchers are shown in Table 3. One specific approach is wire cutting. In a wire cutting test the sample is cleaved into two pieces in a similar way as the wedge test (Figure 3.7 D). The apparent toughness for a given wire diameter, d_1 [m], is calculated as the work of the test divided by the fractured area (Williams and Patel, 2016):

$$R_{d_1} = \frac{1}{wh} \int_0^h F(x) dx \quad 3.17$$

Where R_{d_1} [J/m²] is the apparent toughness for a wire of width d_1 , w [m] the sample width, h [m] the sample height, and $F(x)$ [N] the force response of the sample as it is cut by the wire. The test is repeated for different wire diameters and then extrapolation to a theoretical wire width of zero yields the intrinsic toughness (Figure 3.5 B) (Forte et al., 2015). A consideration for cutting experiments in general is that test speed can be influential, due to the ability of viscoelastic materials to dissipate energy plastically as well as through fracture (Schuldt et al., 2016). Another consideration with cutting experiments involving blades is sharpness. There is no universal definition of blade sharpness, although sharpness indices have been developed and shown to influence the force needed to initiate a cut (McCarthy et al., 2007). This suggests that preserving blade sharpness or changing blades frequently could be important in cutting tests.

With respect to mastication, a previous study found that raw peanuts required more force to cut to a certain depth than roasted peanuts, and also required more work to fully chew as measured using EMG (McKiernan and Mattes, 2010). This is an interesting finding because studies have shown that roasted nuts are more stiff than raw ones (Varela et al., 2008), thus it could be hypothesized that roasted peanuts would require more force to cut to a certain depth than raw peanuts. The fact that the opposite result was observed could be indicative of the cutting test allowing the more brittle roasted peanuts to fracture before a high amount of force was produced, and thus yielding a result that could be directly related to the

desired mastication variable (increased force during cutting, increased work during chewing) (McKiernan and Mattes, 2010). This is indicative of future opportunities using the cutting test to simulate biting using incisors and suggests that it could be valuable when working with brittle foods.

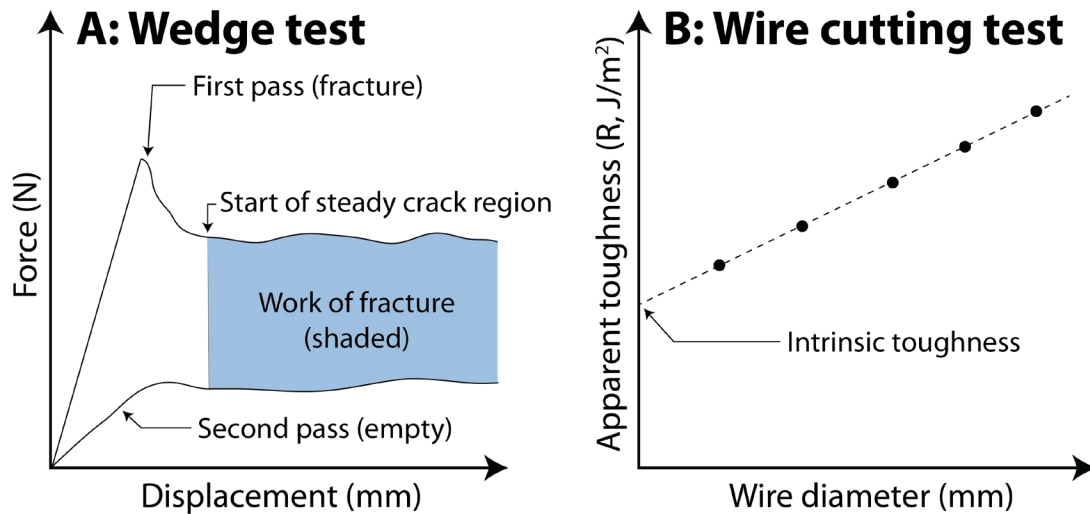


Figure 3.5: The wedge test is used to measure toughness using a two-pass approach. The work of fracture is found by subtracting the work on the second pass from the first pass. Adapted from (Lucas et al., 2012) (A). The wire cutting test can be used to find the intrinsic toughness of a food material by repeating the test with wires of varying width, and then extrapolating to a theoretical wire width of zero. Adapted from Kamyab et al., (1998) (B).

3.5.5 Three-point bend test

The three-point bend test is conducted by placing a food sample between two supports then compressing it from the middle (Figure 3.7 E) (Castro-Prada et al., 2007). For three-point bending, the span between the supports should be at least 16 times larger than the sample height ($s > 16h$) (ASTM D790-17, 2017). Studies have recommended the use of a blunted probe for applying the force to the center of the sample (Saleem et al., 2005). Experimental setups from previous research using the three-point bend test are provided in Table 3.3.

Values that can be obtained from three-point bend test include the fracture stress, fracture strain, and Young's modulus. These can be calculated for solid cylinders and rectangular prisms using formulas in Table 2. The three-point bend test may be useful to measure fracture properties of foods that are relevant during specific tooth/food particle loading geometries, such as when a food particle acts as a beam between molar cusps (Figure 3.2 A). This is the loading geometry that was analyzed by Agrawal et al., (Agrawal et al., 1997) to develop the displacement-limited index for food breakdown (Section 3.3.1). Previous studies have found that the fracture stress, σ_f (Table 3.2), measured using the three point bend test, was correlated with the sensory perception of hardness (Kim et al., 2012). This indicates that values obtained from three-point bend tests can be directly related to certain sensory properties of foods.

Table 3.2. Mechanical properties in three-point bending for two common food sample geometries. Δx_{frac} [m] is the displacement in the direction of the applied force when fracture occurs, F_{frac} [N] is the force when fracture occurs, dF/dx [N/m] is the slope of the linear-elastic region of the force-displacement curve, s [m] is the distance between the supports, D [m] is the diameter of a solid, cylindrical sample, h [m] is the height and w [m] the width of a rectangular prism-shaped sample (Figure 3.7 E).

Property	Sample geometry	Expression	Reference
Fracture stress, σ_f , [Pa]	Solid cylinder	$\sigma_f = \frac{8F_{frac}s}{\pi D^3}$	(Temenoff and Mikos, 2008)
	Rectangular prism	$\sigma_f = \frac{3F_{frac}s}{2wh^2}$	(Chaunier et al., 2007)
Fracture strain, ε_f , [m/m]	Solid cylinder	$\varepsilon_f = \frac{6D}{s^2}\Delta x_{frac}$	(Temenoff and Mikos, 2008)
	Rectangular prism	$\varepsilon_f = \frac{6h}{s^2}\Delta x_{frac}$	(Kim et al., 2012)
Young's modulus, E , [Pa]	Solid cylinder	$E = \frac{dF}{dx} \frac{4s^3}{3\pi D^4}$	(Temenoff and Mikos, 2008)
	Rectangular prism	$E = \frac{dF}{dx} \frac{s^3}{4wh^3}$	(Saleem et al., 2005)

3.5.6 Tensile test

Tensile tests are conducted by placing a sample into grips or clamps and then pulling it apart (test depicted in Figure 3.7 F, examples of previous setups in Table 3.3). Tensile testing of thin sheets (<1 mm width) is covered in ASTM-D882-12 (2012), and for thicker samples in ASTM-D638-14 (2014). Tensile testing has been used to measure the Young's modulus of foods, E [Pa], which is done by taking the slope of the stress vs strain curve of the material in tension. Transforming data recorded as force vs time to stress vs strain can be done using Equations 3.11 and 3.12.

With regards to mastication, tensile testing may be important to study the behavior of foods that self-anchor to teeth and are pulled apart on jaw opening, such as caramels or gums. The tensile test can be used to quantitatively assess the amount of force needed to either deform or fracture these foods. This could be useful for engineering foods with desired sensory properties, such as gums that adhere to teeth but are not so strong as to make jaw opening difficult.

3.5.7 Statistical approaches

One specific statistical approach to fracture analysis is to subject multiple samples to a known stress, σ [Pa], and then define the probability of fracture $P_f(\sigma)$ by direct observation (Courtney, 2005), or with statistical estimators (Guinea et al., 2004). Data can then be fit to the Weibull model (Equation 3.18).

$$P_f(\sigma) = 1 - \exp \left[- \left(\frac{\sigma}{\sigma_o} \right)^m \right] \quad 3.18$$

Here, σ_o [Pa] is a characteristic stress for the material, and m [dimensionless] is a material property describing the variability in material strength, where higher values of m indicate less variability (Quinn and Quinn, 2010). These parameters are determined experimentally. Defining σ_o as the stress at which $P_f(\sigma) = 1 - 1/e = 0.63$ allows it to be found directly from the experimentally determined survivability plot of $P_f(\sigma)$ vs σ (Figure 3.6). An advantage of the Weibull model is that it allows the complexity in fracture to be accounted for under a statistical approach that still yields fundamental material properties (Rojo and Vincent, 2008). This method has been used to obtain the Weibull modulus for fracture of dry peas and spaghetti (Guinea et al., 2004; Łysiak, 2007), as well as to design dental materials that have low

probability of fracture during use (Bütikofer et al., 2015), suggesting its applicability to mastication. A future use could be to engineer foods that will achieve desired failure rates, $P_f(\sigma)$, under stresses that can be exerted by teeth on food during mastication (roughly 0.7 MPa) (Dan et al., 2003).

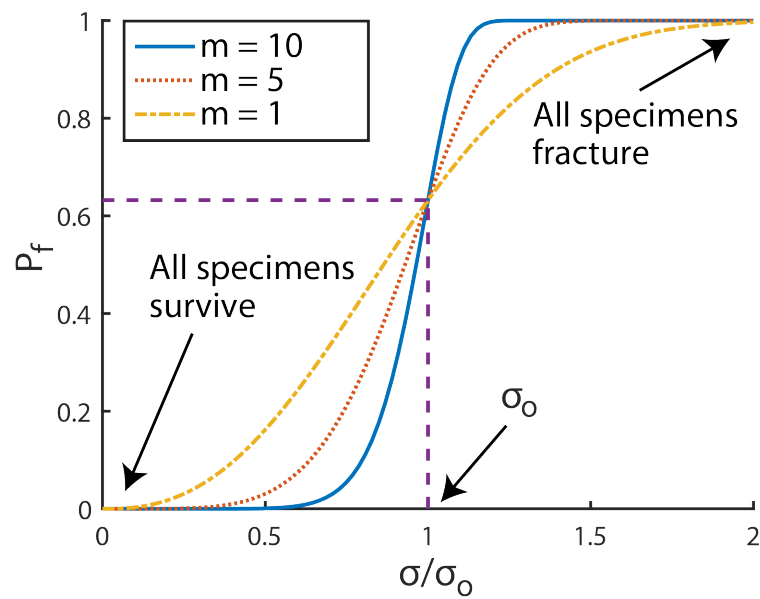


Figure 3.6: Example Weibull survivability plot, showing how Weibull modulus, m , characterizes the consistency of the material. High values of m indicate that all samples fail within a narrow range of stress. By estimating the stress at which $P_f = 1 - 1/e = 0.63$, the characteristic stress, σ_0 , is determined.

Adapted from Burrow et al., (2004).

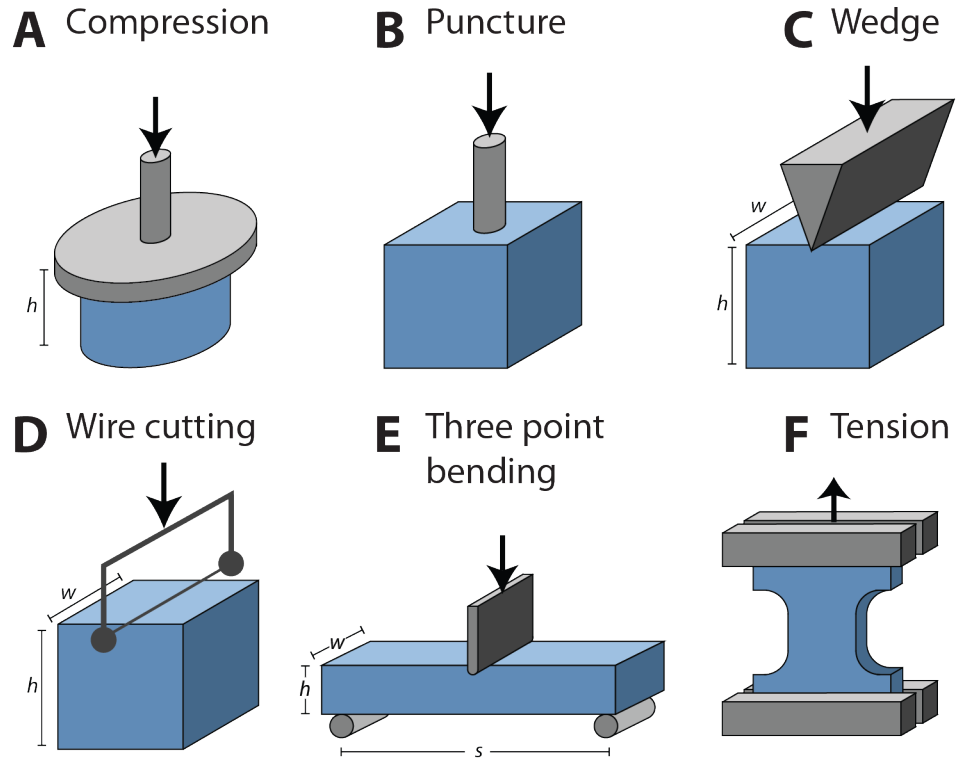


Figure 3.7. Mechanical tests that can be used to measure the fracture properties of foods. Arrows indicate the direction of applied force. Food samples are colored in blue, and selected parts of the test apparatus used to conduct the test are colored grey. Dimensions of the food samples are labeled with lowercase letters and correspond to the variables in the relevant equation for each test (Equations 3.11 to 3.17).

Table 3.3. Parameters of instrumental-mechanical tests used in selected studies to measure the fracture properties of foods. The test food used in each study is indicated. The sample geometry is shown, as well as the geometry of the test probe that was used, the speed at which it was used to deform the sample, and the condition for stopping the test.

Uniaxial compression test					
Food	Sample geometry	Probe dimension	Probe speed	Stoppage condition	Reference
Corn flower extrudates	Rectangular prism, 15 x 15 x varying mm	Cylindrical probe, 25 mm diameter	1.0 mm/s	50% strain	(Paula and Conti-Silva, 2014)
Corn starch puffed snacks	Cylinder, 10 mm diameter x 10 mm height	Cylindrical probe, 20 mm diameter	0.33 mm/s and 10 mm/s	75% strain	(Sanahuja et al., 2018)
Peanuts embedded in chocolate matrix	Rectangular prism, 13 x 20 x 15 mm	Cylindrical probe, 50 mm diameter	0.8 mm/s	80% strain	(Hutchings et al., 2012)
Puncture test					
Food	Sample geometry	Probe dimension	Probe speed	Stoppage condition	Reference
Assorted Japanese foods	Rectangular prism, 10 x 12 x 12 mm	Cylindrical probe, 3.2 mm diameter	1 mm/s	2% strain	(Takahashi et al., 2009)

Extruded crisp bread	Rectangular prism, 7 x 52 x 121 mm	Cylindrical probe, 36 mm diameter	1 mm/s	80% strain	(Jakubczyk et al., 2015)
Cassava flour crackers	Rectangular prism, 3.5 x 3.5 x 1mm	P/2 ball probe	1 mm/s	Complete penetration of sample	(Saeleaw and Schleining, 2010)
Wedge test					
Food	Sample geometry	Probe dimension	Probe speed	Stoppage condition	Reference
Model wheat-based crust	Cylindrical, 60 mm diameter, 1.5 mm height	Wedge with 30° Cutting angle, 32 mm width	40 mm/s	Not reported	(Primo-Martín et al., 2009)
Raw and roasted tubers	Rectangular prism 12-14 mm wide, other dimensions not reported	Wedge with 15° Cutting angle, width not reported	0.5 mm/s	5 mm displacement	(Zink et al., 2014)
Cheeses	Rectangular prism, 12 x 13 x 13 mm	Wedge, angle and width not reported	0.08 mm/s	Not reported	(Agrawal et al., 1998)
Cutting test					
Food	Sample geometry	Probe dimension	Probe speed	Stoppage condition	Reference

Beef muscle	Rectangular prism, 20 x 20 x 15 mm	Double blades at 45° angle	1 mm/s	Not reported	(Mioche et al., 2003)
Elastosil (model food)	Rectangular prism, 20 x 20 x 10 mm	Single blade with tip angle 20°	0.17 and 16.7 mm/s	8 mm cut depth	(Schuldt et al., 2016)
Maize flour extrudates	Cylindrical, diameter not reported	Single blade (0.9 mm thickness)	2.0 mm/s	Until the blade cut through the sample	(Cueto et al., 2015)
Three-point bend test					
Food	Sample geometry	Distance between supports	Probe dimension	Compression speed	Reference
Extruded corn grits	Cylindrical, 50 mm length, roughly 4.5 mm diameter	30 mm	Not reported	1 mm/s	(Wang and Ryu, 2013)
Rice grains	Natural product, average kernel length 6.5 mm	4 mm	Not reported	0.0083 mm/s	(Zhang et al., 2005)
Crisp wafers	Rectangular prism, 16 x 51 x 18 mm	Not reported	HDP/3PB rig (blunted bar)	0.5 mm/s	(Çarşanba et al., 2018)
Tensile test					
Food	Sample geometry	Method of fixing sample to apparatus	Extension speed	Stoppage condition	Reference

Apple	Rectangular prism, 11 x 5 x 2 mm	Glue	0.0083 mm/s	Until fracture	(Alamar et al., 2008)
Bread	Rectangular prism, 70 x 25 x 10 mm	Adhesive tape	0.10 mm/s	Until fracture	(Lapčák et al., 2016)
Elastosil (model food)	Dog bone, narrow section rectangular prism, 50 x 5 x 5 mm	Grips	0.02, 0.17, 1.67 mm/s	Until crosshead displacement of 200 mm	(Boisly et al., 2016)

3.6 Conclusion

Food engineers have used fracture mechanics to define the fundamental fracture properties of foods and developed instrumental tests to evaluate these properties. The connection between food fracture and oral processing has been explored using indices that link fundamental fracture properties to the breakdown of foods during mastication. In general, it has been found that foods with a higher stress-limited index required more stress to fracture than foods with a lower stress-limited index (Agrawal and Lucas, 2003), and foods with a higher displacement-limited index generated less new surface area than foods with a lower-displacement limited index during controlled chewing experiments (Agrawal et al., 1997). Although the stress and displacement-limited indices have informed correlations between food properties and mastication variables, they do not account for the impact of the physiological aspects of mastication on food fracture. A summary of physiological aspects of mastication that affect food fracture in the mouth and some suggested approaches for future research are:

- **Effect of variations in tooth speeds applied to different types of foods:** mechanical tests of food fracture properties could be conducted at speeds similar to those of teeth during mastication of the same food in vivo

- **Effect of multiple cycles of deformation needed to fracture certain foods:** mechanical tests could be used that use multiple cycles to deform and fracture foods, providing a better representation of the way that foods such as caramels are processed in the mouth
- **Occurrence of fracture phenomena on multiple length and time scales:** microscopy could be used in combination with mechanical testing to evaluate changes in food microstructure that occur during mastication
- **Effect of saliva and changing temperatures:** saliva and elevated temperatures could be incorporated into testing procedures to more accurately represent the environment in which foods are fracture in the mouth

Future research in this area is needed. First, more foods must be evaluated using a fracture mechanics approach to measure properties such as fracture stress (σ_F , [Pa]), toughness, (R , [J/m²]), critical stress intensity factor (K_{IC} , [Pa·m^{1/2}]), and Young's modulus (E , [Pa]). There are significant opportunities to characterize the change in fracture properties of foods as time elapses during oral processing. These physical property changes may occur due to temperature increase or saliva uptake by the food and have not been fully explored. Finally, physical relationships between food properties, food structures, and oral processing should be developed. An increased understanding of food fracture and its impact on mastication could guide the engineering of food products and processes with desired function.

Chapter 4 Fatty acid bioaccessibility and structural breakdown from in vitro digestion of almond particles

Originally published as:

Swackhamer, C., Zhang, Z., Taha, A.Y., Bornhorst, G.M., 2019. Fatty acid bioaccessibility and structural breakdown from in vitro digestion of almond particles. *Food Funct* 10, 5174–5187. <https://doi.org/10.1039/C9FO00789J>.

Rationale

The rationale for this chapter was to determine the influence of simulated peristalsis on the breakdown of solid food particles and bioaccessibility of nutrients contained in the solid food. This was the first research objective as identified in Chapter 1 (Introduction). This was conducted by subjecting almond particles to in vitro gastric digestion using either a shaking water bath model, which lacked simulated peristalsis, or the Human Gastric Simulator (HGS), which included simulated peristalsis. The main finding was that almond particles broke down into smaller particles only in the HGS, which led to higher fatty acid bioaccessibility, as compared to the shaking water bath model. This has implications for the design of future in vitro digestion systems and suggests that such systems should include simulated peristalsis. In this study the HGS was used, in which both particle-particle grinding as well as the direct effect of the simulated peristaltic wave could contribute to food particle breakdown. This pointed to the need for a new peristaltic simulator, capable of applying simulated peristaltic contractions to individual food particles, so that the effect of simulated peristalsis on food particle breakdown could be isolated. The results of this study thus called for the development of a novel peristaltic simulator, which was presented in Chapter 6. Furthermore, the physical properties of almonds could not be related to their breakdown due to their anisotropic microstructure and heterogeneous particle size distributions, which highlighted the need for model foods that could be prepared into shapes amenable to standard measurement techniques

used for assessment of textural, rheological, and fracture properties. This need was met through the development of model foods as reported in Chapter 5.

Abstract

Previous studies have shown that the size of almond particles influences lipid bioaccessibility during digestion. However, the extent of structural breakdown of almond particles during gastric digestion and its impact on lipid bioaccessibility is unclear. In this study, in vitro digestion of almond particles was conducted using a dynamic model (Human Gastric Simulator) and a static model (shaking water bath). Structural breakdown of particles during the gastric phase occurred only in the Human Gastric Simulator, as evidenced by a reduction in particle size ($15.89 \pm 0.68 \text{ mm}^2$ to $12.19 \pm 1.29 \text{ mm}^2$, $p < 0.05$). Fatty acid bioaccessibility at the end of the gastric phase was greater in the Human Gastric Simulator than in the shaking water bath ($6.55 \pm 0.85\%$ vs $4.54 \pm 0.36\%$, $p < 0.01$). Results showed that the in vitro model of digestion which included peristaltic contractions (Human Gastric Simulator) led to breakdown of almond particles during gastric digestion which increased fatty acid bioaccessibility.

4.1 Introduction

Almonds have high lipid content (44–61 g per 100 g whole almond) (Yada et al., 2011). However, previous studies have shown that the bioaccessibility of lipids from almond particles is limited by encapsulation within intact almond cells, which resist degradation in the human digestive system (Gallier et al., 2014; Grundy et al., 2015b; M. M. L. Grundy et al., 2016; Mandalari et al., 2008). In accordance with previous researchers, bioaccessibility was defined in this study as the proportion of lipid released from the almond matrix into the aqueous digestive environment (Capuano et al., 2018; Grassby et al., 2014). Understanding the factors that influence bioaccessibility of lipids during digestion of almonds has implications for clinical nutrition in view of studies showing that the limited bioaccessibility of lipids from almonds reduces postprandial lipemia (Berry et al., 2008) and metabolizable energy (Gebauer et al., 2016; Novotny et al., 2012). Limited lipid bioaccessibility from almonds and other nuts has also been linked to improved metabolic markers in type 2 diabetes (Li et al., 2011), cardiovascular disease (Estruch et al., 2018; Rusu et al., 2018), and obesity (Wien et al., 2003).

Previous studies have investigated the digestion of almonds using both in vitro (Grundy et al., 2015b; M. M. L. Grundy et al., 2016; Mandalari et al., 2014, 2008) and in vivo (Berry et al., 2008; Cassady et al., 2009; Ellis et al., 2004; Gebauer et al., 2016; Grassby et al., 2017; Grundy et al., 2015a; Novotny et al., 2012) methods, and it has been observed that smaller particles led to higher lipid bioaccessibility than larger particles (Grassby et al., 2017; Grundy et al., 2015b; Mandalari et al., 2008). Additionally, researchers have reported size reduction of peanut particles during in vitro gastric digestion in a model that simulated the motility of the human stomach (Chen et al., 2011). The relationship between particle size and fatty acid bioaccessibility in the human digestive system has been described using a mathematical model (Grassby et al., 2014), but an assumption was that particle size was constant throughout the digestion. Size reduction of almond particles during gastric digestion has been observed in studies using the growing pig as a model for the adult human, but was not directly linked to lipid bioaccessibility (Bornhorst et al., 2016a, 2014b, 2013c). This points to the need for more data on the breakdown of almond particles during digestion to clarify the relationship between particle breakdown

and lipid bioaccessibility. However, static *in vitro* models of human digestion do not reproduce the peristaltic motion of the stomach (Bornhorst et al., 2015) and thus may not lead to particle breakdown as it occurs *in vivo*. Thus, an *in vitro* model of gastric digestion that included peristaltic contractions, the Human Gastric Simulator (HGS), was used to assess whether peristaltic motion contributed to particle breakdown and lipid bioaccessibility during simulated gastric digestion.

Briefly, the HGS includes a flexible plastic liner which holds the food and simulated gastric juice. Simulated peristaltic contractions are applied to the HGS using rollers, and temperature and pH can be controlled to appropriately simulate the conditions inside the human stomach. An in-depth comparison of the HGS with other dynamic, *in vitro* models of human digestion has been described in a recent review (Dupont et al., 2019). A similar *in vitro* model is the Dynamic Gastric Model, which was used by previous researchers for *in vitro* digestion of almond particles (Mandalari et al., 2014). This model includes simulated peristaltic waves, which are applied by water pressure, in addition to pH and temperature control. Another previously reported *in vitro* model of human digestion is the TIM model (Bellmann et al., 2016; Minekus et al., 1995), which also includes simulated peristaltic contractions applied by water pressure. Previous researchers also used a dynamic *in vitro* model of gastric digestion to show that peanut particles experienced size reduction during simulated gastric digestion (Chen et al., 2011). This model consists of a ball-shaped probe, actuated by a texture analyzer, which was used to gently mix the contents of a vessel containing the food subjected to *in vitro* digestion (Chen et al., 2011).

The objective of this study was to determine whether digestion of almond particles using an *in vitro* model with peristaltic contractions (HGS) led to particle breakdown and whether this affected fatty acid bioaccessibility. This was investigated using *in vitro* digestion of almond particles in either the HGS or a shaking water bath using identical simulated digestive juices. The second objective of the study was to determine the effect of simulated gastric and intestinal juices on the bioaccessibility of fatty acids from almond particles. This was done by digesting almond particles in a shaking water bath model using simulated gastric and intestinal juices or with only pH-adjusted water. Identifying the factors that affect

fatty acid bioaccessibility could have implications for design of appropriate models for simulating human digestion and could assist in the development of functional foods for targeted fatty acid bioaccessibility.

4.2 Materials and methods

4.2.1 Raw materials

Whole, raw nonpareil almonds were generously donated by the Almond Board of California. Almonds had size of 22.69 ± 1.13 mm, 12.72 ± 0.43 mm, 7.82 ± 0.62 mm (length \pm std, width \pm std, height \pm std, $n = 20$ almonds were subjected to measurement with a digital caliper). Almonds were prepared for in vitro digestions by grinding in a food processor (Black & Decker FP2500B, Towson MD). Particles between 2 mm and 4 mm in size were obtained by sieving (WS Tyler, Mentor OH). This size range was chosen to approximate the size of almond particles in a masticated bolus at the point of swallow (McArthur et al., 2018; Peyron et al., 2004). The resulting almond particles, of a size similar to those from mastication in vivo, were then used for in vitro digestions. Almond particles produced using the food processor were prepared fresh each day before conducting in vitro digestions.

4.2.2 Digestive juice formulation

Digestive juices were prepared using a previously described method (Bornhorst and Singh, 2013; Roman et al., 2012) (Table 4.1). Water used for digestive juices was obtained from a Milli-Q Water Purification System (Merck Millipore, Billerica, MA, USA). Saliva has been found to be important for the in vitro digestion of starchy foods due to the prevalence of salivary α -amylase, however, almonds have little to no starch content (Sathe et al., 2008; Yada et al., 2011). Saliva was not used in this study in accordance with previous in vitro digestion research on almond particles (Grundy et al., 2015b; Mandalari et al., 2008). Enzymes were added to simulated gastric and intestinal juices to reflect their activity in vivo, as identified by the INFOGEST international consensus protocol (Minekus et al., 2014) (Table 4.1). Amano Lipase A was used due to its resistance to pepsin (Sams et al., 2016; Zentler-Munro et al., 1992) and for agreement with previous in vitro digestion research (Abrahamse et al., 2012a; Pinheiro et al.,

2013). However, it is acknowledged that the stereospecificity of this lipase is not well described (Sams et al., 2016), which could affect the results of fatty acid bioaccessibility.

Table 4.1. Composition of simulated digestive juices (Bornhorst and Singh, 2013; Minekus et al., 2014; Roman et al., 2012).

	Component	Supplier	Concentration in simulated digestive juice (mg/mL)	Activity in simulated digestive juice
	Pepsin (300 U/mg)	MP Biomedicals CAS: 9001-75-6	6.67	2,000 U/mL
Simulated gastric juice (pH = 1.8)	Gastric mucin (porcine stomach- Type II)	Sigma-Aldrich CAS: 84082-64-4	1.50	-
	Amano Lipase A (120,000 U/g)	Sigma-Aldrich CAS: 9001-62-1	3.33	40 U/mL
	NaCl	Fisher Scientific CAS: 7647-14-5	8.78	-
Simulated intestinal juice (pH = 7)	Pancreatin (8X USP)	Sigma-Aldrich CAS: 8049-47-6	9.60	100 TAME units /mL (for trypsin)
	Bile extract	Sigma-Aldrich CAS: 8008-63-7	10.00	-
	NaHCO ₃	Sigma-Aldrich CAS: 144-55-8	16.80	-

4.2.3 Shaking water bath model

4.2.3.1 Shaking water bath model with simulated gastric and intestinal juices

Digestions in the shaking water bath were conducted by adding simulated gastric juice (Table 4.1, prewarmed to 37 °C) to almond particles in a ratio of 5 mL simulated gastric juice to 1 g almond particles. After adding simulated gastric juice, the pH was recorded (Accumet AE150, Thermo-Fisher, Waltham, MA), and the bottle containing almond particles and simulated gastric juice was placed in a shaking water bath (Thermo-Fisher 2872, Waltham, MA) at 37 °C and 100 rpm. After 60 min elapsed time, the pH was adjusted to 3 ± 0.1 and after 120 min to 2 ± 0.1 to simulate the dynamic pH profile in the human stomach after consumption of a meal (Malagelada et al., 1976; Sams et al., 2016). After 180 min, the intestinal

phase was initiated by adding simulated intestinal juice (Table 4.1, prewarmed to 37 °C) in a 1:1 (v/v) ratio with the simulated gastric juice that was added to begin the gastric phase, and pH was adjusted to 7 ± 0.1 . After 60 min simulated intestinal digestion (240 min total), pH was readjusted to 7 ± 0.1 . After 120 min simulated intestinal digestion (300 min total) pH was again adjusted to 7 ± 0.1 . All pH adjustments were made using 3 M HCl or 3 M NaOH. This pH adjustment protocol was used to resemble the pH in the digestive system after consumption of a meal of almonds in vivo (Bornhorst et al., 2014c). Measured pH values are given in Table 4.6.

Samples were collected for analysis at 8 timepoints (gastric: 1, 5, 15, 30, 180 min, intestinal: 185, 195, 360 min total time). For any timepoint, the entire contents of the bottle in the shaking water bath were collected for analysis (Figure 4.1). The digesta was collected by pouring through a kitchen sieve (aperture size ~0.5 mm) to separate the solid phase (almond particles) from the liquid phase. All digestions were completed in triplicate.

4.2.3.2 Shaking water bath model with only pH-adjusted water

Digestions were also conducted in the shaking water bath model using only pH-adjusted water. The gastric phase was initiated by adding water ($\text{pH} = 1.8 \pm 0.1$) to almond particles in a ratio of 5 mL acidified water to 1 g almond particles. At the end of the gastric phase, water ($\text{pH} = 7 \pm 0.1$) was added in a 1:1 (v/v) ratio with the acidified water that had been added to begin the gastric phase. Adjustments of pH and sample collection were conducted as described previously.

4.3 Human Gastric Simulator model using simulated digestive juices

The Human Gastric Simulator (HGS) is a single-chamber model of human gastric digestion that simulates peristaltic contractions using mechanical rollers on a flexible plastic liner containing food and simulated gastric juice (Dupont et al., 2019; Phinney, 2013). Digestions in the HGS were conducted by adding simulated gastric juice to almond particles in the same ratio as was used for the shaking water bath. During the gastric phase, the contents of the HGS were subjected to peristaltic contractions at a frequency of 3 contractions per minute (Ye et al., 2016). As the HGS was used to test the impact of

peristaltic motion on the breakdown of almond particles in comparison to the shaking water bath model, no secretions were added during the digestion to keep the ratio of solid particles to simulated gastric juice constant for both models. At the end of the gastric phase the contents of the HGS were transferred to a bottle, simulated intestinal juice was added in a 1:1 (v/v) ratio with the simulated gastric juice that was added to begin the gastric phase, and the bottle was transferred to the shaking water bath at 37 °C. The pH in the HGS was adjusted in the same way as for digestions using the shaking water bath. Sampling was conducted by removing the entire contents of the HGS bag (during the gastric phase) or bottle (during the intestinal phase). Solid and liquid phases were separated by sieving in the same way as was done for digestions using the shaking water bath. Each aliquot of almond particles subjected to in vitro digestion in the HGS was ~60 g, and each aliquot used for in vitro digestion in the shaking water bath was ~15 g.

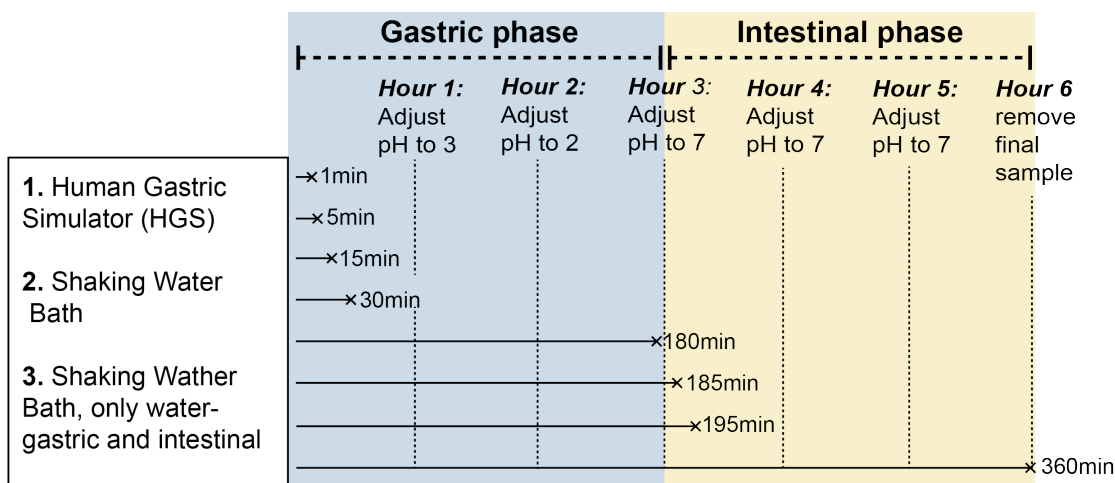


Figure 4.1. The gastric phase of digestion was conducted in either the Human Gastric Simulator (HGS) or a shaking water bath. After the gastric phase, the intestinal digestion was always conducted in the shaking water bath. All digestions were conducted at 37 °C.

4.4 Analysis of liquid phase

After separation of solid and liquid phases by sieving, the liquid phase was homogenized for one minute at 10,000 rpm (Ultra Turrax T18 digital with S18N–19G disperser, IKA Works, Wilmington, NC). °Brix of the homogenized liquid phase was measured in triplicate using a digital refractometer (HI 96800,

Hanna Instruments, Woonsocket, RI), and expressed as the measured value minus the °Brix of the appropriate blank simulated digestive juice. Remaining homogenized digesta was promptly frozen at -20 °C and stored until fatty acid analysis could be completed (less than one month). It has been found that storage of lipids from foods at this temperature for short periods of time does not lead to significant fatty acid oxidation (Ramalhosa et al., 2012; Soyer et al., 2010). No antioxidant was added to the samples during short-term storage, in accordance with previous research on the bioaccessibility of fatty acids from almonds (Grundy et al., 2015b). Although a small amount of fatty acids could have been lost during storage or sample preparation through formation of oxidized products, previous researchers have determined that there was no statistically significant increase in markers of lipid oxidation during storage of food samples at -20 °C for less than one month (Baron et al., 2007).

4.4.1 Fatty acid extraction and preparation

Fatty acids were extracted from liquid digesta and analyzed using gas chromatography with flame ionization detection (GC-FID). The objective was to determine the amount of fatty acids that had left the almond matrix and entered the liquid phase, as a percentage of those initially present in the almonds. Fatty acids were extracted from liquid digesta using the Folch method, a standard method for extraction of total lipids from foods and digesta (Capó et al., 2016; Jang et al., 2014; Taha et al., 2012). Briefly, 0.5 mL of homogenized digesta was combined with 2 mL of a 2:1 chloroform:methanol (v/v) solution containing triheptadecanoin internal standard (Nu-Chek Inc, Elysian MN). The mixture was vortexed and then centrifuged at $458 \times g$ for 10 min (Allegra 6 centrifuge with GH-3.8A rotor, Beckman Coulter, Palo Alto CA). The chloroform layer was transferred to a new test tube. The extraction was repeated a second time and the chloroform layers were combined and then evaporated under nitrogen (Reacti-Vap TS-18826, Thermo-Fisher, Waltham, MA). Dried extracts were reconstituted using 400 µL toluene, 3 mL methanol and 600 µL of a 3% HCl in methanol (v/v) solution, and vortexed. The 3% methanolic HCl solution was prepared by diluting a 37% HCl solution (ACS reagent, 37%, Sigma-Aldrich, St. Louis, MO, USA; Cat #320331) to 8% in methanol. Samples were placed in a heating block at 90 °C for 60 min

for transesterification, obtaining fatty acid methyl esters. After cooling, 1 mL deionized water and 1 mL hexane were added and vortexed. After allowing 15 min for phase separation, the hexane layer was transferred to a microcentrifuge tube containing 450 μ L deionized water which was centrifuged at 16,627 \times g for 2 min at 4 $^{\circ}$ C (5430R Eppendorf micro-centrifuge with FA-45-24-11 rotor, Fisher Scientific, Waltham MA). After centrifuging, the hexane layer was transferred to a new microcentrifuge tube, evaporated under nitrogen, and reconstituted in 100 μ L hexane for analysis using GC-FID.

4.4.2 GC-FID analysis of fatty acids

Samples were run on a Perkin Elmer Clarus 500 GC system (Perkin Elmer, Shelton, CT) with a FFAP column (30 m \times 0.25 mm inner diameter, 0.25 μ m film thickness; Agilent Technologies, Santa Clara, CA) and flame ionization detector sampling at 1.25 Hz. The injector temperature was 240 $^{\circ}$ C and the detector temperature was 300 $^{\circ}$ C. The oven temperature was held at 80 $^{\circ}$ C for 2 min, then increased by 10 $^{\circ}$ C per min to 185 $^{\circ}$ C at the time of injection, and then increased to 240 $^{\circ}$ C at 5 $^{\circ}$ C/min and held at 240 $^{\circ}$ C for 13 min. Total run time was 36.5 minutes. The carrier gas was helium at a flow rate of 1.3 mL/min. The injection volume was 1 μ L and the split ratio was 10:1. A mixture containing 29 fatty acid methyl ester standards was run separately from the experimental samples and used to identify individual fatty acids based on their retention times (Zhang et al., 2017). Fatty acid concentrations in the liquid digesta were determined by comparison of peak areas to the peak from the triheptadecanoin internal standard. Fatty acid analysis was also performed on samples of simulated gastric and intestinal juice, and the fatty acid content of experimental samples of almond digesta was adjusted by subtraction of the appropriate blank. Total bioaccessible fatty acid in the digesta was defined as the sum of palmitic acid (C16:0), oleic acid (C18:1), and linoleic acid (C18:2) extracted from 0.5 mL digesta, multiplied by the total volume of digesta that was collected. It was determined that these three fatty acids constituted > 98% of the total fatty acid content of the whole almonds, which is in agreement with a previous analysis of California-grown almonds (Sathe et al., 2008).

4.5 Analysis of solid phase

After collection of a digestion timepoint and separation of solid and liquid phases by sieving, solid almond particles were drained on the sieve for 15 min. For each timepoint, 5 aliquots of digested particles were randomly selected from the drained solids and used for moisture content analysis. Moisture content was determined gravimetrically using AOAC Official Method 925.4061 by drying at 110 °C to constant weight. Remaining almond particles were used for particle size analysis as well as for Scanning Electron Microscopy.

4.5.1 Particle size analysis

The initial size of almond particles subjected to in vitro digestion was controlled (2 mm – 4 mm), thus, the objective of the particle size analysis was to quantify size reduction of particles that occurred during simulated gastric or intestinal digestion. An image analysis procedure developed by previous researchers to quantify the size distribution of fractured almond particles was used in this study to measure the size of almond particles (Gebauer et al., 2016). Minor modifications were made to adapt the image analysis procedure for this study. Briefly, 6 g almond particles were arranged onto Petri dishes to prevent overlap. Petri dishes were illuminated from beneath using a lightbox (AGPtek HL0163, color temperature 6000 °K). A geometrical reference (ABFO No. 2 photomacrographic standard reference scale) was included in all images for spatial calibration. One image of each dish was captured using a Canon EOS Rebel SL1 digital camera (18-megapixel, APS-C CMOS sensor, Canon USA, San Jose, CA). The camera settings were: no flash, 35 mm focal length, aperture F8.0, ISO 100, and shutter speed 0.1 second, 47 mm distance to the particles. The camera was triggered using a computer interface to reduce disturbances in focus. Images were analyzed using MATLAB R2018b (MathWorks, Natick MA). The number of particles per gram of dry solids was defined as the number of particles that were enumerated during image analysis divided by the dry mass of particles subjected to image analysis (3.68 ± 0.62 g). Particle size analysis was conducted by fitting the cumulative area percentage of the particles to the Rosin–Rammler model (Equation 4.1).

$$C_{area} = 1 - \exp \left(- \left(\frac{x}{x_{50}} \right)^b \ln (2) \right) \quad 4.1$$

Where: C_{area} is cumulative area percentage of each particle (0% to 100%), x_{50} = median particle area (mm^2), and b is the distribution breadth constant (dimensionless), where larger b values represent a narrower distribution spread. This model has previously been used to describe the size of solid food particles as determined by image analysis (Bornhorst et al., 2013c; Gebauer et al., 2016).

4.5.2 Scanning electron microscopy

Scanning electron microscopy (SEM) was conducted on almond particles digested for 180 minutes in the HGS as well as undigested almond particles as a control. Images were obtained using a previously described method (Strobel et al., 2019, 2016). Briefly, almond particles were mounted on double-sided carbon tape and sputter coated in gold. Micrographs were obtained using a scanning electron microscope (Quattro S, Thermo–Fisher, Waltham, MA) in high vacuum mode with acceleration voltage of 5 kV.

4.5.3 Almond composition

The fatty acid content of whole almonds was determined using Folch extraction as well as by direct acid extraction. For both methods almonds were ground in a mortar and pestle. Folch extraction was conducted on 10 mg almond powder as previously described. Direct acid extraction was carried out on 10 mg almond powder by adding 3 mL 3% HCl in methanol, prepared as described previously then following the rest of the steps described previously starting with addition of 400 μL toluene. Composition data from direct acid extraction and Folch extraction are shown in Table 4.2. It was determined that direct acid extraction yielded more fatty acid and was therefore used to establish the initial fatty acid content of almonds. Fatty acid bioaccessibility at different timepoints during the digestion was expressed by dividing total fatty acid in the liquid digesta (g bioaccessible fatty acid) by the fatty acid in the undigested almonds (g initial fatty acid).

4.6 Statistical analysis

Statistical analysis was conducted using SAS Enterprise Guide 7.1 (SAS Institute, Cary NC). Two factor analysis of variance (ANOVA) was used to determine the influence of digestion model (HGS, shaking water bath–gastric fluids, or shaking water bath–only pH adjusted water), digestion time (1, 5, 15, 30, 180, 185, 195, or 360 min) and their interaction on fatty acid bioaccessibility, Rosin–Rammler x_{50} , Rosin–Rammler b , particles per gram of dry solids, moisture content of digesta, and °Brix of digesta. Homogeneity of variance was assessed using the Brown–Forsythe test, and normality of the residuals was assessed using a *qq* plot. Remediation was necessary for °Brix and particles per gram of dry solids and was conducted using the Box–Cox transformation (lambda values 0.33 and -1.83, respectively). When the *F* value for the overall model was found to be significant ($p < 0.05$), post–hoc tests were conducted using Tukey’s HSD and significance was detected for $p < 0.05$. All results are presented as mean \pm standard deviation.

4.7 Results

4.7.1 Fatty acid bioaccessibility

Total bioaccessible fatty acid (%) was significantly influenced by digestion model, digestion time, and their interaction ($p < 0.01$, Figure 4.2). Within each model, total bioaccessible fatty acid (%) significantly increased over time ($p < 0.01$). After the end of the gastric phase (180 min) the total fatty acid bioaccessibility was greater in the HGS ($6.55 \pm 0.85\%$) than in the shaking water bath model with gastric juice ($4.54 \pm 0.36\%$), $p < 0.05$. However, total fatty acid bioaccessibility at the end of the gastric phase in the shaking water bath model with gastric juice ($4.54 \pm 0.36\%$) was not significantly different than in the shaking water bath model with only pH adjusted water ($4.38 \pm 0.37\%$), $p > 0.05$. Thus, total fatty acid bioaccessibility at the end of the gastric phase was significantly higher in the model with peristaltic motion (HGS) than in the models that lacked peristaltic motion (shaking water bath model with gastric juice, shaking water bath model with only pH adjusted water).

After the end of the simulated gastric and intestinal digestion, total fatty acid bioaccessibility was not significantly different in the HGS ($8.88 \pm 0.36\%$) than in the shaking water bath model with gastric juices

($7.87 \pm 0.49\%$), $p > 0.05$. However, total fatty acid bioaccessibility in the HGS as well as the shaking water bath model with gastric juices were both significantly higher than fatty acid bioaccessibility in the shaking water bath model with only pH adjusted water ($5.15 \pm 0.17\%$), $p < 0.05$. Thus, at the end of the intestinal phase total fatty acid bioaccessibility was significantly higher in the models with simulated gastric and intestinal juices (HGS and shaking water bath model with gastric and intestinal juices) than in the model with only pH adjusted water (shaking water bath model with only pH adjusted water).

The percent bioaccessibility of individual fatty acids (C16:0, C18:1, C18:2, Table 4.3) was significantly influenced by the digestion model, digestion time, and their interaction ($p < 0.01$). The percent bioaccessibility of each individual fatty acid increased with time in all three digestion models ($p < 0.01$, Table 4.3). There were no significant differences between the percent bioaccessibility of individual fatty acids (C16:0, C18:1, and C18:2) at any timepoint within the same model. For example, the bioaccessibility of the three fatty acids (C16:0, C18:1, C18:2) in the HGS at the end of the gastric phase (180 min) were $6.38 \pm 0.83\%$, $6.30 \pm 0.82\%$, and $7.44 \pm 0.94\%$, respectively, and there were no significant differences between them ($p > 0.05$). By the end of the gastric and intestinal phase (360 min) the bioaccessibility of all three fatty acids had increased ($8.78 \pm 0.37\%$, $8.60 \pm 0.38\%$, and $9.86 \pm 0.32\%$) but there were still no significant differences between them. However, there were significant differences between the bioaccessibility of fatty acids at certain timepoints between models. For example, at the end of the gastric phase (180 min) the bioaccessibility of C18:1 was $6.30 \pm 0.82\%$, in the HGS, which was significantly higher than both the shaking water bath model with gastric juice ($4.37 \pm 0.34\%$) and the shaking water bath model with only pH-adjusted water ($4.21 \pm 0.36\%$) ($p < 0.05$) (Table 4.3).

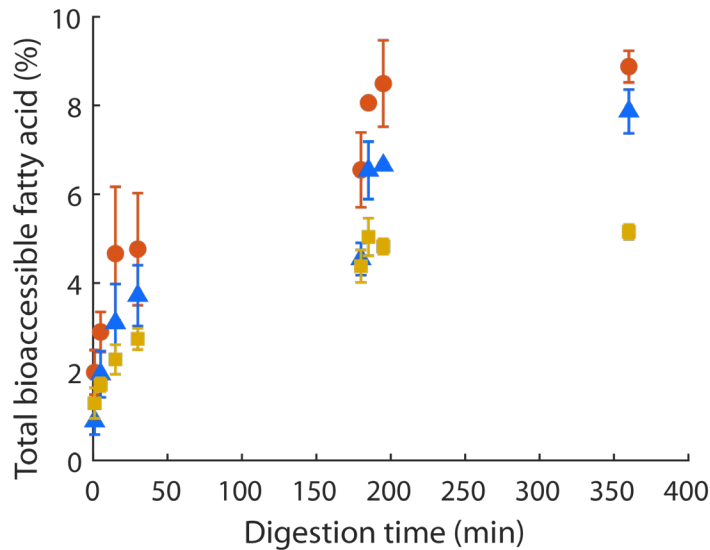


Figure 4.2. Total percent fatty acid bioaccessibility in the Human Gastric Simulator (●), shaking water bath (▲), and shaking water bath with only pH-adjusted water (■) models. All points represent the mean ($n = 3$) \pm standard deviation.

The total lipid content of almonds includes triacylglycerols, phospholipids, and minor contributions of other lipid species such as phytosterols. However, previous researchers have stated that the fat content of almonds is predominantly comprised of esterified fatty acids in the form of triacylglycerols (Yada et al., 2011), therefore the total bioaccessibility of fatty acids as reflected in Figure 4.2 closely reflects the bioaccessibility of total fat. Specifically, it has been determined by previous workers that the combination of oleic and linoleic acid comprises approximately 90% of total fat in almonds (Sathe, 1992). The compositional data gathered in this study showed that extractable fatty acid comprised $58.76 \pm 2.44\%$ of initial almond dry mass (Table 4.2). Previous researchers have determined the total fat content of California-grown almonds to be in the range of 54-56% (Sathe, 1992), which is close to the value of percentage of fatty acids found in this study, suggesting that the total fat content of almonds is primarily represented by fatty acids.

Table 4.2. Fatty acid composition of whole almonds used for in vitro digestion determined by direct acid extraction and Folch extraction (Section 4.4.1). Direct acid extraction was carried out on almond powder (10.08 ± 0.93 mg dry mass) and extractable fatty acid comprised $58.76 \pm 2.44\%$ of initial almond dry mass. Folch extraction was carried out on almond powder (10.42 ± 2.80 mg dry mass) and extractable fatty acid comprised $54.77 \pm 2.68\%$ of initial almond dry mass. All values are means \pm standard deviation ($n = 8$ for direct acid extraction and $n = 9$ for Folch extraction).

Fatty acid	Direct acid extraction			Folch extraction		
	Mass fatty acid extracted (mg)	Percent of initial almond dry mass (%)	Percent of total fatty acid (%)	Mass fatty acid extracted (mg)	Percent of initial almond dry mass (%)	Percent of total fatty acid (%)
Palmitic acid (C16:0)	0.40 ± 0.05	3.98 ± 0.16	6.74 ± 0.07	0.38 ± 0.11	3.62 ± 0.22	6.61 ± 0.33
Oleic acid (C18:1)	4.28 ± 0.57	42.32 ± 1.78	71.67 ± 0.35	3.90 ± 0.97	37.64 ± 2.29	68.79 ± 3.95
Linoleic acid (C18:2)	1.26 ± 0.17	12.45 ± 0.55	21.09 ± 0.29	1.40 ± 0.42	13.51 ± 2.56	24.60 ± 3.95

4.7.2 Particle breakdown

The Rosin–Rammler model provided a satisfactory fit to the cumulative distribution of particles, with the R^2 value for the fit at each timepoint ≥ 0.99 . x_{50} (mm^2) was significantly influenced ($p < 0.05$) by digestion model, digestion time, and their interaction (Table 4.4). To correct for minor differences in the value of x_{50} for the initial almond particles used for different digestion timepoints, particle size was also expressed as Δx_{50} , the change in particle size from initial (undigested) particles to digested particles. Δx_{50} was significantly influenced by digestion model, digestion time, and their interaction ($p < 0.05$,

Figure 4.3). There was a significant decrease in particle size during gastric digestion (15.9 mm^2 to 12.2 mm^2 , $p < 0.05$) but only in the HGS. There were no statistically significant differences between the sizes of the initial (undigested) particles used for any of the three digestion models.

The particle size distribution spread parameter b (dimensionless) was significantly influenced by digestion model, digestion time, and their interaction ($p < 0.01$, Table 4.4). Values of b decreased in the HGS, indicating that the distribution of particles became broader as time elapsed. For example, the value of b decreased from 2.72 ± 0.10 for undigested particles to 2.00 ± 0.14 for particles at the end of the gastric phase ($p < 0.01$). There were no statistically significant differences between the b values of the initial (undigested) particles used for any of the three digestion models.

The number of particles per gram of dry solids was significantly influenced by digestion model, digestion time, and their interaction ($p < 0.01$, Table 4.4). In the HGS, the number of particles per gram increased during digestion, with 60.1 ± 1.3 particles per gram dry solids after one minute of digestion and 216.2 ± 47 particles per gram of dry solids after gastric and intestinal digestion ($p < 0.05$). After 30 min digestion time the number of particles per gram dry solids was significantly higher in the HGS (88.4 ± 15.8) than in the shaking water bath model with gastric juice (61.1 ± 1.5) or the shaking water bath model with only pH-adjusted water (68.5 ± 7.5), $p < 0.05$. For all timepoints after 30 min the number of particles per gram dry solids was highest in the HGS, and there were no significant differences between the number of particles per gram dry solids between the two shaking water bath models. There were no statistically significant differences between the particles per gram of dry solids values of the initial (undigested) particles used for any of the three digestion models. Overall, the HGS was the only model that experienced a significant decrease in particle size as represented by Rosin–Rammler x_{50} as well as a significant increase in the number of particles per gram dry solids.

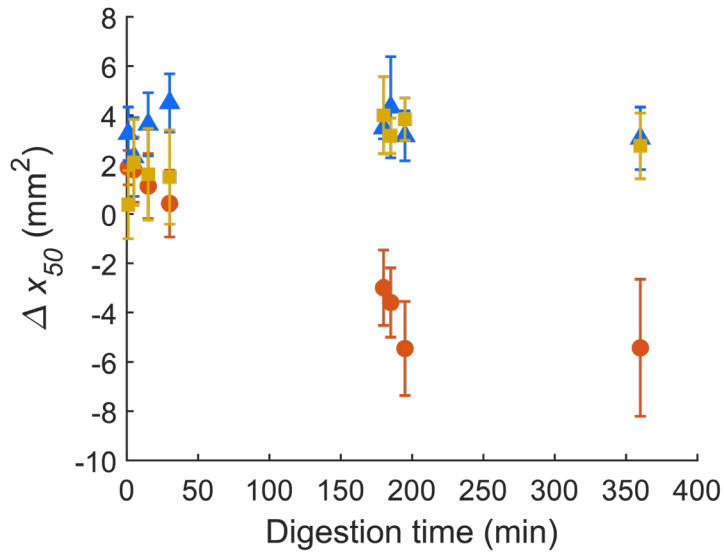


Figure 4.3. Change in Rosin–Rammler x_{50} (Equation 4.1) at each timepoint from x_{50} of the initial almond particles subjected to in vitro digestion shown for Human Gastric Simulator (●), shaking water bath (▲), and shaking water bath with only pH–adjusted water (■) models. All points represent the mean ($n = 3$) \pm standard deviation.

4.7.3 °Brix of liquid phase and moisture content of solid phase

°Brix of the liquid digesta was significantly influenced by digestion model, digestion time, and their interaction ($p < 0.01$, Table 4.5). Within each model, °Brix was significantly influenced by time ($p < 0.01$). For example, in the HGS °Brix increased from 0.40 ± 0.06 at the 1 min timepoint to 3.05 ± 0.06 at the end of the gastric phase (180 min), and 3.21 ± 0.00 at the end of the gastric and intestinal digestion (360 min).

Moisture content (% dry basis) of the solid particles was significantly influenced by digestion model and digestion time ($p < 0.01$, Table 4.5) but not their interaction ($p > 0.05$). Within each model, moisture content significantly increased over time ($p < 0.01$). For example, moisture content (percent dry basis) in the HGS increased from 30.72 ± 4.94 after 1 minute of digestion to 91.47 ± 1.21 after the complete gastric and intestinal digestion.

The pH was recorded and adjusted in each model according to the method described previously, and the measured values are shown in Table 4.6.

4.7.4 Scanning Electron Microscopy Images

Images of almond particles obtained using Scanning Electron Microscopy (SEM) are shown in Figure 4. The particle that was digested in the HGS (Figure 4.4 A) showed that almond cells located on the surface of the particle had ruptured cell walls. The undigested particle (Figure 4.4 B) showed lipid bodies adhering to the surface of the particle.

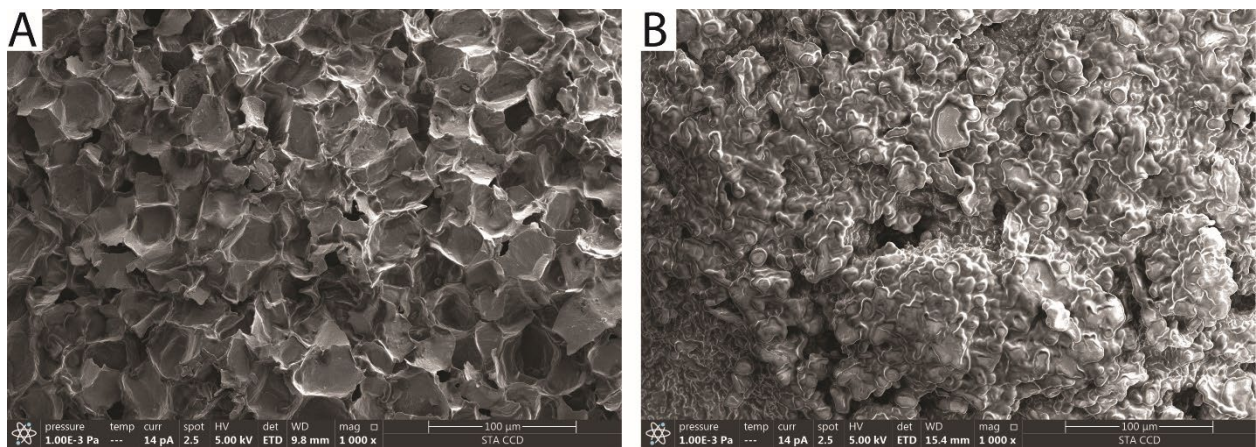


Figure 4.4. SEM images of an almond particle that was either (A) digested in the HGS for 180 min; (B) undigested. Scale bars represent 100 µm.

Table 4.3. Bioaccessible fatty acid in liquid digesta as percentage of initial fatty acid content of almonds. All values are means ($n = 3$) \pm standard deviation. Values in each column with no letter in common (abc) represent significant differences ($p < 0.05$) within a certain model across different digestion times. Values in each row with no letter in common (xyz) represent significant differences ($p < 0.05$) at a certain digestion time across the gastric digestion models for each fatty acid. If no letter is listed, there were no significant differences.

Time (min)	C16:0 (% bioaccessible)			C18:1 (% bioaccessible)			C18:2 (% bioaccessible)		
	HGS	Shaking water bath	Shaking water bath with only pH adjusted water	HGS	Shaking water bath	Shaking water bath with only pH adjusted water	HGS	Shaking water bath	Shaking water bath with only pH adjusted water
1	1.56 \pm 0.86 ^d	0.96 \pm 0.3 ^d	1.27 \pm 0.34 ^e	1.85 \pm 0.36 ^d	0.84 \pm 0.29 ^d	1.24 \pm 0.33 ^b	1.95 \pm 0.64 ^d	1.01 \pm 0.33 ^d	1.49 \pm 0.40 ^b
5	2.87 \pm 0.42 ^d	1.95 \pm 0.48 ^{cd}	1.65 \pm 0.16 ^e	2.79 \pm 0.44 ^d	1.87 \pm 0.51 ^{cd}	1.64 \pm 0.15 ^b	3.25 \pm 0.50 ^d	2.2 \pm 0.57 ^c	1.95 \pm 0.17 ^b
15	4.57 \pm 1.47 ^{c,x}	3.05 \pm 0.80 ^{bc,y}	2.20 \pm 0.32 ^{c,y}	4.48 \pm 1.44 ^{c,x}	2.99 \pm 0.87 ^{bc,y}	2.19 \pm 0.32 ^{b,y}	5.31 \pm 1.72 ^{c,x}	3.5 \pm 0.94 ^{bc,y}	2.59 \pm 0.38 ^{b,y}
30	4.68 \pm 1.22 ^{c,x}	3.63 \pm 0.64 ^{b,xy}	2.64 \pm 0.24 ^{bc,y}	4.57 \pm 1.21 ^{c,x}	3.57 \pm 0.67 ^{b,xy}	2.64 \pm 0.23 ^{b,y}	5.43 \pm 1.47 ^{c,x}	4.21 \pm 0.76 ^{b,xy}	3.12 \pm 0.28 ^{b,y}
180	6.38 \pm 0.83 ^{b,x}	4.43 \pm 0.38 ^{b,y}	4.18 \pm 0.30 ^{ab,y}	6.30 \pm 0.82 ^{b,x}	4.37 \pm 0.34 ^{b,y}	4.21 \pm 0.36 ^{a,y}	7.44 \pm 0.94 ^{b,x}	5.14 \pm 0.43 ^{b,y}	5.02 \pm 0.41 ^{a,y}
185	8.23 \pm 0.22 ^{a,x}	6.88 \pm 0.87 ^{a,y}	4.83 \pm 0.43 ^{az}	7.74 \pm 0.13 ^{ab,x}	6.31 \pm 0.57 ^{a,y}	4.85 \pm 0.40 ^{az}	9.08 \pm 0.15 ^{ab,x}	7.2 \pm 0.84 ^{a,y}	5.72 \pm 0.50 ^{az}
195	8.63 \pm 0.93 ^{a,x}	7.04 \pm 0.24 ^{a,y}	4.63 \pm 0.18 ^{az}	8.18 \pm 0.95 ^{a,x}	6.41 \pm 0.05 ^{a,y}	4.65 \pm 0.16 ^{az}	9.52 \pm 1.09 ^{a,x}	7.35 \pm 0.10 ^{a,y}	5.48 \pm 0.23 ^{az}
360	8.78 \pm 0.37 ^{a,x}	8.18 \pm 0.67 ^{a,x}	4.94 \pm 0.18 ^{a,y}	8.60 \pm 0.38 ^{a,x}	7.61 \pm 0.44 ^{a,x}	4.97 \pm 0.15 ^{a,y}	9.86 \pm 0.32 ^{a,x}	8.63 \pm 0.64 ^{a,x}	5.82 \pm 0.23 ^{a,y}

Table 4.4. Parameters of the Rosin–Rammler model (Equation 4.1) and particles per gram dry solids. The coefficient of determination (R^2) for the Rosin–Rammler distribution fit to the cumulative distribution of particle sizes was ≥ 0.99 in all cases. All values are means ($n = 3$) \pm standard deviation. Values in each column with no letter in common (abc) represent significant differences ($p < 0.05$) within a certain model across different digestion times. Values in each row with no letter in common (xyz) represent significant differences ($p < 0.05$) at a certain digestion time across the different models for each parameter. If no letter is listed, there were no significant differences.

Time (min)	x_{50} (mm ²)			b (dimensionless)			Particles per gram dry solids		
	HGS	Shaking water bath	Shaking water bath with only pH adjusted water	HGS	Shaking water bath	Shaking water bath with only pH adjusted water	HGS	Shaking water bath	Shaking water bath with only pH adjusted water
0	15.89 \pm 0.68 ^a	15.33 \pm 0.17 ^b	16.15 \pm 0.28 ^c	2.72 \pm 0.10 ^a	2.57 \pm 0.03	2.83 \pm 0.02	97.5 \pm 5.3 ^{abc}	109.7 \pm 10.3 ^a	97.8 \pm 4.4 ^a
1	17.62 \pm 0.38 ^a	18.40 \pm 0.52 ^{ab}	16.73 \pm 1.38 ^{bc}	2.80 \pm 0.12 ^a	2.93 \pm 0.13 ^a	2.92 \pm 0.27	60.1 \pm 1.3 ^{e,xy}	54.8 \pm 1.2 ^{e,y}	65.8 \pm 7.0 ^{bc,x}
5	17.65 \pm 1.03 ^a	18.01 \pm 0.03 ^{ab}	18.45 \pm 1.84 ^{abc}	2.64 \pm 0.10 ^a	2.86 \pm 0.27 ^a	2.88 \pm 0.36	67.7 \pm 6.3 ^{de}	61.7 \pm 2.8 ^{de}	59.4 \pm 8.8 ^c
15	16.63 \pm 1.03 ^a	18.78 \pm 1.75 ^a	17.96 \pm 1.92 ^{abc}	2.52 \pm 0.13 ^a	2.78 \pm 0.24 ^{ab}	2.77 \pm 0.12	78.7 \pm 10.9 ^{cd}	66.8 \pm 12.6 ^{cde}	65.1 \pm 7.8 ^{bc}
30	15.92 \pm 0.91 ^{a,y}	19.78 \pm 1.07 ^{a,x}	17.85 \pm 1.89 ^{abc,xy}	2.36 \pm 0.21 ^{ab,y}	2.87 \pm 0.24 ^{a,x}	2.60 \pm 0.15 ^{xy}	88.4 \pm 15.8 ^{bcd,x}	61.1 \pm 1.5 ^{de,y}	68.5 \pm 7.5 ^{bc,y}
180	12.19 \pm 1.29 ^{b,y}	18.84 \pm 0.71 ^{a,x}	20.36 \pm 1.43 ^{a,x}	2.00 \pm 0.14 ^{b,y}	2.81 \pm 0.21 ^{ab,x}	2.84 \pm 0.07 ^x	156.2 \pm 26.9 ^{ab,x}	74.1 \pm 5.2 ^{bcd,y}	63.8 \pm 7.4 ^{bc,y}
185	12.34 \pm 1.53 ^{b,y}	19.68 \pm 1.86 ^{a,x}	18.98 \pm 1.02 ^{abc,x}	2.01 \pm 0.01 ^{b,y}	2.56 \pm 0.26 ^{ab,x}	2.88 \pm 0.11 ^x	172.2 \pm 47.7 ^{a,x}	69.9 \pm 9.0 ^{bcd,y}	72.6 \pm 3.7 ^{ab,y}

195	11.47 ± 1.49 ^{b,y}	18.52 ± 1.19 ^{ab,x}	19.66 ± 0.27 ^{ab,x}	2.03 ± 0.09 ^{b,y}	2.52 ± 0.04 ^{ab,x}	2.85 ± 0.05 ^x	203.2 ± 50.2 ^{a,x}	81.0 ± 10.1 ^{ab,y}	66.2 ± 3.5 ^{bc,y}
360	11.50 ± 2.18 ^{b,y}	18.42 ± 1.20 ^{ab,x}	18.57 ± 0.71 ^{ab,x}	1.93 ± 0.17 ^{b,z}	2.37 ± 0.16 ^{b,y}	2.81 ± 0.14 ^x	216.2 ± 47 ^{a,x}	87.6 ± 10.4 ^{ab,y}	75.6 ± 1.4 ^{ab,y}

Table 4.5. Moisture content of solid particles (g moisture per g dry matter) and °Brix of liquid digesta. All values are means ($n = 3$) ± standard deviation. Values in each column with no letter in common (abc) represent significant differences ($p < 0.05$) within a certain model across different digestion times. Values in each row with no letter in common (xyz) represent significant differences ($p < 0.05$) at a certain digestion time across the different models. If no letter is listed, there were no significant differences.

Time (min)	°Brix			Moisture content (g moisture per g dry matter)		
	HGS	Shaking water bath	Shaking water bath with only pH adjusted water	HGS	Shaking water bath	Shaking water bath with only pH adjusted water
1	0.40 ± 0.06 ^c	0.34 ± 0.03 ^d	0.38 ± 0.07 ^c	30.72 ± 4.94 ^{c,y}	35.02 ± 1.60 ^{d,xy}	42.69 ± 3.78 ^{c,x}
5	0.57 ± 0.15 ^c	0.50 ± 0.03 ^c	0.53 ± 0.03 ^c	37.78 ± 3.40 ^c	40.40 ± 2.86 ^d	45.57 ± 2.45 ^c
15	1.20 ± 0.21 ^{b,x}	1.09 ± 0.23 ^{b,xy}	0.94 ± 0.05 ^{d,y}	50.05 ± 4.17 ^{b,y}	54.0 ± 1.66 ^{c,xy}	61.61 ± 2.77 ^{b,x}
30	1.41 ± 0.14 ^{b,x}	1.33 ± 0.03 ^{b,x}	1.06 ± 0.11 ^{cd,y}	57.56 ± 3.40 ^{b,y}	60.59 ± 6.20 ^{c,y}	71.05 ± 4.24 ^{b,x}
180	3.05 ± 0.06 ^{a,x}	3.10 ± 0.13 ^{a,x}	2.23 ± 0.04 ^{a,y}	81.89 ± 6.50 ^{a,y}	89.83 ± 2.62 ^{b,x}	95.56 ± 6.27 ^{a,x}
185	2.84 ± 0.11 ^{a,x}	2.65 ± 0.08 ^{a,x}	1.17 ± 0.21 ^{bcd,y}	86.59 ± 3.23 ^{a,y}	90.23 ± 0.95 ^{b,y}	98.24 ± 6.47 ^{a,x}
195	3.01 ± 0.07 ^{a,x}	2.68 ± 0.07 ^{a,x}	1.28 ± 0.11 ^{bc,y}	90.23 ± 5.68 ^{a,y}	99.18 ± 4.50 ^{ab,x}	103.72 ± 3.91 ^{a,x}
360	3.21 ± 0.00 ^{a,x}	2.85 ± 0.03 ^{a,x}	1.38 ± 0.04 ^{b,y}	91.47 ± 1.21 ^{a,y}	101.83 ± 1.98 ^{a,x}	104.30 ± 2.31 ^{a,x}

Table 4.6. pH of digesta. When a pH adjustment was called for by the digestion protocol (Section 4.2.3.1), the pH was recorded both before and after the adjustment was made. All values are means \pm standard deviation ($n = 3$).

Time (min)		Human Gastric Simulator	Shaking water bath	Shaking water bath with only pH adjusted water
0		2.02 \pm 0.03	2.00 \pm 0.05	2.02 \pm 0.05
1		2.37 \pm 0.07	2.17 \pm 0.04	2.21 \pm 0.11
5		2.70 \pm 0.11	2.61 \pm 0.05	2.73 \pm 0.14
15		3.15 \pm 0.13	3.14 \pm 0.07	3.52 \pm 0.22
30		3.38 \pm 0.13	3.39 \pm 0.06	4.07 \pm 0.09
60	Before adjusting to 3	3.52 \pm 0.17	3.80 \pm 0.07	4.45 \pm 0.09
	After adjusting to 3	3.01 \pm 0.03	3.01 \pm 0.04	3.00 \pm 0.01
120	Before adjusting to 2	3.47 \pm 0.13	3.52 \pm 0.02	3.94 \pm 0.01
	After adjusting to 2	2.06 \pm 0.01	2.04 \pm 0.01	2.03 \pm 0.02
180	End of gastric phase	2.90 \pm 0.09	2.75 \pm 0.03	3.00 \pm 0.03
	Before adjusting to 7	6.12 \pm 0.10	6.27 \pm 0.06	3.06 \pm 0.02
	After adjusting to 7	7.00 \pm 0.03	7.02 \pm 0.04	7.03 \pm 0.03
185		6.76 \pm 0.07	6.68 \pm 0.17	6.46 \pm 0.12
195		6.72 \pm 0.11	6.80 \pm 0.33	5.88 \pm 0.11
240	Before adjusting to 7	6.57 \pm 0.07	6.70 \pm 0.10	5.57 \pm 0.08
	After adjusting to 7	6.99 \pm 0.06	6.93 \pm 0.03	7.02 \pm 0.03
300	Before adjusting to 7	6.85 \pm 0.09	6.95 \pm 0.02	6.34 \pm 0.10
	After adjusting to 7	6.98 \pm 0.06	6.96 \pm 0.01	7.05 \pm 0.01
360		6.99 \pm 0.05	7.02 \pm 0.03	6.53 \pm 0.10

4.8 Discussion

Fatty acid bioaccessibility increased with time in both the HGS and shaking water bath models. However, fatty acid bioaccessibility at the end of the gastric phase (180 min) was greater for particles digested in the HGS (6.5%) than for those digested in the shaking water bath (4.5%), $p < 0.05$. The fatty acid bioaccessibility measured in the current study can be compared to the results of previous *in vitro* digestions of almonds. Mandalari *et al.*, (2008) (Mandalari et al., 2008) conducted *in vitro* digestion of almond cubes of size 2 mm, which were similar in size to the smallest particles used in the current study. Thus, it was hypothesized that fatty acid bioaccessibility found by Mandalari *et al.*, (2008), (7.6% at the end of simulated gastric digestion) would be higher than the value in the current study. This was supported by the data as the fatty acid bioaccessibility at the end of gastric digestion was 6.5% in the HGS model and was 4.5% in the shaking water bath model with simulated gastric juice. In another recent study it was found that 8.9% of lipid was released from almond particles after mastication (Mandalari et al., 2018). This is slightly higher than the result from this study (6.5% after gastric digestion in the HGS) which is likely due to the size of almond particles (roughly 1-3 mm) in this previous study, which was smaller than the size of particles in the current study (2-4 mm).

After simulated gastric and intestinal digestion, Mandalari *et al.*, (2008) found fatty acid bioaccessibility of 9.9%. This was slightly higher than the values of fatty acid bioaccessibility in the current study after gastric and intestinal digestion (8.9% in the HGS and 7.9% in the water bath model with simulated gastric juice). The fatty acid bioaccessibility in the HGS was closer to the results of Mandalari *et al.*, (2008), and it is hypothesized that this was due to the particle breakdown which occurred in the HGS but not in the shaking water bath model with simulated gastric juice. Although the initial size of the particles in the HGS and the shaking water bath model with simulated gastric juice were not significantly different, particle breakdown in the HGS effectively made the particles closer in size to those used by Mandalari *et al.*, (2008).

There was a significant reduction in the size of almond particles during the gastric phase in the HGS, but an increase in particle size over time for digestions in the shaking water bath. The increase in particle

size in the shaking water bath can be attributed to moisture uptake by almond particles, which also led to increased moisture content. Particle size in the HGS increased from the initial (undigested) timepoint until the 5-minute timepoint, but then began to decrease. This suggests that the magnitude of the particle size reduction in the HGS in the first five minutes of digestion was offset by the simultaneous effect of particle swelling due to moisture uptake. These results were similar to the results of Chen *et al.* who conducted in vitro digestion of peanut particles and found an increase in particle size during the first half hour of digestion, followed by a reduction in particle size by the end of the first hour (Chen et al., 2011). This supports the findings in the current study and suggests that near the beginning of digestion the change in particle size for nuts can be marked by an increase due to swelling followed by a decrease due to particle breakdown at later timepoints. These results are also supported by the conclusions of a recent study where microscopy was conducted on fecal samples from digestion of natural almonds in vivo. In this study, it was determined that the release of lipid during digestion could be in part due to the breakdown of almond particles in the digestive system (Mandalari et al., 2018). Results from the current study provide evidence that some of this breakdown could occur during gastric digestion.

The finding that almond particles broke down during the gastric phase of digestion in the HGS is in contrast to the results of Mandalari *et al.*, (2014) who conducted in vitro digestion of masticated almond particles using a dynamic gastric model and reported no significant change in the particle size distribution during digestion (Mandalari et al., 2014). However, the particles used by Mandalari *et al.*, (2014) (mean particle size ~500 μm) were smaller than those used in the current study (2 – 4 mm) and thus may have been less susceptible to breakdown. This is supported by the results of Chen *et al.* who conducted in vitro digestion using peanut particles of size 1 – 2 mm and reported size reduction of particles initially larger than 1 mm (Chen et al., 2011). It has been proposed that larger particles may be more susceptible to breakdown in the gastric environment than smaller particles (Guo et al., 2015; Lentle, 2018). Overall, the results of the current study, Chen *et al.* (2011), and Mandalari *et al.*, (2014) support this hypothesis, and suggest that nut particles greater than roughly 1 mm in size experience breakdown during in vitro gastric digestion in models that simulate the mechanical motion of the human stomach. In human digestion,

gastric sieving results in the selective retention of particles larger than roughly 1 – 2 mm in the stomach (Gopirajah et al., 2016; Guo et al., 2015). Gastric sieving has been reported during *in vivo* digestion of almonds where the growing pig was used as a model for the adult human (Bornhorst et al., 2014b, 2013c). The results of the current study suggest that nut particles greater than 1 mm can be broken down by *in vitro* models which include simulated peristalsis to a sufficiently small size to resemble those that would be emptied from the human stomach. This data could help future researchers design *in vitro* models for testing hypotheses related to gastric emptying, bioaccessibility, or satiety. To do this, an increased understanding of the mechanisms of particle breakdown during gastric digestion will be essential.

The breakdown of particles in the current study can be attributed to the peristaltic motion of the HGS, because particles in the shaking water bath model with simulated gastric juice did not break down, or increase in size due to swelling. However, it is unclear whether fluid shear, hydrostatic pressure, or particle–particle grinding was responsible for particle breakdown in the HGS (Kozu et al., 2014; Lentle, 2018). Fracture of foods during mastication has been previously reviewed (Skamniotis et al., 2017; Swackhamer and Bornhorst, 2019), but investigating the mechanisms of structural breakdown of solid foods in the gastric environment could be a topic for future research. In addition to particle breakdown, increased mixing of digesta could also have led to the higher lipid bioaccessibility in the HGS as compared to the shaking water bath models. Stronger mixing of *in vitro* digestion systems has been found by previous researchers to result in faster digestion kinetics (Dhital et al., 2014). In the current study, mixing could have led to higher fatty acid bioaccessibility by facilitating removal of lipolysis products from the lipid–aqueous interface, improving the access of lipases to triacylglycerol inside ruptured almond cells. Previous research has proposed that the oil–water interface can become crowded with products of lipolysis, particularly monoacylglycerol and free fatty acid, which have a hydrophilic and a hydrophobic moiety and self–orient around oil droplets in a monolayer, hindering the adsorption of digestive enzymes to the substrate (Capuano et al., 2018; Gallier and Singh, 2012; Singh et al., 2015). During almond digestion there are additional amphiphilic species that could contribute to interface crowding, for example phospholipids, which surround oil bodies inside almond cells, as well as oleosins,

endogenous almond proteins that stabilize oil bodies (Makkhun et al., 2015). The flow of digesta in the HGS could have helped remove these species from the interface, increasing access of digestive enzymes to the contents of almond cells, and contributing to the increased fatty acid bioaccessibility.

Previous researchers have constructed a mathematical model for the bioaccessibility of fatty acids from almonds (Grassby et al., 2014). The model assumed that almond particles were cubical with known, constant size, that all fatty acids from the outermost layer of cells became bioaccessible during digestion, and that no fatty acids from interior layers of cells became bioaccessible. The model was defined as:

$$L = \frac{1}{2} \left(\frac{64}{\pi^2} \left(\frac{d}{p} \right) - 8 \left(\frac{d}{p} \right)^2 + \frac{4}{3} \pi \left(\frac{d}{p} \right)^3 \right) * 100\% \quad 4.2$$

Where L is predicted lipid bioaccessibility (% of initial), d is the diameter of almond parenchymal cells (~36 μm), and p is the size of cubical almond particles. The model was evaluated for $p = 2 \text{ mm}$ and $p = 4 \text{ mm}$ to reflect the smallest and largest particles initially subjected to in vitro digestion in the current study, and the predicted fatty acid bioaccessibility values were 5.7% and 2.9%, respectively. Total bioaccessible fatty acid at the end of the gastric and intestinal digestion was 8.9% in the HGS and 7.9% in the shaking water bath model with simulated gastric juice. The slightly higher bioaccessibility values measured in this study could be due to a partial contribution of fatty acids from cells situated beneath the outermost surface of almond particles (Grundy et al., 2015b; M. M. L. Grundy et al., 2016). In the HGS, the model underprediction can also be attributed to particle breakdown as discussed previously.

Overall, the fatty acid bioaccessibility values found by the current study and previous (Grassby et al., 2017, 2014; Grundy et al., 2015b; Mandalari et al., 2008) in vitro studies are in agreement with the results of a study using human subjects, where it was found that the absorption of fatty acids from almond particles between 1.7 – 3.4 mm in size was approximately 10% (Berry et al., 2008), which is higher than the values predicted by the theoretical model for particles of this size (6.7% for 1.7 mm particles and 3.4% for 3.4 mm particles). This underprediction could have been due to the breakdown of almond particles during gastric digestion by human subjects. Findings of the current study suggest that particle

breakdown can be simulated by dynamic in vitro models, resulting in fatty acid bioaccessibility values more comparable to the in vivo reality.

SEM images suggested that the surfaces of undigested almond particles were coated in lipid bodies (Figure 4.4 B), whereas particles digested in the HGS for 180 min (Figure 4.4 A) had ruptured cell walls and lost their intracellular lipid contents during the digestion. Images of digested particles (Figure 4.4 A) showed the presence of broken cell walls, similar to SEM images of masticated almond particles obtained by previous researchers (Grundy et al., 2015a). This suggests that during either mastication or grinding in a food processor almond cells located on the surfaces of particles are ruptured, and their intracellular contents contribute to bioaccessible lipids during digestion. In this study, SEM images were used as a follow-up investigation and showed that lipid bodies attached to the surface of almond particles were removed during simulated gastric digestion in the HGS. However, in-depth investigation of the lipid release from almonds during digestion could be made using image analysis techniques applied to SEM images. This is an opportunity for future work that has been suggested by previous researchers (Dalmau et al., 2019).

Another objective of the current study was to determine the effect of simulated gastric and intestinal juices on the bioaccessibility of fatty acids from almond particles. Due to the recalcitrance of almond cells it has been proposed that only fatty acids present in cells that are ruptured during mastication or processing can become bioaccessible (Ellis et al., 2004; M. M.-L. Grundy et al., 2016). However, it is not clear whether fatty acids in ruptured cells can be simply washed away from the solid particles in the presence of water, or whether this release is affected by simulated digestive juices. This was investigated by conducting in vitro digestions of almond particles in the shaking water bath model using either simulated gastric and intestinal juices or with only pH adjusted water. Results showed that fatty acid bioaccessibility increased over time in the shaking water bath model with simulated gastric and intestinal juices as well as in the shaking water bath model with only pH-adjusted water ($p < 0.01$). Furthermore, at the end of the gastric phase of digestion (180 min) there was no significant difference in fatty acid bioaccessibility between the shaking water bath model with simulated gastric juice (4.5%) and the

shaking water bath model with only pH-adjusted water (4.4%), $p > 0.05$. However, fatty acid bioaccessibility at the end of gastric and intestinal (360 min) digestion was higher for the shaking water bath model with simulated gastric and intestinal juices (7.9%) than for the shaking water bath model with only pH-adjusted water (5.2%), $p < 0.01$. This suggests that fatty acid bioaccessibility was not significantly affected by the presence of simulated gastric juice but was affected by simulated intestinal juice. This finding did not support the hypothesis that fatty acid bioaccessibility at the end of the gastric phase would be higher for the shaking water bath model using simulated gastric juice than the shaking water bath model using only pH-adjusted water. It suggests, however, that in this system fatty acids in ruptured almond cells can become released under immersion in water at gastric pH (1.8) as efficiently as in simulated gastric juice.

The significant difference in bioaccessible fatty acid at the end of the intestinal phase between the shaking water bath model with simulated gastric and intestinal juices and the shaking water bath model using only pH-adjusted water suggests that intestinal juice affects fatty acid bioaccessibility. Additionally, models that used simulated intestinal juice experienced a greater increase in fatty acid bioaccessibility between the last timepoint in the gastric phase (180 min) and the first timepoint in the intestinal phase (185 min). This increase was 6.5% to 8.1% in the HGS, 4.5% to 6.5% in the shaking water bath model with simulated gastric and intestinal juices, and 4.4% to 5.0% in shaking water bath model using only pH-adjusted water (Figure 4.2). Although the jump in fatty acid bioaccessibility at the beginning of the intestinal phase cannot be attributed to any single component of simulated intestinal juice, it cannot be attributed to a reduction in particle size. This is because there was no significant difference in particle size or number of particles per gram of dry solids between the last timepoint in the gastric phase (180 min) and the first timepoint in the intestinal phase (185 min) for any model. Thus, emulsification by bile salts was likely responsible for the acute increase in fatty acid bioaccessibility at the start of the intestinal phase. This suggests that, even at the end of the gastric phase, there was still some fatty acid within ruptured cells or adhered to almond particles which was not fully released into the aqueous digesta until interaction with bile salts.

The fatty acids that were quantified in this study may have important functional roles *in vivo* (Calder, 2015). Compositional data gathered in this study indicated that 93% of fatty acids extracted from almonds were comprised of unsaturated fatty acids (71.7% oleic acid, 21.1% linoleic acid, Table 4.2). Results of randomized controlled trials have suggested that individuals adhering to diets including nuts or olive oil had reduced risk factors for cardiovascular events (de Lorgeril et al., 1999; Estruch et al., 2018). Furthermore, the high ratio of oleic acid to linoleic acid in almonds could be desirable for some consumers, with preliminary evidence suggesting that a higher ratio of oleic to linoleic acid is associated with reduced risk of obesity (Simopoulos, 2016).

4.9 Limitations

Limitations of this study included the use of a food processor for generation of almond particles that were then used for digestion experiments. Although the resulting particle size was justified as a reasonable approximation of the size of almond particles in a swallowable bolus, the crushing of almond particles by teeth could lead to a different surface structure of the resulting particles than the grinding of the food processor. Another limitation of this study was that only one initial particle size fraction was used. Future work could consider subjecting almond particles of varying initial sizes to *in vitro* gastric digestion either in the presence or in the absence of simulated peristalsis to determine if there is a size below which particles no longer break down into smaller pieces during digestion. In this study, SEM was used to qualitatively examine the surface of almond particles before and after *in vitro* gastric digestion, and it was determined that lipid globules initially present on the surface were removed during digestion. However, a quantitative analysis of almond surface microstructure or topology could be useful, especially if parameters describing the surface of almond particles could be related to outcome variables in digestion such as bioaccessibility of fatty acids. In this study, almond particles and simulated gastric fluid were added to the HGS with no secretion of gastric fluids to ensure that the biochemical conditions of the digestion were as close as possible in the HGS to those of the shaking water bath. However, this represents a limitation of the current study as stomach continuously secretes gastric juices during gastric

digestion and future research could consider conducting in vitro digestion of almond particles in a system that includes both simulated peristalsis as well as continuous secretion of gastric fluids.

4.10 Conclusions

Almond particles broke down in the HGS as evidenced by a significant reduction in particle size and a significant increase in the number of particles per gram of dry solids during the gastric phase. Particle breakdown was attributed to the peristaltic motion of the stomach as it did not occur for in vitro models that lacked peristaltic motion. Fatty acid bioaccessibility was greater in the HGS at the end of the gastric phase than in the shaking water bath model when identical simulated gastric juice was used, suggesting that the change in particle size contributed to higher fatty acid bioaccessibility. There was no significant difference in fatty acid bioaccessibility at the end of the gastric phase between digestions conducted in the shaking water bath with simulated gastric juice and digestions in the shaking water bath with only pH-adjusted water. However, fatty acid bioaccessibility at the end of the intestinal phase was higher in the shaking water bath model when simulated intestinal juice was used than when the intestinal digestion was carried out using only pH adjusted water.

Opportunities for future work include elucidating the effects of peristaltic motion on particle breakdown in the gastric environment and determining in more detail the mechanisms of fatty acid emulsification in the intestinal phase of digestion. Overall, results of this study showed that in vitro digestion of almond particles using a model with simulated peristaltic contractions resulted in particle size reduction and higher fatty acid bioaccessibility than in vitro digestion using a model that lacked peristaltic contractions. Results could assist in the design of future in vitro models for simulating human digestion as well as in the development of functional foods for targeted fatty acid bioaccessibility.

Chapter 5 Development and characterization of standardized model, solid foods with varying breakdown rates during gastric digestion

Rationale

In this study, model, solid foods with varying breakdown rates during gastric digestion were developed, addressing research objective 2 as stated in Chapter 1 (Introduction). This included two model foods that had macronutrient composition based on the Standard American Diet, as well as two model foods based on whey protein hydrogels, which served as a simpler model system. The main purpose for these model foods was to serve as test foods, allowing the physical property changes of solid foods during gastric digestion to be quantified. In Chapter 4 it was determined that simulated peristalsis led to the breakdown of almond particles, however, the physical properties of the almond particles could not be assessed and related to their breakdown as almond particles had an anisotropic microstructure as well as heterogeneous particle size distribution. The four model foods developed in this study can be prepared into sizes and shapes amenable for texture analysis, rheological analysis, or fracture property analysis using standard techniques. The fracture and rheological property changes of the model foods developed in this study during in vitro gastric digestion were assessed in Chapter 7, and then related to the different mechanisms of breakdown experienced by the model foods during in vitro gastric digestion that included simulated peristaltic contractions.

Abstract

Standardized, model solid foods were developed with varying initial hardness and breakdown rates during in vitro digestion. One class of model foods was based on the Standard American Diet, with strong and weak gel versions created by modulating pH. Another class was developed using whey protein hydrogels, with strong and weak gel versions produced by addition of pectin. The initial hardness of the model foods ranged from 6.2 ± 1.0 N (whey protein weak gel) to 56.2 ± 5.7 N (whey protein strong gel; $p < 0.05$), and softening half-times ranged between 58 ± 5 min (standard diet weak gel) and 775 ± 82 min (whey protein strong gel; $p < 0.05$). The model foods were placed into distinct classes according to the Food Breakdown Classification System. These model foods could help future studies develop relationships between food physical property changes during digestion and variables such as gastric emptying and satiety.

5.1 Introduction

Consumption of a solid food involves mastication followed by further breakdown of the food matrix in the gastric environment. However, there is a need for increased quantitative understanding of the breakdown of solid foods during gastric digestion. This could enable links to be established between food breakdown and physiological outcomes such as gastric emptying, nutrient absorption, and satiety (Bornhorst, 2017).

Due to reduced cost, increased throughput, and lesser ethical considerations compared to *in vivo* studies, *in vitro* digestion studies have become increasingly used to elucidate the mechanisms of food breakdown during digestion (Somaratne et al., 2020c). Furthermore, a proposed Food Breakdown Classification System (FBCS) has been developed to provide a systematic framework for categorizing the breakdown of solid foods in the gastric environment (Bornhorst et al., 2015). The FBCS built upon the Biopharmaceutics Classification System (Amidon et al., 1995), which sought to predict the likelihood of an *in vitro* – *in vivo* correlation for data on drug dissolution and absorption based on the breakdown rate of drug delivery systems in the gastrointestinal environment. Although more data is needed, this approach could be extended from drugs to foods, enabling a more detailed understanding of the relationships between food structures, breakdown rates, and physiological variables (Somaratne et al., 2020a).

Several recent studies have investigated the structural and textural changes that occur during digestion of food products such as apples (Olenskyj et al., 2020), cheese (Mulet-Cabero et al., 2017), rice (Schwanz Goebel et al., 2019), and potatoes (Drechsler and Ferrua, 2016). In addition to commercial food products, model foods have been developed and their breakdown assessed during *in vitro* digestion. This has included egg white gels (Nyemb et al., 2016), whey protein gels (Luo et al., 2017), and calcium-alginate gels (Lopez-Sanchez et al., 2018). Although there are many methods that can be used to quantify structural and textural changes in solid foods during digestion, the FBCS classification is based on the initial hardness of the food as determined by a uniaxial compression test and the softening half-time during *in vitro* gastric digestion (Bornhorst et al., 2015). The softening half-time is defined as the time during digestion at which the hardness of the food has decreased to one-half of its initial value. Using

these criteria, previous researchers found that foods with different glycemic indices as measured in vivo (Atkinson et al., 2008) were placed into distinct classes under the FBCS, suggesting the utility of the initial hardness and softening half-time parameters (Drechsler and Bornhorst, 2018). These previous studies demonstrate that the initial hardness and softening half-time are parameters that can be used to classify foods according to their breakdown. However, the targeted development of standardized, model solid foods with varying breakdown rates during in vitro digestion has not yet been reported.

The need for standardized test foods was identified by researchers in the field of nanotoxicology, who noted the significant impact of the food matrix on the bioaccessibility of nanoparticles, and proposed that a standardized food system be developed to increase comparability of results between laboratories (DeLoid et al., 2017; Sohal et al., 2018). Recently, this need has been partially met by the development of a standardized model food system in powder form in which nanoparticles can be encapsulated and their release assessed during digestion (Zhang et al., 2019b). The macronutrient composition of this standard model food system was based on the Standard American Diet, with data from the National Health and Nutrition Examination Survey database (NHANES 2013-2016), and the model food can be prepared in an emulsion form or powdered form. However, roughly 80% of the total calories consumed in the Standard American Diet are from solid foods (Mesirow and Welsh, 2015). Thus, there is a need for standardized model foods that can be prepared in solid form. Such standard test foods would complement the recently developed consensus protocols for in vitro digestion (Brodkorb et al., 2019; Minekus et al., 2014; Mulet-Cabero et al., 2020) and in turn allow for a more mechanistic understanding of the physical processes of digestion. Recent progress in food engineering has made it possible to design model foods with varying breakdown rates using minimal differences in formulation (Foegeding et al., 2017; Funami, 2011).

The aim of this study was to develop standardized, model solid foods with varying values of initial hardness and softening half-time as measured during in vitro digestion. Two model, solid foods with macronutrient composition based on the Standard American Diet but with varying initial hardness and softening half-times were developed. To serve as a simpler model system for studies that require a model food with less complexity than those based on the Standard American Diet, two additional model, solid

foods based on whey protein hydrogels were developed. The breakdown of the standard model foods was assessed using texture analysis, moisture diffusion analysis, and dry solids retention ratio analysis. The model foods were then categorized using the FBCS framework. Previous research using the FBCS has defined the hardness of a food particle as the as the maximum force during uniaxial compression to 50% strain, however, there has not yet been an analysis that considers the softening kinetics of texture parameters defined at other values of strain. In the present study, the forces at varying values of strain were assessed and their associated softening kinetics were determined to develop a more in-depth understanding of the texture change kinetics of the model foods. This analysis could help future studies to define texture properties at appropriate values of strain.

5.2 Materials and Methods

5.2.1 Materials

Whey protein isolate (BiPRO 9500) was generously donated by Agropur Ingredients (Eden Prairie, MN, USA). This batch of whey protein isolate was reported by the manufacturer to contain 97.9% protein (w/w) on a dry mass basis (Nitrogen conversion factor 6.38), 1.7% ash, 0.3% fat, and 4.8% moisture. Pectin (pectin 1400, degree of esterification 69-77%) was generously donated by TIC Gums (White Marsh, MD, USA). Corn starch (PURE-DENT B700) was generously donated by Grain Processing Corporation (Muscatine, IA, USA). Sodium Chloride (CAS 7647-14-5) and sucrose (CAS 57-50-1) were purchased from Sigma-Aldrich. Soybean oil (CAS 8001-22-7) was purchased from Thermo Fisher. Chemicals and ingredients used for preparation of model foods are given in Table 5.1.

Chemicals used for simulated saliva and gastric juice are given in Table 5.2. Water for all experiments was obtained from a Milli-Q Water Purification System (Merck Millipore, Billerica, MA, USA).

5.2.2 Preparation of model foods

Two types of model foods were developed and tested in this study. The first type of model foods were prepared based on the macronutrient composition of the standard US diet as reported by the National

Health and Nutrition Examination Survey (USDA Agricultural Research Service, 2019). This dataset was based on interviews with 15,984 consumers but is subject to limitations of dietary recall survey methods (Arab et al., 2011; Foster and Bradley, 2018). Furthermore, the Standard American Diet represents a population-level average and does not describe the diet of any particular individual. The same macronutrient ratio used for the standard diet model foods in this study has been used by previous researchers to produce a spray-dried model food powder (Zhang et al., 2019b, 2019a). Future studies may investigate development of model foods for specific populations that have a different macronutrient composition from the population-level average values used here.

Model solid foods based on the standard diet were prepared according to the formulations shown in Table 5.1. All dry ingredients were mixed and then slowly added to the appropriate mass of water. The dispersion was stirred for 1 h and then homogenized for 3 min at 10,000 rpm (Ultra Turrax T18 digital with S18N-19G disperser, IKA Works, Wilmington, NC, USA). The pH of the dispersion was then adjusted using 4 M HCl to either 5.2 or 2.5 to minimize changes in volume. Two versions of the standard diet model food were prepared in order to produce a mechanically strong version (standard diet strong gel – prepared at pH 5.2) and a mechanically weaker version (standard diet weak gel – prepared pH 2.5). Different pH levels were used to control the texture as it has been shown by previous researchers that pH can influence the texture of complex model food systems (Lorieau et al., 2018; van der Linden and Venema, 2007).

The second type of model foods prepared in this study were whey protein hydrogels with either 0% pectin or with 0.6% pectin, with both versions at pH 5.2 (Table 5.1). Addition of ingredients, homogenization, and pH adjustment of these model foods was carried out as described above. As with the standard diet model foods, a version of the whey protein model food was developed that was mechanically strong (whey protein strong gel – prepared with 0% pectin) as well as a version that was mechanically weaker (whey protein weak gel – prepared with 0.6% pectin). Pectin was added to change the texture of the whey protein model foods as it has been used by previous researchers (Beaulieu et al., 2001; Munialo et al., 2016).

Table 5.1. Chemicals and other ingredients used for preparation of model foods. All ingredients were dissolved in water so that the total mass of the dispersion was 100 g.

Concentration in model food (g dry matter/100 g)		
Component	Standard diet strong gel	Standard diet weak gel
Corn starch		11.71
Sucrose		10.50
Soybean oil		7.75
Whey protein isolate		7.63
Pectin		1.20
Sodium chloride		0.82
pH of dispersion	5.2	2.5
Component	Whey protein strong gel	Whey protein weak gel
Whey protein isolate		20.00
Sodium Chloride		0.82
Pectin	0.00	0.60
pH of dispersion		5.2

Gelation of model food dispersions was conducted according to a previously reported method (Chantrapornchai and McClements, 2002; Mennah-Govela et al., 2019). Briefly, dispersions were poured into silicone trays, which were covered in plastic to prevent evaporation and heated in a water bath at 90 °C for 60 min. After gelation, model foods were cooled overnight at 4 °C. After resting, model foods were cut into 1.3 cm cubes using a knife and the insert from a potato cutter with 1.3 cm edge length. This geometry was selected so that the texture properties of the model foods such as hardness could be directly compared with food products tested in previous studies (Mennah-Govela and Bornhorst, 2016a; Olenskyj et al., 2020). Steps used to prepare cubes of model foods are presented in a flow diagram in Figure 5.1 A.

After preparation, cubes of model food (Figure 5.2) were subjected to in vitro digestion and used for texture analysis.

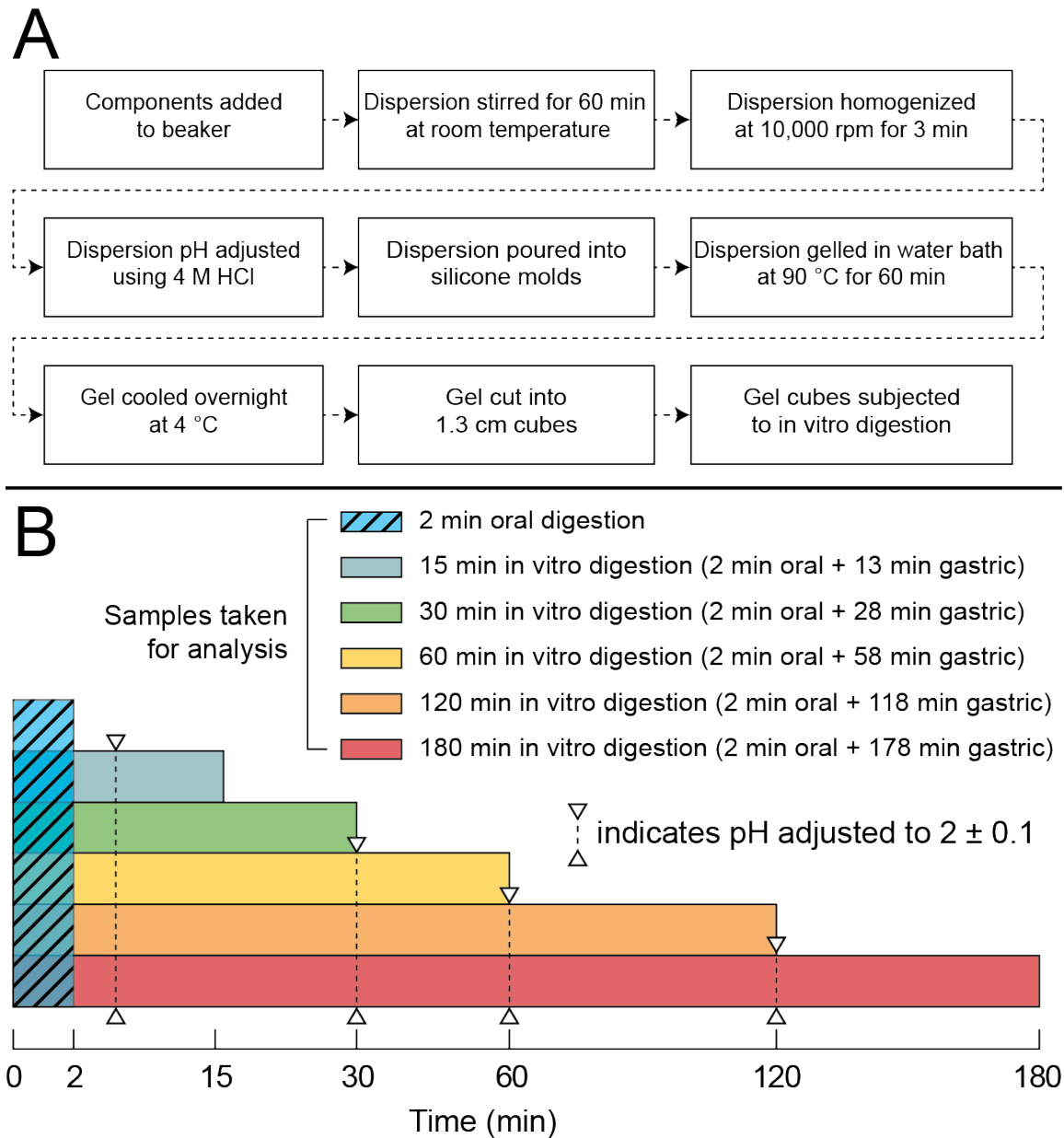


Figure 5.1. Process flow diagram showing steps in the preparation of model foods (A), and diagram showing the in vitro digestion protocol (B). All samples were subjected to in vitro oral digestion (2 min) followed by in vitro gastric digestion, for a maximum total time of 180 min. Samples were taken at 2, 15, 30, 60, 120, and 180 min. Each bottle containing cubes of model food was used for only one timepoint,

i.e., no cubes were removed at 30 min from the bottle designated to be the 60 min timepoint. pH was adjusted to 2 ± 0.1 at 5, 30, 60, and 120 min. Note that bars in the diagram (B) are not to scale.

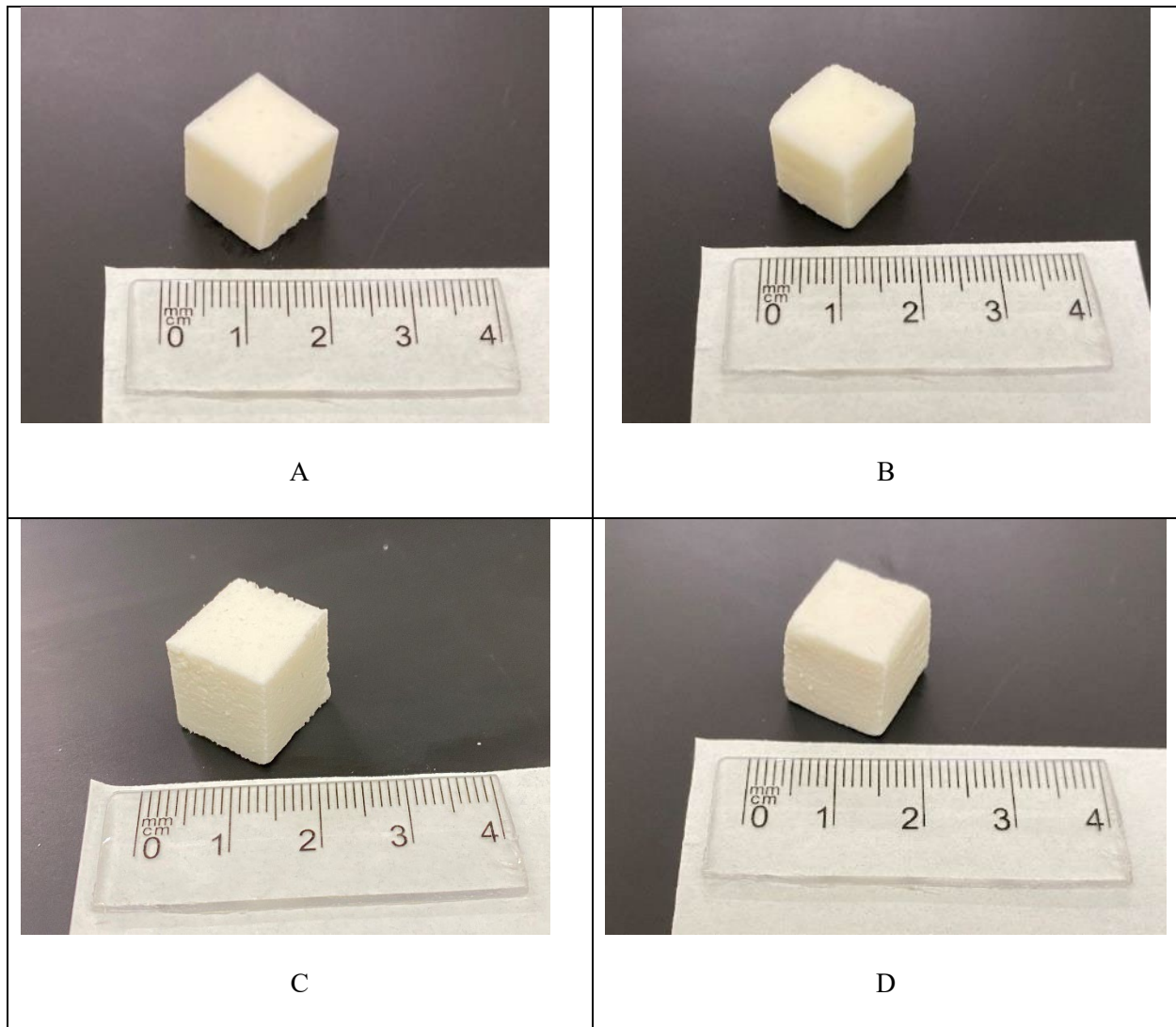


Figure 5.2. Images of undigested model foods cut into cubes of the size and shape that were used for in vitro digestion of the standard diet strong gel (A), standard diet weak gel (B), whey protein strong gel (C), and whey protein weak gel (D).

5.2.3 *Simulated saliva and gastric juice formulation*

Simulated saliva and gastric juice were prepared according to the INFOGEST protocol (Minekus et al., 2014), with the following modifications: Amano Lipase A was chosen as a gastric lipase analogue for its resistance to pepsin and for agreement with previous in vitro digestion research (van Aken et al.,

2011), and mucin was added to simulated saliva (1 mg/mL) and to simulated gastric juice (1.5 mg/mL) in accordance with previous research (Mennah-Govela et al., 2015). The formulation of simulated saliva and gastric juice used in this study is given in Table 5.2. The pH of simulated saliva was adjusted to 7 and the pH of simulated gastric juice was adjusted to 1.8 prior to the digestion. A pH of 1.8 was used for simulated gastric juice as the pH of basal gastric secretions is less than 2, and studies have shown that despite an initial rise in pH following meal consumption stomach pH returns to values between approximately 1.5 and 2 (Nadia et al., 2021b). Using simulated gastric juice at pH 1.8 ensures that pepsin activity is retained, which is important for the digestion of protein-containing foods such as the model foods in this study, as discussed in more detail by Mennah-Govela et al., (2021b).

Table 5.2. Composition of simulated saliva and gastric juice.

Component	Concentration in simulated saliva (mg/mL)	Concentration in simulated gastric juice (mg/mL)	Supplier
KCl	1.13	0.51	Fisher Scientific CAS: 7447-40-7
KH ₂ PO ₄	0.50	0.12	Fisher Scientific CAS: 7778-77-0
NaHCO ₃	1.14	2.10	EMD-Millipore CAS: 144-55-8
NaCl	-	2.76	Fisher Scientific CAS: 7647-14-5
MgCl ₂ (H ₂ O) ₆	0.03	0.02	Fisher Scientific CAS: 7791-18-6
(NH ₄) ₂ CO ₃	0.01	0.05	Fisher Scientific CAS: 506-87-6
CaCl ₂ (H ₂ O) ₂ **	0.22	0.02	Sigma-Aldrich CAS: 10035-04-8
Mucin (porcine stomach-type II)*	1.00	1.50	Sigma-Aldrich CAS: 84082-64-4
α -amylase (190 BAU mL ⁻¹ in simulated saliva)	1.18	-	MP Biomedicals CAS: 9000-90-2
Pepsin** (2000 U mL ⁻¹)	-	2.00	MP Biomedicals CAS: 9001-75-6
Amano Lipase A** (40 U mL ⁻¹)	-	3.33	Sigma-Aldrich CAS: 9001-62-1
pH of simulated saliva or gastric juice	7	1.8	

*Added to stock simulated saliva or gastric juice (used within one week)

**Added 35 min before beginning the digestion experiment

5.2.4 *In vitro* digestion protocol

Eleven cubes of a given type of model food were placed in a bottle and simulated saliva was added (0.2 mL per g model food). The bottle was transferred to a shaking water bath (TSSWB27, Thermo-Fisher, Waltham, MA, USA) which was set to 37 °C and 100 rpm for the 2 min oral digestion, which consisted of treatment with simulated saliva. No simulated mastication was conducted in order to preserve a consistent cubic particle geometry for assessment of food texture property changes during digestion, as has been done by previous researchers (Kozu et al., 2018; Olenskyj et al., 2020; Somaratne et al., 2020d; Wang et al., 2021). At the end of the oral digestion, simulated gastric juice was added (6 mL per g model food) and the bottle was returned to the shaking water bath. After 5 min, the pH in the liquid phase was measured and adjusted to 2 ± 0.1 , if necessary. pH was measured using a digital meter (Thermo-Fisher, Accumet AE150, Waltham, MA, USA) and adjusted in the same way at 30, 60, and 120 min total digestion time. Measured pH values are given in Table 5.13. 4 M HCl was used to adjust pH during *in vitro* digestion. The amount of 4 M HCl used as a percentage of total volume of liquid was 0.06-0.44%. At one of 6 predetermined time points (2 min-oral digestion, 15, 30, 60, 120, 180 min total oral + gastric digestion), all of the cubes were recovered from the bottle for testing. Thus, a separate bottle containing 11 cubes were used at each timepoint. All timepoints represent total *in vitro* digestion time including both oral and gastric digestion, for example, the 60 min timepoint consisted of 2 min oral digestion followed by 58 min simulated gastric digestion (Figure 5.1 B). Cubes were removed from the bottle by pouring through a sieve (aperture size ~0.5 mm) and were drained on the sieve for 1 min after which the mass of the cubes was measured. Cubes were then placed on a plastic cutting board at room temperature for 4 additional min. Next, 8 cubes of model food were subjected to texture analysis and 3 were used for moisture content analysis. Digestions for each model food were completed in triplicate, and the cubes of model food used for each replicate were prepared in a new batch.

5.2.5 Moisture content analysis

Three cubes of model food were cut in half, and their moisture content was determined gravimetrically by drying at 110 °C to constant weight (approximately 16 hours) (Swackhamer et al., 2019). Moisture content was reported on a dry basis (g water per g dry matter).

5.2.6 Diffusion modeling

The effective diffusion coefficient (D_{eff}) of water into cubes of model food during in vitro digestion was estimated using Fick's second law for a cubic geometry, which was adjusted from the solution for an infinite slab using Neumann's rule (Markowski et al., 2009; Yamile A. Mennah-Govela et al., 2020):

$$\frac{C_t - C_e}{C_0 - C_e} = \frac{8^3}{\pi^6} \left[\sum_{i=1}^{\infty} \frac{1}{(2i - 1)^2} \exp \left(-(2i - 1)^2 \pi^2 \frac{D_{\text{eff}} t}{L^2} \right) \right]^3 \quad 5.1$$

where C_t (g moisture/g dry matter) is the dry basis moisture content of cubes of model food during in vitro digestion at time t (s), C_e (g moisture/g dry matter) is the estimated equilibrium dry basis moisture content of cubes of model food during in vitro digestion, C_0 (g moisture/g dry matter) is the initial moisture content of model foods before digestion, L (m) is the length of the cube, D_{eff} (m^2/s) is the estimated effective diffusion coefficient of water in the model food matrix. 100 terms were used in the series. The model was fit to the data using MATLAB R2020a (MathWorks, Natick, MA). The parameter C_t was the dependent variable, t was the independent variable, C_e and D_{eff} were estimated from the fitting procedure, and C_0 and L were constants. C_0 (initial moisture content, g moisture/g dry matter) was based on the measured value for each replicate of each treatment. The normalized moisture content (C_t/C_0) was used to display the change in moisture of model foods during digestion. The assumptions of the model given by Equation 5.1 were: constant effective diffusivity of moisture in the model food matrix and negligible geometric change of the cubes with constant size $L = 1.3$ cm. Additional details on this modeling approach have been discussed by previous researchers (Markowski et al., 2009; Mennah-Govela and Bornhorst, 2016a). The quality of the model fit to experimental data was evaluated using the coefficient of determination (R^2) and relative root mean square error (RRMSE) (Mennah-Govela et al., 2019):

$$RRMSE = \left(\frac{1}{n} \sum_{i=1}^n \left(\frac{y_{model} - y_{obs}}{y_{obs}} \right)^2 \right)^{1/2} \quad 5.2$$

where n is the number of experimental replicates ($n=3$), y_{model} is the model-predicted value using Equation 5.1, and y_{obs} is the experimentally observed value.

5.2.7 Texture analysis of model foods

The texture of cubes of model food before digestion and after in vitro digestion was analyzed using a TA-XT Plus texture analyzer (Texture Technologies, Hamilton, MA, USA). Cubes were compressed at 1 mm/s to 75% strain using a 45 mm diameter cylindrical probe. The pre-test speed was 1 mm/s, the trigger force was 0.1 N, the test speed was 1 mm/s, and the post-test speed was 10 mm/s. The test was carried out at room temperature and data were collected at 500 Hz. The peak force during compression to 50% strain was defined as the hardness in accordance with a previously reported method (Bornhorst et al., 2015; Drechsler and Bornhorst, 2018). The hardness values of 8 cubes of a certain model food were averaged and the result was considered the hardness at that time point.

Additional properties of model foods were determined by expressing texture curves (force vs distance) as stress vs engineering strain. This was determined using a previously reported method (Delprete and Sesana, 2014; Mennah-Govela et al., 2019):

$$\varepsilon_e = \Delta h / h_0 \quad 5.3$$

$$\sigma = F / A_0 \quad 5.4$$

where ε_e (unitless) is engineering strain, Δh (m) is the change in height of the cube due to deformation by the probe, h_0 (m) is the initial height for the cube, σ (Pa) is the stress, F (N) is the normal force on the probe, and A_0 (m²) is the initial surface area of the cube in contact with the probe. The elastic modulus was calculated as the slope of the curve of stress vs strain on the linear elastic region (Munialo et al., 2016). The linear elastic region was defined between 7.5% and 15% strain for the standard diet strong gel, the whey protein strong gel and the whey protein weak gel. The linear elastic region was defined between 5% and 10% strain for the standard diet weak gel. Regression of stress vs. strain on the linear elastic

region was carried out to verify the linearity of the curves on the chosen intervals. The minimum R^2 value for linear regression of stress onto strain on the linear elastic region was 0.993. The fracture strain and fracture stress were estimated as the strain and stress, respectively, at the point when fracture of the cube of model food occurred (Kohyama et al., 2020).

5.2.8 *Dry solids retention ratio analysis*

The breakdown of model foods was assessed by quantifying the loss of dry solids by the cubes subjected to in vitro digestion. This was done according to a mass balance used by previous researchers (Mennah-Govela and Bornhorst, 2016b). The mass of dry solids retained by the cubes after being subjected to in vitro digestion for a given length of time was expressed as a percentage of their initial dry mass:

$$\text{Dry solids retention ratio (\%)} = (1 - S_t/S_0) * 100\% \quad 5.5$$

where S_t (g) is the mass of dry solids retained by the cubes after in vitro digestion for a given time, and S_0 (g) is the initial mass of dry solids in the cubes (before in vitro digestion). The moisture content of the sample of three cubes selected for moisture content analysis was used to calculate the dry mass retained at each timepoint by the 11 cubes that were subjected to in vitro digestion.

5.2.9 *Weibull analysis*

The Weibull function (Equation 5.6) was used to determine the kinetics of the change in hardness, elastic modulus, and dry solids retention ratio of model foods during digestion.

$$Y(t) = Y_0 \cdot \exp(-(kt))^\beta \quad 5.6$$

where $Y(t)$ (N) is the hardness, elastic modulus, or dry solids retention ratio at time t (min) after the start of in vitro digestion, Y_0 (N) is the initial value of the respective variable (before digestion), k (min^{-1}) is the scale parameter, and β (dimensionless) is the shape parameter. The Weibull function given by Equation 5.6 was fit to experimental data using MATLAB R2020a. The goodness of fit of the model to experimental data was evaluated using the coefficient of determination (R^2) as well as the relative root mean square error (RRMSE, Equation 5.2). The half-time was evaluated from the Weibull function as:

$$t_{1/2} = \ln(2)^{1/\beta} / k \quad 5.7$$

where $t_{1/2}$ (min) is the time at which the variable fit to the Weibull function has declined to 50% of its initial value, and β and k are the parameters derived from Equation 5.6.

As a follow up analysis of the softening kinetics of model foods, the Weibull function was used to fit the force obtained at varying values of engineering strain during digestion. Specifically, the force at levels of strain ranging from 5% to 75% in increments of 5% were obtained at each timepoint during digestion and fit to the Weibull function. This was carried out to determine if the level of engineering strain used to define the dependent variable for the Weibull function influenced its parameters (β and k).

5.2.10 Soluble solids analysis

After separating solid cubes from simulated gastric fluids, the soluble solids content of the liquid phase was measured in triplicate using a digital refractometer (HI 96800, Hannah Instruments, Woonsocket, RI) and expressed as °Brix.

5.2.11 Statistical analysis

Statistical analysis was conducted using SAS Enterprise Guide 7.1 (SAS Institute, Cary, NC, USA). Two factor analysis of variance (ANOVA) was used to determine the influence of model food type (whey protein strong gel, whey protein weak gel, standard diet strong gel, standard diet weak gel), and digestion time (0, 2, 15, 30, 60, 120, 180 min) on variables measured at each time point during digestion (hardness, elastic modulus, fracture stress, fracture strain, dry solids retention ratio, dry basis moisture content, and soluble solids content). Two factor analysis of variance (ANOVA) was used to determine the influence of model food type (whey protein strong gel, whey protein weak gel, standard diet strong gel, standard diet weak gel), and strain (5, 10, 15, 20, 25, 30, 35, 40, 45, 50, 55, 60, 65, 70, 75%) on parameters of the Weibull function (k and β) fit to the force at each level of strain. One factor ANOVA was used to determine the influence of model food type (whey protein strong gel, whey protein weak gel, standard diet strong gel, standard diet weak gel) on the initial hardness, initial elastic modulus, and parameters

from fitting the Weibull function to elastic modulus, hardness, and dry solids retention ratio during digestion (k , β , and half-time).

Normality of the model residuals was assessed using a quantile-quantile plot, and homogeneity of variance was assessed using the Brown-Forsythe test. Remediation was necessary for soluble solids content of liquid digesta and for β values from fitting the Weibull function to the force at varying levels of strain and was conducted using the Box-Cox transformation (lambda values -0.69 and -1.06, respectively). In all cases, when the F-statistic for the overall model was significant ($p < 0.05$), post-hoc tests were conducted using Tukey's HSD, and significance was noted for $p < 0.05$.

Linear regressions were conducted using MATLAB 2020a. All results are presented as the mean \pm standard deviation.

5.3 Results

5.3.1 *Texture and fracture properties of model foods*

Model foods softened during digestion, as evidenced through a downward shift in their texture curves (Figure 5.3). Initial hardness ranged between 6.2 ± 1.0 N for the whey protein weak gel to 56.2 ± 5.7 N for the whey protein strong gel ($p < 0.05$). Hardness was significantly influenced by the type of food, digestion time, and their interaction ($p < 0.001$; Table 5.7). Normalized hardness was fit to the Weibull function (Equation 5.6). The Weibull function provided a good fit to the data, with R^2 ranging from 0.95 to 0.99 (Figure 5.4, Table 5.8). The standard diet weak gel had the shortest softening half-time of the four model foods (58 ± 5 min), which was significantly lower ($p < 0.05$) than the softening half-time of the whey protein strong gel (775 ± 82 min), which had the longest softening half-time.

The linear elastic region of the texture curve was used to define the elastic modulus (Table 5.9). The initial elastic modulus was significantly influenced by the type of model food ($p < 0.001$). The smallest value of initial elastic modulus was 107 ± 21 kPa (whey protein weak gel) and the largest was 433 ± 96 kPa (whey protein strong gel, $p < 0.05$). The elastic modulus was significantly influenced by the type of model food and digestion time ($p < 0.001$) but not by their interaction ($p > 0.05$). The elastic modulus averaged across all digestion timepoints was significantly different between the standard diet strong gel

(237 kPa) and standard diet weak gel (180 kPa; $p < 0.001$). Additionally, the average elastic modulus was significantly different between the whey protein strong gel (336 kPa) and the whey protein weak gel (80 kPa; $p < 0.001$).

The normalized elastic modulus was fit to the Weibull function (Equation 5.6; Figure 5.5). The Weibull function provided an acceptable fit to the elastic modulus with R^2 ranging from 0.91 to 0.96 (Table 5.8). The Weibull function was used to define a softening half-time (Equation 5.7) which gives the approximate digestion time at which the modulus would decline by 50% from its initial value. The softening half-time for the elastic modulus was significantly influenced by the type of food ($p < 0.001$) and ranged from 60 ± 9 min for the standard diet weak gel to 543 ± 164 min for the whey protein strong gel ($p < 0.05$).

The standard diet strong gel, standard diet weak gel, and whey protein weak gel model foods fractured during uniaxial compression, which resulted in a local maximum in their texture curves (Figure 5.3). The fracture point was used to define the fracture stress and fracture strain (Table 5.9). The whey protein strong gel did not visibly fracture during the compression. Photographs of the model foods before and after compression to 75% strain are shown in Figure 5.2 and Figure 5.10, respectively.

The fracture stress was significantly influenced by the type of model food, digestion time, and their interaction ($p < 0.001$). The initial fracture stress (for the undigested model foods) was significantly higher than the fracture stress at the final digestion timepoint for the standard diet strong gel and the standard diet weak gel ($p < 0.05$), but not for the whey protein weak gel ($p > 0.05$). The whey protein strong gel did not have an evident fracture point during compression.

The fracture strain was significantly influenced by the type of model food ($p < 0.001$) but not by digestion time or the interaction of food and digestion time ($p > 0.05$). None of the three model foods that fractured during the compression test demonstrated a significant change in fracture strain during digestion. This can be visualized in the example texture curves (Figure 5.3) which show how the curves trended downwards during digestion, but the x -axis location of the fracture point did not significantly change. However, there was a significant difference between the average fracture strain for the standard

diet weak gel (0.20) and the average fracture strain for the standard diet strong gel (0.40) across all digestion timepoints ($p < 0.001$). Additionally, there was a significant difference between the average value of fracture strain for the standard diet weak gel (0.20) and whey protein weak gel (0.42) across all digestion times ($p < 0.001$).

Previous studies have defined hardness as the maximum force achieved during compression to 50% strain (Bornhorst et al., 2015; Drechsler and Bornhorst, 2018), however, the Weibull function given by Equation 5.6 can be fit to the change in force obtained at any level of strain. It was desired to carry out an analysis of Weibull function fits to the force at varying levels of strain to determine the sensitivity of the Weibull parameters (k , β) to the level of strain. This was conducted by obtaining the force at values of strain between 5% and 75% in increments of 5% strain for each model food at each timepoint during in vitro digestion and using these values to determine parameters of the Weibull function (Figure 5.6, Table 5.3 - Table 5.6).

When considering the entire range from 5% to 75% strain, it was found that the Weibull k value was significantly influenced by the type of food ($p < 0.001$), the level of strain ($p < 0.001$), and their interaction ($p < 0.001$). The Weibull β value was significantly influenced by the type of food ($p < 0.05$), but not by the level of strain or their interaction ($p > 0.05$). However, post-hoc tests showed that there were no statistically significant differences in the value of k or β for Weibull functions fit to the force at values of strain between 20% and 60%. This shows that for the model foods in this study the Weibull function could be fit to force measured between 20% and 60% engineering strain and yield parameters (k , β) that were not significantly different. This behavior can be identified visually in the values of k and β between 20% and 60% strain (Figure 5.6 A and B, respectively), where the region with no significant differences lies between the vertical dashed lines.

Table 5.3. Parameters of the Weibull function (Equation 5.6) fit to values of force measured at different levels of strain over time during in vitro digestion for the standard diet strong gel (standard diet model food prepared at pH 5.2). Values represent the mean (n=3) \pm standard deviation.

Strain (unitless)	H_0 (N)	$k * 10^3$ (min⁻¹)	β (dimensionless)	R^2	$t_{1/2}$ (min)
0.05	2.01 \pm 0.30	2.20 \pm 0.71	0.56 \pm 0.19	0.797 \pm 0.231	232 \pm 47
0.10	5.06 \pm 0.52	2.55 \pm 0.50	0.43 \pm 0.11	0.938 \pm 0.054	165 \pm 29
0.15	8.04 \pm 0.76	2.62 \pm 0.54	0.40 \pm 0.08	0.959 \pm 0.021	152 \pm 19
0.20	10.86 \pm 1.06	2.62 \pm 0.61	0.39 \pm 0.07	0.966 \pm 0.021	149 \pm 15
0.25	13.45 \pm 1.47	2.59 \pm 0.65	0.39 \pm 0.07	0.969 \pm 0.025	150 \pm 14
0.30	15.78 \pm 1.91	2.52 \pm 0.67	0.38 \pm 0.07	0.970 \pm 0.025	154 \pm 16
0.35	17.73 \pm 2.45	2.50 \pm 0.68	0.39 \pm 0.07	0.971 \pm 0.02	156 \pm 15
0.40	18.39 \pm 3.11	2.77 \pm 0.64	0.45 \pm 0.10	0.973 \pm 0.012	157 \pm 8
0.45	16.52 \pm 2.69	2.87 \pm 1.06	0.57 \pm 0.18	0.958 \pm 0.044	184 \pm 29
0.50	16.07 \pm 2.30	3.08 \pm 0.97	0.51 \pm 0.14	0.969 \pm 0.023	158 \pm 19
0.55	17.06 \pm 2.29	3.30 \pm 0.61	0.48 \pm 0.11	0.975 \pm 0.011	138 \pm 2
0.60	19.10 \pm 2.50	3.61 \pm 0.37	0.46 \pm 0.11	0.980 \pm 0.009	123 \pm 13
0.65	22.21 \pm 2.76	3.78 \pm 0.32	0.45 \pm 0.11	0.984 \pm 0.007	114 \pm 17
0.70	27.02 \pm 3.15	3.82 \pm 0.35	0.43 \pm 0.10	0.987 \pm 0.007	109 \pm 18
0.75	35.71 \pm 4.12	3.88 \pm 0.40	0.39 \pm 0.08	0.989 \pm 0.006	99 \pm 19

Table 5.4. Parameters of the Weibull function (Equation 5.6) fit to values of force measured at different levels of strain over time during in vitro digestion for the standard diet weak gel (standard diet model food prepared at pH 2.5). Values represent the mean (n=3) \pm standard deviation.

Strain (unitless)	H_0 (N)	$k * 10^3$ (min ⁻¹)	β (dimensionless)	R^2	$t_{1/2}$ (min)
0.05	1.41 \pm 0.21	3.20 \pm 1.06	1.21 \pm 0.32	0.664 \pm 0.355	242 \pm 62
0.10	4.12 \pm 0.45	3.30 \pm 0.76	0.56 \pm 0.11	0.898 \pm 0.121	158 \pm 16
0.15	6.42 \pm 0.82	4.38 \pm 0.98	0.43 \pm 0.08	0.965 \pm 0.037	97 \pm 6
0.20	7.68 \pm 1.02	5.79 \pm 1.17	0.41 \pm 0.08	0.986 \pm 0.014	70 \pm 3
0.25	7.74 \pm 1.02	6.33 \pm 1.20	0.41 \pm 0.08	0.993 \pm 0.006	64 \pm 4
0.30	7.23 \pm 0.87	5.93 \pm 1.19	0.42 \pm 0.09	0.993 \pm 0.007	70 \pm 6
0.35	7.19 \pm 0.82	6.14 \pm 0.97	0.43 \pm 0.08	0.990 \pm 0.009	69 \pm 3
0.40	7.55 \pm 0.86	6.51 \pm 0.89	0.43 \pm 0.08	0.989 \pm 0.010	64 \pm 3
0.45	8.17 \pm 0.98	6.93 \pm 0.79	0.42 \pm 0.08	0.990 \pm 0.009	60 \pm 4
0.50	9.01 \pm 1.10	7.19 \pm 0.76	0.42 \pm 0.08	0.990 \pm 0.009	57 \pm 5
0.55	10.16 \pm 1.29	7.34 \pm 0.72	0.42 \pm 0.08	0.991 \pm 0.008	56 \pm 6
0.60	11.88 \pm 1.60	7.63 \pm 0.73	0.40 \pm 0.08	0.991 \pm 0.008	52 \pm 8
0.65	14.70 \pm 2.13	8.45 \pm 1.07	0.37 \pm 0.08	0.992 \pm 0.007	44 \pm 10
0.70	19.45 \pm 2.99	10.30 \pm 2.01	0.33 \pm 0.06	0.993 \pm 0.005	33 \pm 10
0.75	27.49 \pm 4.46	13.19 \pm 3.50	0.30 \pm 0.05	0.994 \pm 0.005	23 \pm 9

Table 5.5. Parameters of the Weibull function (Equation 5.6) fit to values of force measured at different levels of strain over time during in vitro digestion for the whey protein strong gel (whey protein hydrogel model food with 0% pectin). Values represent the mean (n=3) \pm standard deviation.

Strain (unitless)	H_0 (N)	$k * 10^3$ (min ⁻¹)	β (dimensionless)	R^2	$t_{1/2}$ (min)
0.05	3.05 \pm 0.25	1.80 \pm 1.48	0.98 \pm 0.59	0.794 \pm 0.187	501 \pm 288
0.10	7.79 \pm 0.81	1.40 \pm 0.51	0.51 \pm 0.08	0.935 \pm 0.039	367 \pm 93
0.15	11.84 \pm 1.49	1.20 \pm 0.26	0.46 \pm 0.08	0.963 \pm 0.014	384 \pm 97
0.20	15.59 \pm 2.08	1.02 \pm 0.19	0.45 \pm 0.07	0.970 \pm 0.01	440 \pm 133
0.25	19.56 \pm 2.59	0.91 \pm 0.15	0.45 \pm 0.08	0.973 \pm 0.008	494 \pm 152
0.30	24.08 \pm 3.11	0.83 \pm 0.12	0.45 \pm 0.08	0.973 \pm 0.008	546 \pm 159
0.35	29.46 \pm 3.63	0.76 \pm 0.09	0.46 \pm 0.08	0.973 \pm 0.007	600 \pm 157
0.40	36.10 \pm 4.23	0.70 \pm 0.06	0.47 \pm 0.09	0.972 \pm 0.007	655 \pm 140
0.45	44.68 \pm 4.88	0.65 \pm 0.05	0.48 \pm 0.10	0.971 \pm 0.007	708 \pm 114
0.50	56.18 \pm 5.66	0.61 \pm 0.09	0.50 \pm 0.12	0.968 \pm 0.008	775 \pm 82
0.55	71.52 \pm 6.49	0.56 \pm 0.14	0.52 \pm 0.14	0.964 \pm 0.011	890 \pm 113
0.60	92.41 \pm 7.45	0.51 \pm 0.20	0.55 \pm 0.17	0.957 \pm 0.013	1061 \pm 293
0.65	121.95 \pm 8.45	0.45 \pm 0.25	0.57 \pm 0.20	0.949 \pm 0.017	1357 \pm 645
0.70	165.59 \pm 9.33	0.40 \pm 0.27	0.58 \pm 0.22	0.944 \pm 0.018	1738 \pm 1134
0.75	230.48 \pm 10.08	0.39 \pm 0.28	0.61 \pm 0.24	0.942 \pm 0.015	2090 \pm 1633

Table 5.6. Parameters of the Weibull function (Equation 5.6) fit to values of force measured at different levels of strain over time during in vitro digestion for the whey protein weak gel (whey protein hydrogel model food with 0.6% pectin). Values represent the mean (n=3) \pm standard deviation.

Strain (unitless)	H_0 (N)	$k * 10^3$ (min^{-1})	β (dimensionless)	R^2	$t_{1/2}$ (min)
0.05	0.83 \pm 0.17	1.24 \pm 0.90	0.40 \pm 0.13	0.892 \pm 0.117	373 \pm 148
0.10	1.80 \pm 0.36	1.87 \pm 0.43	0.42 \pm 0.08	0.960 \pm 0.040	224 \pm 20
0.15	2.70 \pm 0.59	2.08 \pm 0.06	0.45 \pm 0.02	0.976 \pm 0.015	214 \pm 7
0.20	3.50 \pm 0.80	1.95 \pm 0.34	0.45 \pm 0.06	0.976 \pm 0.001	230 \pm 18
0.25	4.19 \pm 0.96	1.73 \pm 0.46	0.45 \pm 0.08	0.972 \pm 0.013	259 \pm 31
0.30	4.79 \pm 1.04	1.50 \pm 0.51	0.45 \pm 0.10	0.965 \pm 0.023	304 \pm 58
0.35	5.28 \pm 1.04	1.23 \pm 0.55	0.45 \pm 0.12	0.956 \pm 0.033	390 \pm 128
0.40	5.61 \pm 0.91	0.96 \pm 0.59	0.43 \pm 0.13	0.953 \pm 0.033	562 \pm 332
0.45	5.83 \pm 0.86	0.80 \pm 0.51	0.40 \pm 0.13	0.953 \pm 0.034	657 \pm 411
0.50	6.22 \pm 0.97	0.79 \pm 0.36	0.39 \pm 0.09	0.954 \pm 0.033	536 \pm 187
0.55	6.97 \pm 1.17	0.99 \pm 0.25	0.41 \pm 0.08	0.946 \pm 0.030	417 \pm 35
0.60	8.22 \pm 1.49	1.13 \pm 0.27	0.45 \pm 0.09	0.927 \pm 0.043	395 \pm 74
0.65	10.2 \pm 2.00	1.11 \pm 0.42	0.50 \pm 0.12	0.893 \pm 0.068	466 \pm 169
0.70	13.52 \pm 2.86	0.94 \pm 0.44	0.54 \pm 0.17	0.839 \pm 0.109	613 \pm 284
0.75	19.15 \pm 4.27	0.60 \pm 0.50	0.54 \pm 0.26	0.778 \pm 0.159	1013 \pm 410

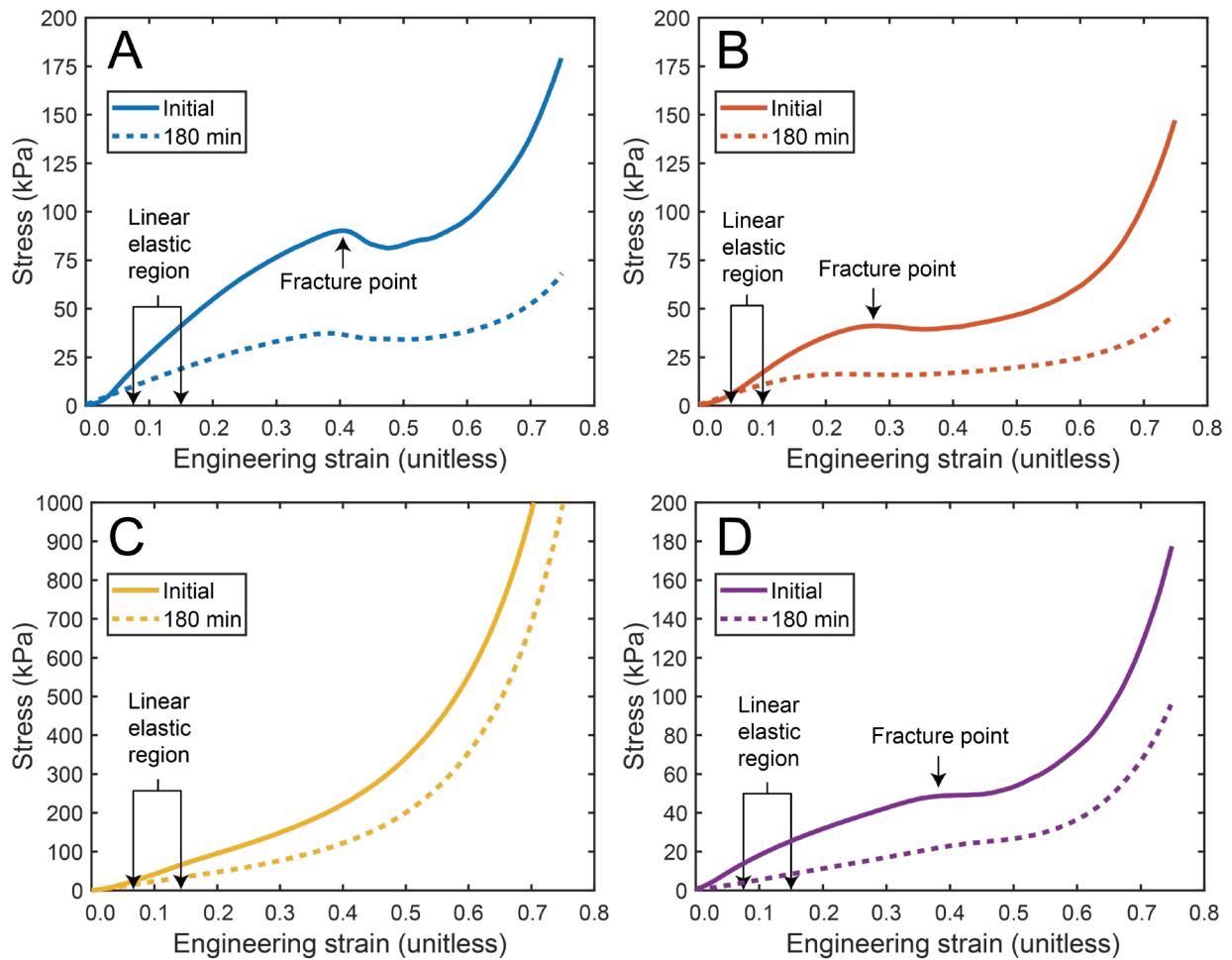


Figure 5.3. Example stress vs strain curves for cubes of the standard diet strong gel (A), standard diet weak gel (B), whey protein strong gel (C), whey protein weak gel (D) model foods before in vitro digestion (initial) and after in vitro digestion (180 min), showing the softening that occurred due to in vitro digestion. Note that the whey protein strong gel did not fracture during the compression and is shown with a different y axis range. The slope of the curve in the linear elastic region was used to define the elastic modulus. Photographs of the model foods before and after compression are shown in Figure 5.1 and Figure 5.9, respectively.

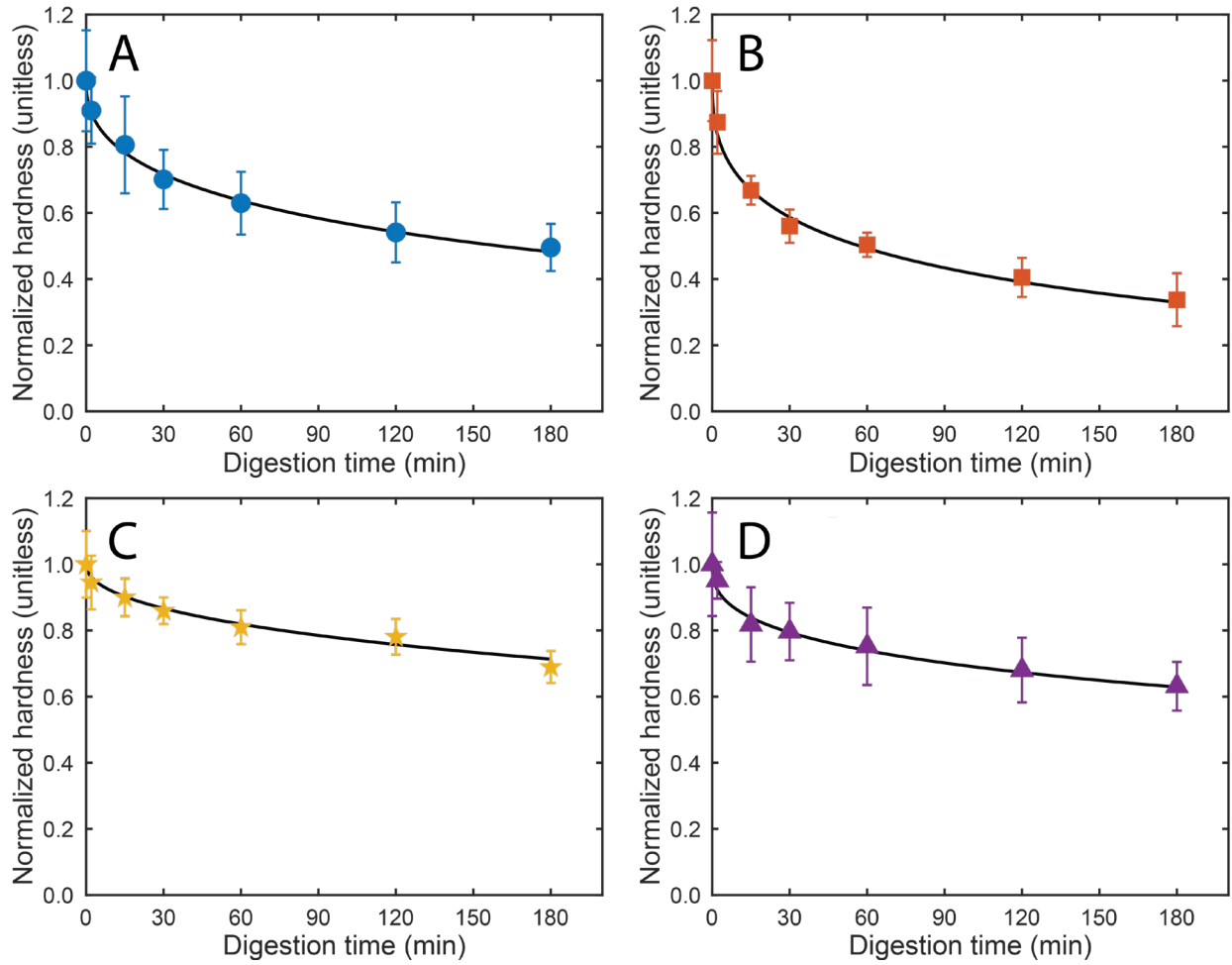


Figure 5.4. Normalized hardness of the standard diet strong gel (A), standard diet weak gel (B), whey protein strong gel (C), whey protein weak gel (D) model foods over time during in vitro digestion (0-180 min) with fit to the Weibull function (Equation 5.6). Markers represent averages with error bars as the standard deviation ($n=3$). Lines represent the Weibull model fit with average parameters (Table 2).

Table 5.7. Hardness (N) of model foods over time during digestion. All values are mean (n=3) ± standard deviation. Values in each column (abc) or each row (zyx) with different letters represent significant differences (p<0.05) between means. If no letter is listed, there were no significant differences within that factor.

Digestion time (min)	Standard diet	Standard diet	Whey protein	Whey protein
	strong gel	weak gel	strong gel	weak gel
0	18.7 ± 2.9 ^{a,y}	9.0 ± 1.1 ^{a,x}	56.2 ± 5.7 ^{a,z}	6.2 ± 1.0 ^x
2	17.0 ± 1.9 ^{ab,y}	7.9 ± 0.9 ^{ab,x}	53.1 ± 4.5 ^{ab,z}	5.9 ± 0.3 ^x
15	15.1 ± 2.7 ^{abc,y}	6.0 ± 0.4 ^{ab,x}	50.5 ± 3.2 ^{bc,z}	5.1 ± 0.7 ^x
30	13.1 ± 1.7 ^{bcd,y}	5.0 ± 0.5 ^{ab,x}	48.3 ± 2.3 ^{bcd,z}	5.0 ± 0.5 ^x
60	11.8 ± 1.8 ^{bcd,y}	4.5 ± 0.3 ^{ab,x}	45.5 ± 2.9 ^{cd,z}	4.7 ± 0.7 ^x
120	10.1 ± 1.7 ^{cd,y}	3.6 ± 0.5 ^{ab,x}	43.9 ± 3.1 ^{de,z}	4.2 ± 0.6 ^x
180	9.3 ± 1.3 ^{d,y}	3.0 ± 0.7 ^{b,x}	38.7 ± 2.7 ^{e,z}	3.9 ± 0.5 ^x

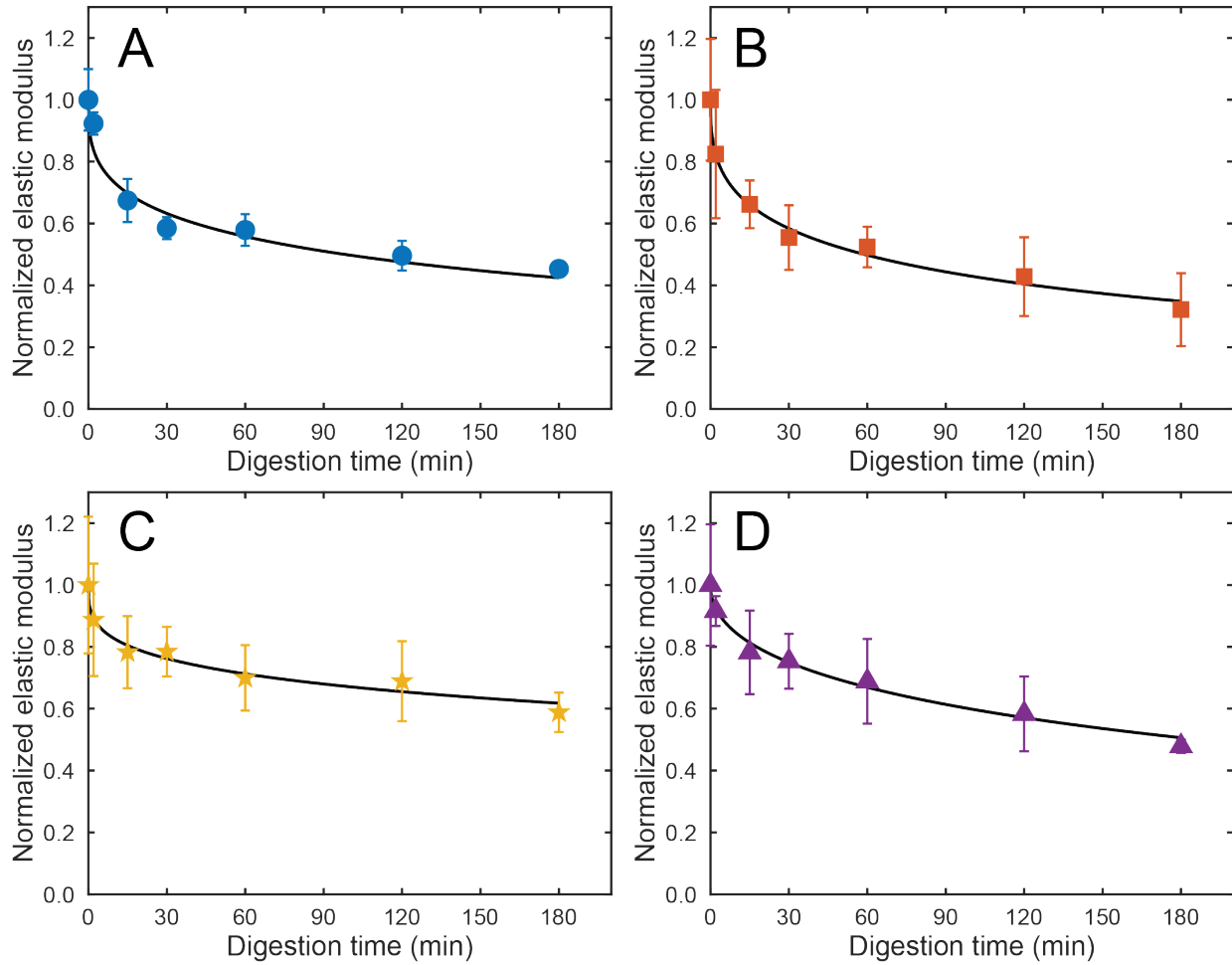


Figure 5.5. Normalized elastic modulus of the standard diet strong gel (A), standard diet weak gel (B), whey protein strong gel (C), whey protein weak gel (D) model foods over time during in vitro digestion (0-180 min) with fit to the Weibull function (Equation 6). Markers represent averages with error bars as the standard deviation ($n=3$). Lines represent the Weibull model fit with average parameters.

Table 5.8. Parameters of the Weibull function (Equation 5.6) used to fit normalized hardness, normalized elastic modulus, and dry solids retention ratio of model foods during in vitro digestion. Values in each row with no letter in common (zyx) represent significant differences ($p < 0.05$) across the different model foods. If no letter is listed, there were no significant differences.

Parameter	Standard diet	Standard diet	Whey protein	Whey protein	
	strong gel	weak gel	strong gel	weak gel	
Hardness	H_0 (N)	18.7 ± 2.9^y	9.0 ± 1.1^x	56.2 ± 5.7^z	6.2 ± 1.0^x
	$k \cdot 10^3$ (min^{-1})	2.79 ± 0.81^y	7.17 ± 0.75^z	0.61 ± 0.09^x	0.80 ± 0.37^x
	β (dimensionless)	0.46 ± 0.11	0.42 ± 0.08	0.50 ± 0.12	0.39 ± 0.09
	$t_{1/2}$ (min)	161 ± 15^y	58 ± 5^y	775 ± 82^z	538 ± 193^z
	R^2	0.97 ± 0.02	0.99 ± 0.01	0.97 ± 0.01	0.95 ± 0.03
	RRMSE (unitless)	0.04 ± 0.01	0.04 ± 0.02	0.02 ± 0.01	0.04 ± 0.01
Elastic modulus	E_0 (kPa)	353 ± 35^z	292 ± 57^z	433 ± 96^z	107 ± 21^y
	$k \cdot 10^3$ (min^{-1})	3.60 ± 0.23^y	6.48 ± 1.01^z	0.64 ± 0.17^x	2.45 ± 0.23^y
	β (dimensionless)	0.35 ± 0.04	0.40 ± 0.11	0.33 ± 0.06	0.47 ± 0.08
	$t_{1/2}$ (min)	99 ± 17^y	60 ± 9^y	543 ± 164^z	187 ± 15^y
	R^2	0.95 ± 0.03	0.96 ± 0.02	0.91 ± 0.07	0.93 ± 0.06
	RRMSE (unitless)	0.07 ± 0.02	0.10 ± 0.04	0.04 ± 0.01	0.07 ± 0.05
Dry solids retention ratio	$k \cdot 10^3$ (min^{-1})	1.09 ± 0.25	0.50 ± 0.20	1.33 ± 0.54	0.64 ± 0.15
	β (dimensionless)	0.67 ± 0.04^y	0.44 ± 0.02^y	1.44 ± 0.33^z	0.83 ± 0.15^y
	$t_{1/2}$ (min)	545 ± 94	970 ± 385	649 ± 268	1019 ± 166
	R^2	0.99 ± 0.01	0.99 ± 0.01	0.92 ± 0.07	0.94 ± 0.06
	RRMSE (unitless)	0.01 ± 0.01	0.01 ± 0.00	0.02 ± 0.01	0.02 ± 0.01

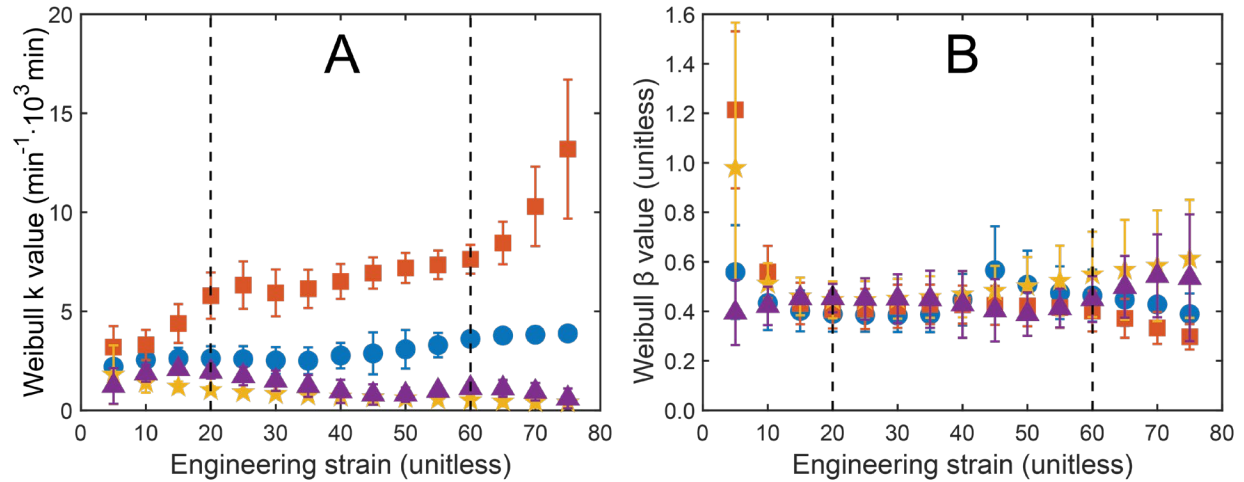


Figure 5.6. Parameters of the Weibull function (Equation 5.6) fit to the force at different values of strain during in vitro digestion. Weibull model parameter k (A) and β (B) are shown for the standard diet strong gel (●), standard diet weak gel (■), whey protein strong gel (★), and whey protein weak gel (▲). Markers represent averages and error bars represent standard deviation (n=3). The region between 20% and 60% strain is shown between the vertical dashed lines as there were no statistically significant differences in the values of k or β between values of strain on this interval.

Table 5.9. Elastic modulus (kPa), fracture stress (kPa), fracture strain (unitless), dry solids retention ratio (%), calculated using Equation 5), and soluble solids (°Brix) for model foods. The whey protein strong gel did not fracture during the compression test and thus its fracture stress and fracture strain are not presented (NA). All values are means (n=3) ± standard deviation. Values in each column (abc) or each row (zyx) with different letters represent significant differences (p<0.05) between means. If no letter is listed, there were no significant differences within that factor. Superscripts are not given for elastic modulus and fracture strain as the interaction effect of model food type and digestion time was not found to be significant for these variables.

Digestion time	Standard diet	Standard diet	Whey protein	Whey protein
(min)	strong gel	weak gel	strong gel	weak gel
Elastic modulus (kPa)				
0	353 ± 35	292 ± 57	433 ± 96	107 ± 21
2	326 ± 13	241 ± 61	384 ± 79	98 ± 5
15	238 ± 25	193 ± 23	339 ± 51	84 ± 15
30	206 ± 13	162 ± 31	340 ± 35	81 ± 10
60	204 ± 18	153 ± 19	303 ± 46	74 ± 15
120	175 ± 17	125 ± 37	298 ± 56	63 ± 13
180	160 ± 4	94 ± 34	255 ± 28	51 ± 2
Fracture stress (kPa)				
0	110 ± 15 ^{a,z}	42 ± 8 ^{a,y}	NA	34 ± 4 ^y
2	102 ± 7 ^{a,z}	37 ± 6 ^{ab,y}	NA	32 ± 2 ^y
15	86 ± 14 ^{b,z}	29 ± 3 ^{abc,y}	NA	27 ± 2 ^y
30	73 ± 6 ^{bc,z}	24 ± 4 ^{bc,y}	NA	27 ± 1 ^y
60	66 ± 7 ^{cd,z}	22 ± 3 ^{bc,y}	NA	26 ± 3 ^y
120	57 ± 7 ^{cd,z}	18 ± 5 ^{e,y}	NA	24 ± 1 ^y
180	52 ± 2 ^{d,z}	13 ± 5 ^{e,y}	NA	21 ± 2 ^y

Fracture strain (unitless)				
0	0.39 ± 0.01	0.22 ± 0.01	NA	0.42 ± 0.04
2	0.39 ± 0.01	0.21 ± 0.01	NA	0.42 ± 0.03
15	0.42 ± 0.01	0.21 ± 0.00	NA	0.42 ± 0.03
30	0.41 ± 0.00	0.21 ± 0.01	NA	0.41 ± 0.02
60	0.40 ± 0.01	0.19 ± 0.01	NA	0.41 ± 0.03
120	0.39 ± 0.02	0.19 ± 0.01	NA	0.42 ± 0.02
180	0.39 ± 0.01	0.22 ± 0.01	NA	0.42 ± 0.04
Dry solids retention ratio (%)				
2	98.9 ± 1.5 ^{a,zy}	96.6 ± 1.4 ^{a,y}	102.3 ± 2.6 ^{a,z}	97.9 ± 2.6 ^{a,zy}
15	93.7 ± 1.3 ^{ab,yx}	89.7 ± 1.4 ^{b,x}	100.2 ± 0.3 ^{a,z}	97.0 ± 1.9 ^{a,zy}
30	91.3 ± 1.1 ^{b,y}	85.9 ± 0.5 ^{bc,x}	100.3 ± 1.1 ^{a,z}	96.9 ± 3.1 ^{ab,z}
60	85.7 ± 1.8 ^{c,x}	81.1 ± 1.4 ^{c,x}	100.2 ± 2.5 ^{a,z}	91.7 ± 2.5 ^{bc,y}
120	76.7 ± 2.2 ^{d,y}	75.4 ± 4.8 ^{d,y}	92.6 ± 0.3 ^{b,z}	88.2 ± 2.9 ^{cd,z}
180	72.4 ± 2.1 ^{d,x}	72.0 ± 2.6 ^{d,x}	89.6 ± 0.7 ^{b,z}	83.9 ± 3.7 ^{d,y}
Soluble solids (°Brix)				
15	1.50 ± 0.07 ^{d,z}	1.66 ± 0.02 ^{d,z}	1.07 ± 0.03 ^{c,y}	1.10 ± 0.03 ^{d,y}
30	1.72 ± 0.04 ^{d,z}	1.90 ± 0.07 ^{cd,z}	1.02 ± 0.05 ^{c,x}	1.12 ± 0.04 ^{c,y}
60	2.16 ± 0.07 ^{c,z}	2.33 ± 0.10 ^{c,z}	1.11 ± 0.05 ^{bc,x}	1.23 ± 0.06 ^{b,y}
120	2.63 ± 0.09 ^{b,z}	2.71 ± 0.05 ^{b,z}	1.29 ± 0.10 ^{ab,y}	1.40 ± 0.12 ^{a,y}
180	2.88 ± 0.13 ^{a,z}	2.91 ± 0.16 ^{a,z}	1.44 ± 0.05 ^{a,y}	1.56 ± 0.08 ^{a,y}

5.3.2 Dry solids retention ratio and soluble solids

The dry solids retention ratio of model foods (Table 5.9) was significantly influenced by the type of model food, digestion time, and their interaction ($p < 0.001$). All four model foods lost dry solids during in vitro digestion, as evidenced by significantly lower values of dry solids retention ratio at the final digestion timepoint (180 min) when compared to their initial values ($p < 0.05$). For example, the standard

diet strong gel model food retained $98.9 \pm 1.5\%$ of its initial dry mass after the 2 min oral phase, which decreased to $72.4 \pm 2.1\%$ after 180 min digestion time ($p < 0.05$).

Analysis of variance was conducted for soluble solids in the liquid digesta during the gastric phase (Table 5.9), as during the oral phase a small volume of simulated saliva was added relative to the amount of simulated gastric juice that was added at the beginning the gastric phase, making the values of °Brix during the oral and gastric phases difficult to compare. During the gastric phase, soluble solids (°Brix) was significantly influenced by the type of model food, digestion time and their interaction ($p < 0.001$). All model foods led to a significant increase in soluble solids content of the liquid digesta during digestion. The decrease in dry solids retention ratio and concomitant increase in soluble solids in the liquid phase shows that during digestion, model foods lost dry solids which became dissolved in the simulated digestive fluids.

5.3.3 *Moisture uptake and diffusion modeling*

The dry basis moisture content of model foods was significantly influenced by the type of food, digestion time, and their interaction ($p < 0.001$). There was a significant difference in the initial dry basis moisture content between the different model foods (Table 5.11). Specifically, the whey protein model foods had higher initial moisture content (3.51 and 3.20 g water per g dry matter for the strong and weak gels, respectively) when compared to the standard diet model foods (1.12 and 1.17 g water per g dry matter for the strong and weak gels, respectively). The effective diffusion coefficient of water in the model food matrix, D_{eff} (m^2/s) and the equilibrium moisture content C_e (g water/g dry matter), were estimated using the diffusion model (Equation 5.1; Table 5.10). The model provided an acceptable fit to the data, with R^2 ranging from 0.89 to 0.97 (Figure 5.7). D_{eff} was significantly influenced by the type of food ($p < 0.05$). D_{eff} was not significantly different between the strong gel and weak gel versions of the standard diet model food ($p > 0.05$) and was also not significantly different between the strong gel and weak gel versions of the whey protein model food ($p > 0.05$). However, D_{eff} values of the whey protein model foods ($9.75 \pm$

$0.03 \cdot 10^{-10} \text{ m}^2/\text{s}$ and $9.27 \pm 0.08 \cdot 10^{-10} \text{ m}^2/\text{s}$, strong gel and weak gel versions, respectively) were significantly higher ($p < 0.05$) than D_{eff} values for the standard diet strong gel ($4.63 \pm 0.10 \cdot 10^{-10} \text{ m}^2/\text{s}$).

The equilibrium moisture content, C_e , was significantly influenced by the type of food ($p < 0.001$). C_e values of the whey protein model foods ($4.01 \pm 0.05 \text{ g water/g dry matter}$ and $3.77 \pm 0.13 \text{ g moisture/g dry matter}$, strong and weak gel versions, respectively) were significantly higher ($p < 0.05$) than the equilibrium moisture content of standard diet model foods ($2.25 \pm 0.09 \text{ g moisture/g dry matter}$ and $2.32 \pm 0.12 \text{ g moisture/g dry matter}$, strong and weak gel versions, respectively). The value of C_e was not significantly different between the strong and weak gel versions of the standard diet model food or between the strong and weak gel versions of the whey protein model food ($p > 0.05$).

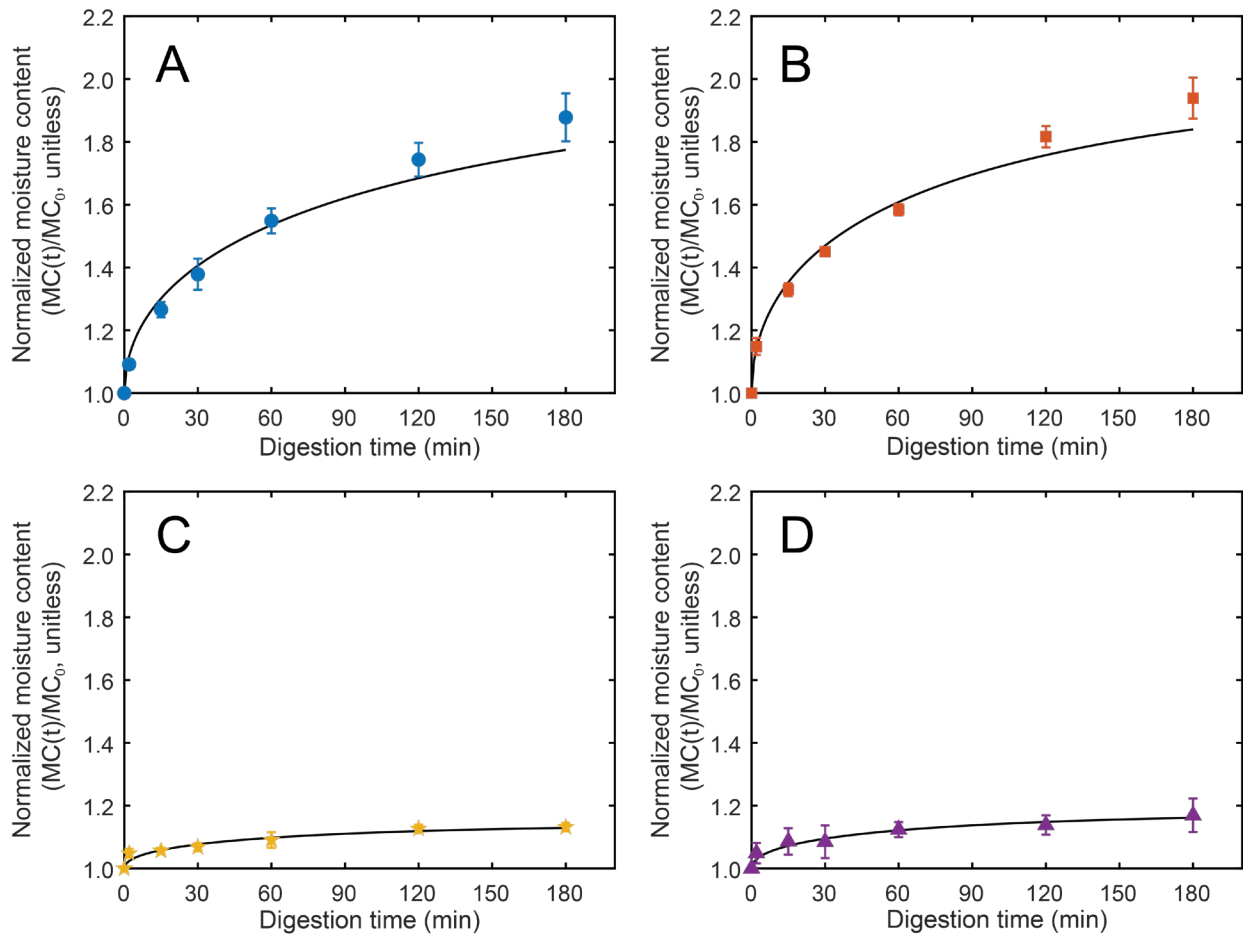


Figure 5.7. Normalized moisture content of standard diet strong gel (A), standard diet weak gel (B), whey protein strong gel (C), whey protein weak gel (D) model foods over time during in vitro digestion. Points represent the mean with error bars as \pm standard deviation, respectively. Error bars may be too small to see in some cases. Lines represent the diffusion model (Equation 5.1) fit with average parameters (Table 5.10).

Table 5.10. Estimated effective diffusivity of moisture (D_{eff}) estimated equilibrium moisture content (C_e) and diffusion model metrics for model foods during in vitro digestion. The relative root mean square error (RRMSE) was calculated using Equation 5.2. Values represent the mean ($n=3$) \pm standard deviation. Values in each row with different letters (zyx) represent significant differences ($p<0.05$) between the model foods.

Parameter	Standard diet	Standard diet	Whey protein	Whey protein
	strong gel	weak gel	strong gel	weak gel
D_{eff} ($\cdot 10^{10}$ m ² /s)	4.63 \pm 0.10 ^y	7.14 \pm 0.19 ^{zy}	9.75 \pm 0.03 ^z	9.27 \pm 0.08 ^z
C_e (g water/g dry matter)	2.25 \pm 0.09 ^y	2.32 \pm 0.12 ^y	4.01 \pm 0.05 ^z	3.77 \pm 0.13 ^z
R ²	0.97 \pm 0.01	0.97 \pm 0.02	0.89 \pm 0.05	0.90 \pm 0.04
RRMSE (unitless)	0.03 \pm 0.01	0.03 \pm 0.01	0.01 \pm 0.00	0.02 \pm 0.01

Table 5.11. Dry basis moisture content (g moisture per g dry matter) of model foods over time during digestion. All values are mean (n=3) ± standard deviation. Values in each column (abc) or each row (zyx) with different letters represent significant differences (p<0.05) between means. If no letter is listed, there were no significant differences within that factor.

Digestion time (min)	Standard diet	Standard diet	Whey protein	Whey protein
	strong gel	weak gel	strong gel	weak gel
0	1.12 ± 0.03 ^{c,x}	1.17 ± 0.01 ^{d,x}	3.51 ± 0.02 ^{c,z}	3.20 ± 0.07 ^{d,y}
2	1.22 ± 0.04 ^{d,x}	1.34 ± 0.03 ^{d,x}	3.68 ± 0.07 ^{b,z}	3.36 ± 0.08 ^{cd,y}
15	1.41 ± 0.01 ^{c,w}	1.55 ± 0.03 ^{c,x}	3.71 ± 0.01 ^{b,z}	3.48 ± 0.14 ^{bc,y}
30	1.54 ± 0.02 ^{bc,w}	1.70 ± 0.01 ^{c,x}	3.75 ± 0.03 ^{b,z}	3.47 ± 0.13 ^{bc,y}
60	1.73 ± 0.01 ^{b,x}	1.85 ± 0.03 ^{b,x}	3.83 ± 0.10 ^{ab,z}	3.60 ± 0.05 ^{ab,y}
120	1.95 ± 0.01 ^{a,w}	2.12 ± 0.05 ^{a,x}	3.96 ± 0.02 ^{a,z}	3.64 ± 0.06 ^{a,y}
180	2.10 ± 0.03 ^{a,w}	2.27 ± 0.09 ^{a,x}	3.98 ± 0.05 ^{a,z}	3.74 ± 0.15 ^{a,y}

5.3.4 Regression analysis

Relationships between the hardness (N), normalized moisture content (unitless), and dry solids retention ratio (%) were examined using linear regression (Figure 5.8, Table 5.12). Significant relationships were found for all four model foods between hardness and dry solids retention ratio (Figure 5.8 A1 and A2), between hardness and normalized moisture content (Figure 5.8 B1 and B2) and between dry solids retention ratio and normalized moisture content (Figure 5.8 C1 and C2). Due to their lower hardness and higher normalized moisture content values, regression relationships for the standard diet model foods are shown in Figure 5.8 A1, B1, and C1, and the corresponding relationships for the whey protein model foods are shown in Figure 5.8 A2, B2, and C2.

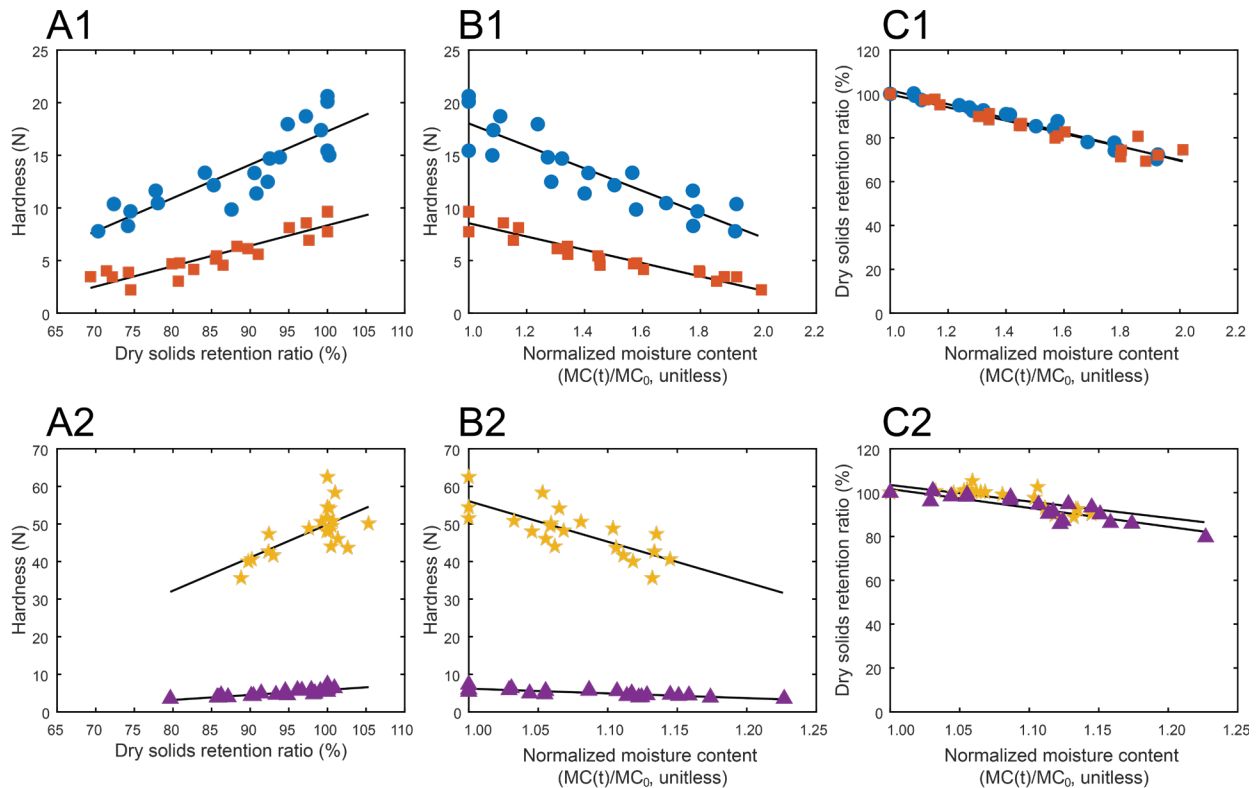


Figure 5.8. Relationships between hardness, dry solids retention ratio, and normalized moisture content analyzed using linear regression, shown for standard diet strong gel (●), standard diet weak gel (■), whey protein strong gel (★), and whey protein weak gel (▲). There was a statistically significant, direct relationship between hardness and dry solids retention ratio for the standard diet model foods (A1) and for

the whey protein model foods (A2). There was a statistically significant, inverse relationship between hardness and normalized moisture content for the standard diet model foods (B1) and for the whey protein model foods (B2). There was a statistically significant, inverse relationship between dry solids retention ratio and normalized moisture content for the standard diet model foods (C1) and for the whey protein model foods (C2).

Table 5.12. Parameters from regression analysis used to determine the relationships between hardness, dry solids retention ratio, and normalized moisture content for model foods. RRMSE was calculated using Equation 5.2.

Regression	Parameter	Standard diet strong gel	Standard diet weak gel	Whey protein strong gel	Whey protein weak gel
Hardness regressed onto dry solids retention ratio	Slope	0.32	0.19	0.88	0.13
	p	<0.0001	<0.0001	0.0014	<0.0001
	R ²	0.74	0.82	0.43	0.71
	RRMSE (unitless)	2.21	2.92	29.39	2.96
Hardness regressed onto normalized moisture content	Slope	-10.68	-6.32	-107.98	-12.58
	p	<0.001	<0.001	<0.001	<0.001
	R ²	0.78	0.906	0.594	0.67
	RRMSE (unitless)	1.022	1.305	8.773	1.091
Dry solids retention ratio regressed onto normalized moisture content	Slope	-32.20	-30.03	-75.18	-86.05
	p	<0.001	<0.001	<0.001	<0.001
	R ²	0.97	0.935	0.527	0.80
	RRMSE (unitless)	0.945	0.944	0.962	0.954

Table 5.13. pH of digesta at each digestion time point. When the in vitro digestion protocol specified a pH adjustment (Section 2.4), the pH was recorded both before and after the adjustment was made. Values represent the mean (n=3) \pm standard deviation. NA indicates that a pH adjustment was not required at the given timepoint, because the pH was already within 2 ± 0.1 .

Digestion time (min)		Standard diet	Standard diet	Whey protein	Whey protein
		strong gel	weak gel	strong gel	weak gel
5	Before adjusting to 2	1.94 \pm 0.01	1.93 \pm 0.06	2.00 \pm 0.10	1.97 \pm 0.09
5	After adjusting to 2	NA	NA	1.97 \pm 0.03	1.94 \pm 0.03
30	Before adjusting to 2	2.13 \pm 0.03	1.98 \pm 0.09	2.18 \pm 0.06	2.19 \pm 0.03
30	After adjusting to 2	1.96 \pm 0.04	1.94 \pm 0.02	1.99 \pm 0.01	1.97 \pm 0.01
60	Before adjusting to 2	2.13 \pm 0.03	2.00 \pm 0.01	2.19 \pm 0.01	2.19 \pm 0.04
60	After adjusting to 2	1.96 \pm 0.03	2.00 \pm 0.01	1.96 \pm 0.03	1.98 \pm 0.01
120	Before adjusting to 2	2.18 \pm 0.05	2.08 \pm 0.05	2.17 \pm 0.16	2.32 \pm 0.05
120	After adjusting to 2	2.01 \pm 0.03	1.95 \pm 0.06	2.09 \pm 0.19	2.05 \pm 0.02
180	After adjusting to 2	2.13 \pm 0.05	2.00 \pm 0.07	2.15 \pm 0.12	2.23 \pm 0.06

5.4 Discussion

5.4.1 Design of standard, model foods with varying breakdown properties

There is a need for standardized, model solid foods to aid the development of relationships between food breakdown and physiological function (Zhang et al., 2019a). In this study, two model solid foods were developed based on the Standard American Diet (strong gel and weak gel version), and two additional model foods were developed using whey protein hydrogels (strong gel and weak gel version) to serve as a simpler model system. An advantage of the model foods developed in this study is the availability of a strong and weak gel version within the standard diet and whey protein classes that had

only minor differences in formulation. This could allow for differences in digestion variables such as emptying rate to be linked to physical properties of the solid food matrix.

The mechanisms leading to formation of the gel in the standard diet model food are complex but likely include a combination of corn starch–whey protein interactions (Considine et al., 2011), corn starch–pectin interactions (Bai et al., 2017) and whey protein–pectin interactions (Munialo et al., 2016; Wijaya et al., 2017). Despite its high solids content (39.6 g dry solids per 100 g dispersion, Table 5.1), the standard diet model food dispersion did not solidify until heating which suggests that its gel structure was due to whey protein gelation and starch gelatinization/retrogradation. Heat-set gels of whey protein isolate are formed by aggregation of β -lactoglobulin, the major protein in whey protein isolate. β -lactoglobulin denatures at high temperature, exposing hydrophobic amino acid residues which form a gel network through disulfide bonding as well as non-covalent interactions (Hansen et al., 2020). Corn starch could also have contributed to the structure of the standard diet model foods, as previous research showed that heating 20% corn starch solutions at temperatures above 80 °C led to gelatinization which was followed by retrogradation during storage at 5 °C (Hirashima et al., 2012). The standard diet model food produced in this study contained 11.7% cornstarch, was heated at 90 °C and was then stored at 4 °C, and thus it is expected that corn starch underwent gelatinization and retrogradation.

The whey protein hydrogel model food developed in this study was comprised of water, whey protein isolate, and NaCl (in order of decreasing mass percentage). The strong gel version contained no pectin, and the weak gel version contained 0.6% pectin (Table 5.1). As with the standard diet model food, the mechanism responsible for forming the whey protein model foods involved β -lactoglobulin gelation.

The strong gel and weak gel versions of the whey protein hydrogel model food differed in their initial texture. For example, the strong gel had a much higher hardness (56.2 ± 5.7 N) than the weak gel version (6.2 ± 1.0 N, $p < 0.05$). Previous research found that at pH greater than the isoelectric point of β -lactoglobulin (pI ca. 5.2) electrostatic repulsion between pectin and β -lactoglobulin resulted in weak intermolecular interactions, but at pH 4.0 an insoluble coacervate was formed (Wang et al., 2007). Formation of pectin– β -lactoglobulin coacervates has also been reported at pH 5.2 (Thongkaew et al.,

2015), and it has been shown that pectin concentrations greater than 0.2% presented as inclusions in whey protein gels (Munialo et al., 2016). Based on these findings it is hypothesized that the whey protein model foods in the current study (20% whey protein, 0.82% pectin, pH 5.2) contained pectin inclusions in the gel matrix. Pectin- β -lactoglobulin inclusions in the gel matrix could have acted as sites of stress concentration, making the whey protein weak gel version more susceptible to fracture during compression than the strong gel version (Foegeding et al., 1995; Swackhamer and Bornhorst, 2019). For example, the whey protein weak gel fractured at approximately 42% strain, whereas the whey protein strong gel achieved 75% strain without fracture (Table 5.9). Furthermore, the whey protein strong gel recovered its initial shape after compression to 75% strain, whereas the whey protein weak gel was destroyed (Figure 5.10 C and D, respectively). Pectin-pectin intermolecular interactions could also have contributed to differences between the strong and weak gel versions of the whey protein model food, since the concentration of pectin (0.6%) was above the overlap concentration (ca. 0.3%) (Capel et al., 2006). It should also be noted that the whey protein strong gel demonstrated syneresis during compression, as evidenced from the expressed liquid surrounding the cube in Figure 5.10 C, whereas the whey protein weak gel did not. A pectin network in the whey protein weak gel could have entrapped moisture, preventing syneresis during compression. Similar findings have been obtained in previous studies (Beaulieu et al., 2001; Khubber et al., 2021).

Future work to characterize the model foods developed in this study could involve microscopy. For example, characterizing the size distribution of soybean oil droplets in the standard diet model food could allow its mechanical behavior to be modeled using mixture theories previously developed for whey protein emulsion gels (Balakrishnan et al., 2017; Sala et al., 2009).

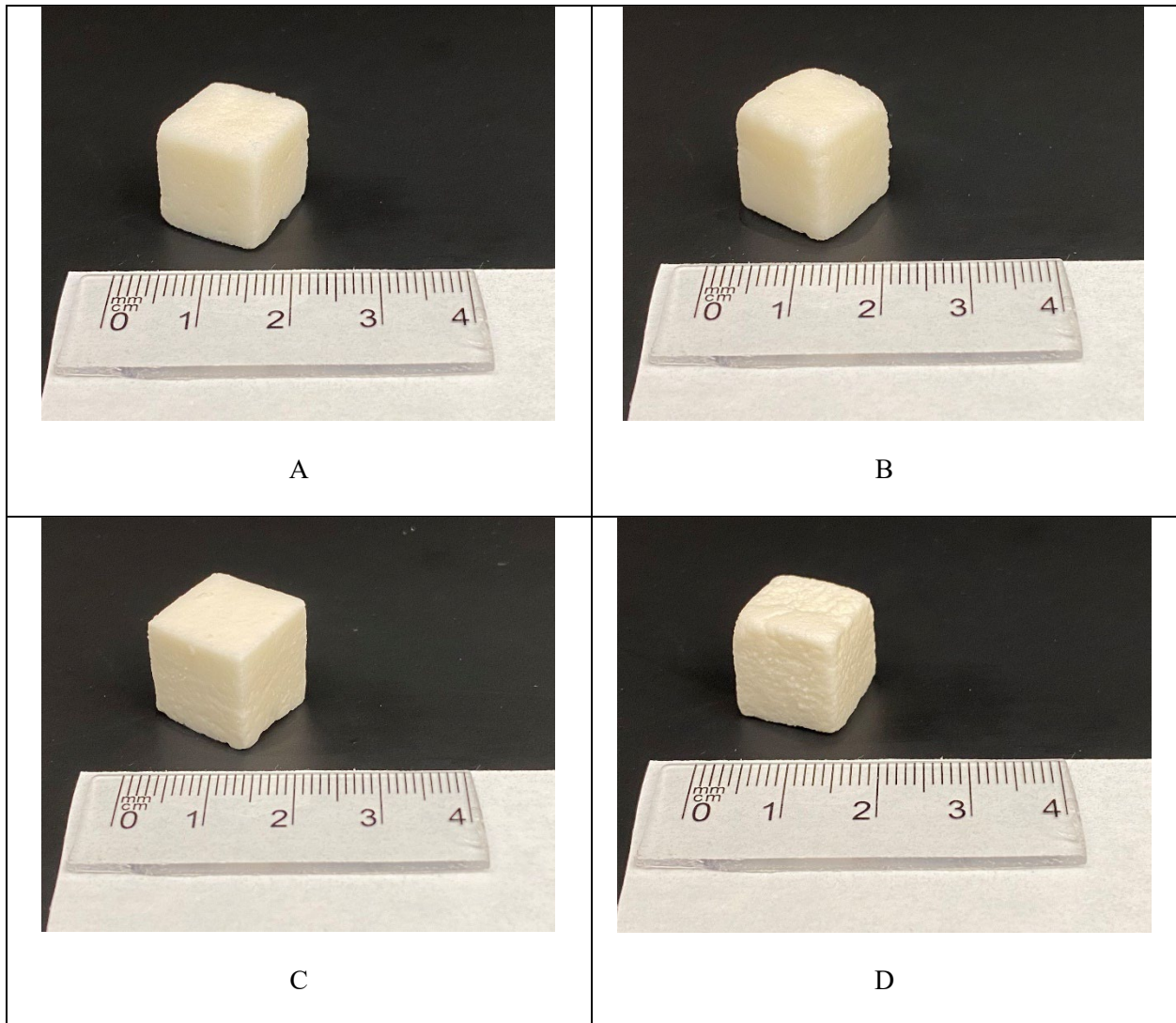


Figure 5.9. Images of model foods after 180 minutes of digestion, as described in Section 2.6 of the standard diet strong gel (A), standard diet weak gel (B), whey protein strong gel (C), and whey protein weak gel (D).

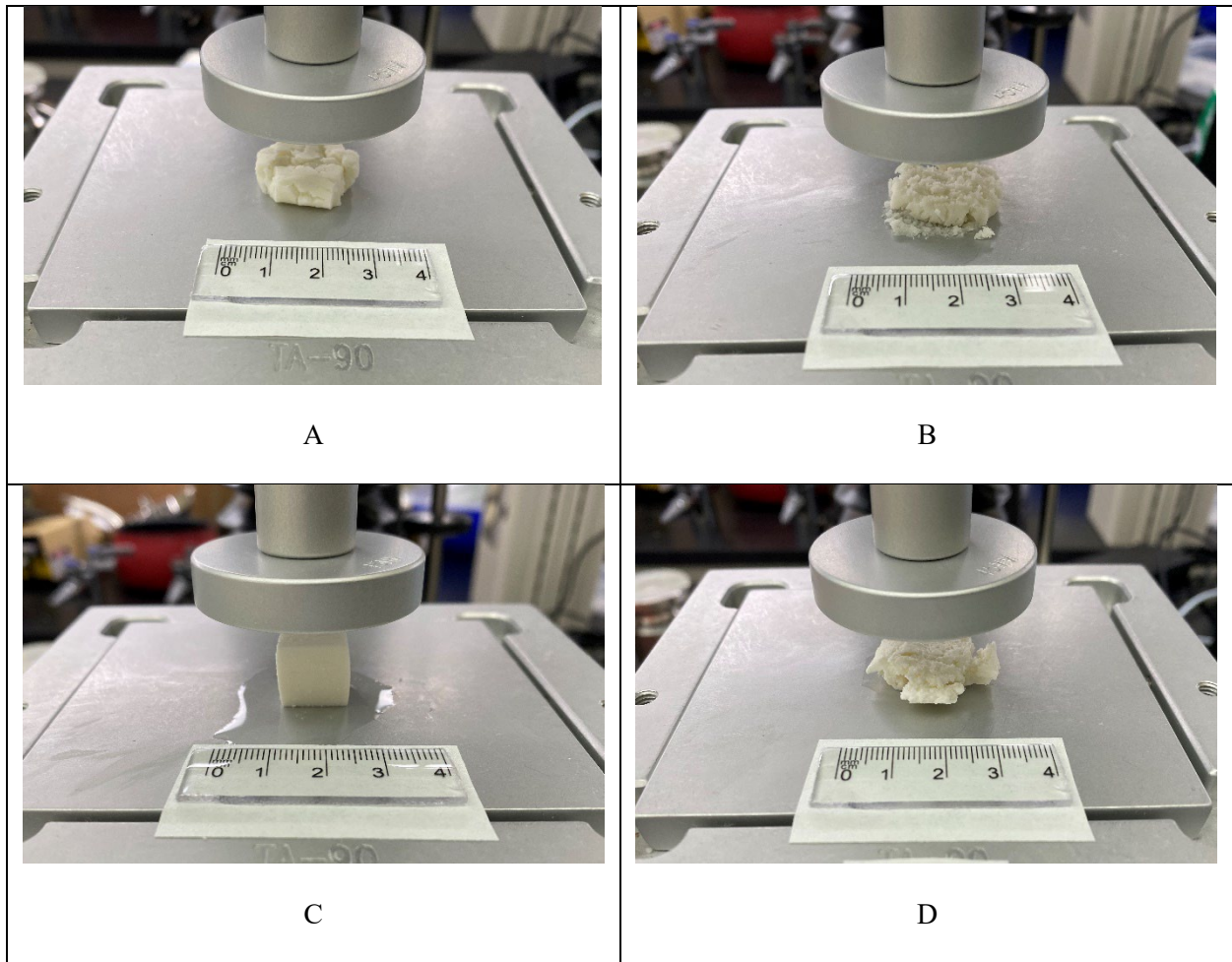


Figure 5.10. Images of undigested model foods after compression to 75% strain, as described in Section 2.7 of the standard diet strong gel (A), standard diet weak gel (B), whey protein strong gel (C), and whey protein weak gel (D). The whey protein strong gel (C) did not fracture during the compression, and thus its fracture stress and fracture strain were not presented in Table 2. It should be noted that the whey protein strong gel (C) expressed water during the compression, resulting in the pool of liquid visible in panel C.

5.4.2 *Physical property changes of model foods during in vitro digestion*

Breakdown of model foods during digestion was assessed using a combination of texture analysis, modeling of moisture uptake, and dry solids retention ratio analysis. All model foods showed a decrease in hardness during digestion (Figure 5.4). Softening half-times were higher for the whey protein model

foods (775 ± 82 min for the strong gel version and 538 ± 193 min for the weak gel version, respectively) than for the standard diet model foods (161 ± 15 min and 58 ± 5 min for the strong and weak gel versions, respectively). Drechsler and Bornhorst (2018) found softening half-times for carbohydrate-based foods ranged between 4 min and 354 min, which are lower than the softening half-times found for whey protein model foods in the current study. However, it is expected that foods based on a protein network such as the whey protein model foods could exhibit greater softening half-times than carbohydrate-based foods, due to the strong internal structure that is provided by whey protein (Kuhn et al., 2019).

Considering softening half-times and Weibull k values together, the model foods can be arranged in the following order: standard diet weak gel (fastest breakdown) > standard diet strong gel > whey protein weak gel > whey protein strong gel (slowest breakdown). Gelation of β -lactoglobulin was likely the greatest contributor to gel matrix integrity and resistance to breakdown during digestion, supported by the finding that the whey protein model foods (20.0% whey protein isolate on a dry mass basis) were slower to break down than the standard diet model foods (7.6% whey protein isolate on a dry mass basis). A microstructure interrupted by pectin may explain why the whey protein weak gel broke down more rapidly than the whey protein strong gel (Munialo et al., 2016; Thongkaew et al., 2015; Wang et al., 2007).

In addition to texture change, all four model foods experienced a significant decrease in dry solids retention ratio (Equation 5.5) during digestion, which was accompanied by a significant increase in the soluble solids content ($^{\circ}$ Brix) of the simulated digestive juices. The standard diet weak gel had the lowest dry solids retention ratio at the final timepoint ($72.0 \pm 2.6\%$) and had the fastest softening half-time of all the model foods (58 ± 5 min), suggesting that rapid softening may indicate loss of dry matter. Previous researchers studied the digestion of 1.2 cm cubes of sweet potato after applying different types of food processing, and found that dry solids retention ratio ranged from 89.4% to 96.1% after 180 min digestion time (Mennah-Govela and Bornhorst, 2016b). These values are comparable to the dry solids retention ratio of the whey protein strong gel ($89.6 \pm 0.7\%$). Mennah-Govela et al. (2016b) also found that the test food with the highest initial hardness exhibited the highest dry solids retention ratio after 180 min

digestion, and that the test food with the lowest initial hardness had the lowest dry solids retention ratio after 180 min digestion. This aligns with the results of the current study, in which the whey protein strong gel had higher initial hardness than the whey protein weak gel (56.2 ± 5.7 N vs. 6.2 ± 1.0 N, $p < 0.05$) and also higher dry solids retention ratio after 180 min digestion ($89.6 \pm 0.7\%$ vs. $83.9 \pm 3.7\%$, $p < 0.05$). Loss of dry mass during digestion can be attributed to erosion of cubes of model food. Erosion is defined by the wearing away of the outer surface of the food particle and has been observed by previous researchers during in vitro digestion of whey protein (Guo et al., 2014a) and other dairy gels (Floury et al., 2018). Slight erosion can be observed by comparing the cubes of model food before and after digestion (Figure 5.2 and Figure 5.9, respectively).

Regression analysis showed that hardness had a significant direct relationship with dry solids retention ratio and a significant inverse relationship with normalized moisture content (Figure 5.8). This suggests that the reduction in hardness of the model foods during digestion can be partly attributed to mass transfer of dry solids out of the cubes of model food, as well as mass transfer of moisture into the cubes of model food. Mass transfer of water into model foods was evidenced by statistically significant increases in the dry basis moisture content of all model foods during in vitro digestion (Table 5.11). The equilibrium moisture content of each model food (C_e , estimated from modeling) was close to the observed moisture content after 180 min digestion (Table 5.11), suggesting that model foods were nearly saturated with water after 180 min in vitro digestion.

Values of D_{eff} obtained in this study are in the same order of magnitude as those obtained by Mennah-Govela (2016b) for sweet potato, where the effective diffusion coefficient of water ranged from 3.52 to $7.85 \cdot 10^{-10}$ m²/s. In general, the whey protein model foods had larger D_{eff} values (average $9.5 \cdot 10^{-10}$ m²/s) than the standard diet model foods (average $5.9 \cdot 10^{-10}$ m²/s). This indicates that the diffusion of water was faster in the matrix of the whey protein gels than in the standard diet gels.

The whey protein model foods had a higher initial moisture content than the standard diet model foods due to their lower dry solids content (ca. 20% dry solids vs ca. 40% dry solids, respectively). As the whey protein model foods were found to have higher D_{eff} values than the standard diet model foods, this

suggests that differences in microstructure between the whey protein and standard diet model foods influenced their diffusion properties. It is hypothesized that the higher dry solids content in the standard diet model foods led to a more compact, less permeable microstructure which slowed diffusion. Similarly, previous research found that the diffusion of fluorescent-labeled dextrans was slower in protein gels with compact microstructure than in gels with a loose microstructure (Somaratne et al., 2020c). An interesting finding is that the whey protein strong gel had high initial hardness and slow softening time, but also a high value of D_{eff} . This demonstrates that a mechanically strong gel matrix does not necessarily have slower diffusion of water than a mechanically weaker gel matrix and suggests that future research should assess both the texture and diffusion properties of model foods to characterize their behavior during *in vitro* digestion.

There were no significant differences in D_{eff} or C_e between the strong gel and weak gel versions of either the standard diet or whey protein model foods. This suggests that the standard diet model foods or whey protein model foods could be used in future studies to isolate the effect of food breakdown as the strong and weak gel versions had differences in their breakdown properties but similar diffusion values.

It is important to note that the diffusion coefficient of water may be different from the diffusion coefficients of acid or enzymes in the model food matrix (Mennah-Govela and Bornhorst, 2016a). Future research could involve fluorescence correlation spectroscopy (Luo et al., 2017), hyperspectral imaging (Somaratne et al., 2019), or fluorescence recovery after photobleaching (Somaratne et al., 2020b) to independently examine the diffusion of acid, enzymes, and moisture in the model foods developed here.

In vitro digestion of the model foods was carried out in a shaking water bath, which did not include simulated peristalsis. Previous research found that particle breakdown occurred for solid foods only when digested using an *in vitro* model which included simulated peristalsis (Swackhamer et al., 2019). The digestion model used in the current study did not include simulated peristalsis so that cubical particle geometries could be maintained, necessary for the assessment of properties such as hardness and elastic modulus. Future research could investigate the breakdown of the model foods developed in the current study using *in vitro* models that include simulated peristalsis, and then relate changes in particle size to

the mechanical properties or diffusion properties measured in the current study. Additionally, intestinal digestion of the model foods could be conducted, which could allow the physical property changes that occur during gastric digestion to be related to variables measured in the intestinal phase such as bioaccessibility of macronutrients. Although the results from the current study focus on the gastric phase, previous studies have found that breakdown during gastric digestion impacts nutrient bioaccessibility during intestinal digestion (Swackhamer et al., 2019), suggesting that the information gained in this study may also be useful in tailoring intestinal nutrient release in future work.

In addition to considering an intestinal phase of digestion, the parameters of the oral phase could be considered in more detail in future studies. All model foods were subjected to an oral digestion phase consisting of incubation with simulated saliva for 2 min despite differences in their initial moisture content and mechanical properties. However, it has been found that oral processing time varies for different foods. For example, foods that are initially dry require more chewing cycles to ensure sufficient lubrication for swallowing (van der Bilt and Abbink, 2017) and foods with greater fracture stress may require more time for oral processing (Kohyama et al., 2017). The standard diet strong gel and whey protein strong gel each had higher fracture stress than the corresponding weak gel versions and thus might conceivably require more time for oral processing. Future research could establish the number of chewing cycles or moisture content at swallowing for these model foods, allowing appropriate parameters for simulated oral digestion to be selected for in vitro experiments.

5.4.3 Weibull analysis of softening using force at varying values of strain

The Weibull function was fit to the force at different values of strain between 20 and 60% in increments of 5% to determine the sensitivity of its parameters to the level of strain. This analysis could be used to determine an appropriate level of strain for texture testing of solid foods during digestion, and to understand if parameters obtained using tests done at different levels of strain can be compared in the future. For values of strain between 20% and 60%, there were no significant differences in the parameters obtained for the Weibull function (k and β) (Figure 5.6). This lends support to the use of a parameter

such as hardness to characterize the texture change of foods during digestion. Since the hardness is defined as the peak force up to 50% strain, it falls near the middle of the range, suggesting that it provides a robust measure of texture change during digestion. Drechsler and Bornhorst (2018) found that the Weibull function could be fit to the force measured from 0 min to 180 min during digestion and yield parameters that were not significantly different from those obtained by fitting the Weibull function to the force measured from 0 min to 240 min. Taken together, these findings suggest that the Weibull analysis is robust with respect to the time interval chosen for the digestion experiment and the level of strain used to define the dependent variable for the Weibull function. Future researchers may consider using Weibull analysis to characterize the softening half-times of foods during in vitro digestion, which could also allow for comparison of softening kinetics between different studies.

5.4.4 *Classification of the standardized, model solid foods using the FBCS*

The FBCS proposes a quantitative approach to characterize the breakdown of solid food during digestion (Bornhorst et al., 2015). It is based on two parameters: the initial hardness of the food, determined through texture analysis, and the softening half-time which is defined as the time during digestion at which the initial hardness decreases by 50%. Using these two parameters, Bornhorst et al. (2015) proposed that six classes could be used to categorize foods with different combinations of initial hardness and softening half-time, and noted that specific values used to define classes could be tuned with additional data from the breakdown of foods with different properties. Although the absolute value of hardness may depend on food particle size, the FBCS uses changes in normalized hardness over time during digestion to classify foods. It is proposed that relative rankings of foods based on the softening kinetics of their normalized hardness will not depend strongly on food particle size, although future research on this topic is needed. The FBCS was used by Drechsler and Bornhorst (2018) where it was found that three levels of softening half-time (slow, intermediate, and fast) and two levels of initial hardness (hard, soft) resulted in an appropriate classification of the six carbohydrate-based foods that were studied. As recommended by Drechsler and Bornhorst (2018), three levels of softening half-time

and two levels of initial hardness were used to classify the standard model foods developed in the current study. However, the cut-off values to define the classes with different softening half-times were modified from those proposed by Drechsler and Bornhorst (2018) to be more appropriate for foods with a wider range of properties. Specifically, it is proposed that the following ranges of softening half-time may be used: fast < 60 min, 60 min < intermediate < 180 min, slow > 180 min (Table 5.14). To assess the applicability of the proposed values, the model foods from the current study and the carbohydrate-based foods studied by Drechsler and Bornhorst (2018) were classified according to the proposed cut off values of hardness and softening time (Table 5.14).

The model foods developed in the current study were designed to fall into four classes, with each model food in its own class. The carbohydrate-based foods studied by Drechsler and Bornhorst (2018) were placed into four different classes according to the criteria. The placement of the model foods as well as carbohydrate-based foods into distinct classes may support the use of the proposed cut-off values of hardness and softening time for classification of whey-protein based model foods and for carbohydrate-based foods.

Results from FBCS classification can be used to identify commercial food products with similar breakdown properties as the model foods developed in the current study. For example, the whey protein weak gel was soft but experienced slow softening (Class II), which was similar to couscous and quinoa studied by Drechsler and Bornhorst (2018). On the other hand, the standard diet weak gel was initially soft but softened rapidly, which was comparable to the behavior of white rice (Class VI). None of the model foods developed in the current study had high initial hardness but rapid softening (Class V), however, it has been determined that pretzel was a member of this class (Drechsler and Bornhorst, 2018).

The initial hardness and softening half-time of the whey protein strong gel were 56.2 N and 775 min, respectively, which are comparable to the corresponding values for apple cubes (70.6 N and 290 min, respectively) (Olenskyj et al., 2020). For the whey protein weak gel, the initial hardness and softening half-time (6.2 N and 538 min, respectively) were similar to steamed sweet potato cubes (6.0 N and 310 min, respectively). The whey protein model foods thus had initial texture and softening times that ranged

roughly from those of a crisp, raw fruit to a softer, thermally processed vegetable. The initial hardness values of the standard diet strong gel and weak gels (18.7 N and 9.0 N, respectively), were similar to those of young cheddar cheese (13.3 N) and aged cheddar cheese (8.8 N) (Fang et al., 2016). The softening half-times of the standard diet strong and weak gels (161 min and 58 min, respectively) were comparable to those of brown rice and pasta for the strong gel, and white rice for the weak gel (Table 5.14) (Drechsler and Bornhorst, 2018). Thus, the standard diet model foods had initial texture that ranged roughly from that of a soft cheddar to a harder cheddar cheese with softening half-times ranging between those of carbohydrate foods with a more easily degradable structure (white rice) to those with a slightly more resistant structure (brown rice, pasta).

By testing the *in vivo* behavior of foods in different FBCS classes, the impact of softening kinetics on variables such as particle breakdown or gastric emptying could be assessed. In a recent *in vivo* study, it was found that softening half times in the stomach were strongly correlated with gastric emptying rates (Nadia et al., 2021b). Drechsler and Bornhorst (2018) found the softening half-time of pretzel and pasta to be 4 min and 71 min, respectively, while the glycemic indices of these foods have been reported to be 83 (Foster-Powell et al., 2002) and 49 (Atkinson et al., 2008). In combination with the findings of Nadia et al., (2021b) this suggests that softening kinetics of food have broad implications for the digestion process. In the future, the FBCS could provide a simple system to rapidly screen foods with different properties by predicting their behavior *in vivo*, leading to improvements in experimental throughput and faster development of foods with health-promoting properties. The model foods developed in the current study could be used as part of this framework. For example, the standard diet strong gel and weak gel were placed into different FBCS classes despite having a minor difference in formulation (0.6% pectin), thus differences in their digestion behavior *in vivo* could yield insights into the role of food softening kinetics on the physiological processes of digestion.

Table 5.14. FBCS classification criteria based on initial hardness (N) and softening half-time (min), modified from Bornhorst et al. (2015) and Drechsler and Bornhorst (2018). NA signifies that no food in the FBCS class was tested in the corresponding study.

Class	Softening half-time	Initial hardness	Classification of model foods developed in the current study	Classification of carbohydrate-based foods (Drechsler and Bornhorst, 2018)
I	Slow softening	Hard (> 20 N)	Whey protein strong gel	NA
II	(> 180 min)	Soft (< 20 N)	Whey protein weak gel	Couscous, Quinoa
III	Intermediate softening	Hard (> 20 N)	NA	NA
IV	(60 – 180 min)	Soft (< 20 N)	Standard diet strong gel	Brown rice, Pasta
V	Fast softening	Hard (> 20 N)	NA	Pretzel
VI	(< 60 min)	Soft (< 20 N)	Standard diet weak gel	White rice

5.5 Limitations

Limitations of this study include the use of a single macronutrient ratio to exemplify the Standard American Diet. Thus, the composition of the two model foods that were based on the Standard American Diet may represent an overall approximation of the diet of an American consumer, however, this composition does not represent the diet of any individual consumer. Future research should consider developing model foods to represent the diet of specialized groups of consumers if a tool is needed for studying the breakdown of solid foods or bioaccessibility of nutrients from the point of view of certain individuals, for instance those with dietary restrictions. Another limitation of this study was the lack of simulated mastication during the oral phase of digestion. This was conducted in order to preserve the cubical geometry of food particles; however, future research could simulate the mastication of the model foods developed in this study and then quantify the breakdown of the particles during digestion or the bioaccessibility of nutrients from those particles. Another limitation of the current study is the lack of examination of the microstructure of the model foods. Future research could investigate the

microstructural changes of model foods during in vitro gastric digestion using techniques such as X-ray micro computed tomography.

5.6 Conclusions

In this study, four standardized, model solid foods were developed and their breakdown during in vitro digestion was assessed. The macronutrient composition of the Standard American Diet was used to design the first model food class, and a strong gel and weak gel version were created by changing the pH at which it was thermally gelled. The second model food class was created using whey protein hydrogels, with a strong gel and a weak gel version created by addition of a small amount of pectin in the weak gel. Model foods were analyzed using the Food Breakdown Classification System (FBCS), confirming that each model food was placed in its own class.

Future work could investigate the digestion of the model foods developed in the current study using in vivo models. Data from the present study could enable relationships to be developed between food physical property changes and variables such as gastric emptying or satiety, leading to potential insights into the digestion process. Overall, this study reports the development and characterization of standard, model solid foods that could assist future researchers to elucidate the physical processes of digestion in more detail, which could accelerate development of novel food products for improved consumer health.

Chapter 6 Video Analysis and Fluid Dynamic Modeling of a Novel Multi-Module Peristaltic Simulator for Gastrointestinal Research

Rationale

A novel peristaltic simulator was developed for gastrointestinal research. The dynamics of the simulated peristaltic wave in the device were characterized using video analysis, and the fluid flow inside the digestion system was predicted using a computational model. The rationale was to design a device in which the effect of the simulated peristaltic wave on the breakdown of solid foods could be isolated without the potentially confounding effect of particle-particle grinding, which may also contribute to the breakdown of solid food particles. The geometry of the peristaltic simulator that was developed in this chapter most closely resembles that of the upper part of the human small intestine. Development of this peristaltic simulator addressed research objective 3 as stated in Chapter 1 (Introduction). In Chapter 4, experiments using almond particles demonstrated that particle size reduction occurred in the Human Gastric Simulator (HGS), an in vitro gastric digestion system that included simulated peristalsis, but particle breakdown did not occur in a digestion system with identical biochemical conditions but without simulated peristalsis. This underscored the importance of peristalsis on the breakdown of solid food particles, however, the HGS was not capable of applying a controllable simulated peristaltic wave to an individual food particle, which pointed to the need for a new experimental device. This device was also designed to permit greater experimental throughput than currently available in vitro digestion systems that include simulated peristalsis. The peristaltic simulator described in this chapter was used in Chapter 7 to apply simulated peristaltic waves to particles of the model foods developed in Chapter 5, so that their physical properties could be related to their hypothesized mechanisms of breakdown.

Abstract

Peristaltic contractions significantly affect food breakdown and mixing of gastrointestinal contents. However, many existing in vitro digestion systems do not accurately represent these peristaltic contractions or are limited by low throughput. A novel peristaltic simulator has been developed that provides peristaltic contractions for up to 12 digestion modules simultaneously. Video analysis showed that the degree of occlusion of the digestion module could be varied from $72.1 \pm 0.4\%$ to $84.6 \pm 1.2\%$ ($p < 0.05$) by changing from thin rollers to thick rollers in the simulator. Manometry was used to determine the forces that could be applied by the system to a food bolus, which were 2.61 ± 0.03 N and 4.51 ± 0.16 N for the thin and thick rollers, respectively, ($p < 0.05$). A multiphysics, Computational Fluid Dynamics model was created to better understand the fluid flow inside a digestion module, and allow future researchers to predict the impact of possible modifications to the simulator on the fluid flow dynamics. This novel peristaltic simulator could allow for high-throughput screening of food materials for health-promoting properties.

6.1 Introduction

Food digestion begins with mastication, which is then followed by the gastric phase, small and large intestinal phases, and colonic fermentation (Bohn et al., 2018). Understanding the physical processes of digestion in more detail could help to design foods for improved consumer health, for instance, by developing products for sustained release of nutrients (Yun et al., 2021), delivery of bioactive compounds (Kuhn et al., 2019), or increased satiety (Norton et al., 2007).

Digestion involves complex physiological processes, however, an engineering point of view has been proposed to allow conceptualization of digestion as a series of processing events (Boland, 2016; Bornhorst et al., 2016b). This approach has been used to guide the development of in vitro systems for studying digestion, which have been increasingly used due to the cost and ethical considerations involved with in vivo experiments (Somaratne et al., 2020a). In vitro experiments, however, require that the biochemical and physical conditions of the digestion environment be recreated in a laboratory setting

(Minekus et al., 2014). Devices that attempt to mimic physiological changes in the digestion environment over time have been referred to as dynamic in vitro digestion systems, and these devices may include pH profiles (Mulet-Cabero et al., 2020), simulated peristaltic contractions (Keppler et al., 2020), and emptying mechanisms (Hayes et al., 2020) that are designed to resemble the in vivo conditions.

The development of in vitro systems is dependent on the availability of data from in vivo experiments, such as the pH profiles and mixing (Bornhorst et al., 2014c), motility (Marciani, 2011), acid secretions (Hoad et al., 2015), and particle breakdown (Bornhorst et al., 2013c) that occur during digestion. Additionally, recent research has applied principles of soft robotics and advanced control systems to develop dynamic in vitro systems with a high level of resemblance to the human stomach (Dang et al., 2020; Li et al., 2019, 2020; D. Liu et al., 2019; Wang et al., 2019) and intestine (Gouseti et al., 2014; Oosterveld et al., 2016; Wright et al., 2016). In certain cases these devices can generate in vitro-in vivo correlations (Dupont et al., 2019). However, the currently available dynamic in vitro digestion systems typically use only one chamber which must be manually loaded and managed during experiments that last for physiologically relevant time periods (approximately 1-4 hours), which limits experimental throughput.

There is a need for dynamic in vitro digestion systems which mimic physiological conditions, but also allow for higher throughput experiments. The advantage of higher experimental throughput could be rapid screening of food materials for health promoting properties. Additionally, a higher throughput platform for in vitro digestion experiments could benefit the food industry, for instance by allowing companies to efficiently assess the effect of different product formulations or processing conditions on variables of interest during the digestion process, such as bioaccessibility or food breakdown. The dynamic in vitro systems mentioned previously were designed at 1:1 scale with the human digestion system. Scaling down the size of the in vitro digestion system could increase throughput. However, modifications in size could also affect the fluid flow inside the simulator, an important consideration as fluid flow driven by peristaltic contractions has been shown to influence mixing (Kozu et al., 2017), and the breakdown of

food particles (Swackhamer et al., 2019). Therefore, there is a need to characterize the fluid flow inside dynamic in vitro digestion systems.

Direct measurement of the fluid flow inside of dynamic in vitro digestion systems has been accomplished using particle imaging velocimetry (Kozu et al., 2014), but due to physical constraints this approach is not possible for every device. Previous research has used Computational Fluid Dynamic (CFD) modeling to predict the fluid flow inside of the stomach (Miyagawa et al., 2016) and intestine (Fullard et al., 2015; Karthikeyan et al., 2021). However, these works did not seek to describe the fluid flow inside of a specific physical device, but instead modeled the fluid flow inside of an average stomach or intestine, based on the available in vivo data on its geometry. In general, the application of CFD modeling to in vitro digestion systems has been limited. This may be related to the difficulty in obtaining a shape function that describes the boundaries of the digestion system, which must be parameterized in time for devices that involve simulated peristalsis, and expressed in a form that can be passed to CFD modeling software. Knowledge of the fluid flow inside of an in vitro system could be used to optimize its operational parameters to better match in vivo conditions. Additionally, relating the breakdown of foods in the in vitro system to the fluid velocity, vorticity, or shear fields could lead to increased understanding of the mechanisms driving food breakdown during digestion (Kozu et al., 2014).

The aim of this study was to design and construct a multi-module peristaltic simulator for higher throughput in vitro digestion research as compared to single-chamber systems. Video analysis and manometry were used to obtain parameters describing the simulated peristaltic wave so that it could be compared to the results of in vivo studies. Additionally, video analysis was used to obtain a function describing the time-dependent shape of the device as it underwent simulated peristalsis, which was used to develop a CFD model of fluid flow inside the device. Results from this modeling were used to better understand the fluid flow inside the peristaltic simulator and were compared to in vivo data. CFD modeling could be used to guide future work on optimization of the simulator, or for understanding the effect of certain experimental conditions such as digesta rheology on the fluid flow, which could in turn enable the mechanisms of food breakdown during digestion to be studied in more detail. The peristaltic

simulator described in this work could have potential applications for studying food breakdown during gastric or intestinal digestion by recreating the peristaltic wave, the velocity, shear, and vorticity fields in the digestion environment while also increasing experimental throughput relative to existing simulators.

6.2 Materials and Methods

6.2.1 *Design and construction of the peristaltic simulator*

The simulator was fabricated in the UC Davis Biological and Agricultural Engineering Department machine shop. Mechanical design was carried out using Computer-Aided Design (CAD) software (SolidWorks, Waltham, MA, USA), shown in Figure 6.1. The device was designed to hold up to 12 individual digestion modules and apply the simulated peristaltic wave using rollers that contacted the digestion modules from both sides as they hung freely from a top rack. The digestion modules (low-density polyethylene, 0.1 mm wall thickness, 25.4 mm diameter, 229 mm length) were used to hold the contents during digestion, such as simulated digestion fluids and food particles. The digestion modules are shown in Figure 6.1 B and Figure 6.1 D as light blue tubes. Each digestion module was connected to the top rack using an embedded piece of a 50 mL conical tube, which allowed a cap to be screwed down, holding the digestion module in place during experiments. Since the modules were comprised of flexible plastic, they were partially occluded as the rollers translated downwards along the sides of the modules, creating the simulated peristaltic wave. A video showing the motion of the rollers creating the simulated peristaltic wave is shown in Supplementary Video 1.

The progression of the peristaltic wave (Figure 6.2) was accomplished through converting the rotational motion of the drive motor to linear motion of the rollers using Hoecken's 4-bar linkage. Individual components of this linkage are shown in Figure 6.1 E. Components of the Hoecken linkage were manufactured from aluminum. The application of the simulated peristaltic wave to the digestion modules is shown in Figure 6.2 A1-A4, with simplified illustrations of the digestion module at the corresponding time in Figure 6.2 B1-B4. At the beginning of the peristaltic wave (Figure 6.2 A1 and B1), the rollers approached the undeformed digestion module. As the rollers moved downwards in the -z direction (Figure 6.2 A2 and B2), they came together, initiating the simulated peristaltic wave. As the

rollers continued downwards (Figure 6.2 A3 and B3), they deformed the digestion module while the simulated peristaltic wave progressed along the module. When the rollers progressed to their lowest point, the simulated peristaltic wave also reached its lowest position on the digestion module (Figure 6.2 A4 and B4). Finally, the rollers separated and returned to the top position, repeating the cycle.

To maintain a constant motor torque throughout the cycle of the simulated peristaltic wave, a pulley and counterweight system were installed (Figure 6.1 B). An alternating current gearmotor (Model 1LPZ1, Dayton Electric Manufacturing Co., Niles, IL, USA) providing 22.6 N-m torque and 3 revolutions per minute was used to drive the system. To minimize intercomponent friction and reduce maintenance, a rail and slide platform supported by plastic linear bearings (NW-02-17, Igus Inc., East Providence, RI, USA) were used to restrain the extended bar (Figure 6.1 E) along its vertical and horizontal axis so that the bar strictly followed the path of the 4-bar Hoecken linkage.

Another consideration in the peristaltic simulator design was allowing for modification according to the needs of future experiments. To accomplish this, the top rack (Figure 6.1 B) was designed to be easily removable, which allows digestion modules of varying width to be used. Additionally, rollers of different widths can be installed in the device, enabling the percent occlusion of the simulated peristaltic wave to be modified. Furthermore, the roller block (Figure 6.1 E) can hold either one or two rollers on each side, which could enable modifications to the shape of the peristaltic wave. This could be used to approximate the dynamics of different types of motility in the gastrointestinal system, as it has been shown by previous researchers that both segmental and longitudinal contractions occur in the intestine (Schulze, 2015). In this study, experiments were carried out using either thin rollers (12.6 mm diameter) or thick rollers (17.4 mm diameter). In both cases, only one roller was used on each side of the digestion modules, resulting in a peristaltic wave with one peak per cycle. When the thin rollers were used to create simulated peristaltic waves, the gap between the rollers during the contraction wave was 7.2 mm, and when the thick rollers were used the gap was 3.9 mm (Figure 6.2 B2). Rollers were manufactured from anodized aluminum.

A control system was designed to control the simulator temperature with a simple user interface (Figure 6.1 F), based on an Arduino Mega microcontroller (Arduino Inc, Turin, Italy). The

microcontroller measured temperature inside a module of the simulator using a DS18B20 digital temperature sensor (Maxim Integrated, San Jose, CA, USA), and recorded data to a removable camera memory card using a datalogger (Product 1141, Adafruit, New York, NY, USA). Temperature and experimental run time were displayed on an LCD screen (Product 1115, Adafruit, New York, NY, USA). The controller was housed inside a box with a cutout for the LCD screen. In Figure 6.1 F, items inside the dashed rectangle were located inside the box. A 400 W ceramic heater was controlled using a relay (IoT Relay II, Digital Loggers Inc, Santa Clara, CA, USA) connected to the microcontroller. An emergency stop button was connected to the relay as a hardware-level interrupt and high-temperature shut off was included in the microcontroller code, either of which turned off the gearmotor and heater and require a reboot of the control system before the system can be re-energized.

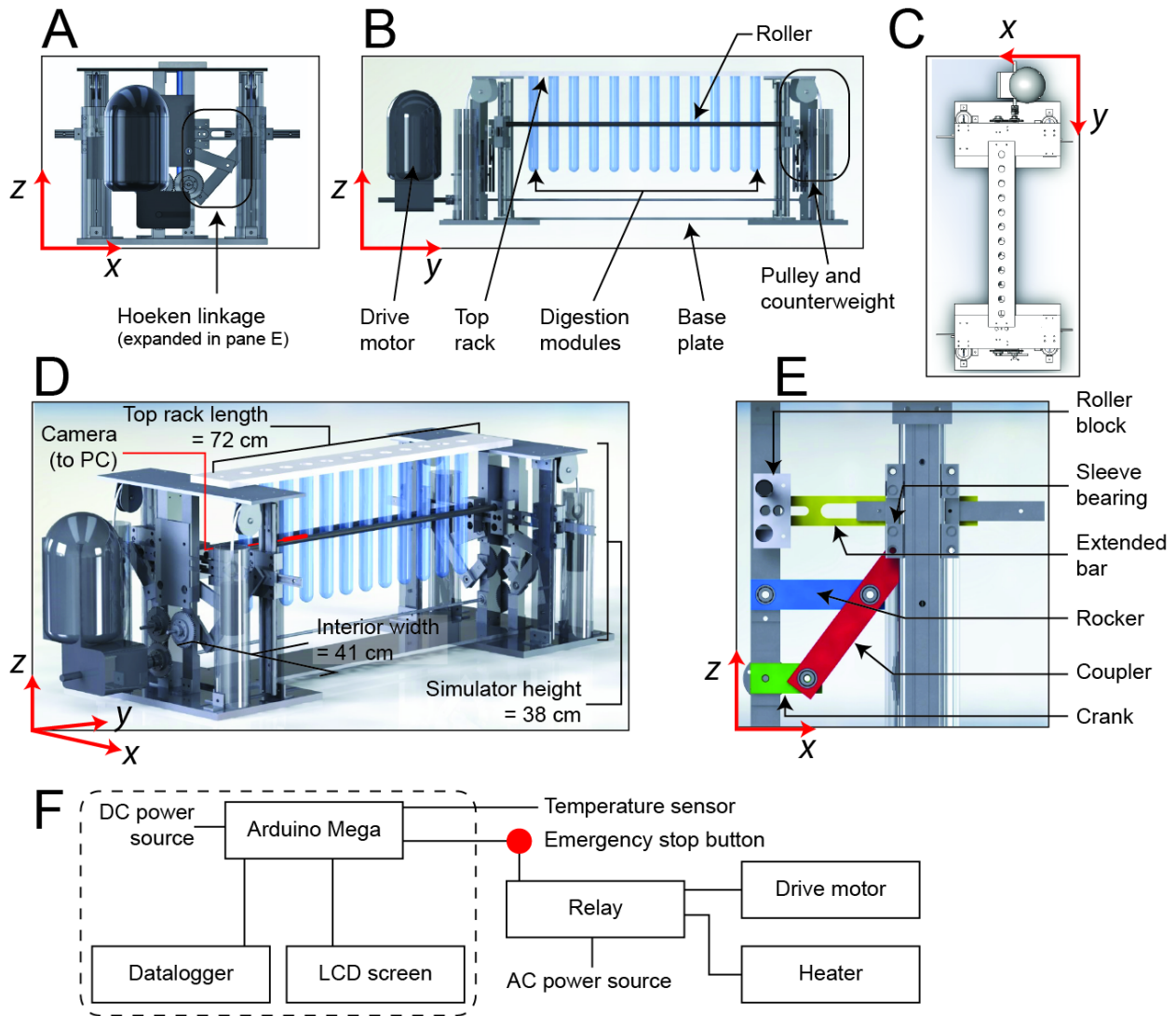
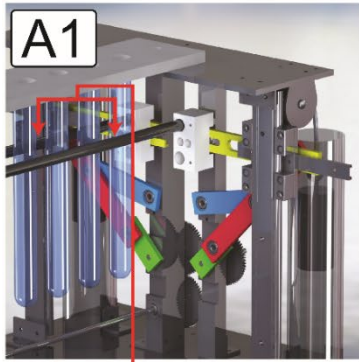
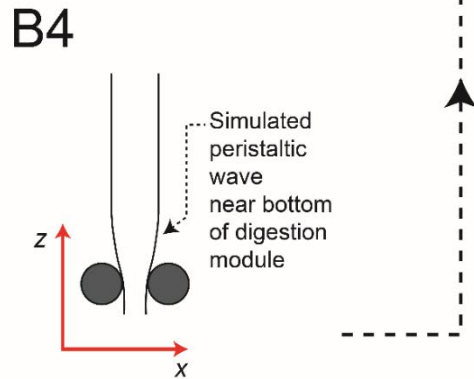
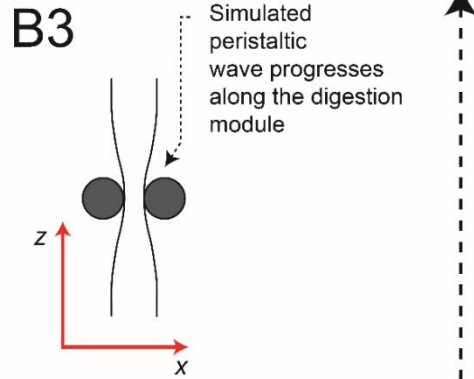
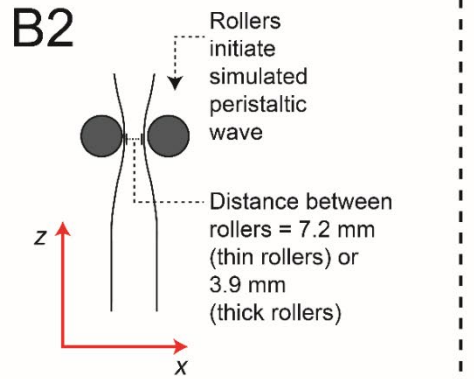
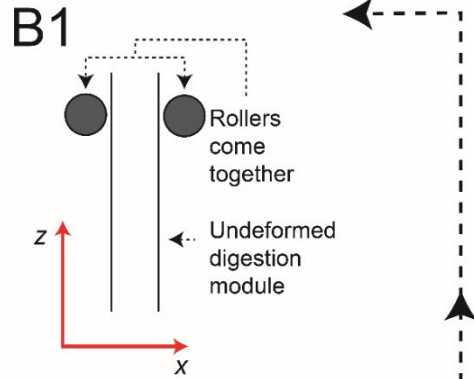
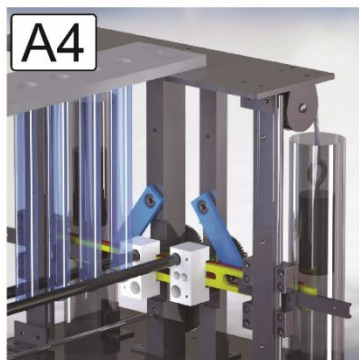
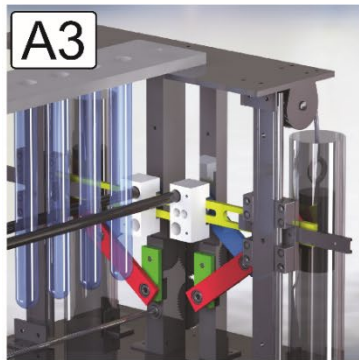
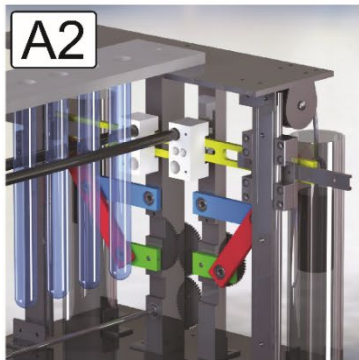


Figure 6.1. Three-dimensional CAD model of the peristaltic simulator showing a side view of the simulator and the Hoecken linkage (A); side view of the peristaltic simulator and the drive motor, digestion modules, base plate, and pulley/counterweight assembly (B); top view of the simulator (C); isometric view of the simulator with the endoscopic camera used for video analysis of the shape of the digestion modules shown in red (D); schematic view of the Hoecken linkage used to drive the motion of the rollers with individual parts shown in different colors for clarity (E); diagram of the control system (F).



Rollers



Rollers separate and return to start position without contacting the digestion module

Figure 6.2. Depiction of the simulated peristaltic wave applied to digestion modules by the simulator. Rollers approach the undeformed digestion modules (A1, B1), Rollers contact the digestion modules, initiating the simulated peristaltic wave (A2, B2), the simulated peristaltic wave progresses to the middle of the digestion modules (A3, B3), rollers reach the lowest point of the path (A4, B4), and rollers then separate and return to the top position, beginning the next cycle. Images in column A represent CAD views of the simulator, and images in column B represent a simplified view showing the interaction of a single digestion module with the rollers.

6.2.2 Characterization of the simulator

6.2.2.1 Manometry

The contraction force exerted by the rollers on the contents of the digestion modules was assessed using manometry, as has been done by previous researchers to characterize the compression force inside dynamic in vitro gastrointestinal models (Keppler et al., 2020; Wang et al., 2021). A manometer (Digi-sense Traceable Digital Manometer, ± 34.5 kPa, Cole-Parmer, Vernon Hills, IL, USA) was used to measure the gauge pressure inside a digestion module by placing the bulb (1.5 cm width, 3.5 cm height) inside the module and then recording the pressure after initiating simulated peristalsis. The manometer bulb was placed inside a digestion module near the middle of the top rack, which was filled with 150 mL of a 1.5 mg/mL mucin solution at 37°C. Each time the manometer was used to measure pressure, two simulated peristaltic contractions (two cycles) were captured (Figure 6.4 A). Pressure readings using the manometer were carried out in triplicate for the thin roller and thick roller types, resulting in 6 total waves per roller type being included in the analysis. Pressure readings were obtained from the manometer every 0.07 s, and data were processed using a 0.5 s moving average filter. The period of the peristaltic wave was determined from manometry data by subtracting the time at which peak pressure was reached during the second wave from the time at which the peak pressure occurred during the first wave.

The contraction force exerted by the rollers on the manometer bulb was estimated by developing a calibration relationship between pressure in the bulb and the force required to compress it. This was done by placing the manometer bulb on a TA-XT Plus texture analyzer (Texture Technologies, Hamilton, MA,

USA) and compressing it at 1 mm/s using a 45 mm diameter flat plate probe until a target force was reached. Target forces from 0 N to 10 N in increments of 0.2 N were used for the calibration. At each target force the resulting pressure was recorded. Each target force was tested in triplicate. The relationship between the target force applied to the bulb by the texture analyzer and the gauge pressure recorded by the manometer was quantified using nonlinear regression. This relationship was used to estimate the contact force between the rollers and the manometer bulb during simulated peristalsis.

6.2.2.2 Video analysis

Video analysis of the peristaltic simulator was used to characterize the simulated peristaltic wave applied to the digestion modules. A high-definition endoscopic video camera (Oiiwak, Marietta, GA, USA) was installed in between the rollers facing a digestion module (Figure 6.1 D). Videos were captured in 1920 x 1080-pixel resolution at 30 frames per second. An individual module was filled with 1.5 mg/mL mucin solution and dyed red to increase contrast prior to starting simulated peristaltic contractions. Analysis was conducted by obtaining videos of the digestion module as it underwent simulated peristalsis, segmenting the digestion module from the background, and then determining a function that described its shape using curve fitting. Briefly, video frames were converted to L*a*b* color space, and then the digestion module was segmented out based on its red color relative to the background using an automated thresholding process. An example raw image is shown in Figure 6.3 A with the corresponding binarized image in Figure 6.3 B. Points defining the edges of the digestion module were obtained (Figure 6.3 C) and then prepared for curve fitting by smoothing with a Savitsky-Golay filter of degree 2 (Figure 6.3 D). The curves obtained from each side of the digestion module were independently fit using a three-parameter Gaussian distribution function given by 6.1:

$$y = a \times \exp(-(x - b)^2/c) \quad 6.1$$

Where (x, y) are the coordinates defining the position of each edge point of the digestion module, and a, b, and c are parameters of the function determined using curve fitting. The function was separately fit to the points defining the left side of the digestion module and then to the points defining the right side

(Figure 6.3 D). This resulted in two sets of parameters, one set (a, b, c) from the fit to the left side of the module and another set of parameters from the fit to its right side. The parameters were averaged, and the function with averaged parameters was used to model the entire deformation (Figure 6.3 E). The result of this analysis was a single function describing the shape of the digestion module as it underwent simulated peristalsis (Figure 6.3 F), which was then used to establish the parameters of the CFD model.

Curve fitting was conducted in two different coordinate spaces. First, distance in each image was expressed in mm. This was accomplished by measuring the width of the digestion module in mm, and then measuring its width in pixels at 6 different vertical locations. The average of these measurements was used as a pixel to mm conversion factor, and applied to each image to express distances in units of mm. It should be noted that this calibration factor is valid in the plane of the digestion module. Curve fitting was also conducted in a nondimensional coordinate space where the length unit was defined as the width of the undeformed digestion module. This was carried out to determine parameters of the function describing the shape of the digestion module in relative units of intestinal widths. The rationale for this analysis was to allow the parameters to be more easily used by future researchers in situations where the intestinal width can be defined more conveniently than a pixel to mm conversion factor. Video analysis for curve fitting was carried out using MATLAB R2020a. Three simulated peristaltic waves (three cycles) were considered for characterizing the shape of the digestion module for the thin rollers and the thick rollers.

Video analysis was also used to quantify the degree to which the simulated peristaltic wave occluded the digestion module. Occlusion was defined using Equation 6.2 (Kwiatek et al., 2006).

$$Occlusion (\%) = (1 - w_d/w_n) \times 100\% \quad 6.2$$

Where w_d (pixels) is the width of the digestion module at the midpoint, and w_n (pixels) is its nominal, undeformed width. The width of the digestion module at its midpoint was determined using the binary images obtained from video of the simulator (Figure 6.3 B) where the digestion module is shown in white on a black background. The nominal width of the module was determined from binary images in the first 10 frames of each video, which corresponded to the module hanging freely before contacting the rollers.

The period of the peristaltic wave was quantified using video analysis by subtracting the time at which maximum occlusion occurred during the first wave from the time at which maximum occlusion occurred during the second wave. Three videos, each encompassing two simulated peristaltic waves, were analyzed for the thin rollers and for the thick rollers.

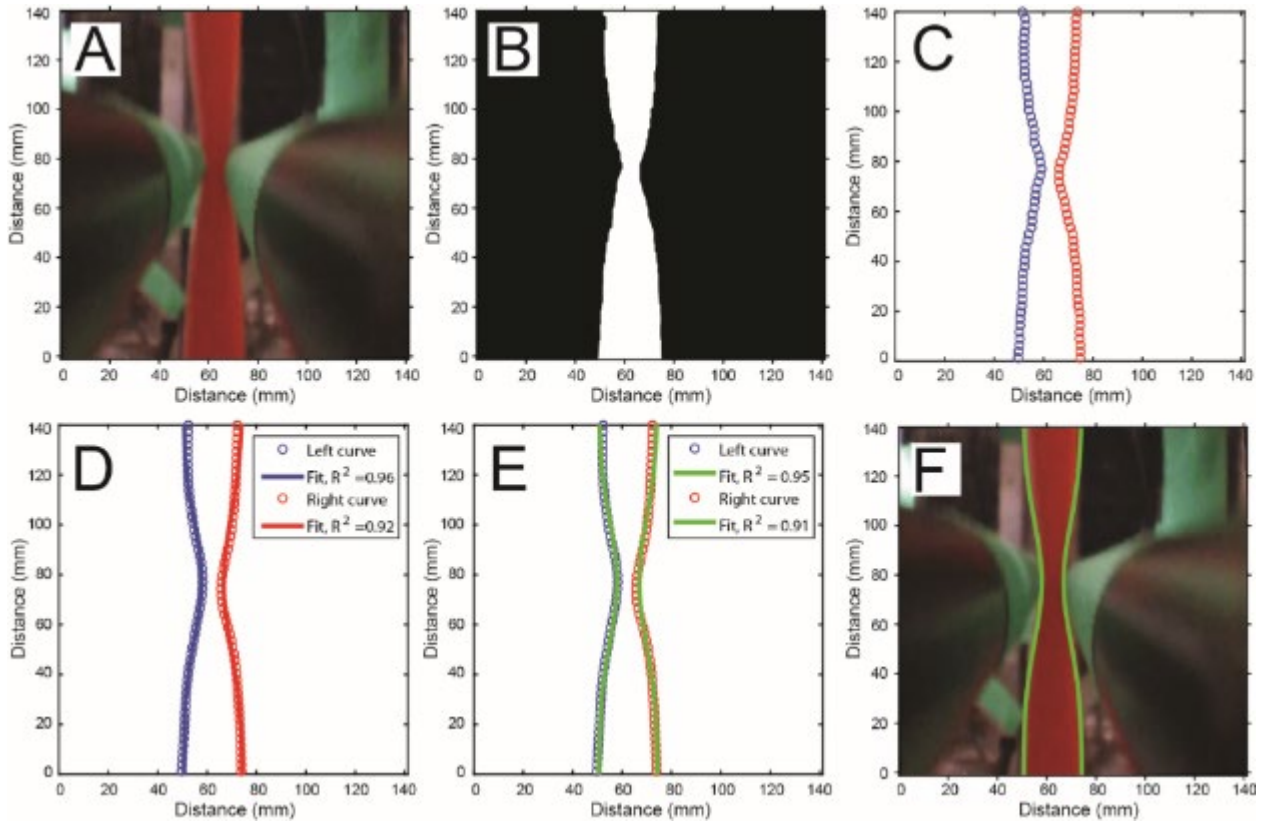


Figure 6.3. Video analysis of the peristaltic simulator. Original image acquired by the endoscopic video camera (A); Binary image showing the digestion module in white and the background in black (B); Points defining the edges of the digestion module with the left edge marked by blue circles and the right edge by red circles (C); Edge points after smoothing, showing the direct fit of the three-parameter Gaussian distribution function (Equation 6.2) to points on the left side with the fit represented by a blue line and the fit to points on the right side of the digestion module represented by a red line (D); Gaussian function with averaged parameters used to model the deformation of both the left and right side of the digestion module (E); Curves generated by the process overlaying the original image (F). The distance axes (in

mm) are valid in the plane of the digestion module, which was located approximately 20 cm from the aperture of the camera.

6.2.2.3 Computational Fluid Dynamic (CFD) modeling of the peristaltic simulator

The contact between rollers and the digestion module leading to fluid flow in the peristaltic simulator was simulated using a multiphysics, finite element model implemented in COMSOL Multiphysics® (Version 5.6, COMSOL Inc., Burlington, MA). The three-dimensional geometry of a single, cylindrical module in the peristaltic simulator was the subject of the simulation. The simulator fitted with the thin rollers was simulated in addition to the simulator fitted with the thick rollers. Model parameters are provided in Table 1. The fluid was assumed to be incompressible and undergoing laminar flow, in agreement with a CFD model for the human intestine developed by previous researchers, where the Reynold's number was estimated ca. 3 (Karthikeyan et al., 2021). The governing equations for fluid flow were the continuity equation (Equation 6.3) and the Navier-Stokes equation (Equation 6.4):

$$\nabla \cdot \underline{u} = 0 \quad 6.3$$

$$\rho \left(\frac{\partial \underline{u}}{\partial t} + \underline{u} \cdot \nabla \underline{u} \right) = -\nabla P + \nabla \cdot \underline{\tau} + \rho \underline{g} \quad 6.4$$

Where \underline{u} (m/s) is the fluid velocity vector, ρ (kg/m³) is the fluid density, t (s) is time, P (Pa) is the pressure, $\underline{\tau}$ (Pa) is the viscous stress tensor, and \underline{g} (m/s²) is the acceleration due to gravity. The model was conducted using a Newtonian fluid, for which the viscous stress tensor is proportional to the rate of strain tensor via the viscosity of the fluid (Equation 6.5):

$$\underline{\tau} = 2\mu \underline{\Gamma} = \mu \left[\nabla \underline{u} + (\nabla \underline{u})^T \right] \quad 6.5$$

Where μ (Pa-s) is the viscosity, $\underline{\Gamma}$ (1/s) is the rate of strain tensor, and T indicates the transpose. Contact between the rollers and the module was modeled using a time and position dependent load function, which applied a specific force density to the outer wall of the module. The governing equation for this structural mechanics computation was Newton's second law of motion (Equation 6.6):

$$\rho_m \left(\frac{\partial^2 \underline{u}_w}{\partial t^2} \right) - \nabla \cdot \underline{\underline{\sigma}} = \underline{F}_v \quad 6.6$$

Where ρ_m (kg/m³) is the density of the wall material of the module, \underline{u}_w (m/s) is the displacement vector of the wall material, $\underline{\underline{\sigma}}$ (Pa) is Cauchy's normal stress tensor, and \underline{F}_v (N/m³) is the body force per unit volume applied to the module wall (Hari et al., 2012). The displacement of the material due to the externally applied force was given by Equation 6.7:

$$\underline{\underline{\varepsilon}} = 1/2 \times \left[(\nabla \underline{u}_w)^T + \nabla \underline{u}_w + (\nabla \underline{u}_w)^T \nabla \underline{u}_w \right] \quad 6.7$$

The load function used to describe the contact force applied by the rollers to the module wall in the radial direction was expressed by Equation 6.8:

$$\underline{F}_{A,r} = -L_{max} \times \exp \left(-\frac{(z - z_0 + v_0 * t)^2}{2\sigma_c^2} \right) \times H_s(t, z) \quad 6.8$$

Where $\underline{F}_{A,r}$ (N/m²) is the load applied in the radial direction to the digestion module, L_{max} (N/m²) is the maximum force density applied by the roller to the module wall, z (m) is the height coordinate, z_0 (m) is the z value where the contraction begins, v_0 (m/s) is the vertical velocity of the rollers, and σ_c^2 (m²) is a variance factor that defines the width of the Gaussian force distribution and H_s (dimensionless) is the function responsible for applying the load according to the desired timing. This function, H_s , was defined using a smoothed Heaviside step function available in the COMSOL library (Equation 6.9):

$$H_s = flc2hs((t_{off} - t)/dt, 1) \times flc2hs((t - t_{on})/dt, 1) \quad 6.9$$

Where $flc2hs$ is the smoothed Heaviside step function, t_{off} (s) is the time when the rollers disengage after reaching the bottom of the module and completing the contraction, dt (s) is the time after rollers engage with the module at which the maximum force was applied, t_{on} (s) is the time when the rollers engage at the top of the module. Equation 6.9 is shown mathematically, along with the conditions for activation of each Heaviside function, in Equation 6.10:

$$H_s = \begin{cases} 0.5 + 0.9375 \times \left(\frac{t_{off} - t}{dt} \right) - 0.625 \times \left(\frac{t_{off} - t}{dt} \right)^3 + 0.1875 \times \left(\frac{t_{off} - t}{dt} \right)^5, & t_{off} - dt < t < t_{off} + dt \\ 0.5 + 0.9375 \times \left(\frac{t - t_{on}}{dt} \right) - 0.625 \times \left(\frac{t - t_{on}}{dt} \right)^3 + 0.1875 \times \left(\frac{t - t_{on}}{dt} \right)^5, & t_{on} - dt < t < t_{on} + dt \end{cases} \quad 6.10$$

As the model consisted of the coupled equations describing the structural mechanics of the module wall deformation and resulting fluid flow inside the module, the deformation of the module due to a given maximum applied force density, L_{max} , could not be predicted *a priori*. Thus, an iterative approach was taken, by varying L_{max} until the predicted shape of the module was in good agreement with the experimentally determined shape functions based on video analysis (Section 6.3.2.2).

The initial condition for laminar flow was a velocity field of zero. An open boundary condition was applied at the top of the module (zero normal force), a closed boundary condition was applied at the bottom of the module, and a no-slip condition was applied at the interface of the fluid and the module wall. The initial conditions for solid structural mechanics were a stress field of zero. The mesh displacement and velocity were coupled through the fluid-structure interface. A mesh for the model was developed using COMSOL's built in method with mesh size set to "fine", and consisted of 390,347 tetrahedral elements, 22,832 triangular elements, 550 edge elements and 8 vertex elements. Mesh quality was evaluated using skewness, which showed an average element quality of 0.6627 and a minimum quality of 0.1792. Multiphysics computations were carried out using a four-step segregated solution technique. On step 1, velocity and pressure fields were solved using COMSOL's built-in Algebraic MultiGrid (AMG) solver with the Generalized Minimal Residual (GMRES) method, a linearized iterative solver. On step 2, the displacement field was solved using PARDISO, a direct solver. On step 3, the spatial mesh displacement was solved using PARDISO. Finally, the fluid-structure interaction was computed using PARDISO. The relative tolerance was 0.001 and the absolute tolerance was 0.01. Results were stored every 0.2 s. The simulation of 8 s of time in the peristaltic simulator was solved on a desktop computer (Intel i7-8700K CPU @3.7 GHz, 64 GB RAM). Solution time was approximately 3 hours.

Table 6.1. Parameters of the CFD model of fluid flow inside the peristaltic simulator

Parameter	Value	Unit	Description
Module diameter	0.0254	m	Diameter of the flexible module holding liquid contents of the simulator
Module height	0.127	m	Height of the flexible module holding liquid contents of the simulator
μ	1.09×10^{-3}	Pa-s	Viscosity of the liquid contents of the simulator (1.5 mg/mL mucin solution, Section 2.2.5)
ρ	1×10^3	kg/m ³	Density of the liquid contents of the simulator
$L_{max,thick\ roller}$	5.290×10^4	N/m ²	Maximum force per unit area applied by thick rollers to the wall of the module
$L_{max,thin\ roller}$	4.475×10^4	N/m ²	Maximum force per unit area applied by thin rollers to the wall of the module
z_0	0.127	m	Z value where the rollers engage with the module at the start of the contraction
v_0	0.0146	m/s	Downwards vertical velocity of rollers
σ_c^2	1.59×10^{-4}	m ²	Variance of the Gaussian distribution describing force applied by rollers to the module
t_{on}	0.75	s	Time when rollers engage at the top of the module
t_{off}	8.0	s	Time when rollers disengage at the bottom of the module
dt	0.5	s	Time after rollers engage at which maximum force (L_{max}) is reached

Young's modulus of wall material	0.171×10^9	Pa	Young's modulus of the wall material of the digestion module (Low-density polyethylene) (Oromiehie et al., 2013)
Poisson ratio of wall material	0.4	Pa	Poisson ratio of the wall material of the digestion module (Low-density polyethylene) (Nitta and Yam, 2012)
Density of wall material	920	kg/m ³	Density of the wall material of the digestion module (Low-density polyethylene) (Oromiehie et al., 2013)

6.2.2.4 Comparison of the motion of the simulator to *ex vivo* porcine tissue

A preliminary analysis was carried out to compare the motility of the simulator to an *ex vivo* porcine intestine. Video of *ex vivo* porcine intestine demonstrating post-mortem motility was obtained from a recent study (Nadia et al., 2021b). The shape of the intestine during the peristaltic wave was quantified using curve fitting. Briefly, a single frame where the intestine was clearly visible was selected, then rotated until the intestine was vertical with the zone of the peristaltic contraction near the midpoint. This image was manually segmented by placing anchor points along the boundary of the intestine. The shape of the intestine during the peristaltic contraction was then quantified using curve fitting with the same approach used for quantification of the shape of the peristaltic simulator (Section 2.2.2). The width of the porcine intestine was determined in pixels using the function `imdistline` in MATLAB. Curve fitting used to determine the shape function representing the porcine intestine was carried out in a nondimensional coordinate space where the length unit was defined as the width of the undeformed intestine.

6.2.2.5 Rheological analysis of simulated digestion fluids

The viscosity of simulated gastric juice and a 1.5 mg/mL mucin solution were assessed to determine an appropriate liquid medium for conducting experiments to characterize the motion of the peristaltic simulator. Simulated gastric juice was prepared using the INFOGEST formulation (Minekus et al., 2014),

with minor modifications. Modifications to the INFOGEST formulation consisted of addition of 1.5 mg/mL mucin to the simulated gastric juice, in accordance with previous research (Mennah-Govela et al., 2015), and adjustment of the simulated gastric juice to pH 1.8. The 1.5 mg/mL mucin solution was also prepared at pH 1.8. The full compositions of simulated gastric juice and the 1.5 mg/mL mucin solution are provided in Table 5.2. Rheological analysis was carried out using an MCR 302 rheometer (Anton Paar, Graz, Austria) using a cup and bob measuring system. Flow curves were generated for each by varying the shear rate logarithmically from 1 to 100 s⁻¹. The test temperature was 37 ± 0.1 °C and each liquid was tested in triplicate.

6.2.3 Statistical analysis

One-way Analysis of Variance (ANOVA) was carried out to determine differences between variables obtained from manometry and video analysis of the peristaltic simulator with the type of roller (thin or thick rollers) as the factor. One-way ANOVA was also used to test for a difference between the viscosity of simulated gastric juice and of the 1.5 mg/mL mucin solution. Post-hoc analysis was carried out using Tukey's test and significance was noted for p<0.05. Results were presented as means ± standard deviation. Statistical analysis was carried out using MATLAB R2020a.

6.3 Results and discussion

6.3.1 Rheology of simulated digestion fluids

Both simulated gastric juice and the 1.5 mg/mL mucin solution displayed Newtonian behavior. The average viscosity across the range of shear rates that were studied was 1.10 ± 0.32 mPa s for simulated gastric juice and 1.09 ± 0.34 mPa s for the 1.5 mg/mL mucin solution. The viscosity of simulated gastric juice was not significantly different from the viscosity of the mucin solution (p>0.05). The 1.5 mg/mL mucin solution at pH 1.8 was used for all video analysis and manometry experiments involving characterization of the peristaltic simulator.

6.3.2 Characterization of the peristaltic simulator

6.3.2.1 Manometry

Results showed that the gauge pressure inside the manometer bulb increased and then decreased as the simulated peristaltic wave passed over it (Figure 6.4 A). The manometer was calibrated by fitting the data of known compression forces applied to the manometer bulb using a texture analyzer and the resulting pressures using a third order polynomial (Figure 6.4 B, $R^2 = 0.9986$). This relationship was used to estimate the contraction force applied by the rollers to the digestion module during simulated peristalsis (Figure 6.4 C). As with the pressure profile, the estimated contraction force on the manometer bulb increased and then decreased as the rollers passed over it. The thick rollers led to a significantly higher peak pressure (7.54 ± 0.29 kPa) than the thin rollers (3.91 ± 0.06 kPa, $p < 0.05$). Likewise, the peak force values were significantly greater when the thick rollers were used (4.51 ± 0.16 N) than when the thin rollers were used (2.61 ± 0.03 N). Between the peristaltic waves, the pressure returned to a baseline of approximately 0.00-0.05 kPa. The period of the peristaltic wave was defined as the elapsed time between the peak pressure value of the first wave and the peak pressure value of the second wave. The period was found to be 17.60 ± 0.18 s when the thick rollers were used, which was not significantly different from the wave period when the thin rollers were used (18.42 ± 1.43 s $p > 0.05$).

The peak pressure values in the peristaltic simulator fell into the range reported by previous researchers based on in vivo manometry measurements in the small intestine. For example, Hansen et al., (2002) found that pressures accompanying peristaltic waves in the small intestine tended to fall between 2.7-5.3 kPa and Samsom et al., (1999) reported peak pressures of 9.5-12.3 kPa. Research using an ingestible pressure sensor (i.e. SmartPill) found peak pressures in the intestine of roughly 6.5 kPa (Cassilly et al., 2008). Based on these results, the peak pressure recorded using the thin rollers (3.91 ± 0.06 kPa) can be considered in the low end of the range of pressures in the small intestine reported in the literature, whereas the peak pressure recorded using the thick rollers (7.54 ± 0.29 kPa) was on the higher side of the range. The ability to study the effect of peristaltic waves with varying amplitudes in terms of peak pressure and force could be an advantage of the peristaltic simulator described in this study.

In clinical settings, manometry has been used to assist in the diagnosis of small intestinal motility disorders, and it has been determined that the presence of pressure events greater than 2.7 kPa is indicative of normal motility (Camilleri et al., 1998). Malagelada (2008) considered the absence of any contractions leading to pressure greater than 1.3 kPa to be indicative of hypomotility, and the presence of sustained pressure in excess of 4.0 kPa to indicate abnormally high luminal pressure. In the peristaltic simulator described in the current study, pressures recorded using manometry would be classified as normal according to both frameworks, suggesting that this model may be appropriate to mimic the pressure in the small intestine during peristaltic contractions.

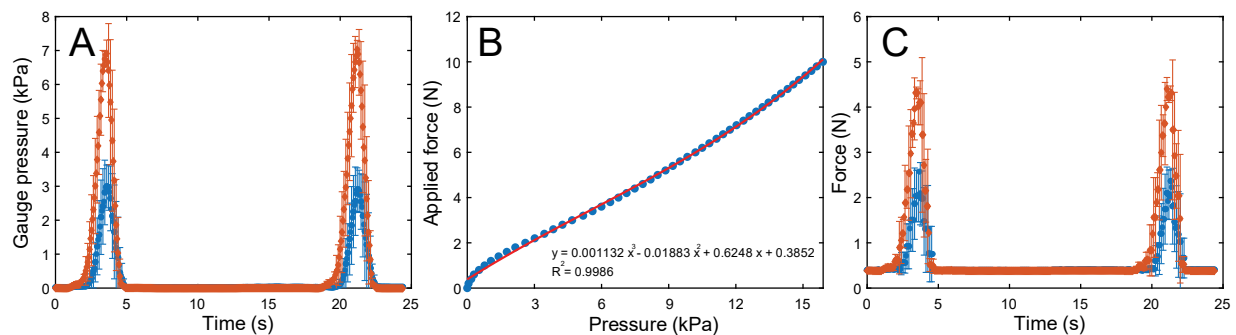


Figure 6.4. Pressure profiles in the digestion module were recorded using the thick rollers (♦) and thin rollers (●) over two simulated peristaltic waves (A). Calibration of the manometer was carried out to determine the estimated contraction force applied to the digestion module during the simulated peristaltic wave by applying force to the bulb using the texture analyzer and recording the resultant pressure recorded by the manometer (B). Force profiles in the digestion module are shown in panel C. The mean values \pm standard deviation from three runs are shown. Error bars are shown on every third point for clarity.

6.3.2.2 Video analysis

Results of video analysis showed that percent occlusion (Equation 6.2) increased as the simulated peristaltic wave passed over the midpoint of the digestion module. As the wave moved downwards, occlusion decreased and the module returned to its nominal width (Figure 6.5). The maximum occlusion

was significantly lower when the thin roller was used ($72.1 \pm 0.4\%$) than when the thick roller was used ($84.6 \pm 1.2\%$, $p < 0.05$).

The percent occlusion of the stomach and intestine have been studied in vivo using Magnetic Resonance Imaging (MRI). It has been determined that the percent occlusion of antral contraction waves in the stomach depends on the distance from the pylorus, with the percent occlusion increasing as the wave reaches the pylorus, reaching values of approximately 58% (L. Marciani et al., 2001b) to 60% (Kwiatek et al., 2006). In the small intestine, maximum occlusion of 75% (Fullard et al., 2015) to 80% (Sinnott et al., 2012) has been reported. The values of occlusion for the small intestine are in good agreement with the values obtained for the simulator in the current study. It should be noted, however, that the simulator can easily be retrofitted with rollers of intermediate width, allowing adjustment of the maximum percent occlusion generated during the simulated peristaltic wave. This could be useful for future studies on the mechanisms of food breakdown, for example, by testing the hypothesis that deeper contractions would lead to greater breakdown of food particles.

It has been previously determined that an in vitro digestion model which included simulated peristaltic waves led to size reduction of almond particles, whereas in vitro digestion in a model which lacked simulated peristalsis did not lead to breakdown (Swackhamer et al., 2019). Additional experiments have confirmed that particle breakdown can occur using in vitro digestion models that include simulated peristalsis (Hayes et al., 2020; Somaratne et al., 2020d; Wang et al., 2021). However, the minimum contraction strength or percent occlusion needed for particle breakdown in an in vitro digestion model has not been determined. The peristaltic simulator described in this work could enable future research on this topic, with potential implications for studying the effect of digestive motility disorders on the digestion process from a mechanistic point of view.

Video analysis was also used to determine the period of the simulated peristaltic wave by subtracting the time of maximum occlusion from the first peak from the time of maximum occlusion at the second peak. Wave period calculated based on max occlusion was significant smaller when the thin rollers were used (17.6 ± 0.1 s) than when the thick roller was used (17.8 ± 0.0 s, $p < 0.05$). For the thin rollers, the

wave period calculated using percent occlusion analysis (17.6 ± 0.1 s) was slightly lower than the period calculated using manometry (18.4 ± 1.4 s). For the thick rollers, the wave period calculated using percent occlusion analysis (17.8 ± 0.0 s) was slightly higher than the value calculated using manometry (17.6 ± 0.2 s). It is possible that during manometry, the response time of the manometer (ca. 0.5 s) made it difficult to establish the true time at which peak pressure occurred. Measured values of wave period made using manometry and percent occlusion analysis were pooled for each roller type to determine an overall average period, which was 18.0 ± 1.0 s for the thin rollers and 17.7 ± 0.2 s for the thick rollers, showing that the average wave period was not significantly influenced ($p > 0.05$) by the roller thickness. The linear speed of the rollers as they progressed downwards across the digestion module was 0.0146 ± 0.00 m/s.

Results of *in vivo* experiments have found the period of peristaltic waves in the gastric antrum to be 23 ± 2 s (Kwiatek et al., 2006) and 20.0 ± 1.3 s (L. Marciani et al., 2001b). However, it has also been found that the frequency of peristaltic contractions in the human stomach was significantly influenced by the type of meal consumed by the subjects. Specifically, a high nutrient density meal led to a wave period of 24.4 ± 1.5 s, whereas a low-nutrient density meal led to a wave period of 19.4 ± 0.87 s (Gopirajah et al., 2016). In the small intestine, the period of peristaltic waves has been found to range from 23-56 s for subjects in the fasted state, and from 27-67 s for subjects in the fed state (Samsom et al., 1998). However, it has also been shown that the frequency of peristaltic waves in the duodenal region of the small intestine (14-29 s) may differ from the frequency of waves in the jejunal region (10-30 s) during the postprandial period (Samsom et al., 1999), with significant variability both between and within human subjects.

The wave periods of the peristaltic simulator are thus in the range of values for gastric and intestinal peristaltic wave period reported in literature. Modifying the wave period in the simulator could be accomplished by adjusting the gear ratio of the drive motor or through on/off control of its power supply. Exploring the effect of wave period on the breakdown of food particles could be a topic of future research, although there is a need for more *in vivo* data on the effect of meal properties on peristaltic wave period.

Small intestinal motility is complex as contractions can be longitudinal, shortening the intestine but having limited impact on lumen width, or segmental, leading to occlusion of the intestinal lumen (Fullard et al., 2015). Furthermore, segmental contractions can be short-lived (phasic), migrating and advancing chyme along the intestinal length, or long-lasting (tonic), leading to reductions in luminal volume without necessary advancing chyme (Lentle, 2018; Schulze, 2015). Small intestinal contractions do not necessarily proceed in an orderly manner, and double contractions as well as simultaneous contractions of different types can occur in vivo (Ailiani et al., 2009; Thuneberg and Peters, 2001). The ability of the peristaltic simulator to be outfitted with double rollers could potentially allow for the study of types of intestinal motility that cannot be reproduced by previously developed in vitro systems.

For the peristaltic simulator described in this report the ends of the digestion modules were sealed, meaning that chyme was not advanced through a long section of intestine by the peristaltic contractions. However, this setup may be advantageous for in vitro experiments as it resembles ex-vivo studies of sections of rabbit intestine that have been carried out by previous researchers (Marcello Costa et al., 2013; Lammers, 2005). Additionally, researchers have developed a computational smooth particle hydrodynamics model of a sealed length of intestine undergoing peristalsis (Sinnott et al., 2017), suggesting the opportunity for future studies comparing results from on ex-vivo intestinal tissue, computational modeling, and in vitro work carried out in the peristaltic simulator.

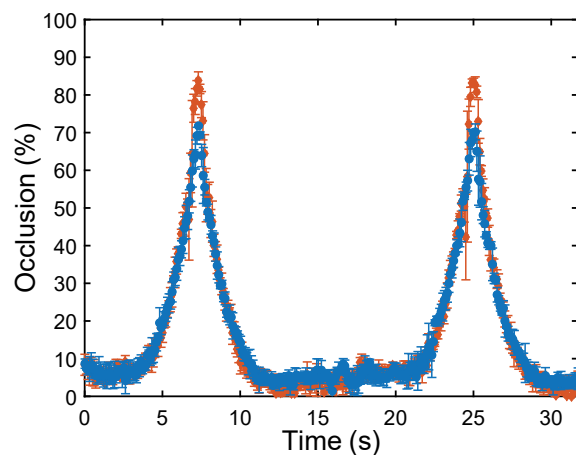


Figure 6.5. Percent occlusion of the midpoint of the digestion module during two compression cycles as determined using video analysis for the thick rollers (◆) and thin rollers (●) over two simulated peristaltic waves, showing the mean values \pm standard deviation from three runs. Every third point is shown for clarity.

The three-parameter Gaussian distribution function (Equation 6.1) was fit to experimental data consisting of points defining the edge of the digestion module as it underwent simulated peristalsis using either the thin or the thick rollers. The Gaussian function provided a good fit to the experimental data consisting of points defining the edge of the digestion module as it underwent simulated peristalsis, as evidenced by R^2 values of 0.96 ± 0.01 (thin rollers) and 0.95 ± 0.02 (thick rollers). Parameters of the shape functions determined using curve fitting in mm coordinates and in nondimensional coordinates are given in Table 2 from the averaged fit to the left- and right-hand sides of the digestion module during the peristaltic wave. In both coordinate spaces there was a significant difference between the “a” parameter of the shape function for the thin and thick rollers ($p < 0.05$). Similarly, there was a significant difference between the “b” parameter of the shape function for the thin and thick rollers ($p < 0.05$). However, the difference between the “c” parameters was not significant ($p > 0.05$). The parameters from curve fitting in mm coordinates may be useful in future research where the size of the intestine can be determined from an external calibration, such as with ex vivo tissue where a scale can be included for image analysis. However, for data collected in vivo it may be more convenient to define the nominal (undeformed) width of the intestine as a relative length unit, and in this case the parameters from curve fitting in nondimensionalized coordinates could be more useful.

Table 6.2. Parameters of the shape function (Equation 6.1) obtained for the digestion module when either the thin rollers or the thick rollers were used.

	Parameters from curve fitting in mm coordinates			
Roller type	a	b	c	R²
Thin	7.55 ± 0.35	63.93 ± 1.71	1296 ± 101	0.96 ± 0.01
Thick	8.75 ± 0.35	49.72 ± 5.77	1047 ± 218	0.95 ± 0.02
	Parameters from curve fitting in nondimensionalized coordinates: length unit set as the width of the undeformed digestion module			
Thin	0.29 ± 0.01	2.52 ± 0.06	1.63 ± 0.18	0.96 ± 0.02
Thick	0.33 ± 0.01	1.96 ± 0.23	1.37 ± 0.28	0.95 ± 0.02

6.3.2.3 Computational Fluid Dynamic Modeling

Fluid flow in the multiphysics CFD model representing one module in the peristaltic simulator was analyzed using its predicted velocity, shear, and vorticity fields. Results showed that fluid flow inside the module began as the roller engaged with the module, deforming its shape and causing a flow field to develop over time. The predicted flow field inside the module is shown in Figure 6.6. As the roller progressed downwards over the module, the initially quiescent fluid developed a flow field characterized by a region of greater velocity near the region of maximum occlusion.

In addition to visualizations of the flow field, the change in velocity over time for the module contacted by either the thin and thick rollers was quantified in terms of the volumetric average magnitude of velocity (Figure 6.10 A1), the average on the xy (horizontal) plane that passed through the center of the module (Figure 6.10 A2) and the volumetric maximum value (Figure 6.10 A3) which represented the maximum magnitude of velocity achieved anywhere on the computational domain as time elapsed. The volumetric average velocity was lower than the average velocity on the center plane, reflecting the presence of regions of mostly still fluid at the distal ends of the module, far away from the region of

occlusion where the velocity was higher. For the thick rollers, the maximum velocity at any point on the domain at any time was 0.0211 m/s, however, this value was maintained for less than 0.1 s with the average velocity values being much lower. For the thin rollers, the maximum velocity was 0.0160 m/s, representing 76% of the maximum value achieved with the thick rollers. Analysis showed that the fluid velocity increased rapidly as the rollers contacted with the module (ca. 0-2 s), achieved a local maximum as the rollers fully engaged with the module (ca. 2 s), then experienced a second local maximum as the rollers reached the bottom of the module and began to disengage (ca. 8 s). Using a CFD model and particle imaging velocimetry studies in a gastric flow simulator, Kozu et al. (2014) found a maximum fluid velocity of ca. 0.02 m/s, which is in good agreement with the results of the CFD model. In this previous study it was determined that the maximum velocity achieved by the fluid was weakly dependent on the fluid viscosity but strongly dependent on peristaltic wave velocity. Taken together with the results of the current study this suggests that both the velocity and occlusion of the applied peristaltic wave can influence the velocity of fluid contents in the gastrointestinal system.

Understanding the development of the velocity field inside the peristaltic simulator could help shed light on certain aspects of digestion that may be difficult to quantify *in vivo*. For example, the mechanisms leading to clinically-relevant phenomena such as gastric emulsion separation (Scheuble et al., 2018) could be studied inside the peristaltic simulator by relating them to the flow conditions that cannot be measured *in vivo*. Furthermore, using a multiphysics CFD model to predict the velocity field developed inside the peristaltic simulator could allow the experimental parameters of the simulator to be tuned to represent specific motility disorders of the gastrointestinal tract, leading to the potential to simulate the gastrointestinal motility of specific individuals, a long term goal in the field of personalized gastroenterology (Wang and Camilleri, 2019).

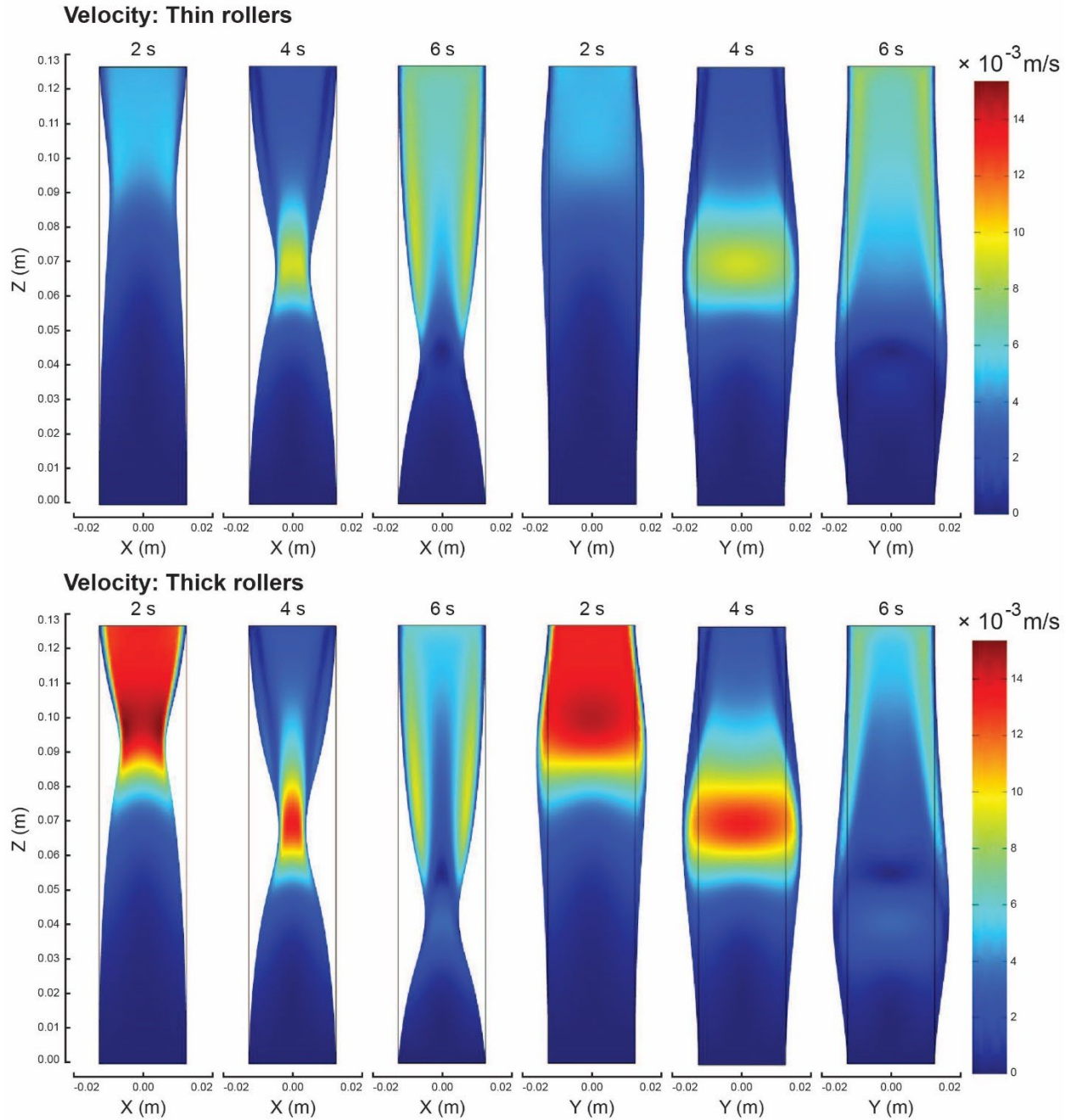


Figure 6.6. Predicted velocity field inside of the peristaltic simulator module using either the thin rollers or thick rollers. The module is shown at three different elapsed times after the start of the simulation (2 s, 4 s, and 6 s) in both the xz and yz plane cutting through the center of the module.

The fluid shear rate and magnitude of vorticity are shown in Figure 6.7 and Figure 6.8, respectively. As with velocity, shear and vorticity fields developed as the roller contacted the module. Shear and vorticity were greatest near the fluid-module wall interface in the region of greatest occlusion. Both variables reached their maximum values as the roller made full contact with the module, as depicted in Figure 6.10 B3 and Figure 6.10 D3. The maximum value of shear rate was 17.6 1/s for the thin rollers and 23.4 1/s for the thick rollers. The maximum values of vorticity were 18.7 1/s for the thin rollers and 24.7 1/s for the thick rollers. As with fluid velocity, the greater occlusion of the thick rollers led to higher values of fluid shear and vorticity. For a fluid with viscosity comparable to the 1.5 mg/mL mucin solution that was used for the simulation in this study, Kozu et al. (2014) obtained a maximum shear rate of 16 1/s. Previous researchers used a CFD model to analyze the flow fields developed in a model of the human stomach and reported a volumetric average shear rate of 0.45 1/s, for a low viscosity Newtonian fluid. Results from the current study showed the average shear rate across all timepoints to be 1.7 1/s for the thin rollers and 2.5 1/s for the thick rollers. The maximum vorticity value from the CFD model can be compared to the results of Ferrua et al. (2010), who found a maximum vorticity of 13 1/s using a CFD model with gastric geometry. Overall, estimates of fluid shear and vorticity in the CFD model of the peristaltic simulator are in the same range as those reported in the literature, although it should be noted that the objective of the CFD model developed in this study was to better understand the flow of fluid inside the peristaltic simulator which had a different geometry than those that were the subject of previous studies. Understanding the shear rate and vorticity experienced by digesta inside the human gastrointestinal system could help for better understanding of the mechanisms of food breakdown (Bornhorst et al., 2016b), mixing (Bornhorst, 2017), and nutrient absorption (Lim et al., 2015; Wang et al., 2010).

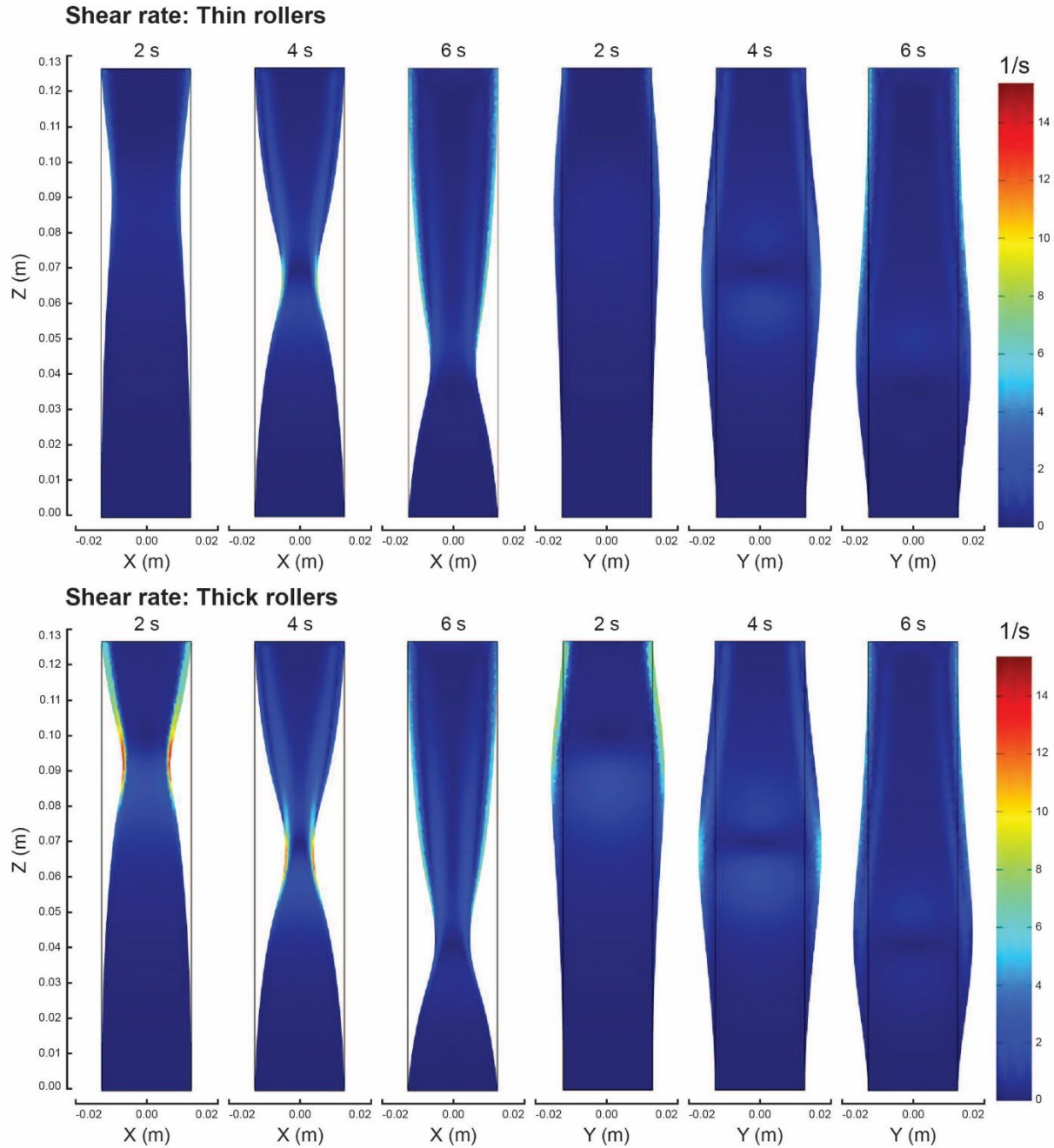


Figure 6.7. Predicted shear field inside of the peristaltic simulator module using either the thin rollers or thick rollers. The module is shown at three different elapsed times after the start of the simulation (2 s, 4 s, and 6 s) in both the xz and yz plane cutting through the center of the module.

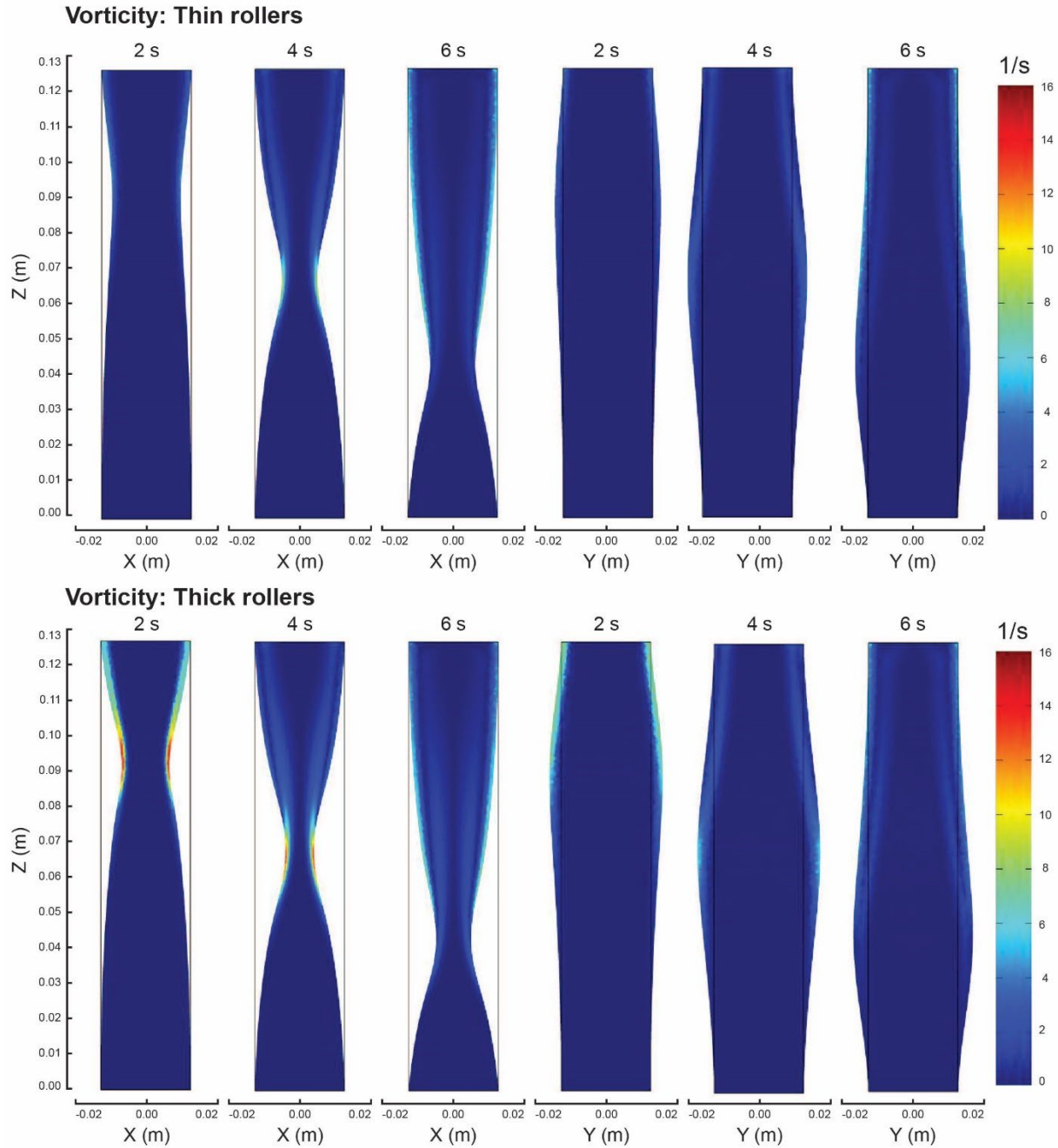


Figure 6.8. Predicted vorticity field inside of the peristaltic simulator module using either the thin rollers or thick rollers. The module is shown at three different elapsed times after the start of the simulation (2 s, 4 s, and 6 s) in both the xz and yz plane cutting through the center of the module.

The pressure field developed in the present study was dominated by the effect of hydrostatic pressure (Figure 6.9). This is due to the open boundary condition imposed on the top surface of the module, which

prevented the imposed peristaltic contraction from leading to a significantly higher pressure than would be expected from hydrostatic effects. This led to an unchanging average and maximum pressure inside the module (Figure 6.10 D1 and Figure 6.10 D3, respectively). The pressure exerted by rollers on a simulated food particle was examined using manometry (Section 3.2.1) which showed that the rollers can exert a physiologically relevant pressure when impinging on a simulated food bolus or particle of food.

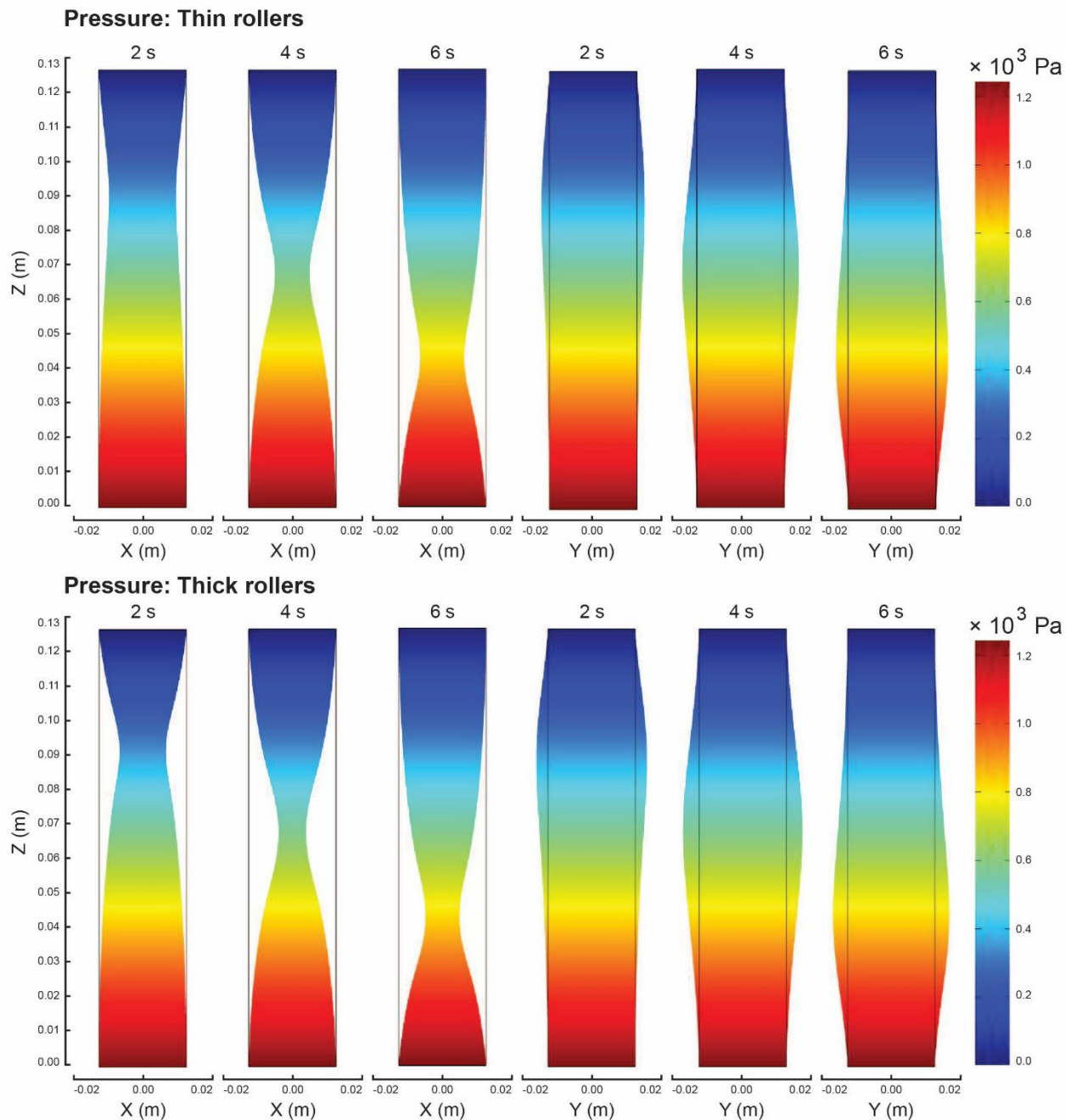


Figure 6.9. Predicted pressure field inside of the peristaltic simulator module using either the thin rollers or thick rollers. The module is shown at three different elapsed times after the start of the simulation (2 s, 4 s, and 6 s) in both the xz and yz plane cutting through the center of the module.

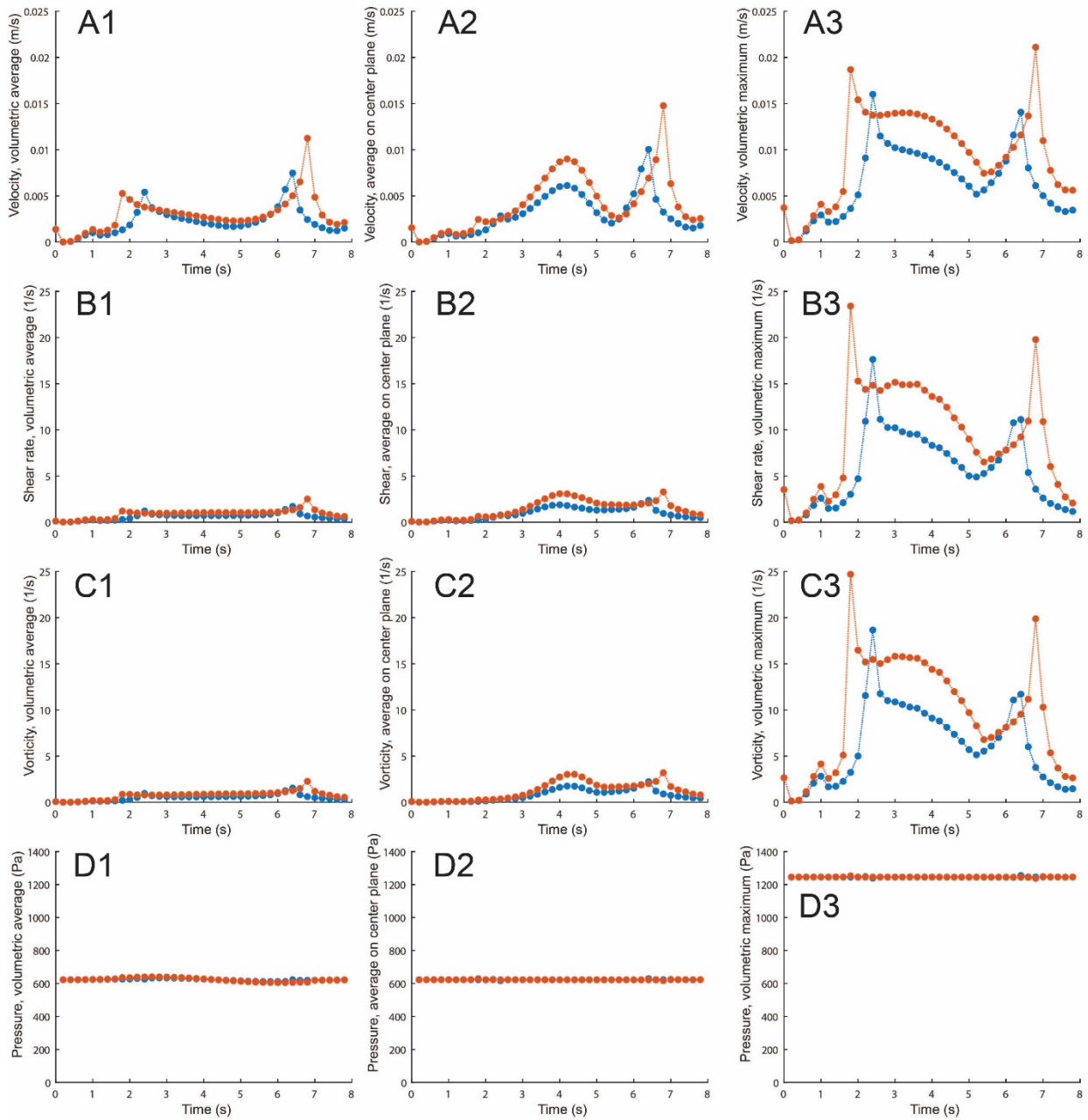


Figure 6.10. Predicted CFD variables for the module in the peristaltic simulator undergoing deformation by either the thick rollers (●) and thin rollers (●). Figures shown the volumetric average fluid velocity on the computational domain (A1), the average fluid velocity on the xy plane passing horizontally through the center of the module (A2), the volumetric maximum fluid velocity (global maximum on the computational domain, A3), the volumetric average shear rate (B1), the average shear rate on the xy plane passing horizontally through the center of the module (B2), the volumetric maximum shear rate (B3), the volumetric average vorticity magnitude rate (C1), the average vorticity magnitude on the xy plane passing horizontally through the center of the module (B2), the volumetric maximum vorticity magnitude (B3), the volumetric average fluid pressure (D1), the average fluid pressure on the xy plane passing horizontally through the center of the module (D2), the volumetric maximum fluid pressure (D3).

Correspondence between the predicted shape of the digestion model and the experimental results was quantitatively assessed by exporting the edge coordinates of the digestion module from COMSOL and then curve fitting them in MATLAB using Equation 6.1, based on the method described in Section 6.2.2.2. The shape of the simulator determined using video analysis can be visually compared to the shape of the module predicted by the CFD module in Figure 6.11 A, with a closer view of the occluded region in Figure 6.11 B. The “a” parameter of the simulated module contacted by the thick rollers was 0.33 ± 0.00 , which was not significantly different ($p > 0.05$) from the “a” parameter obtained using video analysis of the simulator with thick rollers (0.33 ± 0.01). For the simulation of the module contacted by the thin rollers, the “a” parameter was 0.28 ± 0.00 , which was not significantly different ($p > 0.05$) from the results of video analysis (0.29 ± 0.01). In a similar way, the “c” parameter of the simulated module was never significantly different from the “c” parameter from the corresponding roller type measured experimentally. The “b” parameter of the Gaussian function represents the vertical location of the occluded point and thus depends only on the instantaneous position of the rollers with respect to their path along the module and cannot be used to compare the shape of the simulator measured using video analysis with the shape developed by the CFD module.

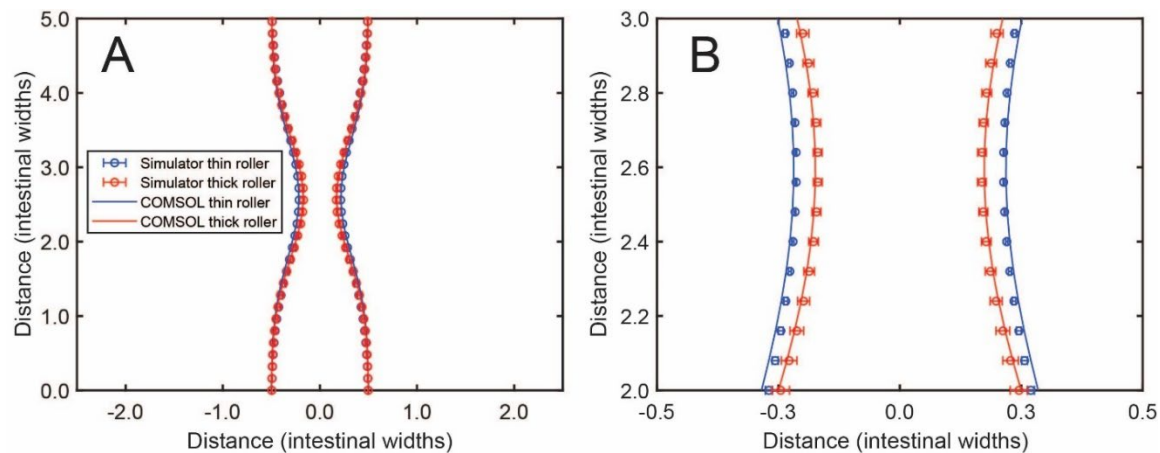


Figure 6.11. Correspondence between the shape of the peristaltic simulator module with either the thin or thick rollers as measured using video analysis with the predicted shape of the module based on the results of the CFD model (A) with a closer view of the occluded region (B).

6.3.2.4 Comparison of the motion of the simulator to the motility of *ex vivo* porcine tissue

Curve fitting was used to compare the shape of an *ex vivo* porcine intestine as it underwent peristalsis to the shape of the digestion module in the peristaltic simulator. One example image from video analysis of the porcine intestine along with the fit to Equation 6.1 is shown in Figure 6.12 A. Four images were used to generate an average shape function for the porcine intestine and each view along with the parameters of the corresponding fit to Equation 6.1 are given in Table 3. The comparison of the shape function from the porcine intestine to the peristaltic simulator is shown in Figure 6.12 B.

The maximum occlusion of the intestine was $27.3 \pm 3.5 \%$, which was significantly lower than the occlusion for the simulator with thin rollers ($72.1 \pm 0.4 \%$) or thick rollers ($84.6 \pm 1.2 \%$), $p < 0.05$ (Figure 6.12 B). The Gaussian function (Equation 6.1) provided a satisfactory fit to the boundaries of the intestinal tissue, with a minimum R^2 value of 0.92. The average value of the “a” parameter was 0.13 ± 0.02 for the intestinal tissue, which was significantly lower than the value for the simulator with thin rollers (0.29 ± 0.01) or with thick rollers (0.33 ± 0.01), $p < 0.05$. This is the amplitude parameter of the Gaussian function, and its lower value for the intestinal tissue reflects how the peristaltic contraction of

the tissue led to a lower degree of occlusion compared to the simulator. The “b” parameter for the intestinal tissue was 0.80 ± 0.22 , which was significantly lower than its value from the simulator with either thin rollers (2.52 ± 0.06) or thick rollers (1.96 ± 0.23), $p < 0.05$. This represents the location of the point of maximum occlusion along the long axis of the section of intestine that was studied, but its value depends only on the location of the region of interest inside the reference frame and thus is not indicative of any differences between the simulator and the intestinal tissue. The “c” parameter for the intestinal tissue was 0.18 ± 0.08 , which was significantly lower than its value for the simulator when thin rollers (1.63 ± 0.18) or thick rollers (1.37 ± 0.28) were used, $p < 0.05$. This is the variance parameter of the Gaussian function and is indicative of the spread of the peristaltic contraction in the direction parallel to the long axis of the intestinal tissue. Overall, the differences between the intestinal tissue and simulator reflect the presence of a more compact peristaltic wave with lower occlusion in the intestinal tissue as compared to a more elongated shape but with greater occlusion generated in the simulator.

It should be noted that gastrointestinal motility patterns are complex, and can be affected by age (Firth and Prather, 2002), body mass index (Miron and Dumitrascu, 2019), sex (Sadik et al., 2003), disease status (Coleski et al., 2015), and prandial state (Khalaf et al., 2018). The results of this analysis cannot capture the biological variability and future research is needed to better quantify the dynamics of gastrointestinal motility that could then be translated to in vitro devices. In addition, the images used for analysis of the intestinal tissue were *ex vivo* samples that may not be fully representative of in vivo conditions, but allow for a preliminary analysis of motion to compare with the in vitro device.

Although previous in vitro devices have been developed that incorporate simulated peristalsis (Bellmann et al., 2016; W. Liu et al., 2019; Ranganathan et al., 2021; Vardakou et al., 2011), comparison of their motion to that of the gastrointestinal tract in vivo has not been widely conducted. This could nevertheless represent an important step in the development of in vitro devices that can accurately assess particle breakdown. The lack of comparisons between the motility of in vitro and in vivo systems could be due to a lack of in vivo data for use in such comparisons, as well as a lack of standard methods for carrying out quantitative analysis of motility in an in vitro device that can be compared to an in vivo

system. The Gaussian function used in this study (Equation 6.1) was able to describe the shape of the peristaltic simulator module (minimum $R^2 = 0.93$) as well as the shape of the intestinal tissue (minimum $R^2 = 0.92$) during contractions. This suggests that future studies could use this approach to characterize the motility of in vitro devices incorporating peristalsis and then compare them to in vivo systems. Such research could lead to the development of an international standard method for representing the peristaltic conditions in the digestion system, which would complement a recently developed standard protocol for static in vitro digestions (Minekus et al., 2014), as well as a system for assessing the breakdown of solid foods (Bornhorst et al., 2015; Swackhamer et al., 2022).

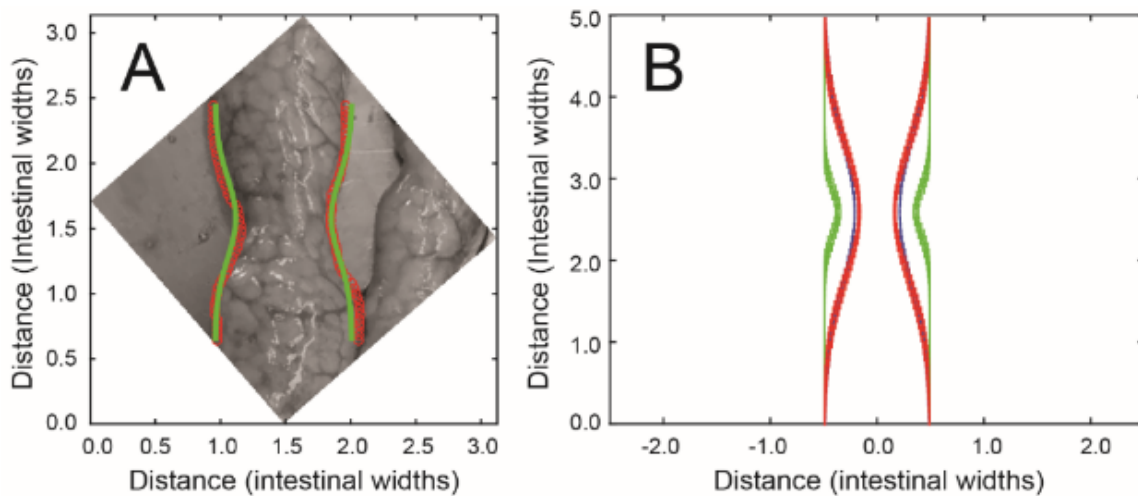
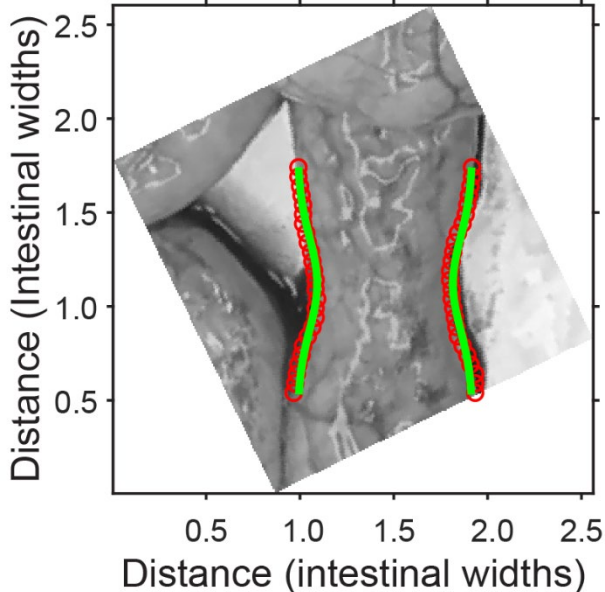
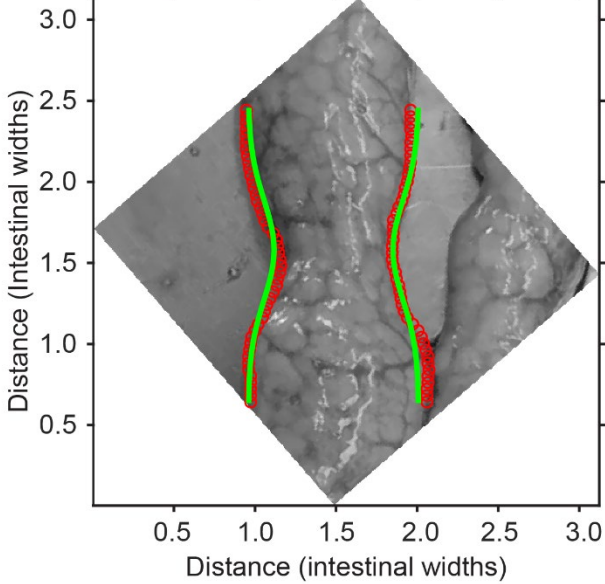
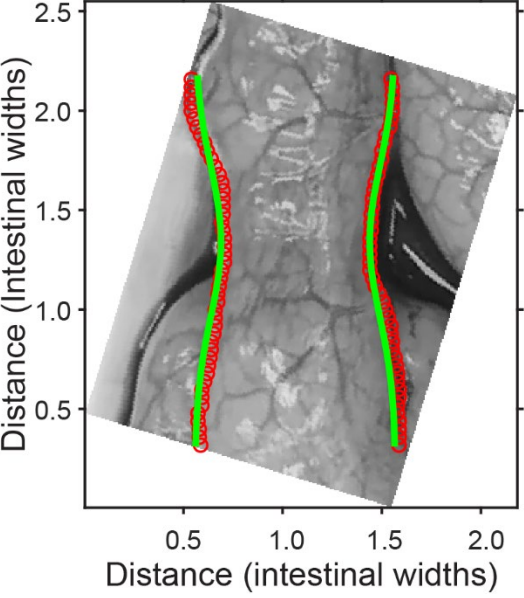


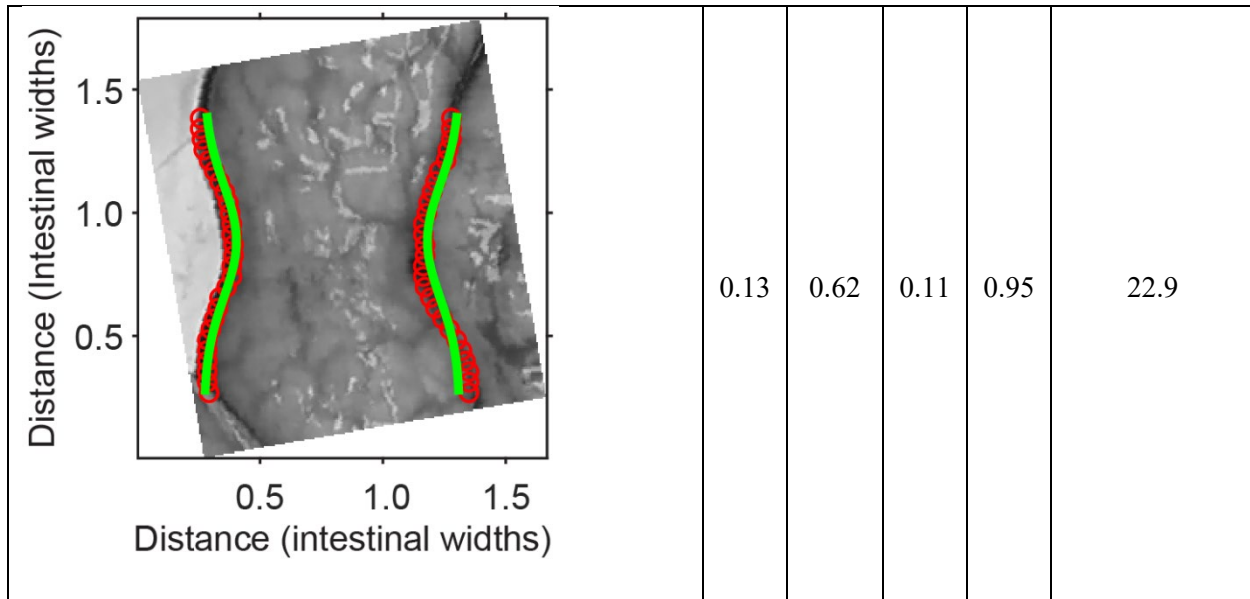
Figure 6.12. Preliminary analysis of the shape of an *ex vivo* porcine intestine (A) and comparison to the peristaltic simulator using either thin or thick rollers (B). One individual image of the porcine intestinal tissue used for curve fitting, with points defining the edge of the intestine shown as red circles and the curve fit shown as green lines (A). The shape function of the digestion module in the peristaltic simulator was shown alongside the shape function from the porcine intestine on the entire region of the contraction (B). The red line represents the shape of the peristaltic simulator with thick rollers, the blue line represents the simulator with thin rollers, and the green line represents the average shape function from curve fitting four images of *ex vivo* intestinal tissue (Table 3). For the peristaltic simulator, error bars

represent the standard deviation from three independent curve fits (Section 2.2.2), and for the intestinal tissue error bars represent the standard deviation from the curve fits generated using four images that were examined (Table 3). Error bars may be too small to be visible.

Table 6.3. Parameters from curve fitting the Gaussian (Equation 6.1) to images of ex vivo porcine intestinal tissue undergoing post mortem motility.

Image of ex vivo porcine intestinal tissue and curve fit using Equation 6.1	Parameters from curve fitting in nondimensionalized coordinates: length unit set as the width of the undeformed digestion module				
	a	b	c	R ²	Maximum percent occlusion (%)
	0.10	0.59	0.12	0.98	28.3

	0.16	0.94	0.19	0.92	31.3
	0.13	1.03	0.29	0.94	26.7



6.4 Limitations

Limitations of this study can be categorized as those pertaining to the analysis techniques carried out on the simulator that was designed and constructed, as well as those pertaining to the device itself. Video analysis was used to characterize the shape of the digestion modules during simulated peristalsis but required the intermediate steps of processing videos on a desktop computer. Future research could consider developing a continuous video analysis system with a human machine interface, allowing for experimental parameters such as roller width or spacing to be quickly related to the shape function describing the digestion modules using real-time video analysis and curve fitting. The CFD model created to predict fluid flow was partially validated by comparing the predicted shape of the digestion module to experimental data, however, follow-up experiments using particle imaging velocimetry to characterize the fluid flow inside the simulator would be necessary to further validate the model. Another limitation of the analysis methods used in this study is that the rheology of digesta was not altered to determine the influence of digesta rheology on the dynamics of the simulated peristaltic wave or the resulting fluid flow field inside the digestion modules. This could be a topic for future research and could be used to determine whether shear stresses exerted from a flowing fluid onto a food particle can contribute to surface erosion of the particle. Limitations of the peristaltic simulator itself include the use of rollers to

simulate the peristaltic contractions of the human digestion system instead of a true peristalsis which would require radial squeezing of the module from all sides to cause occlusion. Another limitation of the device is the lack of online data collection systems, such as built-in turbidity, °Brix, or particle tracking systems. The peristaltic simulator does not include a system to simulate absorption of nutrients by diffusion or active transport through the gut wall. Implementation of a system to study absorption would allow for bioavailability to be predicted through in vitro experiments, which could be useful for development of functional foods, for instance foods with slow starch hydrolysis and absorption for individuals with diabetes. Although the peristaltic simulator can be outfitted with up to 12 digestion modules simultaneous, experiments involving 12 modules at a time were not run in this study, and future work would be needed to test the high-throughput capabilities of the device. The peristaltic simulator most closely resembles the geometry of the upper part of the human small intestine, however, it lacks the capability to simulate certain processes of intestinal digestion, including the transit of intestinal contents, due to the closed nature of the system, and the absorption of nutrients, due to the impermeable material of the digestion module wall. These limitations could be addressed by future engineers through incorporation of a mechanism to empty contents from the bottom of one module and pass them to another, allowing for 12 modules to be potentially linked together in series, allowing for the simulation of digesta transit through a longer portion of the intestine. Semi-permeable wall materials could be used to simulate the absorption of nutrients. A potential way to implement this would be to immerse the digestion modules in a bath of physiological fluid from which samples could be taken to estimate the absorption of nutrients from the intestinal lumen, in this case represented by the interior of the digestion modules in the system.

6.5 Conclusions

A novel, multi-module peristaltic simulator was designed and constructed that can apply simulated peristaltic contractions to as many as 12 flexible plastic modules simultaneously. Using rollers of varying diameter, the degree of occlusion applied to the digestion modules can be adjusted, allowing the simulator to flexibly recreate different types of peristaltic motion that may occur in the human gastrointestinal

system. Video analysis was conducted by installing a high-definition endoscopic video camera inside the simulator. Results showed that the shape of the digestion module was well-characterized by a Gaussian distribution function ($R^2 > 0.95$), and that occlusion of the module could be changed from $72.1 \pm 0.4\%$ when the simulator was outfitted with thin rollers (12.6 mm diameter) to $84.6 \pm 1.2\%$ ($p < 0.05$) when the simulator was outfitted with thick rollers (17.4 mm diameter). Manometry was used to determine the approximate force values that could be applied by the simulator to a food particle or bolus (2.61 ± 0.03 N and 4.51 ± 0.16 N for the thin and thick rollers, respectively, $p < 0.05$). Results from video analysis and manometry were found to be in good agreement with the available in vivo data on the degree of occlusion of the human intestine and the estimated forces that can be applied to a bolus in the gastrointestinal system. A multiphysics, Computational Fluid Dynamics (CFD) model was created to help develop an understanding of the fluid flow patterns inside the digestion modules, and allow future workers to predict the impact of modifications to the device in terms of the impact on fluid flow. Results from CFD model showed that the maximum fluid velocity in the module under deformation by the thin and thick rollers was 0.016 m/s and 0.0211 m/s, respectively. Velocity, shear rate, and vorticity values predicted by the CFD model were found to be in good agreement with those reported by previous researchers. Future research on this device could explore the relationships between gastric motility patterns and the mechanics of food breakdown, for example by determining the impact of occlusion on the rates of particle breakdown of solid foods. The peristaltic simulator described in this work represents a new, high throughput approach to in vitro digestion experiments that could allow for the physical processes of digestion to be understood in more detail, and could have applications in the food industry by allowing for rapid screening of food materials for health-promoting properties.

Chapter 7 Fracture and rheological properties of standardized, model solid foods influence their physical breakdown mechanisms during in vitro gastric digestion with simulated peristalsis

Rationale

The rationale for this chapter was to further characterize the physical property changes of model, solid foods developed in Chapter 5, and then to assess the breakdown of the solid foods during in vitro digestion that included simulated peristalsis. The research in this chapter thus addresses research objectives 2 and 4 as stated in Chapter 1 (Introduction). In Chapter 4, it was determined that size reduction of almond particles during in vitro gastric digestion occurred only in the presence of simulated peristaltic contractions. However, relating the physical properties of solid foods to their breakdown during in vitro digestion with simulated peristalsis was not feasible with almond particles due to their anisotropic microstructure and heterogeneous particle size distribution. This pointed to the need for development of model foods, and then characterization of the changes in textural, fracture, and rheological properties of the model foods during in vitro gastric digestion. In Chapter 5 the hardness, elastic modulus, fracture stress and fracture strain of model foods were assessed after varying durations of in vitro gastric digestion in the absence of simulated peristalsis so that a consistent particle geometry could be maintained. In this study additional physical properties of them model foods including storage modulus (G'), loss modulus (G''), and fracture properties such as toughness and yield stress were quantified at varying timepoints during in vitro digestion in the absence of simulated peristalsis. Then, the model foods were subjected to in vitro gastric digestion for the same timepoints at which their properties had been previously assessed, after which the particles were subjected to in vitro gastric digestion that included simulated peristalsis. This was carried out so that their properties could be linked to their hypothesized breakdown mechanisms during in vitro digestion. The peristaltic simulator developed in Chapter 6 was used in these experiments so that the effect of simulated peristalsis could be isolated without the potential contribution of particle-particle grinding to breakdown.

Abstract

The physical breakdown of solid foods in the stomach is an important aspect of the overall digestion process. However, the mechanisms of breakdown of solid foods in the stomach are not fully understood. In this study, four standardized model solid foods with varying gastric softening kinetics were subjected to static in vitro digestion followed by digestion using either the Human Gastric Simulator (HGS) or a peristaltic simulator to understand their breakdown behavior during simulated peristalsis. The HGS is a dynamic in vitro model of the human stomach that applies simulated peristaltic contractions to multiple food particles contained inside the gastric chamber, and thus includes the potential for particle breakdown due to particle-wall contact as well as particle-particle interactions. The peristaltic simulator applies simulated peristaltic contractions to an individual food particle, allowing the effect of peristalsis to be isolated. The fracture properties of model foods were assessed using wire cutting and knife cutting before digestion or after 30 or 180 min static in vitro gastric digestion. Toughness, yield stress, and stiffness were significantly influenced by digestion time ($p < 0.01$) and the type of model food ($p < 0.01$). Rheological properties of model foods were assessed at the same in vitro gastric digestion time points using parallel plate oscillatory rheology. Storage modulus, loss modulus, and $\tan \delta$ evaluated at 1 Hz ($G' | 1 \text{ Hz}$, $G'' | 1 \text{ Hz}$, and $\tan \delta | 1 \text{ Hz}$, respectively) were significantly influenced by digestion time ($p < 0.01$). Results from experiments in the HGS showed that the model foods experienced physical breakdown dominated by different hypothesized mechanisms. For example, the standard diet strong gel broke down by erosion and chipping, whereas the standard diet weak gel broke down by erosion, chipping, and large-scale fragmentation. It was estimated that that food particles with hardness $< 6 \text{ N}$ may break down by erosion, chipping, and fragmentation but those with hardness $> 9 \text{ N}$ may break down initially by erosion but transition to breakdown by erosion and chipping at later digestion times as the particle softens. Results from experiments in the peristaltic simulator showed that the standard diet strong gel broke down initially by erosion and chipping but began to experience large-scale fragmentation after the application of ca. 30 peristaltic contractions, whereas the standard diet weak gel broke down by

fragmentation with the application of the first peristaltic contractions that were applied. These results suggest that the mechanisms which drive the physical breakdown of food particles in the stomach may change over time as the food matrix is weakened by acids and enzymes in gastric juice as well as the progressive application of peristaltic contractions, for example transitioning from only erosion to erosion, chipping, and fragmentation. It was hypothesized that this transition in breakdown mechanism was attributed to changes in the resistance of the food particle to breakage under large strain, as quantified by its hardness. Overall, results from this study quantified changes in fracture and rheological properties of standardized model solid foods during *in vitro* digestion and established hypothesized breakdown mechanisms for these model foods during *in vitro* digestion with simulated peristalsis. This information could be used by future researchers to develop functional foods with targeted breakdown rates during gastric digestion.

7.1 Introduction

Physical breakdown of solid food particles takes place in the oral cavity and stomach. The rate of food breakdown in the stomach can affect physiological processes such as gastric emptying (Le Feunteun et al., 2014), and satiety (L. Marciani et al., 2001a), yet the physical properties of solid foods that influence their breakdown in the gastric environment are not fully understood (Somaratne et al., 2020a).

The Food Breakdown Classification System (FBCS) was developed to quantify the breakdown of solid foods according to the kinetics of texture change during gastric digestion (Bornhorst et al., 2015). The relative change in hardness has been shown in previous studies to relate to the dry matter lost by solid food particles (Kong and Singh, 2008b), demonstrating its usefulness as a parameter for studying food breakdown. Using the FBCS, previous researchers found that carbohydrate-based foods with different structures were placed into distinct classes (Drechsler and Bornhorst, 2018). Furthermore, trends in softening half-times aligned with trends in glycemic index for similar foods, suggesting that the FBCS could allow future researchers to develop links between food breakdown and physiological response (Drechsler and Bornhorst, 2018).

Standardized model, solid foods have been developed that were categorized into distinct FBCS classes (Swackhamer et al., 2022). Two model foods were designed to have the same macronutrient composition as the Standard American Diet, with a strong gel version and a weak gel version created by modulating pH of the dispersion before it was thermally gelled. Two additional model foods were designed based on whey protein hydrogels to serve as a simpler model system, with a strong gel and a weak gel version created by addition of pectin. Using the FBCS, the whey protein strong gel was determined to be a class I food, indicating it had a slow softening rate (softening half time > 180 min) and high initial hardness (initial hardness > 20 N). The whey protein weak gel was placed in class II, as it had slow softening half time but low initial hardness (initial hardness < 20 N). The standard diet strong gel was a class IV model food due to its intermediate softening rate (softening half time between 60 min and 180 min) and low initial hardness. Lastly, the standard diet weak gel model food was placed in class VI due to its fast softening rate (softening half time < 60 min) and low initial hardness. It was proposed that these model foods could lead to increased understanding of the mechanisms leading to breakdown of solid foods during digestion by relating changes in texture properties such as hardness to changes in fracture and rheological properties as well as to the dynamics of particle size reduction using in vitro digestion systems that include simulated peristalsis.

Using the FBCS, texture change is assessed according to hardness, defined as the maximum force exerted by a food particle on a flat probe during uniaxial compression to 50% engineering strain. Advantages of hardness as a metric for food breakdown are that it can be easily measured for different types of solid foods and does not require specialized equipment. Although the relative change in hardness is an effective way to characterize the overall texture change of food particles during digestion, characterization of the changes in fracture and rheological properties of solid foods during gastric digestion could lead to a more detailed understanding of the mechanisms of food breakdown in the gastric environment, such as the relative contributions of fracture and erosion.

Fracture and erosion have been identified as mechanisms that contribute to breakdown of solid foods in the gastric environment, which can lead to modifications in release of nutrients (Grassby et al., 2014;

Somaratne et al., 2020d). Erosion in the context of food digestion has been defined as the wearing away of the outer surface of the food particle (Guo et al., 2014a), whereas fracture has been defined as the breakage of a solid particle due to an advancing crack (Swackhamer and Bornhorst, 2019). In a previous study, almond particles that were subjected to simulated peristaltic contractions during *in vitro* digestion broke down into smaller and more numerous particles over time, whereas particles that were digested using an *in vitro* system that lacked simulated peristalsis did not break down, which led to differences in the bioaccessibility of fatty acids (Swackhamer et al., 2019). These results suggest that breakdown of solid food particles is influenced by the application of physical stress by peristaltic waves. This agrees with research in the field of fracture mechanics, which states that fracture requires the conversion of mechanical energy stored in a solid material as it undergoes strain into surface energy as a crack elongates through the material (Luyten and Van Vliet, 2006; Williams and Patel, 2016). The resistance of a material to fracture can be quantified in terms of its toughness, which is defined as the force required for a crack to propagate a certain distance through a material, which is equivalent to the energy consumed in creation of a unit area of surface during fracture (Lucas et al., 2012). Materials with a greater toughness are more resistant to fracture. Toughness of foods has been quantified using methods such as knife cutting and wire cutting, however, changes in toughness of solid food during digestion have not yet been quantified.

In addition to properties that are relevant at high values of strain such as hardness and toughness, the rheological properties of foods measured using small-strain oscillatory testing have been shown to change as a result of the breakdown of solid foods during gastric digestion (Nadia et al., 2021b). However, the rheological property changes of solid foods that occur during gastric digestion are not fully understood. Quantifying the changes in fracture and rheological properties of solid foods during digestion could help shed light on their breakdown. For example, food particles with high toughness could conceivably resist fracture but might be susceptible to erosion of the outer surface layer due to softening brought on by the chemical effects of acids and enzymes in gastric juice.

Due to the changes in food physical properties that occur during *in vitro* digestion, the mechanisms that contribute to food breakdown may also vary with digestion time. To shed light on the relationships

between food physical properties and breakdown, previous researchers subjected cubical particles of egg white gels to a static in vitro digestion for varying lengths of time and assessed the changes in hardness demonstrated by the gels (Somaratne et al., 2020d). In the static in vitro digestion egg white gel particles were subjected to the biochemical conditions of gastric digestion consisting of the acids and enzymes in simulated gastric juice but without peristalsis so that consistent particle geometries could be maintained for texture analysis. In parallel experiments, the researchers subjected the gels to static in vitro digestion for the same time points, but afterwards placed the samples into a model of gastric digestion that included simulated peristalsis to assess particle breakdown and relate the breakdown to the changes in hardness that occurred during the static in vitro digestion. This method thus used a static in vitro gastric digestion as a pretreatment after which the breakdown of the foods was tested in a dynamic digestion system. However, the texture analysis of the foods did not include assessment of their fracture or rheological properties.

The first objective of this study was to elucidate the changes in fracture and rheological properties of previously developed model solid foods with varying properties (Swackhamer et al., 2022) during static in vitro gastric digestion. The second objective of the study was to quantify the breakdown of the model foods during in vitro digestion with simulated peristalsis. The HGS was used as a physiologically representative model, in which particle breakdown could occur by direct application of peristaltic contractions to particles but also due to particle-particle grinding inside the gastric chamber. The peristaltic simulator was used to understand the breakdown of the model foods due to the direct effect of peristalsis, as the peristaltic waves were applied to food particles held in isolation from other particles, eliminating the possibility of particle-particle grinding. It was hypothesized that the softening rate categorization of the FBCS would correspond with changes in the fracture properties of the foods during static in vitro digestion, for example, foods in the FBCS classes defined by slow softening rates (whey protein strong gel, whey protein weak gel) would have a slower decline in fracture properties such as toughness as compared to foods in fast softening classes (standard diet weak gel). It was hypothesized that the initial hardness categorization of the FBCS would be predictive of the breakdown mechanism

initially experienced by the foods, with those in classes defined by low initial hardness (standard diet weak gel, whey protein weak gel) breaking down by erosion and fragmentation with the application of the first simulated peristaltic contractions whereas foods in classes defined by high initial hardness (whey protein strong gel) would be too strong to be directly crushed by simulated peristaltic waves and thus would break down only by erosion. The model foods characterized in this study could have applications in future research as they have known rheological and fracture property data which could be correlated with particle size reduction, gastric emptying, satiety, or nutrient bioaccessibility, leading to an improved understanding of food breakdown in the upper gastrointestinal tract. This increased knowledge of the physical processes of gastric digestion could lead to design opportunities for functional foods with physiological benefits.

7.2 Materials and Methods

7.2.1 Materials

Corn starch (PURE-DENT B700) was kindly donated by Grain Processing Corporation (Muscatine, IA, USA). Sucrose (CAS 57-50-1) was purchased from Sigma-Aldrich (St. Louis, MO, USA). Soybean oil (CAS 8001-22-7) was purchased from Thermo Fisher (Waltham, MA, USA). Whey protein isolate (BiPRO 9500) was kindly donated by Agropur Ingredients (Eden Prairie, MN, USA). Pectin (1400, degree of esterification 69-77%) was kindly donated by TIC Gums (White Marsh, MD, USA). Sodium Chloride (CAS 7647-14-5) was purchased from Sigma-Aldrich.

Simulated saliva and simulated gastric juice were prepared based on the INFOGEST protocol (Minekus et al., 2014) with minor modifications. Briefly, Amano lipase A was used (3.3 mg/mL) as an analogue for human gastric lipase (Roman et al., 2012). Mucin was used (1.5 mg/mL) as it has been shown to affect the structure of gastric contents that contain lipid (Scheuble et al., 2018).

Chemicals used to prepare simulated saliva and simulated gastric juice are provided in Table 5.2. Distilled water was used for all experiments (MP-12A System, Corning Inc, Corning, NY, USA).

7.2.2 Overall experimental design

In this study the fracture and rheological property changes of four different model foods were assessed initially (0 min static in vitro digestion) as well as following 30 min or 180 min static in vitro digestion (Figure 7.1 A and B) in a shaking water bath, a system that did not include simulated peristaltic contractions. In parallel experiments, the model foods were subjected to either 0, 30, or 180 min static in vitro digestion after which they were separated from simulated digestive fluids and then subjected to in vitro gastric digestion in either the HGS (Figure 7.1 C) or peristaltic simulator (Figure 7.1 D), systems that included simulated peristaltic contractions. All experiments were conducted in triplicate.

7.2.3 Model food preparation

Model foods were prepared as described in Section 5.2.2. Briefly, components of model foods were added to a beaker, stirred without heating for 1 hour, homogenized for 3 min at 10,000 rpm (Ultra Turrax T18 digital with S18N-19G disperser, IKA Works, Wilmington, NC, USA), adjusted to the target pH (Table 5.1), and then poured into a silicone mold for thermal gelation at 90 °C for 1 h.

Model foods were cut into 1.3 cm cubes for fracture property analysis trials and for breakdown trials in the Human Gastric Simulator (HGS) and peristaltic simulator. Previous studies have found that the size and shape of food particles in the bolus are highly heterogeneous with median sizes of 3 mm (Jalabert-Malbos et al., 2007) and 4 mm (Guo et al., 2013) having been reported but with some particles in the distribution much larger than the median size. Furthermore, it has been shown that particle size distributions in the bolus vary between individual consumers (Ranawana et al., 2010). However, previous studies have recommended the use of cubical food particles of size 1.3 cm for the purpose of standardization, facilitating texture analysis experiments, and allowing for direct comparison of results gathered for different food products between studies (Bornhorst et al., 2015; Koza et al., 2018; Olenskyj et al., 2020; Somaratne et al., 2020d; Wang et al., 2021). The model foods were processed into cubes by first removing a block of model food from the silicone tray and then cutting into 1.3 cm cubes using the insert from a potato cutter. The whey protein strong gel presented too much resistance to cut using the

potato cutter and was instead cut using a knife. Teflon barstock with a 1.3 cm square profile was used as a guide to control cube size.

For rheological property analysis, model foods were cut into 25 mm diameter \times 4.5 mm height disks. This was carried out by removing a block of model food from the silicone tray, slicing a 4.5 mm slab using a cheese slicer, and then stamping out 25 mm disks with a metal punch. The whey protein strong gel could not be cut using the cheese slicer. For this model food, 30 mm cylinders were first punched from the large block of model food. The whey protein strong gel was then gently extruded from the inside of the 30 mm punch to a 4.5 mm thickness and was then cut by hand using a knife to create a 30 mm \times 4.5 mm disk. Finally, a 25 mm disk was stamped from the center of the 30 mm disk using a punch. Previous researchers have used samples with the same geometry for rheological analysis of food with similar texture (Faber et al., 2017a).

7.2.4 Rheological analysis of model food dispersions

Rheological analysis of the model foods in their dispersion form (before thermal gelation) was carried out using a using an MCR 302 stress-controlled rheometer (Anton-Paar, Graz, Austria) with a cup and bob geometry to generate a flow curve of the dispersions with shear rates that varied logarithmically between 0.001 and 100 (1/s). The test was conducted at 37 ± 0.1 °C and the top of the sample was covered in a thin layer of mineral oil to minimize evaporation. Three replicates of the test were conducted, using model food dispersions prepared in separate batches. Data were fit to the power law model (Steffe, 1996):

$$\tau = K \dot{\gamma}^n \quad 7.1$$

Where τ (Pa) is shear stress, K ($\text{Pa}\cdot\text{s}^n$) is the consistency coefficient, $\dot{\gamma}$ is the shear rate (1/s), and n (dimensionless) is the flow behavior index. Fitting was conducted with MATLAB R2020a (The Mathworks, Natick, MA, USA) using nonlinear least squares. The consistency coefficient, K , was restricted to positive values and the flow behavior index, n , was constrained to values between 0 and 1.

7.2.5 Confocal laser scanning microscopy (CLSM)

Model foods were prepared for CLSM by slicing to 150 μm thickness using a tissue slicer (OTS 4500, Electron Microscopy Sciences, Hatfield, PA, USA) and were then stained. The whey protein strong and weak gels were stained using a 10 $\mu\text{g}/\text{mL}$ fluorescein isothiocyanate (FITC) to visualize the whey protein network. Staining of the standard diet strong and weak gels was carried out using a method developed by previous researchers to visualize whey protein and starch that coexisted in a gel, with minor modifications (Lavoisier and Aguilera, 2019). Briefly, samples were stained using 10 $\mu\text{g}/\text{mL}$ FITC followed by 0.5 $\mu\text{g}/\text{mL}$ rhodamine B for simultaneous visualization of starch and whey protein, respectively. Although rhodamine B and FITC can both bind non-covalently with whey protein and starch, staining with a higher concentration of FITC than rhodamine B has been shown to lead to preferential binding of rhodamine B with the protein phase and FITC with the starch (Zheng et al., 2016). As a follow-up analysis, the standard diet strong and weak gel were stained using 0.5 $\mu\text{g}/\text{mL}$ rhodamine B followed by 2.5 $\mu\text{g}/\text{mL}$ BODIPY for simultaneous visualization of whey protein and soybean oil, respectively. In all cases, the sample and stain were incubated for 15 min at room temperature (23 $^{\circ}\text{C}$). Samples were observed using a microscope (Leica TCS SP8 STED 3X, Heidelberg, Germany) with a 40 \times /1.3 objective HC PL APO CS2 oil immersion lens. Samples that were stained using FITC or BODIPY were excited at 488 nm with observation between 500 and 558 nm. Rhodamine B-stained samples were excited at 546 nm and observed between 564 and 661 nm. Images (1024 \times 1024 pixels) were acquired using the Leica Application Suite X version 13 software. Scale bars were added using Fiji (Image J version 1.53c, National Institutes of Health, USA).

7.2.6 Static in vitro gastric digestion

Static in vitro digestion of model foods consisted of an oral phase and then a gastric phase. Model food samples were added to a bottle to which 0.2 mL preheated simulated saliva was added per g model food (Gavião et al., 2004). The bottle was transferred to a shaking water bath (TSSWB27, Thermo-Fisher, Waltham, MA, USA) which was maintained at 37 $^{\circ}\text{C}$ and 100 rpm for the 2 min oral phase, after which 6 mL preheated simulated gastric juice was added per g model food to begin the gastric phase (Drechsler

and Bornhorst, 2018). Simulated mastication was not applied to samples of model foods so that a consistent geometry could be maintained in order to allow for mechanical property measurements, as has been done in previous studies (Kozu et al., 2018; Olenskyj et al., 2020; Wang et al., 2021). There is variability in the time needed for oral processing of solid foods in vivo, with reports of 20 s for 1% (w/v) κ -carageenan/locus bean gum gels (Kohyama et al., 2015), 23 s for whey protein emulsion gels (Lin et al., 2021), and 30 s for gelatine gels (Hutchings et al., 2011), with significant inter individual variability (van der Bilt and Abbink, 2017). As samples in this study were not subjected to simulated mastication, the duration of the simulated oral phase was chosen to be 2 min to allow for simulated saliva to act on the samples as both enzymatic hydrolysis by salivary α -amylase and lubrication by salivary mucins have been shown to exert relevant effects on food samples (Bornhorst et al., 2014a; Vardhanabhuti et al., 2011), as has been recommended for studies that do not include a simulated mastication step (Minekus et al., 2014). During static in vitro digestion the pH was adjusted to 2 ± 0.1 after 5, 30, 60, and 120 min total digestion time. At either 30 min or 180 min samples were removed from the bottle by draining digestion fluids using a sieve (aperture size ca. 0.5 mm). The conditions of static in vitro digestion, including the temperature, ratios of simulated saliva and gastric juice per amount of model food sample, and pH adjustments, were carried out in the same way for samples that were used for fracture property analysis, rheological property analysis, or were subjected to dynamic in vitro digestion in the HGS or peristaltic simulator. The samples used for static in vitro digestion and the analyses that were carried out are shown in Figure 7.1.

For each replicate of fracture property analysis, 10 individual 13 mm cubes of model food were subjected to static in vitro digestion. After either 30 min or 180 min digestion, the cubes were analyzed using either wire cutting or knife cutting to determine changes in their fracture properties (Figure 7.1 A).

For each replicate of rheological property analysis, one 25 mm \times 4.5 mm disk of model food was subjected to static in vitro digestion. After either 30 min or 180 min digestion the disk was removed from the beaker and gently rested on a doubled over paper wipe (Kimwipe, Kimberly-Clark, Irving, TX, USA)

to remove remaining bulk digestive juices before assessment of rheological properties using parallel plate rheometry (Figure 7.1 B).

For each replicate of the trials in the HGS, 100 g of 13 mm cubes (approximately 45 cubes) were subjected to static in vitro digestion. After either 30 min or 180 min digestion, cubes were separated from the digestion fluids using a sieve and were then transferred to the HGS along with 100 mL freshly prepared simulated gastric juice (Figure 7.1 C). The operational parameters of the HGS are given in Section 7.2.9.

For each replicate of the trials in the peristaltic simulator, 5 individual 13 mm cubes were subjected to static in vitro digestion and after either 30 min or 180 min digestion they were separated from digestion fluids using a sieve. Cubes were then transferred to the peristaltic simulator along with freshly prepared simulated gastric juice (Figure 7.1 D). The operational parameters of the peristaltic simulator are given in Section 7.2.11.

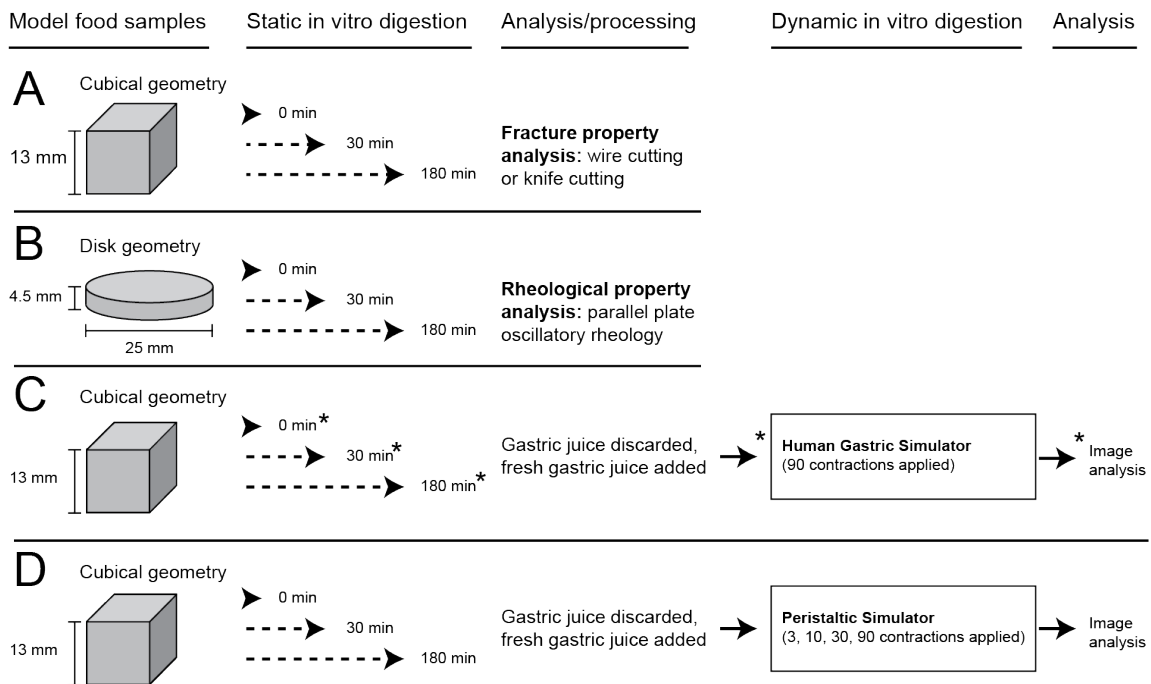


Figure 7.1. Sample geometries used for static in vitro digestion and flowchart showing how samples subjected to static in vitro digestion were then analyzed using fracture property testing (A), rheological

property testing (B), or were processed and then subjected to subsequent dynamic in vitro digestion in the HGS (C), or peristaltic simulator (D). The asterisk (*) in row C, corresponding to experiments carried out in the HGS, indicates when a sample was taken for analysis of protein hydrolysis, as described in Section 7.2.10.

7.2.7 Fracture property analysis

Fracture properties of the standard diet strong gel, standard diet weak gel, and whey protein weak gel were determined using wire cutting. Wire cutting was conducted on 1.3 cm cubes of model food in undigested form, as well as after being subjected to in vitro digestion for either 30 min or 180 min which was carried out as described in Section 7.2.6. For each replicate of each treatment, which consisted of a certain model food at a certain time point (0, 30, or 180 min digestion), 8 cubes of model food were cut by each of 5 total wires, with diameters of 0.11, 0.22, 0.33, 0.54, and 0.64 mm. These 40 tests yielded an estimate of the intrinsic toughness, R , and yield stress, σ_y . Three replicates were conducted. Each replicate was made on a new batch of model food. Model foods were cut using a custom-fabricated wire cutting attachment (Figure 7.2 A) driven by a TA-XT Plus texture analyzer (Texture Technologies, Hamilton, MA, USA) (Figure 7.2 B). Wires were generously donated by Ulbrich Stainless Steels and Special Metals, Inc (North Haven, CT, USA). The force vs displacement data were recorded by the texture analyzer resulting in a curve similar to the example curve shown in Figure 7.2 C. The test was conducted at 1 mm/s and data points were acquired at 500 Hz. The stoppage criterion was 99% strain. Data analysis was carried out using the method of Forte et al (2015). First, the average force during the region of steady crack elongation was determined using Equation 7.2.

$$F_{sce} = \frac{1}{(b - a)} \int_a^b F(x) dx \quad 7.2$$

Where F_{sce} (N) is the average force on the interval of steady crack elongation, a (mm) is the distance traveled by the wire at the start of steady crack elongation, b (mm) is the distance traveled at the end of the steady crack elongation period, and $F(x)$ (N) is the force recorded by the texture analyzer at each point

as the wire cut through the cube of model food. The integral in Equation 2 was approximated using the trapezoidal rule. Parameters of Equation 2 are shown visually in Figure 7.2 C.

It has been determined by previous researchers that the force of steady crack elongation during wire cutting is proportional to wire diameter, but also includes a contribution from the intrinsic toughness, R , as described in Equation 7.3 (Kamyab et al., 1998).

$$\frac{F_{sce}}{w} = R + (1 + \mu_k)\sigma_y\varphi \quad 7.3$$

Where F_{sce} (N) is the average force on the interval of steady crack elongation, w (0.013 m) is the width of the cube of model food that was cut by the wire, R (N/m) is the intrinsic toughness, μ_k (unitless) is the coefficient of kinetic friction between the model food and the wire, σ_y (Pa) is the yield stress of the model food, and φ (m) is the wire diameter. The wire was lubricated before each test using mineral oil (Bluewater Chemgroup, Fort Wayne, IN, USA) in order to ensure that $\mu_k \ll 1$, which allows the slope of the line to be considered approximately equal to the yield stress, σ_y (Forte et al., 2015; Goh et al., 2005). By measuring F_{sce}/w for each of the five different wires, extrapolation to a theoretical wire width of zero can be used to determine the intrinsic toughness of the model food, as shown in Figure 7.2 D (Gamonpilas et al., 2009; Kamyab et al., 1998; Wu et al., 2015). Toughness quantifies the energy needed to advance a crack through a solid material (Skamniotis et al., 2018; Swackhamer and Bornhorst, 2019).

Wire cutting has been used to measure the properties of soft food materials, including starch gels (Gamonpilas et al., 2009), gelatin gels (Czerner et al., 2016), and cheese (Vandenberghe et al., 2017). However, previous researchers have noted that strong foods can significantly deflect or even break the wire during experiments and thus must be tested using alternative methods such as knife cutting (Lucas et al., 2012). The whey protein strong gel was too strong to be cut using wires, and thus its fracture properties were estimated using knife cutting. Briefly, 1.3 cm cubes of the whey protein strong gel were placed onto the texture analyzer platform and cut using a micro carbide utility knife blade (0.6 mm thickness, Product number 2811503, Milwaukee Tool, Brookfield, WI, USA) that was driven by the texture analyzer and lubricated with mineral oil on both sides. The blade was advanced at 1 mm/s, data

points were acquired at 500 Hz, and the stoppage criterion was 99% strain. Each blade was used to cut 4 cubes and then replaced with a new blade to ensure that sharpness was maintained. The apparent toughness from knife cutting of the whey protein strong gel was estimated as the work of the entire curve divided by the surface area revealed by the cut, as given by Equation 7.4 (Anderson, 2009):

$$R_{app} = \frac{1}{wb} \int_0^b F(x) dx \quad 7.4$$

Where R_{app} (N/m) is the apparent toughness of the model food, w (0.013 m) is the width of the cube, and b (m) is the vertical distance traveled by the blade as the cube was cut. The integral in Equation 7.4 was approximated using the trapezoidal rule.

Stiffness (N/m) of the model foods was determined in cutting experiments as the slope of the linear region of the force vs. distance curves. For wire cutting, stiffness was defined using the largest wire (0.64 mm diameter) for comparability to the stiffness from knife cutting experiments (knife thickness = 0.6 mm).

The fracture initiation energy (N/m) of the model foods was determined as the maximum force, which occurred as the wire or knife penetrated the cube surface, divided by the width of the cube (0.013 m) (Duncan et al., 2020; Rattan and Crosby, 2019). As with stiffness, fracture initiation energy was calculated using the largest wire for the samples that were tested using wire cutting (standard diet strong and weak gels, whey protein weak gel) for comparability to the whey protein strong gel which was tested using knife cutting.

The elasto-fracture length of each model food was estimated as its toughness divided by Young's modulus (Rattan and Crosby, 2018). Intrinsic toughness was used for the model foods that were tested using wire cutting, and apparent toughness was used for the whey protein strong gel. Values of Young's modulus were obtained from a previous study (Swackhamer et al., 2022). The elasto-fracture length estimates the size of inherent defects in the model food matrix which were fractured by an advancing wire or knife blade, with small values of elasto-fracture length indicative of brittle behavior and larger values suggesting greater matrix plasticity (Creton and Ciccotti, 2016; Duncan et al., 2020).

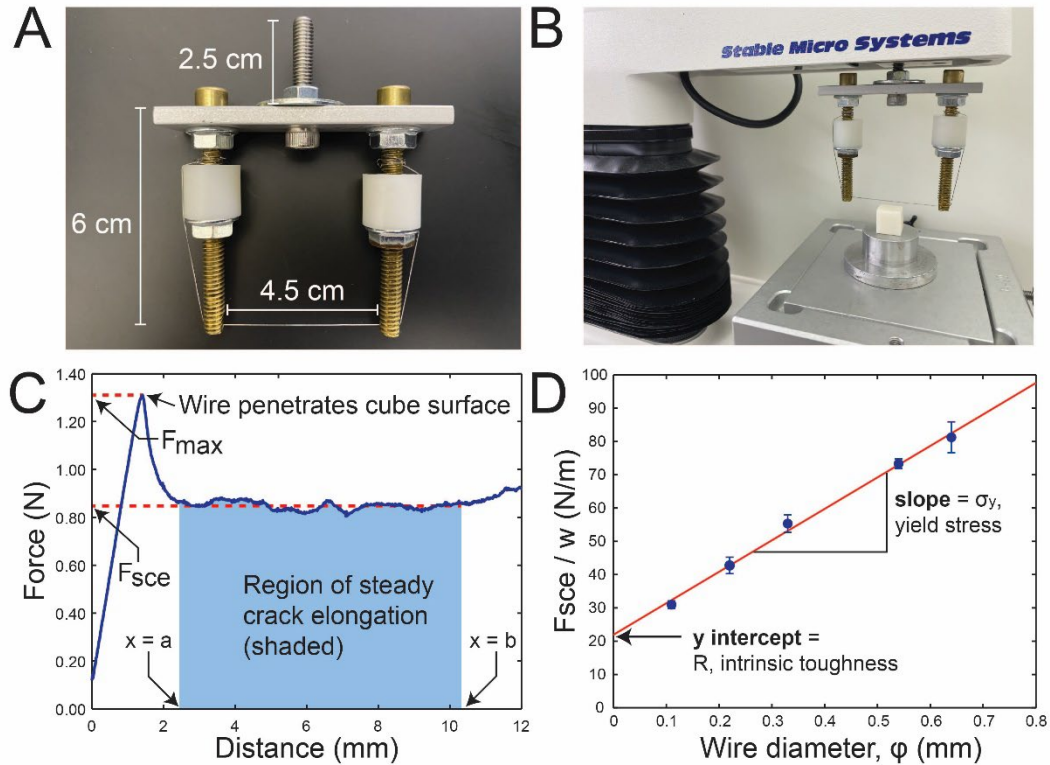


Figure 7.2. Texture analyzer attachment used to conduct wire cutting experiments (A). Wire cutting attachment in use with the texture analyzer (B). Typical curve of force versus distance obtained during wire cutting experiments, with labels showing the parameters of Equation 7.3 (C). Example plot showing regression and extrapolation to a theoretical wire width of zero as used to obtain the intrinsic toughness, R , and yield stress, σ_c (D). Parts C and D were adapted from Swackhamer et al (2019).

7.2.8 Rheological property analysis

Rheological property analysis of model foods was conducted using an MCR 302 stress-controlled rheometer (Anton-Paar, Graz, Austria) with a 25 mm parallel plate geometry. To prevent slip, a profiled upper and lower plate were used (Tsevdou et al., 2015). Rheological properties of the model foods were assessed after 0, 30 or 180 min static in vitro digestion. For each measurement, an individual disk of model food was placed onto the rheometer lower plate. The 25 mm diameter top plate was lowered until a 2 N normal force was achieved in order to achieve adequate contact with the model food (Faber et al., 2017b). Tests were conducted at 37 ± 0.1 °C with a solvent trap to minimize evaporation from the disk

during the test. In preliminary experiments, an amplitude sweep of 0.01-100% shear strain was carried out at 1 Hz to establish the limits of the linear viscoelastic region of the model foods (Wijaya et al., 2017; Young et al., 2020). A frequency sweep was then conducted within the linear viscoelastic range (at 0.1% strain) with frequency varying from 0.1-100 Hz. Storage modulus (G'), loss modulus (G''), and loss factor ($\tan \delta$) were measured as a function of frequency.

The frequency dependence of storage and loss moduli can provide information on gel structure (Ikeda and Foegeding, 1999; Lizarraga et al., 2006), and this was determined by fitting the empirical models given by Equations 7.5 and 7.6.

$$G' = A' \omega^{B'} \quad 7.5$$

$$G'' = A'' \omega^{B''} \quad 7.6$$

Where A' and A'' ($\text{Pa} \cdot \text{Hz}^{-n}$) are constants of proportionality, and B' and B'' (dimensionless) are the slope of a modulus vs frequency plot in log-log coordinates.

7.2.9 Assessment of mechanical breakdown in the Human Gastric Simulator (HGS)

The HGS is a dynamic in vitro digestion system that recreates the peristaltic contractions of the human stomach using mechanical rollers that pass over a flexible plastic liner containing the food and simulated digestion fluids (Keppler et al., 2020; Mennah-Govela et al., 2021). The mechanical motion of the HGS is shown in Figure 7.3 A. Cubes of model food were transferred to the HGS immediately after being subjected to static in vitro digestion for varying periods of time (0, 30, or 180 min, Section 7.2.6). Briefly, 100 g cubes were initially subjected to static in vitro digestion, after which they were separated from digestion fluids by sieving and were then added to the HGS along with 100 mL freshly prepared simulated gastric juice, prewarmed and adjusted to pH 1.8. The HGS was operated at 37 °C and with contractions applied at a rate of 3 per minute, as has been found to represent the frequency of peristaltic waves in the gastric environment in vivo (Gopirajah et al., 2016) After 90 contractions, the contents of the liner were emptied onto a sieve (aperture 250 μm , Retsch GmbH, Haan, Germany). During gastric digestion in vivo food particles may be stored in the proximal region of the stomach where peristaltic

contractions do not reach large values of occlusion but eventually food particles reach the antral region where occlusion from peristaltic waves is greater and particles may experience increased rates of breakdown (L. Marciani et al., 2001a; Pal et al., 2007b). In this study, particles of model food were subjected to static in vitro digestion in a shaking water bath as an analogous treatment to digestion in the proximal stomach where food particles are exposed to gastric juice but are not subjected to strong peristaltic contractions. Following static in vitro digestion for either 30 min or 180 min the particles were transferred to the HGS for a treatment consisting of exposure to simulated gastric juice as well as simulated peristaltic contractions, which represents the digestion of food in the distal stomach. Previous researchers found in an in vivo study using the growing pig as a model for the adult human that after 20 min digestion in the proximal stomach white rice and brown rice had similar particle size distributions, however, after 20 min digestion in the distal stomach white rice broke down into smaller particles than brown rice (Bornhorst et al., 2013c). Based on these in vivo results, an HGS treatment consisting of 90 simulated peristaltic contractions representing 30 minutes was selected, to ensure that differences in particle breakdown due to the application of simulated peristaltic contractions would be observed if they emerged on a physiologically relevant timescale. After being subjected to 90 simulated peristaltic contractions in the HGS and separation of the particles using sieving, the mass of the sieve plus wet particles of model food was recorded using an electronic balance. The particles of model food were then gently rinsed off the sieve using RO purified water and the mass of the empty sieve was recorded.

One particle was selected for moisture content analysis, which was carried out by cutting it in half and placing each half on a separate, pre-dried aluminum pan. Pans were dried in an oven (Lindberg Blue M, Thermo Scientific, Waltham, MA, USA) at 110 °C and 25 mm Hg until constant weight (approximately 16 h). This analysis was carried out to establish the total dry mass of particles remaining on the sieve.

The particles were then analyzed using image analysis according to a previously described method (Swackhamer et al., 2019). Briefly, particles were dispersed onto clear petri dishes with additional RO water applied as necessary to minimize particle overlap. Petri dishes were illuminated from beneath with

a lightbox (AGPtek HL0163, color temperature 6000°K), and a geometric reference object (ABFO no. 2 photomacrographic standard reference scale) was included in each image for spatial calibration. One image of each petri dish was captured using a Canon EOS Rebel SL1 digital camera (18-megapixel, APS-C CMOS sensor, Canon USA, San Jose, CA). To reduce disturbances to particles, image capture was triggered using a computer interface. Images were processed using MATLAB R2020a.

In preliminary trials, it was determined that the cumulative distribution function of particle sizes was bimodal. Specifically, there was a first mode represented by particles much smaller than the initial size of model food cubes, as well as a second mode represented by larger particles that consisted of relatively undamaged cubes of model food. To model this particle size distribution the cumulative area percentage of the particles was fit to the Mixed Weibull model (Equation 7.7) which has been used by previous researchers to analyze the breakdown mechanics during digestion of solid foods that exhibited similar behavior (Drechsler and Ferrua, 2016; Somaratne et al., 2020d).

$$C_{area}(x) = \alpha \left(1 - e^{-(x/x50_1)^{b_1}}\right) + (1 - \alpha) \left(1 - e^{-(x/x50_2)^{b_2}}\right) \quad 7.7$$

Where C_{area} (0% to 100%) is the cumulative area percentage achieved by the distribution at a particle of size x (mm^2), α (dimensionless) is the weight parameter that determines the proportion of total area belonging to the first mode (small particles), $x50_1$ and $x50_2$ (mm^2) are parameters determining the scale of the first and second mode, respectively, and b_1 and b_2 (dimensionless) are the parameters determining the shape of the first and second mode, respectively. After expressing the particle size data as a cumulative size distribution, nearest neighbor interpolation was used to obtain pairs of values (x, C_{area}) at 1000 evenly spaced points between the minimum and the maximum measured particle sizes. The purpose of this step was to ensure that the fitting procedure accurately reflected the shape of the cumulative distribution function of particle areas without being biased by the presence of a much greater number of small particles than large particles. To ensure that the first mode was associated with the smaller particles in the sample, a constraint was imposed (Equation 7.8) to ensure the mean value of the first mode was smaller than that of the second (Drechsler and Ferrua, 2016).

$$x50_1 \times \Gamma(1 + 1/b_1) < x50_2 \times \Gamma(1 + 1/b_2) \quad 7.8$$

Where Γ is the gamma function. Data were fit to Equation 7.7 under the constraint in Equation 7.8 using MATLAB R2020a with the function *fmincon*. The objective function was minimization of the sum of squared deviations between the data and model.

7.2.10 Assessment of free amino group concentration

The *o*-phthalaldehyde assay (OPA) was used to assess the concentration of free amino groups in liquid digesta from experiments in the HGS as a measure of the protein hydrolysis. For the treatments that consisted of model foods that were subjected to 0 min static in vitro digestion, samples for protein hydrolysis analysis were taken by withdrawing three 1.5 mL aliquots of liquid digesta immediately after adding cubes of model food and simulated gastric juice to the HGS, and again after application of 90 simulated peristaltic contractions. For the treatments that consisted of model foods subjected to 30 min or 180 min static in vitro digestion, three 1.5 mL aliquots of liquid digesta were taken for OPA analysis after the conclusion of the static in vitro digestion. Three additional 1.5 mL aliquots were taken immediately after transferring the cubes of model food to the HGS and adding fresh simulated gastric fluid as shown in Figure 7.1 C, to capture the contribution of free amino groups in the small quantity of liquid digesta that adhered to cubes of model food after decanting simulated digestion fluids used in the static in vitro digestion. Finally, three 1.5 aliquots were taken after the application of 90 simulated peristaltic contractions using the HGS.

The concentration of free amino groups in samples of liquid digesta was carried out using a previously reported method (Rios-Villa et al., 2020) with glycine as a standard. For all samples, the concentration of free amino groups of simulated gastric juice was subtracted from the values in liquid digesta so that the reported concentration of free amino groups reflected hydrolysis of the model foods by pepsin.

For the treatments that consisted of model foods subjected to 30 min or 180 min static in vitro digestion, the concentration of free amino groups at the end of the static in vitro digestion was determined

by adding the concentration of free amino groups in samples taken from liquid digesta used in the static in vitro digestion to the concentration in samples taken after decanting the liquid digesta and adding fresh simulated gastric juice.

Two outcome variables were defined based on OPA analysis: the total concentration of free amino groups during the experiment (total $[\text{NH}_2]$), and the increase that occurred in the HGS ($\Delta [\text{NH}_2]$ in the HGS). Total $[\text{NH}_2]$ was determined by adding the concentration of free amino groups in samples after static in vitro digestion (0 min, 30 min, or 180 min) to the value from the corresponding treatment after 90 contractions in the HGS. The increase in the concentration of free amino groups that occurred in the HGS ($\Delta [\text{NH}_2]$ in the HGS) was determined by subtracting the concentration of free amino groups in samples after static in vitro digestion from the value in the corresponding sample after 90 contractions in the HGS.

7.2.11 Assessment of mechanical breakdown in the peristaltic simulator

The peristaltic simulator is a device that allows a single cubical particle of food to be subjected to controlled, simulated peristaltic contractions without being contacted by other particles. The device uses roller bars to apply the simulated peristaltic contraction to food and digestion fluids contained inside of a flexible plastic module (low-density polyethylene, 0.1 mm wall thickness, 25.4 mm diameter, 229 mm length). The rollers start at the top of the module and progress downwards until the contraction has been completed, at which time they return to the top of the device to apply the next contraction (18 s cycle time). The mechanical motion of the HGS is shown in Figure 7.3 B. The contraction applied by the peristaltic simulator has been previously characterized using manometry and video analysis (Chapter 6). This mechanism of operation differs from the HGS, which contained ca. 45 cubical food particles in its plastic liner leading to the possibility of particle/particle interactions as well as particle/liner interactions during simulated peristalsis. The peristaltic simulator was used in this study to understand the breakdown of individual cubical particles of model food due to direct application of a simulated peristaltic contraction, without contact from other particles.

After being subjected to static in vitro digestion for either 0, 30, or 180 min, cubes of model food were gently threaded with a needle and then placed on a holding rig consisting of a piece of monofilament fishing line, with a metal bead beneath the particle to constrain its vertical position as well as a metal bead above the particle to stabilize it. The particle was then placed inside a module containing freshly prepared, prewarmed simulated gastric juice (37°C) and was loaded in the peristaltic simulator. After three contractions, the bottom of the module was sealed off using a heat sealer (Tabletop Impulse Sealer, ULINE, Pleasant Drive, WI, USA), trapping any small particles that broke off the cube during the first three simulated peristaltic contractions. This process was repeated after 10 and 30 contractions. After 90 contractions had been applied, any piece of the cube of model food that remained on the holding rig was collected. Image analysis was used to determine the particle size distribution of the particles of model food that were collected in each interval. Using this method, the sizes and numbers of particles that broke off between 1-3, 4-10, 11-30, and 31-90 contractions were assessed, as well as the size of any remainder of the cube of model food present on the holder rig after 90 contractions were completed. Analysis of the particle sizes was carried out using image analysis with the same method used for particles from the HGS (Section 2.7). Additionally, the progressive breakdown of the particle placed on the holding rig after different numbers of simulated peristaltic contractions were applied was determined. This was done by expressing the estimated volume of particles that broke off the main particle after predetermined numbers of contractions were applied (3, 10, 30, 90 contractions), as a percentage of the total volume of all particles that were imaged at any number of contractions, assuming the particles were spherical:

$$PV_c = 100\% - \frac{\sum_{i=1}^c \sum_{j=1}^{Np} \left(\frac{4}{3\sqrt{\pi}} A_{ij}^{3/2} \right)}{\sum_{i=1}^{Nc} \sum_{j=1}^{Np} \left(\frac{4}{3\sqrt{\pi}} A_{ij}^{3/2} \right)} * 100\% \quad 7.9$$

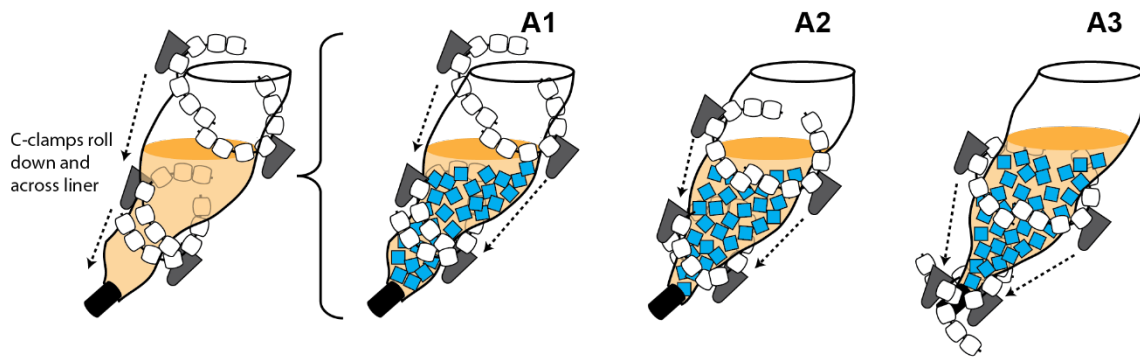
Where PV_c (%) is the percentage of total particle volume remaining on the holding rig after the application of c simulated peristaltic contractions, Nc is the maximum number of peristaltic contractions applied (90), A_{ij} (mm^2) is the area of the j th particle that broke off after i contractions, and Np is the total number of particles that were imaged after a given number of contractions were applied. It was assumed

that particles were spherical to convert the two-dimensional area of each particle to obtain an estimate of its volume. The quantity $\sum_{i=1}^{Nc} \sum_{j=1}^{Np} \left(\frac{4}{3\sqrt{\pi}} A_{ij}^{3/2} \right)$ has units mm^3 and simply indicates the total estimated volume of all particles that were imaged across all contractions. If there was nothing remaining on the holding rig after the application of 90 simulated peristaltic contractions (indicating that the particle was completely removed), then the final *PVc* value (PV_{90}) was zero. This analysis was conducted as a simple method to compare the breakdown of different model foods due to simulated peristaltic contractions applied one at a time to individual food particles.

A. Human gastric simulator

Contraction mechanism:
Rolling C-clamps on J-shaped liner

Contraction sequence:
Applied to ca. 45 cubes in the liner



B. Peristaltic simulator

Contraction mechanism:
Rollers on vertical cylindrical module

Contraction sequence:
Applied to one cube at a time in the module

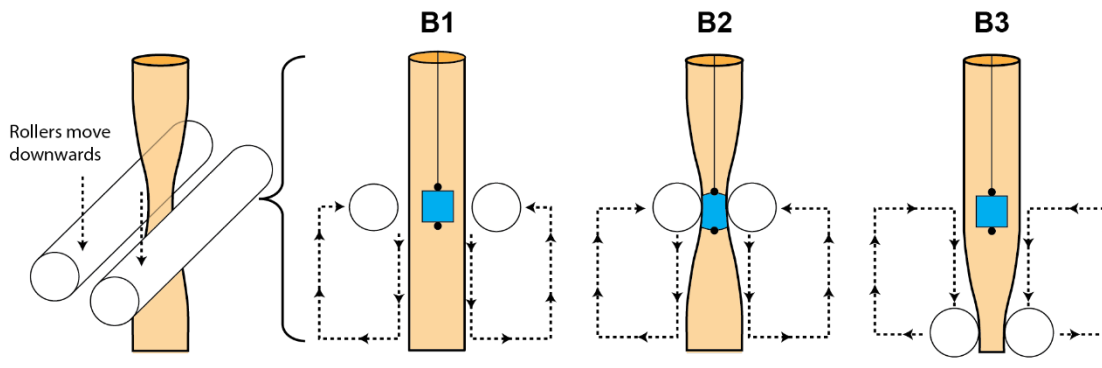


Figure 7.3. Overview of the mechanisms of simulated peristalsis applied to cubes of model food in the HGS (A) and peristaltic simulator (B). In the HGS, simulated peristaltic contractions were applied by

external rollers that progressed along the side of the stomach liner from an initial contact point (A1) to the middle of the liner (A2) and ultimately releasing at the bottom of the liner (A3) after which they began to cycle back to the start position on a chain drive. Simulated peristaltic contractions in the HGS were applied to ca. 45 cubical particles of model food, leading to the possibility for particle breakdown due to particle-particle grinding as well as by direct contact with the liner as the simulated peristaltic wave advanced. The peristaltic simulator (B) consisted of vertical modules hanging from a top rack with the simulated peristaltic contraction applied by rollers that approached the module at a vertical height where the cube was located on the holding rig (B1) then made contact with the module and applied the simulated peristaltic contraction to the cube (B2) then eventually progressed downwards along the module (B3) returning to the top to apply the next simulated peristaltic wave (approximate path shown with dashed lines).

7.2.12 Statistical analysis

Statistical analyses were carried out using SAS Enterprise Guide 7.1 (SAS Institute, Cary, NC, USA). Two-factor Analysis of Variance (ANOVA) was used to determine the influence of the type of model food type (whey protein strong gel, whey protein weak gel, standard diet strong gel, standard diet weak gel), and static in vitro digestion time (0, 30, 180 min) on rheological properties of the model foods ($G' | 1 \text{ Hz}$), $G'' | 1 \text{ Hz}$, $\tan(\delta) | 1 \text{ Hz}$, A' , A'' , B' , B''). Two-factor ANOVA was used to analyze the fracture properties of the standard diet strong gel, standard diet weak gel, and whey protein weak gel as these were measured using wire cutting (toughness, yield stress, stiffness, elasto-fracture length, and fracture initiation energy). Fracture properties of the whey protein strong gel model food were measured using knife cutting and were analyzed separately using one-factor ANOVA with static in vitro digestion time as the factor (apparent toughness, stiffness, elasto-fracture length, and fracture initiation energy).

One-factor ANOVA was used to determine the influence of the type of model food on the rheological properties of the model foods in dispersion form before gelation (K , n).

The concentration of free amino groups in liquid digesta was quantified using total $[\text{NH}_2]$ and $\Delta [\text{NH}_2]$ in the HGS, which were analyzed using two-factor ANOVA with the type of model food and static in vitro digestion time as the factors.

Parameters from the Mixed-Weibull model were used to characterize the particle size of model foods after being subjected to static in vitro digestion and then 90 simulated peristaltic contractions in the HGS. These parameters (α , $x50_1$, $x50_2$, b_1 and b_2) were analyzed using two-factor ANOVA with the type of model food and static in vitro digestion time as the factors. Additionally, particles of model food were classified based on their size, and the percent of all particles belonging to different size classes (debris, partially damaged particles, and mostly undamaged particles) were analyzed using two-factor ANOVA with the type of model food and static in vitro digestion time as the factors.

Breakdown of model foods in the peristaltic simulator was assessed using the estimated percent of total particle volume remaining after a certain number of simulated peristaltic contractions were applied (PV_c) which was analyzed using three-factor ANOVA with the type of model food, static in vitro digestion time, and number of simulated peristaltic contractions applied as the factors. Additionally, the percent of particles belonging to different size classes (debris, partially damaged particles, and mostly undamaged particles) in addition to the number of particles in each class and the average size of particles in each class were assessed using three-factor ANOVA.

Normality of the residuals from ANOVA models was assessed using a quantile-quantile plot, and the Levene test was used to assess homogeneity of variance. Remediation was necessary for the variable representing the average size of particles classified as debris from experiments in the peristaltic simulator (Debris: \bar{x}) and was carried out using the Box-Cox transformation (Box and Cox, 1964) with lambda value equal to 0.5.

For all ANOVA models, when the F-value for the overall model was significant ($p < 0.05$), post-hoc tests were conducted using Tukey's HSD and significance was noted for $p < 0.05$.

ANOVA models were constructed and post-hoc tests were carried out using SAS Enterprise Guide 7.1 (SAS Institute, Cary, NC, USA) and significance was taken at $p < 0.05$. Linear regression was carried out using MATLAB R2020a.

All results are presented as the mean \pm standard deviation.

7.3 Results

7.3.1 *Microstructure of the model foods*

Microstructural differences between the whey protein strong gel (Figure 7.4 A) and the whey protein weak gel (Figure 7.4 B) were observed by staining the whey protein network with FITC. CLSM images showed that both model foods had a continuous whey protein network (shown in green), interspersed with darker pores. The whey protein strong gel had a more cohesive network whereas the microstructure of the whey protein weak gel was interrupted by pectin to create a less homogenous network. Previous researchers have noted that whey protein and pectin formed weak complexes near the isoelectric point of β -lactoglobulin (Lutz et al., 2009), which is ca. 5.2 (Turgeon and Beaulieu, 2001). As both the whey protein strong and weak gel were prepared at 5.2, it is expected that the formation of pectin/ β -lactoglobulin complexes could explain how pectin interrupted the whey protein network, leading to differences in fracture and rheological properties as discussed in Sections 7.3.2 and 7.3.3.

The standard diet strong gel displayed a network of starch after staining with FITC (Figure 7.4 C), as well as a network of whey protein after staining with rhodamine B (Figure 7.4 D). The formation of separate but interpenetrating networks of whey protein and starch in the standard diet strong gel can be contrasted with the standard diet weak gel, where starch (Figure 7.4 F) and protein (Figure 7.4 G) were co-located as shown in the composite image (Figure 7.4 H).

The standard diet strong gel was stained with BODIPY to reveal soybean oil (Figure 7.4 I) and rhodamine B (Figure 7.4 J), the composite of which (Figure 7.4 K) shows that the soybean oil droplets were encapsulated inside the whey protein network. Whey protein is widely used in formation of emulsion gels (Dickinson, 2012), including soybean oil emulsion gels (Guo et al., 2013), and thus the location of soybean oil droplets within the whey protein network likely reflects the emulsification of

soybean oil by whey protein when the dispersion was prepared (before thermal gelation). For the standard diet weak gel, staining with BODIPY (Figure 7.4 L) revealed soybean oil droplets of a similar appearance as those contained by the standard diet strong gel, and staining with rhodamine B (Figure 7.4 M) showed that the oil was encapsulated in the solid network, which consisted of co-located starch and whey protein (Figure 7.4 H). Comparing the composite images of the standard diet strong gel with BODIPY and rhodamine B (Figure 7.4 K) with the corresponding image of the standard diet weak gel (Figure 7.4 N) demonstrated that both gels contained well-emulsified soybean oil droplets that had not coalesced even when located in close proximity to other droplets. The difference between the standard diet strong gel and standard diet weak gel in terms of their oil droplets can be seen in the network surrounding them, specifically that the standard diet weak gel consisted of only one solid network (Figure 7.4 H) holding the oil droplets, whereas the standard diet strong gel consisted of interpenetrating whey protein and starch network (Figure 7.4 E) with the oil being encapsulated by the whey protein. This was apparent from the image of the whey protein strong gel stained with rhodamine B (Figure 7.4 D), where the oil droplets appear as dark spots within the whey protein network that appears in red. Previous research on whey protein emulsion gels with soybean oil have shown a similar appearance (Guo et al., 2014b).

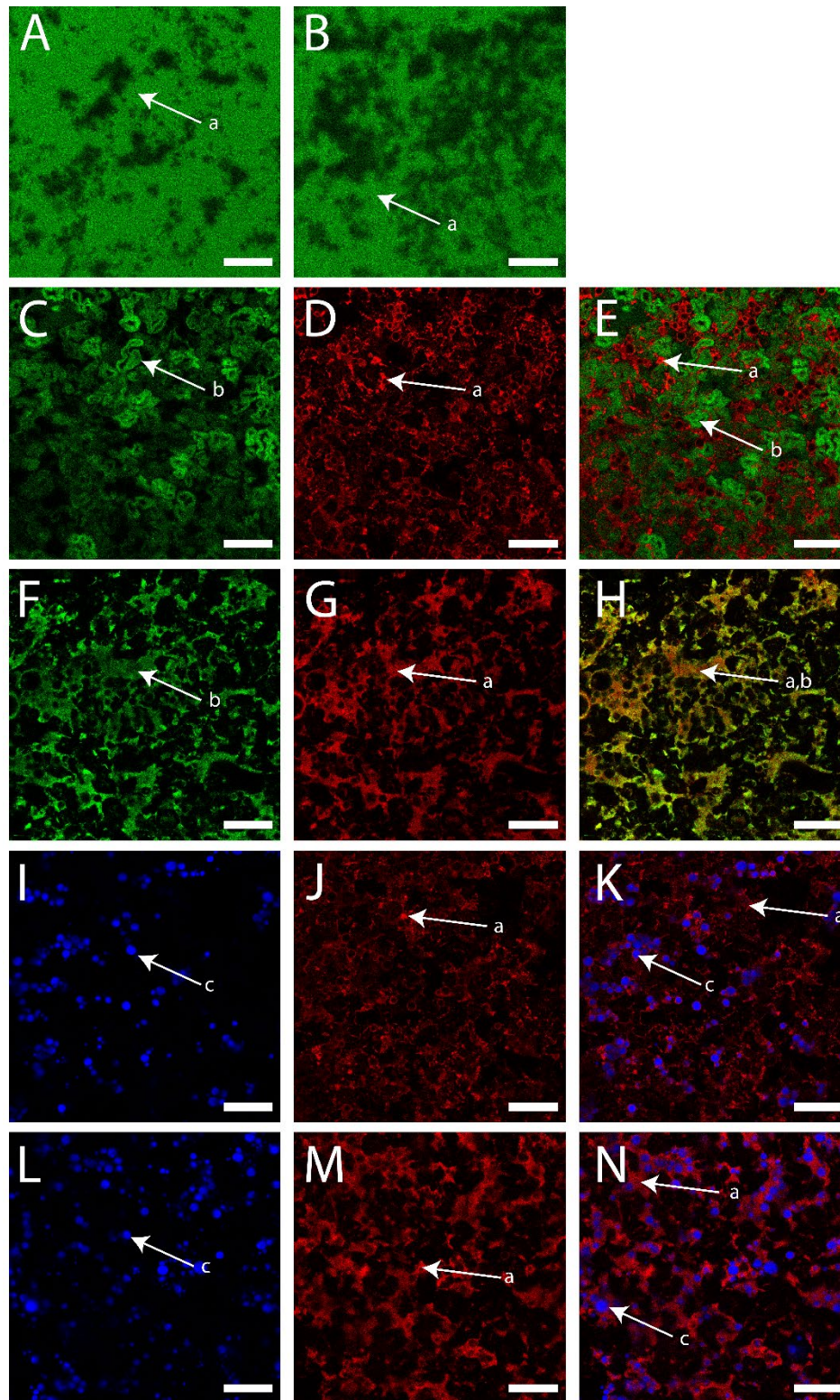


Figure 7.4. CLSM images of the model foods. Lower case letters indicate features in the images, with “a” indicating the protein network, “b” indicating the starch network, and “c” indicating the location of

soybean oil droplets. showing the whey protein strong gel with the protein network shown in green (A), whey protein weak gel with the protein network shown in green (B), standard diet strong gel with the starch network shown in green (C), standard diet strong gel with the protein network shown in red (D), the composite (overlay) of the standard diet strong gel with the protein network shown in red and the starch network shown in green (E), standard diet weak gel the starch network shown in green (F), standard diet weak gel with the protein network shown in red (G), the composite of the standard diet weak gel with the protein network shown in red and the starch network shown in green (H), standard diet strong gel with soybean oil droplets shown in blue (I), standard diet strong gel with the protein network shown in red (J), the composite of the standard diet strong gel with the protein network shown in red and soybean oil droplets shown in blue (K), standard diet weak gel with soybean oil droplets shown in blue (L), standard diet weak gel with the protein network shown in red (M), and the composite of the standard diet strong gel with the protein network shown in red and soybean oil droplets shown in blue (N). Scale bars represent 50 μm .

7.3.2 Changes in fracture properties of model foods during static in vitro gastric digestion

Fracture properties of the standard diet strong gel, standard diet weak gel, and whey protein weak gel model foods were assessed using wire cutting and were analyzed using two-factor ANOVA (Table 7.1). The whey protein strong gel was assessed using knife cutting and results were analyzed using one-factor ANOVA (Table 7.1). For the model foods that were tested using wire cutting, toughness (R), yield stress (σ_y), and fracture initiation energy were each significantly influenced by digestion time ($p < 0.01$) and the type of model food ($p < 0.01$), but not by the interaction of digestion time and the type of model food ($p > 0.05$). The elasto-fracture length (m) and stiffness (N/m) of the model foods measured using wire cutting were significantly influenced by digestion time ($p < 0.01$), type of model food ($p < 0.01$), and their interaction ($p < 0.05$). For the whey protein strong gel, the apparent toughness (R_{app}), fracture initiation energy, elasto-fracture length, and stiffness were significantly influenced by digestion time ($p < 0.01$).

Exemplary curves showing raw force vs distance data for cutting experiments using wires of different diameter are given in Figure 7.5, which showed that the force needed to advance the wire through the material was greater for wires of larger diameter. Specifically, results showed that F_{sce}/w was linear with respect to wire diameter, as expected from Equation 7.3, with a minimum R^2 for the regression of 0.96 (Figure 7.7). Toughness decreased as digestion time elapsed for the three model foods that were tested using wire cutting, which can be visualized as the y-intercepts of the lines in Figure 7.7 were lower for later digestion time points. The average toughness of the three model foods tested using wire cutting was significantly greater at 0 min than after 30 min static in vitro digestion ($p < 0.01$) and significantly greater at 30 min static in vitro digestion than at 180 min ($p < 0.01$). Averaged across all time points, the toughness of the whey protein weak gel (Figure 7.7 C) was significantly ($p < 0.01$) greater than the toughness of the standard diet strong gel (Figure 7.7 A), which was in turn significantly ($p < 0.01$) greater than that of the standard diet weak gel (Figure 7.7 B). The fracture initiation energy results showed the same trends as the results for toughness, for example, the standard diet strong gel had higher fracture initiation energy than the standard diet weak gel when averaged across all time points ($p < 0.01$), and the initial fracture initiation energy averaged across all three model foods was greater than the corresponding value after 180 min in vitro digestion ($p < 0.01$).

The initial yield stress, averaged across the three model foods that were tested using wire cutting, was not different from the yield stress at 30 min elapsed time ($p > 0.05$) but was significantly greater than the yield stress after 180 min elapsed time ($p < 0.01$). The yield stress indicates the stress that can be borne by a material before it loses elastic behavior and undergoes permanent deformation (Berthaume, 2016). The decline in yield stress of model foods measured using wire cutting shows that the model food matrices were weakened during static in vitro digestion. The stiffness of the model foods was calculated as the slope of the linear elastic region during deformation by the 0.64 mm diameter wire, and results showed that all three model foods that were tested using wire cutting demonstrated a significant ($p < 0.05$) reduction in stiffness during in vitro digestion. The elasto-fracture length of the whey protein weak gel was significantly greater after 180 min in vitro digestion than it was initially ($0.40 \pm 0.04 \times 10^{-3}$ m vs 0.29

$\pm 0.03 \times 10^{-3}$ m, $p < 0.05$). Overall, results from wire cutting showed that the model foods were more easily fractured, had a more compliant surface, and experienced plastic deformation at lower values of stress after being subjected to static in vitro digestion, as reflected by reduced toughness, reduced stiffness, and reduced yield stress, respectively.

Apparent toughness of the whey protein strong was measured using knife cutting and was found to be greater in magnitude than the toughness of the other three model foods. For instance, the whey protein strong gel had an initial toughness of 498.0 ± 38.1 N/m, as compared to 31.0 ± 3.3 for the whey protein weak gel. This large difference in toughness between the whey protein strong gel and the whey protein weak gel reflected the disrupting effect of pectin on the whey protein weak gel microstructure, which can be visualized by comparing the CLSM image of the whey protein strong gel microstructure (Figure 7.4 A) with the whey protein weak gel microstructure in Figure 7.4 B. The apparent toughness of the whey protein strong gel increased during static in vitro digestion from an initial value of 498.0 ± 38.1 N/m to a value of 684.0 ± 8.8 N/m after 180 min. This unexpected result reflected the need for a greater force to cause the knife blade to puncture the surface of the whey protein strong at later time points during in vitro digestion. This was quantified by a significantly higher fracture initiation energy at 180 min elapsed digestion time ($1,709.8 \pm 48.0$ N/m) as compared to its initial value ($1,053.0 \pm 57.9$ N/m, $p < 0.05$). Exemplary force vs distance curves from knife cutting are shown in Figure 7.6. Despite a greater force being required to initiate fracture, the surface of the whey protein strong gel became more compliant over time during digestion, as reflected by a significant decrease in stiffness, which can be visualized in Figure 7.6 as the slope of the initial indentation region (before fracture occurred). Overall, the changes in fracture properties of the whey protein strong gel during in vitro digestion showed that the gel became less stiff at the surface, which required the knife blade to travel farther into the gel before fracture was initiated. This resulted in an increase in both fracture initiation energy and apparent toughness.

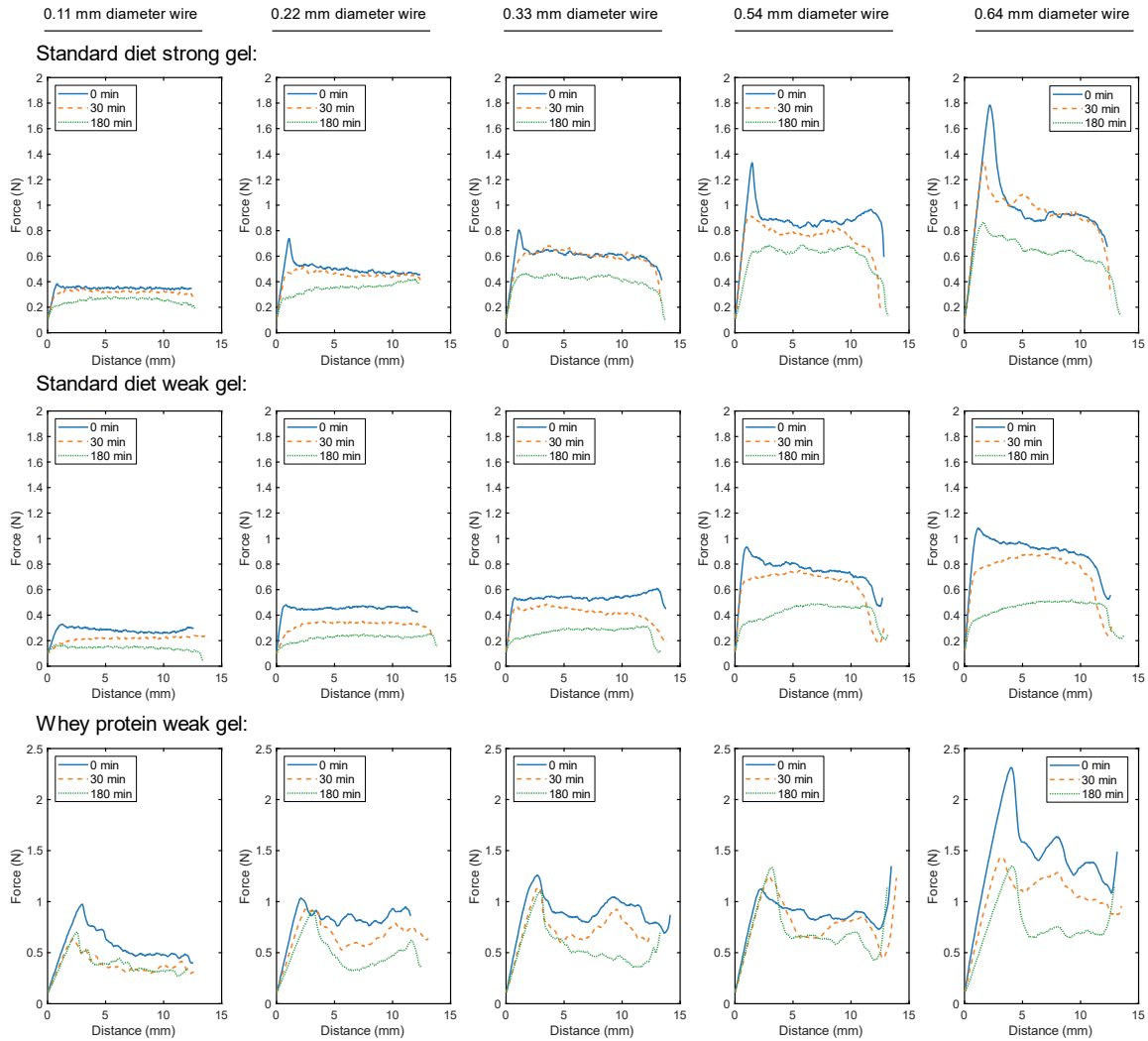


Figure 7.5. Example force vs distance curves for wire cutting experiments on cubes of the standard diet strong gel (top row), standard diet weak gel (middle row), and whey protein weak gel (bottom row) after 30 or 180 min in vitro gastric digestion.

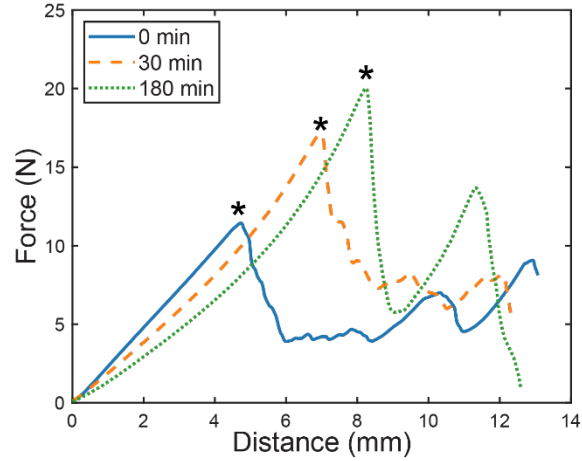


Figure 7.6. Example force vs distance curves for knife cutting experiments on cubes of the whey protein strong gel after 0, 30 or 180 min static in vitro gastric digestion, showing how the initial stiffness of the cubes tended to decrease with digestion time, but the maximum force achieved during the test increased. * indicates the initial fracture point, which occurred when the knife began to penetrate the surface of the model food cube.

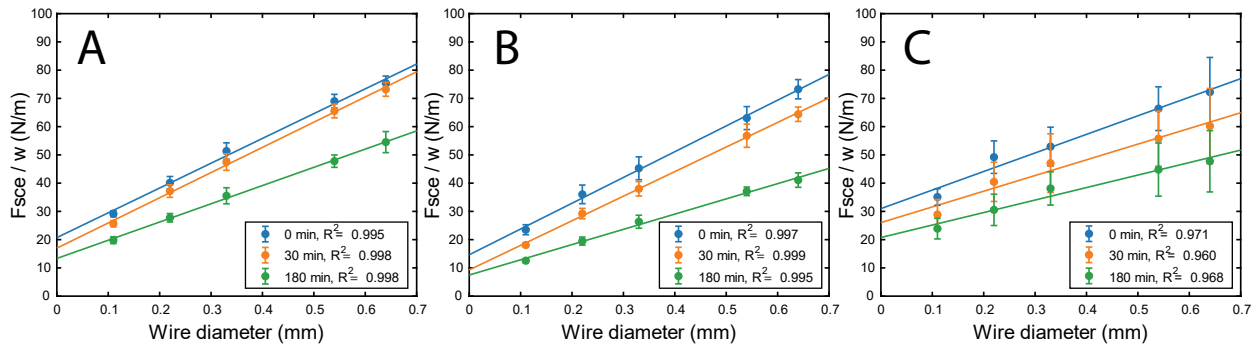


Figure 7.7. Results from wire cutting analysis for the standard diet strong gel (A), standard diet weak gel (B), and whey protein weak gel (C). Points represent the mean with error bars as the standard deviation ($n=3$). Lines represent the linear regression of F_{sce}/w onto wire diameter for each model food at each timepoint, with the R^2 values for the regression shown in the legend. The y-intercept represents the intrinsic toughness of the model food, R (N/m) and the slope represents the yield stress, (σ_y , Pa), which were quantified according to Equation 7.3.

Table 7.1. Fracture properties of model foods over time during in vitro digestion. All values are means ($n=3$) \pm standard deviation. Two-factor ANOVA was used to analyze results for the standard diet strong gel, standard diet weak gel, and whey protein weak gel. For these model foods, values in each column (abc) or each row (zyx) with different letters represent significant differences ($p < 0.05$) between means. If no letter is listed, there were no significant differences within that factor. For variables analyzed using two-factor ANOVA, if the interaction effect of type of model food and time point was not significant ($p > 0.05$), post-hoc tests were not conducted. One-factor ANOVA was used to analyze results for the whey protein strong gel, and values in each row (ijk) with different letters represent significant differences ($p < 0.05$) between means.

Digestion time (min)	Standard diet strong gel	Standard diet weak gel	Whey protein weak gel	Whey protein strong gel
Method used:	Wire cutting	Wire cutting	Wire cutting	Knife cutting
Toughness (R, N/m)				
0	20.7 \pm 1.6	14.7 \pm 2.3	31.0 \pm 3.3	498.0 \pm 38.1 ^j
30	17.0 \pm 1.6	9.3 \pm 0.8	26.0 \pm 4.2	685.5 \pm 35.1 ⁱ
180	13.3 \pm 0.8	7.5 \pm 0.9	20.7 \pm 2.2	684.0 \pm 8.8 ⁱ
Yield stress (σ_y, Pa)				
0	87.8 \pm 6.4	91.2 \pm 2.9	65.7 \pm 22.2	N/A
30	89.2 \pm 1.7	87.0 \pm 4.4	55.6 \pm 13.1	N/A
180	64.5 \pm 3.9	53.9 \pm 2.1	44.2 \pm 13.6	N/A
Stiffness (N/m)				
0	932 \pm 62 ^{a,y}	1,208 \pm 80 ^{a,z}	564 \pm 46 ^{a,x}	2,321 \pm 46 ⁱ
30	905 \pm 31 ^{a,y}	1,046 \pm 137 ^{b,z}	484 \pm 60 ^{ab,x}	1,855 \pm 76 ^j
180	705 \pm 36 ^{b,z}	784 \pm 31 ^{c,z}	393 \pm 15 ^{b,y}	1,607 \pm 35 ^k
Elasto-fracture length $\times 10^3$ (m)				

0	0.06 ± 0.00 ^y	0.05 ± 0.01 ^y	0.29 ± 0.03 ^{b,z}	1.15 ± 0.09 ^k
30	0.08 ± 0.01 ^y	0.06 ± 0.01 ^y	0.32 ± 0.05 ^{b,z}	2.02 ± 0.10 ^j
180	0.08 ± 0.01 ^y	0.08 ± 0.01 ^y	0.40 ± 0.04 ^{a,z}	2.69 ± 0.03 ⁱ
Fracture initiation energy (N/m)				
0	122.7 ± 12.0	88.4 ± 10.7	109.0 ± 24.7	1,053.0 ± 57.9 ^j
30	88.6 ± 5.7	55.4 ± 1.8	100.9 ± 16.8	1,569.2 ± 102.5 ⁱ
180	57.5 ± 6.2	39.4 ± 1.3	92.1 ± 20.8	1,709.8 ± 48.0 ⁱ

7.3.3 Changes in rheological properties of model foods during in vitro digestion

Rheological properties of all four model foods were assessed using oscillatory rheology and were analyzed using two-factor ANOVA (Table 7.4). All variables presented in Table 7.4 were significantly influenced by type of model food ($p < 0.01$), digestion time ($p < 0.01$), and their interaction ($p < 0.01$). Results showed that values of the storage modulus (G') were roughly one order of magnitude higher than the values of the loss modulus (G'') an observation that held true for all model foods across all frequencies of oscillation and static in vitro digestion times that were studied (Figure 7.8). This reflected that the solid, gel-like nature of the model foods was preserved (Cao and Mezzenga, 2020) even after 180 min static in vitro digestion. The relationship between $\tan \sigma$ and frequency of oscillation is shown in Figure 7.9.

The G' and G'' values of the whey protein strong gel were higher than those of the other model foods, reflecting its strong and elastic texture. Both $G'|1 \text{ Hz}$ and $G''|1 \text{ Hz}$ for the whey protein strong gel were significantly ($p < 0.05$) higher than the corresponding values of the other model foods at every time point that was studied (Table 7.4). Differences between the strong and weak gel versions of each model food were evident. The whey protein strong gel had higher values of $G'|1 \text{ Hz}$ and $G''|1 \text{ Hz}$ at all time points compared to the whey protein weak gel ($p < 0.05$). For the standard diet model foods, the initial value of $G'|1 \text{ Hz}$ ($73.1 \pm 2.7 \times 10^3 \text{ Pa}$) was significantly greater for the standard diet weak gel than the

standard diet strong gel ($50.6 \pm 0.6 \times 10^3$ Pa, $p < 0.05$), although at 30 min and 180 min digestion time the difference between them was no longer significant.

Values of G' and G'' decreased during static in vitro digestion for all four model foods that were studied, quantified by significantly lower values of $G'|1$ Hz and $G''|1$ Hz at 180 min digestion time than at 0 min for all four model foods. For example, the standard diet strong gel saw $G'|1$ Hz decrease from an initial value of $50.6 \pm 0.6 \times 10^3$ Pa to a final value of $26.9 \pm 1.5 \times 10^3$ Pa ($p < 0.05$). The intercept parameters of the power law, A' in Equation 7.5 and A'' in Equation 7.6, demonstrated the same trend as $G'|1$ Hz and $G''|1$ Hz, namely, a statistically significant decrease during digestion for all four model foods. In total, these parameter values showed that all model foods experienced softening during static in vitro digestion, leading to a less elastic response.

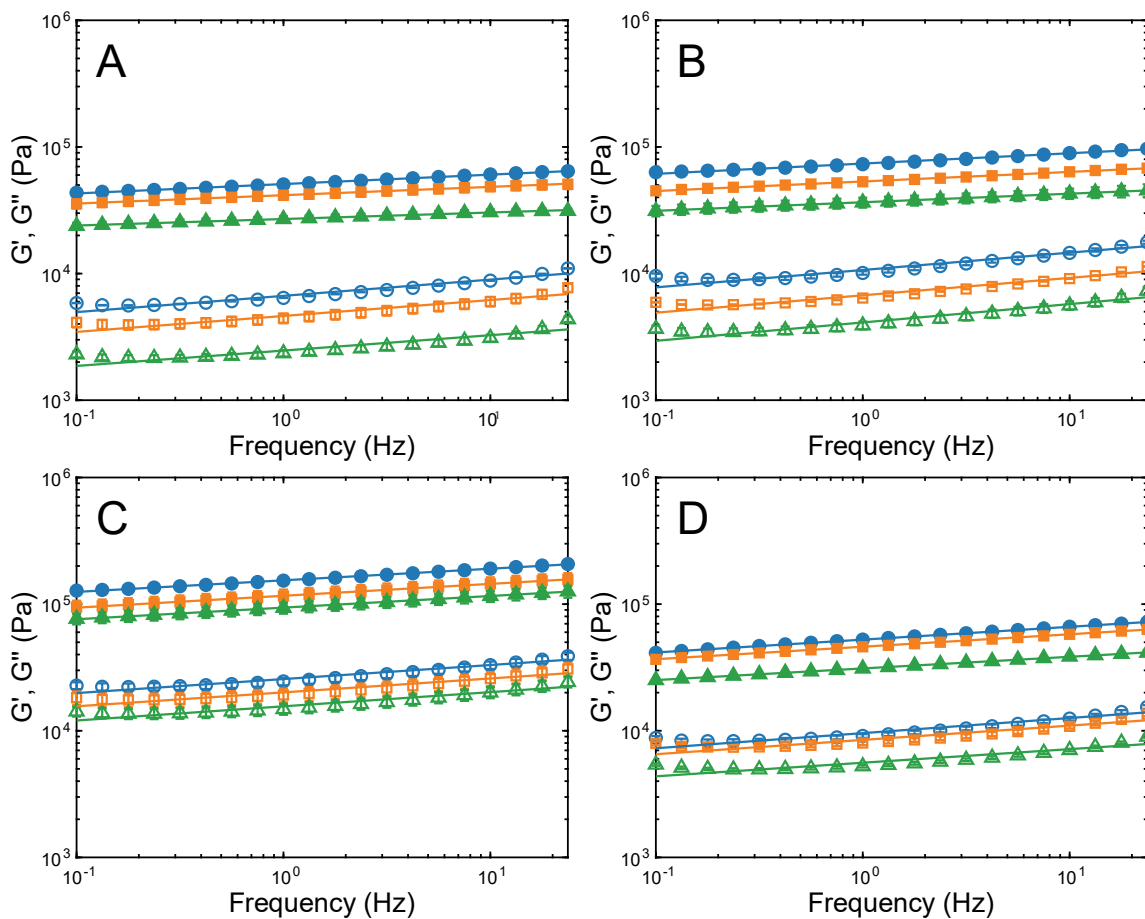


Figure 7.8. Frequency sweeps for the standard diet strong gel (A), standard diet weak gel (B), whey protein strong gel (C), and whey protein weak gel (D). Filled symbols ●, ■, and ▲ represent G' values at 0, 30, and 180 min digestion times, respectively. Open symbols ○, □, and △ represent G'' values at 0, 30, and 180 min digestion times, respectively. All points represent the mean with error bars as the standard deviation ($n=3$). Error bars may be too small to visualize. Lines represent the fit to Equation 7.5 for G' values and Equation 7.6 for G'' values.

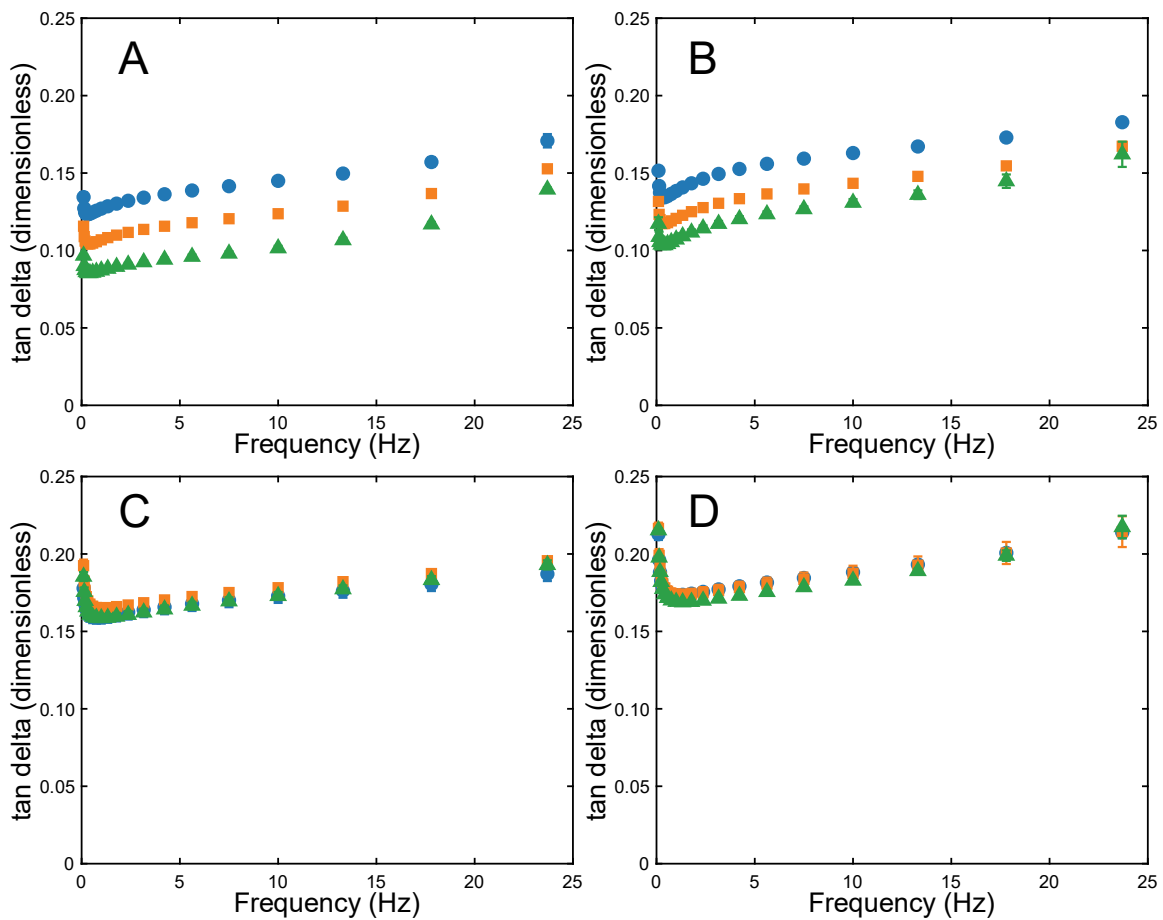


Figure 7.9. $\tan \sigma$ values from frequency sweeps for the standard diet strong gel (A), standard diet weak gel (B), whey protein strong gel (C), and whey protein weak gel (D). Symbols ●, ■, and ▲ represent $\tan \sigma$ values at 0, 30, and 180 min digestion times, respectively. All points represent the mean with error bars as the standard deviation ($n=3$). Error bars may be too small to visualize.

Table 7.2. Rheological properties of model foods over time during in vitro digestion. All values are means (n=3) ± standard deviation. Values in each column (abc) or each row (zyx) with different letters represent significant differences (p < 0.05) between means. If no letter is listed, there were no significant differences within that factor.

Digestion time (min)	Standard diet strong gel	Standard diet weak gel	Whey protein strong gel	Whey protein weak gel
G'² 1 Hz × 10⁻³ (Pa)				
0	50.6 ± 0.6 ^{a,x}	73.1 ± 2.7 ^{a,y}	153.3 ± 6.7 ^{a,z}	52.5 ± 2.3 ^{a,x}
30	41.5 ± 3.4 ^{a,y}	53.1 ± 0.6 ^{b,y}	116.0 ± 14.4 ^{b,z}	46.0 ± 0.9 ^{a,y}
180	26.9 ± 1.5 ^{b,y}	36.4 ± 3.3 ^{c,y}	93.5 ± 9.5 ^{c,z}	31.0 ± 0.6 ^{b,y}
A² × 10⁻³ (Pa·Hz⁻ⁿ)				
0	50.9 ± 0.7 ^{a,x}	73.9 ± 2.8 ^{a,y}	154.2 ± 7.0 ^{a,z}	52.4 ± 2.4 ^{a,x}
30	41.6 ± 3.4 ^{a,y}	53.3 ± 0.6 ^{b,y}	116.4 ± 14.4 ^{b,z}	46.1 ± 0.9 ^{a,y}
180	26.9 ± 1.5 ^{b,y}	36.6 ± 3.4 ^{c,y}	93.8 ± 9.5 ^{c,z}	31.0 ± 0.6 ^{b,y}
B² × 10³ (dimensionless)				
0	74.3 ± 1.0 ^{a,w}	81.4 ± 1.2 ^{a,x}	91.6 ± 2.5 ^y	101.3 ± 1.2 ^{a,z}
30	65.8 ± 1.0 ^{b,x}	75.5 ± 0.6 ^{b,y}	94.0 ± 1.3 ^z	98.5 ± 2.6 ^{a,z}
180	51.5 ± 1.8 ^{c,x}	67.6 ± 2.7 ^{c,y}	91.7 ± 1.4 ^z	91.9 ± 4.9 ^{b,z}
G'' 1 Hz × (10⁻³ Pa)				
0	6.4 ± 0.0 ^{a,x}	10.1 ± 0.3 ^{a,y}	24.5 ± 1.7 ^{a,z}	9.1 ± 0.3 ^{a,y}
30	4.4 ± 0.4 ^{b,x}	6.4 ± 0.0 ^{b,yx}	19.2 ± 2.4 ^{b,z}	8.0 ± 0.3 ^{a,y}
180	2.3 ± 0.1 ^{c,x}	3.9 ± 0.3 ^{c,yx}	14.8 ± 1.5 ^{c,z}	5.2 ± 0.1 ^{b,y}
A'' × 10⁻³ (Pa·Hz⁻ⁿ)				
0	6.7 ± 0.0 ^{a,x}	10.7 ± 0.3 ^{a,y}	25.6 ± 1.7 ^{a,z}	9.6 ± 0.3 ^{a,y}
30	4.6 ± 0.4 ^{a,x}	6.7 ± 0.0 ^{b,yx}	20.1 ± 2.5 ^{b,z}	8.5 ± 0.3 ^{a,y}
180	2.5 ± 0.1 ^{b,x}	4.1 ± 0.3 ^{c,yx}	15.6 ± 1.5 ^{c,z}	5.6 ± 0.1 ^{b,y}
B'' × 10³ (dimensionless)				

0	128.3 ± 1.0 ^{a,y}	137.0 ± 3.7 ^{b,z}	110.9 ± 0.3 ^w	119.4 ± 0.5 ^{a,x}
30	125.9 ± 1.8 ^{a,y}	137.4 ± 0.1 ^{b,z}	109.8 ± 2.1 ^x	112.9 ± 1.8 ^{b,x}
180	121.4 ± 1.2 ^{b,y}	145.0 ± 4.0 ^{a,z}	111.9 ± 1.0 ^x	107.4 ± 0.2 ^{c,w}
tanδ 1 Hz × 10³ (dimensionless)				
0	127.0 ± 1.6 ^{a,w}	138.4 ± 0.8 ^{a,x}	159.9 ± 4.9 ^{b,y}	173.4 ± 2.2 ^{ab,z}
30	106.9 ± 0.7 ^{b,w}	120.7 ± 0.8 ^{b,x}	165.2 ± 2.7 ^{a,y}	173.8 ± 3.3 ^{a,z}
180	87.2 ± 0.8 ^{c,w}	107.1 ± 2.1 ^{c,x}	158.6 ± 2.4 ^{b,y}	169.1 ± 0.8 ^{b,z}

Flow curves of model foods in their dispersion form (before thermal gelation) were analyzed using the power law model in Equation 7.1 and are shown in Figure 7.10. The power law provided a good fit to the data, with R^2 values > 0.99 (Table 7.3). The standard diet model foods developed higher viscosities than the whey protein model foods. The highest value of the consistency index, K , was for the standard diet weak gel ($9.21 \pm 0.50 \text{ Pa}\cdot\text{s}^n$), which was significantly higher than the standard diet strong gel ($4.87 \pm 0.04 \text{ Pa}\cdot\text{s}^n$, $p < 0.05$).

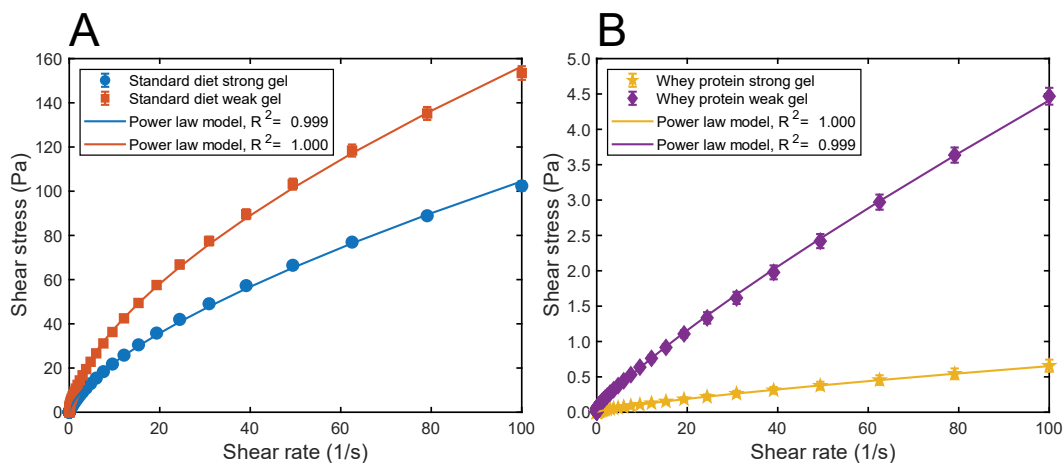


Figure 7.10. Flow curves for the dispersion form of the standard diet model foods (A) as well as the whey protein model foods (B). All points represent the mean with error bars as the standard deviation ($n=3$). Error bars may be too small to visualize. Lines represent the fit to the power law model (Equation 7.1). Standard diet model food dispersions (A) were shown with a greater y-axis scale as they were more viscous than the whey protein model food dispersions (B).

Table 7.3. Rheological properties of model foods in dispersion form with parameters from Equation 7.1. All values are means (n=3) \pm standard deviation. Values in each column (abc) with different letters represent significant differences ($p < 0.05$) between means. If no letter is listed, there were no significant differences within that factor.

Model food	K (Pa·sⁿ)	n (dimensionless)	R²
Standard diet strong gel	4.87 \pm 0.04 ^b	0.67 \pm 0.00 ^c	0.999 \pm 0.000
Standard diet weak gel	9.21 \pm 0.50 ^a	0.62 \pm 0.01 ^c	1.000 \pm 0.000
Whey protein strong gel	0.02 \pm 0.00 ^c	0.77 \pm 0.03 ^b	0.997 \pm 0.004
Whey protein weak gel	0.10 \pm 0.01 ^c	0.83 \pm 0.02 ^a	0.999 \pm 0.001

7.3.4 Breakdown of model foods in the HGS

After being subjected to either 0, 30, or 180 min static in vitro digestion in the shaking water bath, cubes of model food were transferred to the HGS for a treatment consisting of 90 simulated peristaltic contractions. During this treatment, model food cubes experienced mechanical breakdown, which can be visualized in Figure 7.11, showing the presence of food particles of varying sizes. Particle sizes were quantified using image analysis and the cumulative particle size distribution was fit using the Mixed Weibull model (Equation 7.7) with results shown in Figure 7.12. Representative binary images showing particles of the four model foods are given in Figure 7.13.

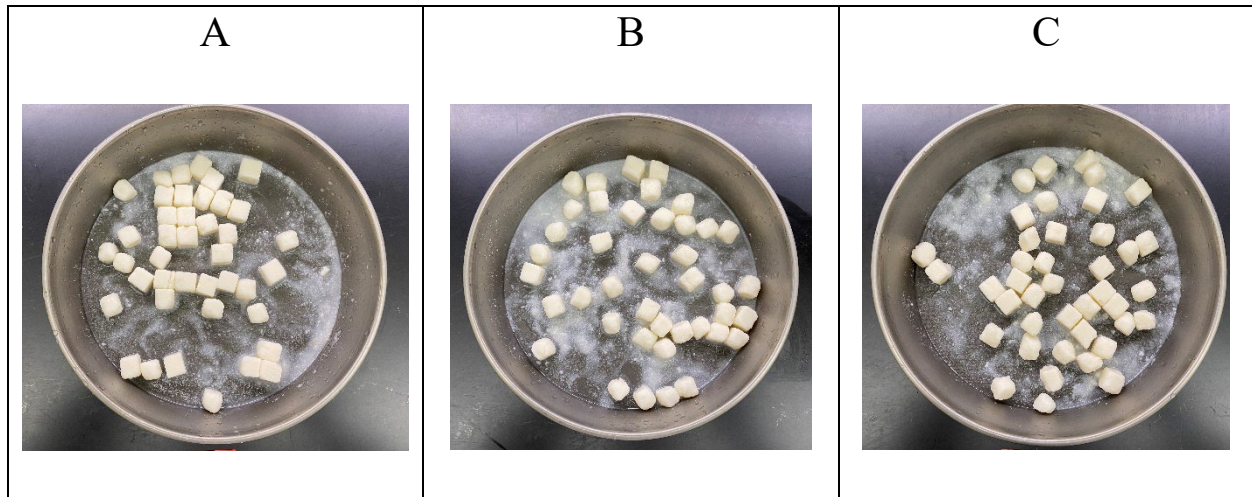


Figure 7.11. Example photographs showing particles of the standard diet weak gel model food after being subjected to 0 min (A), 30 min (B), or 180 min (C) static in vitro digestion, followed by 90 contractions in the HGS

The cumulative distribution functions describing particle sizes resulting from breakdown of model foods in the HGS were bimodal and the Mixed Weibull model provided a satisfactory fit to the data, with R-squared values greater than 0.98 in all cases (Figure 7.12). These cumulative distribution functions were characterized by an initial increase representing the contribution of small particles, a plateau region representing a size range where there were not many particles contributing to the cumulative total, followed by an increase which consisted of large particles. The parameters of the Mixed Weibull function were analyzed using two-factor ANOVA, with type of model food and static in vitro digestion time as the factors, and results are shown in Table 7.4. The contribution of small particles to the total was represented by the weight parameter, α (dimensionless), which was significantly influenced by the type of model food, digestion time, and their interaction (all $p < 0.01$). Notably, this parameter was significantly ($p < 0.05$) larger for the weak gel version of each model food than the corresponding strong gel version regardless of static in vitro digestion time. For example, after being subjected to 30 min static in vitro digestion followed by 90 contractions in the HGS, α for the standard diet weak gel was 0.42 ± 0.04 , which

was significantly larger ($p < 0.05$) than that of the standard diet strong gel (0.20 ± 0.05). This indicates that small particles belonging to the first mode made up approximately 42% of the total area of all particles for the standard diet weak gel, whereas for the standard diet strong gel they made up only 20% of the total. These results demonstrate that the particle size distributions from the weak gel version of each model food included a greater contribution from small particles, which may be related to their weaker structure, leading to a greater extent of particle breakdown in the HGS. For the standard diet weak gel, α was significantly greater ($p < 0.05$) for longer static in vitro digestion times, increasing from a value of 0.44 ± 0.04 for the model food without a static in vitro digestion pretreatment to 0.61 ± 0.05 for the sample after being subjected to 180 min static in vitro digestion. This shows that for the standard diet weak gel, longer static in vitro digestion times were associated with a greater contribution of small particles after the model food was subjected to 90 contractions in the HGS. Conversely, α for the standard diet strong gel experienced a significant decrease ($p < 0.05$) from a value of 0.30 ± 0.09 in the absence of a static in vitro digestion to 0.08 ± 0.05 for the sample after being subjected to 180 min static in vitro digestion. These results highlight how textural differences between model foods with similar composition can lead to different breakdown behavior during in vitro digestion that includes simulated peristalsis.

The $x50_1$ parameter (mm^2) is indicative of the size of particles contributing to the first mode, and it was not significantly influenced by the type of model food or digestion time ($p > 0.05$). This suggests that the small particles which contributed to the first mode were similar in size regardless of the type of model food that they were generated from. Taken together with the α parameter, these results shown that even though the approximate size of particles contributing to the first mode may be the same, their relative contribution to the total distribution can vary between treatments. The value of $x50_1$ may have been more strongly influenced by system characteristics held constant across all treatments, such as the initial model food particle size, cubical geometry, or contact mechanics in the HGS, as opposed to the experimental factors which consisted of model food type and static in vitro digestion time. Another factor that could have contributed to the apparent lack of differences between model foods in terms of the $x50_1$ parameter is the limitations of the computer vision system used to acquire images which were used for particle size

analysis, as these particles were quite small. The b_1 and b_2 parameters (dimensionless) describe the shape of the first and second modes, respectively, and were not significantly influenced by the type of model food or digestion time ($p > 0.05$). The shape of the first mode can be observed in Figure 7.12 as the initial sharp increase in the cumulative particle area, which was consistent across all treatments.

The parameter describing the size of large particles contributing to the second mode ($x50_2$, mm^2) was significantly influenced by the type of model food ($p < 0.01$), digestion time ($p < 0.01$), and their interaction (all $p < 0.05$). Both the whey protein strong and weak gel model foods had significantly smaller ($p < 0.05$) values of $x50_2$ with greater static in vitro digestion times. The particles which made up the mode described by $x50_2$ consisted of mostly undamaged cubes, in contrast to the particles which made up the mode described by $x50_1$ which consisted of small, debris-like particles that had broken away from them. These two groups of particles (debris and mostly undamaged particles) are visible in Figure 7.11. The significantly smaller values of $x50_2$ demonstrated by the whey protein model foods after longer static in vitro digestion times indicates that the large, mostly undamaged particles in the distribution had broken down to smaller sizes after longer static in vitro digestion times. However, the lack of a significant increase in α (proportion of small particles) for longer digestion times suggests that some of the small particles may have been lost, perhaps with the permeate which passed through the sieve that was used to separate particles remaining after the HGS treatment from digestion liquids.

With no static in vitro digestion, the $x50_2$ value for the whey protein weak gel was $227.5 \pm 3.3 \text{ mm}^2$, which was significantly greater ($p < 0.05$) than the value of $x50_2$ for the same model food when particles were subjected to 180 min static in vitro digestion before undergoing 90 contractions of simulated peristalsis in the HGS ($201.5 \pm 6.6 \text{ mm}^2$). The whey protein strong gel demonstrated the same trend, namely, decreased values of $x50_2$ for samples subjected to a longer static in vitro digestion, indicating that more size reduction of the large particles in the distribution occurred during a longer static in vitro digestion. The standard diet model foods did not experience a decrease in $x50_2$. After 30 min and 180 min static in vitro digestion, the whey protein strong gel had significantly greater ($p < 0.05$) values of

$\times 50_2$ than the whey protein weak gel. For example, after 180 min static in vitro digestion the whey protein strong gel had an $\times 50_2$ value of $226.2 \pm 7.8 \text{ mm}^2$, which was greater than that of the whey protein weak gel $201.5 \pm 6.6 \text{ mm}^2$, which shows that the large particles of the whey protein strong gel experienced less size reduction than the large particles of the whey protein weak gel after a given static in vitro digestion time. Overall, results showed that the particle size distributions of all model foods were bimodal, well-represented by the Mixed Weibull function, and had parameters that were affected by both the type of model food and the duration of the static in vitro digestion.

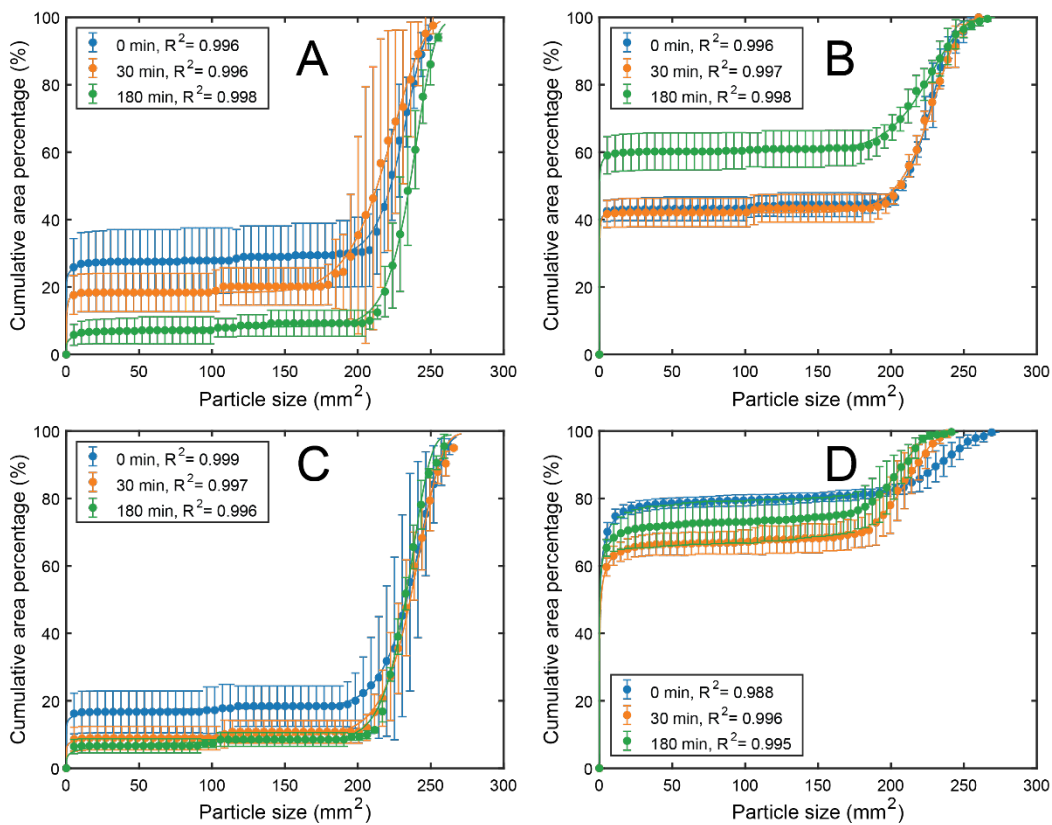


Figure 7.12. Cumulative particle area percentage after varying durations of static in vitro gastric digestion (0, 30, and 180 min), followed by application of 90 contractions in the HGS shown for the standard diet strong gel (A), standard diet weak gel (B), whey protein strong gel (C), and whey protein weak gel (D). All points represent the mean with error bars as the standard deviation ($n=3$). Lines represent the fit to the Mixed Weibull Model (Equation 7.7).

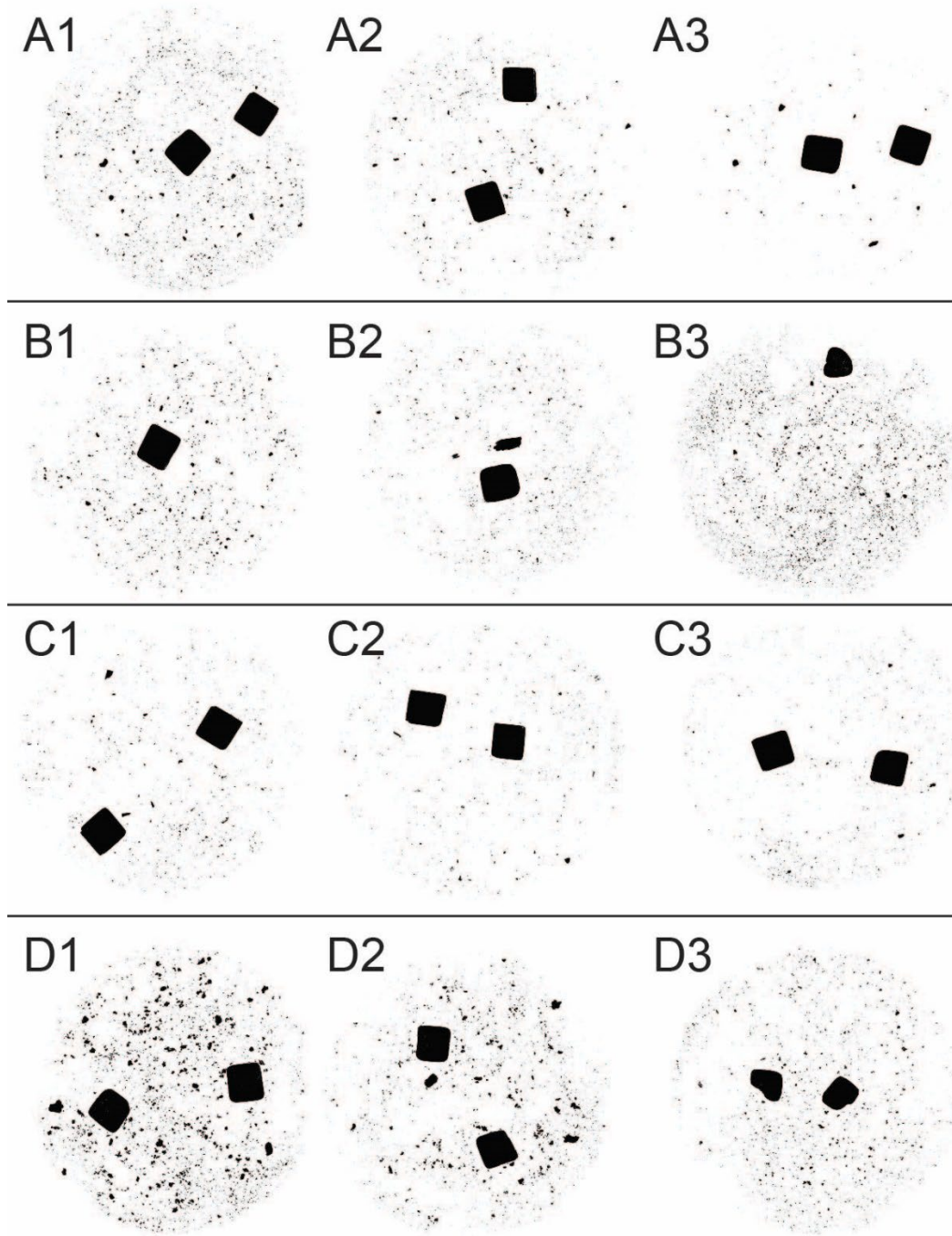


Figure 7.13. Representative binary images showing particles of model foods after static in vitro digestion followed by 90 contractions in the HGS, showing the standard diet strong gel with 0 min static in vitro digestion (A1), standard diet strong gel with 30 min static in vitro digestion (A2), standard diet strong gel with 180 min static in vitro digestion (A3), standard diet weak gel with 0 min static in vitro digestion

(B1), standard diet weak gel with 30 min static in vitro digestion (B2), standard diet weak gel with 180 min static in vitro digestion (B3), whey protein strong gel with 0 min static in vitro digestion (C1), whey protein strong gel with 30 min static in vitro digestion (C2), whey protein strong gel with 180 min static in vitro digestion (C3), whey protein weak gel with 0 min static in vitro digestion (D1), whey protein weak gel with 30 min static in vitro digestion (D2), and the whey protein weak gel with 180 min static in vitro digestion (D3).

Table 7.4. Parameters of the Mixed Weibull Model (Equation 7.7) and percentages of total particle area belonging to distinct size classes for model foods after being subjected to static in vitro digestion for varying time points (0, 30, or 180 min) followed by 90 contractions in the HGS. Values in each column (abc) or each row (zyx) with different letters represent significant differences ($p < 0.05$) between means. For variables where the interaction effect of type of model food and time point was not significant ($p > 0.05$), post-hoc tests were not conducted.

Digestion time (min)	Standard diet strong gel	Standard diet weak gel	Whey protein strong gel	Whey protein weak gel
α (dimensionless)				
0	0.30 ± 0.09 ^{a,x}	0.44 ± 0.04 ^{b,y}	0.19 ± 0.06 ^x	0.80 ± 0.02 ^{a,z}
30	0.20 ± 0.05 ^{a,x}	0.42 ± 0.04 ^{b,y}	0.11 ± 0.04 ^x	0.68 ± 0.05 ^{b,z}
180	0.08 ± 0.05 ^{b,x}	0.61 ± 0.05 ^{a,y}	0.10 ± 0.02 ^x	0.74 ± 0.05 ^{ab,z}
$x50_1$ (mm²)				
0	0.24 ± 0.30	0.12 ± 0.21	1.81 ± 2.77	0.57 ± 0.27
30	0.61 ± 0.79	0.17 ± 0.17	3.39 ± 5.38	0.45 ± 0.19
180	3.59 ± 4.71	0.06 ± 0.05	21.28 ± 24.89	0.42 ± 0.62
b_1 (dimensionless)				
0	0.16 ± 0.01	0.59 ± 0.84	0.18 ± 0.04	0.32 ± 0.06
30	0.24 ± 0.13	0.53 ± 0.31	0.19 ± 0.05	0.30 ± 0.08

180	0.91 ± 0.64	0.27 ± 0.13	0.28 ± 0.07	0.25 ± 0.13
$x50_2$ (mm²)				
0	233.8 ± 6.2^{zy}	223.4 ± 4.7^{yx}	$239.7 \pm 5.8^{a,z}$	$227.5 \pm 3.3^{a,zy}$
30	237.4 ± 6.1^z	228.6 ± 3^z	$229.7 \pm 6.7^{ab,z}$	$213.8 \pm 6.5^{b,y}$
180	230.6 ± 6.3^z	225.4 ± 9.2^z	$226.2 \pm 7.8^{b,z}$	$201.5 \pm 6.6^{b,y}$
b_2 (dimensionless)				
0	22.99 ± 7.64	19.17 ± 3.49	21.43 ± 4.18	12.5 ± 0.87
30	19.83 ± 3.46	15.42 ± 2.01	17.94 ± 3.23	15.78 ± 2.91
180	21.98 ± 5.65	12.37 ± 0.53	21.02 ± 1.49	13.44 ± 0.75
Debris (particles < 4.0 mm², %)				
0	$20.6 \pm 8.5^{a,x}$	$41.6 \pm 2.2^{b,y}$	13.2 ± 6.6^x	66.8 ± 3.0^z
30	$13.8 \pm 5.5^{ab,x}$	$42.0 \pm 3.5^{b,y}$	8.7 ± 3.4^x	58.1 ± 2.1^z
180	$7.3 \pm 0.5^{b,y}$	$58.0 \pm 6.0^{a,z}$	7.1 ± 1.1^y	62.8 ± 1.9^z
Partially damaged particles (4.0 mm² < particles < 170.0 mm², %)				
0	1.8 ± 1.6	0.5 ± 0.1	0.5 ± 0.4	14.2 ± 1.6
30	1.2 ± 0.1	0.6 ± 0.2	0.5 ± 0.2	11.5 ± 2.1
180	2.5 ± 1.4	2.2 ± 0.6	0.4 ± 0.1	12.1 ± 3.9
Mostly intact particles (170.0 mm² < particles, %)				
0	$77.5 \pm 10.1^{b,z}$	$57.8 \pm 2.3^{a,y}$	86.2 ± 7.0^z	$19.1 \pm 1.4^{x,b}$
30	$85.0 \pm 5.6^{ab,z}$	$57.4 \pm 3.7^{a,y}$	90.8 ± 3.2^z	$30.4 \pm 4.2^{x,a}$
180	$90.3 \pm 0.9^{a,z}$	$39.8 \pm 5.4^{b,y}$	92.5 ± 0.9^z	$25.1 \pm 5.7^{x,ab}$
Percent of initial dry mass remaining in cubes retained on sieve (%)				
0	89.2 ± 5.3	91.2 ± 0.5	98.1 ± 2.0	98.9 ± 1.0
30	82.8 ± 1.3	83.3 ± 0.9	96.0 ± 2.2	90.6 ± 1.5
180	71.4 ± 0.5	76.2 ± 4.0	89.8 ± 3.0	82.9 ± 4.7

Follow-up analysis of the breakdown of model foods in the HGS was carried out by classifying the particles that resulted from application of 90 contractions to the cubes of model food subjected to static in

vitro digestion for varying time points. Three classes were used, which consisted of debris, defined as particles smaller than 4 mm², partially damaged particles, defined as those with size between 4 mm² and 170 mm², and mostly intact particles, defined as those with size greater than 170 mm² (Table 7.4). Classification cutoffs were based on the cumulative distribution functions of particle size (Figure 7.12), which showed the presence of an initial increase due to small particles (debris), a relatively flat region that represented the contribution of partially damaged particles, and finally another increase due to mostly intact particles. Histograms showing the contribution of particles in varying size ranges to the cumulative total along with classification cutoffs are shown in Figure 7.14. The percentage of debris was significantly influenced by the type of model food ($p < 0.01$), static in vitro digestion time ($p < 0.05$), and the interaction of the type of model food and static in vitro digestion time ($p < 0.01$). After any duration of static in vitro digestion, the percentage of debris was significantly greater ($p < 0.05$) for the weak gel version of each model food than for the corresponding strong gel version. This can be visualized in Figure 7.14 which shows that the standard diet strong gel (Figure 7.14 A1-A3) and the whey protein strong gel (Figure 7.14 C1-C3) had a minor contribution of debris to the total, whereas the standard diet weak gel (Figure 7.14 B1-B3) and the whey protein weak gel (Figure 7.14 D1-D3) had a greater contribution of debris to the total area represented by all particles in the distribution. In accordance with the α parameter from the Mixed Weibull function analysis, this indicates that the weak gel version of each model food experienced a greater degree of breakdown in the HGS in terms of the total area of small particles relative to the entire particle size distribution.

The percentage of partially damaged particles was significantly influenced by the type of model food ($p < 0.001$), but not by the static in vitro digestion time or their interaction ($p > 0.05$). However, the percentage of partially damaged particles was significantly greater ($p < 0.01$) for the whey protein weak gel than the whey protein strong gel, when averaged across all static in vitro digestion times. The percentage of mostly intact particles was significantly influenced by the type of model food ($p < 0.01$), static in vitro digestion time ($p < 0.05$), and their interaction ($p < 0.01$). For any given static in vitro

digestion time, the whey protein strong gel and standard diet strong gel had a significantly greater ($p < 0.05$) percentage of mostly intact particles than their corresponding weak gel versions.

The moisture content and wet mass of particles retained on the sieve after being subjected to 90 simulated peristaltic contractions in the HGS were used to determine the percentage of initial dry mass that was included in the solid particles fraction and thus used for image analysis. The percent of initial dry mass remaining was significantly influenced by both the type of model food ($p < 0.01$) and the duration of static in vitro gastric digestion ($p < 0.01$) but not their interaction ($p > 0.05$). Averaged across all static in vitro digestion times, the percent of initial dry mass remaining was not significantly different between the standard diet strong gel and standard diet weak gel ($p > 0.05$), however, it was significantly greater ($p < 0.05$) for the whey protein strong gel than the whey protein weak gel. Averaged across the four different model foods, the percent of initial dry mass remaining was significantly greater ($p < 0.05$) when the treatment did not include a static in vitro digestion (0 min) than when the treatment included a 30 min static in vitro digestion, and in the same way was significantly greater ($p < 0.05$) for samples that were subjected to 30 min static in vitro digestion than for those that were subjected to 180 min static in vitro digestion. This demonstrates that the differences in breakdown between the standard diet model foods cannot be ascribed to significantly more dry mass being lost by the weak gel version, however, this cannot be excluded as a potential mechanism leading to differences observed between the whey protein strong gel and whey protein weak gel. Additionally, the influence of static in vitro digestion time shows that more mass was lost by particles that were subjected to a static in vitro digestion in addition to 90 contractions in the HGS as compared to those that were not subjected to static in vitro digestion.

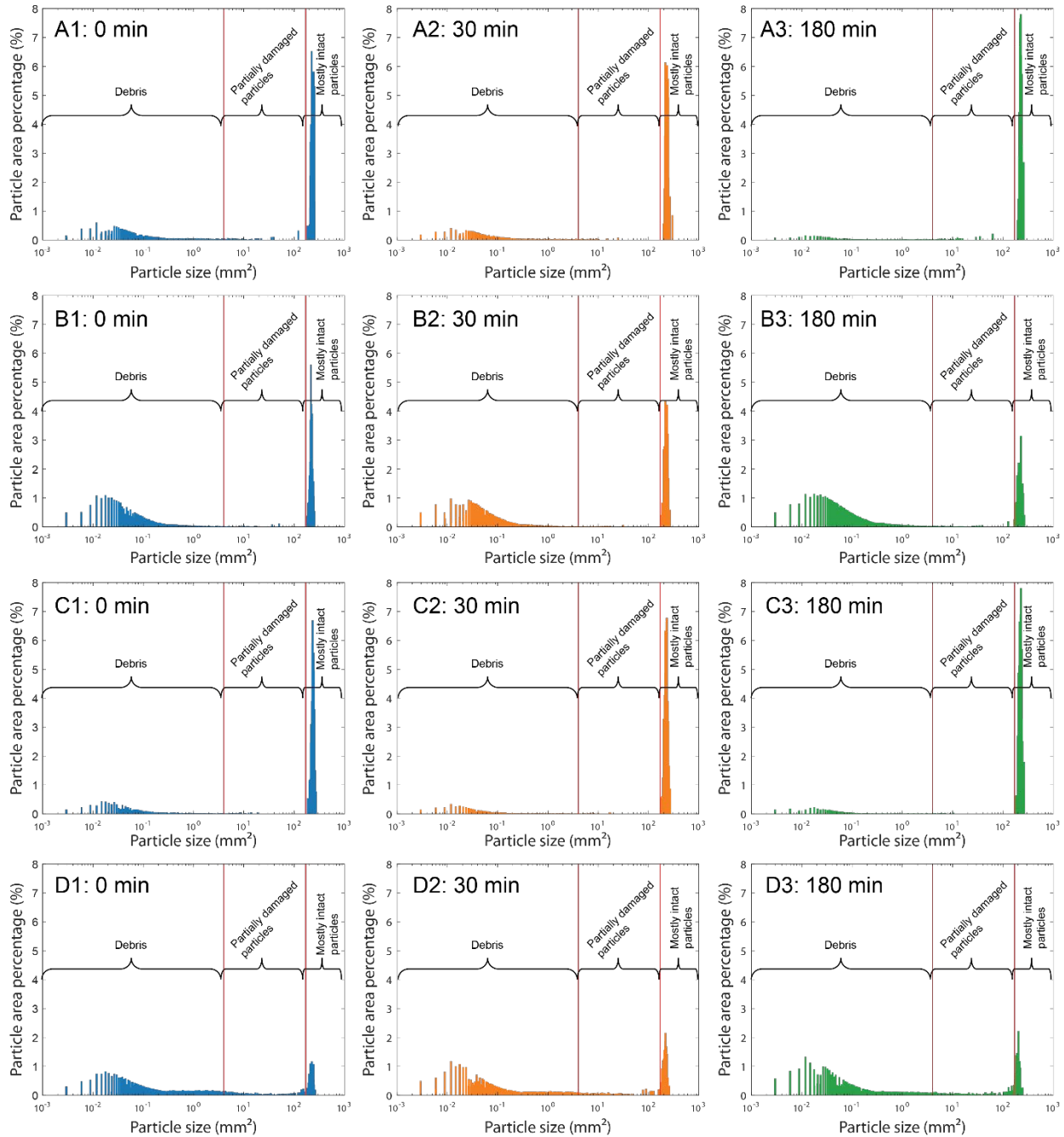


Figure 7.14. Particle size histograms used to classify the particles of model foods that arose from breakdown due to varying durations of static in vitro gastric digestion (0, 30, and 180 min), followed by application of 90 contractions in the HGS shown for the standard diet strong gel (A1-A3), standard diet weak gel (B1-B3), whey protein strong gel (C1-C3), and whey protein weak gel (D1-D3).

7.3.5 *Free amino group concentration*

The concentration of free amino groups in liquid digesta due to hydrolysis of the model foods was assessed using OPA (Section 7.2.10). The total $[\text{NH}_2]$ was significantly influenced by both the type of model food, static in vitro digestion time, and their interaction ($p < 0.01$) (Figure 7.15). For all four model foods, total $[\text{NH}_2]$ was significantly ($p < 0.05$) greater after 180 min static in vitro digestion than after 0 min static in vitro digestion. It should be noted that total $[\text{NH}_2]$ for samples with 0 min static in vitro digestion nevertheless were subjected to 90 simulated peristaltic contractions in the HGS (approximately 30 minutes). For samples subjected to 0 min or 30 min static in vitro digestion, the total $[\text{NH}_2]$ was significantly greater ($p < 0.05$) for the standard diet weak gel than samples from the other model foods. For example, after 30 min static in vitro digestion total $[\text{NH}_2]$ for the standard diet weak gel was 14.4 ± 3.0 Mol/L, which was significantly ($p < 0.05$) higher than that of the standard diet strong gel (9.1 ± 2.0 Mol/L). For all static vitro digestion times, total $[\text{NH}_2]$ was significantly ($p < 0.05$) higher for the standard diet weak gel than for the standard diet strong gel despite their equivalent protein concentration (Table 5.1) potentially reflecting differences in their breakdown. For samples subjected to 180 min static in vitro digestion, total $[\text{NH}_2]$ was significantly ($p < 0.05$) higher for the whey protein strong gel and whey protein weak gel than the standard diet strong and weak gels, reflecting their greater protein content as given in Table 5.1.

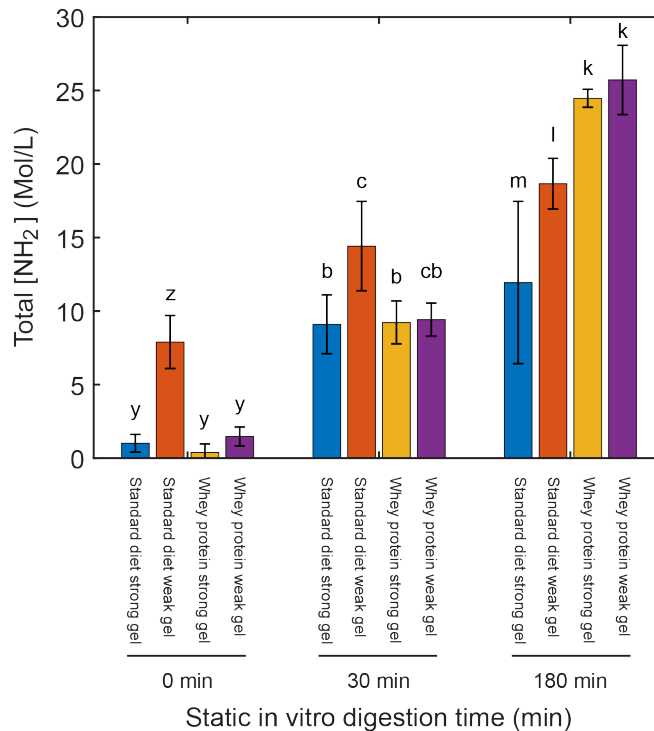


Figure 7.15. Total $[\text{NH}_2]$ as determined using OPA (Section 2.9). Bars within a given in vitro digestion time with different letters were significantly ($p < 0.05$) different.

In addition to total $[\text{NH}_2]$, the change in the concentration of free amino groups during application of 90 simulated peristaltic contractions in the HGS ($\Delta [\text{NH}_2]$ in the HGS) was determined (Table 7.5). $\Delta [\text{NH}_2]$ in the HGS was significantly influenced by the type of model food, static in vitro digestion time, and their interaction ($p < 0.01$). A potentially interesting finding is that the $\Delta [\text{NH}_2]$ in the HGS was always significantly ($p < 0.05$) greater for the standard diet weak gel than for any of the other model foods. Additionally, the whey protein strong gel and whey protein weak gel demonstrated significantly greater ($p < 0.05$) values of $\Delta [\text{NH}_2]$ in the HGS for samples that were subjected to 180 min static in vitro digestion than for samples subjected to 0 min static in vitro digestion. For instance, the whey protein strong gel had a value of $\Delta [\text{NH}_2]$ in the HGS of 0.70 ± 0.31 (Mol/L) after 0 min static in vitro digestion, and a value of 5.27 ± 0.82 (Mol/L) after 180 min static in vitro digestion.

Table 7.5. Change in concentration of free amino groups in liquid digesta Δ [NH₂] (Mol/L) from the end of the static in vitro digestion in the shaking water bath to immediately after 90 simulated peristaltic contractions were applied in the HGS (approximately 30 min). Values in each column (abc) or each row (zyx) with different letters represent significant differences ($p < 0.05$) between means.

Digestion time (min)	Standard diet strong gel	Standard diet weak gel	Whey protein strong gel	Whey protein weak gel
Δ [NH ₂] in the HGS (Mol/L)				
0	1.06 ± 0.49 ^{a,y}	7.87 ± 0.79 ^z	0.70 ± 0.31 ^{a,y}	1.04 ± 0.33 ^{a,y}
30	5.41 ± 1.19 ^{b,y}	8.95 ± 1.61 ^z	3.71 ± 0.88 ^{b,y}	3.42 ± 0.50 ^{b,y}
180	2.45 ± 0.69 ^{a,x}	7.68 ± 2.22 ^z	5.27 ± 0.82 ^{b,zy}	3.63 ± 1.64 ^{b,wx}

7.3.6 Breakdown of model foods in the peristaltic simulator

Breakdown of model food particles in the peristaltic simulator was analyzed using image analysis and was used to estimate the percent of total particle volume remaining after application of c simulated peristaltic contractions (PVc) according to Equation 7.9, with results shown in Figure 7.16. The percent of total volume remaining was significantly influenced by the type of model food ($p < 0.01$), the static in vitro digestion time ($p < 0.01$), the number of simulated peristaltic contractions that were applied ($p < 0.01$), the interaction of type of model food and static in vitro digestion time ($p < 0.01$), the interaction of the type of model food and the number of contractions ($p < 0.01$), the interaction of the static in vitro digestion time and the number of contractions ($p < 0.01$), and the three-way interaction of the type of model food, static in vitro digestion time, and number of contractions ($p < 0.01$). All model foods except for the whey protein strong gel demonstrated a decrease in PVc as the number of simulated peristaltic contractions increased, as evidenced by a significant difference ($p < 0.05$) in their initial and final values of PVc for all static in vitro digestion times, as shown in Figure 7.16.

For all static in vitro digestion times, the whey protein strong gel had a significantly greater ($p < 0.05$) value of PVc after 90 contractions were applied as compared to the whey protein weak gel. For example,

the PV_c for the whey protein strong gel (Figure 7.16 C) after being subjected to 90 simulated peristaltic contractions (PV_{90}) averaged 98.9 % across all static in vitro digestion times, indicating that most of the model food particle remained on the holding rig after being subjected to 90 simulated peristaltic contractions. On the other hand, PV_{90} for the standard diet weak gel (Figure 7.16 D) was always 0 %, indicating that the entire cube of model food had been broken into fragments that fell off the holding rig during the application of 90 simulated peristaltic contractions. For any static in vitro digestion time, PV_{90} for the whey protein strong gel was significantly greater ($p < 0.05$) than PV_{90} for the whey protein weak gel at the corresponding static in vitro digestion time.

The behavior of the standard diet model foods was in between that of the whey protein model foods. Applying 90 simulated peristaltic contractions to the cube of standard diet strong gel (Figure 7.16 A) resulted in some small particles being broken off the main cubical particle immobilized by the holding rig, as quantified by PV_{90} values between 37.9 % and 61.2 %, depending on the static in vitro digestion time. Values of PV_{90} for the standard diet weak gel (Figure 7.16 B) ranged between 1.1 % and 9.6 %. For any static in vitro digestion time, PV_{90} for the standard diet strong gel was significantly greater ($p < 0.05$) than PV_{90} for the standard diet weak gel at the corresponding static in vitro digestion time.

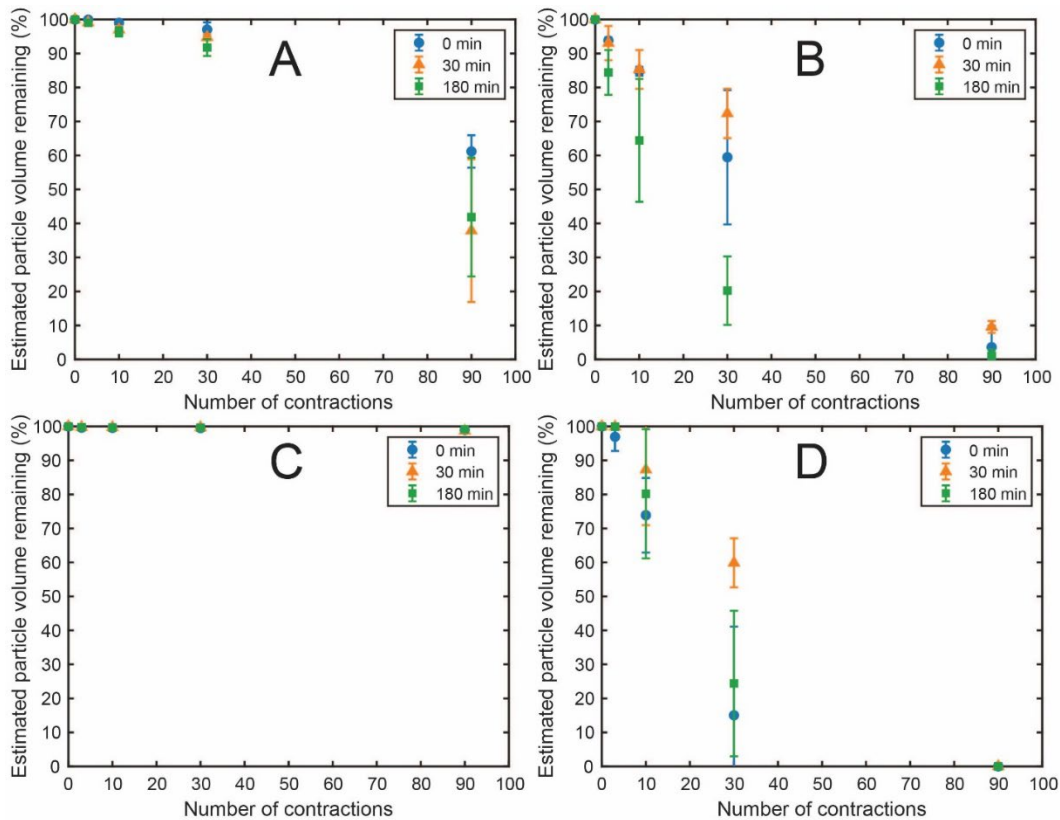


Figure 7.16. Estimated percentage of total particle volume that remained on the holding rig after varying numbers of contractions in the peristaltic simulator (*PVC*) for the standard diet strong gel (A), standard diet weak gel (B), whey protein strong gel (C), and whey protein weak gel (D). All points represent the mean with error bars as the standard deviation ($n=3$).

For each treatment, which consisted of a given combination of type of model food, static *in vitro* digestion time, and number of contractions, the resulting particles were imaged and then classified as either debris, partially damaged, or mostly intact, based on the same size criteria used to classify particles resulting from breakdown in the HGS. Large particles (size > 170 μm^2) that broke away from the cube on the holding rig during the experiment were classified as “mostly intact” for agreement with the terminology used to analyze particle breakdown from experiments in the HGS, however, it should be noted that these particles broke away from the cube that was placed on the holding rig and therefore

resulted from a breakdown event, despite their large size. Additionally, the use of a two-dimensional image analysis method has the limitation of not being able to quantify the three-dimensional volume of particles. The percentage of all particles for a given treatment belonging to each class (% of total), the number of particles in each class (N), and the average size of particles in each class (\bar{x}) were analyzed using three-factor ANOVA with the type of model food, static in vitro digestion time, and number of simulated peristaltic contractions as factors. The significance levels of main effects and their interactions are given in Table 7.6.

For all outcome variables except for the number of mostly undamaged particles, labeled as “mostly undamaged: N” in Table 7.6.), the type of model food was found to be significant ($p < 0.01$). The static in vitro digestion time did not significantly influence any outcome variable except for the contribution of mostly undamaged particles to the total. The number of simulated peristaltic contractions significantly ($p < 0.05$) affected all outcome variables, which reflects the progressive breakdown of cubes of model food that occurred over time as simulated peristaltic contractions were applied. Mean values from three replicate experiments for all outcome variables (% of total, N, \bar{x}) along with results from post-hoc analysis are shown in Table 7.7. In Table 7.7, the sum of debris: % of total, partially damaged: % of total, and mostly undamaged: % of total equate to 100% for each treatment, reflecting that all particles from image analysis were placed into one of the three classes.

Table 7.6. Significance of factors used in three-factor ANOVA to analyze results from trials in the peristaltic simulator. Main effects consisted of the type of model food (F), static in vitro digestion time (T), and number of simulated peristaltic contractions (C). Interaction effects consisted of the interaction of the type of model food and the static in vitro digestion time (F*T), the type of model food and the number of simulated peristaltic contractions (F*C), the interaction of static in vitro digestion time and the number of simulated peristaltic contractions (T*C), and the three-way interaction of the type of model food, static in vitro digestion time, and the number of simulated peristaltic contractions (F*T*C). Significant factors were indicated as $p < 0.01$ or $p < 0.05$. NS indicated that the factor was not significant. Variables labeled as “Debris: N”, “Partially damaged: N”, and “Mostly undamaged: N” indicate the number of particles in each respective class.

Outcome variable	Factor used in three-factor ANOVA						
	Type of model food (F)	Static in vitro digestion time (T)	F*T	Number of simulated peristaltic contractions (C)	F*C	T*C	F*T*C
Debris: % of total	<0.01	NS	<0.01	<0.01	<0.01	NS	<0.05
Debris: N	<0.01	NS	NS	<0.01	<0.01	NS	NS
Debris: \bar{x}	<0.01	NS	NS	<0.01	<0.01	NS	0.0575
Partially damaged: % of total	<0.01	NS	<0.01	<0.01	<0.01	NS	<0.01
Partially damaged: N	<0.01	NS	NS	<0.01	<0.01	NS	<0.05
Partially damaged: \bar{x}	<0.01	NS	<0.05	<0.01	<0.01	<0.05	<0.01
Mostly undamaged: % of total	<0.01	<0.01	<0.01	<0.01	<0.01	<0.01	<0.01
Mostly undamaged: N	NS	NS	NS	<0.01	<0.01	<0.01	NS
Mostly undamaged: \bar{x}	<0.01	NS	NS	<0.05	NS	NS	NS

Table 7.7. Characteristics of particles resulting from application of simulated peristaltic contractions to cubical particles of model food in the peristaltic simulator. For each treatment, consisting of a combination of type of model food (standard diet strong gel, standard diet weak gel, whey protein strong gel, whey protein weak gel), static in vitro digestion time (0, 30, or 180 min), and number of applied contractions (3, 10, 30, 90, or remainder), particles were classified as either debris, partially damaged, or mostly undamaged. The percentage of particles in each class (% total) were reported on an 2D area basis, as well as the number of particles in the respective class, N, and their average size, \bar{x} (mm²). For each treatment, values given are the average of three replicate experiments \pm the standard deviation of those three replicates. Each replicate consisted of results from 5 cubes of model food subjected to simulated peristalsis, each one attached to an individual holding rig. Thus, if in each column (abc) or each row (zyx) with different letters represent significant differences ($p < 0.05$) between means. For variables where the interaction effect of type of model food and number of applied contractions was not significant ($p > 0.05$), post-hoc tests were not conducted. If no particles in a given class were present for a given treatment (which consisted of a combination of type of model food, static in vitro digestion time, and number of contractions), the percent of the total area made up of particles in that class was 0% with $N = 0$, however, their average size was indicated by NA. For example, application of 3 simulated peristaltic contractions to the standard diet strong gel did not result in any particles breaking away from the cube on the holding rig that were large enough to be classified as mostly intact, therefore their percent of total area was 0%, their number, N, was 0, and their average size was indicated by NA.

Digestion time (min)	Number of contractions	Standard diet strong gel				Standard diet weak gel				Whey protein strong gel				Whey protein weak gel			
Debris: particles < 4.0 mm²																	
0	Contractions	% of total	Number of particles (N)	\bar{x} (mm ²)	% of total	Number of particles (N)	\bar{x} (mm ²)	% of total	Number of particles (N)	\bar{x} (mm ²)	% of total	Number of particles (N)	\bar{x} (mm ²)				
	3	100±0 ^{ax}	421±81 ^b	0.04±0.03 ^y	45.6±2.8 ^{ay}	1377±250 ^b	0.18±0.01 ^{ax}	78.7±12.3 ^{ay}	477±40 ^b	0.07±0.02 ^y	54.6±19.3 ^{ay}	1777±1390	0.06±0.01 ^{ay}				
	10	85.3±14 ^{ab,zy}	1147±516 ^b	0.08±0.05 ^{zy}	62.1±7 ^{a,zy}	6310±2423 ^a	0.13±0.01 ^{ab,z}	100±0 ^{ax}	689±200 ^b	0.04±0.01 ^y	20.9±19.4 ^{ab,x}	3103±1440	0.07±0.03 ^{a,zy}				
	30	81.8±4.8 ^{ab,zy}	4274±2799 ^{b,zy}	0.08±0 ^z	55.7±8.3 ^{ay}	12804±6562 ^{ax}	0.08±0 ^{b,z}	100±0 ^{ax}	1204±178 ^{b,x}	0.02±0 ^y	13.5±18.8 ^{b,x}	4241±3415 ^z	0.1±0.03 ^{ax}				
	90	69.4±6.5 ^{ab,zy}	17231±6748 ^{ax}	0.06±0 ^{zy}	46.8±11.8 ^{ay}	16105±5370 ^{ax}	0.09±0.01 ^{ab,z}	99.5±0.9 ^{ax}	22368±5276 ^{ax}	0.02±0 ^{yx}	8.1±33.5 ^{b,x}	3206±5536 ^y	0.03±0.05 ^{b,x}				
	Remainder	7.8±0.3 ^c	1936±439 ^b	0.05±0.01 ^z	4.3±18.1 ^b	176±288 ^b	0.03±0.06 ^{c,zy}	18.8±0.8 ^b	5744±2205 ^b	0.05±0 ^z	0±0 ^b	10±0	0±0 ^{b,y}				
Partially damaged: 4.0 mm² < particles < 170.0 mm² (% of total, N, \bar{x})																	
0	Contractions	% of total	Number of particles (N)	\bar{x} (mm ²)	% of total	Number of particles (N)	\bar{x} (mm ²)	% of total	Number of particles (N)	\bar{x} (mm ²)	% of total	Number of particles (N)	\bar{x} (mm ²)				
	3	0.0±0.0 ^y	0±0	NA	54.4±2.8 ^z	15±3 ^b	20.5±6.0 ^b	21.3±12.3 ^{zy}	1±0	10.2±9.6	45.4±19.3 ^{ab,z}	5±6 ^b	22.1±10.3 ^b				
	10	14.7±14.0 ^y	3±2	11.7±7.1 ^y	37.9±7.0 ^{zy}	38±9 ^{ab}	13.6±3.2 ^{b,y}	0.0±0.0 ^y	0±0	NA	71.3±19.4 ^{ax}	19±13 ^{ab}	43.1±12.3 ^{ax}				
	30	18.2±4.8 ^y	11±6 ^y	6.8±2.0 ^y	30.6±8.3 ^y	25±8 ^{ab,zy}	20.6±2 ^{b,zy}	0.0±0.0 ^y	0±0 ^y	NA	75.5±18.8 ^{ax}	52±33 ^{ax}	35.4±12.2 ^{ab,z}				
	90	13.0±6.5 ^{zy}	30±18 ^{zy}	7.2±1.5	44.2±11.8 ^z	59±21 ^{ax}	23.9±5.0 ^b	0.5±0.9 ^y	0±1 ^y	7.3±0.0	19.3±33.5 ^{bc,zy}	26±44 ^{ab,zy}	24.1±0.0 ^{ab}				
	Remainder	0.2±0.3	0±1	6.0±0.0 ^y	10.5±18.1	0±1 ^b	118.2±0.0 ^{ax}	1.0±0.8	2±1	6.1±2.0 ^y	0.0±0.0 ^c	0±0 ^b	NA				
Mostly intact: 170.0 mm² < particles (% of total, N, \bar{x})																	

0	Contractio ns	% of total	Number of particles (N)	\bar{x} (mm ²)	% of total	Number of particles (N)	\bar{x} (mm ²)	% of total	Number of particles (N)	\bar{x} (mm ²)	% of total	Number of particles (N)	\bar{x} (mm ²)
	3	0.0±0.0 ^b	0±0	NA	0.0±0.0	0±0	NA	0.0±0.0 ^b	0±0	NA	0.0±0.0	0±0	NA
	10	0.0±0.0 ^b	0±0	NA	0.0±0.0	0±0	NA	0.0±0.0 ^b	0±0	NA	7.8±13.6	0±1	200.7±0.0
	30	0.0±0.0 ^b	0±0	NA	13.7±13.1	2±2	189.1±7.7	0.0±0.0 ^b	0±0	NA	11±19	2±3	215.0±0.0
	90	17.5±16.5 ^b	1±1	226.7±19.2	9.0±7.8	2±2	197.3±2.4	0.0±0.0 ^b	0±0	NA	5.9±10.2	1±2	187.9±0.0
	Remainder	92.0±1.5 ^{a,z}	4±1	235.0±2.3	18.5±32.1 ^y	0±1	209.7±0.0	80.3±5.1 ^{a,z}	5±0	235.6±7.8	0.0±0.0 ^y	0±0	NA
Debris (particles < 4.0 mm², %)													
30	Contractio ns	% of total	Number of particles (N)	\bar{x} (mm ²)	% of total	Number of particles (N)	\bar{x} (mm ²)	% of total	Number of particles (N)	\bar{x} (mm ²)	% of total	Number of particles (N)	\bar{x} (mm ²)
	3	57.9±36.9 ^{a,z} _y	514±191 ^b	0.07±0.02 ^y	64.3±13.4 ^{a,z,y}	3089±516 ^c	0.2±0.01 ^{a,z}	57.1±23.2 ^{b,y}	284±30 ^b	0.04±0.01 ^y	92.9±6.2 ^{a,z}	977±471	0.05±0.01 ^{a,y}
	10	47.9±15.2 ^{a,y}	1227±756 ^b	0.11±0.02 ^{z,y}	70.4±11 ^{a,z,y}	8415±1676 ^{b,c}	0.13±0.01 ^{ab,z}	100±0 ^{a,z}	404±93 ^b	0.04±0 ^x	33.2±22.6 ^{b,c,y}	2446±676	0.04±0 ^{a,z,x}
	30	78.7±5.3 ^{a,z,y}	5645±2510 ^{b,y}	0.08±0.01 ^z	78.4±19 ^{a,z,y}	20327±14359 ^{a,z}	0.08±0.01 ^{b,z}	95.3±8.2 ^{a,z}	1031±406 ^{b,y}	0.02±0 ^y	40.9±37.7 ^{b,y}	6473±2083, y	0.04±0.02 ^{a,z,y}
	90	47.2±5.8 ^{a,y}	20044±10907 ^a	0.06±0 ^y	47.7±9.8 ^{a,y}	17485±3810 ^{ab}	0.09±0.01 ^{b,z}	96.9±4.7 ^{a,z}	20753±9900 ^a	0.02±0 ^y	20.4±3.3 ^{b,c,y}	9787±3229	0.06±0.02 ^{a,z,y}
	Remainder	5.6±2 ^c	1043±520 ^b	0.04±0.01 ^z	6.3±1.6 ^b	312±138 ^c	0.06±0.01 ^{b,z}	20.2±4.8 ^c	6747±2380 ^b	0.05±0 ^z	0±0 ^c	10±0	0±0 ^{b,y}
Partially damaged particles (4.0 mm² < particles < 170.0 mm², %)													
30	Contractio ns	% of total	Number of particles (N)	\bar{x} (mm ²)	% of total	Number of particles (N)	\bar{x} (mm ²)	% of total	Number of particles (N)	\bar{x} (mm ²)	% of total	Number of particles (N)	\bar{x} (mm ²)
	3	42.1±36.9 ^{ab}	5±4 ^b	12.1±8.3	35.7±13.4	30±19 ^{ab}	12.8±2.4	42.9±23.2	1±1	7.7±3.3	7.1±6.2 ^b	1±1 ^b	6.4±.07 ^b
	10	52.1±15.2 ^{a,z}	13±6 ^{ab}	10.4±2.1 ^y	29.6±11 ^{z,y}	38±5 ^{ab}	11.5±3.8 ^y	0.0±0.0 ^y	0±0	NA	48.4±16.1 ^{a,z}	5±3 ^b	43.9±26.6 ^{a,z}
	30	21.3±5.3 ^{ab}	12±3 ^{ab}	9.3±2.3	16.0±9.4	27±14 ^{ab}	12.3±6.1	4.7±8.2	0±1	4.7±0.0	33.2±30.9 ^{ab}	25±35 ^{ab}	24.2±2.1 ^{ab}
	90	28.5±9.7 ^{ab,z,y}	49±26 ^{a,z}	14.6±5.8	27.7±7.3 ^{z,y}	62±28 ^{a,z}	16.1±5.8	3.1±4.7 ^y	1±1 ^y	11.5±8	61.0±11.4 ^{a,z}	58±24 ^{a,z}	31.4±4.7 ^a

	Remainder	0.7±1.3 ^b	1±2 ^b	5.7±0.0	0.0±0.0	0±0 ^b	NA	0.9±0.8	2±2	6.4±2.8	0.0±0.0 ^b	0±0 ^b	NA
Mostly intact particles (170.0 mm² < particles, %)													
30	Contractions	% of total	Number of particles (N)	\bar{x} (mm²)	% of total	Number of particles (N)	\bar{x} (mm²)	% of total	Number of particles (N)	\bar{x} (mm²)	% of total	Number of particles (N)	\bar{x} (mm²)
	3	0.0±0.0 ^b	0±0	NA	0.0±0.0 ^b	0±0	NA	0.0±0.0 ^b	0±0	NA	0.0±0.0	0±0	NA
	10	0.0±0.0 ^b	0±0	NA	0.0±0.0 ^b	0±0	NA	0.0±0.0 ^b	0±0	NA	18.5±32	1±1	245.2±0
	30	0.0±0.0 ^b	0±0	NA	5.6±9.7 ^b	1±1	197.6±0	0.0±0.0 ^b	0±0	NA	25.9±37.8	2±2	219.9±12.7
	90	24.3±15.5 ^b	3±2	207.9±11	24.5±3 ^b	5±2	187±5.7	0.0±0.0 ^b	0±0	NA	18.6±14.6	2±2	201.8±21.6
	Remainder	93.7±3.1 ^{a,z}	3±1	226.4±5.1	93.7±1.6 ^{a,z}	1±1	204.2±3.9	78.9±5.4 ^{a,z}	5±0	249.6±7.1	0.0±0.0 ^y	0±0	NA
Debris (particles < 4.0 mm², %)													
180	Contractions	% of total	Number of particles (N)	\bar{x} (mm²)	% of total	Number of particles (N)	\bar{x} (mm²)	% of total	Number of particles (N)	\bar{x} (mm²)	% of total	Number of particles (N)	\bar{x} (mm²)
	3	44.7±19.7 ^{a,y}	560±146 ^b	0.06±0.02 ^y	46.6±16.5 ^{a,y}	4180±2138 ^b	0.19±0.05 ^{a,z}	89.5±10.4 ^{a,z}	576±69 ^b	0.06±0.02 ^y	92.5±13 ^{a,z}	571±134	0.05±0.01 ^{a,y}
	10	52±4.3 ^{a,z,y}	1429±470 ^b	0.11±0.01 ^{z,y}	56.1±11.8 ^{a,z,y}	9342±2895 ^{ab}	0.13±0.01 ^{a,z}	85.5±13.3 ^{a,z}	514±106 ^b	0.04±0.01 ^x	34.5±42.8 ^{bc,y}	1883±144	0.04±0.0 ^{a,y,x}
	30	65.8±2.7 ^{a,z,y}	5691±1420 ^{b,y}	0.08±0.01 ^z	52.9±4 ^{a,y,x}	16110±7361 ^{a,z}	0.11±0.01 ^{a,z}	100±0 ^{a,z}	624±146 ^{b,y}	0.02±0 ^y	18.8±11.9 ^{bc,x}	5651±1693 ^y	0.06±0.01 ^{a,z,y}
	90	55.8±1.8 ^{a,y}	25163±10048 ^{a,z}	0.07±0.01 ^{z,y}	55.2±16 ^{a,y}	6383±2773 ^{ab,y}	0.12±0.01 ^{a,z}	98.2±2 ^{a,z}	13230±9447 ^{a,y}	0.02±0 ^y	13.9±13.9 ^{bc,x}	4023±4515 ^y	0.04±0.04 ^{a,z,y}
	Remainder	6.5±0.8 ^b	1202±136	0.04±0.01 ^z	4.9±8.5 ^b	105±165 ^b	0.03±0.04 ^{b,z,y}	20.6±3.4 ^b	6637±1829 ^{ab}	0.05±0 ^z	0±0 ^c	10±0	0±0 ^{b,y}
Partially damaged particles (4.0 mm² < particles < 170.0 mm², %)													
180	Contractions	% of total	Number of particles (N)	\bar{x} (mm²)	% of total	Number of particles (N)	\bar{x} (mm²)	% of total	Number of particles (N)	\bar{x} (mm²)	% of total	Number of particles (N)	\bar{x} (mm²)
	3	55.3±19.7 ^{a,z}	3±2 ^{b,y}	16.3±5.3	53.4±16.5 ^{z,y}	48±13 ^{ab,z}	17.8±3.4 ^b	10.5±10.4 ^{yx}	1±1 ^y	6.9±3.4	7.5±13.0 ^{bx}	0±1 ^y	7.2±0 ^b
	10	48.0±4.3 ^a	14±4 ^{b,y}	11.0±0.9	40.3±11.1	64±14 ^{a,z}	14.1±4.6 ^b	14.5±13.3	1±1 ^y	6.1±2.2	27.0±33.1 ^{ab}	5±8 ^y	19.5±15.8 ^{ab}

	30	34.2±2.7 ^{ab,y}	26±10 ^{ab,yx}	9.9±0.7 ^y	30.6±14.1 ^y	65±40 ^{az}	17.4±6.8 ^{by}	0.0±0.0 ^y	0±0 ^x	NA	49.2±18.4 ^{az}	24±12 ^{yx}	40.0±8.3 ^{az}
	90	33.8±3.9 ^{ab,zy}	62±32 ^{az}	17.1±1.3 ^{zy}	40.9±13.4 ^{zy}	23±8 ^{bc,zy}	22.9±6 ^{b,zy}	1.8±2 ^y	1±1 ^y	5.7±1.9 ^y	52.7±46.2 ^{az}	26±24 ^{zy}	34.8±8.5 ^{az}
	Remainder	1.4±2.4 ^b	1±2 ^b	9.6±0.0 ^y	28.4±49.2	1±1 ^c	65.3±0 ^{az}	1.3±1.2	3±3	8.7±4.3 ^y	0.0±0.0 ^b	0±0	NA
Mostly intact particles (170.0 mm² < particles, %)													
180	Contractio ns	% of total	Number of particles (N)	\bar{x} (mm²)	% of total	Number of particles (N)	\bar{x} (mm²)	% of total	Number of particles (N)	\bar{x} (mm²)	% of total	Number of particles (N)	\bar{x} (mm²)
	3	0.0±0.0 ^b	0±0	NA	0.0±0.0	0±0	NA	0.0±0.0 ^b	0±0	NA	0.0±0.0 ^b	0±0	NA
	10	0.0±0.0 ^{b,y}	0±0	NA	3.6±6.3 ^y	0±1	183.1±0	0.0±0.0 ^{b,y}	0±0	NA	38.5±47.5 ^{az}	2±2	197.1±6.6
	30	0.0±0.0 ^b	0±0	NA	16.4±11.9	3±2	184.7±12.2	0.0±0.0 ^b	0±0	NA	32±29.3 ^{ab}	4±4	221.9±8.8
	90	10.5±5.7 ^b	1±1	212.0±20.4	3.9±6.7	0±1	202.4±0	0.0±0.0 ^b	0±0	NA	0.0±0.0 ^b	0±0	NA
	Remainder	92.1±3.1 ^{az}	3±1	223.5±21.1	0.0±0.0 ^y	0±0	NA	78.1±4.6 ^{az}	5±0	234.7±6.5	0.0±0.0 ^{b,y}	0±0	NA

From the variables shown in Table 7.7, the manner of breakdown experienced by each model food due to contractions applied by the peristaltic simulator can be determined. For the standard diet strong gel with no static in vitro digestion (0 min), the percentage of all particles consisting of debris significantly decreased ($p < 0.05$) from an initial value of $100 \pm 0\%$ after 3 contractions to a final value of $69.4 \pm 6.5\%$. This was accompanied by an increasing percentage of mostly intact particles, which significantly increased ($p < 0.05$) from an initial value of $0 \pm 0\%$ after 3 contractions to a value of $92.0 \pm 1.5\%$. This reflects how the progressive application of simulated peristaltic contractions broke away small particles from the cubes of the standard diet strong gel that was immobilized on the holding rig but did not completely break them away from the rig as evidenced by the presence of a remainder. However, as the number of peristaltic contractions applied to the cubes increased, the degree of breakdown intensified, as evidenced by the number and sizes of particles breaking away from the cubes increasing. For example, the number of particles classified as debris that broke away from the standard diet strong gel with no static in vitro digestion was 421 ± 81 after 3 contractions, which significantly increased ($p < 0.05$) to $17,231 \pm 6,748$ after 90 contractions. The numbers of partially damaged and mostly intact particles demonstrated the same trend, showing that the standard diet strong gel model food experienced incremental breakdown that increased with the number of simulated peristaltic contractions. The cubes of the standard diet strong gel were not crushed by the initial simulated peristaltic contractions, as demonstrated by the absence of particles large enough to be classified as mostly intact until the sample taken at 90 contractions. These particles could have broken away from the cubes on the holding rig between the application of 30 and 90 contractions, suggesting that at least 30 simulated peristaltic contractions were needed to weaken the standard diet strong gel cubes to the point that the entire cube could be fractured, resulting in the appearance of larger particles in the image analysis results from the sample subjected to 90 contractions. After 90 contractions had been applied, only part of the cubes remained on the holding rig, as evidenced by PV_{90} values between 37.9% and 61.2%, depending on the static in vitro digestion time.

For the standard diet weak gel, particles large enough to be classified as mostly intact were first present in the sample to which 10 contractions had been applied, indicating their appearance between 3 and 10 contractions. This suggests that the standard diet weak gel began to break down soon after the first simulated peristaltic contractions were applied. This can be visualized in Figure 7.16 B, where the estimated percent of total volume of the cubes remaining on the holding rig (PV_c) was found to decrease immediately for the standard diet weak gel after the application of the first simulated peristaltic contractions. The differences in texture and fracture properties between the standard diet strong and weak gels may have influenced their breakdown in the peristaltic simulator so that particles large enough to be classified as mostly intact were produced for the standard diet weak gel between 3 and 10 contractions, whereas such particles first appeared between 30 and 90 contractions for the standard diet strong gel. In support of this finding, the number of particles classified as debris (N) was generally greatest for the standard diet weak gel in the sample imaged after 30 simulated peristaltic contractions. For example, there were $20,327 \pm 14,359$ particles classified as debris for the standard diet weak gel subjected to 30 min static in vitro digestion followed by 30 simulated peristaltic contractions, which was significantly greater ($p < 0.05$) than the number of particles classified as debris after only 3 contractions were applied ($3,089 \pm 516$), suggesting that the greatest rate of breakdown for this model food occurred between 10 and 30 contractions. On the other hand, the standard diet strong gel demonstrated the greatest number of particles classified as debris in the sample that was taken after application of 90 simulated peristaltic contractions, suggesting that its greatest rate of breakdown occurred between the application of 30 and 90 contractions. Observations of the experiment indicated that when the cubes experience fracture events resulting in large particles being broken off the main cube a high number of small particles were also generated during the breakage event. In general, results showed that the standard diet strong gel and standard diet weak gel experienced incremental breakdown as the number of contractions increased, with significant breakage events that resulted in the appearance of large particles as well as high numbers of particles classified as debris that had broken away from the original cubes occurring after 3 contractions for the standard diet weak gel and after 30 contractions for the standard diet strong gel.

The standard diet weak gel demonstrated a significantly lower ($p < 0.05$) value of the percent of total particles made up of debris (debris, % total) for the sample that remained on the holding rig (remainder) when compared to the sample after intermediate numbers of simulated peristaltic contractions. For example, the percentage of particles represented by debris significantly decreased ($p < 0.05$) from $45.6 \pm 2.8\%$ after 3 contractions to $4.3 \pm 18.1\%$ for the sample that consisted of the portion of the original cubes that remained attached to the holding rig after 90 contractions. This is because the remainder of the cubes on the holding rig after 90 simulated peristaltic contractions consisted of a larger particle, as compared to the smaller pieces that were broken away during application of intermediate numbers of simulated peristaltic contractions. This effect was also demonstrated by the other model foods and explains the significant differences between the value of the percent of total particles made up of debris for intermediate numbers of simulated peristaltic contractions and its value for the sample that remained on the holding rig (remainder), as shown in Table 7.7.

The whey protein strong gel experienced little breakdown due to contractions applied by the peristaltic simulator, as evidenced by values of PV_{90} that ranged between 98.7 % and 99.1 %, indicating that roughly 99 % of the initial volume of the cubes that was present on the holding rig remained on the rig after 90 contractions. This is supported by the finding that the mostly intact particles appeared only in the portion of the cubes that remained attached to the holding rig at the end of the experiment. Particles classified as partially damaged (between 4.0 mm^2 and 170 mm^2) were rarely present, with a maximum of one such particle being present in a sample from the whey protein strong gel between 3 to 90 contractions. Observations suggested that particles classified as partially damaged originated from the corners of the original cubes attached to the holding rig, which were occasionally broken away by the simulated peristaltic contractions. The whey protein strong gel experienced less breakdown during the experiment than the whey protein weak gel or either of the standard diet model foods. Additionally, there was not a certain number of simulated peristaltic contractions that could be identified after which the standard diet strong gel began to experience large-scale breakage events, in contrast to the other model foods that demonstrated large-scale breakage events generating particles classified as mostly undamaged

(large particles) as well as high numbers of particles classified as debris (ca. 3-10 contractions for the standard diet weak gel and ca. 30-90 contractions for the standard diet strong gel). This lack of a threshold number of simulated peristaltic contractions after which breakdown intensified was evidenced by the high and relatively constant contribution of debris to the total group of particles that resulted from a given number of peristaltic contractions for the whey protein strong gel. For example, particles classified as debris represented between $78.7 \pm 12.3\%$ and $100 \pm 0\%$ of the total, in the samples that were taken after intermediate numbers of simulated peristaltic contractions for the whey protein strong gel with zero min static in vitro digestion time. These particles had size of ca. 0.02 mm^2 . It is hypothesized that these particles were removed from the outer surface of the cubes of the whey protein strong gel during simulated peristalsis, however, it should be noted that these particles represented only ca. 1% of the total volume of the cubes after 90 simulated peristaltic contractions were applied (PV_{90}), as shown in Figure 7.16 C.

The whey protein weak gel, on the other hand, experienced significant breakdown in the peristaltic simulator as evidenced by PV_{90} values that were always 0%, indicating that the entire cubes of model food had been broken away from the holding rig by the application of 90 simulated peristaltic contractions. Breakdown of the standard diet weak gel model food was evident after the application of 10 simulated peristaltic contractions, with both partially damaged and mostly intact particles being present in the sample, in particular for the cubes subjected to static in vitro digestion of 180 min (Table 7.7). In a manner similar to the standard diet model foods, the numbers of particles classified as partially damaged or as debris generally reached a maximum in the samples that were subjected to 30 simulated peristaltic contractions. For example, there were 52 ± 33 particles classified as partially damaged for the whey protein weak gel subjected to static in vitro digestion for 0 min, which was significantly greater ($p < 0.05$) than the number of such particles present after the application of 3 peristaltic contractions (5 ± 6).

For the whey protein weak gel, particles large enough to be classified as mostly undamaged were first present in samples collected after 10 simulated peristaltic contractions. This suggests that the whey protein weak gel was weakened by the initial simulated peristaltic contractions and began to experience

bulk fragmentation of the cubes attached to the holding rig after ca. 3 simulated peristaltic contractions had been applied. This was similar to the breakdown experienced by the standard diet weak gel and can be visualized in Figure 7.16, where the slope of the graph can be taken as an estimate of the rate at which the cubes of model food was broken down. For the standard diet strong gel (Figure 7.16 A), the greatest rate of breakdown occurred between 30 and 90 contractions, suggesting that roughly 30 contractions were needed to weaken the cubes until large scale breakage could occur, whereas for the standard diet weak gel (Figure 7.16 B) breakdown began after the first peristaltic contractions were applied. The whey protein strong gel did not experience any significant breakdown (Figure 7.16 C), however, the whey protein weak gel (Figure 7.16 D) was weakened by the first 3 contractions, after which rapid breakdown occurred between roughly 10 and 30 contractions.

7.4 Discussion

7.4.1 *Fracture and rheological properties of model foods and relation to their microstructure*

In Chapter 5, one class of model foods based on the Standard American Diet and another class based on whey protein hydrogels were developed and it was demonstrated that the strong and weak gel versions within each class had differing initial texture and softening kinetics during in vitro gastric digestion (Swackhamer et al., 2022).

The standard diet model foods contained the same components (water, corn starch, sucrose, soybean oil, whey protein isolate, pectin, and NaCl), however, the dispersion of the standard diet strong gel was adjusted to pH 5.2 before thermal gelation, whereas the weak gel version was adjusted to pH 2.5. For the standard diet strong gel, CLSM images showed that separate but interpenetrating networks of whey protein and starch were formed (Figure 7.4 E). The whey protein network (Figure 7.4 D) had a similar appearance to particulate whey protein gels formed at pH 5.2 in previous studies (Lambrecht et al., 2019). The formation of separate but interpenetrating networks of whey protein and starch has been found by previous researchers using co-gels of potato starch and whey protein that were visualized using a staining protocol of rhodamine B and FITC (Lavoisier and Aguilera, 2019). In contrast, the standard diet weak gel consisted of a single network which was comprised of both protein and starch (Figure 7.4 H).

The isoelectric point of β -lactoglobulin is ca. 5.2 (Beaulieu et al., 2001) and thus for the whey protein strong gel dispersion which had a pH value close to the isoelectric point, protein-protein interactions would be favored (Ravindra et al., 2004), which could have promoted the formation of a whey protein network that excluded starch and resulted in the formation of the two, interpenetrating networks. In the case of the whey protein weak gel, it is hypothesized that the formation of the combined protein-starch solid phase was due to electrostatic complexation resulting from favorable interactions between whey proteins and starch molecules as the pH of the weak gel dispersion was lowered towards its endpoint (pH 2.5). At this pH, whey proteins would become increasingly positively charged (Wu et al., 2020), entangling with starch in a combined protein-starch solid phase and preventing the formation of separate networks. The whey protein weak gel dispersion attained a higher viscosity than that of the standard diet strong gel (Figure 7.10), as quantified by a significantly greater ($p < 0.05$) consistency index (Equation 7.1, 9.21 ± 0.50 vs 4.87 ± 0.04 , respectively). It is hypothesized that this was in part due to protein-starch interactions increasing at the low pH of the dispersion, in addition to acid-induced gelation of whey proteins (Kharlamova et al., 2018). The formation of a whey protein network during thermal gelation occurs in a two-step process consisting of denaturation followed by aggregation of whey proteins, with the aggregation step commonly assumed to be rate-limiting (Quevedo et al., 2021). The higher viscosity of the standard diet strong gel as compared to the weak gel when in the form of dispersions could have reduced the mobility of protein molecules (Zhu et al., 2018), hindering the aggregation of denatured whey proteins and leading to the formation of a weaker gel matrix.

In Chapter 5 it was shown that the initial hardness of the standard diet strong gel was significantly greater ($p < 0.05$) than the initial hardness of the standard diet weak gel (18.7 ± 2.9 N vs 9.0 ± 1.1 N, respectively) (Swackhamer et al., 2022). In the present study, the toughness of the standard diet model foods was quantified using wire cutting, and it was found that the average toughness across all in vitro digestion times was significantly greater ($p < 0.05$) for the standard diet strong gel than for the standard diet weak gel. Since the macronutrient composition of these model foods was the same, these results suggest that the presence of separate, interpenetrating starch and whey protein networks led to greater

resistance of the standard diet strong gel to compression as well as to fracture as compared to the standard diet weak gel. From curve fitting the frequency sweep data from small strain oscillatory rheology it was found that the values of B' and B'' of the standard diet strong gel were significantly lower ($p < 0.05$) than those of the standard diet weak gel at all digestion times (Table 7.2). Since this parameter is lower for covalently linked gels than for physically entangled gels (Raei et al., 2018), this finding reflects the microstructural differences observed using CLSM and supports the hypothesis that the whey protein strong gel was comprised of a distinct whey protein network whereas the whey protein weak gel was not.

The whey protein strong and weak gels were both thermally gelled at pH 5.2 but differed in the presence of 0.6% pectin (w/w) in the weak gel version. The effect of pectin was the disruption of the continuous whey protein network of the whey protein weak gel as compared to the strong gel version, as shown in confocal images of the gel microstructure (Figure 7.4 B and Figure 7.4 A, respectively). It is hypothesized that the presence of pectin- β -lactoglobulin coacervates was responsible for the disrupted microstructure of the whey protein weak gel as compared to the whey protein strong gel. Similar findings have been reported by previous researchers, who noted the formation of pectin- β -lactoglobulin coacervates at pH 5.2 (Thongkaew et al., 2015). The isoelectric point of β -lactoglobulin is ca. 5.2 with the pKa of the carboxyl groups of high-methoxyl pectin ca. 2.9-3.3 (Lan et al., 2018). At pH 4.5 the zeta potential of pectin and β -lactoglobulin in aqueous solution were found to be -27.4 mV and +6.4 mV, respectively (Li et al., 2022), leading to strong electrostatic interactions. At the pH of the whey protein model food dispersions (5.2) these electrostatic interactions would not be as favorable. Nevertheless, the formation of pectin- β -lactoglobulin complexes has been reported even at pH 6.0, and it was proposed that electrostatic interactions between the negatively charged pectin and positively charged moieties of whey protein could have been responsible (Lutz et al., 2009). An alternative view has also been proposed, which is that these complexes formed due to hydrophobic interactions that arose between the heat treated whey protein, which reveals hydrophobic amino acid residues upon denaturation, and high methoxyl pectin, with only minor contributions from electrostatic effects (Thongkaew et al., 2015). Flow curves of the whey protein strong and weak gel dispersions showed that the weak gel was more viscous (Figure

7.10) as quantified by a significantly greater flow index ($p < 0.05$). However, this does not necessitate that pectin/whey protein complexes were solely responsible for the difference in viscosity as the concentration of pectin (0.6 %) was greater than the overlap concentration of pectin (ca. 0.3%) (Capel et al., 2006) meaning that pectin-pectin intermolecular interactions could have contributed to the increased viscosity.

Previous researchers have shown that pectin in a concentration of 0.2% formed inclusions in whey protein hydrogels (Munialo et al., 2016). Such inclusions could act as local inhomogeneities in the gel microstructure, leading to stress concentration and reducing the resistance of the matrix to fracture (Gravelle and Marangoni, 2021; Swackhamer and Bornhorst, 2019). In Chapter 5, uniaxial compression was used to analyze the texture of the model foods, with the hardness defined as the maximum force achieved during compression to 50 % engineering strain. It was found that the whey protein strong gel had hardness of 56.7 ± 5.7 N, which was significantly greater ($p < 0.05$) than the hardness of the whey protein weak gel 6.2 ± 1.0 N (Swackhamer et al., 2022). The difference in texture between these two model foods was such that the whey protein strong gel could not be cut using wires, instead requiring the use of knife cutting to allow its fracture properties to be estimated. The initial toughness of the whey protein weak gel was 31.0 ± 3.3 N/m and the initial apparent toughness of the whey protein strong gel was 498.0 ± 38.1 N/m. Together with hardness, these values indicate that pectin diminished the strength of the whey protein weak gel in resistance to both large strain compression and fracture. However, the initial stiffness of the whey protein weak gel model food 564 ± 46 N/m was also much lower than that of the whey protein strong gel ($2,321 \pm 46$ N/m). Since stiffness was defined on the linear elastic region, the stress concentration due to pectin inclusions facilitating fracture was not the only mechanism by which pectin modified the texture of the whey protein weak gel. Similarly, results from small-strain oscillatory rheology (Section 2.6) showed that the whey protein weak gel had a significantly lower ($p < 0.05$) initial value of $G' |_{1\text{Hz}}$ (52.5 ± 2.3 kPa) as compared to the whey protein strong gel (153.3 ± 6.7 kPa). The complexation of pectin and β -lactoglobulin could have reduced the integrity of the protein network that was formed during thermal gelation, leading to the observed disruptions in the microstructure (Figure 7.4 A and B) and leading to the reductions in both large and small strain strength properties of the whey

protein weak gel. As with the standard diet model foods, the greater viscosity of the whey protein weak gel dispersion could have led to slower kinetics of aggregation for proteins during thermal gelation and contributed to a weaker gel. Results from the present study underscore the effect of pectin on the mechanical properties of whey protein hydrogels and suggest that future research may be needed to clarify whether the interactions between whey proteins and high methoxyl pectin at pH values close to the isoelectric point of β -lactoglobulin are due to electrostatic effects or hydrophobic interactions. Additionally, future experiments could determine the effect of viscosity of whey protein dispersions on the strength of the gels that are formed after thermal treatment.

7.4.2 *Changes in fracture and rheological properties of model foods during in vitro digestion*

Fracture and rheological properties of model foods were assessed after 0, 30, or 180 min static in vitro digestion. Wire cutting was used to determine the fracture properties of the standard diet model foods as well as the whey protein weak gel and knife cutting was used to estimate the fracture properties of the whey protein strong gel. After longer static in vitro digestion times, the force on the wire cutting attachment during the steady crack elongation phase of wire cutting was lower (Figure 7.5), leading to the finding that static in vitro digestion time significantly influenced ($p < 0.01$) toughness. For the standard diet strong gel, the initial toughness was 20.7 ± 1.6 N/m, and after 180 min static in vitro digestion the toughness was 13.3 ± 0.8 N/m (Table 7.1). Previous researchers found the toughness of mild cheddar cheese to be 20.4 N/m (Goh et al., 2005) and the toughness of 10% (w/w) gelatin gels as ca. 10 N/m (Czerner et al., 2016), values comparable to the initial and final toughness values of the standard diet strong gel model food, respectively. As with toughness, the yield stress of model foods decreased with increasing digestion time (Table 7.1). The yield stress ranged between 44.2 ± 13.6 Pa for the whey protein weak gel after 180 min static in vitro digestion to 91.2 ± 2.9 Pa for the standard diet weak gel after zero min static in vitro digestion (initial value). These values of yield stress are comparable in magnitude to the yield stress obtained using wire cutting by previous researchers for a 20% (w/w) gel of sago starch in water (73.9 Pa) (Gamonpilas et al., 2009).

The elasto-fracture length is indicative of the sizes of flaws in the gel matrix during fracture (Duncan et al., 2020), with higher values suggesting greater dissipation of mechanical energy in the vicinity of the crack tip due to plastic deformation (Mishra et al., 2019). Smaller values of elasto-fracture length may suggest brittle behavior during fracture, whereas larger values suggest greater matrix plasticity (Creton and Ciccotti, 2016; Duncan et al., 2020). Elasto-fracture length was significantly influenced ($p < 0.05$) by static in vitro digestion time, type of model food, and their interaction. However, post-hoc analysis showed that there were no significant differences in the values of elasto-fracture length of the standard diet model foods between any digestion times (Table 7.1). The values of elasto-fracture length for the standard diet model foods ranged between 0.05 mm and 0.08 mm, comparable to previously reported values for the elasto-fracture length of gellan gels which ranged from .025 mm to 0.140 mm (Duncan et al., 2020). In contrast to the standard diet model foods, the whey protein strong and weak gels saw significant ($p < 0.05$) increases in elasto-fracture length during static in vitro digestion of 133 % and 38 %, respectively (Table 7.1). The influence of this parameter can be understood using a mechanical energy balance that has been previously used to describe the fracture process (Luyten et al., 2005) (Equation 7.10):

$$U_s = U_f + U_p + U_d + U_e \quad 7.10$$

Where U_s (J) is the total energy applied to the model food, U_f (J) is fracture energy, U_p (J) is energy dissipated due to plastic deformation, U_d (J) is the energy dissipated by other processes, and U_e (J) is elastically stored strain energy. At steady state there is no accumulation of stored strain energy, and thus the energy applied to the model food by an advancing knife or wire can either be converted to surface energy through fracture or can be allocated to plastic deformation of the material (Williams and Patel, 2016). For the whey protein model foods, the increase in elasto-fracture length during static in vitro digestion suggests an increase in the plasticity of the material, which could be due to water uptake or hydrolysis of the biopolymers that comprise the model food matrix. The effective diffusion coefficient of water in the model food matrix was estimated in Chapter 5, and it was determined that the whey protein model foods had significantly greater ($p < 0.05$) values (ca. $9.5 \cdot 10^{-10} \text{ m}^2/\text{s}$) than the standard diet model

foods (ca. $5.9 \cdot 10^{-10} \text{ m}^2/\text{s}$), which was attributed to differences in the total solids content (40% for the standard diet model foods vs. 20% for the whey protein model foods) (Swackhamer et al., 2022). This suggests that increased diffusivity of water in the model food matrix could have given rise to the significantly increased values of elasto-fracture length during digestion for the whey protein model foods. During digestion water uptake by foods may promote plasticity, increasing resistance to fracture, while hydrolysis by acids and enzymes weakens the matrix, lowering the resistance to fracture. In the case of the standard diet model foods and whey protein weak gel model food, the net effect of these hypothesized mechanisms was a decreased toughness after being subjected to in vitro digestion for any length of time. For the whey protein strong gel, the apparent toughness from knife cutting significantly increased ($p < 0.05$) during digestion, from $498.0 \pm 38.1 \text{ N/m}$ to $684.0 \pm 8.8 \text{ N/m}$. It is hypothesized that these increases were due to an enhanced ability of the model food matrix to dissipate energy through plastic deformation. A follow-up experiment was conducted to determine whether the whey protein strong gel would eventually experience a decrease in toughness during digestion, which was carried out by subjecting it to static in vitro digestion for 24 hours. After this length of time the apparent toughness had decreased to $541.3 \pm 34.7 \text{ N/m}$, which was significantly lower ($p < 0.05$) than its apparent toughness after 180 min static in vitro digestion ($684.0 \pm 8.8 \text{ N/m}$). This suggests that a crossing-over had occurred between 3 h and 24 h static in vitro digestion, during which the hydrolysis of the matrix decreased its intrinsic toughness enough to overcome the increased energy requirement for fracture due to greater plasticity. To further examine this hypothesized effect, the distance that the knife indented into the gel matrix before initiating fracture was quantified. For undigested samples of the whey protein strong gel, it was found that the knife indented $5.4 \pm 0.2 \text{ mm}$ into the matrix before fracture was initiated, which was significantly ($p < 0.05$) lower than the distance of indentation after 180 min digestion ($8.4 \pm .08 \text{ mm}$). After 24 h static in vitro digestion, the knife indented $7.2 \pm 0.5 \text{ mm}$ into the gel before fracture was initiated, which was significantly ($p < 0.05$) greater than the value for undigested samples and significantly ($p > 0.05$) lower than the value for samples subjected to 180 min static in vitro digestion. It is hypothesized that the undigested gel was fractured at small indentation due to a reduced ability to dissipate applied energy in

the vicinity of the knife blade by mechanisms other than fracture. By 180 min static in vitro digestion, the matrix had been softened by water uptake allowing for the blade to indent far into the matrix before fracture was initiated, building up force on the texture analyzer and resulting in the increase in apparent toughness from 0 min to 180 min. However, after 24 h static in vitro digestion the matrix had been weakened by hydrolysis to the extent that fracture was initiated at smaller indentation values despite greater plasticity, leading to the observed decrease in apparent toughness. This may be due to a relatively rapid change in matrix properties due to water uptake relative to the changes occurring due to hydrolysis by pepsin. The increased apparent toughness of the whey protein strong gel and its hypothesized relationship with microstructural changes was summarized in Figure 7.17. Future research on energy partitioning in hydrogels during digestion is needed, particularly if a combination of recoverable energy methods on the linear elastic region and fracture methods at large value of strain are used in tandem.

Rheological property changes of model foods were also quantified at varying static in vitro digestion times. It was determined that both the storage and loss moduli of model foods decreased during digestion, as evidenced by a significant decrease ($p < 0.05$) in $G' | 1 \text{ Hz}$ and $G'' | 1 \text{ Hz}$ for all four model foods from their initial values to their values after 180 min static in vitro digestion (Table 7.2). As the frequency sweeps that were used to analyze rheological properties were carried out on the linear viscoelastic region, these changes indicate softening of the model foods which could have been due to moisture uptake or hydrolysis by digestive enzymes. Similar findings were reported by Nadia et. al. (2021b) who found that the G' and G'' values of digesta decreased over time during digestion.

The slope parameters from the power law model, B' in Equation 7.5 and B'' in Equation 7.6, reflect the influence of oscillatory frequency on the values of G' and G'' . For perfectly elastic materials these parameters are zero, with higher values indicative of frequency dependence due to viscous dissipation of stress (Ikeda and Foegeding, 1999). Typically, covalently-linked gels have lower values of B' and B'' than gels of physically entangled biopolymers (Raei et al., 2018). For all model foods except the whey protein strong gel, B' and B'' experienced a significant change over time during digestion ($p < 0.05$). This suggests that the mechanical response of the whey protein strong gel was less affected by the static in

in vitro digestion than the other model foods. Additionally, the values of B' and B'' for the standard diet weak gel were significantly higher at each time point than the corresponding values for the whey protein strong gel ($p < 0.05$). This may reflect microstructural differences between them, specifically, that the standard diet strong gel contained a continuous whey protein network (Figure 7.4 C) whereas the standard diet weak gel did not (Figure 7.4 F).

The changes in fracture and rheological properties measured in this study could have implications for design of functional foods with targeted physiological benefit. For example, designing a food matrix that resists breakdown in the gastrointestinal system to promote sustained delivery of nutrients could consider the coupled trade-offs between matrix plasticity and matrix hydrolysis that can affect the rheological and fracture property changes of solid foods during digestion.

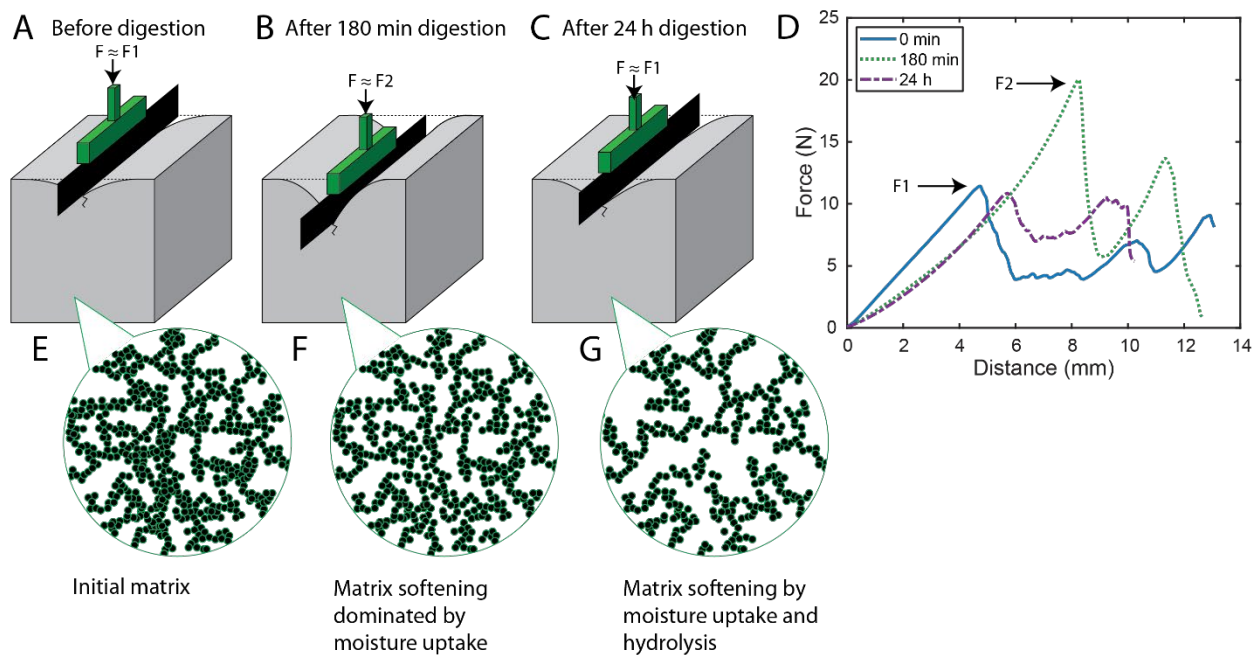


Figure 7.17. Knife cutting was used to estimate the fracture properties of the whey protein strong gel, which was too strong to be cut with wires. Before digestion, the whey protein strong gel had higher stiffness but lower apparent toughness and fracture initiation energy than after 180 min static in vitro digestion (Table 7.1). It was observed that fracture was initiated by the knife blade after a small distance

of indentation at the onset of fracture for the undigested samples (A) but after 180 min static in vitro digestion the cube deformed around the advancing knife blade resulting in a greater distance of indentation at the onset of fracture, greater force achieved at fracture, and greater apparent toughness (B). After 24 h digestion the distance of indentation at the onset of fracture was intermediate to the undigested and 180 min digested samples and the apparent toughness had decreased relative to its value at 180 min (C). These differences were shown using representative force vs distance profiles (D). It is hypothesized that these differences were due to changes in the microstructure of the whey protein strong gel that occurred during static in vitro digestion, namely that the microstructure was strong before digestion (E), after 180 min digestion was softened by moisture with a minor contribution of hydrolysis (F) causing the gel to become less stiff but able to dissipate energy by bending or flow of serum, resulting in the increased apparent toughness between 0 min and 180 min. After 24 h digestion it was hypothesized that the matrix was extensively weakened by hydrolysis (G), leading to the observed decrease in apparent toughness between 180 min and 24 h. Hypothesized microstructures of the whey protein model foods (E, F, and G) were adapted from Schmitt et. al., (2010).

7.4.3 Hypothesized mechanisms of breakdown of model foods in the HGS

Model foods were subjected to static in vitro digestion for either 0 min, 30 min, or 180 min, followed by 90 simulated peristaltic contractions in the HGS, after which particles were separated from liquid digesta using a sieve and assessed using image analysis (Section 2.8). Previous researchers used a similar experimental protocol to elucidate the mechanisms of breakdown of egg white gels with varying initial properties (Somaratne et al., 2020d). The previously identified mechanisms of breakdown for solid foods under simulated peristaltic contractions were erosion, chipping, and fragmentation (Drechsler and Ferrua, 2016), a categorization originally developed in the field of powder technology to understand the breakdown of catalyst beads (Couroyer et al., 2000). Erosion has been defined as the wearing away of the outer surface of the food particle (Guo et al., 2014a). Chipping has been defined as a fracture event resulting in localized damage to a particle, and fragmentation has been defined as a fracture event leading

to generation of a small number of large fragments which have comparable size to the original particle (Papadopoulos and Ghadiri, 1996). Discerning between chips and fragments has been conducted based on size cutoffs relative to the original particle. Drechsler and Ferrua (2016) defined chips as particles between 4 % and 7 % of the 2D area of the original particle as determined using image analysis, whereas Papadopolous and Ghadiri (1996) defined chips as particles retained by a sieve two standard mesh sizes below the largest size that retained the original particles. In either case the size cutoff for particles between chips and fragments was chosen with reference to the size of the original particles due to the mechanistic interpretation of the event that produces a chip, that is, a fracture event that breaks off a piece of the original particle.

In this study, a modified terminology was used, under which particles were classified as either debris, partially damaged, or mostly intact (Section 2.8), reflecting their size relative to the size of the original particles. Particles with two-dimensional area less than 1.7 % of the initial area of the cubes were defined as debris ($\text{debris} < 4 \text{ mm}^2$). Particles from 1.7 % to 71 % of the theoretical area of the initial cubes were defined as partially damaged ($4 \text{ mm}^2 \leq \text{partially damaged} < 170 \text{ mm}^2$). Particles with area equal to or larger than the theoretical area of the initial cubes were defined as mostly intact ($\text{mostly intact} \geq 170 \text{ mm}^2$). After static in vitro digestion followed by treatment in the HGS, the percentage of the total particle area made up of debris was always significantly ($p < 0.05$) greater for the standard diet weak gel than the standard diet strong gel, and likewise always greater for the whey protein weak gel than the whey protein strong gel (Table 7.4). These differences can be visualized in Figure 7.13 in the number of small particles in representative binary images resulting from treatment in the HGS. It is hypothesized that the softer texture of the weak gel version of each model food led to these differences. In a similar way, the percentage of mostly intact particles was always significantly ($p < 0.05$) lower for the standard diet weak gel than the standard diet strong gel, and always significantly lower for the whey protein weak gel than the whey protein strong gel (Table 7.4). For example, after 180 min static in vitro digestion followed by 90 contractions in the HGS, mostly intact particles represented 92.5 ± 0.9 % of the total particle area from digestion of the whey protein strong gel but only 25.1 ± 5.7 % of the total particle area from digestion of

the whey protein weak gel. These differences highlight the effect of pectin on the breakdown of this model food, with 0.6 % pectin (w/w) in the whey protein weak gel leading to more breakdown than the strong gel version that lacked pectin. It is hypothesized that the breakdown of the whey protein strong gel and whey protein weak gel in the HGS were dominated by different mechanisms. Specifically, the treatment of the whey protein strong gel resulted in either mostly intact particles or debris, with less than 0.5 % of the total particle distribution made up of partially damaged particles. The whey protein weak gel, on the other hand, had a contribution of partially damaged particles between 11.5 % and 14.2 %. This shows that the type of breakage events that could generate particles of intermediate size did not occur during application of 90 simulated peristaltic contractions in the HGS for the whey protein strong gel but did occur for the whey protein weak gel. It is hypothesized that erosion was the only significant mechanism contributing to particle breakdown of the whey protein strong gel in the HGS as evidenced by the presence of large, mostly intact particles with a minor contribution of debris, whereas the whey protein weak gel broke down by both erosion, chipping, and fragmentation as evidenced by the presence of partially damaged particles, as can be seen in Figure 7.13 D1 - D3. The hypothesized mechanisms of breakdown of the whey protein strong gel and whey protein weak gel in the HGS are depicted in Figure 7.18 C and D, respectively.

In contrast to the significant changes in α that were observed for the standard diet model foods between different static in vitro digestion times, no statistically significant changes in the values of $x50_1$ or $x50_2$ were observed for the standard diet model foods between different static in vitro digestion times (Table 7.4). This could have been due to a minor contribution of particle swelling for the standard diet model foods. The standard diet model foods experienced a greater moisture uptake during static in vitro digestion as compared to the whey protein model foods (Table 5.11), which may have explained their lack of significant changes in $x50_2$ as compared to the whey protein model foods which demonstrated significant decreases in this parameter after longer static in vitro digestion times.

For the standard diet strong gel, it is hypothesized that its dominant breakdown mechanisms were erosion and chipping as evidenced by the large contribution of mostly intact particles to the total

distribution (77.5 % to 90.3 %), the relatively small contribution of partially damaged particles (ca. 2%) and the presence of debris, which represented 7.3 % to 20.6 % of the total particle area distribution. The standard diet weak gel exhibited similar results to the standard diet strong gel except with a much higher contribution of debris and some larger damaged particles evident in the binary images (Figure 7.13 B2 and B3) indicating the contribution of erosion, chipping, and fragmentation to its particle size reduction.

The effect of static in vitro digestion time varied between the different model foods. For example, the standard diet weak gel had a significantly ($p < 0.05$) lower contribution of mostly intact particles to the total after 180 min static in vitro digestion (39.8 ± 5.4 %) as compared to the value after 0 min static in vitro digestion (57.8 ± 2.3 %) (Table 7.4). Accordingly, the percentage of debris was greater for 180 min static in vitro digestion than for 0 min static in vitro digestion. Overall, these results showed that the standard diet weak gel experienced more particle breakdown in the HGS when it was exposed to a longer duration of static in vitro digestion. On the contrary, the standard diet strong gel exhibited significantly ($p < 0.05$) lower contributions of debris and greater contributions of mostly intact particles to the overall particle size distribution for samples subjected to 180 min static in vitro digestion than for samples subjected to 0 min static in vitro digestion. The whey protein strong gel and whey protein weak gel did not display any trend in the proportion of particles in various classes with respect to static in vitro digestion time.

The model foods in this study had differences in their fracture (Table 7.1) and rheological properties (Table 7.2), and it is hypothesized that these differences in physical properties influenced their breakdown in the HGS. It was proposed that the standard diet strong gel broke down predominantly by erosion with a minor contribution of chipping (Figure 7.18 A), whereas the standard diet weak gel broke down by erosion, chipping, and fragmentation (Figure 7.18 B). The standard diet weak gel demonstrated a greater degree of breakdown than the standard diet strong gel, as evidenced by an increased contribution of debris for samples subjected to longer static in vitro digestion times. Additionally, the standard diet weak gel demonstrated the greatest value of $\Delta [\text{NH}_2]$ out of the four model foods (Table 7.5) which may have been due to its breakdown in the HGS.

For the standard diet strong gel, it is hypothesized that the small particles which resulted from erosion may have been generated near the beginning of static in vitro digestion, perhaps due to particle-particle contact in the shaking water bath leading to erosion of small imperfections at the surface. However, after longer static in vitro digestion time points such eroded particles from the standard diet strong gel may have dissolved and been too small to be retained by the 250 μm sieve that was used to separate particles from liquid digesta, leading to the apparent decrease in the contribution of debris for samples that were subjected to a longer static in vitro digestion. Some small particles resulting from erosion of the standard diet weak gel could also have degraded during static in vitro digestion to sizes too small to be retained on the sieve, however, the standard diet weak gel experienced chipping and fragmentation events leading to generation of new particles during the HGS whereas the standard diet strong gel did not, which may be due to its high values of toughness ($20.7 \pm 1.6 \text{ N/m}$, Table 7.1) or hardness ($18.7 \pm 2.9 \text{ N}$) as compared to the corresponding values for the standard diet weak gel ($14.7 \pm 2.3 \text{ N/m}$ and $9.0 \pm 1.1 \text{ N}$, respectively (Swackhamer et al., 2022).

For the whey protein weak gel, the contributions of particles in different classes to the total distribution were not affected by static in vitro digestion time, suggesting that its hypothesized breakdown mechanisms (erosion, chipping, and fragmentation Figure 7.18 D) were not influenced by the changes in its fracture and rheological properties that occurred during static in vitro digestion. Previous experiments showed that the whey protein weak gel had the lowest initial hardness of the four model foods ($6.2 \pm 1.0 \text{ N}$) (Swackhamer et al., 2022), perhaps indicating that foods with hardness beneath a certain threshold can break down via a combination of all three mechanisms at the onset of static in vitro digestion. The standard diet weak gel had initial hardness of $9.0 \pm 1.1 \text{ N}$ (Swackhamer et al., 2022), and its hypothesized breakdown mechanism in the HGS consisted of erosion but with an increased importance of chipping for samples subjected to a longer static in vitro digestion, which may have been due to the reduced hardness of the particles entering the HGS after longer static in vitro digestion times.

For the whey protein strong gel, the extent of breakdown in the HGS was small and unaffected by static in vitro digestion time with erosion serving as the only hypothesized mechanism of breakdown

(Figure 7.18 C). This model food had the highest values of toughness (Table 7.1), stiffness (Table 7.1), G' (Table 7.2) and hardness (56.2 ± 5.7 N) (Swackhamer et al., 2022), and in general displayed the slowest changes in these parameters out of the four model foods, suggesting that across the different static in vitro digestion times that were studied its particles were too strong to undergo chipping or fragmentation events in the HGS that would result in partially damaged particles or significant amounts of debris. As this model food was designed for high hardness and had slow breakdown kinetics dominated by surface erosion, it could potentially serve in future studies as a benchmark for food products that are slow to break down during digestion.

Based on the breakdown of these four model foods in the HGS, it can be estimated that food particles with hardness values lower than ca. 10 N, such as the standard diet weak gel and whey protein weak gel, may break down by erosion, chipping, and fragmentation at the onset of digestion, whereas particles with hardness ca. 20 N, such as the standard diet strong gel, may break down by erosion and chipping. Food particles with hardness ca. 40 N or greater, such as the whey protein strong gel, would be expected to undergo erosion, but with minimal overall breakdown occurring. Based on the softening profiles of the model foods characterized in Chapter 5, there was not a model food with hardness between ca. 20 N and ca. 40 N at any point during static in vitro digestion, however, the standard diet strong gel with initial hardness ca. 20 N broke down by erosion and chipping whereas the whey protein strong gel, which had a hardness ca. 40 N after 180 min static in vitro gastric digestion broke down only by erosion, thus this region from 20 N to 40 N could be considered a transitional zone between foods highly resistant to breakdown and only experiencing erosion and those that may break down by erosion as well as chipping. The softening profiles of the model foods in addition to their hypothesized mechanisms of breakdown and proposed cutoff values of hardness between these hypothesized mechanisms is shown in Figure 7.18 E.

It should be noted that in this study erosion was considered as a potential mechanism for food breakdown without distinguishing between surface erosion and bulk erosion. However, research in the field of polymer science has defined surface erosion as the incremental wearing away of the surface of a degradable particle when the hydrolysis of the particle matrix occurs quickly in the surrounding

environment (such as by acids and enzymes in the case of digestion) relative to the rate of diffusion of the hydrolytic entities into the particle matrix (Burkersroda et al., 2002; Fu and Kao, 2010). In a limiting case of surface erosion, the matrix in the interior of a particle remains unchanged until the boundary of the particle has eroded inwards far enough to reach it. On the other hand, bulk erosion occurs when the acids or enzymes quickly diffuse into the matrix and hydrolysis of the particle occurs throughout its entire volume simultaneously. Future research could extend the classification system for food breakdown used in this study, which considers only one type of erosion, to distinguish between surface erosion and bulk erosion.

Breakdown of model foods in the Human Gastric Simulator (HGS)

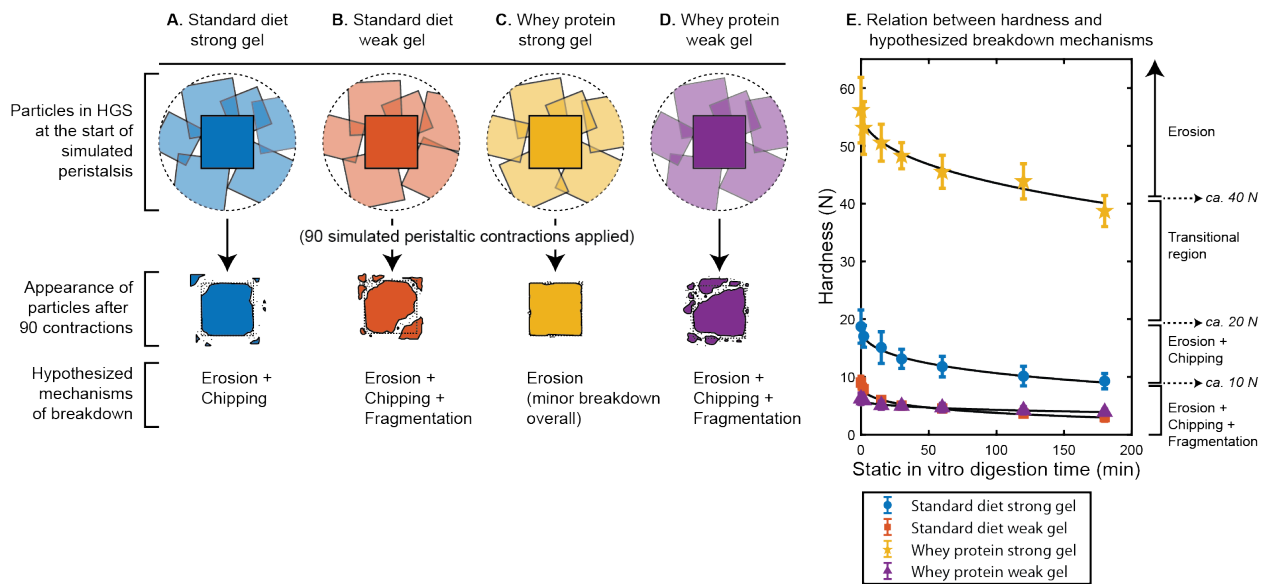


Figure 7.18. Appearance of particles after application of 90 simulated peristaltic contractions in the HGS and hypothesized mechanisms of breakdown for the standard diet strong gel (A), standard diet weak gel (B), whey protein strong gel (C), and the whey protein weak gel (D). The hypothesized mechanisms of particle breakdown varied more between different model foods than between different static in vitro digestion times for a given model food. For instance, the hypothesized mechanism of breakdown for the whey protein strong gel was erosion regardless of static in vitro digestion time. The relation between changes in hardness and hypothesized mechanisms of breakdown are shown in panel E (modified from Chapter 5).

7.4.4 Hypothesized mechanisms of breakdown of model foods in the peristaltic simulator

In the peristaltic simulator, cubes of model food were subjected to simulated peristaltic contractions applied by rollers (Figure 7.3 B). The rationale for this experiment was to isolate the effect of simulated peristaltic contractions on the breakdown of model food cubes without the potential for particle-particle interactions, which make breakdown behavior in the HGS more complex.

The cubical particles of the standard diet strong gel began to experience fragmentation after ca. 30 simulated peristaltic contractions had been applied, whereas particles of the standard diet weak gel began to demonstrate such events with the first contractions that were applied. Thus, it is hypothesized that fragmentation of the standard diet strong gel required the cubes to first be weakened by the application of simulated peristaltic contractions, whereas the standard diet weak gel was vulnerable to fragmentation events without necessitating that it was first weakened by the initial simulated peristaltic contractions. This parallels the findings for these model foods in the HGS, where the standard diet strong gel did not undergo fragmentation, and experienced breakdown dominated by erosion whereas the standard diet weak gel was broken down by a combination of erosion and chipping.

The whey protein strong gel did not experience any significant breakdown in the peristaltic simulator, as it was the only model food that did not see a significant decrease in PV_c during the experiment. The whey protein weak gel, however, demonstrated fragmentation after application of ca. 3 peristaltic contractions. In the HGS, the whey protein weak gel broke down by a hypothesized mechanism of erosion, chipping, and fragmentation, which is consistent with its behavior in the peristaltic simulator. Similarly, the whey protein strong gel experienced minimal overall breakdown in the HGS, with the small degree of breakdown that was experienced due to erosion, in agreement with its behavior in the peristaltic simulator.

Comparing the whey protein weak gel and standard diet weak gel potentially reveals the impact of toughness on the breakdown in the peristaltic simulator. The standard diet weak gel had slightly higher hardness than the whey protein weak gel (9.0 ± 1.1 N vs 6.2 ± 1.0 N), yet the whey protein weak gel resisted fragmentation until ca. 3 simulated peristaltic contractions had been applied (Figure 7.16 D)

whereas the standard diet weak gel fragmented with the initial contractions (Figure 7.16 B). This difference in their breakdown behavior may be related to a greater toughness of the whey protein weak gel (31.0 ± 3.3 N/m) as compared to the standard diet weak gel (14.7 ± 2.3 N/m). The hypothesized breakdown mechanisms for the different model foods in the peristaltic simulator are shown in Figure 7.19.

With the finding that some model foods experienced a fragmentation breakdown mechanism in the peristaltic simulator only after certain numbers of simulated peristaltic contractions had been applied (ca. 30 contractions for the standard diet strong gel and ca. 3 contractions for whey protein weak gel, Figure 7.16), future studies might consider that the dominant breakdown mechanisms for a given food could change depending on the number of peristaltic contractions that the food matrix has been exposed to. Specifically, food particles might experience erosion during the initial peristaltic contractions applied to them but then transition to a period of more rapid breakdown by chipping or fragmentation after a “threshold” number of contractions that weaken their internal structure. The toughness of a food particle may be an influential property in this regard, as justified by the finding that the standard diet weak gel experienced fragmentation during the initial 3 simulated peristaltic contractions whereas the whey protein weak gel did not experience fragmentation during the initial 3 simulated peristaltic contractions. Despite the higher hardness of the standard diet weak gel (9.0 ± 1.1 N) than the whey protein weak gel (6.2 ± 1.0 N), the whey protein weak gel had higher toughness (31.0 ± 3.3 N/m) than the standard diet weak gel (14.7 ± 2.3 N/m) potentially explaining why it survived the initial three simulated peristaltic contractions without experiencing fragmentation.

In general, the effect of the number of simulated peristaltic contractions applied to a food particle was more influential on its breakdown than the static in vitro digestion time. This agrees with previous research on almond particles (Chapter 1) that showed solid food particles only experienced particle size reduction in dynamic digestion systems that included simulated peristaltic contractions. Due to the influence of peristaltic contractions on food breakdown, it is recommended that future studies consider

using dynamic digestion systems that include simulated peristalsis to better understand the breakdown of solid foods (Bornhorst, 2017; Bornhorst and Singh, 2014; Dupont et al., 2019).

In the HGS particles were able to move within the stomach liner as the simulated peristaltic contractions were applied, whereas the cubes in the peristaltic simulator were fixed on a holding rig. The fragmentation of the standard diet strong gel occurred in the peristaltic simulator but not in the HGS (only erosion and chipping) which suggests the importance of particle mobility. It is conceivable that in the stomach large particles which become trapped in a certain position could undergo fragmentation that would not be experienced by smaller particles that could move out of the path of an advancing peristaltic contraction, preventing sufficient stress from being achieved to cause fracture. A similar trapping mechanism has been shown to allow food particles to be more efficiently fractured by teeth during mastication when their position is constrained (Anderson and LaBarbera, 2008) and it was proposed that evolution of teeth in animals that consume foods with high toughness has resulted in fang-like tooth geometries that function to constrain the position of food particles. In the distal region of the stomach (antrum) the diameter is reduced as compared to the corpus (Schulze, 2006) as shown in Figure 2.1. In the antral region, peristaltic contractions lead to greater occlusion as the wave approaches the pylorus (Ferrua and Singh, 2010). The antral region is known as a site of significant food particle breakdown, referred to as antral grinding (L. Marciani et al., 2001a). In this study it was demonstrated that food particles are more vulnerable to fracture by an advancing peristaltic wave when their position is fixed on a holding rig, and thus it is conceivable that the roughly funnel-shaped human stomach efficiently grinds particles in the antrum as their position is constrained in this region by neighboring particles, stomach walls, and the intermittent closing of the pylorus (Faas et al., 2001).

Breakdown of model foods in the peristaltic simulator

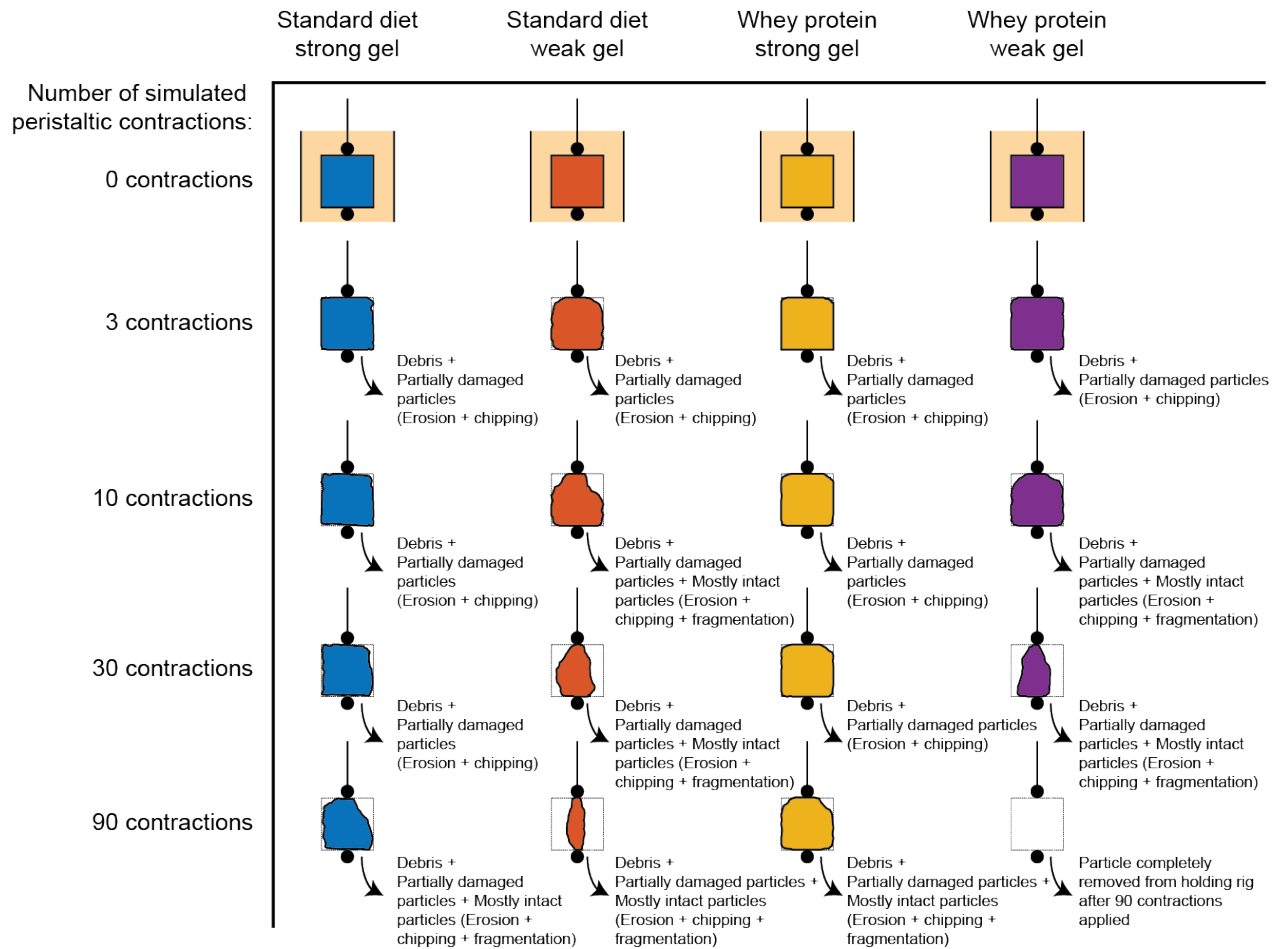


Figure 7.19. Appearance of particles during progressive application of contractions in the peristaltic simulator and hypothesized mechanism of breakdown. In general, variations in breakdown behavior were greater between different model foods than between different static in vitro digestion times for a given model food.

7.4.5 Implications for the FBCS

In the FBCS, foods are classified according to initial hardness as well as the kinetics of hardness change during digestion, as quantified by the softening half-time (Bornhorst et al., 2015). In this study, model foods that were previously demonstrated to fall into distinct FBCS classes were subjected to simulated peristaltic contractions in either the HGS or the peristaltic simulator and demonstrated breakdown that was dominated by different hypothesized mechanisms (Table 7.8). Previous researchers determined that trends in softening half-time aligned with trends in the glycemic index for carbohydrate-based foods (Drechsler and Bornhorst, 2018). Taken together with the results of this study, it is proposed that foods in different FBCS classes can exhibit different breakdown mechanisms, potentially explaining differences in their physiological responses such as glycemic index. Future research should consider using the FBCS to categorize the breakdown of solid foods during digestion as well as report the hypothesized breakdown mechanisms experienced by the foods so that an improved understanding of food breakdown can be established.

Table 7.8. Summary of FBCS classifications of the model foods used in the current study as described by Swackhamer et. al., (2022), along with summary of hypothesized mechanisms of breakdown in the HGS and peristaltic simulator.

FBCS class	Softening half-time	Initial hardness	Classification of model foods used the current study	Summary of hypothesized breakdown mechanisms in the HGS	Summary of hypothesized breakdown mechanisms in the peristaltic simulator
I	Slow softening (> 180 min)	Hard (> 20 N)	Whey protein strong gel	Erosion, minimal breakdown overall	Erosion, minimal breakdown overall
II		Soft (< 20 N)	Whey protein weak gel	Erosion + chipping + fragmentation	Erosion + chipping until application of ca. 3 simulated peristaltic contractions, then erosion + chipping + fragmentation
III	Intermediate softening (60 – 180 min)	Hard (> 20 N)	NA	NA	NA
IV		Soft (< 20 N)	Standard diet strong gel	Erosion + chipping	Erosion + chipping until application of ca. 30 simulated peristaltic contractions, then erosion + chipping+ fragmentation
V	Fast softening (< 60 min)	Hard (> 20 N)	NA	NA	NA
VI		Soft (< 20 N)	Standard diet weak gel	Erosion + chipping + fragmentation	Erosion + chipping + fragmentation

7.5 Limitations

The use of only four model foods was a limitation of this study. Before the mechanisms of breakdown attributed to solid food particles with certain textural properties can be considered representative of all solid foods, additional research on the breakdown of food products with varying properties and types of internal structure is needed. Additionally, experiments where model foods were subjected to *in vitro* gastric digestion in the presence of simulated peristalsis were conducted only on food particles with a homogenous initial particle size distribution, whereas food particles in the swallowable bolus have a heterogenous particle size distribution. Future research is needed to clarify the relationships between particle size and physical property changes. To this end the FBCS may be informative as the normalized hardness is recommended, which may allow the softening times of particles of varying sizes to be considered. Analysis carried out in this study involved two-dimensional image analysis to quantify particle size, a limitation that required particle volume to be estimated based on the assumption that particles had a spherical geometry. Future research could consider development of a particle size analysis system capable of determining three-dimensional particle geometry so that the breakdown can be analyzed in more detail. To analyze the percentage of dry matter remaining in food particles retained by the sieve after 90 simulated peristaltic contractions were applied in the HGS, it was assumed that the particles of all sizes had the same moisture content, which was measured for the corresponding model food at the appropriate timepoint. Future research could consider establishing the moisture content of particles of varying sizes, allowing for a more appropriate determination of the percentage of dry matter remaining as part of model food cubes after treatment in an *in vitro* digestion system that includes simulated peristalsis.

Conclusions

In this study, four previously developed standardized, model solid foods were subjected to static *in vitro* digestion for varying lengths of time (0 min, 30 min, and 180 min) and changes in their fracture and rheological properties were assessed. In general, it was found that model foods experienced reduced toughness, yield stress, stiffness, and shear modulus (G') over time during static *in vitro* digestion. These

changes were attributed to the breakdown of the model food matrices by acids and enzymes in simulated gastric fluids. In parallel experiments, cubical particles of each model food were subjected to static in vitro digestion followed by application of 90 contractions using either the Human Gastric Simulator (HGS), a physiologically representative model of the human stomach, or up to 90 contractions using the peristaltic simulator, which was used to apply peristaltic contractions to particles directly without the involvement of particle-particle interactions. The model foods broke down by varying hypothesized mechanisms. In the HGS, the standard diet strong gel broke down by erosion and chipping, the standard diet weak gel broke down by erosion, chipping, and fragmentation, the whey protein strong gel broke down by erosion, and the whey protein weak gel broke down by erosion, chipping, and fragmentation. In the peristaltic simulator the standard diet strong gel began to experience fragmentation (large-scale fracture of the particle) after application of ca. 30 simulated peristaltic contractions, the standard diet weak gel experienced fragmentation as soon as simulated peristaltic contractions were applied, the whey protein strong gel did not experience fragmentation after any number of contractions, and the whey protein weak gel began to experience fragmentation after ca. 3 contractions. CLSM results showed that the standard diet strong gel and whey protein strong gel were each comprised of a continuous whey protein network, whereas the standard diet weak gel was a physical gel of entangled starch and whey protein but lacking a distinct whey protein network, and the whey protein weak gel's protein network was disrupted by pectin. Due to the different hypothesized breakdown mechanisms experienced by these model foods, it is proposed that the presence of a continuous whey protein network in a hydrogel model food may strengthen its structure and restrict its breakdown to mechanisms consisting of erosion and chipping, without fragmentation such as may occur in foods which lack a distinct whey protein network in their microstructure. The breakdown of foods in this study was related to the FBCS classes of the foods, with the finding that foods in classes defined by low initial hardness may break down by erosion, chipping, and fragmentation, whereas those in FBCS classes defined by high initial hardness may experience breakdown by erosion, and potentially chipping. Experiments in the HGS showed that the breakdown mechanisms experienced by model foods were not strongly influenced by the duration of

static in vitro digestion that cubes were subjected to before application of simulated peristalsis, however, the breakdown mechanisms of model foods in the peristaltic simulator changed, for example from erosion and chipping to erosion, chipping, and fragmentation, as the number of simulated peristaltic contractions applied to a particle increased. Considering these results together, it can be concluded that foods may not experience fragmentation after the first peristaltic contraction applied to them in the stomach, but nevertheless may undergo fragmentation with the progressive application of additional contractions. These results point to the need to conduct in vitro gastric digestion experiments in the presence of simulated peristaltic contractions to determine the breakdown of solid food particles. Overall, results from this study established the changes in fracture and rheological properties of standardized model foods and shed light on their breakdown mechanisms during in vitro digestion that includes simulated peristalsis. The model foods tested in this study, which were previously placed in distinct classes according to the Food Breakdown Classification System (FBCS), experienced different breakdown mechanisms, suggesting that the FBCS class of solid foods may help to understand the breakdown mechanisms of foods during digestion. Future work could use the range of hardness of the model foods in this study as a guide to design functional foods with desired breakdown rates using a forward-engineering approach, although the breakdown of such food products would need to be confirmed in vivo.

Chapter 8 Overall conclusions

The first main conclusion from this project was that particle breakdown of solid foods, as determined using experiments with almonds, was triggered by simulated peristaltic contractions during in vitro gastric digestion. The second main conclusion was that the physical properties of solid foods, as determined using experiments with novel model foods based on the Standard American Diet, influenced their breakdown rates during in vitro digestion, and that the progressive application of simulated peristaltic contractions led to transitions in the breakdown mechanisms of the solid food particles.

The main limitations of this project were that the work was conducted in vitro using simulators that do not perfectly represent the digestion process in vivo, and that a small number of solid foods were tested (almonds as well as four standardized model solid foods), pointing to the need for future research to characterize the breakdown of additional food products with a wide range of properties during gastric digestion.

The following overall conclusions were reached as part of this research project:

1. Almond particles experienced a statistically significant ($p < 0.05$) particle size reduction from $15.89 \pm 0.68 \text{ mm}^2$ to $12.19 \pm 1.29 \text{ mm}^2$ in the HGS, a dynamic in vitro model of gastric digestion that includes simulated peristaltic contractions, but particles did not experience size reduction in a shaking water bath model of gastric digestion that included only agitation. Thus, it was concluded that simulated peristaltic contractions can lead to the breakdown of solid food particles during in vitro gastric digestion that may not occur under agitation, even if identical biochemical conditions are applied such as pH values and enzyme activity.
2. Particle size reduction of almond particles during in vitro gastric digestion influenced the bioaccessibility of fatty acids contained within the solid food matrix. After a three-hour in vitro gastric digestion, the total bioaccessibility of fatty acids from almond particles subjected to in vitro digestion in the HGS was $6.55 \pm 0.85 \%$, which was significantly ($p < 0.01$) greater than the fatty acid bioaccessibility from particles digested in the shaking water bath ($4.54 \pm 0.36 \%$). This

suggests that in vitro digestion experiments on solid foods should be carried out in the presence of simulated peristalsis to achieve appropriate nutrient bioaccessibility even if assessment of particle breakdown itself is not a primary research goal.

3. Model solid foods with varying initial hardness and softening half-times were developed to serve as test system for studying the role of food properties on food breakdown (Figure 8.1). Two model foods with macronutrient composition of the Standard American Diet in addition to two based on whey protein hydrogels were designed. The initial hardness of the standard diet strong gel (pH 5.2) was 18.7 ± 2.9 N, which was significantly ($p > 0.05$) greater than that of the standard diet weak gel version (pH 2.5) which was 9.0 ± 1.1 N. The initial hardness of the whey protein strong gel version was 56.2 ± 5.7 N which was significantly ($p < 0.05$) greater than that of the weak gel version (6.2 ± 1.0 N). Varying softening-half times were achieved between the standard diet model foods (161 ± 15 min and 58 ± 5 min, strong and weak gel versions, respectively) and the whey protein hydrogel model foods (775 ± 82 min and 538 ± 193 min, strong and weak gel versions, respectively).
4. The model foods were classified according to the Food Breakdown Classification System:
 - a. Class I – slow softening rate, high initial hardness: whey protein strong gel
 - b. Class II – slow softening rate, low initial hardness: whey protein weak gel
 - c. Class IV – intermediate softening rate, low initial hardness: standard diet strong gel
 - d. Class VI – fast softening rate, low initial hardness: standard diet weak gel
5. A novel, multi-module peristaltic simulator was developed so that the direct effect of simulated peristalsis on food particle breakdown could be studied without the potential for particle-particle grinding which can occur in the HGS. It was demonstrated that the occlusion of the simulated peristaltic wave could be adjusted from $72.1 \pm 0.4\%$ to $84.6 \pm 1.2\%$ ($p < 0.05$) by changing from thin rollers to thick rollers. The corresponding forces applied to a food particle or bolus were estimated as 2.61 ± 0.03 N and 4.51 ± 0.16 N ($p < 0.05$) for the thin rollers and thick rollers, respectively. A Multiphysics CFD simulation was used to obtain insight into the fluid flow in the

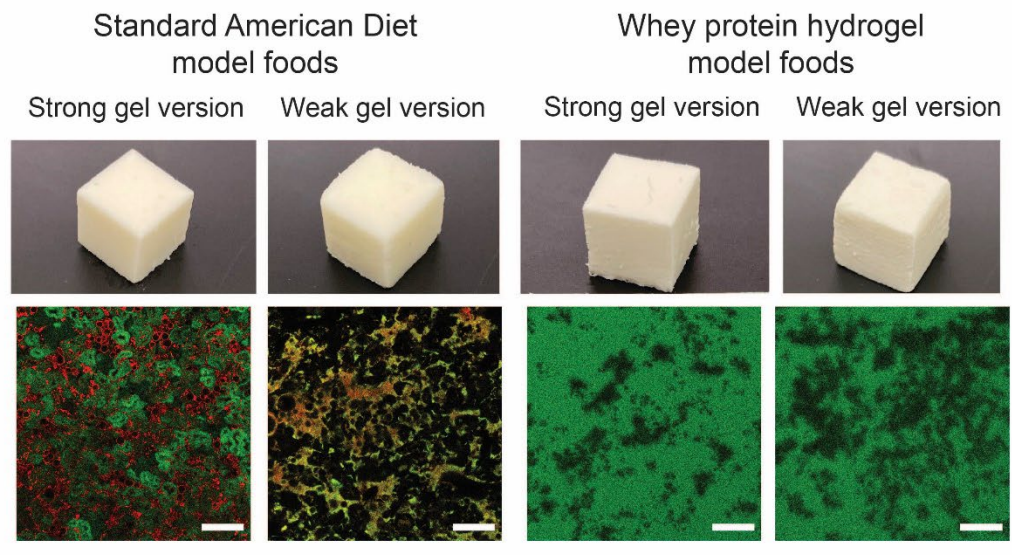
peristaltic simulator, and it was found that the maximum predicted fluid velocity for the thick rollers at any point in the computational domain was 0.0211 m/s and for the thin rollers was 0.0160 m/s. From the development and characterization of this device, it can be concluded that varying the occlusion of the peristaltic wave can affect the force on a simulated food particle as well as the fluid velocity in the system, factors which should be considered by future engineers designing in vitro gastric digestion systems that incorporate simulated peristalsis.

6. Particles of the model foods were subjected to static in vitro digestion for either 0, 30, or 180 min followed by the application of 90 simulated peristaltic contractions in the HGS, and it was found that model foods experienced particle size reduction by different hypothesized mechanisms. Specifically, the standard diet strong gel broke down by erosion and chipping, the standard diet weak gel broke down by erosion, chipping, and fragmentation, the whey protein strong gel broke down by erosion, and the whey protein weak gel broke down by erosion, chipping, and fragmentation (Figure 8.1). These mechanisms were not affected by the static in vitro digestion time applied to the model foods before treatment in the HGS. It was estimated that in a physiologically representative gastric digestion system including simulated peristalsis such as the HGS, food particles with hardness values lower than ca. 10 N, such as the standard diet weak gel and whey protein weak gel, may break down by erosion, chipping, and fragmentation at the onset of digestion, whereas particles with hardness ca. 20 N, such as the standard diet strong gel, may break down by erosion and chipping. Food particles with hardness ca. 40 N or greater, such as the whey protein strong gel, would be expected to undergo erosion, but with minimal overall breakdown occurring.
7. Particles of the model foods were subjected to static in vitro digestion for either 0, 30, or 180 min followed by the application of up to 90 simulated peristaltic contractions in the novel peristaltic simulator in order to isolate the direct effect of simulated peristalsis on food breakdown, and it was concluded that the breakdown mechanisms of model foods changed, for example from erosion and chipping to erosion, chipping, and fragmentation, as the number of simulated

peristaltic contractions applied to a particle increased. This may shed light on the breakdown of solid foods in the stomach, suggesting that food particles may not experience fragmentation after the first peristaltic contraction but still may undergo fragmentation with the progressive application of additional contractions (Figure 8.1). It was concluded that the applied forces from peristaltic contractions affect the breakdown of solid food particles, with initial contractions functioning to weaken particles that may be fragmented by subsequent contractions. This finding from experiments in the peristaltic simulator, that food particles transitioned from only erosion to erosion as well as chipping and fragmentation after the application of additional simulated peristaltic contractions, can be contrasted with experiments using the HGS. In the HGS it was determined that food particles did not demonstrate a transition in their breakdown mechanisms regardless of the duration of static in vitro gastric digestion to which particles were subjected, before exposure to simulated peristaltic contractions. Taking these findings together, it can be concluded that the transition in the breakdown mechanism of solid food particles may be attributed to weakening of the particle by progressive contractions rather than exposure to gastric fluids for longer periods of time. This may support the findings from previous studies that report the antrum of the stomach as the principal region for food particle breakdown. In the antrum peristaltic contractions lead to greater occlusion than in the proximal region and particles may be more physically constrained than in the proximal region due to the presence of other food particles and narrower stomach geometry. These factors may allow food particles to transition from erosion to erosion, chipping, and fragmentation upon reaching the antrum, potentially explaining why the rate of food particle breakdown in the antrum is high.

8. In general, results from this study demonstrate the foods can break down by varying mechanisms (erosion, chipping, fragmentation) based on their mechanical properties, with stronger foods breaking down predominantly by erosion and softer foods breaking down by a combination of all three mechanisms (Figure 8.1). Furthermore, the changes in food properties that occur over time during gastric digestion due to the action of enzymes and gastric acid may lead to changes in the

dominant breakdown mechanisms for a certain food as digestion time elapses. For example, a food that has high initial hardness, but experiences intermediate to rapid softening (FBCS classes III and V, respectively) could see breakdown dominated by erosion during the first few minutes of gastric digestion but transition to breakdown dominated by fragmentation after longer digestion times. It is recommended that future researchers assess the hardness and softening-half times of solid food particles as recommended by the FBCS as these were the most salient physical properties that were assessed in this project with respect to determining the hypothesized mechanisms of breakdown of the model foods.



Microstructure	Interpenetrating whey protein and starch networks	Physical gel of entangled whey protein and starch	Whey protein network	Whey protein network disrupted by pectin
Initial Hardness (N)	18.7	9.0	56.2	6.2
Softening half-time (min)	161	58	775	538
FBCS Class	IV	VI	I	II
Mechanisms of breakdown in the HGS	Erosion + chipping	Erosion + chipping + fragmentation	Erosion	Erosion + chipping + fragmentation
# of contractions at first fragmentation in the peristaltic simulator	10	1	N/A	3

Figure 8.1. Overall conclusions from this project. Images of model foods cut into a cubical geometry are shown along with CLSM images from microstructural analysis. The initial hardness, softening half-time, and resulted FBCS classifications are provided, along with the hypothesized mechanisms of breakdown in

the HGS. The number of contractions at which point particles began to break down by fragmentation in the peristaltic simulator are provided.

Chapter 9 **Recommendations for future work**

The most direct next step for research in this topic area could be to assess the breakdown of the model foods developed in this project in vivo. This could potentially allow for assessment of the correspondence between the hypothesized breakdown mechanisms observed using in vitro systems such as the HGS and peristaltic simulator and an in vivo model for the adult human, such as a growing pig. However, such experiments generally require euthanasia of test animals after certain timepoints in the postprandial period so that food breakdown can be determined by collection of intragastric contents and could thus involve cost and ethical considerations. An alternative approach could be to link breakdown mechanisms of model foods to physiologically relevant parameters such as the blood glucose profile in the postprandial period, which could simplify study design as collection of stomach contents would not be strictly necessary. It is hypothesized that the standard diet weak gel would lead to a greater peak in blood glucose than the standard diet strong gel due to its more rapid breakdown by erosion, chipping, and fragmentation, as compared to only erosion and chipping for the standard diet strong gel. Since the standard diet strong and weak gel have identical macronutrient composition, differences in physiological outcomes from their digestion in vivo such as postprandial blood glucose profile, satiety, or gastric emptying rate could be related to differences in their breakdown during gastric digestion.

A general recommendation for future work is to gather additional data on food breakdown and classify foods based on the Food Breakdown Classification System (FBCS), eventually leading to a dataset containing data on food breakdown for many foods, representing a range of properties and microstructures. In this project four model foods were characterized according to the FBCS, however, these model foods do not represent all possible foods, such as those with low moisture content, cellular structure microstructure, or potential to melt at physiological temperature. Additionally, model foods could be developed with a wider dynamic range in hardness than those developed in the current study. For example, the whey protein strong gel experienced a reduction in hardness during 180 min static in vitro gastric digestion from 56.2 ± 5.7 N to 38.7 ± 2.7 N. During digestion of this model food in the HGS, erosion was the only hypothesized mechanism of breakdown. However, the whey protein weak gel model

food, which experienced a hardness decrease from 6.2 ± 1.0 N to 3.9 ± 0.5 N broke down by erosion, chipping, and fragmentation. If a model food could be developed with rapid softening, for instance from 60 N to 5 N in 180 min, it would be interesting to subject such a food to digestion in the HGS and determine whether the dominant mechanisms of breakdown transitioned from erosion to erosion, chipping, and fragmentation as hardness declined. This approach could allow for more accurate determination of hardness thresholds below which the mechanisms of particle breakdown would change. This could be done by fitting the profile of hardness vs time using the Weibull function and using the function to determine a specific value of hardness by interpolation at the time when the particles began to fragment.

Model foods could be developed that fall into the classes that were not represented by model foods developed in this study (Classes III and V). Furthermore, research could focus on the breakdown of foods that are not currently part of the FBCS, such as semi solids like yogurt, emulsions such as milk, or foods that initially have small particle sizes whose initial hardness and softening half times cannot be easily established, such as particles resulting from mastication of solid foods. For semi-solid foods or those with small particles, an alternative framework could be pursued based on particle size reduction kinetics instead of texture change kinetics. For example, the time for the median particle size to decrease by $\frac{1}{2}$ could be determined using a fit with the Weibull function in the same manner as is used to determine the softening half-time by the FBCS. Since bioaccessibility has been shown to relate to surface area in numerous previous studies, this approach could be promising for prediction of bioaccessibility. Another specific approach could be using curve fitting to establish the relationship between particle size and softening half-time. Using this method, extrapolation or interpolation could be employed to estimate the softening half times of particles with arbitrary sizes, including those too small to measure using a texture analyzer. It is hypothesized that softening half-time will scale according to two parameters: the diffusion coefficient of water in the food matrix and the particle size cubed (to the third power), due to the need for gastric juice to diffuse into a three-dimensional particle. Similar scaling laws have been developed in the field of drug delivery which could be adapted by future researchers seeking to develop such relationships

in the field of food engineering (Burkersroda et al., 2002). This approach could generate a library of softening functions, linking particle size to the expected softening half-times, which could be useful for designing functional foods, such as a snack with slow softening particles for sustained fullness or energy release.

Future work could improve the peristaltic simulator developed in the current study, for example by incorporating options to create the types of peristaltic contractions that were seen in the post-mortem motility analysis of porcine intestinal tissue which had shallower occlusion and smaller width than those produced by the peristaltic simulator. Since in vivo intestinal motility includes both segmental and propagating contractions, a specific recommendation would be to create a system in which both of these types of motility can be represented by the simulator. Another suggestion for future work in this area is to establish collaborations between medical professionals involved with gastrointestinal imaging and develop a workflow for analysis and modeling of human motility data which could be used to inform the design of future digestion simulators. One additional suggestion for future research in this area is to consider scaling down in vitro digestion to smaller volumes, potentially allowing for in vitro digestions to be carried out in the cells of a 96 well plate on a plate reader instrument, which could enable dramatically higher throughput and lower cost. This approach might not be feasible for digestion of solid food particles but could potentially find use in the digestion of beverages. To achieve a degree of correspondence between the digestion conditions in vivo and in such a hypothetical small-scale digestion system, dimensionless numbers could be matched, such as the Reynolds number or Stokes number.

Chapter 10 References

- Abarca-Gómez, L., Collaborators*, 2017. Worldwide trends in body-mass index, underweight, overweight, and obesity from 1975 to 2016: a pooled analysis of 2416 population-based measurement studies in 128·9 million children, adolescents, and adults. *Lancet* 390, 2627–2642. [https://doi.org/10.1016/S0140-6736\(17\)32129-3](https://doi.org/10.1016/S0140-6736(17)32129-3)
- Abrahamse, E., Minekus, M., Ludwig, T., van Aken, G.A., van de Heijning, B., Knol, J., Bartke, N., Oozeer, R., van der Beek, E.M., Ludwig, T., 2012a. Development of the Digestive System — Experimental Challenges and Approaches of Infant Lipid Digestion. *Food Dig.* 3, 63–77. <https://doi.org/10.1007/s13228-012-0025-x>
- Abrahamse, E., Minekus, M., van Aken, G.A., van de Heijning, B., Knol, J., Bartke, N., Oozeer, R., van der Beek, E.M., Ludwig, T., 2012b. Development of the Digestive System—Experimental Challenges and Approaches of Infant Lipid Digestion. *Food Dig.* 3, 63–77. <https://doi.org/10.1007/s13228-012-0025-x>
- Afshin, A., Collaborators*, 2017. Health effects of overweight and obesity in 195 countries over 25 years. *N. Engl. J. Med.* 377, 13–27. <https://doi.org/10.1056/NEJMoa1614362>
- Agrawal, K., Lucas, P., Bruce, I., 2000. The effects of food fragmentation index on mandibular closing angle in human mastication. *Arch. Oral Biol.* 45, 577–584. [https://doi.org/10.1016/S0003-9969\(00\)00019-4](https://doi.org/10.1016/S0003-9969(00)00019-4)
- Agrawal, K.R., Lucas, P.W., 2003. The mechanics of the first bite. *Proc. R. Soc. London. Ser. B Biol. Sci.* 270, 1277–1282. <https://doi.org/10.1098/rspb.2003.2361>
- Agrawal, K.R., Lucas, P.W., Bruce, I.C., Prinz, J.F., 1998. Food Properties that Influence Neuromuscular Activity During Human Mastication. *J. Dent. Res.* 77, 1931–1938. <https://doi.org/10.1177/00220345980770111101>
- Agrawal, K.R., Lucas, P.W., Prinz, J.F., Bruce, I.C., 1997. Mechanical properties of foods responsible for resisting food breakdown in the human mouth. *Arch. Oral Biol.* 42, 1–9. [https://doi.org/10.1016/S0003-9969\(96\)00102-1](https://doi.org/10.1016/S0003-9969(96)00102-1)
- Ailiani, A.C., Neuberger, T., Basseur, J.G., Banco, G., Wang, Y., Smith, N.B., Webb, A.G., 2009. Quantitative analysis of peristaltic and segmental motion in vivo in the rat small intestine using dynamic MRI. *Magn. Reson. Med.* 62, 116–126. <https://doi.org/10.1002/mrm.21982>
- Alamar, M.C., Vanstreels, E., Oey, M.L., Moltó, E., Nicolai, B.M., 2008. Micromechanical behaviour of apple tissue in tensile and compression tests: Storage conditions and cultivar effect. *J. Food Eng.* 86, 324–333. <https://doi.org/10.1016/j.jfoodeng.2007.10.012>
- Alfonso, M., Neyraud, E., Blanc, O., Peyron, M.A., Dransfield, E., 2002. Relationship between taste and chewing patterns of visco-elastic model foods. *J. Sens. Stud.* 17, 193–206. <https://doi.org/10.1111/j.1745-459X.2002.tb00342.x>
- Alvarez, M.D., Saunders, D.E.J., Vincent, J.F.V., Jeronimidis, G., 2000. An engineering method to evaluate the crisp texture of fruit and vegetables. *J. Texture Stud.* 31, 457–473. <https://doi.org/10.1111/j.1745-4603.2000.tb00302.x>
- Amado, F.M.L., Vitorino, R.M.P., Domingues, P.M.D.N., Lobo, M.J.C., Duarte, J.A.R., 2005. Analysis of the human saliva proteome. *Expert Rev. Proteomics* 2, 521–539. <https://doi.org/10.1586/14789450.2.4.521>
- Amidon, G.L., Lennernäs, H., Shah, V.P., Crison, J.R., 1995. A theoretical basis for a biopharmaceutical drug classification: the correlation of in vitro drug product dissolution and in vivo bioavailability. *Pharm. Res.* 12, 413–20. <https://doi.org/10.1023/A:1016212804288>
- Anderson, P.S.L., 2009. The effects of trapping and blade angle of notched dentitions on fracture of biological tissues. *J. Exp. Biol.* 212, 3627–3632. <https://doi.org/10.1242/jeb.033712>
- Anderson, P.S.L., LaBarbera, M., 2008. Functional consequences of tooth design: effects of blade shape on energetics of cutting. *J. Exp. Biol.* 211, 3619–3626. <https://doi.org/10.1242/jeb.020586>
- Andreuccetti, C., Carvalho, R.A., Galicia-García, T., Martínez-Bustos, F., González-Nuñez, R., Grosso,

- C.R.F., 2012. Functional properties of gelatin-based films containing *Yucca schidigera* extract produced via casting, extrusion and blown extrusion processes: A preliminary study. *J. Food Eng.* 113, 33–40. <https://doi.org/10.1016/j.jfoodeng.2012.05.031>
- Arab, L., Estrin, D., Kim, D.H., Burke, J., Goldman, J., 2011. Feasibility testing of an automated image-capture method to aid dietary recall. *Eur. J. Clin. Nutr.* 65, 1156–1162. <https://doi.org/10.1038/ejcn.2011.75>
- Ashby, M.F., Gibson, L.J., 1988. *Cellular solids - Structure and Properties*. Pergamon Press, Oxford.
- ASTM-D638-14, 2014. Standard test method for tensile properties of plastics. West Conshohocken PA. <https://doi.org/https://doi.org/10.1520/D0638-14.1>
- ASTM-D882-12, 2012. Standard test method for tensile properties of thin plastic sheeting. West Conshohocken PA. <https://doi.org/https://doi.org/10.1520/D0882-12.2>
- ASTM D790-17, 2017. Standard test method for flexural properties of unreinforced and reinforced plastics and electrical insulating materials. West Conshohocken PA. <https://doi.org/https://doi.org/10.1520/D0790-17.2>
- Atkins, A.G., Mai, Y.W., 1985. *Elastic and plastic fracture*. Ellis Horwood Ltd, West Sussex.
- Atkinson, F.S., Foster-Powell, K., Brand-Miller, J.C., 2008. International Tables of Glycemic Index and Glycemic Load Values: 2008. *Diabetes Care* 31, 2281–2283. <https://doi.org/10.2337/dc08-1239>
- Avantaggiato, G., Havenaar, R., Visconti, A., 2007. Assessment of the multi-mycotoxin-binding efficacy of a carbon/aluminosilicate-based product in an in vitro gastrointestinal model. *J. Agric. Food Chem.* 55, 4810–4819. <https://doi.org/10.1021/jf0702803>
- Bai, Y., Wu, P., Wang, K., Li, C., Li, E., Gilbert, R.G., 2017. Effects of pectin on molecular structural changes in starch during digestion. *Food Hydrocoll.* 69, 10–18. <https://doi.org/10.1016/j.foodhyd.2017.01.021>
- Balakrishnan, G., Nguyen, B.T., Schmitt, C., Nicolai, T., Chassenieux, C., 2017. Heat-set emulsion gels of casein micelles in mixtures with whey protein isolate. *Food Hydrocoll.* 73, 213–221. <https://doi.org/10.1016/j.foodhyd.2017.07.005>
- Banerjee, P., Maitra, S., 2020. The Role of Small Millets as Functional Food to Combat Malnutrition in Developing Countries The Role of Small Millets as Functional Food to Combat Malnutrition in Developing Countries 10, 20412–20417.
- Baron, C.P., Kjærsgård, I.V.H., Jessen, F., Jacobsen, C., 2007. Protein and Lipid Oxidation during Frozen Storage of Rainbow Trout (*Oncorhynchus mykiss*). *J. Agric. Food Chem.* 55, 8118–8125. <https://doi.org/10.1021/jf070686f>
- Barrett, K., 2014. *Gastrointestinal physiology*, 2nd ed. McGraw-Hill, New York.
- Barros, L., Retamal, C., Torres, H., Zúñiga, R.N., Troncoso, E., 2016. Development of an in vitro mechanical gastric system (IMGS) with realistic peristalsis to assess lipid digestibility. *Food Res. Int.* 90, 216–225. <https://doi.org/10.1016/j.foodres.2016.10.049>
- Beaulieu, M., Turgeon, S.L., Doublier, J.-L., 2001. Rheology, texture and microstructure of whey proteins/low methoxyl pectins mixed gels with added calcium. *Int. Dairy J.* 11, 961–967. [https://doi.org/10.1016/S0958-6946\(01\)00127-3](https://doi.org/10.1016/S0958-6946(01)00127-3)
- Bellmann, S., Krishnan, S., de Graaf, A., de Ligt, R.A., Pasman, W.J., Minekus, M., Havenaar, R., 2019. Appetite ratings of foods are predictable with an in vitro advanced gastrointestinal model in combination with an in silico artificial neural network. *Food Res. Int.* 122, 77–86. <https://doi.org/10.1016/j.foodres.2019.03.051>
- Bellmann, S., Lelieveld, J., Gorissen, T., Minekus, M., Havenaar, R., 2016. Development of an advanced in vitro model of the stomach and its evaluation versus human gastric physiology. *Food Res. Int.* 88, 191–198. <https://doi.org/10.1016/j.foodres.2016.01.030>
- Berry, S.E., Tydeman, E.A., Lewis, H.B., Phalora, R., Rosborough, J., Picout, D.R., Ellis, P.R., 2008. Manipulation of lipid bioaccessibility of almond seeds influences postprandial lipemia in healthy human subjects. *Am. J. Clin. Nutr.* 88, 922–929. <https://doi.org/10.1093/ajcn/88.4.922>
- Berthaume, M.A., 2016. Food mechanical properties and dietary ecology. *Am. J. Phys. Anthropol.* 159, 79–104. <https://doi.org/10.1002/ajpa.22903>

- Berthaume, M.A., Dumont, E.R., Godfrey, L.R., Grosse, I.R., 2013. How does tooth cusp radius of curvature affect brittle food item processing? *J. R. Soc. Interface* 10, 20130240.
<https://doi.org/10.1098/rsif.2013.0240>
- Bhatka, R., Throckmorton, G., Wintergerst, A., Hutchins, B., Buschang, P., 2004. Bolus size and unilateral chewing cycle kinematics. *Arch. Oral Biol.* 49, 559–566.
<https://doi.org/10.1016/j.archoralbio.2004.01.014>
- Bohn, T., Carriere, F., Day, L., Deglaire, A., Egger, L., Freitas, D., Golding, M., Le Feunteun, S., Macierzanka, A., Menard, O., Miralles, B., Moscovici, A., Portmann, R., Recio, I., Rémond, D., Santé-Lhoutelier, V., Wooster, T.J., Lesmes, U., Mackie, A.R., Dupont, D., 2018. Correlation between in vitro and in vivo data on food digestion. What can we predict with static in vitro digestion models? *Crit. Rev. Food Sci. Nutr.* 58, 2239–2261.
<https://doi.org/10.1080/10408398.2017.1315362>
- Boisly, M., Schuldt, S., Kästner, M., Schneider, Y., Rohm, H., 2016. Experimental characterisation and numerical modelling of cutting processes in viscoelastic solids. *J. Food Eng.* 191, 1–9.
<https://doi.org/10.1016/j.jfoodeng.2016.06.019>
- Boland, M., 2016. Human digestion - a processing perspective. *J. Sci. Food Agric.* 96, 2275–2283.
<https://doi.org/10.1002/jsfa.7601>
- Bornhorst, G.M., 2017. Gastric Mixing During Food Digestion: Mechanisms and Applications. *Annu. Rev. Food Sci. Technol.* 8, 523–542. <https://doi.org/10.1146/annurev-food-030216-025802>
- Bornhorst, G.M., 2012. Breakdown and Mixing of Brown and White Rice during Gastric digestion in vivo. University of California, Davis.
- Bornhorst, G.M., Chang, L.Q., Rutherford, S.M., Moughan, P.J., Singh, R.P., 2013a. Gastric emptying rate and chyme characteristics for cooked brown and white rice meals in vivo. *J. Sci. Food Agric.* 93, 2900–2908. <https://doi.org/10.1002/jsfa.6160>
- Bornhorst, G.M., Drechsler, K.C., Montoya, C.A., Rutherford, S.M., Moughan, P.J., Singh, R.P., 2016a. Gastric protein hydrolysis of raw and roasted almonds in the growing pig. *Food Chem.* 211, 502–508. <https://doi.org/10.1016/j.foodchem.2016.05.085>
- Bornhorst, G.M., Ferrua, M.J., Rutherford, S.M., Heldman, D.R., Singh, R.P., 2013b. Rheological Properties and Textural Attributes of Cooked Brown and White Rice During Gastric Digestion in Vivo. *Food Biophys.* 8, 137–150. <https://doi.org/10.1007/s11483-013-9288-1>
- Bornhorst, G.M., Ferrua, M.J., Singh, R.P., 2015. A Proposed Food Breakdown Classification System to Predict Food Behavior during Gastric Digestion. *J. Food Sci.* 80, R924–R934.
<https://doi.org/10.1111/1750-3841.12846>
- Bornhorst, G.M., Gouseti, O., Wickham, M.S.J., Bakalis, S., 2016b. Engineering Digestion: Multiscale Processes of Food Digestion. *J. Food Sci.* 81, R534–R543. <https://doi.org/10.1111/1750-3841.13216>
- Bornhorst, G.M., Hivert, H., Singh, R.P., 2014a. Rice bolus texture changes due to α -amylase. *LWT - Food Sci. Technol.* 55, 27–33. <https://doi.org/10.1016/j.lwt.2013.09.014>
- Bornhorst, G.M., Kostlan, K., Singh, R.P., 2013c. Particle Size Distribution of Brown and White Rice during Gastric Digestion Measured by Image Analysis. *J. Food Sci.* 78, E1383–E1391.
<https://doi.org/10.1111/1750-3841.12228>
- Bornhorst, G.M., Roman, M.J., Dreschler, K.C., Singh, R.P., 2014b. Physical Property Changes in Raw and Roasted Almonds during Gastric Digestion In vivo and In vitro. *Food Biophys.* 9, 39–48.
<https://doi.org/10.1007/s11483-013-9315-2>
- Bornhorst, G.M., Roman, M.J., Rutherford, S.M., Burri, B.J., Moughan, P.J., Singh, R.P., 2013d. Gastric Digestion of Raw and Roasted Almonds In Vivo. *J. Food Sci.* 78, H1807–H1813.
<https://doi.org/10.1111/1750-3841.12274>
- Bornhorst, G.M., Rutherford, S.M., Roman, M.J., Burri, B.J., Moughan, P.J., Singh, R.P., 2014c. Gastric pH Distribution and Mixing of Soft and Rigid Food Particles in the Stomach using a Dual-Marker Technique. *Food Biophys.* 9, 292–300. <https://doi.org/10.1007/s11483-014-9354-3>
- Bornhorst, G.M., Singh, R.P., 2014. Gastric Digestion In Vivo and In Vitro: How the Structural Aspects of Food Influence the Digestion Process. *Annu. Rev. Food Sci. Technol.* 5, 111–132.

- <https://doi.org/10.1146/annurev-food-030713-092346>
- Bornhorst, G.M., Singh, R.P., 2013. Kinetics of in Vitro Bread Bolus Digestion with Varying Oral and Gastric Digestion Parameters. *Food Biophys.* 8, 50–59. <https://doi.org/10.1007/s11483-013-9283-6>
- Bornhorst, G.M., Singh, R.P., 2012a. Bolus Formation and Disintegration during Digestion of Food Carbohydrates. *Compr. Rev. Food Sci. Food Saf.* 11, 101–118. <https://doi.org/10.1111/j.1541-4337.2011.00172.x>
- Bornhorst, G.M., Singh, R.P., 2012b. Bolus formation and disintegration during digestion of food carbohydrates. *Compr. Rev. Food Sci. Food Saf.* 11, 101–118. <https://doi.org/https://doi.org/10.1111/j.1541-4337.2011.00172.x>
- Bornhorst, G.M., Ströbinger, N., Rutherford, S.M., Singh, R.P., Moughan, P.J., 2013e. Properties of Gastric Chyme from Pigs Fed Cooked Brown or White Rice. *Food Biophys.* 8, 12–23. <https://doi.org/10.1007/s11483-012-9277-9>
- Boulby, P., Moore, R., Gowland, P., Spiller, R.C., 1999. Fat delays emptying but increases forward and backward antral flow as assessed by flow-sensitive magnetic resonance imaging. *Neurogastroenterol. Motil.* 11, 27–36. <https://doi.org/10.1046/j.1365-2982.1999.00133.x>
- Bower, A.F., 2010. Applied mechanics of solids. Taylor & Francis, Boca Raton, FL.
- Box, G.E.P., Cox, D.R., 1964. An Analysis of Transformations. *J. R. Stat. Soc. Ser. B* 26, 211–243. <https://doi.org/10.1111/j.2517-6161.1964.tb00553.x>
- Brandstaeter, S., Fuchs, S.L., Aydin, R.C., Cyron, C.J., 2019. Mechanics of the stomach: A review of an emerging field of biomechanics. *GAMM-Mitteilungen* e201900001. <https://doi.org/10.1002/gamm.201900001>
- Brodkorb, A., Egger, L., Alming, M., Alvito, P., Assunção, R., Ballance, S., Bohn, T., Bourlieu-Lacanal, C., Boutrou, R., Carrière, F., Clemente, A., Corredig, M., Dupont, D., Dufour, C., Edwards, C., Golding, M., Karakaya, S., Kirkhus, B., Le Feunteun, S., Lesmes, U., Macierzanka, A., Mackie, A.R., Martins, C., Marze, S., McClements, D.J., Ménard, O., Minekus, M., Portmann, R., Santos, C.N., Souchon, I., Singh, R.P., Vegarud, G.E., Wickham, M.S.J., Weitschies, W., Recio, I., 2019. INFOGEST static in vitro simulation of gastrointestinal food digestion. *Nat. Protoc.* 14, 991–1014. <https://doi.org/10.1038/s41596-018-0119-1>
- Burkersroda, F. von, Schedl, L., Göpferich, A., 2002. Why degradable polymers undergo surface erosion or bulk erosion. *Biomaterials* 23, 4221–4231. [https://doi.org/10.1016/S0142-9612\(02\)00170-9](https://doi.org/10.1016/S0142-9612(02)00170-9)
- Bütikofer, L., Stawarczyk, B., Roos, M., 2015. Two regression methods for estimation of a two-parameter Weibull distribution for reliability of dental materials. *Dent. Mater.* 31, e33–e50. <https://doi.org/10.1016/j.dental.2014.11.014>
- Butt, S.S., Mohammed, I.K., Raghavan, V., Osborne, J., Powell, H., Charalambides, M.N., 2018. Quantifying the differences in structure and mechanical response of confectionery products resulting from the baking and extrusion processes. *J. Food Eng.* 238, 112–121. <https://doi.org/10.1016/j.jfoodeng.2018.05.039>
- Calder, P.C., 2015. Functional Roles of Fatty Acids and Their Effects on Human Health. *J. Parenter. Enter. Nutr.* 39, 18S–32S. <https://doi.org/10.1177/0148607115595980>
- Camilleri, M., Hasler, W.L., Parkman, H.P., Quigley, E.M.M., Soffer, E., 1998. Measurement of gastrointestinal motility in the GI laboratory. *Gastroenterology* 115, 747–762. [https://doi.org/10.1016/S0016-5085\(98\)70155-6](https://doi.org/10.1016/S0016-5085(98)70155-6)
- Campanella, O.H., 2011. Instrumental techniques for measurement of textural and rheological properties of foods, in: Cho, Y.-J., Kang, S. (Eds.), *Emerging Technologies for Food Quality and Food Safety Evaluation*. Routledge.
- Campbell, C.L., Daubert, C.R., Drake, M., Foegeding, E.A., 2016. An ISO-Protein Model Food System for Evaluating Food Texture Effects. *J. Texture Stud.* 47, 377–391. <https://doi.org/10.1111/jtxs.12182>
- Campbell, C.L., Wagoner, T.B., Foegeding, E.A., 2017. Designing foods for satiety: The roles of food structure and oral processing in satiation and satiety. *Food Struct.* 13, 1–12. <https://doi.org/10.1016/j.foostr.2016.08.002>

- Canet, W., Alvarez, M.D., Gil, M.J., 2007. The analysis of frictional, displacement rate and sample dimension effects on fracture parameters from uniaxial compression of potato. *J. Food Eng.* 80, 342–352. <https://doi.org/10.1016/j.jfoodeng.2006.06.002>
- Cao, Y., Mezzenga, R., 2020. Design principles of food gels. *Nat. Food* 1, 106–118. <https://doi.org/10.1038/s43016-019-0009-x>
- Capel, F., Nicolai, T., Durand, D., Boulenguer, P., Langendorff, V., 2006. Calcium and acid induced gelation of (amidated) low methoxyl pectin. *Food Hydrocoll.* 20, 901–907. <https://doi.org/10.1016/j.foodhyd.2005.09.004>
- Capó, X., Martorell, M., Busquets-Cortés, C., Sureda, A., Riera, J., Drobnic, F., Tur, J.A., Pons, A., 2016. Effects of dietary almond- and olive oil-based docosahexaenoic acid- and vitamin E-enriched beverage supplementation on athletic performance and oxidative stress markers. *Food Funct.* 7, 4920–4934. <https://doi.org/10.1039/C6FO00758A>
- Capuano, E., Pellegrini, N., Ntone, E., Nikiforidis, C. V., 2018. In vitro lipid digestion in raw and roasted hazelnut particles and oil bodies. *Food Funct.* 9, 2508–2516. <https://doi.org/10.1039/C8FO00389K>
- Carpenter, G., Bozorgi, S., Vladescu, S., Forte, A.E., Myant, C., Potineni, R.V., Reddyhoff, T., Baier, S.K., 2019. A study of saliva lubrication using a compliant oral mimic. *Food Hydrocoll.* 92, 10–18. <https://doi.org/10.1016/j.foodhyd.2019.01.049>
- Çarşamba, E., Duerrschmid, K., Schleining, G., 2018. Assessment of acoustic-mechanical measurements for crispness of wafer products. *J. Food Eng.* 229, 93–101. <https://doi.org/10.1016/j.jfoodeng.2017.11.006>
- Cassady, B.A., Hollis, J.H., Fulford, A.D., Considine, R. V., Mattes, R.D., 2009. Mastication of almonds: effects of lipid bioaccessibility, appetite, and hormone response. *Am. J. Clin. Nutr.* 89, 794–800. <https://doi.org/10.3945/ajcn.2008.26669>
- Cassilly, D., Kantor, S., Knight, L.C., Maurer, A.H., Fisher, R.S., Semler, J., Parkman, H.P., 2008. Gastric emptying of a non-digestible solid: Assessment with simultaneous SmartPill pH and pressure capsule, antroduodenal manometry, gastric emptying scintigraphy. *Neurogastroenterol. Motil.* 20, 311–319. <https://doi.org/10.1111/j.1365-2982.2007.01061.x>
- Castro-Prada, E.M., Luyten, H., Lichtendonk, W., Hamer, R.J., van Vliet, T., 2007. An improved instrumental characterization of mechanical and acoustic properties of crispy cellular solid food. *J. Texture Stud.* 38, 698–724. <https://doi.org/10.1111/j.1745-4603.2007.00121.x>
- Castro-Prada, E.M., Meinders, M.B.J., Primo-Martin, C., Hamer, R.J., van Vliet, T., 2012. Why coarse toasted rusk rolls are crispier than fine ones. *J. Texture Stud.* 43, 421–437. <https://doi.org/10.1111/j.1745-4603.2012.00353.x>
- Channer, K.S., Virjee, J.P., 1986. The effect of size and shape of tablets on their esophageal transit. *J. Clin. Pharmacol.* 26, 141–146. <https://doi.org/10.1002/j.1552-4604.1986.tb02922.x>
- Chantrapornchai, W., McClements, D.J., 2002. Influence of glycerol on optical properties and large-strain rheology of heat-induced whey protein isolate gels. *Food Hydrocoll.* 16, 461–466. [https://doi.org/10.1016/S0268-005X\(01\)00123-0](https://doi.org/10.1016/S0268-005X(01)00123-0)
- Chaunier, L., Della Valle, G., Lourdin, D., 2007. Relationships between texture, mechanical properties and structure of cornflakes. *Food Res. Int.* 40, 493–503. <https://doi.org/10.1016/j.foodres.2006.07.014>
- Chen, J., 2009a. Food oral processing—A review. *Food Hydrocoll.* 23, 1–25. <https://doi.org/10.1016/j.foodhyd.2007.11.013>
- Chen, J., 2009b. Food oral processing—A review. *Food Hydrocoll.* 23, 1–25. <https://doi.org/https://doi.org/10.1016/j.foodhyd.2007.11.013>
- Chen, J., Feng, M., Gonzalez, Y., Pugnaroni, L.A., 2008. Application of probe tensile method for quantitative characterisation of the stickiness of fluid foods. *J. Food Eng.* 87, 281–290. <https://doi.org/10.1016/j.jfoodeng.2007.12.004>
- Chen, J., Gaikwad, V., Holmes, M., Murray, B., Povey, M., Wang, Y., Zhang, Y., 2011. Development of a simple model device for in vitro gastric digestion investigation. *Food Funct.* 2, 174. <https://doi.org/10.1039/c0fo00159g>

- Chen, J., Karlsson, C., Povey, M., 2005. Acoustic envelope detector for crispness assessment of biscuits. *J. Texture Stud.* 36, 139–156. <https://doi.org/10.1111/j.1745-4603.2005.00008.x>
- Chen, J., Khandelwal, N., Liu, Z., Funami, T., 2013. Influences of food hardness on the particle size distribution of food boluses. *Arch. Oral Biol.* 58, 293–298. <https://doi.org/10.1016/j.archoralbio.2012.10.014>
- Chen, J., Lolivret, L., 2011. The determining role of bolus rheology in triggering a swallowing. *Food Hydrocoll.* 25, 325–332. <https://doi.org/10.1016/j.foodhyd.2010.06.010>
- Chen, L., Opara, U.L., 2013a. Approaches to analysis and modeling texture in fresh and processed foods – A review. *J. Food Eng.* 119, 497–507. <https://doi.org/10.1016/j.jfoodeng.2013.06.028>
- Chen, L., Opara, U.L., 2013b. Texture measurement approaches in fresh and processed foods — A review. *Food Res. Int.* 51, 823–835. <https://doi.org/10.1016/j.foodres.2013.01.046>
- Cichero, J.A.Y., Steele, C., Duivesteyn, J., Clavé, P., Chen, J., Kayashita, J., Dantas, R., Lecko, C., Speyer, R., Lam, P., Murray, J., 2013. The Need for International Terminology and Definitions for Texture-Modified Foods and Thickened Liquids Used in Dysphagia Management: Foundations of a Global Initiative. *Curr. Phys. Med. Rehabil. Reports* 1, 280–291. <https://doi.org/10.1007/s40141-013-0024-z>
- Cisse, F., Erickson, D., Hayes, A., Opekun, A., Nichols, B., Hamaker, B., 2018. Traditional Malian Solid Foods Made from Sorghum and Millet Have Markedly Slower Gastric Emptying than Rice, Potato, or Pasta. *Nutrients* 10, 124. <https://doi.org/10.3390/nu10020124>
- Coleski, R., Wilding, G.E., Semler, J.R., Hasler, W.L., 2015. Blunting of colon contractions in diabetics with gastroparesis quantified by wireless motility capsule methods. *PLoS One* 10, 1–15. <https://doi.org/10.1371/journal.pone.0141183>
- Colombo, R., Ferron, L., Frosi, I., Papetti, A., 2021. Advances in static in vitro digestion models after COST action Infogest consensus protocol. *Food Funct.* 0–48. <https://doi.org/10.1039/d1fo01089a>
- Considine, T., Noisuwan, A., Hemar, Y., Wilkinson, B., Bronlund, J., Kasapis, S., 2011. Rheological investigations of the interactions between starch and milk proteins in model dairy systems: A review. *Food Hydrocoll.* 25, 2008–2017. <https://doi.org/10.1016/j.foodhyd.2010.09.023>
- Corral-Acero, J., Margara, F., Marciniak, M., Rodero, C., Loncaric, F., Feng, Y., Gilbert, A., Fernandes, J.F., Bukhari, H.A., Wajdan, A., Martinez, M.V., Santos, M.S., Shamohammdi, M., Luo, H., Westphal, P., Leeson, P., DiAchille, P., Gurev, V., Mayr, M., Geris, L., Pathmanathan, P., Morrison, T., Cornelussen, R., Prinzen, F., Delhaas, T., Doltra, A., Sitges, M., Vigmond, E.J., Zacur, E., Grau, V., Rodriguez, B., Remme, E.W., Niederer, S., Mortier, P., McLeod, K., Potse, M., Pueyo, E., Bueno-Orovio, A., Lamata, P., 2020. The “Digital Twin” to enable the vision of precision cardiology. *Eur. Heart J.* 41, 4556–4564B. <https://doi.org/10.1093/eurheartj/ehaa159>
- Costa, M., Dodds, K.N., Wiklendt, L., Spencer, N.J., Brookes, S.J.H., Dinning, P.G., 2013. Neurogenic and myogenic motor activity in the colon of the guinea pig, mouse, rabbit, and rat. *Am. J. Physiol. - Gastrointest. Liver Physiol.* 305, 749–759. <https://doi.org/10.1152/ajpgi.00227.2013>
- Costa, Marcello, Wiklendt, L., Arkwright, J.W., Spencer, N.J., Omari, T., Brookes, S.J.H., Dinning, P.G., 2013. An experimental method to identify neurogenic and myogenic active mechanical states of intestinal motility. *Front. Syst. Neurosci.* 7, 1–18. <https://doi.org/10.3389/fnsys.2013.00007>
- Couroyer, C., Ghadiri, M., Laval, P., Brunard, N., Kolenda, F., 2000. Methodology for Investigating the Mechanical Strength of Reforming Catalyst Beads. *Oil Gas Sci. Technol.* 55, 67–85. <https://doi.org/10.2516/ogst:2000004>
- Courtney, T.H., 2005. Fracture Mechanics, in: *Mechanical Behavior of Materials*. Waveland Press, INC., Long Grove, Illinois, pp. 404–453.
- Creton, C., Ciccotti, M., 2016. Fracture and adhesion of soft materials: A review. *Reports Prog. Phys.* 79. <https://doi.org/10.1088/0034-4885/79/4/046601>
- Cueto, M., Porrás-Saavedra, J., Farroni, A., Alamilla-Beltrán, L., Schöenlechner, R., Schleininger, G., Buera, P., 2015. Physical and mechanical properties of maize extrudates as affected by the addition of chia and quinoa seeds and antioxidants. *J. Food Eng.* 167, 139–146. <https://doi.org/10.1016/j.jfoodeng.2015.07.027>

- Czerner, M., Fasce, L.A., Martucci, J.F., Ruseckaite, R., Frontini, P.M., 2016. Deformation and fracture behavior of physical gelatin gel systems. *Food Hydrocoll.* 60, 299–307. <https://doi.org/10.1016/j.foodhyd.2016.04.007>
- Dalmau, M.E., Eim, V., Rosselló, C., Cárcel, J.A., Simal, S., 2019. Effects of convective drying and freeze-drying on the release of bioactive compounds from beetroot during in vitro gastric digestion. *Food Funct.* 10, 3209–3223. <https://doi.org/10.1039/C8FO02421A>
- Dan, H., Okamoto, M., Wada, Y., Dan, I., Kohyama, K., 2007. First bite for hardness judgment as haptic exploratory procedure. *Physiol. Behav.* 92, 601–610. <https://doi.org/10.1016/j.physbeh.2007.05.006>
- Dan, H., Watanabe, H., Dan, I., Kohyama, K., 2003. Effects of textural changes in cooked apples on the human bite, and instrumental tests. *J. Texture Stud.* 34, 499–514. <https://doi.org/10.1111/j.1745-4603.2003.tb01078.x>
- Dang, Y., Liu, Y., Hashem, R., Bhattacharya, D., Allen, J., Stommel, M., Cheng, L.K., Xu, W., 2020. SoGut: A Soft Robotic Gastric Simulator. *Soft Robot.* 00, soro.2019.0136. <https://doi.org/10.1089/soro.2019.0136>
- de Lorgeril, M., Salen, P., Martin, J.-L., Monjaud, I., Delaye, J., Mamelle, N., 1999. Mediterranean Diet, Traditional Risk Factors, and the Rate of Cardiovascular Complications After Myocardial Infarction. *Circulation* 99, 779–785. <https://doi.org/10.1161/01.CIR.99.6.779>
- de Loubens, C., Dubreuil, A., Lentle, R.G., Magnin, A., Kissi, N. El, Faucheron, J.L., 2020. Rheology of human faeces and pathophysiology of defaecation. *Tech. Coloproctol.* 24, 323–329. <https://doi.org/10.1007/s10151-020-02174-0>
- DeLoid, G.M., Wang, Y., Kapronezai, K., Lorente, L.R., Zhang, R., Pyrgiotakis, G., Konduru, N. V., Ericsson, M., White, J.C., De La Torre-Roche, R., Xiao, H., McClements, D.J., Demokritou, P., 2017. An integrated methodology for assessing the impact of food matrix and gastrointestinal effects on the biokinetics and cellular toxicity of ingested engineered nanomaterials. Part. *Fibre Toxicol.* 14, 40. <https://doi.org/10.1186/s12989-017-0221-5>
- Delprete, C., Sesana, R., 2014. Mechanical characterization of kernel and shell of hazelnuts: Proposal of an experimental procedure. *J. Food Eng.* 124, 28–34. <https://doi.org/10.1016/j.jfoodeng.2013.09.027>
- Deng, R., Seimys, A., Mars, M., Janssen, A.E.M., Smeets, P.A.M., 2022. Monitoring pH and whey protein digestion by TD-NMR and MRI in a novel semi-dynamic in vitro gastric simulator (MR-GAS). *Food Hydrocoll.* 125, 107393. <https://doi.org/10.1016/j.foodhyd.2021.107393>
- Denis, S., Sayd, T., Georges, A., Chambon, C., Chalancon, S., Santé-Lhoutellier, V., Blanquet-Diot, S., 2016. Digestion of cooked meat proteins is slightly affected by age as assessed using the dynamic gastrointestinal TIM model and mass spectrometry. *Food Funct.* 7, 2682–2691. <https://doi.org/10.1039/c6fo00120c>
- Dewulf, E.M., Cani, P.D., Claus, S.P., Fuentes, S., Puylaert, P.G.B., Neyrinck, A.M., Bindels, L.B., De Vos, W.M., Gibson, G.R., Thissen, J.P., Delzenne, N.M., 2013. Insight into the prebiotic concept: Lessons from an exploratory, double blind intervention study with inulin-type fructans in obese women. *Gut* 62, 1112–1121. <https://doi.org/10.1136/gutjnl-2012-303304>
- Dhital, S., Dolan, G., Stokes, J.R., Gidley, M.J., 2014. Enzymatic hydrolysis of starch in the presence of cereal soluble fibre polysaccharides. *Food Funct.* 5, 579. <https://doi.org/10.1039/c3fo60506j>
- Dickinson, E., 2012. Emulsion gels: The structuring of soft solids with protein-stabilized oil droplets. *Food Hydrocoll.* 28, 224–241. <https://doi.org/10.1016/j.foodhyd.2011.12.017>
- Dirven, S., Allen, J., Xu, W. (Peter), Cheng, L.K., 2017. Soft-robotic esophageal swallowing as a clinically-inspired bolus rheometry technique. *Meas. Sci. Technol.* 28, 035701. <https://doi.org/10.1088/1361-6501/aa544f>
- Drechsler, K.C., Bornhorst, G.M., 2018. Modeling the softening of carbohydrate-based foods during simulated gastric digestion. *J. Food Eng.* 222, 38–48. <https://doi.org/10.1016/j.jfoodeng.2017.11.007>
- Drechsler, K.C., Ferrua, M.J., 2016. Modelling the breakdown mechanics of solid foods during gastric digestion. *Food Res. Int.* 88, 181–190. <https://doi.org/10.1016/j.foodres.2016.02.019>
- Dressman, J.B., Berardi, R.R., Dermentzoglou, L.C., Russell, T.L., Schmaltz, S.P., Barnett, J.L., Jarvenpaa, K.M., 1990. Upper Gastrointestinal (GI) pH in Young, Healthy Men and Women. *Pharm.*

- Res. An Off. J. Am. Assoc. Pharm. Sci. <https://doi.org/10.1023/A:1015827908309>
- Duncan, T.T., Sarapas, J.M., Defante, A.P., Beers, K.L., Chan, E.P., 2020. Cutting to measure the elasticity and fracture of soft gels. *Soft Matter* 16, 8826–8831. <https://doi.org/10.1039/d0sm01174f>
- Dupont, D., Alric, M., Blanquet-Diot, S., Bornhorst, G., Cueva, C., Deglaire, A., Denis, S., Ferrua, M., Havenaar, R., Lelieveld, J., Mackie, A.R., Marzorati, M., Menard, O., Minekus, M., Miralles, B., Recio, I., Van den Abbeele, P., 2019. Can dynamic in vitro digestion systems mimic the physiological reality? *Crit. Rev. Food Sci. Nutr.* 59, 1546–1562. <https://doi.org/10.1080/10408398.2017.1421900>
- Egger, L., Schlegel, P., Baumann, C., Stoffers, H., Guggisberg, D., Brügger, C., Dürr, D., Stoll, P., Vergères, G., Portmann, R., 2017. Physiological comparability of the harmonized INFOGEST in vitro digestion method to in vivo pig digestion. *Food Res. Int.* 102, 567–574. <https://doi.org/10.1016/j.foodres.2017.09.047>
- Ehrlein, H.-J., Reich, H., Schwinger, M., 1982. Physiological Significance of the Contractions of the Rabbit Proximal Colon. *Q. J. Exp. Physiol.* 67, 407–417. <https://doi.org/10.1113/expphysiol.1982.sp002656>
- Ellis, P.R., Kendall, C.W.C., Ren, Y., Parker, C., Pacy, J.F., Waldron, K.W., Jenkins, D.J.A., 2004. Role of cell walls in the bioaccessibility of lipids in almond seeds. *Am. J. Clin. Nutr.* 80, 604–613. <https://doi.org/10.1093/ajcn/80.3.604>
- Erlanson-Albertsson, C., Weström, B., Pierzynowski, S., Karlsson, S., Ahrén, B., 1991. Pancreatic procolipase activation peptide-enterostatin-inhibits pancreatic enzyme secretion in the pig. *Pancreas* 6, 619–624. <https://doi.org/10.1097/00006676-199111000-00001>
- Estruch, R., Ros, E., Salas-Salvadó, J., Covas, M.-I., Corella, D., Arós, F., Gómez-Gracia, E., Ruiz-Gutiérrez, V., Fiol, M., Lapetra, J., Lamuela-Raventos, R.M., Serra-Majem, L., Pintó, X., Basora, J., Muñoz, M.A., Sorlí, J. V., Martínez, J.A., Fitó, M., Gea, A., Hernán, M.A., Martínez-González, M.A., 2018. Primary Prevention of Cardiovascular Disease with a Mediterranean Diet Supplemented with Extra-Virgin Olive Oil or Nuts. *N. Engl. J. Med.* 378, e34. <https://doi.org/10.1056/NEJMoa1800389>
- Everard, C.D., O’Callaghan, D.J., O’Kennedy, B.T., O’Donnel, C.P., Sheehan, E.M., Delahunty, C.M., 2007. A three-point bending test for prediction of sensory texture in processed cheese. *J. Texture Stud.* 38, 438–456. <https://doi.org/10.1111/j.1745-4603.2007.00106.x>
- Faas, H., Hebbard, G.S., Feinle, C., Kunz, P., Brasseur, J.G., Indireskumar, K., Dent, J., Boesiger, P., Thumshirn, M., Fried, M., Schwizer, W., 2001. Pressure-geometry relationship in the antroduodenal region in humans. *Am. J. Physiol. - Gastrointest. Liver Physiol.* 281, 1214–1220. <https://doi.org/10.1152/ajpgi.2001.281.5.g1214>
- Faber, T.J., Jaishankar, A., McKinley, G.H., 2017a. Describing the firmness, springiness and rubberiness of food gels using fractional calculus. Part II: Measurements on semi-hard cheese. *Food Hydrocoll.* 62, 325–339. <https://doi.org/10.1016/j.foodhyd.2016.06.038>
- Faber, T.J., Van Breemen, L.C.A., McKinley, G.H., 2017b. From firm to fluid – Structure-texture relations of filled gels probed under Large Amplitude Oscillatory Shear. *J. Food Eng.* 210, 1–18. <https://doi.org/10.1016/j.jfoodeng.2017.03.028>
- Fang, X., Rioux, L.-E., Labrie, S., Turgeon, S.L., 2016. Commercial cheeses with different texture have different disintegration and protein/peptide release rates during simulated in vitro digestion. *Int. Dairy J.* 56, 169–178. <https://doi.org/10.1016/j.idairyj.2016.01.023>
- Ferrua, M.J., Kong, F., Singh, R.P., 2011. Computational modeling of gastric digestion and the role of food material properties. *Trends Food Sci. Technol.* 22, 480–491. <https://doi.org/10.1016/j.tifs.2011.04.007>
- Ferrua, M.J., Singh, R.P., 2010. Modeling the fluid dynamics in a human stomach to gain insight of food digestion. *J. Food Sci.* 75, 151–162. <https://doi.org/10.1111/j.1750-3841.2010.01748.x>
- Ferrua, M.J., Xue, Z., Paul Singh, R., 2014. On the kinematics and efficiency of advective mixing during gastric digestion – A numerical analysis. *J. Biomech.* 47, 3664–3673. <https://doi.org/10.1016/j.jbiomech.2014.09.033>

- Firth, M., Prather, C.M., 2002. Gastrointestinal motility problems in the elderly patient. *Gastroenterology* 122, 1688–1700. <https://doi.org/10.1053/gast.2002.33566>
- Fisher, R.S., Malmud, L.S., Applegate, G., Rock, E., Lorber, S.H., 1982. Effect of bolus composition on esophageal transit: concise communication. *J. Nucl. Med.* 23, 878–82.
- Floury, J., Bianchi, T., Thévenot, J., Dupont, D., Jamme, F., Lutton, E., Panouillé, M., Boué, F., Le Feunteun, S., 2018. Exploring the breakdown of dairy protein gels during in vitro gastric digestion using time-lapse synchrotron deep-UV fluorescence microscopy. *Food Chem.* 239, 898–910. <https://doi.org/10.1016/j.foodchem.2017.07.023>
- Foegeding, E.A., Bowland, E.L., Hardin, C.C., 1995. Factors that determine the fracture properties and microstructure of globular protein gels. *Food Hydrocoll.* 9, 237–249. [https://doi.org/10.1016/S0268-005X\(09\)80254-3](https://doi.org/10.1016/S0268-005X(09)80254-3)
- Foegeding, E.A., Stieger, M., van de Velde, F., 2017. Moving from molecules, to structure, to texture perception. *Food Hydrocoll.* 68, 31–42. <https://doi.org/10.1016/j.foodhyd.2016.11.009>
- Forte, A.E., D'Amico, F., Charalambides, M.N., Dini, D., Williams, J.G., 2015. Modelling and experimental characterisation of the rate dependent fracture properties of gelatine gels. *Food Hydrocoll.* 46, 180–190. <https://doi.org/10.1016/j.foodhyd.2014.12.028>
- Foster-Powell, K., Holt, S.H., Brand-Miller, J.C., 2002. International table of glycemic index and glycemic load values: 2002. *Am. J. Clin. Nutr.* 76, 5–56. <https://doi.org/10.1093/ajcn/76.1.5>
- Foster, E., Bradley, J., 2018. Methodological considerations and future insights for 24-hour dietary recall assessment in children. *Nutr. Res.* 51, 1–11. <https://doi.org/10.1016/j.nutres.2017.11.001>
- Foster, K.D., Woda, A., Peyron, M.A., 2006. Effect of Texture of Plastic and Elastic Model Foods on the Parameters of Mastication. *J. Neurophysiol.* 95, 3469–3479. <https://doi.org/10.1152/jn.01003.2005>
- Freitas, D., Le Feunteun, S., Panouillé, M., Souchon, I., 2018. The important role of salivary α -amylase in the gastric digestion of wheat bread starch. *Food Funct.* 9, 200–208. <https://doi.org/10.1039/C7FO01484H>
- Fu, Y., Kao, W.J., 2010. Drug release kinetics and transport mechanisms of non-degradable and degradable polymeric delivery systems. *Expert Opin. Drug Deliv.* 7, 429–444. <https://doi.org/10.1517/17425241003602259>
- Fujinaga, M., Chernaia, M.M., Mosimann, S.C., James, M.N.G., Tarasova, N.I., 2008. Crystal structure of human pepsin and its complex with pepstatin. *Protein Sci.* 4, 960–972. <https://doi.org/10.1002/pro.5560040516>
- Fullard, L.A., Lammers, W.J., Ferrua, M.J., 2015. Advective mixing due to longitudinal and segmental contractions in the ileum of the rabbit. *J. Food Eng.* 160, 1–10. <https://doi.org/10.1016/j.jfoodeng.2015.03.017>
- Funami, T., 2011. Next target for food hydrocolloid studies: Texture design of foods using hydrocolloid technology. *Food Hydrocoll.* 25, 1904–1914. <https://doi.org/10.1016/j.foodhyd.2011.03.010>
- Gallier, S., Rutherford, S.M., Moughan, P.J., Singh, H., 2014. Effect of food matrix microstructure on stomach emptying rate and apparent ileal fatty acid digestibility of almond lipids. *Food Funct.* 5, 2410–2419. <https://doi.org/10.1039/C4FO00335G>
- Gallier, S., Singh, H., 2012. Behavior of almond oil bodies during in vitro gastric and intestinal digestion. *Food Funct.* 3, 547. <https://doi.org/10.1039/c2fo10259e>
- Gamonpilas, C., Charalambides, M.N., Williams, J.G., 2009. Determination of large deformation and fracture behaviour of starch gels from conventional and wire cutting experiments. *J. Mater. Sci.* 44, 4976–4986. <https://doi.org/10.1007/s10853-009-3760-9>
- Gao, J., Wong, J.X., Lim, J.C.-S., Henry, J., Zhou, W., 2015. Influence of bread structure on human oral processing. *J. Food Eng.* 167, 147–155. <https://doi.org/10.1016/j.jfoodeng.2015.07.022>
- Gargouri, Y., Pieroni, G., Riviere, C., Saunier, J.-F., Lowe, P.A., Sarda, L., Verger, R., 1986. Kinetic assay of human gastric lipase on short- and long-chain triacylglycerol emulsions. *Gastroenterology* 91, 919–925. [https://doi.org/10.1016/0016-5085\(86\)90695-5](https://doi.org/10.1016/0016-5085(86)90695-5)
- Gavião, M.B.D., Engelen, L., Van Der Bilt, A., 2004. Chewing behavior and salivary secretion. *Eur. J. Oral Sci.* 112, 19–24. <https://doi.org/10.1111/j.0909-8836.2004.00105.x>

- Gebauer, S.K., Novotny, J.A., Bornhorst, G.M., Baer, D.J., 2016. Food processing and structure impact the metabolizable energy of almonds. *Food Funct.* 7, 4231–4238. <https://doi.org/10.1039/C6FO01076H>
- Goh, S.M., Charalambides, M.N., Williams, J.G., 2005. On the mechanics of wire cutting of cheese. *Eng. Fract. Mech.* 72, 931–946. <https://doi.org/10.1016/j.engfracmech.2004.07.015>
- Gopirajah, R., Raichurkar, K.P., Wadhwa, R., Anandharamakrishnan, C., 2016. The glycemic response to fibre rich foods and their relationship with gastric emptying and motor functions: an MRI study. *Food Funct.* 7, 3964–3972. <https://doi.org/10.1039/C6FO00659K>
- Gouseti, O., Jaime-Fonseca, M.R., Fryer, P.J., Mills, C., Wickham, M.S.J., Bakalis, S., 2014. Hydrocolloids in human digestion: Dynamic in-vitro assessment of the effect of food formulation on mass transfer. *Food Hydrocoll.* 42, 378–385. <https://doi.org/10.1016/j.foodhyd.2014.06.004>
- Grassby, T., Mandalari, G., Grundy, M.M.L., Edwards, C.H., Bisignano, C., Trombetta, D., Smeriglio, A., Chessa, S., Ray, S., Sanderson, J., Berry, S.E., Ellis, P.R., Waldron, K.W., 2017. In vitro and in vivo modeling of lipid bioaccessibility and digestion from almond muffins: The importance of the cell-wall barrier mechanism. *J. Funct. Foods* 37, 263–271. <https://doi.org/10.1016/j.jff.2017.07.046>
- Grassby, T., Picout, D.R., Mandalari, G., Faulks, R.M., Kendall, C.W.C., Rich, G.T., Wickham, M.S.J., Lapsley, K., Ellis, P.R., 2014. Modelling of nutrient bioaccessibility in almond seeds based on the fracture properties of their cell walls. *Food Funct.* 5, 3096–3106. <https://doi.org/10.1039/C4FO00659C>
- Gravelle, A.J., Marangoni, A.G., 2021. A new fractal structural-mechanical theory of particle-filled colloidal networks with heterogeneous stress translation. *J. Colloid Interface Sci.* 598, 56–68. <https://doi.org/10.1016/j.jcis.2021.03.180>
- Grundy, M.M.L., Lapsley, K., Ellis, P.R., 2016. A review of the impact of processing on nutrient bioaccessibility and digestion of almonds. *Int. J. Food Sci. Technol.* 51, 1937–1946. <https://doi.org/10.1111/ijfs.13192>
- Grundy, M.M.L., Carrière, F., Mackie, A.R., Gray, D.A., Butterworth, P.J., Ellis, P.R., 2016. The role of plant cell wall encapsulation and porosity in regulating lipolysis during the digestion of almond seeds. *Food Funct.* 7, 69–78. <https://doi.org/10.1039/C5FO00758E>
- Grundy, M.M.L., Grassby, T., Mandalari, G., Waldron, K.W., Butterworth, P.J., Berry, S.E.E., Ellis, P.R., 2015a. Effect of mastication on lipid bioaccessibility of almonds in a randomized human study and its implications for digestion kinetics, metabolizable energy, and postprandial lipemia. *Am. J. Clin. Nutr.* 101, 25–33. <https://doi.org/10.3945/ajcn.114.088328>
- Grundy, M.M.L., Wilde, P.J., Butterworth, P.J., Gray, R., Ellis, P.R., 2015b. Impact of cell wall encapsulation of almonds on in vitro duodenal lipolysis. *Food Chem.* 185, 405–412. <https://doi.org/10.1016/j.foodchem.2015.04.013>
- Guinea, G., Rojo, F., Elices, M., 2004. Brittle failure of dry spaghetti. *Eng. Fail. Anal.* 11, 705–714. <https://doi.org/10.1016/j.engfailanal.2003.10.006>
- Guo, Q., Ye, A., Lad, M., Dalgleish, D., Singh, H., 2014a. Effect of gel structure on the gastric digestion of whey protein emulsion gels. *Soft Matter* 10, 1214–1223. <https://doi.org/10.1039/c3sm52758a>
- Guo, Q., Ye, A., Lad, M., Dalgleish, D., Singh, H., 2014b. Behaviour of whey protein emulsion gel during oral and gastric digestion: effect of droplet size. *Soft Matter* 10, 4173. <https://doi.org/10.1039/c4sm00598h>
- Guo, Q., Ye, A., Lad, M., Dalgleish, D., Singh, H., 2013. The breakdown properties of heat-set whey protein emulsion gels in the human mouth. *Food Hydrocoll.* 33, 215–224. <https://doi.org/10.1016/j.foodhyd.2013.03.008>
- Guo, Q., Ye, A., Lad, M., Ferrua, M., Dalgleish, D., Singh, H., 2015. Disintegration kinetics of food gels during gastric digestion and its role on gastric emptying: an in vitro analysis. *Food Funct.* 6, 756–764. <https://doi.org/10.1039/C4FO00700J>
- Guo, Q., Ye, A., Singh, H., Rousseau, D., 2020. Deconstructing and restructuring of foods during gastric digestion. *Compr. Rev. Food Sci. Food Saf.* 19, 1658–1679. <https://doi.org/10.1111/1541-4337.12558>

- Hamaker, B.R., Tuncil, Y.E., 2014. A perspective on the complexity of dietary fiber structures and their potential effect on the gut microbiota. *J. Mol. Biol.* 426, 3838–3850. <https://doi.org/10.1016/j.jmb.2014.07.028>
- Hansen, M.B., 2002. Small intestinal manometry. *Physiol. Res.* 51, 541–556.
- Hansen, M.M., Maidannyk, V.A., Roos, Y.H., 2020. Thermal gelation and hardening of whey protein beads for subsequent dehydration and encapsulation using vitrifying sugars. *J. Food Eng.* 279. <https://doi.org/10.1016/j.jfoodeng.2020.109966>
- Hari, B., Bakalis, S., Fryer, P., Kingdom, U., 2012. Computational Duodenum Modelling and Simulation of the.
- Harrison, S.M., Cleary, P.W., 2014. Towards modelling of fluid flow and food breakage by the teeth in the oral cavity using smoothed particle hydrodynamics (SPH). *Eur. Food Res. Technol.* 238, 185–215. <https://doi.org/10.1007/s00217-013-2077-8>
- Harrison, S.M., Cleary, P.W., Eyres, G., D. Sinnott, M., Lundin, L., 2014. Challenges in computational modelling of food breakdown and flavour release. *Food Funct.* 5, 2792–2805. <https://doi.org/10.1039/C4FO00786G>
- Hayes, A.M.R.R., Swackhamer, C., Mennah-Govela, Y.A., Martinez, M.M., Diatta, A., Bornhorst, G.M., Hamaker, B.R., 2020. Pearl millet (*Pennisetum glaucum*) couscous breaks down faster than wheat couscous in the Human Gastric Simulator, though has slower starch hydrolysis. *Food Funct.* 11, 111–122. <https://doi.org/10.1039/c9fo01461f>
- He, L.H., Swain, M. V., 2007. Enamel — A “metallic-like” deformable biocomposite. *J. Dent.* 35, 431–437. <https://doi.org/https://doi.org/10.1016/j.jdent.2006.12.002>
- Herrero, M., Thornton, P.K., Mason-D’Croz, D., Palmer, J., Benton, T.G., Bodirsky, B.L., Bogard, J.R., Hall, A., Lee, B., Nyborg, K., Pradhan, P., Bonnett, G.D., Bryan, B.A., Campbell, B.M., Christensen, S., Clark, M., Cook, M.T., de Boer, I.J.M., Downs, C., Dizyee, K., Folberth, C., Godde, C.M., Gerber, J.S., Grundy, M., Havlik, P., Jarvis, A., King, R., Loboguerrero, A.M., Lopes, M.A., McIntyre, C.L., Naylor, R., Navarro, J., Obersteiner, M., Parodi, A., Peoples, M.B., Pikaar, I., Popp, A., Rockström, J., Robertson, M.J., Smith, P., Stehfest, E., Swain, S.M., Valin, H., van Wijk, M., van Zanten, H.H.E., Vermeulen, S., Vervoort, J., West, P.C., 2020. Innovation can accelerate the transition towards a sustainable food system. *Nat. Food* 1, 266–272. <https://doi.org/10.1038/s43016-020-0074-1>
- Hirashima, M., Takahashi, R., Nishinari, K., 2012. The gelatinization and retrogradation of cornstarch gels in the presence of citric acid. *Food Hydrocoll.* 27, 390–393. <https://doi.org/10.1016/j.foodhyd.2011.10.011>
- Hoad, C.L., Parker, H., Hudders, N., Costigan, C., Cox, E.F., Perkins, A.C., Blackshaw, P.E., Marciani, L., Spiller, R.C., Fox, M.R., Gowland, P.A., 2015. Measurement of gastric meal and secretion volumes using magnetic resonance imaging. *Phys. Med. Biol.* 60, 1367–1383. <https://doi.org/10.1088/0031-9155/60/3/1367>
- Hofmann, A.F., 1999. The continuing importance of bile acids in liver and intestinal disease. *Arch. Intern. Med.* 159, 2647–2658. <https://doi.org/10.1001/archinte.159.22.2647>
- Hutchings, S.C., Foster, K.D., Bronlund, J.E., Lentle, R.G., Jones, J.R., Morgenstern, M.P., 2012. Particle breakdown dynamics of heterogeneous foods during mastication: Peanuts embedded inside different food matrices. *J. Food Eng.* 109, 736–744. <https://doi.org/10.1016/j.jfoodeng.2011.11.011>
- Hutchings, S.C., Foster, K.D., Bronlund, J.E., Lentle, R.G., Jones, J.R., Morgenstern, M.P., 2011. Mastication of heterogeneous foods: Peanuts inside two different food matrices. *Food Qual. Prefer.* 22, 332–339. <https://doi.org/10.1016/j.foodqual.2010.12.004>
- Ikeda, S., Foegeding, E.A., 1999. Dynamic viscoelastic properties of thermally induced whey protein isolate gels with added lecithin. *Food Hydrocoll.* 13, 245–254. [https://doi.org/10.1016/S0268-005X\(99\)00006-5](https://doi.org/10.1016/S0268-005X(99)00006-5)
- Ioannides, Y., Seers, J., Defernez, M., Raithatha, C., Howarth, M.S., Smith, A., Kemsley, E.K., 2009. Electromyography of the masticatory muscles can detect variation in the mechanical and sensory properties of apples. *Food Qual. Prefer.* 20, 203–215. <https://doi.org/10.1016/j.foodqual.2008.09.007>

- Jakubczyk, E., Linde, M., Gondek, E., Kamińska-Dwórznicza, A., Samborska, K., Antoniuk, A., 2015. The effect of phytosterols addition on the textural properties of extruded crisp bread. *J. Food Eng.* 167, 156–161. <https://doi.org/10.1016/j.jfoodeng.2015.07.013>
- Jalabert-Malbos, M.-L., Mishellany-Dutour, A., Woda, A., Peyron, M.-A., 2007. Particle size distribution in the food bolus after mastication of natural foods. *Food Qual. Prefer.* 18, 803–812. <https://doi.org/10.1016/j.foodqual.2007.01.010>
- Jang, A., Kim, D., Sung, K.-S., Jung, S., Kim, H.J., Jo, C., 2014. The effect of dietary α -lipoic acid, betaine, L-carnitine, and swimming on the obesity of mice induced by a high-fat diet. *Food Funct.* 5, 1966–1974. <https://doi.org/10.1039/C4FO00246F>
- Jean, A., 2001. Brain stem control of swallowing: Neuronal network and cellular mechanisms. *Physiol. Rev.* 81, 929–969. <https://doi.org/10.1152/physrev.2001.81.2.929>
- Jiamjariyatam, R., Kongpensook, V., Pradipasena, P., 2016. Prediction Models for Textural Properties of Puffed Rice Starch Product by Relative Crystallinity. *J. Food Qual.* 39, 445–455. <https://doi.org/10.1111/jfq.12218>
- Jiang, M., Wang, Y., van Santen, E., Chappell, J.A., 2008. Evaluation of textural properties of channel catfish (*Ictalurus punctatus* Rafinesque) fillet with the natural contour method. *LWT - Food Sci. Technol.* 41, 1548–1554. <https://doi.org/10.1016/j.lwt.2007.11.022>
- John, J., Seifi, A., 2017. Total parenteral nutrition usage trends in the United States. *J. Crit. Care* 40, 312–313. <https://doi.org/10.1016/j.jcrc.2017.04.018>
- Joubert, M., Septier, C., Brignot, H., Salles, C., Panouillé, M., Feron, G., Tournier, C., 2017. Chewing bread: impact on alpha-amylase secretion and oral digestion. *Food Funct.* 8, 607–614. <https://doi.org/10.1039/C6FO00963H>
- Kamba, M., Seta, Y., Kusai, A., Ikeda, M., Nishimura, K., 2000. A unique dosage form to evaluate the mechanical destructive force in the gastrointestinal tract. *Int. J. Pharm.* 208, 61–70. [https://doi.org/10.1016/S0378-5173\(00\)00552-4](https://doi.org/10.1016/S0378-5173(00)00552-4)
- Kamyab, I., Chakrabarti, S., Williams, J.G., 1998. Cutting cheese with wire. *J. Mater. Sci.* <https://doi.org/10.1023/A:1017517332112>
- Karthikeyan, J.S., Salvi, D., Karwe, M. V., 2021. Modeling of fluid flow, carbohydrate digestion, and glucose absorption in human small intestine. *J. Food Eng.* 292, 110339. <https://doi.org/10.1016/j.jfoodeng.2020.110339>
- Keppler, S., Huynh, K., Reinhold, D., Bornhorst, G.M., 2021. Fate of Phytometabolites of Antibiotics during In Vitro Digestion and Implications for Human Health . *J. Agric. Food Chem.* 69, 12598–12607. <https://doi.org/10.1021/acs.jafc.1c03934>
- Keppler, S., O’Meara, S., Bakalis, S., Fryer, P.J., Bornhorst, G.M., 2020. Characterization of individual particle movement during in vitro gastric digestion in the Human Gastric Simulator (HGS). *J. Food Eng.* 264, 109674. <https://doi.org/10.1016/j.jfoodeng.2019.07.021>
- Khalaf, A., Hoad, C.L., Menys, A., Nowak, A., Taylor, S.A., Paparo, S., Lingaya, M., Falcone, Y., Singh, G., Spiller, R.C., Gowland, P.A., Marciani, L., Moran, G.W., 2018. MRI assessment of the postprandial gastrointestinal motility and peptide response in healthy humans. *Neurogastroenterol. Motil.* 30, 1–9. <https://doi.org/10.1111/nmo.13182>
- Kharlamova, A., Chassenieux, C., Nicolai, T., 2018. Acid-induced gelation of whey protein aggregates: Kinetics, gel structure and rheological properties. *Food Hydrocoll.* 81, 263–272. <https://doi.org/10.1016/j.foodhyd.2018.02.043>
- Khubber, S., Chaturvedi, K., Thakur, N., Sharma, N., Yadav, S.K., 2021. Low-methoxyl pectin stabilizes low-fat set yoghurt and improves their physicochemical properties, rheology, microstructure and sensory liking. *Food Hydrocoll.* 111, 106240. <https://doi.org/10.1016/j.foodhyd.2020.106240>
- Kim, E.H.-J., Corrigan, V.K., Wilson, A.J., Waters, I.R., Hedderley, D.I., Morgenstern, M.P., 2012. Fundamental fracture properties associated with sensory hardness of brittle solid foods. *J. Texture Stud.* 43, 49–62. <https://doi.org/10.1111/j.1745-4603.2011.00316.x>
- Klein, T., Anderegg, W.R.L., 2021. A vast increase in heat exposure in the 21st century is driven by global warming and urban population growth. *Sustain. Cities Soc.* 73, 103098.

- <https://doi.org/10.1016/j.scs.2021.103098>
- Koç, H., Vinyard, C.J., Essick, G.K., Foegeding, E.A., 2013. Food Oral Processing: Conversion of Food Structure to Textural Perception. *Annu. Rev. Food Sci. Technol.* 4, 237–266.
<https://doi.org/10.1146/annurev-food-030212-182637>
- Kohyama, K., Gao, Z., Watanabe, T., Ishihara, S., Nakao, S., Funami, T., 2017. Relationships Between Mechanical Properties Obtained from Compression Test and Electromyography Variables During Natural Oral Processing of Gellan Gum Gels. *J. Texture Stud.* 48, 66–75.
<https://doi.org/10.1111/jtxs.12211>
- Kohyama, K., Hayakawa, F., Kazami, Y., Ishihara, S., Nakao, S., Funami, T., Nishinari, K., 2015. Electromyographic texture characterization of hydrocolloid gels as model foods with varying mastication and swallowing difficulties. *Food Hydrocoll.* 43, 146–152.
<https://doi.org/10.1016/j.foodhyd.2014.05.016>
- Kohyama, K., Ishihara, S., Nakauma, M., Funami, T., 2020. Fracture phenomena of soft gellan gum gels during compression with artificial tongues. *Food Hydrocoll.*
<https://doi.org/10.1016/j.foodhyd.2020.106283>
- Kohyama, K., Sasaki, T., Hayakawa, F., 2008. Characterization of Food Physical Properties by the Mastication Parameters Measured by Electromyography of the Jaw-Closing Muscles and Mandibular Kinematics in Young Adults. *Biosci. Biotechnol. Biochem.* 72, 1690–1695.
<https://doi.org/10.1271/bbb.70769>
- Kong, F., Singh, R.P., 2009a. Modes of disintegration of solid foods in simulated gastric environment. *Food Biophys.* 4, 180–190. <https://doi.org/10.1007/s11483-009-9116-9>
- Kong, F., Singh, R.P., 2009b. Digestion of Raw and Roasted Almonds in Simulated Gastric Environment. *Food Biophys.* 4, 365–377. <https://doi.org/10.1007/s11483-009-9135-6>
- Kong, F., Singh, R.P., 2008a. Disintegration of Solid Foods in Human Stomach. *J. Food Sci.* 73, R67–R80. <https://doi.org/10.1111/j.1750-3841.2008.00766.x>
- Kong, F., Singh, R.P., 2008b. A Model Stomach System to Investigate Disintegration Kinetics of Solid Foods during Gastric Digestion. *J. Food Sci.* 73, E202–E210. <https://doi.org/10.1111/j.1750-3841.2008.00745.x>
- Kozu, H., Kobayashi, I., Nakajima, M., Neves, M.A., Uemura, K., Isoda, H., Ichikawa, S., 2017. Mixing characterization of liquid contents in human gastric digestion simulator equipped with gastric secretion and emptying. *Biochem. Eng. J.* 122, 85–90. <https://doi.org/10.1016/j.bej.2016.10.013>
- Kozu, H., Kobayashi, I., Nakajima, M., Uemura, K., Sato, S., Ichikawa, S., 2010. Analysis of Flow Phenomena in Gastric Contents Induced by Human Gastric Peristalsis Using CFD. *Food Biophys.* 5, 330–336. <https://doi.org/10.1007/s11483-010-9183-y>
- Kozu, H., Kobayashi, I., Neves, M.A., Nakajima, M., Uemura, K., Sato, S., Ichikawa, S., 2014. PIV and CFD studies on analyzing intragastric flow phenomena induced by peristalsis using a human gastric flow simulator. *Food Funct.* 5, 1839–1847. <https://doi.org/10.1039/C4FO00041B>
- Kozu, H., Wang, Zheng, Wang, Zaitian, Nakajima, M., Neves, M.A., Uemura, K., Sato, S., Kobayashi, I., Ichikawa, S., 2018. In vitro digestion of oil-containing hydrogels using gastric digestion simulator: A model analysis for oil release control inside human stomach. *Japan J. Food Eng.* 19, 89–102.
<https://doi.org/10.11301/jsfe.17505>
- Kuhn, K.R., e Silva, F.G.D., Netto, F.M., da Cunha, R.L., 2019. Production of whey protein isolate – gellan microbeads for encapsulation and release of flaxseed bioactive compounds. *J. Food Eng.* 247, 104–114. <https://doi.org/10.1016/j.jfoodeng.2018.12.002>
- Kwiatk, M.A., Steingoetter, A., Pal, A., Menne, D., Brasseur, J.G., Hebbard, G.S., Boesiger, P., Thumshirn, M., Fried, M., Schwizer, W., 2006. Quantification of distal antral contractile motility in healthy human stomach with magnetic resonance imaging. *J. Magn. Reson. Imaging* 24, 1101–1109.
<https://doi.org/10.1002/jmri.20738>
- Laird, M.F., Vogel, E.R., Pontzer, H., 2016. Chewing efficiency and occlusal functional morphology in modern humans. *J. Hum. Evol.* 93, 1–11. <https://doi.org/10.1016/j.jhevol.2015.11.005>
- Lamart, S., Imran, R., Simon, S.L., Doi, K., Morton, L.M., Curtis, R.E., Lee, Choonik, Drozdovitch, V.,

- Maass-Moreno, R., Chen, C.C., Whatley, M., Miller, D.L., Pacak, K., Lee, Choonsik, 2013. Prediction of the location and size of the stomach using patient characteristics for retrospective radiation dose estimation following radiotherapy. *Phys. Med. Biol.* 58, 8739–8753. <https://doi.org/10.1088/0031-9155/58/24/8739>
- Lambrecht, M.A., Jansens, K.J.A., Rombouts, I., Brijs, K., Rousseau, F., Schymkowitz, J., Delcour, J.A., 2019. Conditions Governing Food Protein Amyloid Fibril Formation. Part II: Milk and Legume Proteins. *Compr. Rev. Food Sci. Food Saf.* <https://doi.org/10.1111/1541-4337.12465>
- Lammers, W.J.E.P., 2005. Spatial and temporal coupling between slow waves and pendular contractions. *Am. J. Physiol. - Gastrointest. Liver Physiol.* 289, 898–903. <https://doi.org/10.1152/ajpgi.00070.2005>
- Lammers, W.J.E.P., Ver Donck, L., Stephen, B., Smets, D., Schuurkes, J.A.J., 2009. Origin and propagation of the slow wave in the canine stomach: the outlines of a gastric conduction system. *Am. J. Physiol. Liver Physiol.* 296, G1200–G1210. <https://doi.org/10.1152/ajpgi.90581.2008>
- Lamond, A.R., Janssen, A.E.M., Mackie, A., Bornhorst, G.M., Bakalis, S., Gouseti, O., 2019. An Engineering Perspective on Human Digestion, in: *Interdisciplinary Approaches to Food Digestion*. Springer International Publishing, Cham, pp. 255–273. https://doi.org/10.1007/978-3-030-03901-1_12
- Lan, Y., Chen, B., Rao, J., 2018. Pea protein isolate–high methoxyl pectin soluble complexes for improving pea protein functionality: Effect of pH, biopolymer ratio and concentrations. *Food Hydrocoll.* 80, 245–253. <https://doi.org/10.1016/j.foodhyd.2018.02.021>
- Landa, S.T., Dumon, K.R., Dempsey, D.T., 2019. *The SAGES Manual of Foregut Surgery, The SAGES Manual of Foregut Surgery*. Springer International Publishing, Cham. <https://doi.org/10.1007/978-3-319-96122-4>
- Lapčik, L., Vašina, M., Lapčíková, B., Valenta, T., 2016. Study of bread staling by means of vibro-acoustic, tensile and thermal analysis techniques. *J. Food Eng.* 178, 31–38. <https://doi.org/10.1016/j.jfoodeng.2016.01.004>
- Lassauzay, C., Peyron, M.-A., Albuissou, E., Dransfield, E., Woda, A., 2000. Variability of the masticatory process during chewing of elastic model foods. *Eur. J. Oral Sci.* 108, 484–492. <https://doi.org/10.1034/j.1600-0722.2000.00866.x>
- Lavoisier, A., Aguilera, J.M., 2019. Starch gelatinization inside a whey protein gel formed by cold gelation. *J. Food Eng.* 256, 18–27. <https://doi.org/10.1016/j.jfoodeng.2019.03.013>
- Lazou, A., Krokida, M., 2011. Thermal characterisation of corn – lentil extruded snacks. *Food Chem.* 127, 1625–1633. <https://doi.org/https://doi.org/10.1016/j.foodchem.2011.02.029>
- Le Feunteun, S., Barbé, F., Rémond, D., Ménard, O., Le Gouar, Y., Dupont, D., Laroche, B., 2014. Impact of the Dairy Matrix Structure on Milk Protein Digestion Kinetics: Mechanistic Modelling Based on Mini-pig In Vivo Data. *Food Bioprocess Technol.* 7, 1099–1113. <https://doi.org/10.1007/s11947-013-1116-6>
- Le Feunteun, S., Mackie, A.R., Dupont, D., 2020. In silico trials of food digestion and absorption: how far are we? *Curr. Opin. Food Sci.* 31, 121–125. <https://doi.org/10.1016/j.cofs.2020.04.006>
- Le Feunteun, S., Verkempinck, S., Floury, J., Janssen, A., Kondjoyan, A., Marze, S., Mirade, P.-S., Pluschke, A., Sicard, J., van Aken, G., Grauwet, T., 2021. Mathematical modelling of food hydrolysis during in vitro digestion: From single nutrient to complex foods in static and dynamic conditions, *Trends in Food Science & Technology*. Elsevier Ltd. <https://doi.org/10.1016/j.tifs.2021.08.030>
- Le Révérend, B., Saucy, F., Moser, M., Loret, C., 2016. Adaptation of mastication mechanics and eating behaviour to small differences in food texture. *Physiol. Behav.* 165, 136–145. <https://doi.org/10.1016/j.physbeh.2016.07.010>
- Leach, S.D., Modlin, I.M., Scheele, G.A., Gorelick, F.S., 1991. Intracellular activation of digestive zymogens in rat pancreatic acini stimulation by high doses of cholecystokinin. *J. Clin. Invest.* 87, 362–366. <https://doi.org/10.1172/JCII14995>
- Leal-Calderon, F., Cansell, M., 2012. The design of emulsions and their fate in the body following enteral

- and parenteral routes. *Soft Matter* 8, 10213. <https://doi.org/10.1039/c2sm26215k>
- Lentle, R.G., 2018. Deconstructing the physical processes of digestion: reductionist approaches may provide greater understanding. *Food Funct.* 9, 4069–4084. <https://doi.org/10.1039/C8FO00722E>
- Lentle, R.G., Hemar, Y., Hall, C.E., 2006. Viscoelastic behaviour aids extrusion from and reabsorption of the liquid phase into the digesta plug: Creep rheometry of hindgut digesta in the common brushtail possum *Trichosurus vulpecula*. *J. Comp. Physiol. B Biochem. Syst. Environ. Physiol.* 176, 469–475. <https://doi.org/10.1007/s00360-006-0068-9>
- Lentle, R.G., Janssen, P.W.M., 2008. Physical characteristics of digesta and their influence on flow and mixing in the mammalian intestine: A review. *J. Comp. Physiol. B Biochem. Syst. Environ. Physiol.* 178, 673–690. <https://doi.org/10.1007/s00360-008-0264-x>
- Lewicki, P.P., 2004. Water as the determinant of food engineering properties. A review. *J. Food Eng.* 61, 483–495. [https://doi.org/10.1016/S0260-8774\(03\)00219-X](https://doi.org/10.1016/S0260-8774(03)00219-X)
- Lewicki, P.P., Pawlak, G., 2003. Effect of Drying on Microstructure of Plant Tissue. *Dry. Technol.* 21, 657–683. <https://doi.org/10.1081/DRT-120019057>
- Li, H., Wang, T., Su, C., Wu, J., Van der Meeren, P., 2022. Effect of ionic strength on the sequential adsorption of whey proteins and low methoxy pectin on a hydrophobic surface: A QCM-D study. *Food Hydrocoll.* 122, 107074. <https://doi.org/10.1016/j.foodhyd.2021.107074>
- Li, S.-C., Liu, Y.-H., Liu, J.-F., Chang, W.-H., Chen, C.-M., Chen, C.-Y.O., 2011. Almond consumption improved glycemic control and lipid profiles in patients with type 2 diabetes mellitus. *Metabolism* 60, 474–479. <https://doi.org/10.1016/j.metabol.2010.04.009>
- Li, Y., Fortner, L., Kong, F., 2019. Development of a Gastric Simulation Model (GSM) incorporating gastric geometry and peristalsis for food digestion study. *Food Res. Int.* 108598. <https://doi.org/10.1016/j.foodres.2019.108598>
- Li, Z., Zhu, L., Zhang, W., Zhan, X., Gao, M., 2020. New dynamic digestion model reactor that mimics gastrointestinal function. *Biochem. Eng. J.* 154, 107431. <https://doi.org/10.1016/j.bej.2019.107431>
- Lillford, P.J., 2011. The Importance Of Food Microstructure In Fracture Physics And Texture Perception. *J. Texture Stud.* 42, 130–136. <https://doi.org/10.1111/j.1745-4603.2011.00293.x>
- Lim, Y.F., de Loubens, C., Love, R.J., Lentle, R.G., Janssen, P.W.M., 2015. Flow and mixing by small intestine villi. *Food Funct.* 6, 1787–1795. <https://doi.org/10.1039/C5FO00285K>
- Lin, Q., Liang, R., Zhong, F., Ye, A., Singh, H., 2021. In vivo oral breakdown properties of whey protein gels containing OSA-modified-starch-stabilized emulsions: Impact of gel structure. *Food Hydrocoll.* 113, 106361. <https://doi.org/10.1016/j.foodhyd.2020.106361>
- Liu, D., Dhital, S., Wu, P., Chen, X.-D., Gidley, M.J., 2019. In Vitro Digestion of Apple Tissue Using a Dynamic Stomach Model: Grinding and Crushing Effects on Polyphenol Bioaccessibility. *J. Agric. Food Chem.* [acs.jafc.9b05649](https://doi.org/10.1021/acs.jafc.9b05649). <https://doi.org/10.1021/acs.jafc.9b05649>
- Liu, W., Fu, D., Zhang, X., Chai, J., Tian, S., Han, J., 2019. Development and validation of a new artificial gastric digestive system. *Food Res. Int.* 122, 183–190. <https://doi.org/10.1016/j.foodres.2019.04.015>
- Liu, W., Jin, Y., Wilde, P.J., Hou, Y., Wang, Y., Han, J., 2020. Mechanisms, physiology, and recent research progress of gastric emptying. *Crit. Rev. Food Sci. Nutr.* 0, 1–14. <https://doi.org/10.1080/10408398.2020.1784841>
- Lizarraga, M.S., Pianta Vicin, D.D., Gonzalez, R., Rubiolo, A., Santiago, L.G., 2006. Rheological behaviour of whey protein concentrate and λ -carrageenan aqueous mixtures. *Food Hydrocoll.* 20, 740–748. <https://doi.org/10.1016/j.foodhyd.2005.07.007>
- Lopez-Sanchez, P., Fredriksson, N., Larsson, A., Altskär, A., Ström, A., 2018. High sugar content impacts microstructure, mechanics and release of calcium-alginate gels. *Food Hydrocoll.* 84, 26–33. <https://doi.org/10.1016/j.foodhyd.2018.05.029>
- Lorieau, L., Halabi, A., Ligneul, A., Hazart, E., Dupont, D., Flourey, J., 2018. Impact of the dairy product structure and protein nature on the proteolysis and amino acid bioaccessibility during in vitro digestion. *Food Hydrocoll.* 82, 399–411. <https://doi.org/10.1016/j.foodhyd.2018.04.019>
- Loubens, C.D.E., Lentle, R.G., Love, R.J., Hulls, C., Janssen, P.W.M., 2013. Fluid mechanical

- consequences of pendular activity, segmentation and pyloric outflow in the proximal duodenum of the rat and the guinea pig. *J. R. Soc. Interface* 10. <https://doi.org/10.1098/rsif.2013.0027>
- Love, R.J., Lentle, R.G., Asvarujanon, P., Hemar, Y., Stafford, K.J., 2013. An Expanded Finite Element Model of the Intestinal Mixing of Digesta. *Food Dig.* 4, 26–35. <https://doi.org/10.1007/s13228-012-0017-x>
- Lucas, P.W., Copes, L., Constantino, P.J., Vogel, E.R., Chalk, J., Talebi, M., Landis, M., Wagner, M., 2012. Measuring the Toughness of Primate Foods and its Ecological Value. *Int. J. Primatol.* 33, 598–610. <https://doi.org/10.1007/s10764-011-9540-9>
- Lucas, P.W., Prinz, J.F., Agrawal, K.R., Bruce, I.C., 2002. Food physics and oral physiology. *Food Qual. Prefer.* 13, 203–213. [https://doi.org/10.1016/S0950-3293\(00\)00036-7](https://doi.org/10.1016/S0950-3293(00)00036-7)
- Luo, Q., Borst, J.W., Westphal, A.H., Boom, R.M., Janssen, A.E.M., 2017. Pepsin diffusivity in whey protein gels and its effect on gastric digestion. *Food Hydrocoll.* 66, 318–325. <https://doi.org/10.1016/j.foodhyd.2016.11.046>
- Lutz, R., Aserin, A., Portnoy, Y., Gottlieb, M., Garti, N., 2009. On the confocal images and the rheology of whey protein isolated and modified pectins associated complex. *Colloids Surfaces B Biointerfaces* 69, 43–50. <https://doi.org/10.1016/j.colsurfb.2008.10.011>
- Luyten, H., Plijter, J. J., van Vliet, T., 2005. Crispy/crunchy crusts of cellular solid foods: A literature review with discussion. *J. Texture Stud.* 35, 445–492. <https://doi.org/10.1111/j.1745-4603.2004.35501.x>
- Luyten, H., Van Vliet, T., 2006. Acoustic emission, fracture behavior and morphology of dry crispy foods: A discussion article. *J. Texture Stud.* 37, 221–240. <https://doi.org/10.1111/j.1745-4603.2006.00049.x>
- Luyten, H., van Vliet, T., Walstra, P., 1992. Comparison of various methods to evaluate fracture phenomena in food materials. *J. Texture Stud.* 23, 245–266. <https://doi.org/10.1111/j.1745-4603.1992.tb00524.x>
- Łysiak, G., 2007. Fracture toughness of pea: Weibull analysis. *J. Food Eng.* 83, 436–443. <https://doi.org/10.1016/j.jfoodeng.2007.03.034>
- Makkhun, S., Khosla, A., Foster, T., McClements, D.J., Grundy, M.M.L., Gray, D.A., 2015. Impact of extraneous proteins on the gastrointestinal fate of sunflower seed (*Helianthus annuus*) oil bodies: a simulated gastrointestinal tract study. *Food Funct.* 6, 124–133. <https://doi.org/10.1039/C4FO00422A>
- Malagelada, C., De Iorio, F., Azpiroz, F., Accarino, A., Segui, S., Radeva, P., Malagelada, J.R., 2008. New Insight Into Intestinal Motor Function via Noninvasive Endoluminal Image Analysis. *Gastroenterology* 135, 1155–1162. <https://doi.org/10.1053/j.gastro.2008.06.084>
- Malagelada, J.-R., Longstreth, G.F., Summerskill, W.H.J., Go, V.L.W., 1976. Measurement of Gastric Functions During Digestion of Ordinary Solid Meals in Man. *Gastroenterology* 70, 203–210. [https://doi.org/10.1016/S0016-5085\(76\)80010-8](https://doi.org/10.1016/S0016-5085(76)80010-8)
- Malagelada, J.R., Go, V.L.W., Summerskill, W.H.J., 1979. Different gastric, pancreatic, and biliary responses to solid-liquid or homogenized meals. *Dig. Dis. Sci.* 24, 101–110. <https://doi.org/10.1007/BF01324736>
- Maldonado-Valderrama, J., Wilde, P., Macierzanka, A., Mackie, A., 2011. The role of bile salts in digestion. *Adv. Colloid Interface Sci.* 165, 36–46. <https://doi.org/10.1016/j.cis.2010.12.002>
- Malik, Z., Sankineni, A., Parkman, H.P., 2015. Assessing pyloric sphincter pathophysiology using EndoFLIP in patients with gastroparesis. *Neurogastroenterol. Motil.* 27, 524–531. <https://doi.org/10.1111/nmo.12522>
- Mandalari, G., Faulks, R.M., Rich, G.T., Lo Turco, V., Picout, D.R., Lo Curto, R.B., Bisignano, G., Dugo, P., Dugo, G., Waldron, K.W., Ellis, P.R., Wickham, M.S.J., 2008. Release of Protein, Lipid, and Vitamin E from Almond Seeds during Digestion. *J. Agric. Food Chem.* 56, 3409–3416. <https://doi.org/10.1021/jf073393v>
- Mandalari, G., Grundy, M.M.L., Grassby, T., Parker, M.L., Cross, K.L., Chessa, S., Bisignano, C., Barreca, D., Bellocco, E., Laganà, G., Butterworth, P.J., Faulks, R.M., Wilde, P.J., Ellis, P.R.,

- Waldron, K.W., 2014. The effects of processing and mastication on almond lipid bioaccessibility using novel methods of in vitro digestion modelling and micro-structural analysis. *Br. J. Nutr.* 112, 1521–1529. <https://doi.org/10.1017/S0007114514002414>
- Mandalari, G., Parker, M., Grundy, M., Grassby, T., Smeriglio, A., Bisignano, C., Raciti, R., Trombetta, D., Baer, D., Wilde, P., 2018. Understanding the Effect of Particle Size and Processing on Almond Lipid Bioaccessibility through Microstructural Analysis: From Mastication to Faecal Collection. *Nutrients* 10, 213. <https://doi.org/10.3390/nu10020213>
- Marciani, L., 2011. Assessment of gastrointestinal motor functions by MRI: a comprehensive review. *Neurogastroenterol. Motil.* 23, 399–407. <https://doi.org/10.1111/j.1365-2982.2011.01670.x>
- Marciani, L., Gowland, P.A., Fillery-Travis, A., Manoj, P., Wright, J., Smith, A., Young, P., Moore, R., Spiller, R.C., 2001a. Assessment of antral grinding of a model solid meal with echo-planar imaging. *Am. J. Physiol. Liver Physiol.* 280, G844–G849. <https://doi.org/10.1152/ajpgi.2001.280.5.G844>
- Marciani, Luca, Gowland, P.A., Spiller, R.C., Manoj, P., Moore, R.J., Young, P., Fillery-Travis, A.J., 2001. Effect of meal viscosity and nutrients on satiety, intragastric dilution, and emptying assessed by MRI. *Am. J. Physiol. Liver Physiol.* 280, G1227–G1233. <https://doi.org/10.1152/ajpgi.2001.280.6.G1227>
- Marciani, L., Hall, N., Pritchard, S.E., Cox, E.F., Totman, J.J., Lad, M., Hoard, C.L., Foster, T.J., Gowland, P.A., Spiller, R.C., 2012. Preventing Gastric Sieving by Blending a Solid/Water Meal Enhances Satiety in Healthy Humans. *J. Nutr.* 142, 1253–1258. <https://doi.org/10.3945/jn.112.159830>
- Marciani, L., Young, P., Wright, J., Moore, R., Coleman, N., Gowland, P.A., Spiller, R.C., 2001b. Antral motility measurements by magnetic resonance imaging. *Neurogastroenterol. Motil.* 13, 511–518. <https://doi.org/10.1046/j.1365-2982.2001.00285.x>
- Markowski, M., Bondaruk, J., Błaszczak, W., 2009. Rehydration Behavior of Vacuum-Microwave-Dried Potato Cubes. *Dry. Technol.* 27, 296–305. <https://doi.org/10.1080/07373930802606600>
- Martinez, R.C.R., Cardarelli, H.R., Borst, W., Albrecht, S., Schols, H., Gutiérrez, O.P., Maathuis, A.J.H., de Melo Franco, B.D.G., De Martinis, E.C.P., Zoetendal, E.G., Venema, K., Saad, S.M.I., Smidt, H., 2013. Effect of galactooligosaccharides and *Bifidobacterium animalis* Bb-12 on growth of *Lactobacillus amylovorus* DSM 16698, microbial community structure, and metabolite production in an in vitro colonic model set up with human or pig microbiota. *FEMS Microbiol. Ecol.* 84, 110–123. <https://doi.org/10.1111/1574-6941.12041>
- Mazumder, P., Roopa, B.S., Bhattacharya, S., 2007. Textural attributes of a model snack food at different moisture contents. *J. Food Eng.* 79, 511–516. <https://doi.org/10.1016/j.jfoodeng.2006.02.011>
- McArthur, B., Considine, R., Mattes, R., 2018. Mastication of Nuts under Realistic Eating Conditions: Implications for Energy Balance. *Nutrients* 10, 710. <https://doi.org/10.3390/nu10060710>
- McCarthy, C.T., Hussey, M., Gilchrist, M.D., 2007. On the sharpness of straight edge blades in cutting soft solids: Part I – indentation experiments. *Eng. Fract. Mech.* 74, 2205–2224. <https://doi.org/10.1016/j.engfracmech.2006.10.015>
- McFeeters, R.F., Balbuena, M.B., Fleming, H.P., 1995. Softening Rates of Fermented Cucumber Tissue: Effects of pH, Calcium, and Temperature. *J. Food Sci.* 60, 786–788. <https://doi.org/10.1111/j.1365-2621.1995.tb06229.x>
- McKiernan, F., Mattes, R.D., 2010. Effects of Peanut Processing on Masticatory Performance during Variable Appetitive States. *J. Nutr. Metab.* 2010, 1–6. <https://doi.org/10.1155/2010/487301>
- Mennah-Govela, Y.A., Bornhorst, G.M., 2021a. Breakdown mechanisms of whey protein gels during dynamic in vitro gastric digestion. *Food Funct.* 12, 2112–2125. <https://doi.org/10.1039/d0fo03325a>
- Mennah-Govela, Y.A., Bornhorst, G.M., 2021b. Food buffering capacity: quantification methods and its importance in digestion and health. *Food Funct.* <https://doi.org/10.1039/D0FO02415E>
- Mennah-Govela, Y.A., Bornhorst, G.M., 2016a. Mass transport processes in orange-fleshed sweet potatoes leading to structural changes during in vitro gastric digestion. *J. Food Eng.* 191, 48–57. <https://doi.org/10.1016/j.jfoodeng.2016.07.004>
- Mennah-Govela, Y.A., Bornhorst, G.M., 2016b. Acid and moisture uptake in steamed and boiled sweet

- potatoes and associated structural changes during in vitro gastric digestion. *Food Res. Int.* 88, 247–255. <https://doi.org/10.1016/j.foodres.2015.12.012>
- Mennah-Govela, Y.A., Bornhorst, G.M., Singh, R.P., 2015. Acid Diffusion into Rice Boluses is Influenced by Rice Type, Variety, and Presence of α -Amylase. *J. Food Sci.* 80, E316–E325. <https://doi.org/10.1111/1750-3841.12750>
- Mennah-Govela, Yamile A, Cai, H., Chu, J., Kim, K., Maborang, M.-K., Sun, W., Bornhorst, G.M., 2020. Buffering capacity of commercially available foods is influenced by composition and initial properties in the context of gastric digestion. *Food Funct.* 11, 2255–2267. <https://doi.org/10.1039/C9FO03033F>
- Mennah-Govela, Yamile A., Keppler, S., Januzzi-Guerreiro, F., Follador-Lemos, C., Vilpont, K., Bornhorst, G.M., 2020. Acid and Moisture Uptake into Red Beets during in Vitro Gastric Digestion as Influenced by Gastric pH. *Food Biophys.* 15, 261–272. <https://doi.org/10.1007/s11483-019-09623-w>
- Mennah-Govela, Y.A., Singh, R.P., Bornhorst, G.M., 2019. Buffering capacity of protein-based model food systems in the context of gastric digestion. *Food Funct.* 10, 6074–6087. <https://doi.org/10.1039/C9FO01160A>
- Mennah-Govela, Y.A., Swackhamer, C., Bornhorst, G.M., 2021. Gastric Secretion Rate and Protein Concentration Impact Intragastric pH and Protein Hydrolysis during Dynamic in Vitro Gastric Digestion. *Food Hydrocoll. Heal.* 1, 100027. <https://doi.org/10.1016/j.fhfh.2021.100027>
- Mesirow, M.S.C., Welsh, J.A., 2015. Changing Beverage Consumption Patterns Have Resulted in Fewer Liquid Calories in the Diets of US Children: National Health and Nutrition Examination Survey 2001–2010. *J. Acad. Nutr. Diet.* 115, 559–566. <https://doi.org/10.1016/j.jand.2014.09.004>
- Meyer, M.A., 2020. The role of resilience in food system studies in low- and middle-income countries. *Glob. Food Sec.* 24, 100356. <https://doi.org/10.1016/j.gfs.2020.100356>
- Miao, M., Hamaker, B.R., 2021. Food Matrix Effects for Modulating Starch Bioavailability. *Annu. Rev. Food Sci. Technol.* 12, 1–23. <https://doi.org/10.1146/annurev-food-070620-013937>
- Minekus, M., Alminger, M., Alvito, P., Ballance, S., Bohn, T., Bourlieu, C., Carrière, F., Boutrou, R., Corredig, M., Dupont, D., Dufour, C., Egger, L., Golding, M., Karakaya, S., Kirkhus, B., Le Feunteun, S., Lesmes, U., Macierzanka, A., Mackie, A., Marze, S., McClements, D.J., Ménard, O., Recio, I., Santos, C.N., Singh, R.P., Vegarud, G.E., Wickham, M.S.J., Weitschies, W., Brodkorb, A., 2014. A standardised static in vitro digestion method suitable for food – an international consensus. *Food Funct.* 5, 1113–1124. <https://doi.org/10.1039/C3FO60702J>
- Minekus, M., Marteau, P., Havenaar, R., H.J. Huis int't Veld, J., 1995. A multicompartamental dynamic computer-controlled model simulating the stomach and small intestine. *ATLA-Alternatives to Lab. Anim.* 23, 197–209.
- Mioche, L., Bourdiol, P., Martin, J.-F., Noël, Y., 1999. Variations in human masseter and temporalis muscle activity related to food texture during free and side-imposed mastication. *Arch. Oral Biol.* 44, 1005–1012. [https://doi.org/10.1016/S0003-9969\(99\)00103-X](https://doi.org/10.1016/S0003-9969(99)00103-X)
- Mioche, L., Bourdiol, P., Monier, S., 2003. Chewing behaviour and bolus formation during mastication of meat with different textures. *Arch. Oral Biol.* 48, 193–200. [https://doi.org/10.1016/S0003-9969\(03\)00002-5](https://doi.org/10.1016/S0003-9969(03)00002-5)
- Miron, I., Dumitrascu, D.L., 2019. Gastrointestinal motility disorders in obesity. *Acta Endocrinol. (Copenh).* 15, 497–504. <https://doi.org/10.4183/aeb.2019.497>
- Miyagawa, T., Imai, Y., Ishida, S., Ishikawa, T., 2016. Relationship between gastric motility and liquid mixing in the stomach. *Am. J. Physiol. Liver Physiol.* 311, G1114–G1121. <https://doi.org/10.1152/ajpgi.00346.2016>
- Morais, J.A., Heydecke, G., Pawliuk, J., Lund, J.P., Feine, J.S., 2003. The effects of mandibular two-implant overdentures on nutrition in elderly edentulous individuals. *J. Dent. Res.* 82, 53–58. <https://doi.org/10.1177/154405910308200112>
- Morell, P., Hernando, I., Fiszman, S.M., 2014. Understanding the relevance of in-mouth food processing. A review of in vitro techniques. *Trends Food Sci. Technol.* 35, 18–31.

- <https://doi.org/10.1016/j.tifs.2013.10.005>
- Mulet-Cabero, A.-I., Egger, L., Portmann, R., Ménard, O., Marze, S., Minekus, M., Le Feunteun, S., Sarkar, A., Grundy, M.M.-L., Carrière, F., Golding, M., Dupont, D., Recio, I., Brodkorb, A., Mackie, A., 2020. A standardised semi-dynamic in vitro digestion method suitable for food – an international consensus. *Food Funct.* 11, 1702–1720. <https://doi.org/10.1039/C9FO01293A>
- Mulet-Cabero, A.-I., Rigby, N.M., Brodkorb, A., Mackie, A.R., 2017. Dairy food structures influence the rates of nutrient digestion through different in vitro gastric behaviour. *Food Hydrocoll.* 67, 63–73. <https://doi.org/10.1016/j.foodhyd.2016.12.039>
- Mulet-Cabero, A.I., Mackie, A.R., Wilde, P.J., Fenelon, M.A., Brodkorb, A., 2019. Structural mechanism and kinetics of in vitro gastric digestion are affected by process-induced changes in bovine milk. *Food Hydrocoll.* 86, 172–183. <https://doi.org/10.1016/j.foodhyd.2018.03.035>
- Mullane, M., 2006. *Riding rockers: The outrageous tales of a space shuttle astronaut*. Scribner, New York.
- Munialo, C.D., van der Linden, E., Ako, K., Nieuwland, M., Van As, H., de Jongh, H.H.J., 2016. The effect of polysaccharides on the ability of whey protein gels to either store or dissipate energy upon mechanical deformation. *Food Hydrocoll.* 52, 707–720. <https://doi.org/10.1016/j.foodhyd.2015.08.013>
- N’Gom, P.I., Woda, A., 2002. Influence of impaired mastication on nutrition. *J. Prosthet. Dent.* 87, 667–673. <https://doi.org/10.1067/mpr.2002.123229>
- Nadia, J., Bronlund, J., Singh, R.P., Singh, H., Bornhorst, G.M., 2021a. Structural breakdown of starch-based foods during gastric digestion and its link to glycemic response: In vivo and in vitro considerations. *Compr. Rev. Food Sci. Food Saf.* 20, 2660–2698. <https://doi.org/10.1111/1541-4337.12749>
- Nadia, J., Olenskyj, A.G., Stroebinger, N., Hodgkinson, S.M., Estevez, T.G., Subramanian, P., Singh, H., Singh, R.P., Bornhorst, G.M., 2021b. Tracking physical breakdown of rice- and wheat-based foods with varying structures during gastric digestion and its influence on gastric emptying in a growing pig model. *Food Funct.* <https://doi.org/10.1039/D0FO02917C>
- Nativ-Zeltzer, N., Ueha, R., Nachalon, Y., Ma, B., Pastenkos, G., Swackhamer, C., Bornhorst, G.M., Lefton-Greif, M.A., Anderson, J.D., Belafsky, P.C., 2020. Inflammatory Effects of Thickened Water on the Lungs in a Murine Model of Recurrent Aspiration. *Laryngoscope lary.* 28948. <https://doi.org/10.1002/lary.28948>
- Nishinari, K., Fang, Y., 2021. Molar mass effect in food and health. *Food Hydrocoll.* 112, 106110. <https://doi.org/10.1016/j.foodhyd.2020.106110>
- Nitta, K., Yam, M., 2012. Poisson’s Ratio and Mechanical Nonlinearity Under Tensile Deformation in Crystalline Polymers, in: Vincente, J.D. (Ed.), *Rheology*. InTech, pp. 113–132. <https://doi.org/10.5772/34881>
- Norton, I., Moore, S., Fryer, P., 2007. Understanding food structuring and breakdown: engineering approaches to obesity. *Obes. Rev.* 8, 83–88. <https://doi.org/10.1111/j.1467-789X.2007.00324.x>
- Novotny, J.A., Gebauer, S.K., Baer, D.J., 2012. Discrepancy between the Atwater factor predicted and empirically measured energy values of almonds in human diets. *Am. J. Clin. Nutr.* 96, 296–301. <https://doi.org/10.3945/ajcn.112.035782>
- Nyemb, K., Guérin-Dubiard, C., Pézennec, S., Jardin, J., Briard-Bion, V., Cauty, C., Rutherford, S.M., Dupont, D., Nau, F., 2016. The structural properties of egg white gels impact the extent of in vitro protein digestion and the nature of peptides generated. *Food Hydrocoll.* 54, 315–327. <https://doi.org/10.1016/j.foodhyd.2015.10.011>
- Olenskyj, A.G., Donis-González, I.R., Bornhorst, G.M., 2020. Nondestructive characterization of structural changes during in vitro gastric digestion of apples using 3D time-series micro-computed tomography. *J. Food Eng.* 267, 109692. <https://doi.org/10.1016/j.jfoodeng.2019.109692>
- Oosterveld, A., Minekus, M., Bomhof, E., Zoet, F.D., van Aken, G.A., 2016. Effects of inhomogeneity on triglyceride digestion of emulsions using an in vitro digestion model (Tiny TIM). *Food Funct.* 7, 2979–2995. <https://doi.org/10.1039/C4FO01045K>

- Oromiehie, A.R., Lari, T.T., Rabiee, A., 2013. Physical and thermal mechanical properties of corn starch/LDPE composites. *J. Appl. Polym. Sci.* 127, 1128–1134. <https://doi.org/10.1002/app.37877>
- Pal, A., Brasseur, J.G., Abrahamsson, B., 2007a. A stomach road or “Magenstrasse” for gastric emptying. *J. Biomech.* 40, 1202–1210. <https://doi.org/10.1016/j.jbiomech.2006.06.006>
- Pal, A., Brasseur, J.G., Abrahamsson, B., 2007b. A stomach road or “Magenstrasse” for gastric emptying. *J. Biomech.* 40, 1202–1210. <https://doi.org/10.1016/j.jbiomech.2006.06.006>
- Pal, A., Indireskumar, K., Schwizer, W., Abrahamsson, B., Fried, M., Brasseur, J.G., 2004. Gastric flow and mixing studied using computer simulation. *Proc. R. Soc. London. Ser. B Biol. Sci.* 271, 2587–2594. <https://doi.org/10.1098/rspb.2004.2886>
- Papadopoulos, D.G., Ghadiri, M., 1996. Impact breakage of poly-methylmethacrylate (PMMA) extrudates: I. Chipping mechanism. *Adv. Powder Technol.* 7, 183–197. [https://doi.org/10.1016/S0921-8831\(08\)60495-1](https://doi.org/10.1016/S0921-8831(08)60495-1)
- Paula, A.M., Conti-Silva, A.C., 2014. Texture profile and correlation between sensory and instrumental analyses on extruded snacks. *J. Food Eng.* 121, 9–14. <https://doi.org/10.1016/j.jfoodeng.2013.08.007>
- Peyron, M.-A., Mishellany, A., Woda, A., 2004. Particle Size Distribution of Food Boluses after Mastication of Six Natural Foods. *J. Dent. Res.* 83, 578–582. <https://doi.org/10.1177/154405910408300713>
- Peyron, M.-A., Santé-Lhoutellier, V., Dardevet, D., Hennequin, M., Rémond, D., François, O., Woda, A., 2019. Addressing various challenges related to food bolus and nutrition with the AM2 mastication simulator. *Food Hydrocoll.* 97, 105229. <https://doi.org/10.1016/j.foodhyd.2019.105229>
- Phinney, D.M., 2013. Design, construction, and evaluation of a reactor designed to mimic human gastric digestion. University of California, Davis.
- Pilkey, W.D., Pilkey, D.F., 2008. Peterson’s stress concentration factors, 3rd ed. John Wiley & Sons, Inc., Hoboken, NJ. <https://doi.org/https://doi.org/10.1002/9780470211106>
- Pinheiro, A.C., Lad, M., Silva, H.D., Coimbra, M.A., Boland, M., Vicente, A.A., 2013. Unravelling the behaviour of curcumin nanoemulsions during in vitro digestion: effect of the surface charge. *Soft Matter* 9, 3147. <https://doi.org/10.1039/c3sm27527b>
- Poppitt, S.D., Shin, H.S., McGill, A.-T., Budgett, S.C., Lo, K., Pahl, M., Duxfield, J., Lane, M., Ingram, J.R., 2017. Duodenal and ileal glucose infusions differentially alter gastrointestinal peptides, appetite response, and food intake: a tube feeding study. *Am. J. Clin. Nutr.* 106, ajcn157248. <https://doi.org/10.3945/ajcn.117.157248>
- Primo-Martín, C., Sözer, N., Hamer, R.J., Van Vliet, T., 2009. Effect of water activity on fracture and acoustic characteristics of a crust model. *J. Food Eng.* 90, 277–284. <https://doi.org/10.1016/j.jfoodeng.2008.06.039>
- Quevedo, M., Karbstein, H.P., Emin, M.A., 2021. Concentration-dependent changes in the reaction behavior of whey proteins: Diffusion-controlled or transition state-controlled reactions? *Food Hydrocoll.* 118, 106745. <https://doi.org/10.1016/j.foodhyd.2021.106745>
- Quinn, J.B., Quinn, G.D., 2010. A practical and systematic review of Weibull statistics for reporting strengths of dental materials. *Dent. Mater.* 26, 135–147. <https://doi.org/10.1016/j.dental.2009.09.006>
- Raei, M., Rafe, A., Shahidi, F., 2018. Rheological and structural characteristics of whey protein-pectin complex coacervates. *J. Food Eng.* 228, 25–31. <https://doi.org/10.1016/j.jfoodeng.2018.02.007>
- Ramalhosa, M.J., Paíga, P., Morais, S., Rui Alves, M., Delerue-Matos, C., Oliveira, M.B.P.P., 2012. Lipid content of frozen fish: Comparison of different extraction methods and variability during freezing storage. *Food Chem.* 131, 328–336. <https://doi.org/10.1016/j.foodchem.2011.07.123>
- Ranawana, V., Monro, J.A., Mishra, S., Henry, C.J.K., 2010. Degree of particle size breakdown during mastication may be a possible cause of interindividual glycemic variability. *Nutr. Res.* 30, 246–254. <https://doi.org/10.1016/j.nutres.2010.02.004>
- Ranganathan, K., Subramanian, V., Shanmugam, N., 2016. Effect of Thermal and Nonthermal Processing on Textural Quality of Plant Tissues. *Crit. Rev. Food Sci. Nutr.* 56, 2665–2694. <https://doi.org/10.1080/10408398.2014.908348>

- Ranganathan, S., Vasikaran, E.M., Elumalai, A., Moses, J.A., Anandharamakrishnan, C., 2021. Gastric emptying pattern and disintegration kinetics of cooked rice in a 3D printed in vitro dynamic digestion model ARK®. *Int. J. Food Eng.* <https://doi.org/10.1515/ijfe-2020-0159>
- Rattan, S., Crosby, A.J., 2019. Effect of Polymer Volume Fraction on Fracture Initiation in Soft Gels at Small Length Scales. *ACS Macro Lett.* 492–498. <https://doi.org/10.1021/acsmacrolett.9b00086>
- Rattan, S., Crosby, A.J., 2018. Effect of far-field compliance on local failure dynamics of soft solids. *Extrem. Mech. Lett.* 24, 14–20. <https://doi.org/10.1016/j.eml.2018.08.003>
- Ravindra, P., Genovese, D.B., Foegeding, E.A., Rao, M.A., 2004. Rheology of heated mixed whey protein isolate/cross-linked waxy maize starch dispersions. *Food Hydrocoll.* 18, 775–781. <https://doi.org/10.1016/j.foodhyd.2003.12.004>
- Reynaud, Y., Buffière, C., David, J., Cohade, B., Vauris, M., Lopez, M., Souchon, I., Dupont, D., Rémond, D., 2020. Temporal changes in postprandial intragastric pH: comparing measurement methods, food structure effects, and kinetic modelling. *Food Res. Int.* 128, 108784. <https://doi.org/10.1016/j.foodres.2019.108784>
- Rico, D., Martín-Diana, A.B., Barat, J.M., Barry-Ryan, C., 2007. Extending and measuring the quality of fresh-cut fruit and vegetables: a review. *Trends Food Sci. Technol.* 18, 373–386. <https://doi.org/10.1016/j.tifs.2007.03.011>
- Rios-Villa, K.A., Bhattacharya, M., La, E.H., Barile, D., Bornhorst, G.M., 2020. Interactions between whey proteins and cranberry juice after thermal or non-thermal processing during: In vitro gastrointestinal digestion. *Food Funct.* 11, 7661–7680. <https://doi.org/10.1039/d0fo00177e>
- Rivière, A., Selak, M., Lantin, D., Leroy, F., De Vuyst, L., 2016. Bifidobacteria and Butyrate-Producing Colon Bacteria: Importance and Strategies for Their Stimulation in the Human Gut. *Front. Microbiol.* 7. <https://doi.org/10.3389/fmicb.2016.00979>
- Rockström, J., Edenhofer, O., Gaertner, J., DeClerck, F., 2020. Planet-proofing the global food system. *Nat. Food* 1, 3–5. <https://doi.org/10.1038/s43016-019-0010-4>
- Rogalska, E., Ransac, S., Verger, R., 1990. Stereoselectivity of lipases. II. Stereoselective hydrolysis of triglycerides by gastric and pancreatic lipases. *J. Biol. Chem.* 265, 20271–20276. [https://doi.org/10.1016/s0021-9258\(17\)30500-8](https://doi.org/10.1016/s0021-9258(17)30500-8)
- Rojo, F.J., Vincent, J.F. V., 2008. Fracture properties of potato crisps. *Int. J. Food Sci. Technol.* 43, 752–760. <https://doi.org/10.1111/j.1365-2621.2007.01531.x>
- Roman, M.J., Burri, B.J., Singh, R.P., 2012. Release and Bioaccessibility of β -Carotene from Fortified Almond Butter during in Vitro Digestion. *J. Agric. Food Chem.* 60, 9659–9666. <https://doi.org/10.1021/jf302843w>
- Roopa, P.M.B.S., Bhattacharya, S., 2009. Fracture behavior and mechanism of puffed cereal during compression. *J. Texture Stud.* 40, 157–171. <https://doi.org/10.1111/j.1745-4603.2009.00174.x>
- Ross, K.A., Scanlon, M.G., 2004. A fracture mechanics analysis of the texture of fried potato crust. *J. Food Eng.* 62, 417–423. [https://doi.org/10.1016/S0260-8774\(03\)00274-7](https://doi.org/10.1016/S0260-8774(03)00274-7)
- Rusu, M.E., Gheldiu, A.-M., Mocan, A., Vlase, L., Popa, D.-S., 2018. Anti-aging potential of tree nuts with a focus on the phytochemical composition, molecular mechanisms and thermal stability of major bioactive compounds. *Food Funct.* 9, 2554–2575. <https://doi.org/10.1039/C7FO01967J>
- Sadik, R., Abrahamsson, H., Stotzer, P.O., 2003. Gender differences in gut transit shown with a newly developed radiological procedure. *Scand. J. Gastroenterol.* 38, 36–42. <https://doi.org/10.1080/00365520310000410>
- Saeleaw, M., Dürschmid, K., Schleining, G., 2012. The effect of extrusion conditions on mechanical-sound and sensory evaluation of rye expanded snack. *J. Food Eng.* 110, 532–540. <https://doi.org/10.1016/j.jfoodeng.2012.01.002>
- Saeleaw, M., Schleining, G., 2011a. A review: Crispness in dry foods and quality measurements based on acoustic-mechanical destructive techniques. *J. Food Eng.* 105, 387–399. <https://doi.org/10.1016/j.jfoodeng.2011.03.012>
- Saeleaw, M., Schleining, G., 2011b. Effect of frying parameters on crispiness and sound emission of cassava crackers. *J. Food Eng.* 103, 229–236. <https://doi.org/10.1016/j.jfoodeng.2010.10.010>

- Saeleaw, M., Schleining, G., 2010. Effect of blending cassava starch, rice, waxy rice and wheat flour on physico-chemical properties of flour mixtures and mechanical and sound emission properties of cassava crackers. *J. Food Eng.* 100, 12–24. <https://doi.org/10.1016/j.jfoodeng.2010.03.020>
- Sakaguchi, E., 2003. Digestive strategies of small hindgut fermenters. *Anim. Sci. J.* 74, 327–337. <https://doi.org/10.1046/j.1344-3941.2003.00124.x>
- Sala, G., van Vliet, T., Cohen Stuart, M.A., van Aken, G.A., van de Velde, F., 2009. Deformation and fracture of emulsion-filled gels: Effect of oil content and deformation speed. *Food Hydrocoll.* 23, 1381–1393. <https://doi.org/10.1016/j.foodhyd.2008.11.016>
- Saleem, Q., Wildman, R.D., Huntley, J.M., Whitworth, M.B., 2005. Material properties of semi-sweet biscuits for finite element modelling of biscuit cracking. *J. Food Eng.* 68, 19–32. <https://doi.org/10.1016/j.jfoodeng.2004.05.020>
- Salles, C., Tarrega, A., Mielle, P., Maratray, J., Gorria, P., Liaboeuf, J., Liodenot, J.-J., 2007. Development of a chewing simulator for food breakdown and the analysis of in vitro flavor compound release in a mouth environment. *J. Food Eng.* 82, 189–198. <https://doi.org/10.1016/j.jfoodeng.2007.02.008>
- Sams, L., Paume, J., Giallo, J., Carrière, F., 2016. Relevant pH and lipase for in vitro models of gastric digestion. *Food Funct.* 7, 30–45. <https://doi.org/10.1039/C5FO00930H>
- Sansom, M., Fraser, R., Smout, A.J.P.M., Verhagen, M.A.M.T., Adachi, K., Horowitz, M., Dent, J., 1999. Characterization of small intestinal pressure waves in ambulant subjects recorded with a novel portable manometric system. *Dig. Dis. Sci.* 44, 2157–2164. <https://doi.org/10.1023/A:1026659414507>
- Sansom, M., Smout, A.J.P.M., Hebbard, G., Fraser, R., Omari, T., Horowitz, M., Dent, J., 1998. A novel portable perfused manometric system for recording of small intestinal motility. *Neurogastroenterol. Motil.* 10, 139–148. <https://doi.org/10.1046/j.1365-2982.1998.00093.x>
- Sanahuja, S., Fédou, M., Briesen, H., 2018. Classification of puffed snacks freshness based on crispiness-related mechanical and acoustical properties. *J. Food Eng.* 226, 53–64. <https://doi.org/10.1016/j.jfoodeng.2017.12.013>
- Sanahuja, S., Upadhyay, R., Briesen, H., Chen, J., 2017. Spectral analysis of the stick-slip phenomenon in “oral” tribological texture evaluation. *J. Texture Stud.* 48, 318–334. <https://doi.org/10.1111/jtxs.12266>
- Sanders, K.M., Kito, Y., Hwang, S.J., Ward, S.M., 2016. Regulation of gastrointestinal smooth muscle function by interstitial cells. *Physiology* 31, 316–326. <https://doi.org/10.1152/physiol.00006.2016>
- Sanson, G., 2016. Cutting food in terrestrial carnivores and herbivores. *Interface Focus* 6, 20150109. <https://doi.org/10.1098/rsfs.2015.0109>
- Santagiuliana, M., Christaki, M., Piqueras-Fizman, B., Scholten, E., Stieger, M., 2018. Effect of mechanical contrast on sensory perception of heterogeneous liquid and semi-solid foods. *Food Hydrocoll.* 83, 202–212. <https://doi.org/10.1016/j.foodhyd.2018.04.046>
- Santangelo, A., Peracchi, M., Conte, D., Fraquelli, M., Porrini, M., 1998. Physical state of meal affects gastric emptying, cholecystokinin release and satiety. *Br. J. Nutr.* 80, 521–527. <https://doi.org/10.1017/S0007114598001615>
- Sathe, S.K., 1992. Solubilization, electrophoretic characterization and in vitro digestibility of almond (*prunus amygdalus*) proteins. *J. Food Biochem.* 16, 249–264. <https://doi.org/10.1111/j.1745-4514.1992.tb00450.x>
- Sathe, S.K., Seeram, N.P., Kshirsagar, H.H., Heber, D., Lapsley, K.A., 2008. Fatty Acid Composition of California Grown Almonds. *J. Food Sci.* 73, C607–C614. <https://doi.org/10.1111/j.1750-3841.2008.00936.x>
- Scheuble, N., Schaffner, J., Schumacher, M., Windhab, E.J., Liu, D., Parker, H., Steingoetter, A., Fischer, P., 2018. Tailoring Emulsions for Controlled Lipid Release: Establishing in vitro–in Vivo Correlation for Digestion of Lipids. *ACS Appl. Mater. Interfaces* 10, 17571–17581. <https://doi.org/10.1021/acsami.8b02637>
- Schmitt, C., Moitzi, C., Bovay, C., Rouvet, M., Bovetto, L., Donato, L., Leser, M.E., Schurtenberger, P.,

- Stradner, A., 2010. Internal structure and colloidal behaviour of covalent whey protein microgels obtained by heat treatment. *Soft Matter* 6, 4876–4884. <https://doi.org/10.1039/c0sm00220h>
- Schubert, M.L., Peura, D.A., 2008. Control of Gastric Acid Secretion in Health and Disease. *Gastroenterology* 134, 1842–1860. <https://doi.org/10.1053/j.gastro.2008.05.021>
- Schuldt, S., Boden, L., Schneider, Y., Rohm, H., 2016. Pre-crack cutting properties of viscoelastic food models. *J. Food Eng.* 169, 272–277. <https://doi.org/10.1016/j.jfoodeng.2015.09.005>
- Schuldt, S., Witt, T., Schmidt, C., Schneider, Y., Nündel, T., Majschak, J.-P., Rohm, H., 2018. High-speed cutting of foods: Development of a special testing device. *J. Food Eng.* 216, 36–41. <https://doi.org/10.1016/j.jfoodeng.2017.08.001>
- Schulze, K.S., 2015. The imaging and modelling of the physical processes involved in digestion and absorption. *Acta Physiol.* 213, 394–405. <https://doi.org/10.1111/apha.12407>
- Schulze, K.S., 2006. Imaging and modelling of digestion in the stomach and the duodenum. *Neurogastroenterol. Motil.* 18, 172–183. <https://doi.org/10.1111/j.1365-2982.2006.00759.x>
- Schwanz Goebel, J.T., Kaur, L., Colussi, R., Elias, M.C., Singh, J., 2019. Microstructure of indica and japonica rice influences their starch digestibility: A study using a human digestion simulator. *Food Hydrocoll.* 94, 191–198. <https://doi.org/10.1016/j.foodhyd.2019.02.038>
- Schwizer, W., Steingoetter, A., Fox, M., 2006. Magnetic resonance imaging for the assessment of gastrointestinal function. *Scand. J. Gastroenterol.* 41, 1245–1260. <https://doi.org/10.1080/00365520600827188>
- Sender, R., Fuchs, S., Milo, R., 2016. Revised Estimates for the Number of Human and Bacteria Cells in the Body. *PLoS Biol.* 14, 1–14. <https://doi.org/10.1371/journal.pbio.1002533>
- Sendler, M., Lerch, M.M., 2020. The Complex Role of Trypsin in Pancreatitis. *Gastroenterology* 158, 822–826. <https://doi.org/10.1053/j.gastro.2019.12.025>
- Shani-Levi, C., Alvito, P., Andrés, A., Assunção, R., Barberá, R., Blanquet-Diot, S., Bourlieu, C., Brodkorb, A., Cilla, A., Deglaire, A., Denis, S., Dupont, D., Heredia, A., Karakaya, S., Giosafatto, C.V.L., Mariniello, L., Martins, C., Ménard, O., El, S.N., Vegarud, G.E., Ulleberg, E., Lesmes, U., 2017. Extending in vitro digestion models to specific human populations: Perspectives, practical tools and bio-relevant information. *Trends Food Sci. Technol.* 60, 52–63. <https://doi.org/10.1016/j.tifs.2016.10.017>
- Sharma, S., Bhattacharya, S., 2014. Strain and strain rate dependence of gellan, agar and agar – gellan gels as model systems. *J. Food Eng.* 141, 93–98. <https://doi.org/https://doi.org/10.1016/j.jfoodeng.2014.05.001>
- Shiau, Y.Y., Peng, C.C., Hsu, C.W., 1999. Evaluation of biting performance with standardized test-foods. *J. Oral Rehabil.* 26, 447–452. <https://doi.org/10.1046/j.1365-2842.1999.00411.x>
- Shimada, A., Yamabe, Y., Torisu, T., Baad-Hansen, L., Murata, H., Svensson, P., 2012. Measurement of dynamic bite force during mastication. *J. Oral Rehabil.* 39, 349–356. <https://doi.org/10.1111/j.1365-2842.2011.02278.x>
- Simopoulos, A., 2016. An Increase in the Omega-6/Omega-3 Fatty Acid Ratio Increases the Risk for Obesity. *Nutrients* 8, 128. <https://doi.org/10.3390/nu8030128>
- Singh, H., Ye, A., Ferrua, M.J., 2015. Aspects of food structures in the digestive tract. *Curr. Opin. Food Sci.* 3, 85–93. <https://doi.org/10.1016/j.cofs.2015.06.007>
- Sinnott, M.D., Cleary, P.W., Arkwright, J.W., Dinning, P.G., 2012. Investigating the relationships between peristaltic contraction and fluid transport in the human colon using Smoothed Particle Hydrodynamics. *Comput. Biol. Med.* 42, 492–503. <https://doi.org/10.1016/j.combiomed.2012.01.002>
- Sinnott, M.D., Cleary, P.W., Harrison, S.M., 2017. Peristaltic transport of a particulate suspension in the small intestine. *Appl. Math. Model.* 44, 143–159. <https://doi.org/10.1016/j.apm.2017.01.034>
- Skamniotis, C.G., Charalambides, M.N., 2020. Development of computational design tools for characterising and modelling cutting in ultra soft solids. *Extrem. Mech. Lett.* 40, 100964. <https://doi.org/10.1016/j.eml.2020.100964>
- Skamniotis, C.G., Elliott, M., Charalambides, M.N., 2017. On modeling the large strain fracture

- behaviour of soft viscous foods. *Phys. Fluids* 29, 121610. <https://doi.org/10.1063/1.4993754>
- Skamniotis, C.G., Patel, Y., Elliott, M., Charalambides, M.N., 2018. Toughening and stiffening of starch food extrudates through the addition of cellulose fibres and minerals. *Food Hydrocoll.* 84, 515–528. <https://doi.org/10.1016/j.foodhyd.2018.06.004>
- Smeets-Peeters, M.J.E., Minekus, M., Havenaar, R., Schaafsma, G., Versteegen, M.W.A., 1999. Description of a dynamic in vitro model of the dog gastrointestinal tract and an evaluation of various transit times for protein and calcium. *ATLA Altern. to Lab. Anim.* 27, 935–949. <https://doi.org/10.1177/026119299902700608>
- Sohal, I.S., O’Fallon, K.S., Gaines, P., Demokritou, P., Bello, D., 2018. Ingested engineered nanomaterials: state of science in nanotoxicity testing and future research needs. Part. *Fibre Toxicol.* 15, 29. <https://doi.org/10.1186/s12989-018-0265-1>
- Somaratne, G., Ferrua, M.J., Ye, A., Nau, F., Flourey, J., Dupont, D., Singh, J., 2020a. Food material properties as determining factors in nutrient release during human gastric digestion: a review. *Crit. Rev. Food Sci. Nutr.* 1–17. <https://doi.org/10.1080/10408398.2019.1707770>
- Somaratne, G., Nau, F., Ferrua, M.J., Singh, J., Ye, A., Dupont, D., Singh, R.P., Flourey, J., 2020b. Characterization of egg white gel microstructure and its relationship with pepsin diffusivity. *Food Hydrocoll.* 98, 105258. <https://doi.org/10.1016/j.foodhyd.2019.105258>
- Somaratne, G., Nau, F., Ferrua, M.J., Singh, J., Ye, A., Dupont, D., Singh, R.P., Flourey, J., 2020c. In-situ disintegration of egg white gels by pepsin and kinetics of nutrient release followed by time-lapse confocal microscopy. *Food Hydrocoll.* 98, 105228. <https://doi.org/10.1016/j.foodhyd.2019.105228>
- Somaratne, G., Reis, M.M., Ferrua, M., Ye, A., Nau, F., Flourey, J., Dupont, D., Singh, R.P., Singh, J., 2019. Mapping the spatiotemporal distribution of acid and moisture in food structures during gastric juice diffusion using hyperspectral imaging. *J. Agric. Food Chem.* 67, 9399–9410. <https://doi.org/10.1021/acs.jafc.9b02430>
- Somaratne, G., Ye, A., Nau, F., Ferrua, M.J., Dupont, D., Paul Singh, R., Singh, J., 2020d. Egg white gel structure determines biochemical digestion with consequences on softening and mechanical disintegration during in vitro gastric digestion. *Food Res. Int.* 138, 109782. <https://doi.org/10.1016/j.foodres.2020.109782>
- Soyer, A., Özalp, B., Dalmiş, Ü., Bilgin, V., 2010. Effects of freezing temperature and duration of frozen storage on lipid and protein oxidation in chicken meat. *Food Chem.* 120, 1025–1030. <https://doi.org/10.1016/j.foodchem.2009.11.042>
- Speksnijder, C.M., Abbink, J.H., van der Glas, H.W., Janssen, N.G., van der Bilt, A., 2009. Mixing ability test compared with a comminution test in persons with normal and compromised masticatory performance. *Eur. J. Oral Sci.* 117, 580–586. <https://doi.org/10.1111/j.1600-0722.2009.00675.x>
- Springmann, M., Clark, M., Mason-D’Croz, D., Wiebe, K., Bodirsky, B.L., Lassaletta, L., de Vries, W., Vermeulen, S.J., Herrero, M., Carlson, K.M., Jonell, M., Troell, M., DeClerck, F., Gordon, L.J., Zurayk, R., Scarborough, P., Rayner, M., Loken, B., Fanzo, J., Godfray, H.C.J., Tilman, D., Rockström, J., Willett, W., 2018. Options for keeping the food system within environmental limits. *Nature* 562, 519–525. <https://doi.org/10.1038/s41586-018-0594-0>
- Steffe, J.F., 1996. *Rheological methods in food process engineering*. Freeman press, East Lansing.
- Stokes, D.J., Donald, A.M., 2000. In situ mechanical testing of dry and hydrated breadcrumb in the environmental scanning electron microscope (ESEM). *J. Mater. Sci.* 35, 599–607. <https://doi.org/10.1023/A:1004720209547>
- Strobel, S.A., Scher, H.B., Nitin, N., Jeoh, T., 2019. Control of physicochemical and cargo release properties of cross-linked alginate microcapsules formed by spray-drying. *J. Drug Deliv. Sci. Technol.* 49, 440–447. <https://doi.org/10.1016/j.jddst.2018.12.011>
- Strobel, S.A., Scher, H.B., Nitin, N., Jeoh, T., 2016. In situ cross-linking of alginate during spray-drying to microencapsulate lipids in powder. *Food Hydrocoll.* 58, 141–149. <https://doi.org/10.1016/j.foodhyd.2016.02.031>
- Sui, Z., Agrawal, K.R., Corke, H., Lucas, P.W., 2006. Biting efficiency in relation to incisal angulation. *Arch. Oral Biol.* 51, 491–497. <https://doi.org/10.1016/j.archoralbio.2005.11.002>

- Sun, W., Lo, C.-M., Tso, P., 2009. Intestinal Lipid Absorption, in: Textbook of Gastroenterology. Blackwell Publishing Ltd., Oxford, UK, pp. 445–463. <https://doi.org/10.1002/9781444303254.ch18>
- Swackhamer, C., Bornhorst, G.M., 2019. Fracture properties of foods: Experimental considerations and applications to mastication. *J. Food Eng.* 263, 213–226. <https://doi.org/10.1016/j.jfoodeng.2019.07.002>
- Swackhamer, C., Doan, R., Bornhorst, G.M., 2022. Development and characterization of standardized model, solid foods with varying breakdown rates during gastric digestion. *J. Food Eng.* 316, 110827. <https://doi.org/10.1016/j.jfoodeng.2021.110827>
- Swackhamer, C., Zhang, Z., Taha, A.Y., Bornhorst, G.M., 2019. Fatty acid bioaccessibility and structural breakdown from in vitro digestion of almond particles. *Food Funct.* 10, 5174–5187. <https://doi.org/10.1039/C9FO00789J>
- Swinburn, B.A., Kraak, V.I., Allender, S., Atkins, V.J., Baker, P.I., Bogard, J.R., Brinsden, H., Calvillo, A., Larijani, B., Lobstein, T., Long, M.W., Matsudo, V.K.R., Mills, S.D.H., Morgan, G., Morshed, A., Nece, P.M., Wolfenden, L., Dietz, W.H., 2019. The Global Syndemic of Obesity, Undernutrition, and Climate Change: The Lancet Commission report. *Lancet* 6736, 1–56. [https://doi.org/10.1016/S0140-6736\(18\)32822-8](https://doi.org/10.1016/S0140-6736(18)32822-8) See
- Szczesniak, A.S., 2002. Texture is a sensory property. *Food Qual. Prefer.* 13, 215–225. [https://doi.org/10.1016/S0950-3293\(01\)00039-8](https://doi.org/10.1016/S0950-3293(01)00039-8)
- Taha, A.Y., Metherel, A.H., Stark, K.D., 2012. Comparative analysis of standardised and common modifications of methods for lipid extraction for the determination of fatty acids. *Food Chem.* 134, 427–433. <https://doi.org/10.1016/j.foodchem.2012.02.087>
- Takahashi, T., Hayakawa, F., Kumagai, M., Akiyama, Y., Kohyama, K., 2009. Relations among mechanical properties, human bite parameters, and ease of chewing of solid foods with various textures. *J. Food Eng.* 95, 400–409. <https://doi.org/10.1016/j.jfoodeng.2009.05.023>
- Taniwaki, M., Kohyama, K., 2012. Mechanical and acoustic evaluation of potato chip crispness using a versatile texture analyzer. *J. Food Eng.* 112, 268–273. <https://doi.org/10.1016/j.jfoodeng.2012.05.015>
- Temenoff, J.S., Mikos, A.G., 2008. Mechanical properties of biomaterials, in: Biomaterials-The Intersection of Biology and Materials Science. Pearson Prentice Hall, New Jersey, p. 152.
- Thévenot, J., Cauty, C., Legland, D., Dupont, D., Floury, J., 2017. Pepsin diffusion in dairy gels depends on casein concentration and microstructure. *Food Chem.* 223, 54–61. <https://doi.org/10.1016/j.foodchem.2016.12.014>
- Thongkaew, C., Hinrichs, J., Gibis, M., Weiss, J., 2015. Sequential modulation of pH and ionic strength in phase separated whey protein isolate - Pectin dispersions: Effect on structural organization. *Food Hydrocoll.* 47, 21–31. <https://doi.org/10.1016/j.foodhyd.2014.11.006>
- Thuneberg, L., Peters, S., 2001. Toward a concept of stretch-coupling in smooth muscle. I. Anatomy of intestinal segmentation and sleeve contractions. *Anat. Rec.* 262, 110–124. [https://doi.org/10.1002/1097-0185\(20010101\)262:1<110::AID-AR1016>3.0.CO;2-0](https://doi.org/10.1002/1097-0185(20010101)262:1<110::AID-AR1016>3.0.CO;2-0)
- Tokoro, K., Hashimoto, T., Kobayashi, H., 2014. Development of robotic defecation simulator. *J. Robot. Mechatronics* 26, 377–387. <https://doi.org/10.20965/jrm.2014.p0377>
- Toro-Urbe, S., López-Giraldo, L.J., Alvarez-Rivera, G., Ibáñez, E., Herrero, M., 2019. Insight of Stability of Procyanidins in Free and Liposomal Form under an in Vitro Digestion Model: Study of Bioaccessibility, Kinetic Release Profile, Degradation, and Antioxidant Activity. *J. Agric. Food Chem.* 67, 1990–2003. <https://doi.org/10.1021/acs.jafc.9b00351>
- Tritsch, G.L., Sachatello, C.R., 1971. Kinetic comparison of human, canine and porcine pepsins. *Comp. Biochem. Physiol. Part B Comp. Biochem.* 39, 715–718. [https://doi.org/10.1016/0305-0491\(71\)90096-4](https://doi.org/10.1016/0305-0491(71)90096-4)
- Tsevdou, M., Gogou, E., Dermesonluoglu, E., Taoukis, P., 2015. Modelling the effect of storage temperature on the viscoelastic properties and quality of ice cream. *J. Food Eng.* 148, 35–42. <https://doi.org/10.1016/j.jfoodeng.2014.07.002>
- Turgeon, S.L., Beaulieu, M., 2001. Improvement and modification of whey protein gel texture using

- polysaccharides. *Food Hydrocoll.* 15, 583–591. [https://doi.org/10.1016/S0268-005X\(01\)00064-9](https://doi.org/10.1016/S0268-005X(01)00064-9)
- USDA Agricultural Research Service, 2019. Usual Nutrient Intake from Food and Beverages, by Gender and Age, What We Eat in America (NHANES 2013-2016).
- Valdes, A.M., Walter, J., Segal, E., Spector, T.D., 2018. Role of the gut microbiota in nutrition and health. *BMJ* 361, k2179. <https://doi.org/10.1136/bmj.k2179>
- van Aken, G.A., Bomhof, E., Zoet, F.D., Verbeek, M., Oosterveld, A., 2011. Differences in in vitro gastric behaviour between homogenized milk and emulsions stabilised by Tween 80, whey protein, or whey protein and caseinate. *Food Hydrocoll.* 25, 781–788. <https://doi.org/10.1016/j.foodhyd.2010.09.016>
- Van Der Bilt, A., 2011. Assessment of mastication with implications for oral rehabilitation: a review. *J. Oral Rehabil.* 38, 754–780. <https://doi.org/10.1111/j.1365-2842.2010.02197.x>
- van der Bilt, A., Abbink, J.H., 2017. The influence of food consistency on chewing rate and muscular work. *Arch. Oral Biol.* 83, 105–110. <https://doi.org/10.1016/j.archoralbio.2017.07.011>
- van der Linden, E., Venema, P., 2007. Self-assembly and aggregation of proteins. *Curr. Opin. Colloid Interface Sci.* 12, 158–165. <https://doi.org/10.1016/j.cocis.2007.07.010>
- Van Hecke, E., Allaf, K., Bouvier, J.M., 1998. Texture and structure of crispy-puffed food products Part II: Mechanical properties in puncture. *J. Texture Stud.* 29, 617–632. <https://doi.org/10.1111/j.1745-4603.1998.tb00189.x>
- van Vliet, T., 2014. Rheology and fracture mechanics of foods. CRC Press, Boca Raton, FL.
- van Vliet, T., Primo-Martin, C., 2011. Interplay between product characteristics, oral physiology and texture perception of cellular brittle foods. *J. Texture Stud.* 42, 82–94. <https://doi.org/10.1111/j.1745-4603.2010.00273.x>
- Van Wey, A.S., Cookson, A.L., Roy, N.C., McNabb, W.C., Soboleva, T.K., Wieliczko, R.J., Shorten, P.R., 2014. A mathematical model of the effect of pH and food matrix composition on fluid transport into foods: An application in gastric digestion and cheese brining. *Food Res. Int.* 57, 34–43. <https://doi.org/10.1016/j.foodres.2014.01.002>
- Vandenberghe, E., Charalambides, M.N., Mohammed, I.K., De Ketelaere, B., De Baerdemaeker, J., Claes, J., 2017. Determination of a critical stress and distance criterion for crack propagation in cutting models of cheese. *J. Food Eng.* 208, 1–10. <https://doi.org/10.1016/j.jfoodeng.2017.04.005>
- Vandenberghe, E., Choucharina, S., De Ketelaere, B., De Baerdemaeker, J., Claes, J., 2014. Spatial variability in fundamental material parameters of Gouda cheese. *J. Food Eng.* 131, 50–57. <https://doi.org/10.1016/j.jfoodeng.2014.01.016>
- Vardakou, M., Mercuri, A., Barker, S.A., Craig, D.Q.M., Faulks, R.M., Wickham, M.S.J., 2011. Achieving Antral Grinding Forces in Biorelevant In Vitro Models: Comparing the USP Dissolution Apparatus II and the Dynamic Gastric Model with Human In Vivo Data. *AAPS PharmSciTech* 12, 620–626. <https://doi.org/10.1208/s12249-011-9616-z>
- Vardhanabhuti, B., Cox, P.W., Norton, I.T., Foegeding, E.A., 2011. Lubricating properties of human whole saliva as affected by β -lactoglobulin. *Food Hydrocoll.* 25, 1499–1506. <https://doi.org/10.1016/j.foodhyd.2011.02.021>
- Varela, P., Salvador, A., Fiszman, S., 2009. On the assessment of fracture in brittle foods II. Biting or chewing? *Food Res. Int.* 42, 1468–1474. <https://doi.org/10.1016/j.foodres.2009.08.004>
- Varela, P., Salvador, A., Fiszman, S., 2008. On the assessment of fracture in brittle foods: The case of roasted almonds. *Food Res. Int.* 41, 544–551. <https://doi.org/10.1016/j.foodres.2008.03.009>
- Verboven, P., Defraeye, T., Datta, A.K., Nicolai, B., 2020. Digital twins of food process operations: the next step for food process models? *Curr. Opin. Food Sci.* 35, 79–87. <https://doi.org/10.1016/j.cofs.2020.03.002>
- Verkempinck, S.H.E., Salvia-Trujillo, L., Infantes Garcia, M.R., Hendrickx, M.E., Grauwet, T., 2019. From single to multiresponse modelling of food digestion kinetics: The case of lipid digestion. *J. Food Eng.* 260, 40–49. <https://doi.org/10.1016/j.jfoodeng.2019.04.018>
- Ville, E., Carrière, F., Renou, C., Laugier, R., 2002. Physiological Study of pH Stability and Sensitivity to Pepsin of Human Gastric Lipase. *Digestion* 65, 73–81. <https://doi.org/10.1159/000057708>

- Vincent, J.F.V., 2004. Application of fracture mechanics to the texture of food. *Eng. Fail. Anal.* 11, 695–704. <https://doi.org/10.1016/j.engfailanal.2003.11.003>
- Vincent, J.F.V., Jeronimidis, G., Khan, A.A., Luyten, H., 1991. The wedge fracture test a new method for measurement of food texture. *J. Texture Stud.* 22, 45–57. <https://doi.org/10.1111/j.1745-4603.1991.tb00005.x>
- Vogel, E.R., Zulfa, A., Hardus, M., Wich, S.A., Dominy, N.J., Taylor, A.B., 2014. Food mechanical properties, feeding ecology, and the mandibular morphology of wild orangutans. *J. Hum. Evol.* 75, 110–124. <https://doi.org/10.1016/j.jhevol.2014.05.007>
- Wang, J., Wu, P., Liu, M., Liao, Z., Wang, Y., Dong, Z., Chen, X.D., 2019. An advanced near real dynamic in vitro human stomach system to study gastric digestion and emptying of beef stew and cooked rice. *Food Funct.* 10, 2914–2925. <https://doi.org/10.1039/C8FO02586J>
- Wang, X., Lee, J., Wang, Y.-W., Huang, Q., 2007. Composition and Rheological Properties of β -Lactoglobulin/Pectin Coacervates: Effects of Salt Concentration and Initial Protein/Polysaccharide Ratio. *Biomacromolecules* 8, 992–997. <https://doi.org/10.1021/bm060902d>
- Wang, X.J., Camilleri, M., 2019. Personalized medicine in functional gastrointestinal disorders: Understanding pathogenesis to increase diagnostic and treatment efficacy. *World J. Gastroenterol.* 25, 1185–1196. <https://doi.org/10.3748/wjg.v25.i10.1185>
- Wang, Y.-Y., Ryu, G.-H., 2013. Physical properties of extruded corn grits with corn fibre by CO₂ injection extrusion. *J. Food Eng.* 116, 14–20. <https://doi.org/10.1016/j.jfoodeng.2012.10.041>
- Wang, Y., Brasseur, J.G., Banco, G.G., Webb, A.G., Ailiani, A.C., Neuberger, T., 2010. A multiscale lattice Boltzmann model of macro- to micro-scale transport, with applications to gut function. *Philos. Trans. R. Soc. A Math. Phys. Eng. Sci.* 368, 2863–2880. <https://doi.org/10.1098/rsta.2010.0090>
- Wang, Z., Kozu, H., Uemura, K., Kobayashi, I., Ichikawa, S., 2021. Effect of hydrogel particle mechanical properties on their disintegration behavior using a gastric digestion simulator. *Food Hydrocoll.* 110, 106166. <https://doi.org/10.1016/j.foodhyd.2020.106166>
- Welcome, M.O., 2018. *Gastrointestinal Physiology*. Springer International Publishing, Cham. <https://doi.org/10.1007/978-3-319-91056-7>
- Wien, M.A., Sabaté, J.M., Iklé, D.N., Cole, S.E., Kandeel, F.R., 2003. Almonds vs complex carbohydrates in a weight reduction program. *Int. J. Obes.* 27, 1365–1372. <https://doi.org/10.1038/sj.ijo.0802411>
- Wijaya, W., Van der Meeren, P., Patel, A.R., 2017. Cold-set gelation of whey protein isolate and low-methoxyl pectin at low pH. *Food Hydrocoll.* 65, 35–45. <https://doi.org/10.1016/j.foodhyd.2016.10.037>
- Williams, J.G., Patel, Y., 2016. Fundamentals of cutting. *Interface Focus* 6, 20150108. <https://doi.org/10.1098/rsfs.2015.0108>
- Williams, S.H., Wright, B.W., Truong, V. den, Daubert, C.R., Vinyard, C.J., 2005. Mechanical properties of foods used in experimental studies of primate masticatory function. *Am. J. Primatol.* 67, 329–346. <https://doi.org/10.1002/ajp.20189>
- Witt, T., Stokes, J.R., 2015. Physics of food structure breakdown and bolus formation during oral processing of hard and soft solids. *Curr. Opin. Food Sci.* 3, 110–117. <https://doi.org/10.1016/j.cofs.2015.06.011>
- Woda, A., Mishellany-Dutour, A., Batier, L., François, O., Meunier, J.-P., Reynaud, B., Alric, M., Peyron, M.-A., 2010. Development and validation of a mastication simulator. *J. Biomech.* 43, 1667–1673. <https://doi.org/10.1016/j.jbiomech.2010.03.002>
- Wright, N.D., Kong, F., Williams, B.S., Fortner, L., 2016. A human duodenum model (HDM) to study transport and digestion of intestinal contents. *J. Food Eng.* 171, 129–136. <https://doi.org/10.1016/j.jfoodeng.2015.10.013>
- Wright, W., Vincent, J.F.V., 1996. Herbivory and the mechanics of fracture in plants. *Biol. Rev.* 71, 401–413. <https://doi.org/10.1111/j.1469-185X.1996.tb01280.x>
- Wu, D., Lin, Q., Singh, H., Ye, A., 2020. Complexation between whey protein and octenyl succinic

- anhydride (OSA)-modified starch: Formation and characteristics of soluble complexes. *Food Res. Int.* 136, 109350. <https://doi.org/10.1016/j.foodres.2020.109350>
- Wu, K., Gunaratne, A., Collado, L.S., Corke, H., Lucas, P.W., 2015. Adhesion, Cohesion, and Friction Estimated from Combining Cutting and Peeling Test Results for Thin Noodle Sheets. *J. Food Sci.* 80, E370–E376. <https://doi.org/10.1111/1750-3841.12758>
- Wu, P., Bhattarai, R.R., Dhital, S., Deng, R., Chen, X.D., Gidley, M.J., 2017. In vitro digestion of pectin- and mango-enriched diets using a dynamic rat stomach-duodenum model. *J. Food Eng.* 202, 65–78. <https://doi.org/10.1016/j.jfoodeng.2017.01.011>
- Xu, X., 2016. On the Oral Health and Chewing Enjoyment of the Elderly: A Review from the Point of Mechanics. *J. Texture Stud.* 47, 323–341. <https://doi.org/10.1111/jtxs.12206>
- Yada, S., Lapsley, K., Huang, G., 2011. A review of composition studies of cultivated almonds: Macronutrients and micronutrients. *J. Food Compos. Anal.* 24, 469–480. <https://doi.org/10.1016/j.jfca.2011.01.007>
- Yang, P.J., Lee, A.B., Chan, M., Kowalski, M., Qiu, K., Waid, C., Cervantes, G., Magondu, B., Biagioni, M., Vogelnest, L., Martin, A., Edwards, A., Carver, S., Hu, D.L., 2021. Intestines of non-uniform stiffness mold the corners of wombat feces. *Soft Matter* 17, 475–488. <https://doi.org/10.1039/d0sm01230k>
- Ye, A., Cui, J., Dagleish, D., Singh, H., 2016. The formation and breakdown of structured clots from whole milk during gastric digestion. *Food Funct.* 7, 4259–4266. <https://doi.org/10.1039/C6FO00228E>
- Young, P.W.W., Mills, T.B.B., Norton, I.T.T., 2020. Influence of pH on fluid gels produced from egg and whey protein isolate. *Food Hydrocoll.* 111, 106108. <https://doi.org/10.1016/j.foodhyd.2020.106108>
- Yun, P., Devahastin, S., Chiewchan, N., 2021. In vitro glycemic index, physicochemical properties and sensory characteristics of white bread incorporated with resistant starch powder prepared by a novel spray-drying based method. *J. Food Eng.* 294, 110438. <https://doi.org/10.1016/j.jfoodeng.2020.110438>
- Yven, C., Guessasma, S., Chaunier, L., Della Valle, G., Salles, C., 2010. The role of mechanical properties of brittle airy foods on the masticatory performance. *J. Food Eng.* 101, 85–91. <https://doi.org/10.1016/j.jfoodeng.2010.06.012>
- Zentler-Munro, P.L., Assoufi, B.A., Balasubramanian, K., Cornell, S., Benoliel, D., Northfield, T.C., Hodson, M.E., 1992. Therapeutic Potential and Clinical Efficacy of Acid-Resistant Fungal Lipase in the Treatment of Pancreatic Steatorrhea due to Cystic Fibrosis. *Pancreas* 7, 311–319. <https://doi.org/10.1097/00006676-199205000-00007>
- Zhang, Q., Yang, W., Sun, Z., 2005. Mechanical properties of sound and fissured rice kernels and their implications for rice breakage. *J. Food Eng.* 68, 65–72. <https://doi.org/10.1016/j.jfoodeng.2004.04.042>
- Zhang, Z., Richardson, C.E., Hennebelle, M., Taha, A.Y., 2017. Validation of a One-Step Method for Extracting Fatty Acids from Salmon, Chicken and Beef Samples. *J. Food Sci.* 82, 2291–2297. <https://doi.org/10.1111/1750-3841.13850>
- Zhang, Z., Zhang, R., McClements, D.J., 2019a. Establishing the impact of food matrix effects on the bioaccessibility of nutraceuticals and pesticides using a standardized food model. *Food Funct.* 10, 1375–1385. <https://doi.org/10.1039/C8FO02368A>
- Zhang, Z., Zhang, R., Xiao, H., Bhattacharya, K., Bitounis, D., Demokritou, P., McClements, D.J., 2019b. Development of a standardized food model for studying the impact of food matrix effects on the gastrointestinal fate and toxicity of ingested nanomaterials. *NanoImpact* 13, 13–25. <https://doi.org/10.1016/j.impact.2018.11.002>
- Zheng, Z., Stanley, R., Gidley, M.J., Dhital, S., 2016. Structural properties and digestion of green banana flour as a functional ingredient in pasta. *Food Funct.* 7, 771–780. <https://doi.org/10.1039/c5fo01156f>
- Zhu, M., Xu, W., Cheng, L.K., 2017. Esophageal Peristaltic Control of a Soft-Bodied Swallowing Robot by the Central Pattern Generator. *IEEE/ASME Trans. Mechatronics* 22, 91–98. <https://doi.org/10.1109/TMECH.2016.2609465>

- Zhu, Y., Bhandari, B., Prakash, S., 2018. Tribo-rheometry behaviour and gel strength of κ -carrageenan and gelatin solutions at concentrations, pH and ionic conditions used in dairy products. *Food Hydrocoll.* 84, 292–302. <https://doi.org/10.1016/j.foodhyd.2018.06.016>
- Zink, K.D., Lieberman, D.E., Lucas, P.W., 2014. Food material properties and early hominin processing techniques. *J. Hum. Evol.* 77, 155–166. <https://doi.org/10.1016/j.jhevol.2014.06.012>